Evolution of two-layer oxide scale on the steel surface in a lead circuit during NPP operation

V.V. Alekseyev, E.A. Orlova, F.A. Kozlov, E.V. Varseyev

State Scientific Center of Russian Federation – Institute for Physics and Power Engineering (SSC IPPE), Obninsk, Russia

Abstract. The analysis of mass transfer process of corrosion products in non-isothermal loop with lead is submitted. The calculations were performed for the primary circuit of BREST-300 using a model previously proposed by us. The distributions of corrosion products fluxes along the installation hydraulic path are obtained. The mass transfer process was calculated taking into account the variable during the time the thickness of the two-layer oxide scale on the steel surface. In circuit areas with high temperature the magnetite sub-layer is absent, and in areas with low temperatures calculation showed an increasion in its thickness: at exit of the steam generator in 2 times approximatly, and at the core entrance in 5.5 times in 365 days. The Fe-Cr spinel sub-layer thickness changing with time in the circuit is positive, the rate of growth in areas with high temperature by one order of magnitude higher than in areas with low temperature. The data on the thickness change of the cladding along the core length over time are obtained.

Description of the mathematical model used to study corrosion products mass transfer in the circuit with lead was presented in [1, 2]. The case of a two-layer oxide film is observed, taking into account data [3]. The formation of the inner zone of oxidation is not considered. Depending on the local coolant conditions the upper layer which is in contact with lead, (denoted its thickness by the x_2) consists of magnetite, or absent in all. The bottom layer (thickness x_1) is thermodynamically more stable than the top layer, its composition is identified as a mixture of magnetite and double oxide $FeCr_2O_4$ and in some cases it is described by the formula $(Fe_{0,88}Cr_{0,12})_3O_4$. The last one composition of spinel is adopted in our analysis.

Additionally the diffusion layer thickness of chromium in steel wall x_{Cr} is introduced. The x_{Cr} value is proportional to the thickness of spinel sub-layer x_1, so $x_{Cr} = k_{sp} \cdot x_1$, where k_{sp} – coefficient, which depends on the stoichiometry of spinel.

The second part of model of steel corrosion products mass transfer in circuits with the lead coolant considers processes of chemical interaction of iron with oxygen in lead and transfer of products of the reaction in circuit from stainless steel. It is supposed that in liquid metal the reaction (1) between the dissolved impurity proceeds.

$$3Fe + 4PbO \Leftrightarrow Fe_3O_4 + 4Pb. \qquad (1)$$

In order to describe the transferring process the parameters that characterize concentration of reaction (1) components close to the wall surface in coolant are introduced [4].

The model takes into account that the supersaturation of impurities is removed when it is sufficient for the nucleation of a solid phase in the bulk fluid, and the resulting dispersion system is added to the already existing particles system in the coolant. Evolution of the disperse system is described by the basic kinetic equation of coagulation [4].

The solution of the obtained equations system together with the closing relations was carried out in the coordinate system related with the coolant flow. This allowed us to calculate the distribution of dissolved and suspended reaction components on the circuit length, and the output rate of iron from the steel and the formation or decomposition rate of the oxide covering and other mass transfer characteristics in the lead circuit.

Currently, there are no accurate data on the value of some physical and chemical constants characterizing the mass transfer of corrosion products in the circuits with lead.

As follows of the analysis in the previous studies [2], it is necessary to assess the value of two fundamental constants: solubility and reaction rate of formation (dissociation) of magnetite in the lead. Estimates of the approximate values of these constants were obtained in [6]. For the constant of reaction rate of magnetite formation in lead $K = 10^{59}\exp(-274200 / 8.314T)$, $1/(s\cdot(m.f.)^6)$. For the value of the magnetite saturation concentration in lead $C_S = 2\cdot10^{-11}$ m.f. (molar fraction).

The calculations with the proposed model were carried out for the primary circuit of BREST-300 setup [4]. For this purpose the hydraulic path with the bulk coolant circulation was separated on blocks, see Fig. 1 and Table 1. The primary circuit is modeled by a number of sections, which are characterized by constant geometrical and hydraulic parameters along their length. The sections are modeled as straight round channels. The estimations of the coolant passage time in each circuit section at nominal regime of reactor operation were carried out. As the calculation shows, the time for lead to pass through the whole circuit is 136.7 s.

Table 1. Times of coolant passage through different sections of BREST-300 setup

Section number	Section name	Residence time of lead in section, s	Time from start of cycle, s
1	Core 1	0.659	112.27
2	Core 2	0.679	112.50
3	Core 3	0.764	112.73
4	Upper reflector	0.857	113.59
5	Side reflector	50	117.35
6	Lifting zone	15.76	133.11
7	Steam generator inlet compartment	3.59	136.7
	Steam generator inlet		Cycle start (zero)
8	Steam generator	9.26	9.26
9	Pump suction	0.76	10.2
10	Pump pressure chamber	3.21	13.23
11	Pool	63.16	76.39
12	Sinking zone	30.59	107.34
13	Pressure chamber	3.87	111.21
14	Lower reflector	0.83	112.04

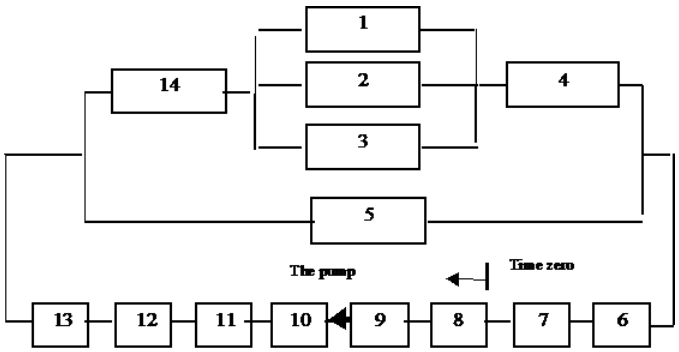

FIG. 1. The diagram of the primary circuit of the BREST-300 setup

The density of weight distribution of magnetite particles on their sizes after 200 coolant passes through the circuit is presented in Fig. 2. After a large number of coolant passes through the circuit the equilibrium disperse system with an average size of particles about 10^{-6} m is established.

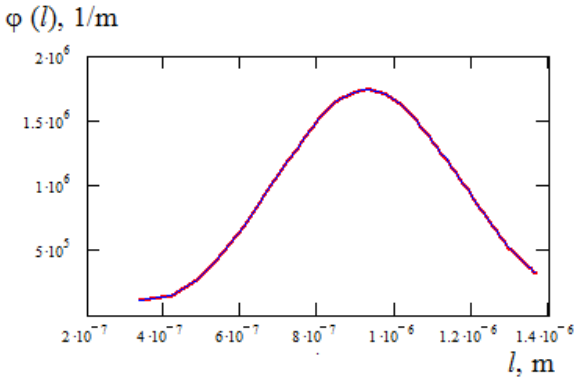

FIG. 2. The density of weight distribution of corrosion products particles on their sizes after 200 coolant passes through the circuit

The fluxes distribution along the BREST-300 primary circuit of corrosion products (dissolved and particles) deposited on the channel surface see in Fig. 3. Here time corresponds to the residence coordinate along the circuit.

Initial value of oxide film thickness on the entire surface is set to equal 10 microns. Negative flux values correspond to dissociation of magnetite. The time point of the cycle start is at the inlet of the steam generator. There takes place magnetite dissociation at the inlet of the steam generator. Along the length of the steam generator the direction of magnetite flux changes.

The flux of particles to the surface of the channels in the steam generator at the entrans has a maximum value of $2 \cdot 10^{-9}$ kg/(m^2·s) and gradually decreases to the exit to the value of 9^{-10} kg/(m^2·s). On the surface of the pool there is an accumulation of corrosion products: from the solution at a rate of 9^{-10} kg/(m^2·s) and to the particles flow around $8 \cdot 10^{-11}$ kg/(m^2·s). Fluxes of magnetite on the walls increases intensely in the channels of the core (in the figure 3 the passage of coolant of the core channels from 112.04 s to 112.73 s includes the passage of each of the three parallel sections at an appropriate scale). At the exit of the core may be a thinning of the oxide layer due to the dissociation of magnetite.

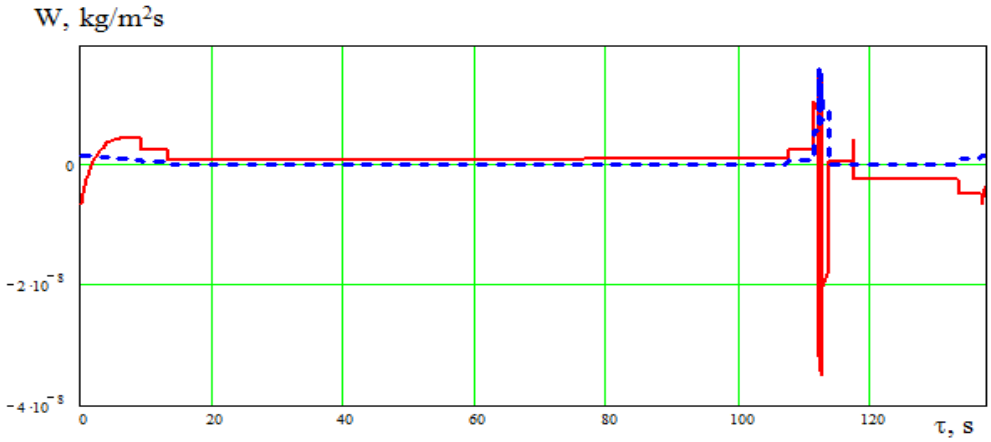

FIG. 3. The distribution of fluxes of dissolved (continuous line) and particles (dotted line) of corrosion products on length of the BREST-300 primary circuit

The calculation results of dissolved iron fluxes distribution, outgoing of steel, on hydraulic path length of the primary circuit setup BREST-300 are shown in Fig. 4. As we can see on this figure, the maximum flux of iron from steel occurs at the exit of the core channels. At the extreme point the iron flux reaches $7.5 \cdot 10^{-9}$ kg/(m^2·s), which corresponds to the thinning of the steel wall with a rate of 30 micron/year. The obtained dissolution rates are consistent with the known experimental data [5].

The dissolution rate of steel $6.5 \cdot 10^{-9}$ kg/(m^2·s) will be kept in the loop throughout the high-temperature zone (550 °C), prior to entry into steam generator. As follows from the calculation, at the most cold areas of the circuit (420 °C) the iron flux from the wall is negligible small. The iron that goes out of steel depends on thickness of oxide scale, see Fig. 5. For a long periods of installation operation a change of thickness of the oxide scale due to the mass transfer process is occurred.

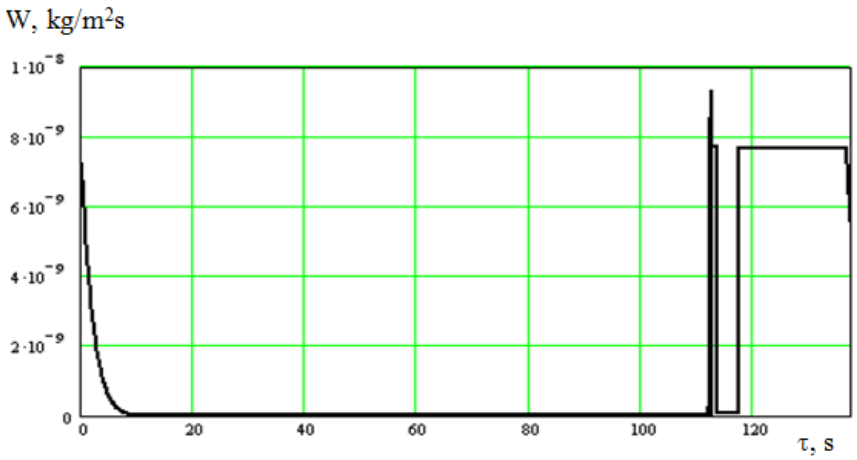

FIG. 4. The distribution of iron fluxes outgoing of steel on length of a primary circuit

When the equilibrium state of oxygen concentration in the lead is reached, it will probably increase the thickness of the oxide coating in some parts of the circuit, and in the other cases will decrease it, depending on the temperature and the flow rate of coolant. Moreover, if we consider each sub-layer of the oxide coating, their thickness can be reduced or increased separately, depending on the location in the circuit.

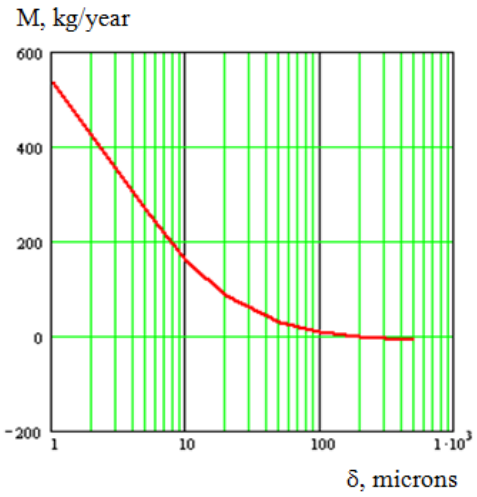

FIG. 5. The outgoing of iron from steel in BREST-300 as a function of oxide film thickness

As follows from the foregoing analysis, magnetite sub-layer dissociates in the circuit parts with high temperature, and with a certain time it disappears. Oxide layer of iron-chromium spinel the only layer that remains on the steel surface, changes in which are evaluated in our calculations. It was previously shown that iron-chromium spinel is thermodynamically stable in a wide range of oxygen concentrations in the lead and temperature [1], so we can assume that it's dissociation does not occur under these conditions. With transformation of oxide coating distribution on steel along the length of the primary circuit the whole picture of the mass transfer of corrosion products in the circuit is changed, including the distribution of iron and oxygen fluxes.

In [6] is considered the modeling of corrosion products mass transfer in the circuit for a long time of setup operation. It is assumed that at the initial time (start of operation) the oxide coating is uniformly distributed over the entire surface of the primary circuit and consists of two sub-layers: the outer layer of magnetite having 10 mkm thickness and the inner sub-layer of Fe-Cr spinel known composition having 0.1 mkm thickness. As a result of the calculations the distributions of thickness of magnetite and spinel sub-layers on the steel surface along the length of the BREST-300 circuit after 365 days from the start of operation in nominal mode are obtained, see Fig. 6. In circuit areas with high temperature (steam generator inlet pipe, outlet of the core and tracts behind core till steam generator) magnetite sub-layer is absent, and in areas with low temperature has been an increase in thickness of it: at the outlet of the steam generator is about 2 times, and at the core entrance of 5.5 times for 365 days. During 730 days magnetite sub-layer thickness increases approximately 4 and 11 times respectively. Changing the thickness of the spinel sub-layer along the length of BREST-300 circuit over time is positive, Fig. 7, and the rate of growth in the areas of circuit with high temperature about one order higher than in areas with low temperature. In 730 days from the start of the circuit operation the spinel sub-layer thickness is one and a half times higher than in 365 days.

The dissociation time of magnetite sub-layer at the core outlet is about 37 days, after which the oxide coating on this circuit part consists only of Fe-Cr spinel sub-layer, see Fig. 8.

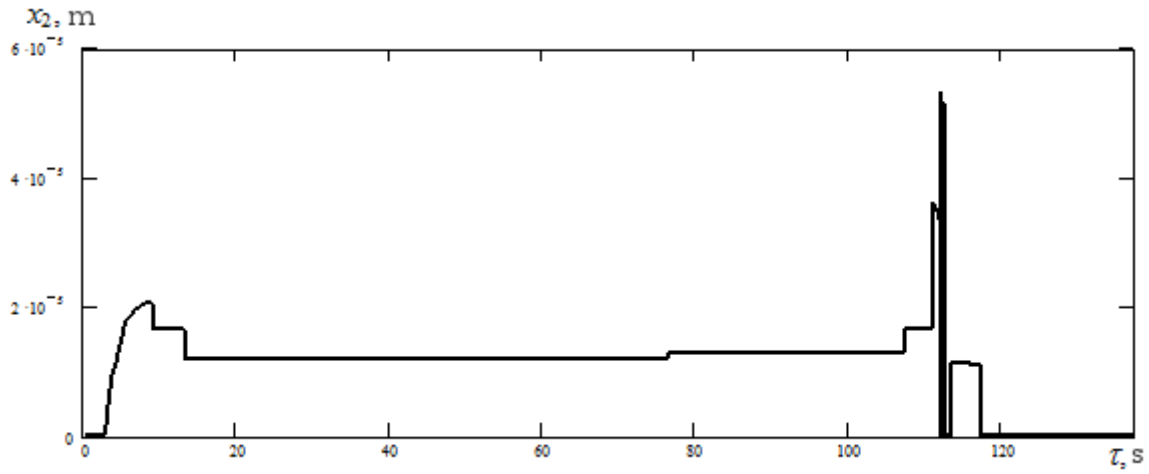

FIG. 6. Magnetite sub-layer thickness distribution along the length of the BREST-300 circuit after 365 days from the start at rated regime of operation

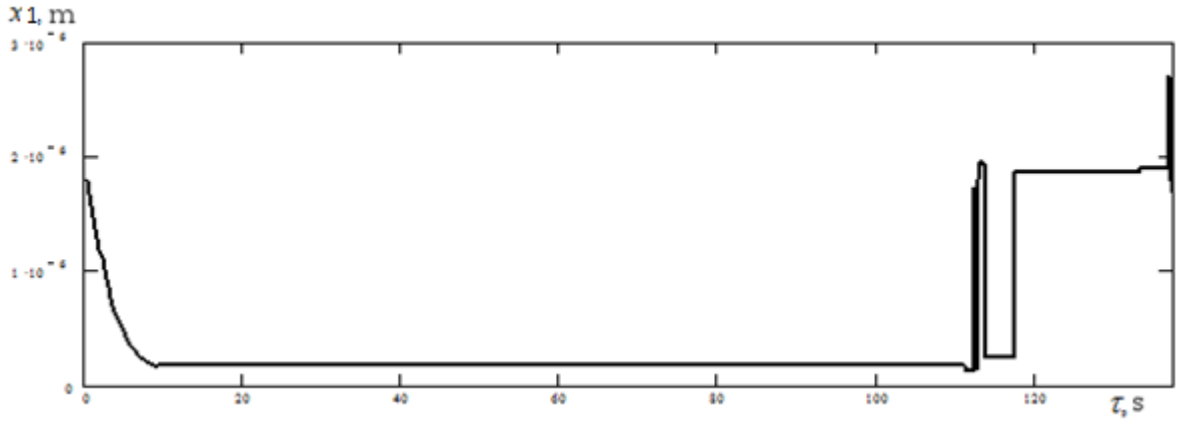

FIG. 7. Spinel sub-layer thickness distribution along the length of the BREST-300 circuit after 365 days from the start at rated regime of operation

The thickness change of magnetite sub-layer on the steel surface at the core entrance over time in relation to the conditions of the BREST-300 in Fig. 9 is submitted. As follows from the calculations, the highest growth rate of the oxide coating thickness is in the areas of circuit with the lowest temperature. The growth of magnetite sub-layer thickness on steal surface at core entrance is relatively large, it can be a reason for violations of the core thermal-hydraulic operational conditions.

The change of the thickness of Fe-Cr spinel sub-layer at the core inlet and outlet over time is calculated, see Fig. 10 and 11. This result suggests that the growth of Fe-Cr spinel sub-layer thickness is small and it not leads to violations of the core thermal-hydraulic operational conditions.

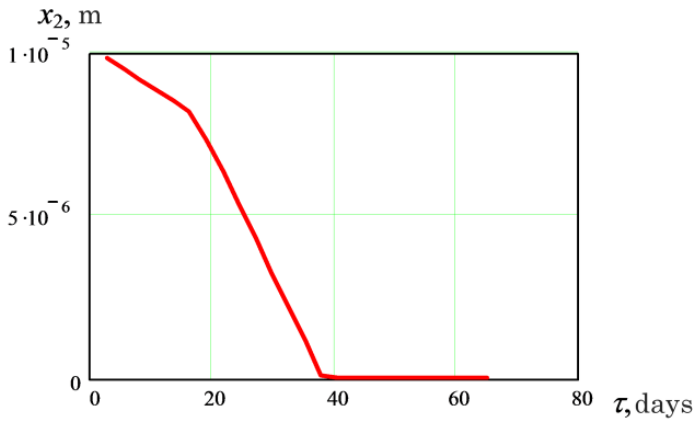

FIG. 8. Changing the thickness of the magnetite sub-layer at the core outlet

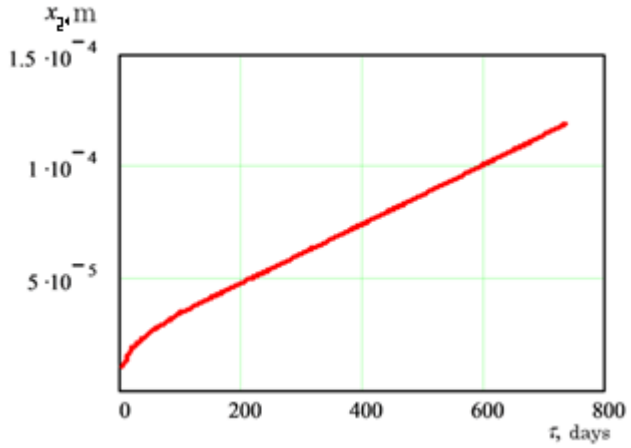

FIG. 9. Changing the thickness of the magnetite sub-layer at the core inlet

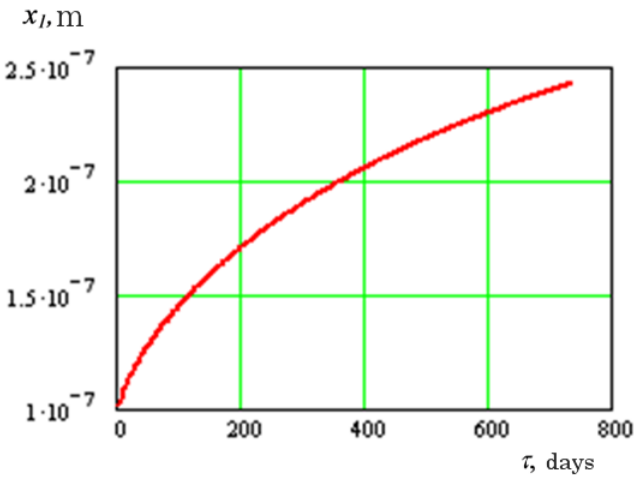

FIG. 10. Changing the thickness of the Fe-Cr spinel sub-layer at the core inlet

During reactor operation decrease of the cladding thickness will occur. Calculations in accordance with our model permit to derive a quantitative description of this process. In Fig. 12 and 13 shows the change in the thickness of the cladding at the inlet and outlet of the

core over time. During the first year of continuous reactor operation the fuel cladding at the core outlet will decrease on approximately 8 microns, which is an acceptable value.

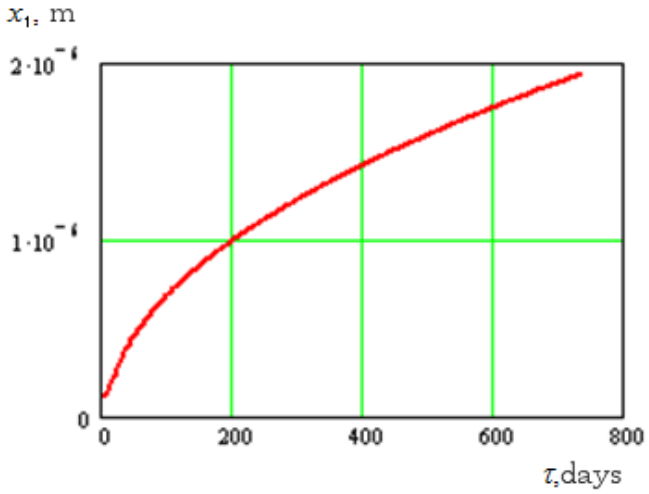

FIG. 11. Changing the thickness of the Fe-Cr spinel sub-layer at the core outlet

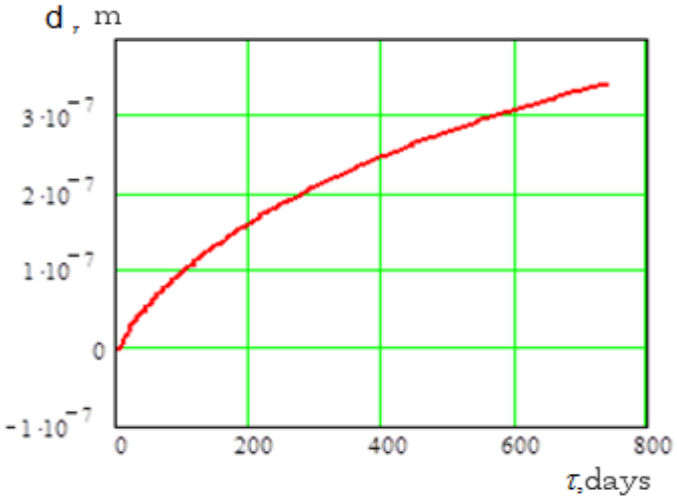

FIG. 12. Changing the thickness of the cladding (d) at the core inlet

Using the proposed model the distribution magnetite sub-layer on the core length for different times from the beginning of circuit operation was calculated, see Fig. 14. With increasing time of the plant operation the area of decayed magnetite sub-layer is shifted to the core entrance and at the same time the thickness of the magnetite sub-layer at the core inlet is increased.

As follows from the calculated data, an increasing of the time operation results in increase of Fe-Cr spinel sub-layer thickness on the entire length of the core, and at its entrance there is only a slight increase, and at the same time, at the exit there is a more significant increase.

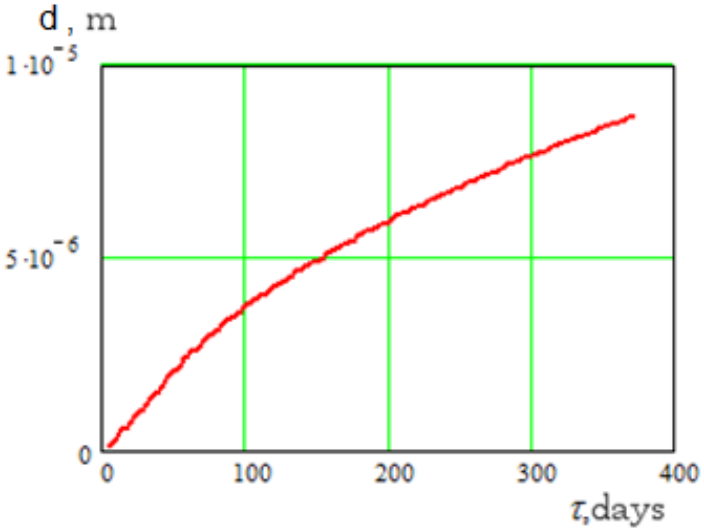

FIG. 13. Changing the thickness of the cladding (d) at the core outlet

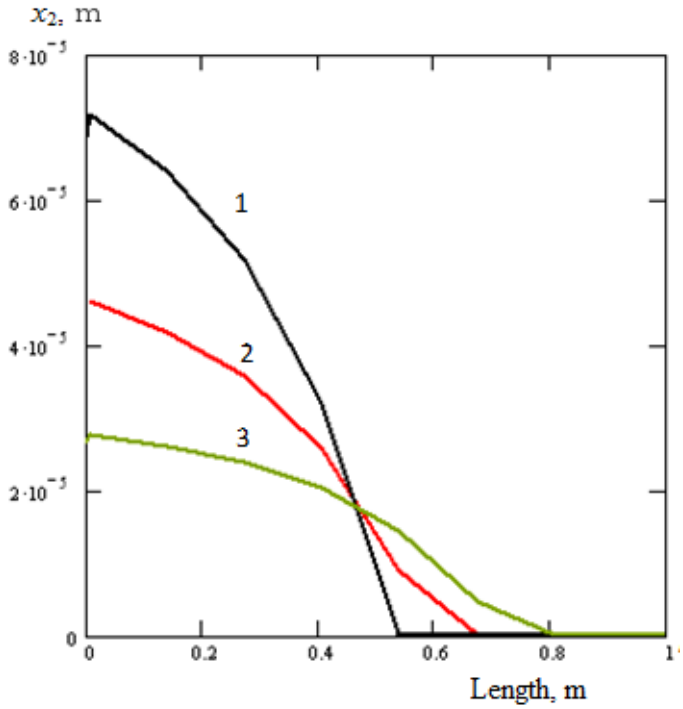

FIG. 14. Distribution of the magnetite sub-layer on the core length for different times from the start of operation: 1 – 365 days, 2 – 180 days, 3 – 60 days

ACKNOWLEDGEMENT

This work was supported by the Russian Foundation for Basic Research (grant 10-08-00524-a).

REFERENCES

[1] ALEKSEYEV V.V., ORLOVA E.A., KOZLOV F.A., TORBENKOVA I.YU., Modeling of mass transfer and corrosion of steel in nuclear power plants with lead coolant (part 1) Preprint № 3128. Obninsk: IPPE (2008) (in Russian).

[2] ALEKSEYEV V.V., ORLOVA E.A., KOZLOV F.A. et al., Modeling of mass transfer and corrosion of steel in nuclear power plants with lead coolant (Part 3: specification preliminary calculations. Developing three-dimensional model.) Preprint № 3179. Obninsk: IPPE (2010) (in Russian).

[3] MARTINELLI L., COUROUAU J-L., BALBAUD-CELERIER F., Oxidation of steels in liquid lead-bismuth: oxygen control to achieve efficient corrosion protection. 3rd Conference Heavy Liquid-Metal Coolants In Nuclear Technologies (HLMC-2008). Obninsk, Russia, September 15-19 (2008).

[4] ALEKSEYEV V.V., ORLOVA E.A., KOZLOV F.A. et al., Modeling of mass transfer and corrosion of steel in nuclear power plants with lead coolant (Part 2: Development of a one-dimensional model of mass transfer) Preprint № 3154. Obninsk: IPPE (2009) (in Russian).

[5] ABRAMOV V.Y., BOZIN S.N., EVROPIN S.V. et al., Corrosion and mechanical properties of BREST-OD-300 reactor structural materials. 11-th International conference on nuclear engineering. Tokyo, Japan, April 20-23, ICONE11-36413 (2003).

[6] ALEKSEYEV V.V., ORLOVA E.A., KOZLOV F.A. et al., Investigation of fundamental laws of mass transfer and corrosion of steel in nuclear power plants with lead coolant (Part 2: The Evolution of a two-layer oxide coating on the steel surface of the primary circuit during operation NPP) Preprint № 3209. Obninsk: IPPE (2011) (in Russian).

Inverted Steam Generators for Sodium Cooled Fast Reactors

Oldřich Matal, Tomáš Šimo, Oldřich Matal, jun.

ENERGOVÝZKUM, Ltd, Božetěchova 17, Brno, Czech Republic

Presented by Oldřich Matal

Abstract.

Inverted steam generators (ISG) are tube bundle heat exchangers with sodium flow on the inside the tubes and water and steam flow on the shell side.

Two types of inverted steam generators, one so called micro modular (MMISG) and one modular (MISG), were developed by Czech institutes in cooperation with Russian organizations and designed and manufactured by Czech organizations in the past. Both still operate successfully at BOR 60 in RIAR Dimitrovgrad, Russian Federation. The MMISG has operated since 1981 (thus 31 year of operation) and the MISG has operated since 1991 (thus 21 year of operation).

Design studies of ISG modules with 100 MW thermal power have been performed in the framework the CP European Sodium Fast Reactor (CP ESFR) project (7^{th} EUFP).
In the paper selected design parameters of Czech provenience ISGs that are in operation at the BOR 60 as well as design and safety and reliability features if the ISG 100 MW modules for CP ESFR are described and discussed.

STEAM GENERATORS OF THE CZECH PROVENIENCE

Steam generator types and design parameters

Four types of steam generators for plants with sodium cooled fast reactors were developed in cooperation with Russian (Soviet Union) organizations and Czech (Czechoslovak) organizations. These steam generators were manufactured in the Czech organizations and delivered to BOR 60 in the RIAR Dimitrovgrad (Micro Modular Steam Generator - MMSG, Micro Modular Inverted Steam Generator - MMISG and Modular Inverted Steam Generator - MISG) and to BN 350 (MMSG NADA I and NADA II) in the period of 1966 to 1992.

A summary of selected design parameters of the steam generators of the Czech provenance is shown in Table 1.

Table 1. Some design parameters of steam generators of the Czech provenance and reactor inlet/outlet sodium temperatures

Design parameters	MMSG (BOR 60)	MMISG (BOR 60)	MISG (BOR 60)	MMSG NADA I NADA II (BN350)
Thermal power, MW	30	28	26,3	200
Sodium temperature reactor outlet, °C	550	550	550	500
Sodium temperature reactor inlet, °C	340	340	340	300
Sodium temperature SG inlet, °C	565 (max)	500	505	453
Sodium temperature SG outlet, °C	320	302	309	273
Superheated steam temperature, °C	540 (max)	475	490	435
Superheated steam pressure, MPa	10	11,6	11	5
Feed water temperature, °C	215	210	210	158
Water/steam system	forced	forced	forced	natural circulation
Sodium side	shell side	in tubes (inverted)	in tubes (inverted)	shell side

Micro Modular Steam Generator (MMSG)

The MMSG operated in one of two loops of the BOR 60 experimental reactor in Dimitrovgrad, Russia, from 1973 to 1980.

The MMSG predominant design features are [1]:

- 8 branches parallel connected to the inlet and outlet sodium chambers,
- each branch consisting of 3 modules (economiser, evaporator and superheater modules),
- each module – U shaped shell tube of 159 mm O.D. with inserted tube bundle and sodium at the shell side,
- once-through design at the water/steam side,
- thermal power of 30 MW (for BOR 60 application).

MMSG safety tests were performed by artificial water/steam into sodium leaks (series of leak rates of 0,05 to 1 g/s and one steam into sodium injection of 0,17 kg/s of duration of 60 seconds) at one branch of the operating MMSG in October and November 1979. The responses of sensors and diagnostic systems based on chemical as well physical principles of actions were recorded at the same time [2][3].

After the safety testing, the MMSG was shut down, cooled and the leaked branch was cut out and corresponding pipes were plugged by covers at the MMSG side. In the time period of only two months (sodium purification, inspections etc.) the MMSG was taken into operation at BOR 60 in 1980 again to demonstrate the SG repairability and ability to operate after the large steam into sodium accident.

Micro Modular Steam Generator NADA I and NADA II

Two steam generators of the type NADA were developed and manufactured by companies in Czechoslovakia and operated at two of the five loops of the nuclear power plant BN 350 NADA I was taken in operation in May 1980 and NADA II in June 1982 [4].

The BN 350 was configurated into loops and operated to provide electricity and to desalinate the seawater.

SG NADA design features include:

- each SG consisted of branches and the steam drum,
- each branch consisted of two modules (one was the evaporator and one was the superheater),
- each module – U shaped shell tube with inserted tube bundle and sodium at the shell side,
- natural circulation of the water/steam in the system steam drum and evaporator modules,
- SG unit thermal power of 200 MW (for BN 350 application).

Some design parameters of the SG NADA are in Table 1.

The schematic disgram of NADA steam generators is in Fig. 1

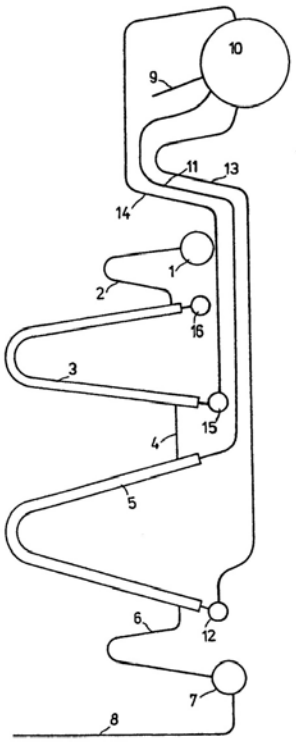

1 – Na inlet chamber
2 – Na pipe
3 – superheater module
4 – Na pipe
5 – evaporator module
6 – Na outlet pipe
7 – Na outlet chamber
8 – Na pipe into buffer tank
9 – feed water inlet
10 – steam drum
11 – rising pipe
12 – water chamber
13 – water supply pipe
14 – saturated steam pipe
15 – inlet steam chamber into the superheater
16 – superteated steam outlet chamber

FIG. 1. Schematic diagram of the NADA steam generators with natural water/steam circulation

Micro Modular Inverted Steam Generator (MMISG)

The MMISG was developed in cooperation with Czech and Russian organizations and manufactured by companies from the Czech Republic [5][6][7][8].

The MMISG has been in operation at one of the two loops of the BOR 60 reactor facility since September 1981 with no water into sodium leaks.

MMISG design features include:

- 8 branches connected in parallel to the inlet and outlet sodium chambers,
- SIGMA shaped branch,
- each branch consists of 3 modules (economiser, evaporator and superheater modules),
- module - shell tube O.D. of 194 mm and tube bundle of 19 tubes,

- once - through design at the water/steam side,
- sodium in tubes concept – a basis of the inherent steam generator safety if a water/steam leak into sodium should occur,
- thermal power of 28 MW (for BOR 60 application).

Some design parameters of the MMISG are in Table 1.
Micro Modular Inverted Steam Generator front view is schematically in Fig. 2.

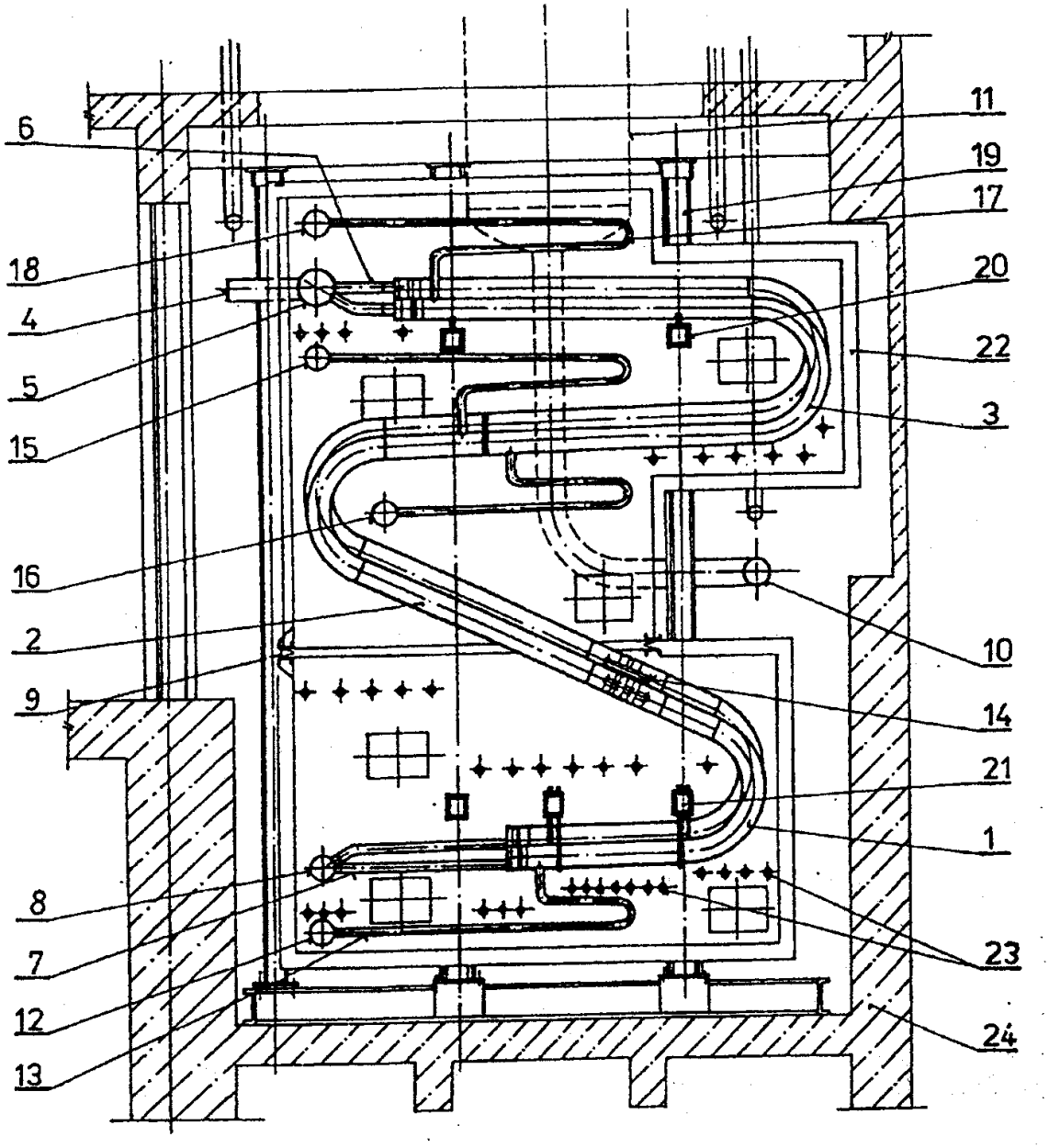

1, 2, 3 – economiser, evaporator and superheater moduls
4 – sodium inlet pipe
5 – sodium chamber
6 – sodium inlet pipes into a branch
7 – sodium outlet pipes
8 - sodium outlet chamber
9 – N/A
10 – sodium pipe (SG – buffer tank)
11 – buffer tank
12 – feed water chamber
13 – feed water pipes to branches
14 – connecting pipes
15 – steam chamber (evaporator outlet)
16 – steam chamber (separator outlet)
17 – steam outlet (from branch)
18 – steam outlet chamber (superheated steam)
19, 20, 21 – support structure
22 – isolation box
23 – electic heaters
24 – SG concrete cell

FIG. 2. Micro Modular Steam Generator front view

Modular Inverted Steam Generator (MISG)

The MISG technology was developed and manufactured by companies from the Czech Republic [8]. The MISG has been in operation at one of the two loops of the BOR 60 reactor facility since March 1991 with no water into sodium leak.
MISG design features include:

- one module SG design,
- banana shaped vertical oriented module,
- module - shell tube O.D. of 521 mm and tube bundle of 246 tubes,
- once - through design at the water/steam side,
- sodium in tubes concept – a basis of the SG inherent safety,
- thermal power of 26,3 MW (for BOR 60 application).

Some design parameters of the MISG are in Table 1.

INVERTED STEAM GENERATOR SAFETY BENEFITS

There are some specific design features of an inverted steam generator that positively contribute to its inherent safety, namely:

Overpressure at the outer surface of tubes in the ISG mitigates or eliminates potential crack growth in the tube walls.

Cross section of the one tube at the sodium side in the ISG is considerably smaller that the cross section at the shell side with sodium of the traditional steam generator. Consequently, in case of even small water into sodium leak flow regime of displacement can start and (a) the liquid sodium does not flow in the leaked tube and (b) the heated tube is filled by the gas and (c) no wastage of the target tube wall to the leak location can occur.

Crystallization of products of the water - sodium reaction, namely of NaOH, on the tube wall at the temperatures below 350 °C is a phenomenon that can lead to a self blockade of the sodium flow into the tube with the leaked wall [9].

Many parallel channels (parallel tubes in the tube bundle) to the leaked tube at the sodium side in the ISG module are available and only a redistribution of sodium flow inside the tubes of the module bundle is a consequence of many of water into sodium situations.

All these above mentioned items that have an inherent safety character are reasons, why there are substantial positive safety differences in an ISG in comparison to a traditional SG design in water into sodium leak situations.

STUDIES ON ISG MODULE SELECTION FOR ESFR

Module design selection criteria

In the framework of the European Sodium Fast Reactor project [10] studies on heat transfer and optimization of inverted steam generator (ISG) modules were performed. To evaluate results, selected criteria were used, namely predesign criteria, like tube bundle length, inner diameter (I.D.) of the module shell tube, mean heat flux at the tube bundle, tube bundle mass to module thermal power ratio, and safety criteria like resistance to water/steam into sodium leaks and ISG response to water sodium reaction etc.

A brief summary of study results

Tube bundle length limits

The tube bundle length is limited by the tube manufacturer´s technological limits, steam generator box dimensions and the goal to avoid tube to tube welds in the heat transfer area.

Module shell tube I.D. or O.D.

Module shell tube I.D. or/and O.D. is strongly influenced by the manufacturer´s technological limits and steam generator box dimensions. Module shell tube I.D. decreases when the bundle length increase.

Dependence of the tube bundle length on module shell I.D. for one ISG module of 100 MW thermal power and CP ESFR media parameters and two types of tube materials is shown in Fig. 3.

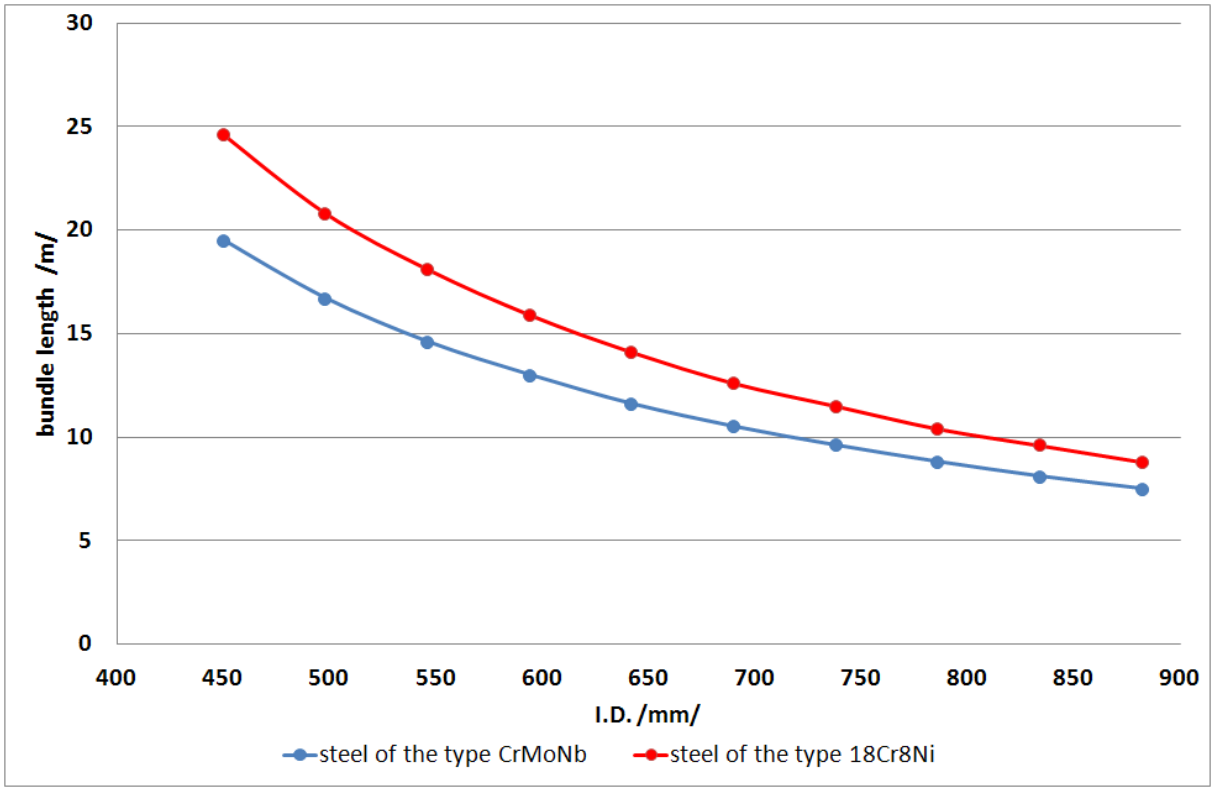

FIG. 3. Dependence of tube bundle length on module shell I.D.

Tube bundle length is increasing with decreasing diameter of the module shell tube. Our results of studies indicate that long and slim ISG modules promise an acceptable mass to thermal power ratio.

Mean heat flux at the tube bundle

Heat flux at the tube bundle influences the ISG modules long term operational availability, design life time as well as hydrodynamic stability of the H_2O module side. The mean heat flux increases with the increase in tube bundle length.

Pressure losses at the sodium side

Pressure losses at the ISG module sodium side contribute to the sodium loop total pressure losses and play an important role in the inherent safety considerations in the case of water into sodium leaks. The pressure losses at the sodium side increase with the increase in tube bundle length.

ISG mass and thermal power ratio

ISG mass and thermal power ratio values characterize investment costs and module dimensions and are strongly influenced by available ISG box dimensions and decay heat removal requirements. In general the ISG mass to thermal power ratio values are decreasing with the increase in tube bundle length.

ISG MODULE CANDIDATES FOR ESFR

Based on preliminary ESFR design data [10] with reactor heat output of 3600 MW and six secondary sodium loops each of the thermal power of 600 MW, the following IHX and ISG design parameters were considered, Table 2.

Table 2. ISG module design parameters

Parameter	Dimension	Value
ISG module thermal power	MW	100
Sodium temperature - IHX inlet - IHX outlet	°C	 525 340
ISG outlet superheated steam - temperature - pressure	 °C MPa	 490 18,5

Keeping in mind the successful design concept of the MISG being still in operation at BOR 60 since 1991 and having the aim of a cost most interesting as well as safety most interesting feasible steam generator design preliminary two ISG module candidates for ESFR has been considered, Table 3.

Table 3. 100 MW ISG module candidates for the ESFR application

Item	Dimension	ISG module	
		Option 1	Option 2
ISG module thermal power	MW	100	100
Module O.D.	mm	850	720
Number of tubes in bundle	1	593	520
Length of the tube bundle	m	11,2	12,5
Mean heat flux	kW/m^2	285	325
Estimated pressure drop at the sodium side	MPa	0,21	0,52
Expected module mass to thermal power ratio, approximately	kg/MW	250	210
Module shape and orientation	1	banana shaped, vertical orientation	banana shaped, vertical orientation

The option 2 provides estimated total pressure drop at the ISG module sodium side of 0,52 MPa, which seems too be to high in practice. Nevertheless, the comparison of pressure drop values at the sodium side of both options demonstrates the tendencies that decreasing module mass to thermal power ratios (decreasing investment costs) are paid by increasing module pressure losses, module length and as well as increasing mean heat fluxes at the tube bundle.

A comparison of needed space and ground plan area for ISGs of 100 MW thermal power that would use micro-modules of the O.D. 194 mm (same as used at the micro modular inverse steam generator – MMISG), modules of the O.D. 521 mm (same as used at the modular inverse steam generator – MISG) and one module concept with the shell tube of O.D. 850 mm is in the Table 4.

Table 4. Comparison of estimated space and ground plan area needed for a SG of 100 MW thermal power in the three variants of inverse steam generators (ISG)

ISG type	Module O.D. [mm]	Number of needed modules	Space (approx.) [m^3]	Ground plan area (approx)[m^2]
MMISG	194	28	140	26
MISG	521	4	115	12
ISG one module	850	1	55	5

INDUSTRIAL DEVELOPMENT OF MATERIAL AND TECHNOLOGY FOR STEAM GENERATOR COMPONENTS IN THE CZECH REPUBLIC

Development of material and technology for SFR steam generator components was performed in the framework of the research and development project of the same name initiated by ENERGOVYZKUM and supported by the Ministry of Industry and Trade [11][12]. The production of the steel of the type CrMoNb with very high purity (B factor smaller then 8) and forging, heat treatment, welding and machining technologies were verified in the Czech Republic industrial conditions in years 2003 and 2004. Manufacturing of tubes of 10 mm, 20 mm and 22 mm O.D. (heat exchanging tubes for liquid sodium heated steam generators) was verified in industrial conditions too.

Realization of an industrial steel melt

The realization of a steel melt of the CrMoNb type steel in the industrial conditions was performed in four steps:

- metal charge and direct reduced iron process
- hot melt processed in an electric arc furnace
- vacuum processed steel
- pot furnace and ingot mould

Realization of forged ISG components

This was proven in three steps:

- ingot long term homogenization in preheating furnace
- forming process
- component semi-products

Fabrication of heat exchanging tubes

Fabrication of heat exchanging tubes for ISG applications was carried out also in industrial conditions in four steps:

- tube rolling and piercing process
- tube drawing process
- tube inspections and testing
- verification of tube material and mechanical properties (R_m, $R_{p0,2}$, A5, …)

CONCLUSIONS

Two inverted steam generators of the Czech industry provenance have still been in successful operation with no water into sodium leaks at BOR 60 (RIAR Dimitrovgrad, Russian Federation). Micromodular inverted steam generator (MMISG) since 1981 and modular inverted steam generator (MISG) since 1991.

In the framework of the CP ESFR project, predesign studies of 100 MW (thermal) ISG modules were performed with the consideration of MMISG and MISG design, operational and safety benefits and experience.

Development of material and technology for sodium heated steam generators components reflecting contemporary domestic industrial conditions in the Czech Republic was restarted in the years 2003 to 2004 and supported in the years 2008 to 2011 by the European CP ESFR project and by the Ministry of Industry and Trade of the Czech Republic.

ACKNOWLEDGEMENTS

The authors acknowledge the Ministry of Industry and Trade of the Czech Republic for the financial support of the projects registration number 2A-1TP1/067 and FD-K3/078 as well as European Commission for the financial support of the CP ESFR project.

REFERENCES

[1] Dubšek, F., Jaderná energie 22 (1976), Nr. 8, p. 283.
[2] Matal, O. et al., Jaderná energie 29 (1983), Nr. 5, p. 193.
[3] Matal, O. at al., Jaderná energie 30 (1984), Nr. 4, p. 143.
[4] Dubšek, F. at al., Strojírenství 33 (1983), Nr. 6/7, p. 394.
[5] Matal, O., Korolkov, A. S., Thirty years of operation of the BOR 60 reactor facility, Energetika 50 (2000), Nr. 11, pages 376-378, ISSN 0375-8842.
[6] Matal, O. et al., Thermal and hydraulic characteristics of the second Czechoslovak experimental steam generator 30 MW heated by liquid sodium, Jaderná energie 33 (1987), No. 1, p. 21.
[7] Matal, O. et al., Operating experience with the second Czechoslovak 30 MW steam generator and concept of steam generators with double-wall heat exchangers tube, IAEA-SM-28437,In. Proceedings of an Int. Symp. on Fast Breeder Reactors: Experience and Future Trends, IAEA Vienna, 1986.
[8] Fast reactor steam generators with sodium on the tube side, IAEA-TEC-DOC-730, IAEA, January, 1994.
[9] Srojelov, V.S. et al., Atomnaja energija, T. 63, 1987.
[10] Fiorini, G. L. et al., The collaborative project on European sodium fast reactor (CP ESFR project), In: FISA 2009, 7th European Commission Conference on Euratom research and training in reactor systems, 22 - 24 June 2009, Prague, ISBN 13-978-92-79-13302-2.
[11] Steam generator material and component technology development, National project registration number FD-K3/078, supported by the Ministry of Industry and Trade of the Czech Republic, 2003-2004.
[12] Research into high - potential heat transfer technologies from a nuclear source, National project supported by the Ministry of Industry and Trade of the Czech Republic (CR), Project registration number 2A-1TP1/067, 2008 - 2011.

Study on Chemical Reactivity Suppression and Coolant Applicability of Sodium with Suspended Nanoparticles

Jun-ichi SAITO[a], Naoki YOSHIOKA[b], Masahiko NAGAI[c], Kuniaki ARA[a]

[a] Japan Atomic Energy Agency, Ibaraki, JAPAN

[b] Mitsubishi FBR Systems, Inc., Tokyo, JAPAN

[c] Mitsubishi Heavy Industries, Ltd., Nagasaki, JAPAN

Presented by Jun-ichi SAITO

Abstract

Liquid sodium is used as a coolant for fast breeder reactors because of its superior heat-transfer property, low neutron absorption property and wide liquid phase temperature region. The purpose of this study is to suppress the chemical reactivity of liquid sodium using nanotechnology. An atomic interaction between nanoparticle and sodium atom is applied to suppress the chemical reactivity of liquid sodium. The fundamental properties of surface tension and evaporation rate which relate to the reaction were changed by suspension of nanoparticles. By these changes the reaction heat and reaction rate with water or oxygen of sodium with suspended nanoparticles were suppressed. The thermal property and fluidity of sodium with suspended nanoparticles were same as sodium, because the nanoparticles in liquid sodium are quite small (nano-meter size) and small amount. From these results, it was found that the chemical reactivity was suppressed by suspension of nanoparticles, keeping the superior coolant properties of liquid sodium.

1. Introduction

Liquid sodium as a coolant for fast breeder reactor (FBR) has superior heat-transfer characteristics and compatibility with structural material. However, it exhibits a high chemical reactivity with oxygen and water. The amount of released heat by reaction is large and the reaction rate is extremely rapid, which are caused by accidents of sodium fire and sodium-water reaction. The severe reaction behavior may affect the safety and maintenance of the FBR plant. Today's development of a commercial FBR concept is pursued based on safety facilities and component design. If the high chemical reactivity of sodium can be suppressed by new technology, an innovative concept for the FBR plant which possesses higher safety and economic potential will be proposed.

The concept of suspended nanoparticles in liquid sodium has been studied to identify the possibility to suppress the chemical reactivity of the sodium itself using the atomic interaction between sodium and nanoparticles.

Sodium coolant utilized in FBRs is required to possess chemical reactivity suppression and maintain excellent thermal hydraulics property. In order to suppress the chemical reactivity of sodium, nanoparticles are suspended in liquid sodium. We can reduce the amount of nanoparticles by decreasing the diameter of the nanoparticle and enlarging the specific surface area to manage both the reaction suppression and the superior thermal hydraulics property.

The purpose of this study is to suppress the chemical reactivity of sodium itself based on nanotechnology. Furthermore, safety and economic efficiency of FBR are enhanced by suppressing the reactivity suppression of sodium itself. Flexibility in the plant design increases and a new concept of the FBR plant will be created. This study is to research the possibility of overcoming sodium's chemical reactivity by using innovative technology.

We have been studying the chemical reactivity suppression by suspended nanoparticles. In this paper, we summarize the previous research[1-3]. Additionally the effect of chemical reactivity suppression on plant design is described.

2. Idea of Chemical Reactivity Suppression by Nanoparticles

An image of the suspension of nanoparticles in liquid sodium is shown in Fig.1(a). According to theoretical calculations, it is clear that the atomic bonding between nanoparticles and sodium atoms is twice that of sodium atoms as exlained later. It seems that the nanoparticle forms a cluster with the surrounding sodium atoms. In other words, the nanoparticle catches the surrounding sodium atoms via atomic bonding. Furthermore, charge transfer takes place from the surrounding sodium atoms to the nanoparticle. This means that the surface of the nanoparticle becomes positively charged and that the nanoparticles repulse each other. Hence, it is expected that the clusters are suspended in liquid sodium.

An image of the reaction between sodium with suspended nanoparticles and water is shown in Fig.1(b). There are many free sodium atoms which do not interact with the nanoparticles. The free sodium atoms react readily with water. On the other hand, the sodium atoms captured with the nanoparticle react later than the free sodium atoms because the captured sodium atoms must break the strong atomic bond in order to react with water. Excess energy and extra time are necessary for the reaction with water. Hence, it is thought that the chemical reactivity of sodium with suspended nanoparticles is suppressed.

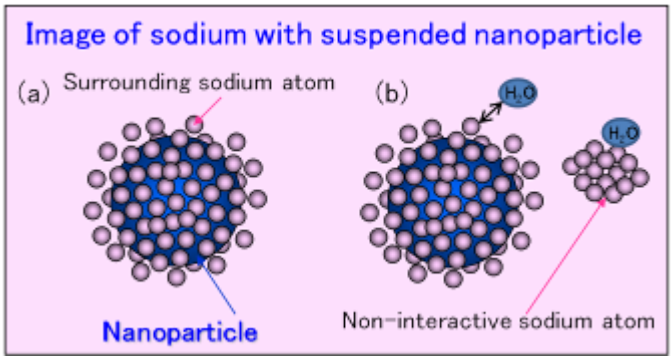

Fig. 1 Image of chemical reactivity of sodium dispersing nanoparticles

The specific surface of the nanoparticle becomes larger by the minimization of its diameter. The effect of reducing reactivity is proportional to the area of the contact surface between the nanoparticle and the

sodium. Therefore, the specific surface is enhanced by decreasing the diameter of the nanoparticle and even a small amount of nanoparticles can obtain a larger effect. For this reason the superior thermal hydraulics of sodium will be kept. The feature of this idea is to satisfy both the chemical reactivity suppression and thermal hydraulics at the same time. Hereafter, we call sodium suspended with nanoparticles, “sodium nanofluid”.

3. Verification of Idea and Chemical Reactivity Suppression

When nanoparticles disperse into liquid sodium, an atomic interaction between the nanoparticles and the sodium occurs. However, the state of atomic interaction is not clear. In this chapter, we estimate the atomic bond and charge state by theoretical calculations. The chemical reaction properties which relate to the atomic bond of the sodium nanofluid are measured in comparison with sodium.

(1) Atomic Interaction between Nanoparticle and sodium

The atomic interaction of a pair of sodium atoms was calculated using the two atoms model which substitutes a sodium atom for the metal element (constituting nanoparticle) of the two atoms model. The atomic interaction was calculated using density functional theory (B3LYP)[4-6]. The basic function used was LanL2D (Los Alamos ECP+DZ). Transition elements were selected for candidate metals because they have a large difference in electronegativity compared with sodium which leads to significant atomic interaction, and because they possess the low density and the low solubility in liquid sodium. The requirements for the FBR coolant are large heat capacity and low density from the viewpoint of heat transport and low solubility in liquid sodium from the viewpoint of compatibility with structural materials. Also the large difference of electronegativity is required from the viewpoint of strong atomic interaction between nanoparticle and sodium.

(a) Atomic Bond

An atomic bond between the sodium and the nanoparticle metal atom is shown in Fig.2. The atomic bond between sodium atoms was approximately 0.5eV, as shown by the broken line in Fig.3. The atomic bond between the sodium atom and transition metal, except for chromium and manganese, is more than two times larger than that between sodium atoms. The atomic bond between sodium and manganese is the smallest among them. Because five electrons occupy the d-orbital, the atomic bond is not formed. It became clear that the atomic bond between sodium and transition metal is significantly larger than that between sodium atoms. This means that the nanoparticle bonds strongly interact with the surrounding sodium atoms. And it is expected that the nanoparticle and sodium atoms form a cluster.

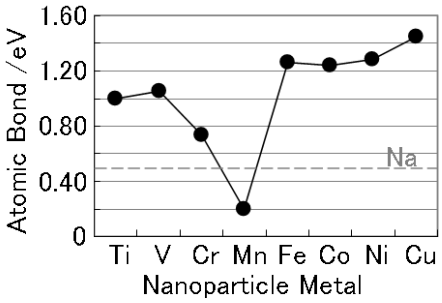

Fig. 2 Atomic bond between the sodium and the nanoparticle metal atom

(b) Charge state

The charge transfer of the nanoparticle metal atom is shown in Fig.3**.** The minus value of the vertical axis denotes charge transfer to the nanoparticle atom from the sodium atom. For example, approximately 0.23 electrons transfer to titanium from sodium. This means that titanium nanoparticles absorb electrons from surrounding sodium atoms. This charge state is due to the difference in electronegativity between sodium and transition element.

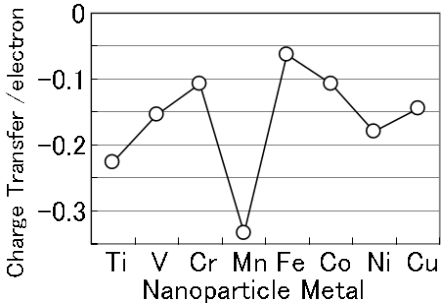

Fig. 3 Charge transfer of the nanoparticle metal atom

It is inferred that an uneven distribution of electrons between sodium and the nanoparticle of the formed cluster occurs. The sodium located at the external surface of the cluster becomes positive charge and a repulsive force develops between clusters. It is expected that the clusters suspend stably in liquid sodium, and it is suggested that the charge state contributes to the suspension of nanoparticles in liquid sodium.

It became clear that the atomic bond between sodium and the nanoparticle is larger than that between sodium atoms. This means that the strong atomic bond is obtained by the selection of the nanoparticle element. The strength of the atomic bond between sodium and the nanoparticle atom does not change irrespective of the number of nanoparticle atoms or sodium atoms. Because the atomic bond increased more than two times, there is a possibility of change in the properties that relate to the atomic bond. Therefore, in order to verify the inferred atomic interaction, we investigate the properties of the sodium nanofluid.

(2) Reaction Properties of Sodium Nanofluid and Effect on Plant Design

(a) Oxdation Reaction

The released reaction heat of the sample during reaction with oxygen was estimated by the following procedure. The integrated quantity of released heat received by the insulated steel vessel from the reaction was calculated from the heat capacity and temperature trend of the vessel wall as shown in Fig. 4. The weight of the sodium in the sample was normalized in the same way as in the case of reaction with water. The time trend of the integrated heat is shown in Fig. 5. A significant suppression was also confirmed in the oxidation reaction.

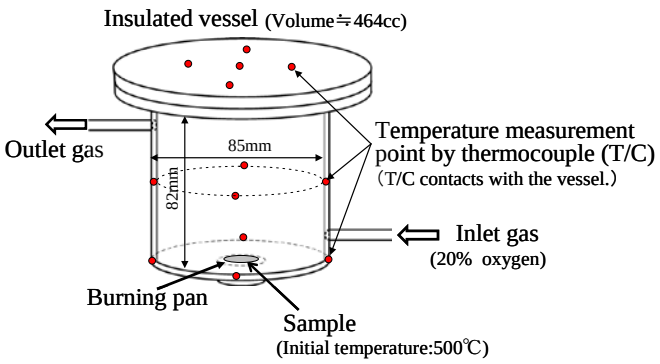

Fig. 4 Schematic diagram of experimental apparatus for measuring the released

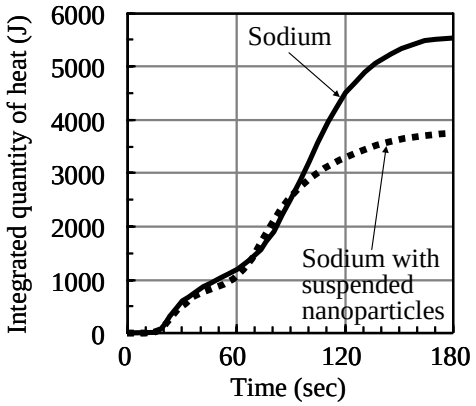

Fig. 5 Released reaction heat about reaction with oxygen

The residual reaction products were identified by X-ray diffraction. And it was confirmed that they included nanoparticles. Even if there is a possibility that nanoparticles react directly with sodium, since the released reaction heat of the nanoparticle-sodium reaction is larger than that of sodium, suppression of the chemical reactivity is certain. Also the influence of impurity elements such as oxygen and hydrogen on suppression is considered possible. Therefore, the released reaction heat of sodium nanofluid including impurity elements was measured and it was verified from the reduction rate of released reaction heat that there was no significant influence of impurity elements on reaction suppression.

Furthermore, in order to confirm the change of reaction rate, which has a close relation with the evaporation rate, the apparatus was used. We measured the weight of sample during reaction. In Fig. 6, the x-axis is time from the start of oxygen supply and the y-axis is the weight of the sample. As the reaction products are released from this apparatus during the reaction, the weight of the sample decreases. Therefore, the slope of the line shows the reaction rate. During the surface reaction at the first stage of reaction, the difference in the rate of reduction of the sample weight between sodium and sodium nanofluid was very small. In the gas phase reaction, the rate of decrease of the sample weight became large. As a result, the difference between sodium and sodium nanofluid was identified. Suppression of the rate of reaction of the sodium nanofluid was confirmed from the inclination of decreasing weight.

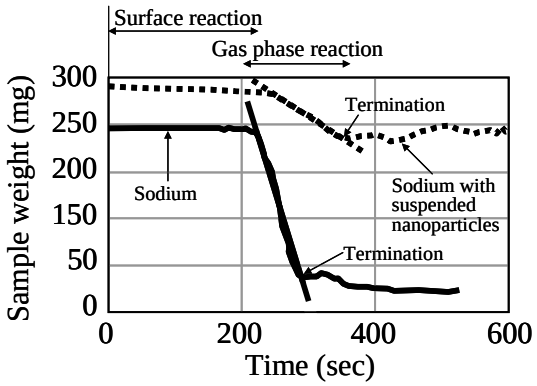

Fig. 6 Rate of reaction for reaction with oxygen 20%O_2

The released reaction heat (temperature) and reaction progress phenomenon (reactive continuity) were investugated, respectively. The time trend of sodium sample temperature is shown in Fig. 7. Comparison of maximum temperature showed that sodium nanofluis did not reach 600℃ while sodium exceeded 800℃. From the difference of temperature the decrease of the pool temperature was verified.

The pool temperature is a result of the balance of released heat and cooling by blowing gas. Since the cooling condition is the same, this means that the released reaction heat is reduced.

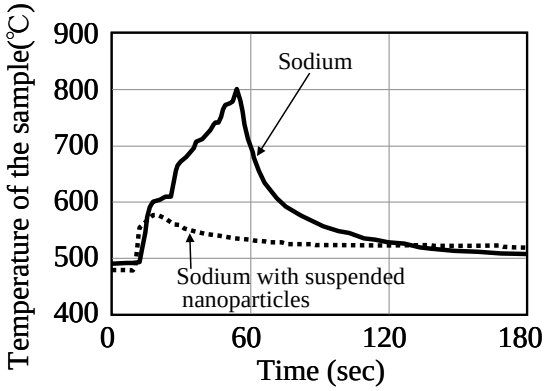

Fig. 7 Temperature of the pool 20%O_2

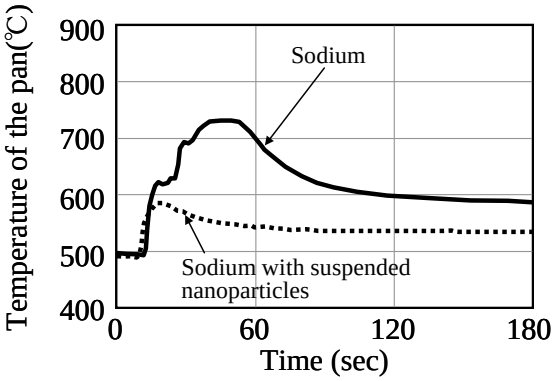

Fig. 8 Temperature of the steel pan under the pool 20%O_2

It is expected that the thermal load to the combustion pan can be decreased by the reduction of pool temperature. The resulting comparison of pan temperature is shown in Fig. 8. The temperature of the sodium nanofluid did not reach 600℃ while that of sodium exceeded 700℃. From the viewpoint of the mechanical strength of steels in, for example, the floor structure, this means that there is a significant difference in safety allowance. In the FBR plant, it contributes to the improvement of sodium fire countermeasures.

The time transition of the reaction interface in the pool combustion is shown in Fig. 9. Initially, there is no difference in shape or size between sodium and the sodium nanofluid. The difference appeared as the reaction progressed. In the case of sodium, the reaction products grow as many projections which appeared one after another on the reaction surface and are piled on top of one another; however, the projection of the sodium nanofluid is small and the products are not piled on top of one another. The reaction products of sodium grow in the direction of supplied oxygen; however, this is not observed in the case of the sodium nanofluid. Therefore, the growth of reaction products was clearly suppressed and the mitigation of reaction was verified.

Observed in detail, it seems to come to the end of reaction earlier in the sodium nanofluid. Therefore, the remaining sample in the combustion pan was analyzed to identify the unreacted sodium by amalgam method after the reaction test. It was confirmed that the entire sample had reacted with oxygen in the sodium sample; however, approximately 21 % unreacted metal sodium remained in the sodium nanofluid. There is a possibility that the reaction will stop with non-reacted sodium left in the sodium nanofluid.

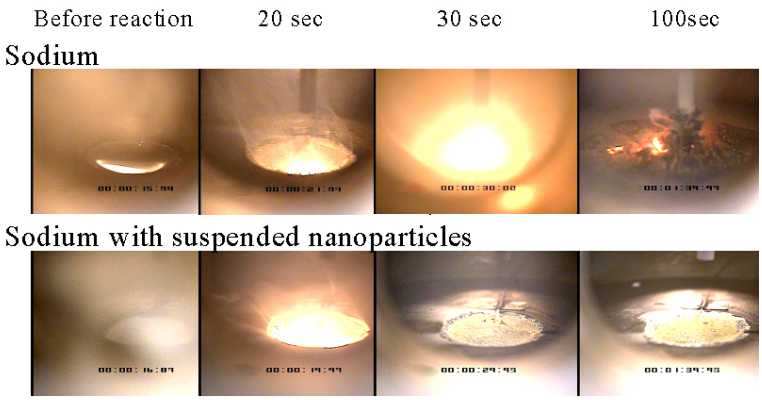

Fig. 9 Reactivity suppression of sodium nanofluid (Self-extinguishing effect)

From these results the chemical reactivity suppression of sodium nanofluid was confirmed. Then an effect of chemical reactivity suppression on plant design was investigated. There are many countermeasures for sodium fire as shown in Fig.10. For example, there is the thermal liner for protection from the high temperature. And there is N_2 gas injection system for early fire extinguishing. If a sodium nanofluid will be used as the coolant of secondary loop, these countermeasures are not necessary, because sodium fire is suppressed. For example, N_2 gas injection system, heat sink material and thermal insulation

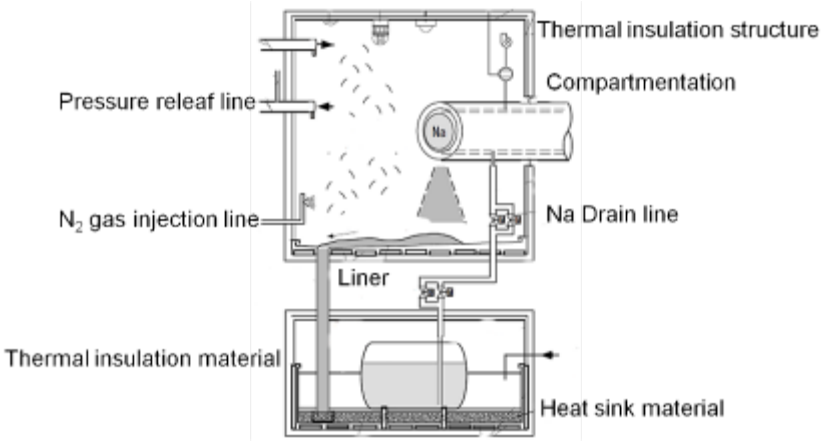

Fig. 10 Countermeasures of secondary loop against sodium fire

structure are not necessary. And thickness of the thermal liner can be reduced. In this way, not only reduction of countermeasures but also the flexibility of plant design will be enhanced.

(b) Water Reaction

The generated heat of reaction and the reaction rate were selected to evaluate the change of behavior between sodium and the sodium nanofluid. We conducted experiments using a sample of a sodium nanofluid to identify the difference in the generated heat of reaction and the reaction rate between sodium and the sodium nanofluid.

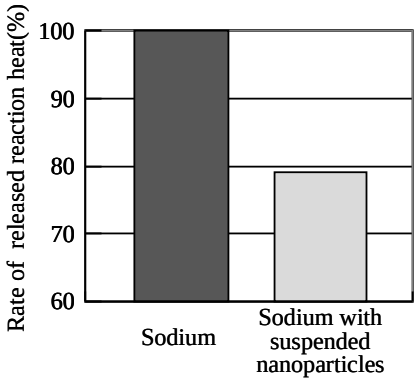

Fig. 11 Released reaction heat about reaction with water

The generated heat of reaction of the sample during reaction with water was measured by Twin Condition Calorimeter (OmniCal Technologies, Inc, Super-CRC). Measurement error was less than 10%. The weight of the sodium in the sample was normalized and the released reaction heat of the sodium nanofluid was compared with sodium. The typical data of the results is shown in Fig. 11. It was confirmed that the released reaction heat was significantly reduced. The reproducibility of results in the samples was also checked.

We performed an experiment to examine the primitive reaction behavior of the initially solid sample with water. The heat of reaction and hydrogen gas are generated in the sodium-water reaction as shown in Eq(1).

$$Na\ (sl) + H_2O\ (g) \rightarrow NaOH\ (sl) + 1/2\ H_2\ (g) - 183.7\ [kJ/mol] \quad (1)$$

It is necessary to measure the temperature change of the heat of reaction or the pressure change of the generated hydrogen gas to investigate the time trend of the reaction behavior. Reaction with water is too fast for the accurate measurement of temperature by thermocouples. The measured temperature varies by location of measurement, and it involves time delay. On the other hand, pressure measurement is quick and expresses reaction behavior with relative accuracy. Therefore, the pressure change time trend is used to evaluate the reaction behavior of sodium-water, and the pressure due to generated hydrogen gas was measured. As Fig. 12 shows, suppression of the reaction of sodium nanofluid was confirmed.

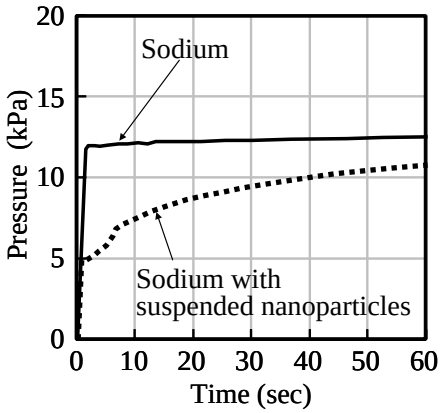

Fig. 12 Reaction rate about reaction with water

An explanation of the reaction suppression effect on the released reaction heat follows. On the basis of the result of reduction of the generated heat of reaction in this study, the reaction temperature was estimated using the sodium-water temperature reaction evaluation method[7,8] used in the previous study. In the method, it is considered that an axisymmetric-high-velocity steam jet leaks at high pressure into an unbounded region of molten sodium at a relatively low pressure. The steam jet passes through three physical zones as it penetrates the molten sodium, an expansion zone, a sodium entrainment/reaction zone, and a reaction-free

sodium entrainment zone, within which the jet cools down to the temperature of the surrounding sodium.

The entrainment/reaction zone is treated as a one-dimensional two phase zone and all the properties of the jet (temperature, species concentration, etc.) are assumed to be constant over the local cross section of the jet and to change depending only on the distance downstream from the crack opening. The conservation equations of momentum, mass and energy are solved with comparative ease by this approach.

The evaluation results are shown in Fig. 13 and Fig. 14. Analysis conditions are a large scale reactor, a straight type single wall tube SG, full power condition and initial leak rate 15g/s. From this figure, a significant reduction of the reaction temperature of sodium nanofluid was expected. In the future, the generated heat of reaction and reaction phenomena including the reaction between nanoparticles and sodium and water will be experimentally evaluated.

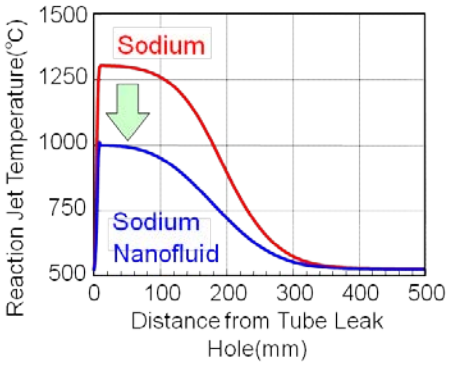

Fig. 13 Comparison of analyzed reaction temperature of sodium-water reaction with sodium and sodium nanofluid

From this result, we predict an actual situation of sodium-water reaction. The peak temperature of reaction decreases by the reduction of generated heat of reaction. For that reason overheating and tube rupture will be avoided. Also, wastage of tube will be reduced by a decrease of reaction jet temperature. Furthermore the leak propagation of tubes by wastage will be avoided by improvement of sodium nanofluid, too. Hence the double wall tube may become a single wall tube.

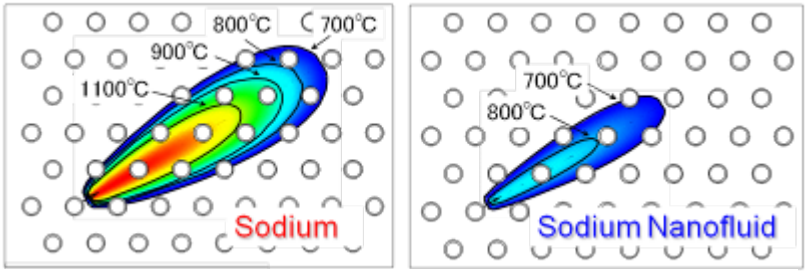

Fig. 14 Comparison of analyzed reaction temperature distribution of sodium-water reaction with sodium and sodium nanofluid

(c) Applicability for FBR Plant

The purpose of this section is to investigate subjects related to the application of sodium nanofluid as coolant. Subjects related to the application of sodium nanofluid to the FBR plant were identified from the viewpoint of design, operation and maintenance, and from these, priority subjects were selected for investigation. The result is shown in Fig. 15. The applicable conditions for FBR plants are as follows. Sodium temperature is ～530℃ and sodium velocity is ～10 m/s. The subjects were evaluated on the basis of current knowledge, calculations,

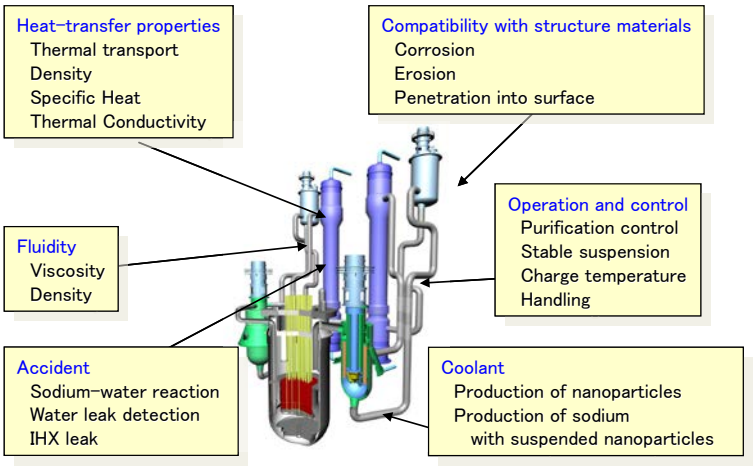

Fig. 15 Subjects of sodium fluid which relate to applicability to the FBR plant

and fundamental physical properties. As a result, it was determined that there was no need for concern, and it was verified that there were no issues with coolant of the FBR.

4. Conclusion

An original idea which overcomes the weak point of sodium was created. The original idea is realized and it was gotten a prospect of the realization of the idea. The flexibility of plant design will be explanded utilizing the creative idea. And it is found that there is a possibility of creation of new concept.

ACKNOWLEDGEMENTS

Present study includes the result of "Development of application technology of sodium with suspended nanoparticles to fast reactor" entrusted to Japan Atomic Energy Agency by the Ministry of Education, Culture, Sports, Science and Technology of Japan (MEXT).

REFERENCES

[1] K. Ara, K. Sugiyama, H. Kitagawa, M. Nagai and N. Yoshioka, "Study on Chemical Reactivity Control of Sodium by Suspended Nanoparticles I," *J. Nucl. Sci. Technol.*, **47**, pp1165-1170 (2010).

[2] K. Ara, K. Sugiyama, H. Kitagawa, M. Nagai and N. Yoshioka, "Study on Chemical Reactivity Control of Sodium by Suspended Nanoparticles II," *J. Nucl. Sci. Technol.*, **47**, pp1171-1181 (2010).

[3] J. Saito and K. Ara, "A study on atomic interaction between suspended nanoparticle and sodium atoms in liquid sodium," Nucl. Eng. and Design, **240**, pp.2664-2673 (2010).

[4] A. D. Becke, "Density-functional thermochemistry. III. The role of exact exchange", *J. Chem. Phys.*, **98**, 5648(1988).

[5] C. Lee, W. Yang and R.G. Parr, "Development of the Colle-Salvetti correlation-energy formula into a functional of the electron density", *Phys. Rev.* **B37**, 785(1988).

[6] A. D. Becke, "Density-functional exchange-energy approximation with correct asymptotic behavior", *Phys. Rev.* **A38**, 3098(1988).

[7] M. Epstein, H. K. Fauske, N. Yoshioka, M. Tashimo, “Analytical Model for Peak Temperature within a Sodium-Water Reaction Jet,” *J. Nucl. Sci.*, **43**, 43(2006).

[8] N. Yoshioka, Abstracts of 2004 Fall Meeting of Japan Atomic Energy Society of Japan, (2004) B22. [in Japanese].

Preliminary design of a large scale Sodium Gas Heat Exchanger (SGHE) for the Nitrogen Power Conversion System envisaged on the ASTRID SFR prototype

L. CACHON, E. RIGAL[1], A. WOAYE HUNE[2], Ch. GARNIER, I. CHU[1], J. CALAPEZ[1], S. MENOU[2], F. DELASSALE, G. RODRIGUEZ, S. MADELEINE, G. LAFFONT

French Commission for Atomic Energy and Alternative Energies, F- 13 108 Saint PAUL Lez Durance, France
[1]French Commission for Atomic Energy and Alternative Energies,F- 38 054 GRENOBLE, France
[2]AREVA NP, Rue Juliette Récamier 69006 Lyon, France.
Tel : +33 4 42 25 74 25, Email : lionel.cachon@cea.fr

ABSTRACT: *The ASTRID prototype (Advanced Sodium Technological Reactor for Industrial Demonstration), is foreseen in operation by the 20's. It will have to demonstrate progresses in Sodium Fast Reactor (SFR) technology at industrial scale, by qualifying innovative options. Some of these options still require development especially in the field of operability and safety.*

Thus, two power conversion systems (PCS) are investigated in parallel: the steam water Rankine PCS and the Gas Brayton PCS. This paper is placed in the context of a gas PCS with pure nitrogen which is mainly motivated by an enhanced safety and acceptability considerations with the "de facto" elimination of the sodium / water reaction risk.

In this gas PCS, the main critical and innovative component is the sodium gas heat exchanger (SGHE) which transfers heat from the secondary sodium loops to the tertiary gas loop.

This paper presents the development status of this component through the different topics, i.e. design, material studies, manufacturing process development, thermo-hydraulic and thermo-mechanical program, and a preliminary qualification plan as a conclusion.

1- Introduction

The French 1500 MWth GEN IV Sodium Fast Reactor (SFR) named ASTRID [1], which stands for Advanced Sodium Technological Reactor for Industrial Demonstration, is an integrated technology prototype designed for industrial-scale demonstration of 4th-generation sodium-cooled fast reactor (SFR) safety and operation. This "integrated technology demonstrator" is planned to be put in operation after 2020. It is the precursor of a commercial SFR of 2500-3600 MWth foreseen after 2040.

The four main criteria expected for ASTRID are:

- ✓ Sustainability, with a fuel and a core designs allowing for an optimal use of uranium resources and so multiple recycling of plutonium is adopted. Additionally, it should offer a minor actinide transmutation capability (in the scope of the June 2006 French Parliament act regarding sustainable management of radioactive material and waste) [1] [2].
- ✓ Safety, with the safety level being at least equivalent to that of current generation III reactors. An improved and robust safety demonstration with regard to former fast reactors is expected, which will include an enhanced prevention of whole core melting accidents, mitigation of a whole core accident, prevention and mitigation of risks due to sodium chemical reactivity and robustness to external hazards.
- ✓ Economy, with competitive costs compared to other sources of energy. This leads to large efforts to reduce investment and operation costs but also to improve the plant availability.

- ✓ Non-proliferation, with a strong resistance and protection against any external hazard.

The first phase of the ASTRID conceptual design ended in 2012 with the choice of the main reference technology options. The end of the second conceptual design phase is planned for 2014. Then the basic design is foreseen for 2017.

Two power conversion systems (PCS) are investigated in parallel: the classical steam water Rankine PCS and an innovative Gas Brayton PCS. This paper is discusses the gas PCS (pure nitrogen) which is mainly motivated by an enhanced safety and acceptability considerations with the "de facto" elimination of the sodium / water reaction risk.

In this gas PCS, the main critical and innovative component (see below) is the sodium gas heat exchanger (SGHE) which transfers heat from the secondary sodium loops to the tertiary gas loop.

This paper presents the development status of the SGHE through the discussion of different topics, i.e. design, material studies, manufacturing development, thermo-hydraulic and thermo-mechanical program and a preliminary qualification plan as a conclusion.

2- The nitrogen power conversion system

Thermodynamic performances analyses [2] were carried out taking into account these main input data :

- Thermal power delivered to the gas cycle: 1500 MWth
- Inlet core temperature : 395°C
- Sodium gas heat exchanger outlet temperature: 515°C
- Sodium gas heat exchanger inlet temperature: 330°C
- Outlet cooler temperature : 27°C (air-cooling tower)

The main parameters of this study [2] were the pressure and nature of the pure gas and gas mixtures (neon, argon, nitrogen, helium, He/N_2). Their influence on the cycle efficiency was studied. In complement to this thermodynamic comparison, the impact of these parameters on the heat exchangers compactness [2][3] and the turbomachinery size [2] was also assessed.

The nitrogen cycle was chosen because it is viewed pragmatically as the most reliable candidate compatible with the ASTRID schedule, due to the industrial experience gained with air-breathing fossil fueled turbomachines. Additionally, the use of a single gas, nitrogen, rather than a mixture is expected to significantly simplify cycle operations. With this choice decided, the optimization of the nitrogen cycle has been going on with the investigation of the optimal turbine inlet pressure. A 180 bar maximum operating pressure has been selected [2].

The resulting nitrogen-gas reference cycle option for ASTRID is presented in Figure 1. The net cycle efficiency is 37.5%: this value takes into account the realistic turbomachinery efficiencies, the pressure losses on the gas loop and the thermal efficiency and pressure losses of heat exchangers, as presented below.

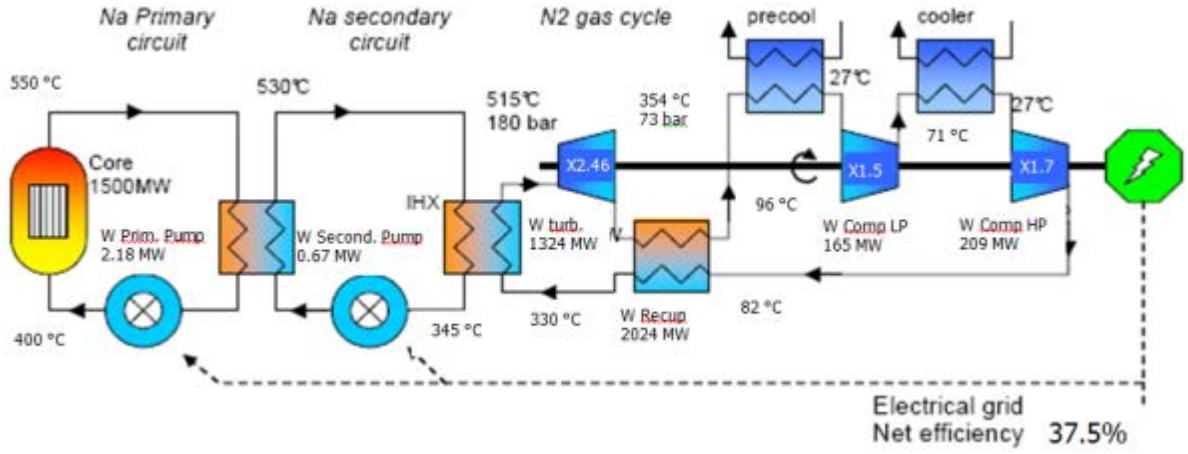

Figure 1 - Nitrogen power conversion cycle, ASTRID design option [2].

3- Heat exchangers

The tertiary gas loop (N_2 gas cycle in figure 1) is composed of three heat exchanger components:

- Na / gas heat exchanger,
- Gas / Gas economizer,
- Coolers.

In the following paragraphs, we are going to present only the studies performed on the Na/gas heat exchanger (SGHE). During this preliminary phase, two heat exchanger technologies have been evaluated:

- The reference technology and the most innovative is based on compact plate heat exchanger technology. The objective is to compensate for the poor intrinsic thermal exchange performance of nitrogen by using a high thermal efficiency technology.
- The backup solution is based on a classical tube-and-shell heat exchanger.

3.1- Compact SGHE

The technology selected for compact heat exchangers is Plates Machined Heat Exchangers (PMHE), where the corrugations are made by machining (milling, chemical etching, etc.). The diversity of feasible heat transfer patterns is very large: classical micro-channels of different cross-section area could be used, up to fins which could be machined in the plate.

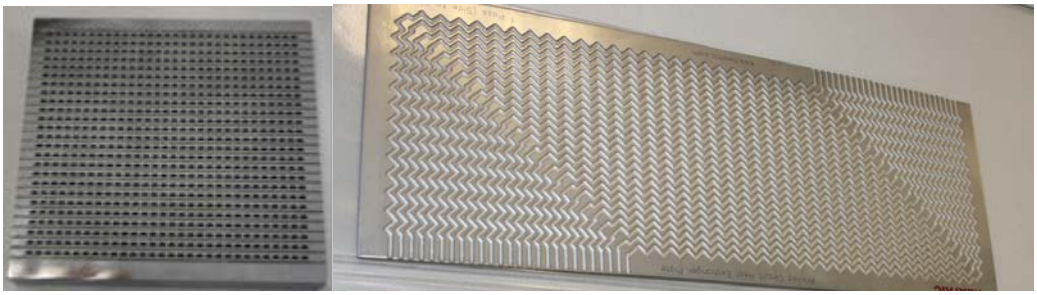

Figure 2 – Illustration of PMHE

The design phase [3], especially for these non-standard nuclear reactor components, requires essential knowledge to be investigated from a number of parameters, specifications, and rules; in particular:

- ✓ The thermal-hydraulic design requires the knowledge of heat transfer and friction factor correlations. These parameters directly affect the size of the components and the input data for the thermal-mechanical analysis.
- ✓ The thermal-mechanical analysis has to be done with validated materials data, in particular for assembly areas where the base material properties will be modified during the welding process. Also the design / manufacturing code, i.e. ASME or RCC MRx, must integrate this component exchange, with all its features, in order to allow its manufacturing with nuclear rules.
- ✓ The assembly process plays a major role on the thermal-mechanic behavior of the component. Its knowledge, qualification and integration into the design / manufacturing code are essential. The proposed method for compact heat exchangers assembly is diffusion welding (DW).
- ✓ The identification and eventual partnership with a manufacturer which is able to integrate the overall process and adopt the tools to manufacture a compact heat exchanger will complete the process.

3.1.1- Thermohydraulic program

The bibliography studies and pre-design work already carried out demonstrated the difficulty in finding thermal-hydraulic correlations able to adequately describe the specific exchange geometries. Indeed, the literature is full of studies and correlations, more or less adapted to the geometries studied, leading to a significant discrepancy in the calculational results. In addition, in the case of the PMHE, it is difficult to find a geometrical description of a heat transfer pattern associated with a complete set of correlations.

Finally, having as an ultimate goal to optimize the heat transfer pattern, it is essential to have a more detailed knowledge of the hydraulic phenomena induced by the corrugations.

A computational fluid-dynamic study has been carried out on the PMHE concept [3], and consists of a parametric study which aims to assess the influence of many geometrical parameters of a PMHE type fluid stream (shape of the section, hydraulic diameter, radius elbows, straight length between bends, angle between straight lengths) on the correlations for friction factor and heat transfer coefficient.

These correlations were used in a finite volume 1D code developed in CEA. They show that 125 MWth can be exchanged using 8 bundles of plates with a dimension of 1x0,65x3 m^3.

3.1.2- Bundle of plates assembly process

Diffusion welding by hot isostatic pressing (HIP-DW) is the selected process. A furnace is used for warming up, but it is included in a pressurized vessel: compression of the stack is achieved by gas pressure. A canister is used to prevent gas ingress inside the stack. This difference allows greater flexibility in the tools for implementing the HIP-DW. However, industrial HIP furnaces, working at high temperature and high pressure, have difficulty to operate at low pressure, which might be required for our applications, i.e. to avoid excessive channels deformation.

A large program has been launched in order to adapt HIP-DW for compact heat exchanger assemblies. The objective of this study is to investigate the diffusion weldability (DW) of 316 Type steel. The required material properties favorable to DW are:

- grain boundaries that easily cross interfaces during welding,
- no formation of compounds embrittling the interfaces or detrimental to grains to cross of the interfaces during their growth during welding,
- moderate grain coarsening at welding temperature,
- low distortion during welding.

Some of these features are antagonistic and therefore require a compromise, specifically:

- a good crossing of interfaces by grain boundaries seems antithetical to a low grain coarsening,
- low distortion of the channels during welding goes against the need to apply sufficient force to weld.

In this study, material suitability is assessed through different characterizations. Data on materials and their influence on the diffusion weldability are also evaluated by the characterization of joint mechanical properties and the tendency to grain coarsening via metallographic analysis (figure 3).

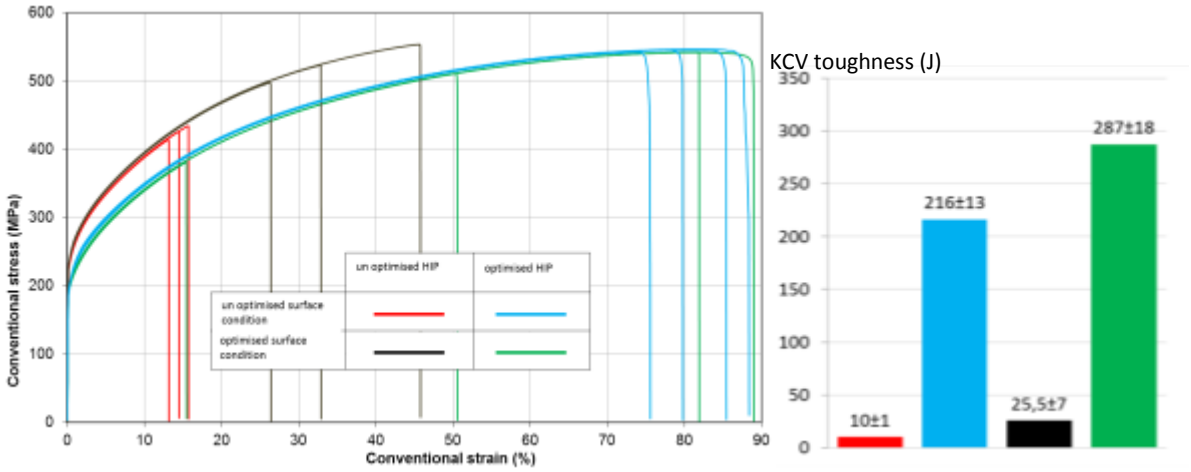

Figure 3 – room temperature tensile testing (left) and impact toughness (right) of HIP-DW joints

3.1.3 - Codification - Inspection

The aim of the study is to describe the existing rules and the gaps in the design and manufacturing code RCC-MRx for innovative compact heat exchangers. The objective is to define the R&D program to eventually meet specific requirements of a nuclear quality design, procurement of materials, manufacturing, production control and welding.

One of the identified key points is the manufacturing control. Depending upon the component safety classification level, 100 % “Non Destructive Testing” of welding joints might be required. Acceptable method to control the welding has to be developed.

Inspection tools and techniques best suited to carry out 100% volumetric control checks of compact heat exchangers are expected to be based upon ultrasonic and electromagnetic processes.

The CIVA software platform will be used to model these applications in order to assess their feasibility. An optimization of the design of the heat exchangers could also be made in order to favor ultrasound propagation. Experimental tests on a mock-up assembled by HIP-DW will also be performed to validate the CIVA simulation results.

3.1.4 - Na / gas heat exchanger design

The main constraints taken into account in the design presented in this section deal with the ease of inspection, disassembly of the component during phases of maintenance and component compactness. The design is made using the French design and manufacturing code RCC-MRx. The materials used are listed in table 1.

Material / designation	Location	Sm (300°C, MPa) Rpt $_{0.2}$min (300°C, MPa) Rm (300°C, MPa)	Negligible creep temperature limit for an infinite hold time	St at 425°C t = 1.10^5 h
X2CrNiMo17-12-2(N) (316LN)	Plates, Sodium pipes	115 128 410	450°C	137 MPa
2 ¼ Cr1Mo 11CrMo9-10 (thickness 200 < t < 500 mm, forged)	Pressurized pipes, vessel.	133 200 450 (20°C)	375°C	129 MPa

Table 1 – Material used for Na / gas heat exchanger.

The main design criterion is including multiple modules in a pressurized chamber with nitrogen at 180 bar. The main reasons for this design criterion are:

- Minimization of losses on the gas system: the pressure vessel also plays the role of a gas collector, thereby avoiding the integration of gas collectors in the modules and saving about 20% of pressure losses of the current heat transfer zone. The vessel is pressurized to 180 bar but manufacturing constraints limit its diameter to about 4m.
- Access to modules for ease of maintenance and inspection: the major advantage of this provision is to provide direct access to the modules without having to open the sodium loop. Inspection of the enclosure and the outer wall of the modules are facilitated.
- Sodium confinement: this design has two barriers between the sodium and the outside, i.e. the plate bundle and the pressure vessel shell.

The main design elements (figure 4) are:

- A set of "modules support" removable from the pressure chamber and composed of:
  - the four modules installed on a support plate (sealed connection), suspended by four flexible bars (managing the radial and axial thermal expansion) to a flange, integrated Na outlets by means of thermal sleeve.
  - the Na inlet which is coaxial with the inlet / outlet gas; it is vertical allowing for an easy Na draining,
  - the gas outlet manifold attached to the support plate modules,
  - the gas outlet pipe, coaxial and containing Na piping.
  - a yoke guide modules in the middle part,
  - an inner shell gas, composed of four parts mounted on flexible bars. It helps guide the inlet gas along the pressure vessel wall and thus establishes and homogenizes its operating temperature.
- The pressure vessel during the maintenance phases of the modules can remain on site. It comprises:
  - the pressure vessel,
  - the top cover,
  - the inlet/outlet gas coaxial pipe.

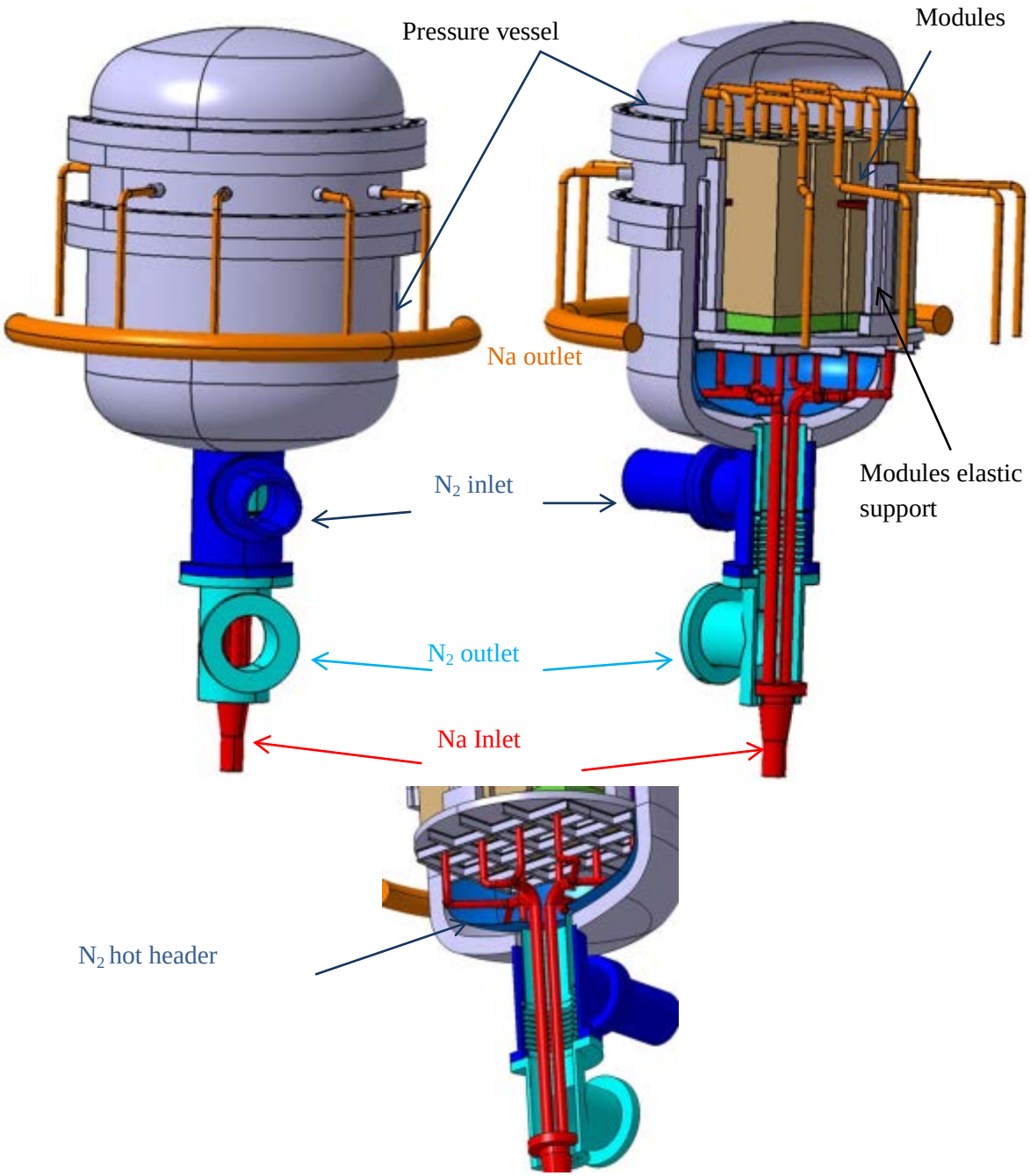

Figure 4 – CEA Na / Gas heat exchanger design (125 MWth)

3.2 - SGHE - Shell and Tube Heat Exchanger concept

Within the R&D development program, this option is proposed as a back-up option. The component is derived from conventional shell-and-tube heat exchangers.

Adaptation of such a component for use in ASTRID conditions will require limited investment and R&D for component justification and demonstration as compared to the compact option. The assessment of power capability is performed under the requirements of reactor conditions (high temperature and pressure levels).

3.2.1 - Exchanger description:

The tubes & shell SGHE is composed by :

- "U" shaped tube bundle implemented within a surrounding shell structure,

- Heat exchange tubes are fixed at each end into two thick tube-plates,
- Two spherical headers are welded on tube-plates for gas feeding,
- Two annular headers are implemented for sodium homogeneous feeding,
- Nitrogen is flowing within the tubes ,
- Sodium is flowing outside the tubes within the surrounding shell structure,
- The two coolants (sodium and gas) are flowing in counter-flow,
- Tubes are stabilized along their length by machined grid spacer plates,
- Nozzles are implemented on spherical headers for coolant feeding and in service inspection access from gas side.

3.2.3 - Main characteristics

The main characteristics are:

- Component power 22 MWth,
- Pressure drop on gas side is less than 1 bar,
- The whole component is composed of 316 LN material,
- Tube bundle is composed of 2500 tubes (triangular pitch),
- Tubes are linked on tube-plates by hard rolling and a leak-tight weld,
- Total component length is 9.8 m.

The U-shaped shell and tube exchanger power is limited by the strength of the tube-plate. This strength is limited by the maximum thickness that may be provided for the thick 316 LN forged plate required for the tube-plate.

3.2.4 - Upcoming studies:

Sodium coolant has a high thermal ability compared to gas coolant. Using these two coolants at the same time within one heat exchanger requires assessing the general thermal hydraulic behavior in nominal and transient conditions. Upcoming R&D studies on the heat exchanger sodium side should focus on:

- Flow stability
- Flow maldistribution assessment
- Accidental conditions such as tube rupture

Possible heat exchanger design adaptations may be envisioned in a following step.

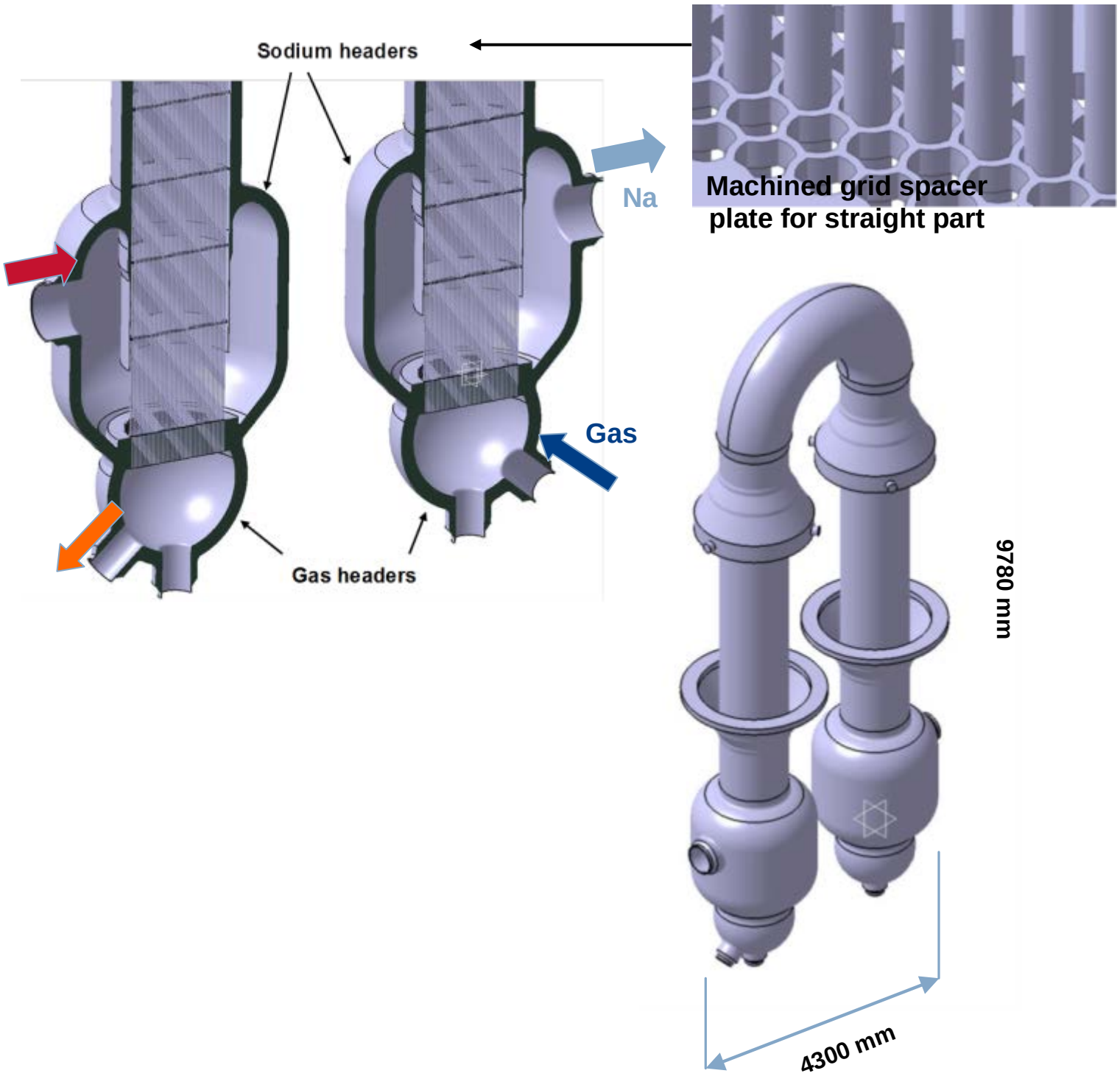

Figure 5 : © AREVA *Na/Gas heat exchanger design (shell & tubes concept)*

4 - Summary & Conclusions

As part of the GenIV SFR R&D program and in order to avoid issues related to the fast and energetic Na/water reaction, an alternative gas cycle power conversion system is considered by CEA to replace the standard water steam cycle. This paper has presented the current R&D program devoted to one of the most critical component of the Nitrogen Power Conversion System, the SGHE.

Numerous development areas have been completed. First, a better understanding of thermal-hydraulical correlations of PMHE was acquired by CFD calculations on various geometric channels. A program carried out on the assembly process has confirmed the potential of diffusion welding as a assembling method for a plate bundles, including the production of a technological mock up.

The design studies offer components combining thermal-hydraulic and thermal-mechanic performances, inspection, instrumentation and maintenance capacities :

- The reference plate compact SGHE has the advantages of a good thermal power per component (125 MWth), and a good compactness. The drawbacks concern the lack of technological maturity and a higher difficulty for inspection. The R&D qualification program has to improve the confidence in this technology. The main topics to be studied are materials (characterisation, behavior in sodium and nitrogen environment), manufacturing process, inspection, justification of design and manufacturing, …
- The back up tube-and-shell heat exchanger solution has better technological maturity. The conclusion is that tube-and-shell heat exchanger technology could be used. The main issue concerns the low intrinsic compactness and the low thermal power of the component which induces a penalty on investment cost and a complex installation around the reactor.

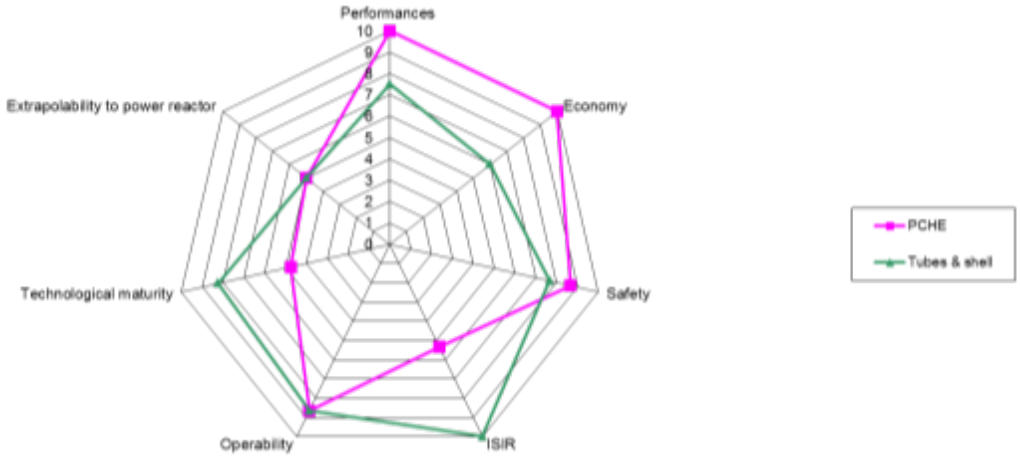

Figure 6 – Comparison between the two SGHE technologies

Nomenclature

ASTRID : Advanced Sodium Technological Reactor for Industrial Demonstration
SFR : Sodium Fast Reactors
PCS : Power Conversion System
PMHE : Plates Machined Heat Exchangers
DW : diffusion welding
U-DW : Uniaxial diffusion welding
HIP : hot isostatic pressing
HIP-DW : hot isostatic pressing - Diffusion welding
RCC-MRx : French nuclear design and manufacturing code

References

[1] Lecoz P. & al, “Sodium-cooled Fast Reactors: the ASTRID plant project”, Proceedings of ICAPP ’11, Nice, France, May 2-5 , 2011, Paper 11249.

[2] N. ALPY et al, “Gas Cycle testing opportunity with ASTRID, the French SFR prototype”, Supercritical CO2 Power Cycle Symposium, May 24-25, 2011, Boulder, Colorado.

[3] L. CACHON et al, “Innovative power conversion system for the French SFR prototype, ASTRID”, ICAPP '12, Chicago - June 24-28, 2012.

Cooperation on impingement wastage experiment of Mod. 9Cr-1Mo steel using SWAT-1R sodium-water reaction test facility

F. Beauchamp[a1], **M. Nishimura**[b2], **R. Umeda**[b], **A. Allou**[a]

[a] CEA (French Alternative Energies and Atomic Energy commission),
Nuclear Energy Directorate,
Cadarache center, France

[b] JAEA (Japan Atomic Energy Agency),
Oarai R&D center,
Narira, Oarai, Ibaraki,
Japan

Abstract. The loss of tightness from a Steam Generator Unit (SGU) tube results in high-pressure steam or water leak into sodium causing a Sodium-Water Reaction (SWR), highly exothermic, with corrosive products leading to a local erosion-corrosion called "wastage" of neighbouring tubes. Under the collaboration between CEA and JAEA, wastage experiments were carried out on Mod. 9Cr-1Mo steel (T91) tubes. T91 is one of the material candidates of SGU tubes for future sodium-cooled fast reactors (SFRs). Wastage characterization of T91 is needed to evaluate the consequences for safety and the availability of the SGU. Six T91 target tubes were incorporated in the SWR test facility (SWAT-1R) of JAEA and subjected to reaction jets. All tubes were successfully penetrated by the reaction jets, and the wastage rates were determined. The main results are discussed in this paper. These test results contribute to the improvement of wastage rates prediction and to the safety demonstration of future SFRs.

1. Introduction and context

Tubes of a Steam Generator Unit (SGU) in a Sodium Fast Reactor (SFR) system are the only one physical barrier between sodium and water. The loss of tightness from one tube results in high-pressure steam or water leak into sodium causing a Sodium-Water Reaction (SWR), highly exothermic, with corrosive products leading to a local erosion-corrosion called impingement "wastage" of neighbouring tubes [1]. The consequences of an initial small leak are the propagation towards intermediate and large leaks if the detection and protection means are failing. Therefore, high reliability is required for the SGU to minimize the effect of SWR events on the plant system and availability.

Impingement wastage phenomenon is very strongly correlated with the nature of the tubes material and with its intrinsic behaviour. Wastage experiments data are needed to investigate the phenomenon of wastage due to steam leaks in SGU tubes and to quantify the wastage resistance of materials [2]. Modified 9Cr-1Mo (T91) steel is one of the material candidates of SGU tubes for future sodium-cooled fast reactors (SFRs). To expand the wastage database of the T91 steel, sodium-water reaction experiments were performed under the collaboration between CEA and JAEA.

Six T91 test straight tubes were provided by CEA, and the tubes were then incorporated in the sodium-water reaction test facility (SWAT-1R) of JAEA Oarai R&D Center. The tubes were subjected to sodium-water reaction jets from leaking tubes in a sodium vessel, to obtain its wastage resistance characteristics. The water injection rate, the sodium temperature and the distance between the water injection point and the target tube wall were selected as test parameters, because the wastage rate is known to be dependent on these factors in previous studies [2][3][4].

This paper describes the SWAT-1R facility, the test procedure and operating conditions, and brings out the main results and experience gained through the wastage experiments.

[1] Present address: CEA, DEN, Cadarache, DTN/STPA/LTRS, 13108 Saint-Paul lez Durance Cedex, France
[2] Present address: JAEA, Oarai R&D center, 4002 Narira, Oarai, Ibaraki, Japan

2. Objectives and definition of the experiments

The goal of this cooperation was to perform additional impingement wastage experiments on Mod. 9Cr-1Mo steel in order to have a more thorough and reliable database of experimental wastage tests covering all the required characteristic data. This updated experimental database supports the optimization of the wastage modelling of CEA and JAEA codes [2][5][6]. These codes are used to quantify the tubes penetration times for any kind of leak, in order to assess the leak evolution in the SGU and to define the system required to detect an initial leak before the propagation to a secondary leak and the failures of many tubes.

For this purpose, it was decided to retain the two following leak conditions:

(a) Three leaks with a sodium temperature of 500°C which correspond to leaks located at the upper part of the SGU where the wastage rate is maximal due to the high sodium temperature and the hydraulic transit time towards the hydrogen detection system is the longest. Those leaks are representative of undesirable events occurring under nominal operating conditions (100% of the nominal power).

(b) Three leaks with a sodium temperature of 350°C which correspond to leaks located at the lower part of the SGU where the fraction of hydrogen dissolved in sodium, and detectable with the first turn of loop, is weaker. It may penalize the response time of the hydrogen detection system, particularly if a leak occurred under low operating conditions (20% of the nominal power).

Figure 1 illustrates the distribution of these six wastage tests performed in the SWAT-1R (red squares) with all the other wastage experimental data currently available from the CEA database on the Mod. 9Cr-1Mo (T91) [2]. No experiments at temperatures close to 350°C were performed before. Those at 400°C were conducted with steam/water at 13MPa, too far away from the conditions of Experiments 1-2-3. These three experiments performed provide some new determining data on wastage resistance of Mod. 9Cr-1Mo steel at low temperature 350°C.

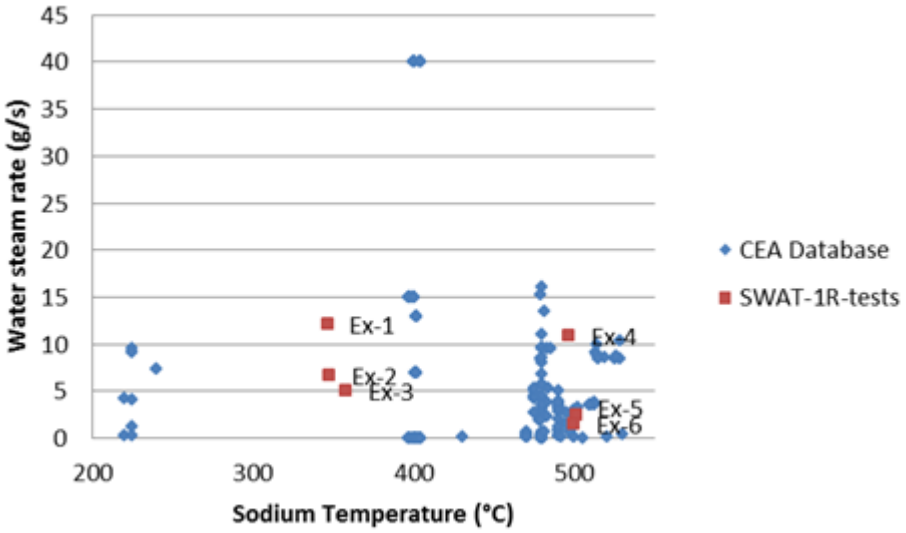

FIG. 1. Distribution of SWAT-1R experiments versus database as a function of the sodium temperature and the water/steam leak rate

3. SWAT-1R test facility

The sodium-water reaction test facility (SWAT-1R) is established in JAEA Oarai R&D Center. This test facility is dedicated to study the phenomenon of impingement wastage on different SG tube materials when SG tubes are submitted to a sodium-water reaction jet. The schematic diagram of the

SWAT-1R is shown in FIG. 2.

SWAT-1R consists of:

(c) Two steam-water supply systems:
  (i) A water tank with electric heater (WT) for larger injection rates (more than approx. 10g/sec)
  (ii) A water holding pipe (WH) pressurized in argon gas for smaller injection rates (less than approx. 10g/sec);
(d) A reaction vessel (RV) that contains test tubes (target tubes)
(e) A sodium dump tank (DT)
(f) A reaction products release tank (RT)
(g) Sodium circuit, water circuit, argon gas lines
(h) Temperature and pressure measuring instruments and level meters
(i) Power supply system and instrumentation and control system for monitoring and control of the operation
(j) A data acquisition system using personal computers.

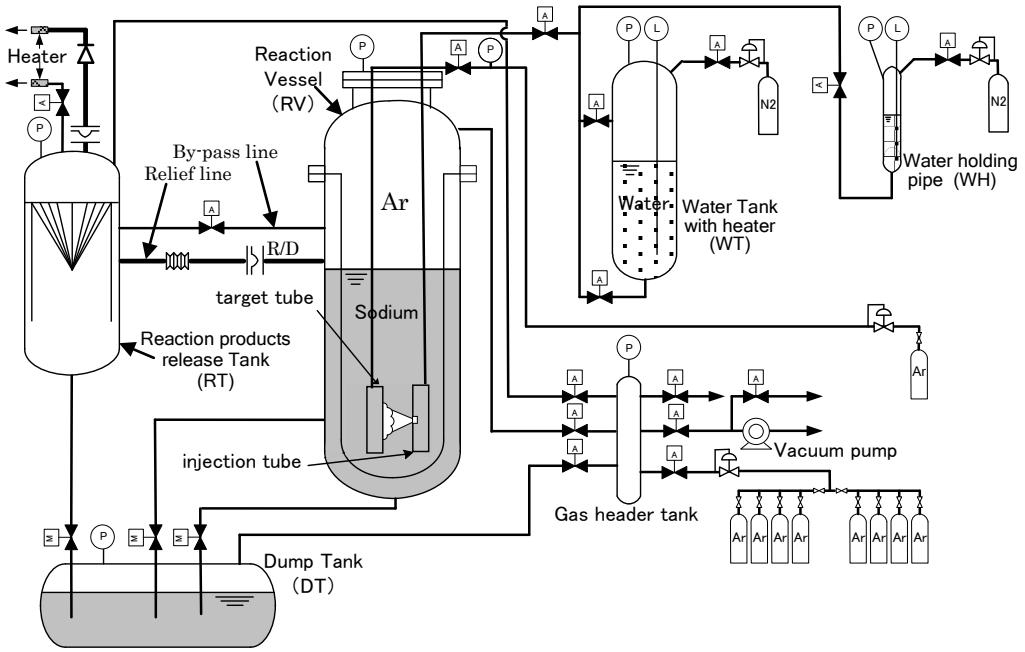

FIG. 2. SWAT-1R test facility

The total sodium inventory of the SWAT-1R is 0.8m^3. Half of the capacity of the dump tank (DT) is supplied to the reaction vessel (RV). The DT also provides a function of sodium purification. The sodium temperature in the DT is lowered to 200ºC to precipitate impurity substances such as NaOH. After the impurity substances are separated from the sodium, the sodium is charged into the RV at the same temperature. Sodium in the RV is heated and maintained up to 520°C by the electric heaters fixed around the vessel. The DT and the RV have an argon space over the sodium free surface level.

For the larger water injection rates, the water is heated up to 350ºC in the WT, and saturated steam at approx. 18 MPa is then fed through the water injection lines to the water injection tube in the RV. For the smaller water injection rates, the water is fed from the WH by Ar gas pressure at room temperature. For the two steam-water supply systems, each water injection line is equipped with air-operated valves to prevent unintentional injection of water towards the reaction vessel. These valves are opened approx. 60 seconds before starting the tests.

Safety against over pressurization is ensured by a rupture disc on a relief line and an air operated by-pass valve line between the RV and the RT. The by-pass valve releases hydrogen gas from the RV to the RT and maintains the RV cover gas pressure between 0.02MPa and 0.05MPa.

The test section in the RV contains the six target tubes and six water injection tubes, as shown in FIG. 3.

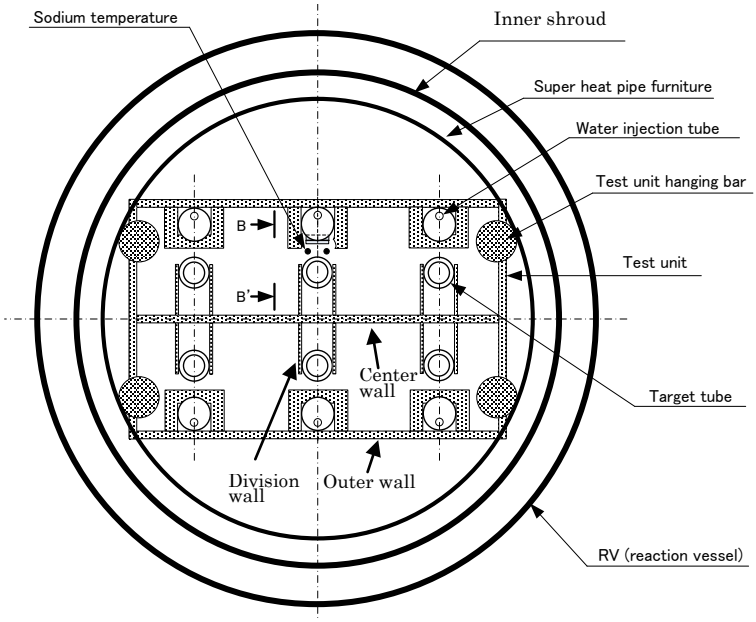

FIG. 3. Target tube / water injection tube arrangement in test section

The water injection tubes and the target tubes are fixed on the outer wall and the center wall of the test section, respectively. Target tubes are precisely arranged in front of each water injection tube with a determined tube to tube spacing. Division walls prevent the influence of a reaction jet on adjacent target tubes. An inner shroud is placed between the test unit and the reaction vessel, to protect the inner surface of the reaction vessel from reaction jets. Steam/water supply lines are partly coiled in the sodium of the RV, so that the temperature of the injected steam is increased to the test conditions in the coils by the heat of the sodium before water injection. Figure 4 shows details of one set of a target tube and a water injection tube. Steam/water is fed to the top of water injection tube through the water feed line from the water supply system. Temperature and pressure of the injected water are continuously monitored during the steam injection.

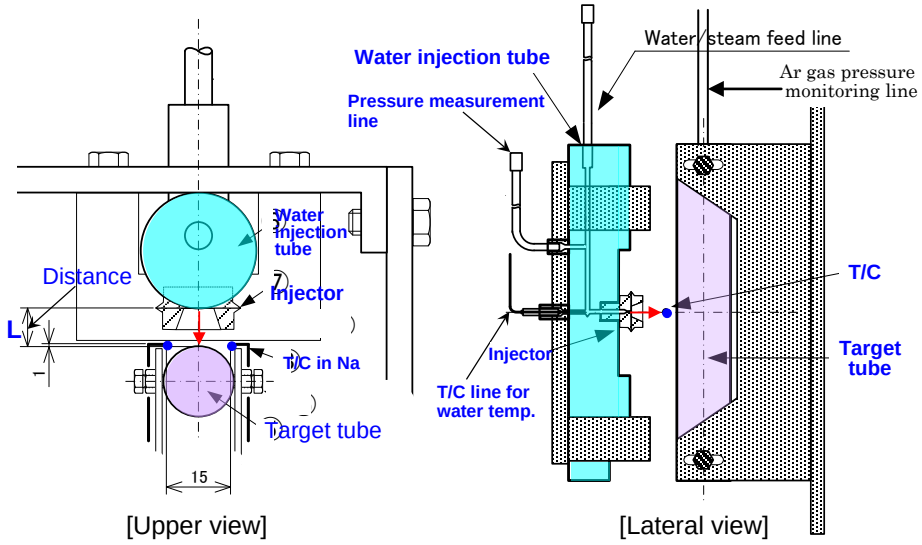

FIG. 4. Details of the target and water injection tubes

An injector with an orifice is welded to the water injection tube. The injector is made in stainless steel to limit the self-wastage process. A thin stainless steel film is sandwiched by lip welding between a retainer plate and a nozzle base. The water supply pressure is increased which then opens the thin stainless steel film, and then the water injection starts. Two thermocouples (type K) are located between each target and water injection tubes to confirm the initiation of a SWR.

Plugs were welded at both ends of the target tubes, and an argon gas line was connected to the upper end. 0.5MPa argon gas pressure is maintained in the target tube during the experiment. Once the target tube is punctured by a reaction jet (wastage), argon is released to the sodium side, and tube failure is then detected by the gas pressure fall.

4. Experimental conditions and test procedure

Once the RV is filled with sodium, the sodium is progressively heated up to the temperature required for the experiment. At the same time, the water injection lines are pre-heated. Before the steam/water injection, a little amount of sodium is sampled from the RV for chemical analysis.

The impingement wastage experiments are performed on Mod. 9Cr-1Mo steel (T91) tubes materials. All the original tubes (T91) were provided by CEA. The six experiments were conducted in series over two days, one target tube after the other. Three tubes were tested at approx. 350ºC during the first day, and the other three tubes at approx. 500ºC during the second day. The initial experimental conditions of each test (before the beginning of the injection) are those of:

(a) The steam/water pressure set up in one of the two steam-water supply systems (approx. 18MPa)
(b) The temperature of the sodium in the RV before the steam/water injection
(c) The temperature of the steam/water in the water injection tube at the starting point of the injection (close to that of sodium).

The other main parameters of the wastage experiments are the steam/water injection rate and the distance between the injector and the outer surface of the target tube. The water injection rate is determined by the injector diameter, the steam/water pressure and temperature. The injector diameters were designed to be 0.3mm, 0.4mm, 0.85mm or 1.6mm depending on the expected steam/water injection rate. Intertube distances are set to be 8mm, 15mm or 17mm.

Steam/water injection is started by the opening of the air-operated water valves. The stainless steel foil covering the water injection nozzle is burst open by the steam/water pressure, and the steam/water injection into the sodium then starts. Supplying steam/water into the RV is confirmed by the valve opening start signal, the pressure increase in the steam/water injection tube and the sudden decrease of the water level meter in the WH or the WT. The SWR is instantaneously detected by the temperature rise of the two thermocouples in sodium. Steam/water injection is continued until the target tube is punctured by the reaction jet. Puncturing of target tube is noticed by the fall in argon pressure. The air-operated water valves are then manually closed to terminate the water supply. The steam/water injection, however, continues for a certain period, because of the residual water in the water supply piping. At the end of reaction, the sodium in the RV is cooled down by natural heat release for the next test. Once the three tests are completed in the first day, sodium dumping into the DT is initiated. The sodium is cooled down to 200ºC and then charged-up to the RV in the second day. The sodium is heated up to 500ºC. The other three wastage experiments are conducted by following the same procedure of the first day. The temperatures in the SWAT-1R are slowly lowered after all the experiment completion.

The steam/water injection rates (g/s) are calculated by the changes of the water level meters in the water tank (WT) or the water holding pipe (WH). Both the level meters are differential pressure type. These level meters were calibrated in order to establish the relation between the output voltage and the water mass in the water tank. As calibrations were performed under the atmospheric condition (1atm, room temperature) and the level meters were used at the conditions of 18MPa/room temperature or

18MPa/350ºC during the steam/water injection, their outputs were corrected by the comparison of the data between the pressure and the level meter output obtained in the pressure rising process of the WH or WT.

The wastage rate is obtained by the ratio of the tube thickness (mm) to the penetration time (second). The penetration time (second) is taken as the span from the time of response of the thermocouples indicating a rise of sodium temperature to the time of response of the pressure transmitter indicating the fall of argon gas pressure in the target tube. There is a time delay estimated to be 0.1~ 0.35 seconds between the sodium temperature rise and the beginning of the steam/water injection (valve opening start signal) due to the time for the water to arrive at the water injection tube and to open the metal film. The tube thickness is measured by a vernier caliper after the wastage test. Since the difference between the measurement thickness and the nominal thickness (2.2mm) is small (within 2.3% error), the wastage rates are calculated based on the nominal value (2.2mm) in this paper. The results of the experiments are shown in FIG. 5.

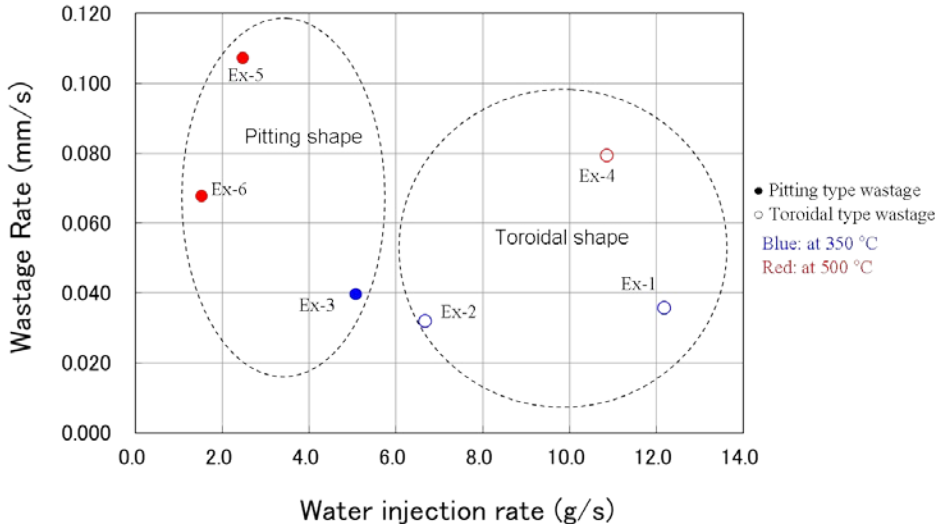

FIG. 5. Impingement wastage experiments results: wastage rate vs water injection rate

5. Experimental results and discussion

The six experiments were conducted successfully. All the tubes were punctured by the SWR jet. No self-wastage was observed in any injector of the injection tubes. Diameters of the injectors were measured before and after each test by an optical profile projector, and the measurement results showed no significant change after the wastage experiment.

Finally the steam/water leak rate was known and the wastage rate was determined for all the cases (see FIG. 5).

At low sodium temperatures of approx. 350°C, Experiments 2 and 3 were in the same range of leak rate compared to Experiment 1 performed with a higher leak. Figures 6, 7 and 8 show respectively for Experiment 1, 2 and 3 the wastage occurred. Experiments 1 and 2 have a toroidal wastage shape whereas a pit shape occurred for Experiment 3. Main parameters influencing the wastage profile are the distance between the injector and the target tube (intertube distance), the water-steam leak rate and the morphology of the jet (lengths of expansion and penetration) which depends on the hydrodynamics of the reaction jet.

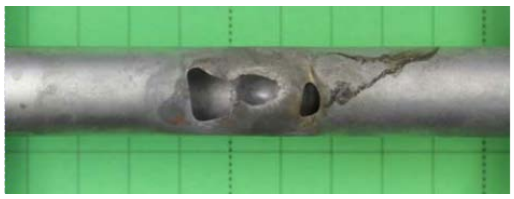

FIG. 6. Impingement wastage occurred on target tube experiment 1

FIG. 7. Impingement wastage occurred on target tube experiment 2

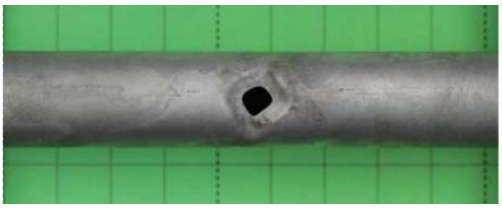

FIG. 8. Impingement wastage occurred on target tube experiment 3

Experiments 2 and 3 were conducted under similar conditions of temperature and water leak rate. Only the intertube distance was different. In order to explain this difference in the wastage shape between the two experiments, Figure 9 illustrates for a similar form and length of the jet that the intertube distance determines the wastage profile (pit/toroidal). The pointy end of the jet in which may combine a high temperature, a high impact velocity and corrosive reaction products such as sodium hydroxide is in contact with the wall of the target tube that results in pit type shape wastage, as shown in FIG. 9a. Due to the shorter intertube distance, the hydrodynamics of the jet is modified compared with a free jet. The core of the jet rich in steam/water is colder and gets close to the target tube. The end of the jet (rich in reaction products) is spread out against the wall of the tube, and the high temperature area deviates from the axis of the jet to affect a wider surface of the target tube, as shown in FIG. 9b. Consequently the toroidal wastage appears.

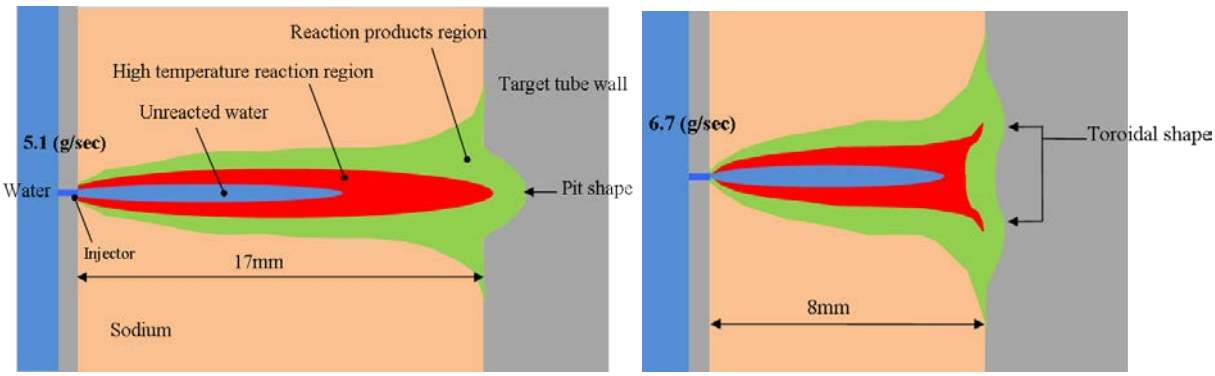

FIG. 9. Wastage profile. (a) Pitting wastage of experiment 3. (b) Toroidal wastage of experiment 2.

Experiments 4, 5 and 6 were performed at higher sodium temperature, near 500°C. Pitting wastage was observed for Experiments 5 and 6, as shown in FIGs. 10 and 11.

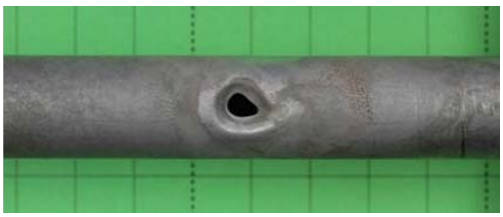

FIG. 10. Impingement wastage occurred on target tube experiment 5

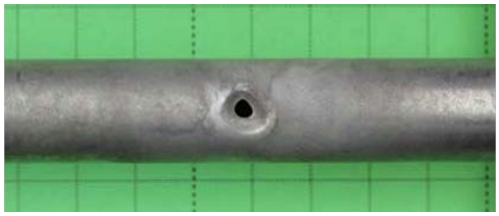

FIG. 11. Impingement wastage occurred on target tube experiment 6

The relation between the wastage profile, the intertube distance and the water injection rate explains the wastage shape of Experiment 4. Figure 12 shows images of the wastage development, a photographic picture of the wastage that occurred on the target tube, and the temperature and pressure evolution versus time. Figure 12 illustrates at 27.8 seconds (puncture time) the toroidal wastage process supported by a high steam flow rate (10.9 g/s). As soon as the tube penetration was detected, the steam/water side was depressurized and the steam injection rate gradually decreased. This reduction in the steam injection rate modified the profile of the reaction jet and the resulting wastage shape changed from the toroidal to the pitting one, as shown in FIG. 12b, with the jet puncturing the centre area of the tube front wall. At this stage, the target tube began to fill with sodium. The water injection lasted approx. 73 seconds. The jet penetrated inside the tube, then reached the opposite internal wall and finally punctured it (FIG. 12c). The same wastage development occurred during Experiment 1 (see FIG. 6) which was conducted with a high water injection rate. However, no failure occurred at the opposite wall because of the lower temperature (350ºC).

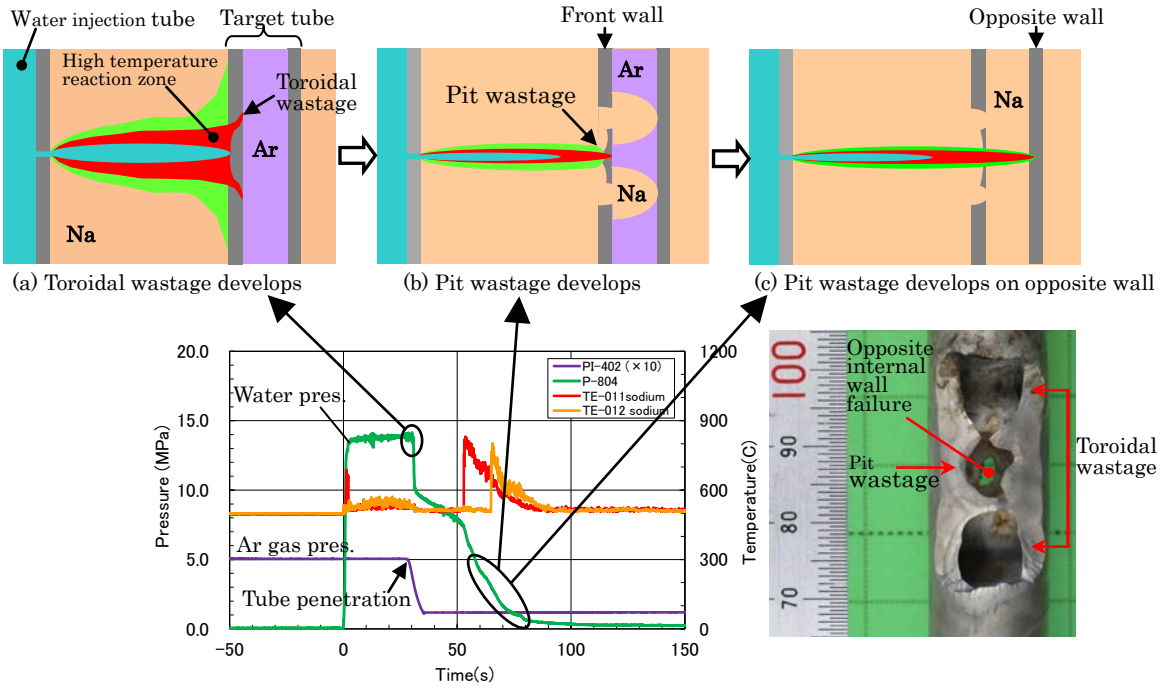

FIG. 12. Wastage development scenario in experiment 4

As discussed previously, the impingement wastage observed on the target tubes does not indicate the status soon after the tube penetration occurrence. Photographic pictures represent the final state of the SWR because admission of residual water into sodium lasted several tens of seconds after the end of the water/steam injection. Nevertheless, it does not affect the determination of the wastage rates.

The experimental results confirm that wastage rates are higher at the high temperatures (500°C) than at the low temperatures (350°C). Wastage rates for Experiments 4, 5 and 6 are in the range from 0.06 to 0.11 mm/s compared to those obtained for Experiments 1, 2 and 3 that are close to 0.03-0.04 mm/s. Depending on leak characteristics, wastage resistance of Mod. 9Cr-1Mo steel (T91) at 350°C is found about 2 times to 4 times higher than the wastage resistance at 500°C.

Other trends are observed in these experiments. Wastage rates at lower temperature 350°C are much less sensitive to the variations of parameters (intertube distance, water/steam leak rate) than those at 500°C (see FIG. 5). Comparison between Experiments 5 and 6 shows that for quasi similar intertube distance and high sodium temperature slight increase of the leak rate (1.5 g/s to 2.5 g/s) induces a rise of the wastage rate. Globally, considering the same conditions of temperature, wastage rates are found to be higher for pitting wastage than for toroidal type, which was usually observed in the past for different types of tube materials.

6. Comparison of experimental results with database and modelling

Most of the previous wastage experiments on Mod. 9Cr-1Mo steel (T91) were performed at higher temperature, around 500°C. The wastage rates obtained from Experiments 4, 5 and 6 are plotted in FIG. 13 with those from the available literature data carried out under the closest conditions (high sodium temperature, intertube distance and leak rate). Considering some differences in the test conditions, it has been concluded that both data are distributed in the same range.

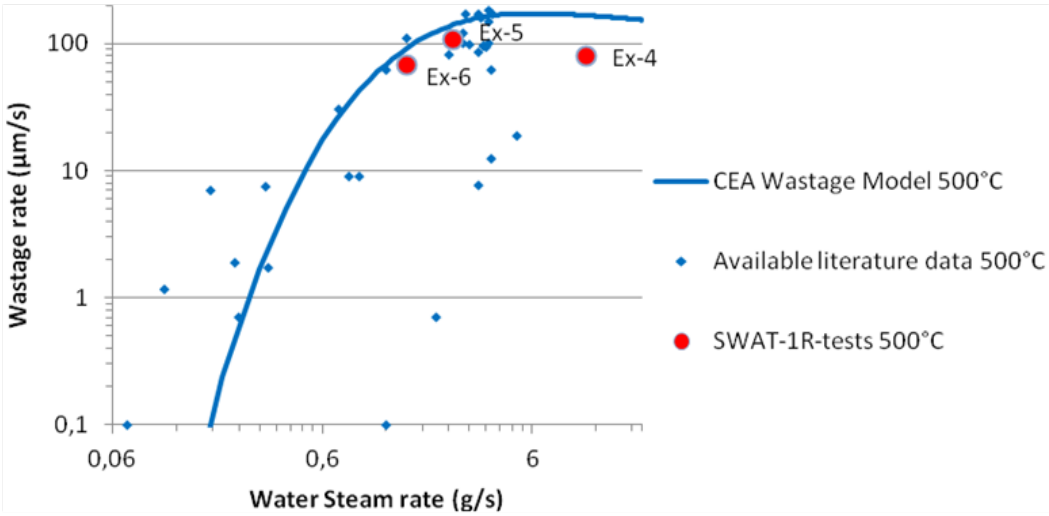

FIG. 13. Distribution of wastage rate from SWAT-1R Experiments 4-5-6 with available literature data and modelling results and as a function of the water/steam leak rate

Figure 13 highlights the good correlation between the wastage rate predicted by the CEA modelling and those obtained for the three experiments performed at 500°C. Wastage rate predictions are close to those obtained in the SWAT-1R and remain higher than most of the experiments results obtained at higher leak rate (>0.5g/s). However data experiments have a largest dispersion for lower leak rate (<0.3g/s), and the predicted values are not conservative in this field of smaller leak.

7. Conclusion

Sodium-water reaction experiments were carried out in the SWAT-1R facility of JAEA Oarai R&D Center to study the wastage resistance of the Mod. 9Cr-1Mo steel (T91) straight tubes. These experiments were performed under the cooperation between CEA and JAEA. Six wastage experiments were conducted successfully. All the tubes were punctured by the reaction jet. The wastage rates were obtained by the ratios of the tubes thickness (mm) to the penetration times (second). These experiments bring some new determining sets of wastage data on Mod. 9Cr-1Mo steel and expand the wastage database of CEA and JAEA. Comparison with wastage resistance of SG helical tubes made of alloy 800 shows that the wastage rates of Mod. 9Cr-1Mo steel obtained at low sodium temperatures are about the twice the wastage rates of alloy 800 material under the same operating conditions. At high sodium temperatures, wastage of Mod. 9Cr-1Mo steel is definitely faster than for alloy 800 material, with a variable factor (> 6) according to the steam leak flow rate.

The experimental results have contributed to upgrading wastage rates prediction from CEA modelling and to the safety demonstration of future steam generators units.

REFERENCES

[1] SAEZ, M., MENOU, S., BEAUCHAMP, F., BERTRAND, C., ALLOU, A., RODRIGUEZ, G., PRELE, G., Sodium-Water Reaction approach and mastering for ASTRID Steam Generator design, Proceedings of IAEA FR13 meeting, 2013.

[2] GERBER, A., PIRUS, J.P., BEILS, S., CARLUEC, B., BEAUCHAMP, F., JEANNOT, J.P., PRELE, G., Safety improvement research to design a sodium fast reactor steam generator with regard to sodium-water reaction risk, Proceedings of ICAPP-2010; San Diego, USA, June 13-17, 2010.

[3] HORI, M., Sodium /water Reaction in Steam Generators of Liquid Metal Fast Breeder Reactors, Atomic Energy Review, Vol. 18, No. 3, 1980.

[4] NEI, H., Evaluation of Heat Transfer Tube Failure Propagation due to Sodium-Water Reaction in Steam Generator, Journal of Nuclear Science and Technology, 15[3], pp. 192~199, March, 1978.

[5] THOMINE, G., MAUPRE, J.P., REMY, F.N., HOBBES., Modelling of water leakage effects in fast breeder reactor steam generators", Proceedings of 13th Int. Conf. on Structural Mechanics in reactor Technology (SMiRT 13), Porto Alegre, Brazil, August 13-18, 1995.

[6] HAMADA, H., TANABE, H., Analysis of Design Basis Leak Event in an LMFBR Steam Generator, Proceedings of ANP'92, Tokyo, Japan, 1992.

Synthesis of results obtained on sodium components and technology through the Generation IV International Forum SFR Component Design and Balance-of-Plant Project

J. J. SIENICKI[1], G. RODRIGUEZ[2], N. KISOHARA[3], J. B. KIM[4], A. GERBER[5], Y. ASHURKO[6], S. TOYAMA[7]

[1] : *ANL - Argonne National Laboratory, 9700 South Cass Avenue, Argonne Illinois 60439, USA, Email:* sienicki@anl.gov
[2] : *CEA-Commissariat à l'Énergie Atomique, CEA/CADARACHE DTN/DIR, 13108 St Paul Lez Durance, France. Email:* gilles.rodriguez@cea.fr
[3] : *JAEA - Japan Atomic Energy Agency, 4002 Narita, Oarai, Ibaraki Pref. 311-1393, Japan. Email:* kisohara.naoyuki@jaea.go.jp
[4] : *KAERI - Korea Atomic Energy Research Institute, 150 Dukjindong, Yuseong, Deajeon, 305-353, Republic of Korea. Email:* jbkim@kaeri.re.kr
[5] : *AREVA, NP, 10 Rue Juliette Recamier 69456 Lyon Cedex, France. Email:* alain.gerber@areva.com
[6] : *IPPE, Institute for Physics & Power Engineering, Bondarenko Sq1 249033 Obninsk, Kaluga Region, Russia. Email :* ashurko@ippe.ru
[7] : *OECD-NEA, Le Seine St-Germain, 12, boulevard des Iles, 92130 Issy-les-Moulineaux, France. Email:* Shinichi.toyama@oecd.org

Abstract

In the framework of the Generation IV International Forum (GIF), the Sodium-Cooled Fast Reactor (SFR) Component Design and Balance-of-Plant Project Management Board (CD&BOP PMB) was composed until 2011 of four research organizations representing nations participating in research and development of SFR concepts : DOE/ANL from USA, CEA from France, JAEA from Japan, and KAERI from the Republic of Korea. From 2007 to 2011, the CD&BOP Program has been conducted according to the initial Project Plan and completed. This paper aims at presenting the major achievements of the Project, mainly in four technological domains : Supercritical CO_2 Brayton cycle energy conversion systems coupled with a SFR, In-Service Inspection & Repair, innovation in Steam generators design, and Leak-Before-Break assessment. The Project is continuing under a new Project Plan (2012-2016) which includes two new partners : the European Community and the Russian Federation.

1. INTRODUCTION & CONTEXT

The SFR Component Design and Balance of Plant Project was formally initiated on October 11th, 2007, with the signature of the Project Arrangement by the Commissariat à l'Énergie Atomique (CEA), the U.S. Department of Energy (DOE), the Japan Atomic Energy Agency (JAEA), and the Korea Atomic Energy Research Institute (KAERI). U.S. participants are Argonne National Laboratory (ANL) and Sandia National Laboratories (SNL). The main objective of the Project is to enhance the performance and economic competitiveness of Sodium-Cooled Fast Reactors (SFRs) through the development of advanced components and component-related technologies or through research and development of advanced energy conversion approaches like the supercritical carbon dioxide Brayton cycle or improvement in steam generator design and monitoring. In addition, the Project recognizes the significance of the experience that has been gained from SFR operation and upgrading in France, Japan, as well as the United States. Since 2007, the CD&BOP Project Management Board is holding one meeting per semester animated by a technical secretary from OECD. Every country has nominated a representative plus one alternative. A yearly program of the CD&BOP PMB is defined with contribution of the respective countries through technical deliverables and associated presentation to the audience during the planned meetings. These meetings are therefore the occasion for representatives to present and evaluate the respective actions in progress, and allow this PMB to gain a coherent overall view of R&D performed (national programs) and to plan for a future set of harmonized program of work. End 2011 the first CD&BOP Project Plan has been accomplished. The objective of this paper is therefore to draw a synthesis of these studies carried on during this first project plan and to present some trends of the second one in progress (2012-2016) where a significant modification relies in the integration process of two new members: the European Community and the Russian Federation.

2. GOALS AND OBJECTIVES

The viability of designing appropriate Sodium-Cooled Fast Reactor (SFR) components and balance of plant (BOP) has been demonstrated with the design, construction and operation of previous sodium-cooled reactors. The main objective of this research and development (R&D) project is related to system performance, either through the design of advanced components and technologies to enhance the economic competitiveness of the plant, or by research and development on the use of advanced energy conversion systems in the BOP that could allow further cost improvements. This R&D project is dedicated to essential efforts to support the design at component level.

The objective of the Project is to conduct collaborative research and development of components and balance-of-plant (BOP) for the SFR System. Therefore the Project has to satisfy the GIF's criteria of

safety, economy, sustainability, proliferation resistance and physical protection. Activities within this Project are addressing experimental and analytical evaluation of advanced in-service inspection, instrumentation and repair technologies, leak before break assessment, development of advanced energy conversion systems with Brayton cycles including the supercritical carbon dioxide (S-CO_2) Brayton cycle, advanced steam generator technologies, detection of steam generator failure, sodium-water reactions, and include other relevant activities related with components and BOP system designs. The project will ultimately include assessment of the feasibility of the technology for desired utilization. Project activities will be based in part on the extensive historical R&D experience with component design and balance of plant for sodium-cooled fast reactors.

3. COMPONENT DESIGN & BALANCE OF PLANT : DESCRIPTION OF THE MAIN TECHNOLOGICAL DOMAINS AND WORKS PERFORMED

3.1. COMPONENT DESIGN

The main area of R&D for component design is related to development of in-service inspection and repair (ISI&R) technologies that can enhance plant availability and lifetime of advanced SFR designs. The R&D category of ISI&R also contains development of the assessment procedure of leak before break (LBB). For sodium-cooled plants, it is believed that sodium leakage monitoring is a method that has enough precision and reliability to early detect the breach of the sodium coolant boundary and being able to localize it as well. However, for highly stressed structural components filled with sodium coolant and sodium boundaries, Non-Destructive Evaluations (NDE) are also required. While not a viability issue, advanced in-service inspection instrumentation and repair methods must be developed to enhance the performance of advanced SFR designs and to improve their load factor. Thus, improvement of ISI&R technologies is important to confirming the integrity of safety related structures, and to repair them in place in case of some identified default. Development of high quality sensors, remote-handling systems in sodium, and maintenance and repair equipment is necessary and has been presented all along this project. In particular :

- Improvement of ultrasonic application to non-destructive volumetric examination, telemetry, and visualization;
- Perspective/approach on reactor core surveillance;
- Study of two sensor types for double-walled tubes of steam generators;
- ISI&R requirements taking into account demands of utilities and main objectives of future SFRs;
- Repair technologies development and specifically remote sodium removal with laser techniques.

In addition, the guide for high temperature LBB analysis and defect assessment has been presented recently in several countries. While these guidelines propose comparatively well-established evaluation procedures for high temperature defect assessment of austenitic steels, the guidelines applicable to ferritic martensitic steels (FMS) such as Modified 9Cr-1Mo steel are comparatively incomplete. The creep-fatigue crack initiation and growth behavior in ferritic martensitic steels (FMS) such as Modified 9Cr-1Mo steel are to be studied by both experimental efforts and analytical approach. The tentative guides for high temperature defect assessment applicable to steels - including FMS structure - are to be developed :

- Experimental studies of the kinetics of crack growth under creep condition;
- Determination of requirements for sensitivity of sodium leak detection methods;
- Development of the technique of justification of the “leak before break” concept in application to SFR reactor facilities;
- Calculational validation of the technique.

3.2. BALANCE OF PLANT

S-CO_2 Brayton cycle

From the economic point of view, Advanced Energy Conversion Systems (AECSs), such as Brayton cycles in the BOP offer the possibility of increasing the thermal efficiency of the plant and decreasing the capital costs by replacing the typically larger turbomachinery components in a Rankine steam cycle.

Supercritical CO_2 (S-CO_2) has been identified as a candidate fluid because of the temperatures involved in the cycle and the potential compactness of the BOP equipment, the turbine and compressors, in particular. The S-CO_2 cycle offers the potential for surpassing 40 % efficiency in energy conversion, even at the typical 550°C sodium coolant outlet temperature of reference SFR designs. The S-CO_2 cycle is therefore well matched to the SFR. The cycle wants to operate with a CO_2 temperature rise in the sodium-to-CO_2 heat exchanger of about 150°C which is approximately the primary sodium temperature rise through the reactor core. The use of a Brayton cycle is maintained as an advanced alternative to the reference design using a Rankine steam cycle BOP. Therefore, the R&D stages for S-CO_2 BOP development, to assess the feasibility of coupling a Brayton cycle to an SFR and the development of technology for coupling the S-CO_2 cycle to SFR reactors, have been identified in this project. The R&D should focus on the conceptual design of a S-CO_2 power generating system coupled to a reference SFR and the evaluation of its performance and potential safety implications. Research and development activities of interest are including :

- Conceptual design studies and assessments, including thermodynamic optimization for SFR conditions, studies of S-CO_2 cycle components, conceptual designs for sodium-to-CO_2 heat exchangers, and investigation of material implications including reactions of the CO_2 working fluid with candidate materials.
- Studies of technical performance and cost, including investigation of the safety implications of failure of the sodium-CO_2 boundary.
- Experiments investigating the behavior of sodium-CO_2 interactions and heat exchanger phenomena including the performance of heat exchanger technologies for sodium-to-CO_2 heat exchange.
- Investigation, development and verification of control strategies for S-CO_2 Brayton cycles with SFRs encompassing normal operation, operational transients and postulated accidents.
- System level dynamic analyses of S-CO_2 cycles coupled to SFRs encompassing operational transients and postulated accidents.
- Validation of individual models in the dynamic analyses as well as integrated dynamic analyses through comparison with experiment data from separate effects testing of turbomachinery and heat exchangers as well as integral S-CO_2 cycle demonstrations.

Steam Generators (SGs)

As described before, the CD&BOP R&D activities include and started with the development of Advanced Energy Conversion Systems (AECS) based on the S-CO_2 Brayton cycle which represents an advanced alternative to the Rankine steam cycle for SFRs. In parallel, studies of sodium-heated steam generators have been joined in this Project Plan since 2010, and are still on-going. Indeed, steam generators are one of the key components of SFRs (current and future generation) and require high reliability because of the possibility of sodium-water reaction. Various kinds of steam generators have been examined and evaluated since the early stages of SFR development in the world. But recently, most of the nations that are developing SFRs are reinvestigating innovations in steam generator design to enhance their robustness regarding sodium-water reaction as well as their efficiency. Thus, even if S-CO_2 is considered as a promising advanced alternative to steam, it is still considered as not mature enough to be implemented on an industrial SFR reactor in the near future. This situation justifies that both energy conversion systems and thermodynamic cycles (steam/Rankine cycle and S-CO_2/Brayton cycle) are studied in parallel in this Project. For the Rankine cycle, the works performed are focused on :

- Conceptual design studies and assessments, including thermodynamic optimization for SFR conditions, and comparison between SG designs or options (modular versus monolithic, straight-tube versus helical-coiled tube, double-tube walled versus single-tube walled).
- Studies of technical performance and cost, including investigation of the safety implications of failure of the sodium-steam boundary, recent performance of rapid detection systems.

4. SOME SIGNFICANT RESULTS OBTAINED DURING THE CD&BOP FIRST PROGRAM PLAN (2007-2011)

The purpose of this chapter is not to provide an exhaustive presentation of all the fields covered by CD&BOP because the list would be too long. It must be kept in mind that around 20 deliverables are produced per year from the whole group (leading to an average of five deliverables per country). This chapter will therefore highlight some significant achievements and will try to show through these selected examples how this GIF collaborative organization is revealing synergies.

ISI&R

In the field of In Service Inspection & Repair, KAERI developed an Ultrasonic Waveguide Sensor for Under-Sodium Visualization. After a first feasibility test performed in water, the program realized under-sodium test (performance test phase) using sodium test facility with glove box system and they realize performance verification by the ultrasonic beam propagation test and C-scan resolution test in sodium. The good resolution of some representative typical defects and sleeve in sodium at 200°C allows to confirm the potentially of this instrument for under sodium visualization with a good accuracy and comply the default detection limit. The program is now pursued towards some performance enhancement of the sensor and of some specific inspections.

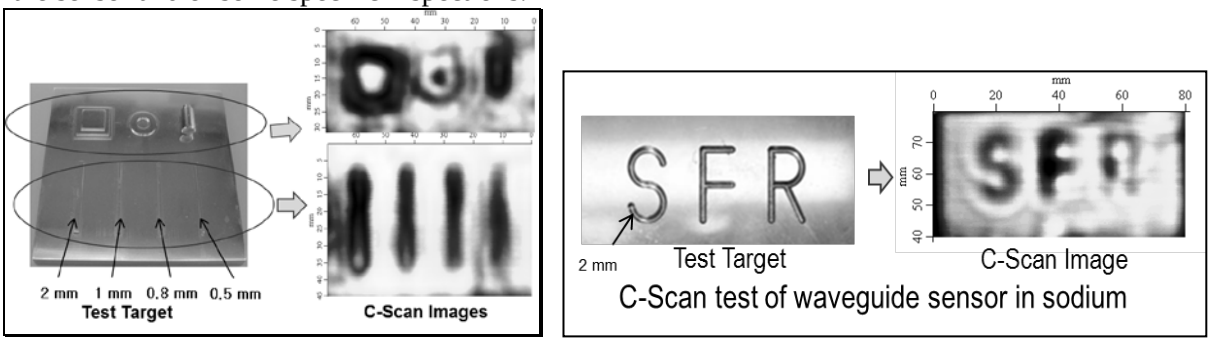

Fig 1. : In sodium test of several targets

Complementary, CEA has performed a thorough investigation of the wetting effects of metallic pieces in hot sodium. Metallic structures are not wetted by sodium at 200°C or below, and this phenomenon could induce a total blockage of the UltraSonic wave transmission. This wetting phenomenon is therefore of prime importance to allow a good signal transmission and further under-sodium image scanning resolution. This study revealed the importance of the temperature in the wetting effect where 350°C appears to be a transition temperature between non wetting (below this T°) and wetting (over this value). In addition some experimental tests revealed the influence of metallic material, coatings (nickel, gold, and beryllium) and the surface treatment (roughness) of the sensor. All these fundamentals studies have direct applications on every in sodium sensor or instrument that must be efficient during the reactor shutdown (with a sodium temperature at around 200°C).

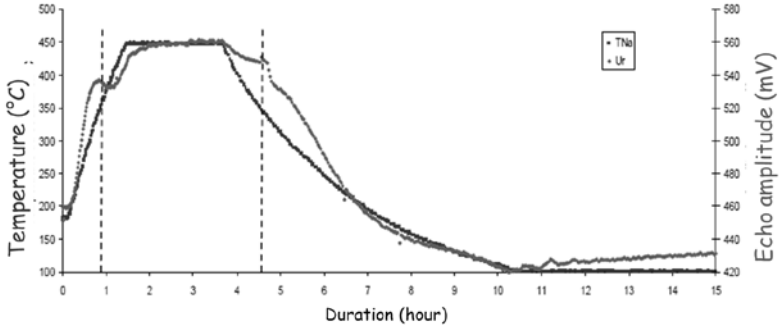

Fig 2. : Correlation between the temperature of sodium and the amplitude of the first echo reflected by the immersed end of the wave guide.

JAEA also performed the development of a New Inspection Technology for ISI of Double-Wall Steam Generator tubes in JSFR using multi-coil, remote field eddy current and magnetic sensors in coherence with the design of their Double-Wall tube steam generator for JSFR.

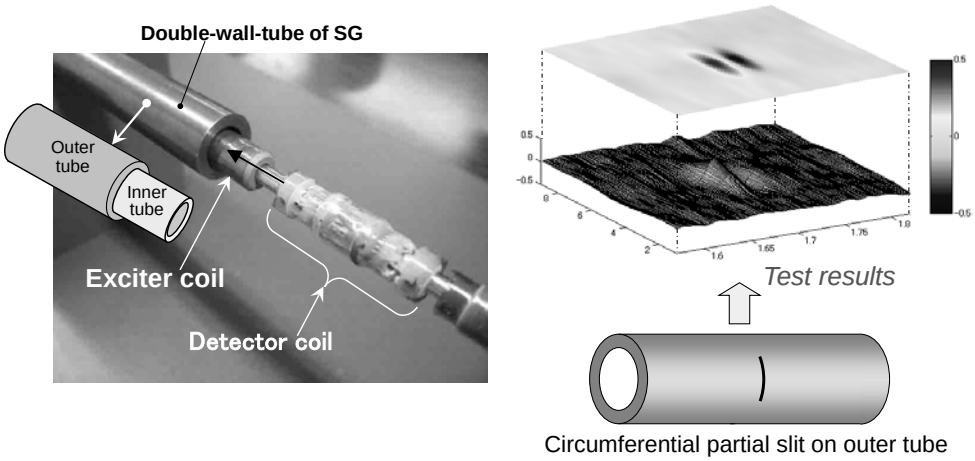

Fig 3. : Multi-coil RF-ECT (Remote Field - Eddy Current Testing) sensor

LBB

Mod.9Cr-1Mo steel is currently favored structural material for several of the high temperature components in a Sodium-cooled Fast Reactor. However it is not feasible to conduct a high temperature leak before break and flaw assessment for Mod.9Cr-1Mo structures due to the lack of material data concerning its fracture toughness, fatigue crack growth, and creep-fatigue crack growth at elevated temperature conditions, and also the assessment technologies are not accomplished yet. The objective of this work performed by KAERI to GIF/CD&BOP is to develop high temperature defect assessment procedure for a leak before break evaluation for Mod.9Cr-1Mo steel structures. To achieve this object, the fatigue crack behavior, fracture toughness and creep-fatigue crack behavior have been studied by both experimental efforts and analytical approach since 2008. Latest works were focused on fatigue crack growth tests at elevated conditions and low cycle of loading frequencies in parallel with creep crack growth tests for Mod.9Cr-1Mo base metal CT specimen.

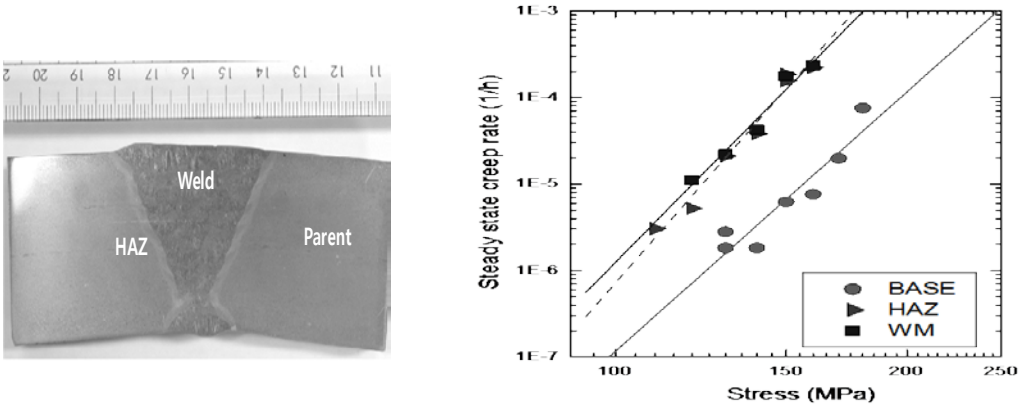

Fig 4. : Comparison of the Creep Crack Growth Rates lines for the Base Metal, Welded Medium and HAZ at 600 ℃

In the coming years, these studies will be pursued and might be complemented by LBB studies performed by Russia.

S-CO2 AECS

The field of investigations in the frame of the S-CO2 Advanced Energy Conversion System is wide and constitutes the most significant collaborative work performed within CD&BOP. From 2007 to now, several studies have been carried out by the four countries leading to complementary work or parallel studies that could lead to efficient benchmarks (in the frame of the Na-CO2 interaction or in S-CO2 corrosion studies for instance) or collaborative works (development and use of PDC code).

$S\text{-}CO_2$ R&D items	DOE/USA	JAEA/Japan	CEA/France	KAERI/Korea
1. Power cycle				
1,1 Conceptual design				
(1) $S\text{-}CO_2$ system	x	x	x	x
(2) Thermodynamic efficiency	x	x	x	x
1.2 Experiments				
(1) $CO_2\text{-}CO_2$ Heat exchanger	x	x		x
(2) $Na\text{-}CO_2$ heat exchanger	x		x	x
(3) Compressor	x	x		
(4) Turbine	x			
(5) Power cycle ($S\text{-}CO_2$ loop)	x	x		
2. Operation and control of $S\text{-}CO_2$ cycle				
2,1 Steady state	x		x	x
2,2 Transient state	x		x	x
2,3 Controllability	x		x	
3. Sodium/CO_2 reaction				
3,1 Reaction mechanism	x	x	x	x
3,2 Failure detection	x		x	x
3.3 Safety device regarding HX failure	x			
3.4 Specific Na technology development	x		x	
4. Material tests				
4.1 Corrosion effect vs time		x	x	
4.2 Material compatibility and choice			x	
5. Cost Evaluation				

Fig 5. : R&D Work Partition among the CD&BOP Members (Current Situation updated from the 2010 Table)

This entire subject has been already presented on a previous 2010 paper. Since then major progresses have been carried out in :

- Analysis of Control Strategies and Component Performance for the S-CO2 Brayton Cycle Using the DOE/ANL Plant Dynamics Code.
  - Control strategy for S-CO2 Brayton cycle has been extended to enable use of cycle to remove heat from a SFR at decay heat power levels (down to 3 % nominal) at which time switchover can be made to the normal shutdown heat removal system or a passive decay heat removal system such as a DRACS - Capability achieved through introduction of shaft speed control for single turbomachinery shaft following reduction in grid load to zero and disconnection of generator from grid.
- Investigation of Sodium Plugging in Compact Diffusion-Bonded Heat Exchanger Channel Configurations.
  - A series of experiments was performed at DOE/ANL to investigate the potential for plugging of narrow flow channels of sodium by impurities (e.g., oxides). The primary objective was to see if small channels whose cross sections are semicircles of 2, 4, and 6 mm in diameter are usable in liquid sodium applications where sodium purity is carefully controlled. It was concluded that the smallest of the three, could be used in clean sodium systems at temperatures even as low as 100 to 110°C without plugging. In the second phase, sodium oxide was added to the loop, and the oxygen concentration in the liquid sodium was controlled. Intentional plugging was induced by creating a cold spot in the test sections, and the subsequent plugging behavior was observed. Unplugging of the plugged channels was accomplished by heating the affected test section.

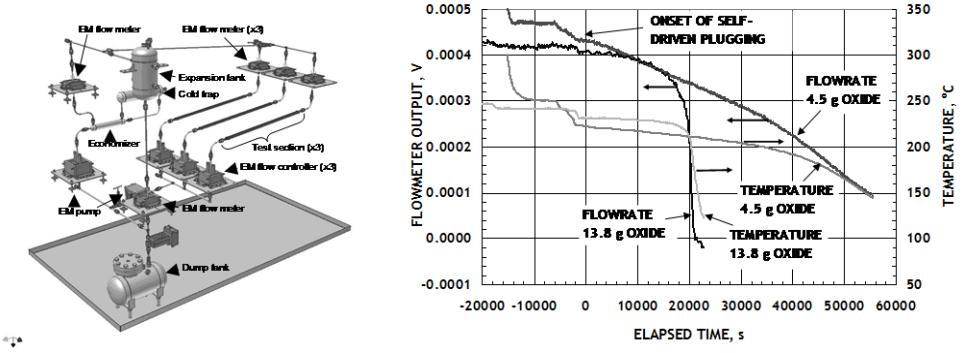

Fig 6. : Some typical results produced by the ANL Na plugging loop

- Study of the corrosion kinetic of different steel in contact with S-CO2.
    - The cross comparison between JAEA and CEA corrosion tests is coherent : JAEA is working with long term coupon over 8000 hours and CEA with 1000 hours. The purpose now is to provide a corrosion phenomenology explanation in order to propose either specific steels or preliminary treatment enable to reduce this corrosion rate with ferritic steels.

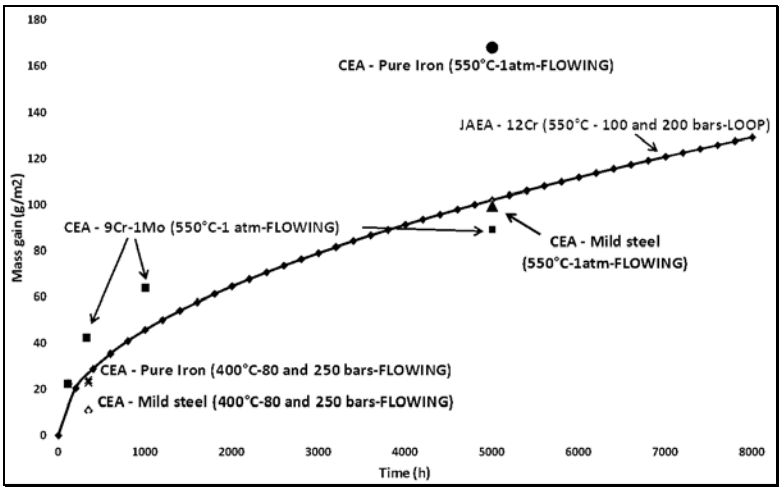

Fig 7. : Corrosion rate curve where is plotted CEA and JAEA experimental tests.

- In addition we shall mention other numerous studies like :
    - Development of compact Na/CO2 heat exchanger with optimized channel shape on CO2 side performed by KAERI,
    - Continuation of the Na-CO2 interaction by modeling (CEA) or by future experimental tests ore reproducible of a channel CO2 leak through failure or small breach (ANL &KAERI projects).

STEAM GENERATOR IMPROVEMENTS

This subject has been recently added to CD&BOP (since 2011). KAERI and JAEA are presenting the design of their respective double-walled tube steam generator and mainly focus on the double-walled tube fabrication constraints. CEA has presented its safety approach on steam generator regarding the occurrence of sodium/water reaction, its monitoring and the development of relative specific instrumentation (hydrogen diffusion membrane, hydrogen-meter performances and passive acoustic detection systems).

5. SYNTHESIS AND CONTINUATION OF THE CD&BOP PMB

This brief overview of all subjects covered by GENIV SFR CD&BOP is illustrating the coherence of the studies carried on within this group especially under the ISI&R and S-CO2 AECS items.

For continuation of this collaborative studies performed by the four countries, a new five year project plan (2012-2016) is now scheduled, with the continuation of these current items plus new proposals around instrumentation, repair technologies & monitoring. This project plan remains to be officially signed by state members but has already started by anticipation.

Furthermore, the most significant evolution of this new project plan would be the integration of two new members : the European community and the Russian federation. Both have been accepted since end 2011 as observers and have proposed future studies to be produce through VD&BOP PMB, and that are matching with the items currently treated (mainly in ISI&R, LBB and SG).

6. CONCLUSION

This paper wanted to summarize and highlight the excellence of the works performed and shared by the four member countries since 2007. Beyond the current program of work and due deliverables, the CD&BOP Project Management Board has largely facilitated the exchanges through national research organisms and searchers to produce a very interesting and efficient international network in the field of

SFR technology. The enlargement of the CD&BOP PMB to new members is a real asset to confirm the high level of expertise of this enlarged international commnity.

ACKNOWLEDGMENTS
The reported work represents the efforts of over sixty individuals at CEA Cadarache Marcoule and Saclay, DOE/ANL, Kansas State University, DOE/SNL, JAEA O Arai and Monju research centers, Tokyo Institute of Technology, Mitsubishi Heavy Industries, and KAERI.
PMB members would also like to recognize the precious role and the large contribution to the CD&BOP PMB efficiency of the OECD technical secretaries: Y. OKANO from end 2006 until mid-2009, M. TAKANO (mid 2009 until 2011) and S. TOYAMA the present one.

REFERENCES

1. The Generation IV International Forum, http://www.gen-4.org
2. M. ICHIMIYA, “The Status of Generation IV Sodium-Cooled Fast Reactor Technology Development and its Future Project”, Energy Procedia, Volume 7, 2011, Pages 79-87.
3. J. SIENICKI et al., “International collaboration on development of the supercritical carbon dioxide brayton cycle for sodium-cooled fast reactors under the generation IV international Forum Component Design and Balance of Plant project”, Proc. of ICAPP 2010, San-Diego, CA, USA, June 13-17, 2010.
4. G. L. FIORINI et al., “European Commission – 7th Framework program. The collaborative Project on European Sodium Fast Reactor (CP ESFR)”, Proc. of ICAPP ’09, Tokyo, Japan, May 10-14, 2009.

Development of experimental facility platform in support of the ASTRID program

G. RODRIGUEZ, L. AYRAULT, J. DUMESNIL E. SANSEIGNE, F. DUJET,
B. COLLARD, F. SERRE, C. JOURNEAU
CEA Cadarache -CEA/DEN/CAD/DTN
Blg 710, 13108 St Paul lez Durance - FRANCE
Contact author : Gilles RODRIGUEZ, +33442257437, gilles.rodriguez@cea.fr,

Abstract

The design of the ASTRID French Sodium Fast reactor prototype implies the development of innovative concepts in multiple and various domains such as energy conversion system, thermo hydraulic, core design, fuel handling, In Service Inspection & Repair, Large Flow Electro Magnetic Pump, etc... In many cases the qualification of innovative options has to be confirmed thanks to experimental tests. Thus, the development of the ASTRID project is including in parallel the development of technological infrastructures in support of the R&D program to be performed; and also in support to the future qualification of specific ASTRID components. Therefore the identification of technological facility needs and their construction is a process in operation since 2007, and that has led to the definition of four technological facility platforms. This paper is presenting this infrastructure definition and then describes the potentiality of these four platforms devoted to innovation in sodium technology (PAPIRUS platform), in water testing for hydraulic qualification (GISEH platform), large scale component qualification (CHEOPS platform), severe accident behaviour and mitigation demonstration (PLINIUS SFR platform and FOURNAISE facility). The international involvement is also described.

1. INTRODUCTION & CONTEXT

The design of the ASTRID French Sodium Fast reactor prototype implies the development of innovative concepts in multiple and various domains such as energy conversion system, thermo-hydraulic analysis, core design, fuel handling, In Service Inspection & Repair, Large Flow Electro Magnetic Pump, etc... In many cases the qualification of innovative options has to be confirmed with experimental tests. Thus, the development of the ASTRID project is including, in parallel, the development of the technological infrastructure in support of the R&D program to be performed; and also in support to the future qualification of specific ASTRID components.

Historically the sodium facility infrastructures in support of Fast Reactor Program were located mainly at CEA/CADARACHE research centre for technology, and at CEA/GRENOBLE research centre for thermo-hydraulic studies [1, 2]. This sodium technology infrastructure has been in permanent evolution to be in coherence with the French SFR program and chronologically in phase with the SUPERPHENIX final shutdown (1998) – and its subsequent decommissioning phase, the technical support to the Phénix reactor operation (1974-2009) and afterwards the launch of R&D innovation studies in Fast Reactor (2006-2009) leading to the ASTRID project (starting in 2010). In 1995, CEA began cleaning all dated and non-upgradable sodium facilities no longer in use. From 1995 to 2005, over twenty sodium facilities at Cadarache were dismantled or put under cocooning situation. The CEA/Grenoble sodium technology platform has been entirely decommissioned. In that period of time, CEA aimed to relocate all the necessary sodium loops into the same building with other test facilities used in R&D studies focusing on different coolants such as lead, lead/bismuth, helium and lithium. Fig. 1 shows the evolution of the number of sodium loops under operation.

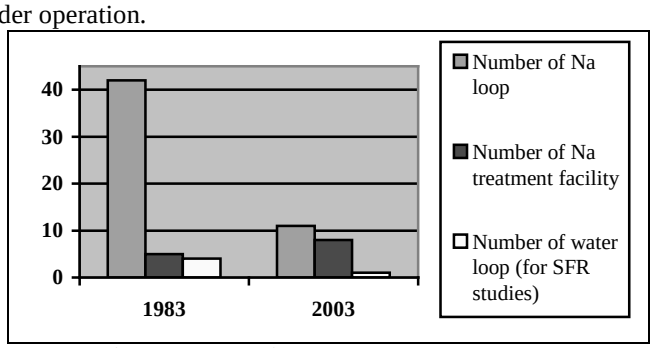

Figure 1: Inventory of sodium coolants facilities used at Cadarache in 1983 and 20 years later

As soon as an ambitious R&D SFR program was set towards the definition of innovative concepts in SFRs [3, 4], a thorough analysis of the future qualification and experimental tests and the corresponding facility needs was started. Since 2007, this evaluation, performed in parallel with the R&D studies, has led to structure the facility infrastructure in four technological platforms covering actual and future R&D needs plus ASTRID component qualification [5]. The paper will start by describing the general approach leading to this platform definition, and then a technical presentation of every proposed technological platform.

2. DEFINITION OF THE TECHNOLOGICAL FACILITY PLATFORM FOR ASTRID PROGRAM

2.1. The methodology

As presented in chapter 1, there was already a CEA fleet of sodium testing facilities which was not – at the time of the SFR-ASTRID program launching – in total adequacy with the project's future need. Therefore, a methodology was performed by starting three actions:

- Action 1: By anticipation, we defined the future R&D needs and experimental qualification tests with respect to the pre-selected innovative options to investigate.
- Action 2: An identification of the facility requirement has been carried out with respect to the needs determined on the previous action. The different facility requirements were set in terms of technological possibility, power, performance, accuracy and instrumentation needs.
- Action 3: In parallel, a detailed examination of the different existing sodium loops has been launched in order to determine the status of each loop: actual load factor, potential performance, whether the facility is in good or bad repair, etc. In case of bad repair, the cost and delay of this refurbishment was evaluated. At this step, it was possible to determine every sodium facilityaccording to the following criteria : 1- facility interesting to be refurbished, 2– facility in an outdated state which drives to complete decommissioning.

These three actions had led to identify an exhaustive table list of the future R&D needs & the facility requirements. It becomes then easier to determine line by line if:

- Case 1 : the R&D needs were already fulfilled by an existing facility in operation,
- Case 2 : the R&D needs can be fulfilled by a facility which requires first refurbishment actions,
- Case 3 : the R&D needs were not fulfilled by any existing facility. In that case the design of a brand new facility has to be considered. It is also investigated the opportunity to find out if some international program or foreign facility could reply to this situation.

This important work allowed proposing a development and action plan in terms of needs, requirements, facility fleet, performances, budget, and schedule for the SFR R&D supporting facility platform. This pluri-annual action plan has been initially validated by the CEA SFR Program Direction and confirmed by external experts from EDF and AREVA. Since, this Action Plan is yearly re-evaluated, principally to adjust the platform orientation from the R&D and ASTRID orientations and potential evolutions. End of 2009, in a broader investment plan for the future, ASTRID was identified as one of the priorities to receive governmental funding [6]. The funding of this Facility platform plan is integrated within this government funding.

2.2. Synthesis of this work

This work has led to the following main conclusions :

- A large number of already existing sodium facilities could be involved in the ASTRID supporting R&D works; bearing in minds that in most cases significant refurbishment works were necessary to remove asbestos, and to integrally renew the electricity and control panel board,
- A debate has taken place between the refurbishment of an aged sodium facility with the possibility of getting "bad news" during the refurbishment work[1] in balance with designing a brand new facility[2]. The compromise was to put a go-no go decision either to refurbish or not the facility, after its heat insulator removal and after a diagnosis phase checking the overall tightness of the facility, some representative weldings and some highly thermally solicited structures.
- It appears impossible to transform or adapt a lead or lead/bismuth facility to a sodium facility. This idea has been quickly abandoned.
- For new facilities to be commissioned, it is necessary to keep in mind at their early design stage that they must keep a large flexibility in their performance to be adjusted to R&D needs in permanent evolution.
- With time, it is necessary to investigate the effect of ageing not only for the existing facility but also the ageing of the building containing those facilities. Rules and regulations in civil engineering are in constant evolution too, and in some cases the building refurbishment work has to be investigated too.
- In some specific cases, we identified that some technological gaps could be covered by a foreign facility. This has led to identify some international collaborative works. One significant example is the Wastage tests performed at O Arai research centre (Japan) by JAEA in 2011 [7].

The number of facilities identified to support the ASTRID program is quite large (around 50 facilities or specific programs). Therefore for sake of simplicity and to rationalize the renovation and design works, this amount of facilities was shared into four technological platforms covering the entire R&D and component qualification domains. These four platforms are :

- PAPIRUS[3] platform : It is a set of small sodium loops for in sodium experimental tests. These facilities can be devoted for modelling code qualification, in sodium instrumentation, specific technological or mechanical concepts, or determination of dissolution & corrosion laws in sodium for core or structure materials.
- GISEH[4] platform : It is a set of loops and mock up used with simulant fluid (water or air) allowing the qualification of thermo-hydraulic codes or validating hydraulic data of the primary vessel (hot/cold plenum),

[1] *For instance discovering unexpected sodium small leak or material/weldings cracks when the whole facility is removed from its heat insulator.*
[2] *With no risk links to facility obsolescence but with longer construction delays and greater investment costs.*
[3] ***PAPIRUS** for **Pa**rc des **P**etites **I**nstallations de **r**echerche sur l'**U**tilisation du **S**odium (Fleet of Small research Facilities on the use of Sodium)*
[4] ***GISEH** for **G**roupement des **I**nstallations en **S**imulant **E**au pour l'**H**ydraulique (Group of facilities in water simulant for hydraulic studies)*

or some complex part of specific SFR components (water collector in Steam Generator, hydraulic in Fuel Assemblies).

- CHEOPS[1] platform : This platform is a group of large sodium facilities devoted to qualify either the future ASTRID components (Fuel handling Machine, Fuel Cask,…), or mock-up of ASTRID components at significant and representative scale (Steam Generator mock up (scale around $1/10^{th}$), Large Flow Electro Magnetic Pump, Sodium/Gas heat exchanger (in case of selection of a gas Brayton cycle [8],…).
- PLINIUS[2] SFR platform : PLINIUS platform is a set of facilities dedicated to studies linked to severe accident for GEN 2/ GEN 3 reactors. PLINIUS SFR will be an adaptation/extension of this platform to take into account the specificity of Sodium Fast Reactors in this domain.

3. DESCRIPTION OF THE FOUR TECHNOLOGICAL PLATFORMS IN SUPPORT OF ASTRID

It would be fastidious having an exhaustive description of all the facility involved in ASTRID program. The total list of operational, under project and in construction is representing a number of around fifty facilities that cannot be extensively presented in this paper. Therefore for each platform, the purpose will be to present its overall structure and then to highlight only some significant or remarkable facilities.

3.1. The PAPIRUS platform

PAPIRUS platform is gathering the group of small non-active sodium loop. The generic term of «small non-active sodium loop» means a technological facility where non-radioactive sodium is in circulation. The volume of sodium involved in this kind of facility can vary from 1 to 1000 liters. This ensemble of facilities is used for :

- Item n°1 : The qualification of in-sodium instrumentation at SFR representative operating conditions in terms of flow and temperature. It gathers the qualification of instrumentation for core surveillance [9], coolant quality control (Hydrogen meter, Oxygen meter, plugging indicators), sodium leak detection, sodium water reaction fast detection [10], In Service Inspection tools (US sensors, EMAT sensors, …) [11].
- Item n°2 : The technological qualification of innovative and complex systems or components such as : robots for repair or ISI measurement, qualification of complex mechanical device like SEPIA system [12], Electromagnetic pumps with high Reynolds number [13], Sodium/Gas heat exchanger mock-up [14], …
- Item n°3 : acquisition of specific data to qualify modeling code, in particular for : sodium mass transfer [15], kinetic of sodium impurities crystallization [16], sodium aerosols behavior in air [17] (for sodium fire scenario) or at sodium/gas interface, heat exchange correlation of sodium/gas compact heat exchanger [14],
- Item n°4 : Adjustment of innovative SFR processes that will be used on ASTRID reactor or validated on larger scale on the CHEOPS platform : cleaning process, sodium purification process, sodium aerosol trapping process, passive safety system (physical principles), decay heat removal systems, …
- Item n°5 : Testing and/or qualification of SFR innovative materials, coatings, weldings in contact with hot sodium to identify their behavior in time (ageing, corrosion resistance, creep fatigue, ductility) and their tribology properties [18].
- Item n°6 : In support of facilities constituting the PAPIRUS platform, it is necessary to get specific facilities directly linked with the specificity of sodium technology :
    - Sodium cleaning systems, glove boxes to operate under inert gas, adequate post testing examination capabilities mainly in physico-chemistry and in metallography,
    - Plus the entire infrastructure devoted to sodium technology knowledge transfer assured today at CEA by the Sodium School [19].

PAPIRUS platform is therefore today composed of twenty facilities in operation, under refurbishment or under construction phase. These facilities are dispatched between two CEA research centers :

- CEA/SACLAY where are located material studies performed by two in sodium corrosion benches (named CORRONa1 [20] and CORRONa2) supplying the needs for item 5, and a small bench testing specific instrumentation in sodium.
- CEA/CADARACHE which is concentrating in a same area (mainly in one building named HR4 : Reactor Hall n°4) all the other sodium facilities devoted to sodium technology and test qualification as described in Item 1 to 4.

3.2. Significant sodium facilities belonging to the PAPIRUS platform

a/ The CORRONa facilities

As soon as the innovative studies on SFR wanted to investigate the use of new materials, it was necessary to design a new set of experimental facilities to investigate material behavior in sodium. Therefore the design and construction of a first facility called CORRONa facility (Corrosion in Na) has been anticipated by the CEA-Saclay Corrosion

[1] ***CHEOPS*** *for* ***C****ircuits et* ***H****all d'Essais des gr****O****s com****P****osants en* ***S****odium (Circuit and facility hall of sodium large components test).*
[2] ***PLINIUS SFR****, PLatform for Increase of Nuclear Industry and Utility Safety.*

Study Service, and lead to its first in service testing early 2010. A complete description of the CORRONa1 facility can be found in the following reference [20]. CORRONa1 is a combination of two glove boxes (Figure 2). Each glove box contains a thermal well with a sodium crucible controllable in temperature, designed with a system of rotating cylinders to simulate the hydrodynamic, and a mini sodium-loop to control the chemistry (Figure 3).

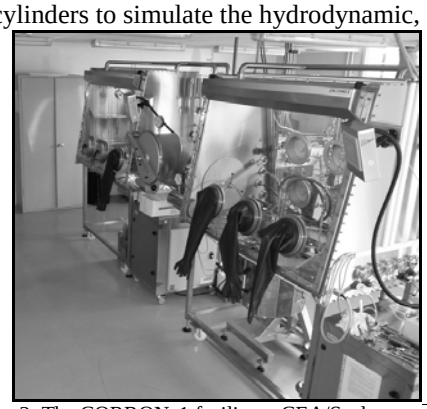

Figure 2: The CORRONa1 facility at CEA/Saclay research centre

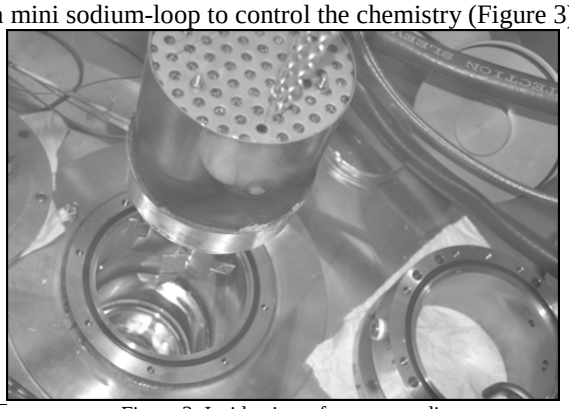

Figure 3: Inside view of an open sodium pot

The development of the R&D program and the increasing demand for in-sodium tests for material investigation (new materials for structures and steam generators [18], [21], for sub-assembly hexagonal cladding tube, or sacrificial material for core catcher [22]) has rapidly highlighted an important need of experiments arguing for the construction of a second complementary facility. The design of this second facility named CORRONa2 started in 2011 and its commissioning tests start in 2013. This second facility will largely extend the potentiality of CEA to realize in-sodium corrosion test. In addition it will open the scope of performances with the possibility to realize tribo-corrosion studies to qualify for instance hard coatings in sodium environment with continuous translation movements. Thus since 2010, CEA has acquired a brand new facility enable to respond with experimental tests to material corrosion behavior in static or dynamic hot sodium. In 2013, it is able to realize numerous tests in parallel, and will extend the performance towards the tribology domain.

b/ The PEMDYN facility

To ensure heat transfer from the core to the energy conversion system through the secondary circuit, the requirement on the pump flow is in a range of 2 to 4 m^3s^{-1} (120 to 240 m^3/min) and a pressure head of around 3 bar. One innovative option envisaged on ASTRID reactor is to provide all intermediate sodium loops to large flow Electro Magnetic Pumps (EMP), ALIP (Annular Linear Induction Pump) type. The design work of these EMP will be performed in collaboration with TOSHIBA Company who already experienced such type of large flow EMP (160 m^3/min) [23]. Neither the less, the following points require improvements and justified the creation a new test facility specifically devoted :

- The actual modeling tools are validated for pumps in a scale of flow from $10^{-5}m^3s^{-1}$ to $10^{-3}m^3s^{-1}$. It is required a validation domain up in a range from $10^{-2}m^3s^{-1}$ to 10 m^3s^{-1}.
- Experience in operating such ALIP EMPs (endurance tests, reliability, net efficiency of the pump, heat dissipation, …) is necessary.

Therefore, the construction of a new facility specifically devoted to the test of ALIP EMP was decided beginning of 2011. This facility called PEMDYN will consists in a simple closed loop connecting in a serial arrangement an ALIP EMP, heat exchangers and a regulating valve. A test section is placed for reservation for implementing additional instrumentations. The facility will be instrumented in order to acquire data on mass flow measurement, pressure drop and to measure the magnetic field.

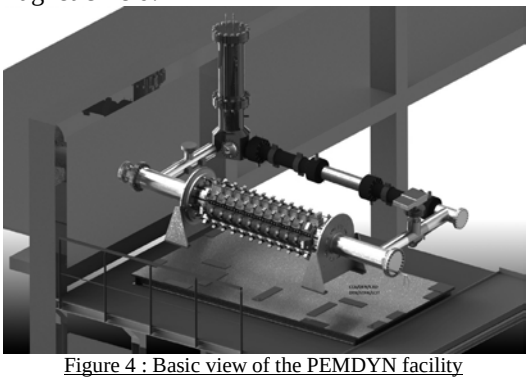

Figure 4 : Basic view of the PEMDYN facility

The ALIP EMP pump used on this facility will have an active length of 1 to 2 m, gap thickness : 0.02 to 0.05 m, frequency : 20 Hz, typical value of the magnetic field : from 0.05 to 0.1 T, flow rate : between 500 and 1000 m^3h^{-1},

magnetic Reynolds number : higher than 10, operating temperature of sodium : 120°C. Commissioning tests of the PEMDYN facility are planned in 2014.

c/ The DIADEMO Na facility

The study of an ASTRID option with Gas Energy Conversion System (ECS) is leading to an important R&D and design program work which is largely described in [13]. In this gas ECS, the key component remains the sodium/gas heat exchanger design which is integrating PCHE type modules in order to get a better heat power density compared to a standard shell & tubes HX type.

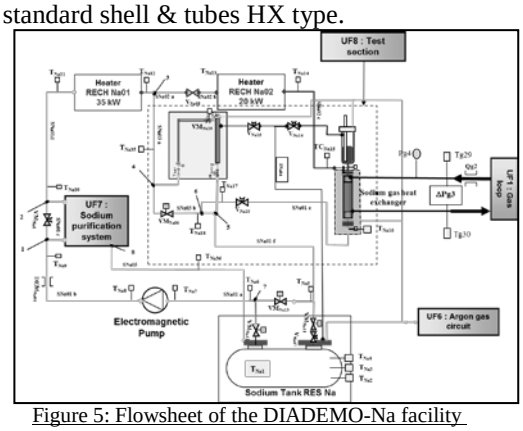

Figure 5: Flowsheet of the DIADEMO-Na facility

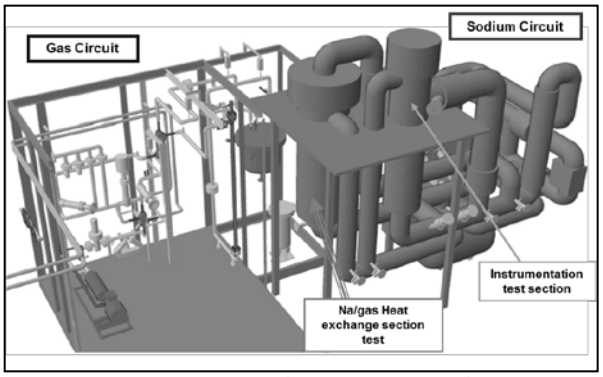

Figure 6: Partial 3D view of the DIADEMO Na facility

A PCHE type heat exchanger has never been used with sodium and it is therefore necessary to test mock-up in order to qualify this concept, to quantify the heat exchange correlations, to investigate challenges of the flow and metallic sodium in narrow channels (draining, cleaning, potential self-plugging, stop and restart, inspection, …).

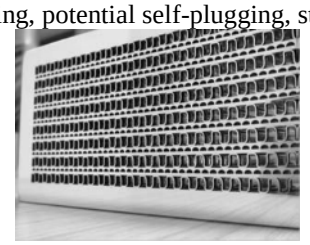

Figure 7 : Cut view of a PCHE type sodium/gas heat exchanger module, large channels are devoted to sodium circulation

Thus a facility named DIADEMO is under refurbishment and adaptation to allow the test of a sodium/gas heat exchanger mock-up with a 30 to 40 kWth power (see Figure 5 and 6). To do so, the DIADEMO facility which was a gas circulation loop for ITER tests, is under modification to implement a sodium circuit and to allow a heat exchange test section fully instrumented. In the design of the additional sodium loop, an independent sodium pot has been included to enlarge this facility potentiality. Specific instrumentation will be tested in this sodium pot. The modification of this DIADEMO facility shall end at the end of 2012 and the commissioning test plus first mock-up tests start first trimester 2013, the name of the facility will be changed to DIADEMO Na.

d/ Synthesis of the PAPIRUS platform

In addition to these facilities previously described, the PAPIRUS platform is today fulfilling an important program of work linked with ISI&R program and instrumentation qualification : six facilities are entirely devoted to this item. Today, the PAPIRUS platform is composed of 19 facilities or experimental benches (15 at Cadarache and 4 at Saclay) in operation or being operational before end 2013. It is planned to extend this platform to a maximum of 25 facilities at the end of 2017 (with the refurbishment of two other old sodium facilities and the creation of four new ones). At this time, PAPIRUS platform will be completed and fully adapted to the ASTRID R&D requirements.

3.2. The GISEH platform

GISEH platform is gathering the facilities working with simulant fluids (water or air) in support of the SFR program. This set of facilities will allow to :

- Item 1 : study and understand complex hydraulic phenomena that can occur in the internals of the primary vessel or in some specific components or group of components (hydraulic of the core outlet, impact of the Cover Core Structure, outlet of one fuel assembly or between two assemblies, …),
- Item 2 : validate numerical approaches and some hydraulic computing codes,
- Item 3 : highlight and investigate some complex physical hydraulic phenomenon like : unstable vortex, gas trapping at the free turbulent surface, vibrations and self-vibration of the whole system, …

Unlike sodium loops, the use of water or air simulant is bringing much more flexibility in the loop concept. The approach used in this case was to design two multipurpose water facilities distributing fluids in parallel to several Plexiglas mock-up designed according to the requested needs. Thus the GISEH platform is mainly based of two gross distribution facilities named ATHENA and PLATEAU (see Fig. 8), both located at Cadarache. In addition several existing facilities are under refurbishment or design process.

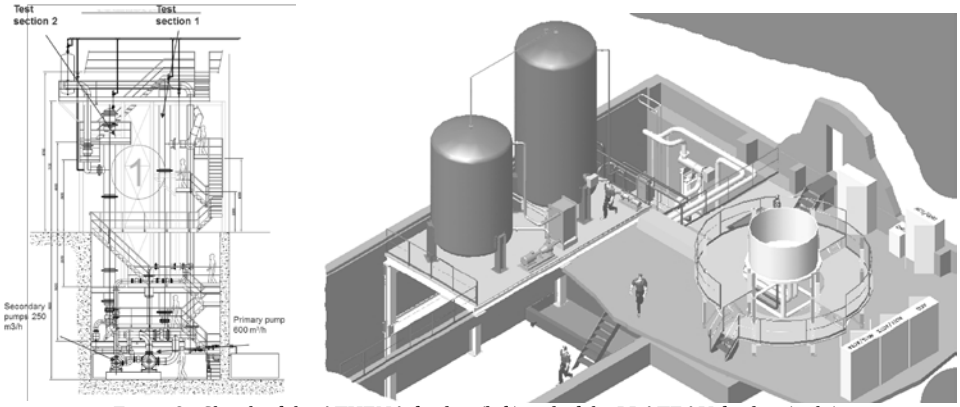

Figure 8 : Sketch of the ATHENA facility (left) and of the PLATEAU facility (right)

a/ Description of the CEA-CADARACHE-ATHENA facility

The main purpose of this facility in a realization phase is to provide water supply to all studies in connection with the core assembly technology and mechanical design : hydraulic, pressure drop, vibration, hydraulic jack, A scale 1 mock-up of all kinds of core assemblies (fuel, fertile, reflector, control rods,…) will have to be hydraulically tested within this facility. The commissioning tests of the ATHENA facility are planned for 2014.

b/ Description of the PLATEAU facility

The purpose of this facility is to test hydraulically different sections of the ASTRID primary vessel (when all options will be settled). By anticipation of this reactor vessel design, the work consists in implementing a water service facility to enable the distribution of water to several Plexiglas mocks-up in parallel. The needs are anticipated by analogy by the R&D and qualification works performed for the EFR project where mainly three Plexiglas mocks-up were necessary to describe the hydraulic behavior of the Reactor Vessel (see Fig. 9). The commissioning tests of the ATHENA facility are planned for 2013/2014.

Figure 9 : Picture of the several Plexiglas mocks-up used for EFR hydraulic qualification, from left to right : COCO mock-up representing the EFR cold plenum (scale 1/15th), COLCHIX mock-up representing the EFR hot plenum (scale 1/8th), JESSICA mock-up representing a section of the EFR hot plenum (scale 1/3rd)

c/ Description of the BANGA facility

The BANGA facility[1] is a new facility devoted to the study of the creation of unstable vortex and the condition of gas entrainment (see Figure 10). The principle of this facility is based on similar works performed by JAEA for JSFR application [23].

[1] *BANGA for Boucle d'ANalyse de l'entrainement de GAz – Analytical loop for Gas Entrainment.*

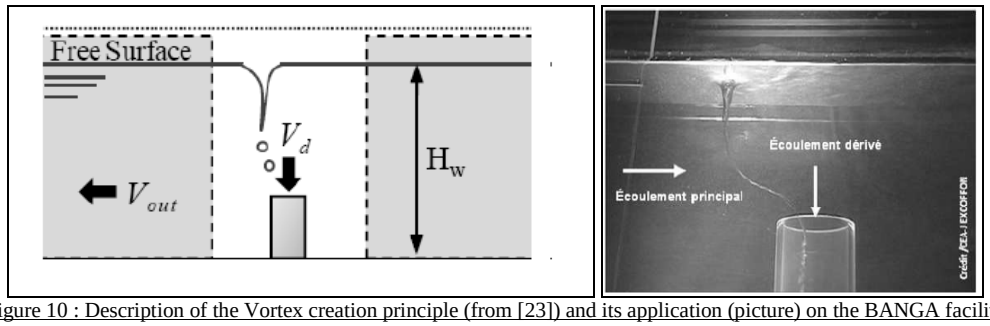

Figure 10 : Description of the Vortex creation principle (from [23]) and its application (picture) on the BANGA facility

The creation of unstable vortex is done with a rectangular vessel (mm 700x100x400) with a resting zone and a flooding zone. The height of the free surface can be adjusted, as well as height of the section nozzle. This facility has been built at CEA/Grenoble research center and the commissioning tests have been performed in the second semester 2012. This facility is in operation (see Fig. 11).

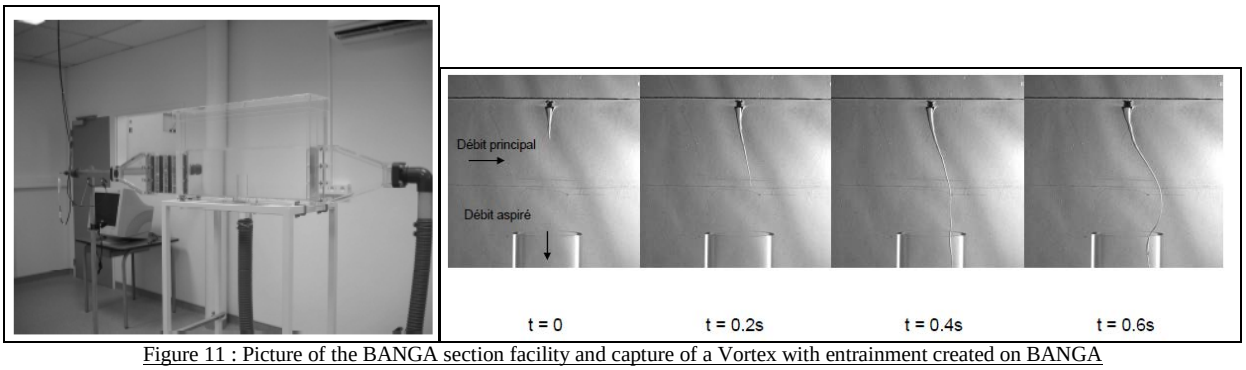

Figure 11 : Picture of the BANGA section facility and capture of a Vortex with entrainment created on BANGA

d/ Synthesis of the GISEH platform

In addition to the facilities previously described, it is interesting to note that some experimental facility used in R&D studies for Gas Fast Reactor technology have been extended to SFR needs with gas simulant, mainly in the area of high or very high temperature : i.e. 550°C and over. The completion of the GISEH platform is planned for 2016, at this time this platform will be composed of two major facilities (ATHENA and PLATEAU) and several (maximum 5) basic facilities, as BANGA. The number and scale of Plexiglas mocks-up are not entirely determined today, and will be fixed by the ASTRID primary vessel design option selected during the second phase of studies (2013-2015).

In first assumption, by analogy and according to the EFR feedback, the construction of three large Plexiglas mocks-up is today envisaged.

3.3. The CHEOPS platform

The CHEOPS platform is integrating a group of sodium facilities that will be necessary to qualify:

- Future components of the ASTRID prototype in representative conditions of the reactor operating conditions (pressure, flow, Na temperature, transients …).
- Scale 1:1 mock-up of the ASTRID fuel assemblies, to test mechanical behavior of these non-active mocks-up in core representative conditions and in case of thermal shocks (safety demonstration of the mechanical strength of the fuel assembly to fast transients during reactor SCRAM).
- Validation of active or passive safety systems in representative conditions (especially in terms of fast transients and high temperature).
- Validation of components at an intermediate scale between the R&D study and the ASTRID component, to reduce the scaling factor and to minimize the technological risks between the mock-up and the final component design. This is particularly important in the case of energy conversion system where the whole steam generator cannot be tested before due to its large power (100 to 150 MWth). Consequently an intermediate test with a mock-up of about $1/10^{th}$ power is unavoidable.
- Qualification of detection systems and measuring devices for ISI&R plus robots operating in an environment equivalent to reactor conditions.
- In addition, it is necessary to take into account sodium removal of all mocks-up after being tested and immersed in sodium. A large scale cleaning pit is then necessary.

The CHEOPS platform is therefore a large infrastructure grouping five to six facilities (depending on ASTRID option choices) to cover all ASTRID qualification needs in terms of components.

- NADYNE[1] facility will be a dynamic sodium facility enable to provoke thermal shock and fast transients to mocks-up representing all sub-assemblies family. This facility will be able to qualify ASTRID valves until a diameter of 300 mm too. Depending on ASTRID option choices, a part of NADYNE will be able to reproduce fast transient up to 700°C.
- NAIMMO[2] is a facility with large static sodium pots where fuel handling system, control rod mechanisms, ISI&R tools, core surveillance instrumentation can be tested. Due to the larger pot (diameter 4.4 m) some tests to improve Na-aerosols behavior in reactor cover gas will be possible too.
- NSET[3] loop is a facility to be devoted to the test of a steam generator mock-up (power from 10 to 12 MWth), in stable conditions (different steps between 100% Nominal Power (NP) to 30% NP) and transients conditions (in case of fast reactor trip). An equivalent facility is envisaged if the gas conversion system is selected. In that case this facility will be devoted to qualify the sodium/gas heat exchanger coupling the intermediate sodium loop to the Brayton tertiary cycle.
- NAPEM facility will be a dynamic facility able to test the ALIP EMP of the secondary loops of ASTRID.
- In addition a large cleaning pit is designed allowing the cleaning of all mocks-up and simulated fuel assemblies tested in NADYNE.

The CHEOPS platform will be a large building that regrouping these facilities. It will be located at Cadarache research center. The CHEOPS platform project is based on a completely new infrastructure (building + facilities). It must be noted that prior to this decision, the option of reusing past facilities and building developed for the PHENIX & SUPERPHENIX component qualification has been investigated. But these infrastructures were two old (in particular the building) and could not reply to new safety standards. Since one year, studies for CHEOPS platform are engaged and first tests will be possible at 2016/2017 after 4 years of building.

3.4. The PLINIUS SFR platform

The PLINIUS platform is a coherent set of facilities devoted to test severe accident with core melting. Indeed, severe accident prevention will necessitate the development of means for allowing to exclude highly energetic sequences in case of core melting. It will also necessitate proposing robust passive solutions for core catching and evacuation of the residual power in case of severe accident. It could also be used for out of pile tests with prototypic material that would be necessary to study the severe accident behaviour of innovative systems. CEA disposed of a platform for the testing and simulation of severe accidents. This platform called PLINIUS [27] is today devoted to GEN II/GEN III reactors, the purpose would be to adapt it to in-sodium core melting tests. The PLINIUS platform (www.plinius.eu) is made of:

- VULCANO: VULCANO is a 50-100 kg corium melting facility. It is possible to melt oxides and metals (in depleted uranium) and to mix them for a VULCANO experiment. VULCANO can be used to test the interaction of corium with core catcher molten materials. Both facilities cannot operate with sodium and will not be converted to handle sodium.
- COLIMA: COLIMA is a small scale (few kg) facility with induction heating (up to 170 kW) and a thermostatic 1.5 m^3 enclosure in which it is possible to monitor the gas atmosphere. COLIMA has been up to now used to study aerosols, material interactions, and physical properties. It is planned to test the effect of mixing with core catcher sacrificial materials on aerosol releases.
- KROTOS: KROTOS is a Corium-Water Interaction facility in which up to 5 kg corium is molten and dropped into water. Energetic steam explosions can be triggered and studied.
- VITI: VITI is suitable to small scale interaction experiments and to study of thermophysical and thermochemical properties. A levitating droplet device has been developed to measure corium viscosity and surface tension. Crucible tests have also been performed in VITI. It has already been used to test the interaction of potential SFR core-catcher sacrificial materials with UO_2-Fe [28, 29].

[1] *NADYNE for DYNamic Na*
[2] *NAIMMO for IMMObilised Na*
[3] *NSET for New Sodium Experimental Testing*

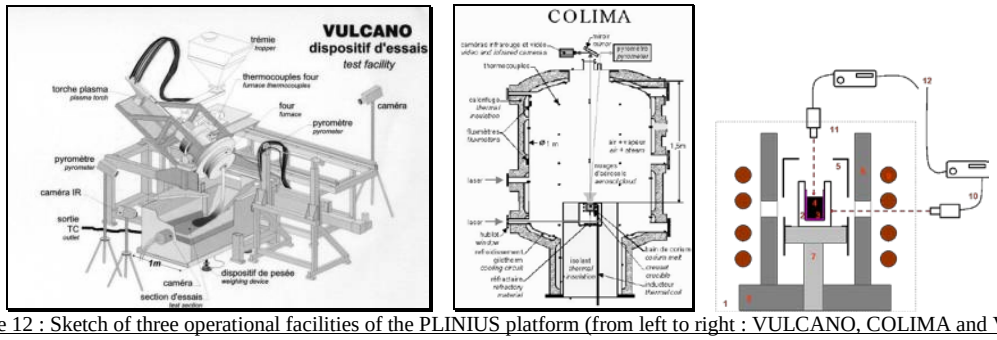

Figure 12 : Sketch of three operational facilities of the PLINIUS platform (from left to right : VULCANO, COLIMA and VITI)

Without sodium, the platform is already operational. With sodium, an analysis has concluded that a new facility shall be added to this PLINIUS platform devoted to SFR. This facility is now under detailed definition phase and called FOURNAISE [30].

a/ Description of the FOURNAISE facility

CEA is studying the construction of a new large scale corium facility to extend its current PLINIUS prototypic corium platform. This new versatile facility, called FOURNAISE (Furnace for Oxides of Uranium aimed at simulating Nuclear severe Accidents In large Scale Experiments), shall be devoted to both water and sodium-cooled reactor severe accident experimental simulation. Fuel Coolant Interaction experiments in the FARO facility at JRC ISPRA had shown the importance of large masses, allowing the study of steady state interaction with respect to premixing as well as debris bed and "cake" formation. Large oxide and metal pools are also necessary to study melt coolability issues. The FOURNAISE facility dedicated to 100-500 kg corium is currently under study at CEA, based on the FARO experimental feedback. Therefore, the FOURNAISE facility (Fig. 13) will be composed of:

- A furnace able to melt 100 to 500 kg of UO_2 containing corium (parametric calculations are underway to estimate the optimum mass to be considered).
- A transfer device, allowing also for the insulation of the furnace from the test section during energetic interaction. It also enables to predefine the jet initial conditions (diameter - as it has been done in the latest KROTOS experiments at Cadarache [8], pressure, temperature…).
- Various test sections, depending on the experimental programmes (e.g. fuel coolant interaction FCI (Fig. 14), jet ablation, corium material interaction).
- A sodium circuit, a steam quenching system and a corium powder workshop and storage and service rooms.

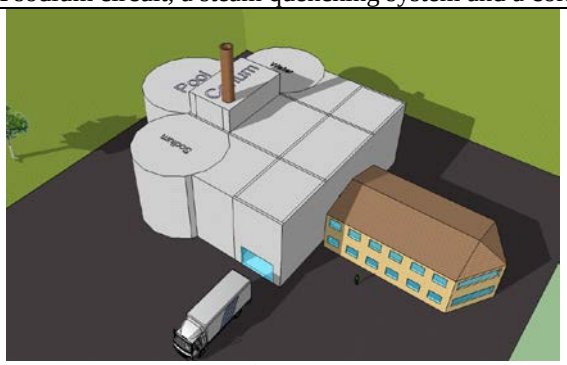

Figure 13 : Sketch of the FOURNAISE building

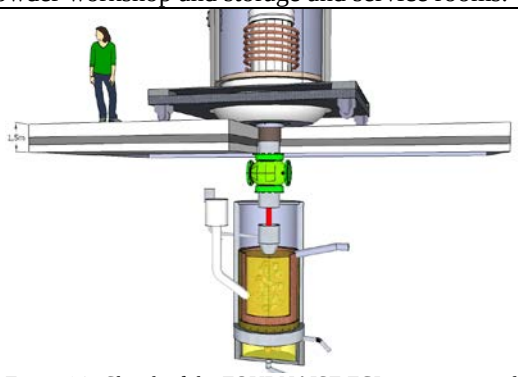

Figure 14 : Sketch of the FOURNAISE FCI test section and melting furnace

4. THE CEA POSITION OF SFR TECHNOLOGICAL STRUCTURE IN THE INTERNATIONAL CONTEXT

All countries working on SFR development have or had to develop their own testing facility infrastructure. Beyond the national program for ASTRID needs, it is necessary to integrate those facility platforms in an international context. Therefore cross-cutting activities have been initiated to find coherence between the various national testing infrastructures and also to identify common needs and potential lack of infrastructure in regards with the SFR R&D future challenges.

It is the reason why, in parallel of the development of its own facility platforms, CEA has pursued information exchanges and international contacts to:

- get the most accurate vision of the facility potentiality throughout the SFR International community,
- identify the R&D needs and gaps coming for other national SFR program and corresponding facility needs,

- evaluate the opportunity to mutualize R&D needs that can be performed in common existing facilities, or investigate the possibility to externalize some specific experimental tests necessary for ASTRID.

Thus, CEA participated in several expert groups aiming to exchange and present their list of facilities and to share their views on R&D needs/technological gaps/corresponding Na facility necessity. These expert groups were:

- TAREF[1] group organised by OECD [24]. The TAREF work (2008-2011), was an expert group to provide overview of facilities suitable for carrying out the safety research that was considered necessary for SFRs. The group started with a PIRT-like approach to identify the technical areas to address and establish a ranking with regard to safety relevance. For each of the safety issues, the TAREF members identified the related facilities that were deemed appropriate to address the issue in question, providing relevant information such as operating conditions, operating range, description of the section, type of testing, instrumentation, current status and availability, uniqueness, etc.
- ADRIANA[2] European project funded by the European Community (EURATOM) [25].The coordinating action ADRIANA has been initiated to set up a network dedicated to the construction and operation of research infrastructures in support of developments for the European Industrial Initiative for sustained nuclear fission. The project sets these objectives for the following reactor systems: SFR, LFR (Lead Fast reactor), GFR (Gas Fast reactor), Irradiation facilities and hot laboratories, Zero power reactors.

In addition, through bilateral or trilateral collaboration exchanges on SFR, CEA has recently engaged significant common works on foreign or French facilities, i.e.:

- In 2011, 9Cr tube wastage tests were performed on the SWAT-1R facility at the JAEA/O Arai research centre [7],
- In 2012, sodium leak detection test were performed on the FUTUNA facility[3] for IGCAR needs,
- Sodium aerosols behaviour performed on the MINA facility at IGCAR to improve the CEA model of sodium aerosols dispersion 2011-2012 [17],
- JAEA-CEA joint analysis of EAGLE1&2 in-pile tests on fuel discharge through mitigation devices in severe accident conditions, performed by JAEA and IAE/NNC RK[4] in IGR facility (Kazakhstan) [26].

Moreover, the CEA involvement in the GEN IV International Forum (GIF), and especially in all SFR Project Management Boards, allows CEA personnel to be informed of the program evolution and the corresponding capabilities in terms of technological infrastructures of the main actors in the field of Sodium Fast Reactors.

5. FACILITY REFURBISHMENT AND PLATFOM ORGANISATION

At the beginning the early identification of the R&D needs and corresponding facility needs was endorsed by the TECNA project (R&D project of sodium technology & Component development) with the help of numerous experts. When the definition of the four platforms was achieved (2010), a responsible person for each of them was identified. The four platforms are now connected to the corresponding R&D projects:

- PAPIRUS and GISEH linked with the so-called TECNA project,
- CHEOPS platform is linked with the so-called KEOPS project (project ownership of the corresponding platform),
- PLINIUS SFR platform is linked with the so-called SFRAG (SFR Acc. Grave - severe accident) project.

6. CONCLUSIONS

This paper is describing the studies performed on the development of experimental platforms in support of ASTRID program. At 2020 horizon, the four platforms comprising a total of around 50 facilities will enable system and component qualification and research data required by the ASTRID program. Thus the evolution of the facility infrastructure fleet is summarized in the following Fig. 15.

[1] *: TAREF for Task group on Advanced Reactor Experimental Facilities. Countries participating to the TAREF expert group were Canada, China, Czech Republic, Finland, France, Germany, Hungary, Italy, Japan, Republic of Korea, and United States.*
[2] : *ADRIANA for Advanced reactor Initiative And Network Arrangement.*
[3] : *FUTUNA for Fuite Tuyauterie Na (Sodium Pipe leak). FUTUNA is a CEA/CADARACHE sodium loop belonging to the PAPIRUS platform.*
[4] *: IAE/NNC RK : Institut of Atomic Energy of National Nuclear Center of the Republic of Kazakhstan.*

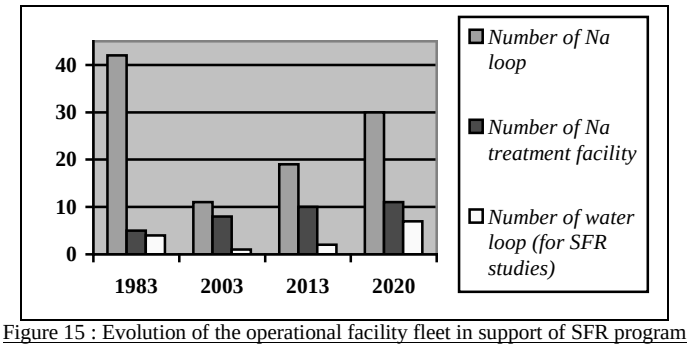

Figure 15 : Evolution of the operational facility fleet in support of SFR program

This chart is summarizes the evolution of the technology infrastructures in support of CEA SFR program. It shows the decrease of facilities as a consequence of the SUPERPHENIX shutdown (1998), the evolution towards sodium treatment facility in support of decommissioning activities, then the restart of a significant and coherent technological facility fleet to support ASTRID project.

ACKNOWLEGMENTS

Many people are involved in this vast program and it was not possible to put all of them as co-authors. Neither the less authors would like to thank O. GASTALDI and his entire lab for their daily strong involvement in the PAPIRUS and CHEOPS platforms; R. ROBIN, J.L. COUROUAU and F. ROUILLARD in charge of the CORRONA 1&2 facilities; S. MADELEINE and his lab for their important involvement in the PEMDYN and DIADEMO Na facilities; I. TKATSCHENKO and E. TEVISSEN and their respective labs, for their involvement in the GISEH platform; G. WILLERMOZ, J.M. RUGGIERI his lab and for their involvement in the PLINIUS SFR platform; E. CHALAYE for his participation in the TAREF group; and C. LATGE for his involvement in all international actions.

REFERENCES

[1] : J. LECLERE, B. GIRAUD, G. HUBERT, J.C. LEFEVRE, "Thirty years of fast reactors development in France", ENC'98, Nice, France, Oct. 25-28, 1998, Trans. Vol. IV, pp 31-39.
[2] : G. RODRIGUEZ., F. BAQUE, J.C. ASTEGIANO, "Evolution of Sodium Technology R&D Actions Supporting French Liquid-Metal Fast Breeder Reactors", Nuclear Technology, Volume 150, Number 1, April 2005, pages 3-15.
[3] : P. ANZIEU, J.P. SERPANTIE, D. VERWAERDE, Ph DUFOUR, Ph. MARTIN, A program on Innovative SFR in France, Proc. of ICAPP 2007, May 13-18, Nice Acropolis, France, 2007.
[4] : P. MARTIN, J. ROUAULT, J-P. SERPANTIE, D. VERWAERDE, French program towards a GEN IV sodium cooled fast reactor, ENC 2007, Sept 16-20, Brussels, Belgium, 2007.
[5] : P. LE COZ, J. F. SAUVAGE, J.P. SERPANTIE, "Sodium-cooled Fast Reactors : the ASTRID plant project", Proc. of ICAPP'11, Nice, France, May 2-5, 2011.
[6] : F. GAUCHE, J. ROUAULT, "French SFR R&D Program and Design Activities for SFR Prototype ASTRID". Energy Procedia 7, pages 314-316, 2011.
[7] : F. BEAUCHAMP, A. ALLOU, N. NISHIMURA, R. UMEDA. "Cooperation on impingement wastage experiment of Mod. 9Cr-1Mo steel using SWAT-1R sodium-water reaction test facility", Proc. of IAEA FR13 meeting, 2013.
[8] : M. SAEZ, D. HAUBENSACK, A. GERBER, F. DAVID, "The use of Gas based Energy Conversion cycles for Sodium Fast Reactor", Proc. of ICAPP 2008, Anaheim, CA, USA, June 8-12, 2008
[9] : J.P. JEANNOT, G. RODRIGUEZ, C. JAMMES, B. BERNARDIN, J.L. PORTIER, F. JADOT, S. MAIRE, D. VERRIER, F. LOISY, G. PRELE, "R&D program for core instrumentation improvements devoted for French Sodium Fast reactors", Proc. of ANIMMA 2011, Ghent, Belgium, June 6-9, 2011.
[10] : J.P. JEANNOT, T. GNANASEKARAN, C. LATGE, L. MARTIN, R. GANESAN, J.M. AUGEM, J.L. COUROUAU, G. GOBILLOT, "In-sodium hydrogen detection in the Phenix fast reactor steam generator : a comparison between two detection methods", Proc. of ANIMMA 2009, Marseille, France, June 7-10, 2009.
[11] : F. BAQUE, F. REVERDY, J.M. AUGEM, J. SIBILO, "Development of tools, instrumentation and codes for improving periodic examination and repair of SFRs", Science and Technology of nuclear Installations, Hindawi Publishing Corporation, Volume 2012, Article ID 718054, 2012.
[12] : S. BEILS et al. "Safety objectives of SEPIA Systems for Sodium-Cooled Fast Reactors", Proc. of ICAPP 2010, San-Diego, CA, USA, June 13-17, 2010.
[13] : S. VITRY, A. MORCILLO, F. REY, G. LAFFONT, G. RODRIGUEZ, M. DUMONT, J. ETAY, Y. FAUTRELLE, "Development of large flow ALIP EMP for application in ASTRID sodium cooled fast reactor and future power plant reactors", Proc. of the 8th PAMIR Intl Conf, Borgo, France, Sept. 5-9, 2011
[14] : L. CACHON, et al., "Innovative power conversion system for the French SFR prototype, ASTRID", Proc. of ICAPP 2012, Chicago, USA, June 24-28, 2012.
[15] : J.B. GÉNIN, L. BRISSONNEAU, T. GILARDI, G. BÉNIER, "OSCAR-Na V1.3 : a new code for simulating corrosion product contamination in SFR reactors", Proc. of IAEA FR13 meeting, 2013.
[16] : N. KHATCHERESSIAN, X. JOULIA, C. LATGE, X. MEYER, T. GILARDI, "Modelling of sodium oxide and hydride crystallization in colp traps for sodium purification in fast breeder reactor", Proc. of ESCAPE 22, London, UK, June 17-20, 2012.
[17] : T. GILARDI, A. CHASSERY, R. BASKARAN, V. SUBRAMANIAN, C. PERRAIS, C. LATGÉ, "Modelling of the chemical behaviour of sodium fire aerosols during atmospheric dispersion", Proc. of IAEA FR13 meeting, 2013.
[18] : O. GELINEAU, S. DUBIEZ le GOFF, P. DUBUISSON, F. DALLE, M. BLAT, "Materials challenges supporting new sodium fast reactor designs", Proc. of ICAPP 2009, Tokyo, Japan, May 10-14, 2009.
[19] : C. LATGE, G. RODRIGUEZ, F. BAQUE, A. LECLERC, L. MARTIN, B. VRAY, P. ROMANETTI, "Teaching sodium fast reactors technology and operation for the present and future generations of SFR users", Journal of Nuclear Science and Technology, Vol. 48, N°. 4, pages 701-708, 2011.

[20] : J.L. COUROUAU, F. BALBAUD-CELERIER, V. LORENTZ, T. DUFRENOY, "Corrosion by liquid sodium of materials for sodium fast reactors : the CORRONa testing device", Proc. of ICAPP'11, Nice, France, May 2-5, 2011.
[21] : S. DUBIEZ-le GOFF, S. GARNIER, O. GELINEAU, F. DALLE, M BLAT-YRIEX, J.M. AUGEM, "Selection of materials for sodium fast reactor steam generator", Proc. of ICAPP 2012, Chicago, USA, June 24-28, 2012.
[22] : C. JOURNEAU, K. PLEVACOVA, G. RIMPAULT, S. POUMEROULY, "Sacrificial materials for SFR severe accident mitigation", Proc. of ICAPP 2010, San-Diego, CA, USA, June 13-17, 2010.
[23] : T. IZURE, N. KIMURA, H. MIYAKOSHI, H. KAMIDE, "Experimental investigation on bubble characteristics entrained by surface vortex", Nuclear Engineering and Design 241 (2011), 4575-4584.
[24] : OECD Book, "Experimental Facilities for Sodium Fast Reactors Safety Studies", Task group on Advanced Reactor Experimental Facilities (TAREF), NEA/AEN n°6908, ISBN 978-92-64-99155-2, 2011.
[25] : C. LATGE et al., "ADRIANA Project : identification of research infrastructure for the SFR, within the frame of European Industrial Initiative for Sustainable Nuclear Fission", Proc. of ICAPP 2012, Chicago, USA, June 24-28, 2012.
[26] : K. KONISHI et al. "The result of a wall-failure in-pile experiment under the EAGLE project", Nuclear Engineering and Design 273 (2007), pages 2165-2174.
[27] : C. JOURNEAU, É. BOCCACCIO, J.-M. BONNET, P. FOUQUART, L. GODIN-JACQMIN, J.-F. HAQUET, D. MAGALLON, S. MALAVAL, K. MWAMBA, P. PILUSO, V. SALDO, "Severe Accident Research at the PLINIUS Prototypic Corium Platform", In: Proc. Int. Congr. Advances nuclear Power plants (ICAPP05), Seoul, Korea, 2005.
[28] : K. PLEVACOVA, C. JOURNEAU, P. PILUSO, J. POIRIER, "An experimental study of the effect of Boron carbide on the SFR corium composition", Proc. Int Young Nuclear Conf., IYNC 2010, Capetown, South Africa, 2010.
[29] : K. PLEVACOVA, « Etude des matériaux sacrificiels absorbants et diluants pour le contrôle de la réactivité dans le cas d'un accident hypothétique de fusion du cœur de réacteurs de quatrième génération », PhD Thesis, University of Orléans, 2010.
[30] : C. JOURNEAU, J.M. RUGGIERI, P. PILUSO, "Plans for a new large scale facilty at CEA Cadarache: the FOURNAISE project", European Review Meeting on Severe Accident Research (ERMSAR 2012), Cologne, Germany, 2012.

Study and evaluation of innovative fuel handling systems for Sodium cooled Fast Reactors. Single Component Optimization

F. DECHELETTE, S. CHRISTIN, E. SANSEIGNE, F. MORIN, G. LAFFONT, G. RODRIGUEZ, X. MOGNOT, A. MORCILLO

CEA CADARACHE, St paul lez durance, France

Abstract. The prototype ASTRID (Advances Sodium Technological Reactor for Industrial Demonstration) sets out to demonstrate the progress made in SFR technology at industrial scale by qualifying innovative options, some of which still remain open in the areas requiring improvements, especially safety and operability. Among all ASTRID requirements, two are specifically impacting the Fuel Handling Systems (FHS) : the reactor load factor (up to 90%) and the investment costs of the prototype (the ratio of the Fuel Handling System to the total reactor investment cost is estimated to be from 15% to 20%. A large set of fuel handling routes has been investigated. The options considered include in-vessel fuel handling systems (under rotating plugs) and options for the transfer of fuel between the reactor vessel and the external storage. The work performed realized a characterization of solutions, a performance review and an analysis of the advantages and drawbacks of the options compared to a so-called starting reference solution (SRS option) based upon well-known French SFR options or some option already envisaged in French project i.e. EFR reactor. The conclusion of this technological feasibility study is presented later for each option, and a macro-criteria grid analysis has been performed to highlight the innovative options enabled to be pursued for ASTRID. The following options were investigated: a cover core structure (CCS) designed in two independent parts, design of the "Dual Location Rotor" and design of the "Simultaneous Handling of two assemblies".

1. Introduction

In the framework of the French Act of the 28th of June 2006 about nuclear materials and waste management, a GENIV and actinides incineration demonstration prototype is to be commissioned in the 2020 decade ([5]). This prototype, called ASTRID (Advances Sodium Technological Reactor for Industrial Demonstration), sets out to demonstrate the progress made in SFR technology in an industrial scale by qualifying innovative options, some of which still remain open and require improvement, especially safety and operability. The current R&D program that supports the selection of ASTRID technology options is particularly focused on the following topics:

- Core design with the objective of improvement of its intrinsic behavior in case of events with scram, development of innovative third shutdown system, improvement in core monitoring,
- Improvement of the decay heat removal system performance and development of an efficient decay heat removal system,
- development of a strategy for the limitation of core degradation consequences in support to the development of the core catcher,
- development of innovative fuel handling systems and energy conversion systems.

Among all ASTRID requirements, two are specifically impacting the fuel handling system (FHS): 1) after a learning period the reactor shall have a high load factor (up to 90%) and 2) the investment costs of the prototype that shall be kept to the lowest possible, with technical options compatible with the later deployment in a commercial facility. This option is particularly important in the ASTRID FHS selection which can influence numerous parts of the reactor design, i.e., from the primary vessel diameter to the balance of plant and overall plant layout.

Between 2007 and 2009, R&D investigations in FHSs focused on collecting past design options ([14], [4]), obtaining experimental feedback from previous SFR French and international reactors ([12], [13], [15] and [9]), and reviewing it with recent innovative options proposed by the scientific community

([3], [8] and [1]). This work led to a first set of innovative preselected options ([2]) and to determine several axis of R&D development to pursue for ASTRID design options. This papers aims to describe the different studies carried out since 2011 by CEA in the field of SFR fuel handling system innovation and to characterize them according to the ASTRID criteria.

2. Scope of work

A large set of fuel handling routes has been investigated. They were based on past achievements (usually used as a first reference for comparison) compared with innovative alternatives and sometimes based on a mix of options already studied. The options considered relate to in-vessel fuel handling systems (under the rotating plugs), to options of transfer between the reactor vessel and the external storage, and also, in the particular case of fuel handling through the gas corridor, to fuel handling in the external storage. The work performed realized characterization of solutions, a performance review and an analysis of the advantages and drawbacks of the options compared to a so-called starting referenced solution (SRS option) that is based upon well-known French SFR options or some option already envisaged in French project i.e. EFR reactor. The main features of the SRS options are as follows (the SRS options are represented bellow) :

- the “in vessel” fuel handling system is carried out with two rotating plugs (Superphenix option),
- definition of a direct lift machine placed in the centre of the cover core structure (EFR option),
- a fuel handling arm with fixed offset is placed on the large rotating plug (Phenix option),
- the fuel assembly is extracted from the primary vessel through a loading/unloading station (Phenix and Superphenix option),
- the transfer of the fuel is performed using a sodium pot to maintain adequate cooling (Phenix and Superphenix options),
- a fuel handling cask is used for transfer from the primary vessel to the in-sodium external vessel storage tank (Rapsodie and EFR option (but it was designed with no sodium pot in both cases)),
- the fuel handling transfer uses no rotor system, neither in the vessel nor in the external storage.

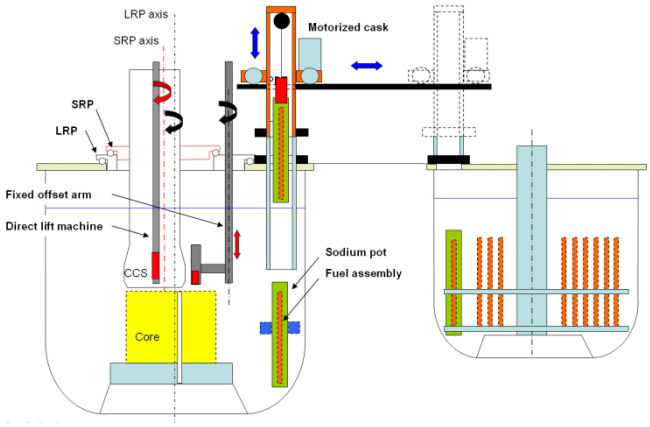

FIG. 1. View of the fuel handling route called SRS (Starting Referenced Solution)

3. List of the Main Innovations Selected

Starting from the SRS case, several innovations were selected either on some specific and targeted study on a single component or on a global approach of the fuel handling route (from the primary vessel to the EVST). The aim is to favour in this first step a very large survey of different innovative ideas without putting too many constraints or restrictions regarding their maturity level or cost impact. Then the conclusion of a technological feasibility study is presented later for each option, and a macro-criteria grid analysis has been performed to highlight the innovative options that can potentially be pursued for ASTRID. Thus, the following options have been investigated :

- Single component optimization :
  - Cover Core Structure (CCS) designed in two independent parts.
  - Design of the “Dual Location Rotor”.
  - Design of the “Simultaneous Handling of two assemblies”.
- Fuel Handling Route optimization :
  - Design of a “Mixed Way” option (defined as a fuel ramp and transfer lock plus a gas corridor for transfer).
  - Design of the “Three rotating plugs, ramp and gas corridor option”.
  - Design of the “Cask and direct fuel handling option”.

This review deals with specific component optimization and is defined as Part 2. Part 1 of this review deals with innovations of the fuel handling route definition is provided in another paper ([17]).

4. Cover Core Structure (CCS) designed in two independent parts

4.1. Motivations

A previous study ([14]) has evaluated the optimum between the fuel handling system and the reactor vessel diameter but with the assumption that the cover core structure was made of a single component. Due to this constraint, optimization of the fuel handling system with two rotating plugs does not reduce significantly the reactor vessel diameter. Indeed EFR optimization had reached only 10 % gain compared to a Superphenix-like option. In this option the CCS is assumed to be in two independent parts. With such a concept, it is envisaged to handle fuel assemblies without exchange position, to reduce size of the system and consequently to reduce the primary vessel diameter. Furthermore this option can provide solutions to improve fuel handling speed and reduce the reactor manufacturing costs.

4.2. Technical description of the solution

Thus, in this option the CCS is in two parts, one is the large rotating plug (LRP) and the other one is the small rotating plug (SRP) (see Fig. 2.). The LRP is slightly off-center from the reactor core centerline. The SRP located in the LRP is off-center from the LRP. The particular feature of this solution is that the track of the SRP has to go between the control rod linkage mechanisms. Therefore, the instrumented part of the CCS is separated into two parts, one on the LRP and the other on the SRP. A fixed offset arm is set on the SRP. Thus, this single arm with its basic design is able to reach all the fuel assemblies (because of the rotation of the SRP and the LRP and their eccentricity from the center) and also the transfer pot for extraction from the reactor vessel located outside the core.

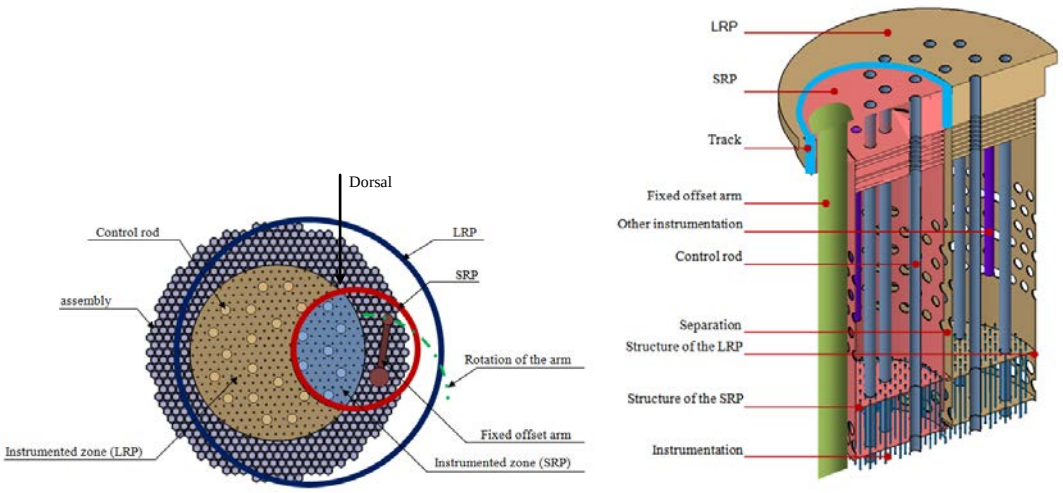

FIG. 2. Location of the CCS in two parts for a 1500 MWth type core

The installation of the track between the LRP and the SRP has been dimensioned for a 180 mm width. Analytical calculations have been carried out to validate the resistance of the structures, pins, jacks and rolls. The sealing technology used for this track is a combination of a molten metallic seal (MMS) + inflatable seal + metal-metal support (this technology was used in Phénix and SPX). This solution is not optimized for such a narrow track. Indeed, the operating clearance (for rotation) is low and the thermal characteristics of the MMS are not ideal. Thus, the development of an innovative sealing system is an requirement issue to improve these aspects. Because of the runway between the LRP and the SRP, the space required for the control rods and their relevant drive systems is reduced. The ability to install a control rod handling cask close to the runway path remains one of the major challenges of this option.

To validate the two-part CCS concept, studies have been carried out on the pre-dimensioning of the structures. The purpose of this calculation is to compare thermomechanical behaviour of this concept with a classic concept selected in previous French fast reactors (i.e., Phénix- and SPX). Finite element calculations are thus carried out and compared. Table1 below provides the maximum equivalent stress (Von Mises) of the SRP and the LRP. They have been compared with the stress (for the same conditions) of a single CCS. We can see that the stress is higher for the SRP and the LRP due to the non-axisymmetric shape of the plugs. The highest stress is found on the lower part of the CCS slab.

Standard CCS	Max stress (MPa)	Value	**99**
		Location	Cover link(similar over the whole circumference)
SRP	Max stress (MPa)	Value	**217**
		Location	Cover link (dorsal)
LRP	Max stress (MPa)	Value	**219**
		Location	Cover link (dorsal)

Table 1. : Maximum Von Mises stress values / comparison

4.3. Optimization of Stresses

Increasing the bend radius of the connections: A groove and a radius have been set up at the junction between the cover and the vertical part of the SRP. The objective is to have a better stress distribution over the entire surface of the connection. This solution does not provide satisfactory performance when the constraints remain unchanged. The maximum values remain too high. We also observe a change in the maximum stress positions, originally located just under the cover link, they move down the groove or down the radius.

Increasing the thickness of the structures: An increase of the thickness of the upper part of the structure has been envisaged. But this modification has a negative impact to the maximum stress of the structure. It is mainly due to the fact that the displacements are because of the thermal dilatations and in that case, distance from the neutral axis is the parameter that governs the constraints.

Increasing the radius of the dorsal: The maximum stresses measured on the different geometries are usually located under the cover at the dorsal radius. A work on the geometry has been performed to increase these radiuses to reduce stress concentrations. The maximum value that the dorsal radius can reach is limited by the control rods. Their position is fixed and therefore represents a physical limit to the increase in the radius. On the SRP, the maximum stresses reduce significantly with increasing the radius of the dorsal (up to 50% with a dorsal radius of 550mm. This solution is then an interesting way for improvement. The results obtained with the LRP are less conclusive (-4.5% with a radius of 300mm). Compared to the base case of standard CCS used in the same conditions, the value of the maximum stress after improvement remains too high and above the yield strength of 316L(N).

Conclusions about the optimizations: the improvement that provides the best results is the increase of the dorsal radius. Constraints on the SRP were divided by half to reach 114 MPa. However, this solution has shown its limits on the LRP and results in a smaller decrease on the maximum stresses. The geometry optimizations will reduce significantly the maximum stresses in the CCS. However, it remains no doubt that the thermo-mechanical design of such a component is significantly more difficult than a cylindrical core cover structure. In SFR design, this matter is particularly relevant with this component which is one of the most structures thermo-mechanically loaded.

4.4. Option performance review

Technical data for qualification of the option: The main qualifications will include the runway between the control rod mechanisms (qualification of compact rolling mechanisms operated in air and behaviour with sodium aerosols of the compact sealing system) and the core cover structure detailed design with its cutting zone. It must integrate the thermo-mechanical behaviour of the core cover structure and the cutting zone as regards sodium and temperature, precision of the instrumentation near the cutting zone, and behaviour of the CCS in the event of earthquake.

Economic review: Rotating plug dimensions can directly impact the reactor vessel diameter. The reactor vessel diameter is estimated at 6,500 mm when the optimized solution with a single CCS is adopted and is estimated at 7,200 mm with two rotating plugs, with an expected reactor vessel diameter gain of around 14%. In addition, this solution eliminates the direct lift machine and the takeover position. The fuel handling technology is similar from the SRS concept, only the SRP rotation mecanism is more complex. The development cost can therefore be estimated slightly higher or equivalent to the EFR-type solution.

Safety review: As regards safety, the two-part CCS concept raises several issues: rotation inhibition following an incident on the cutting zone and earthquake resistance of the whole system. In addition, the good mechanical behaviour of the two-part CCS solution still has to be proven over its entire lifespan. There is no feedback for this solution.

ISIR review: The two-part CCS solution requires a runway that must pass between the control rods which may thus be difficult to implement. The two-part CCS cutting zone requires additional inspection points, the ISIR review is therefore slightly negative, compared with the reference solution.

Operability review: The two-part CCS solution offers a real advantage for certain fuel handling cases where the transfer times between the reactor and the vessel of the external storage unit are optimized. This required time due to movement of the rotating plugs to access one specific fuel assembly and to place it in a loading/unloading station can be significantly reduced (no takeover position).

Design complexity review: Despite the removal of the direct lift machine, the pick-up station and the reduction of the plug dimension, the two-part CCS is in itself a complex system. This assumption is

mainly due to the runway and the cutting zone that have to pass between control rods. Therefore the main points rendering the solution more complex are as follows: compact runway dimensions (mechanical support + sealing system + rotation system); thermo-hydraulic dimensioning in the cutting zone at the core exit; thermo-mechanical dimensioning of a non axisymmetrical CCS; location of the control rods close to the runway (space required for their removal).

5. Description of the "Dual location rotor" option

5.1. Motivations

The dual location rotor has the advantage of improving fuel handling times by simultaneously managing a new assembly and a spent fuel assembly, thus decoupling the fuel handling inside the vessel and outside the vessel. This system integrated into the primary vessel has to be designed to have minimal impact on the vessel diameter.

5.2. Technical description of the solution

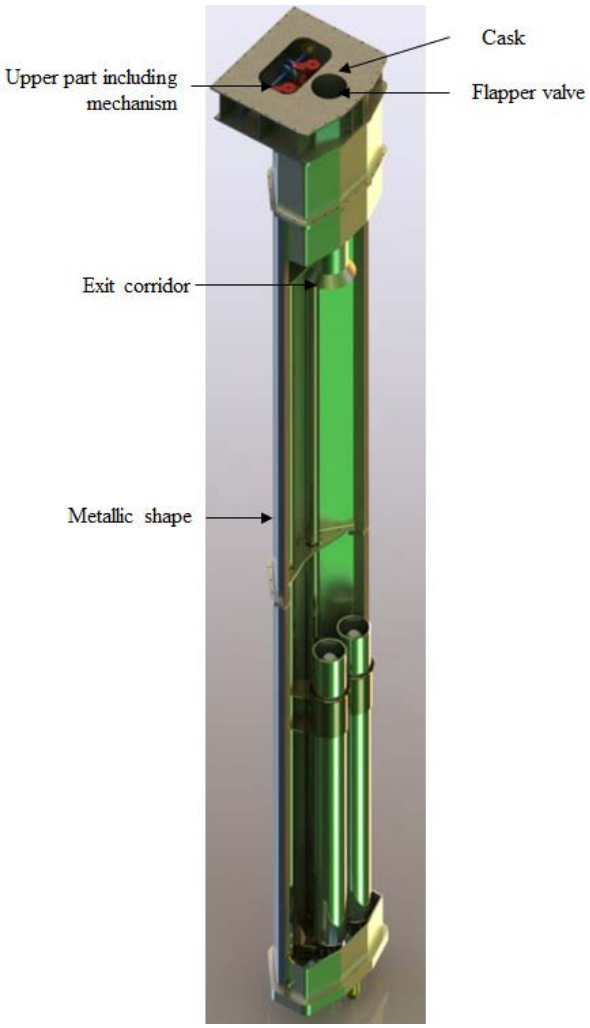

FIG. 3. Plan of the rotor switch

The principle is patented and detailed below. The system is structured inside a metallic shape open on one side to be accessible for the fuel handling arm, except on the upper part where the rotation mechanisms are located. The main components of the system are : two sodium pot-holder systems, two rotating shafts, one link rods system to couple the pots, ball pivot link systems and annular linear links for movements and guides, a structure system, a shaft drive and upper part motorization unit, an

isolation valve and an instrumentation system. This “rotor switch” configuration has been chosen to reduce the impact of such a mechanism on the diameter of the reactor vessel. Such a system impacts the reactor vessel diameter by approx 0.5m (to be compared with a cylindrical rotor solution which would have an impact of approx. 1.50m on the reactor vessel diameter). This solution also has an advantage compared to a cylindrical rotor as the exit pot can still be accessed by the fuel handling arm in the event the rotor movement is inhibited. Disassembling the entire system remains possible to carry out maintenance operations. While in a rotorless theory, we could consider for the entire fuel handling campaign a single sodium pot that is part of the transfer cask, because of the presence of the rotor, the rotor and the pot must be separate, which requires an additional pot and a grab system enabling the sodium pot to be locked/unlocked from the cask before and after each rotation of the rotor.

5.3. Option performance review

Technical data for qualification of the option: tests that have been identified are the valves or sealing flapper valves interfacing between the reactor vessel and the fuel handling cask (in the presence of sodium aerosols) and all the mechanism in liquid sodium or in sodium aerosols.

Economic review: Compared to a rotorless solution, and therefore with a single pot constantly placed in the exit corridor, adding this mechanism therefore has an economic impact on the cost of the entire nuclear plant. The impact concerns: the vessel diameter (+500mm), the additional mechanism installed in the reactor vessel and the grab required for the cask to pick up and set down the pot.

Safety review: the system gives rise to additional safety constraints by adding a device in the reactor vessel. Furthermore, the two sodium pots require a grab system to set down and pick up the sodium pots at the bottom of the rotor. However, compared with a cylindrical rotor solution, the design of the rotor switch makes it possible to introduce the irradiated assembly directly into the exit corridor.

Operability review: The time gain is notable, but it must nonetheless be qualified by the maintenance operations to be carried out on this rotor. Such an operation would indeed lead to special “large component”-type fuel handling and would demand several days of downtime.

Design complexity review: From this point of view, the rotor switch solution, given the multiple links involved, is inevitably more complex than a rotorless solution. Moreover, the necessity to uncouple the pot from the fuel handling cask before the inversion operation means that the cask must be fitted with a grab system thus making it more complex. This is true regardless of the type of rotor considered. Nevertheless, note should be taken of the possibility of dismantling this system for maintenance operations.

6. DESCRIPTION OF THE “SIMULTANEOUS HANDLING OF 2 ASSEMBLIES” OPTION

6.1. Motivations

This solution aims to optimize the transfer speed of the fuel handling cask from the reactor vessel to the storage vessel by handling two fuel assemblies. A similar solution is notably investigated in the Japanese JSFR project. The reasons in favor of this solution relate exclusively to availability.

6.2. Technical description of the solution

This is therefore an extension of the sodium pot capacity to transport 2 fuel assemblies. The pot comprises 2 locations for fuel assemblies, each one being fitted with a convection liner to optimize heat exchange. The 2 assemblies are located in a pot with an externally finned structure. Thermal studies may define the maximum assembly power admissible in the double pot. The fuel handling cask will be larger due to the increased thickness of biological shielding required for two irradiated assemblies.

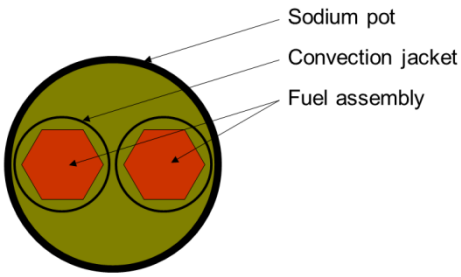

FIG. 4. Plan view of the double assembly pot

6.3. Technical characteristics

- Pot dimensions : L = ~ 5,000 mm, D = ~500 mm inner, Volume of sodium : 1 m^3
- Total weight : Approx 3 tons
- Impact on the vessel diameter (if it is on the critical path of the vessel diameter) : + 500 mm

6.4. Option performance review

Technical data for qualification of the option: This option does not, at first sight, have any particular impact on the qualification of the sodium pot compared to a classic option with a single sodium pot.

Economic review: The economic impacts are as follows: the cost of the pot itself, the increase in the vessel diameter, and the increase in the cost of the fuel handling cask (effective diameter and thickness of the biological protection). This solution would thus result in an economic loss compared to the SRS solution.

Safety review: As regards to safety, the main difference lies in the consideration of two assemblies instead of one in the event of an incident, such as the cask movement being inhibited during fuel handling for example.

Operability review: This system significantly improves the fuel handling time.

Design complexity review: Design of a double pot is relatively similar to a single pot, so no major change. It should be noted that the diameter of the reactor slab opening increases.

7. Review of the options

7.1. Advantages / drawbacks and difficult points

Advantages and drawbacks of each solution are listed below. Major difficulties are marked in bold.

	Advantages	**Drawbacks**
SRS	Simplicity of systems Little impact on the reactor geometry Extrapolability to power reactor	**Fuel handling time** **Fuel handling cask dimensions** Moving mass Reactor bulding opening
2-PART CCS	Reduced vessel diameter Reduced number of mechanisms Fuel handling time No pick-up	**CCS dimensioning** Limited space for runways, requires adaptation of the control rod positions or rod mechanisms
DUAL LOCATION	Improved fuel handling time Component can be removed	Increased vessel diameter Additional mechanism in the vessel

ROTOR		Sodium pot disconnection from the cask (complexity of mechanisms)
HANDLING OF 2 Irradiated Assemblies	Mechanism inexpensive at first sight but significantly increasing fuel handling speed	Increase in the vessel diameter **Increase in the size and weight of the cask** Power of the assemblies handled to be defined

Table 3: Advantages and drawbacks of the reference solution plus the innovative solution investigated

7.2. Quantification and comparison of each option

Criteria grid: Based on the technical elements above, a set of micro-criteria has been generated in order to quote all of them and to determine the maturity level of the options that can be translated in performance index. A graphical representation of a succinct summary of the analysis with a focus on cost and risk can be plotted which provides a relative comparison with each option

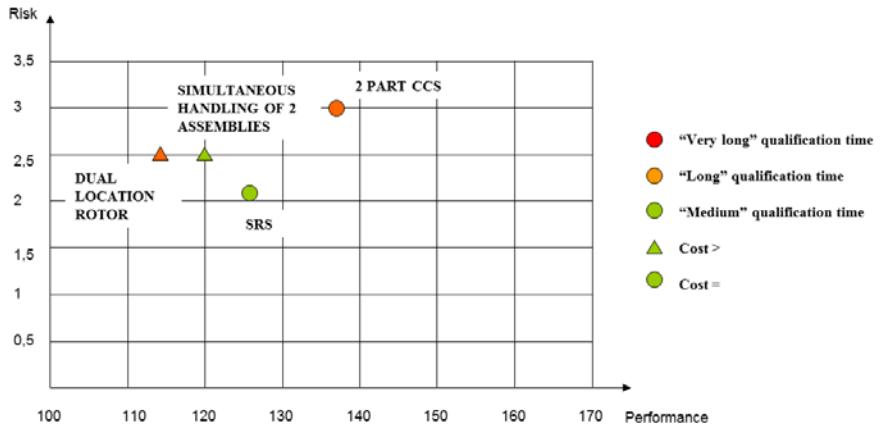

FIG. 5. Graphical representation of the assessment of solutions

Thus, based on the analysis above, the following orientations are recommended :

- Due to the expected difficulties and the foreseeable time required to dimension and qualify the sensitive component, i.e. the CCS, we suggest discarding the **2 part CCS** option.
- The **dual location rotor** is interesting in term of availability, but, because of the fact that we have added a new component into the reactor vessel, and also because of its design complexity, it is proposed to not continue in this option.
- **Simultaneous handling of two assemblies:** a substancial improvement of the fuel handling speed is obtained with a minor change in the design. The complexity of the cask and the moving masses are points to be studied. Thus, this option should be studied in more detail. An alternative solution that may be promising is this dual location sodium pot but transfering only one assembly, using the pot as a new assembly / irradiated assembly exchange.

8. Conclusion

This study has revealed that several options are available to improve availability, but, because of their design complexity, consequences in term of safety, many do not appear practically feasible. However, the dual location sodium pot, transfering simultaneously two assemblies or optionally one is a promising option that should be moved forward. The search for integral innovative systems without severe constraints on the technical feasibility is interesting in the way that it helps in providing new ideas and some specific innovative points can therefore be selected even if the whole system appears to be, at the end of the study, technically unfeasible and/or too challenging.

9. ACRONYMS, ABBREVIATIONS AND TERMINOLOGY

CCS : Cover Core Structure

EVST: External Vessel Storage Tank

FHS : Fuel Handling System

ISIR: In Service Inspection and Repair

LRP: Large Rotating plug

RP : Rotating Plug

SRP: Small Rotating plug

REFERENCES

[1] Cacuci, D., 2010, Handbook of nuclear Engineering, Chap. 21 : Sodium Fast Reactor design, Springer editor, ISBN 978-0-387-98130-7, 2321-2711.

[2] Chassignet, M., Dumas, S., Penigot, C., Prèle, G., Capitaine, A., Rodriguez, G., Sanseigne, E., Beauchamp, F., 2011, Challenges and innovative technologies on fuel handling systems for future sodium-cooled fast reactors, Journal of Nuclear Science and Technology, VOL. 48, No. 4, 662-668.

[3] Chellapandi, P., Puthiyavinayagam, P., Balasubramaniyan, V., Ragupathy, S., 2010. Design concepts for reactor assembly components of 500 MWe future SFRs. Nuclear Engineering and Design 240, 2948-2956.

[4] Chikazawa, Y., Farmer, M., Grandy, C., 2009. Technology gap analysis on sodium-cooled reactor fuel-handling system supporting advanced burner reactor development. Nuclear Technology VOL. 165, 270-292.

[5] Gauché, F., Rouault, J., 2011. French SFR R&D Program and Design Activities for SFR Prototype ASTRID. Energy Procedia 7, 314-316.

[6] Henry, K.J., 1971, Technical description of PFR. Nucl. Eng. Int. Aug. 1971, 632-636.

[7] Hunt, C. R., Riley, P. L., Campbell, N., 1974. Fuel handling and other In-reactor mechanisms in PFR, Proc Int. Conf. Fast reactor Power Stations, London, UK, March 11-14, BNES. IAEA, 2006. Fast Reactor Database, IAEA TECDOC n°1531.

[8] Katoh, A., Chikazawa, Y., Obata, H., Kotake, S., 2010. Development of Advanced Fuel Handling Machine for JSFR. Journal of Nuclear Science and Technology, VOL. 47, No. 7, 642–651.

[9] Kumar, K. V. S., Babu, A., Anandapadmanaban, B., Srinivasan, G; 2011. Twenty five years of operating experience with the Fast Breeder Test Reactor, Energy Procedia 7, pp 323-332.Lefèvre, J.C., Mitchell. C. H., Hubert, G., 1994. European fast reactor design, Nuclear Engineering and Design 162 (1996), 133-143.

[10] Melhuish, D. B., 1992. Engineering improvements to PFR, Nucl. Energy, 31, 3, 193.

[11] Morin, F., Dechelette, F., 2012. Transfert innovant d'assemblages combustibles pour un RNRNA de la cuve réacteur vers un stockage externe déporté, French Patent HD 13521, June 2012.

[12] Prèle, G., Latgé, C., Dupraz, R., Dirat, J.P., 2009. Feedback experience from sodium technology, Revue Générale Nucléaire RGN n°1, Janvier-Février 2009.

[13] Prèle, G., Rodriguez, G., Sanseigne, E., Chassignet, M., Majot, C., 2008. Some experimental feedback of the fuel handling system of French sodium fast reactors regarding specific operations : cleaning, refuelling, final defueling. IAEA Technical Meeting on Fuel Handling Systems of Sodium Cooled Fast Reactors, 24 – 27 November, IGCAR, Kalpakkam,Tamil Nadu, India.

[14] Rodriguez, G., Saez, M., Levy, M., Astegiano, J.C., Le Coz, P., Ravenet, A., Martin, P.,2007. Review and innovative technologies on Fuel Handling System for Sodium Fast Reactors. Proc of GLOBAL '07, September 9-13, Boise, Idaho.

[15] Srinivasan, G., Kumar, K. V. S., Rajendram, B., Ramalingan, P. V., 2006. The Fast Breeder Test Reactor –Design and operating experiences, Nuclear Engineering and Design 236, 796-811.

[16] Dechelette, F, Sanseigne, E, Morcillo, A, 2010. Dispositif et procédé de remplacement d'un assemblage combustible irradié par un assemblage combustible neuf dans la cuve d'un réacteur nucléaire et réacteur nucléaire comprenant un tel dispositif, French Patent HD1058641, October 2010

[17] Dechelette, F, Morin, F, Laffont, G, Rodriguez, G, Sanseigne, E, Christin, S, Mognot, X, Morcillo, A.
Study and evaluation of innovative Fuel Handling System for Sodium-cooled Fast Reactors – Part1 : Fuel Handling Route Optimization. to be published in Nuclear Engineering & Design in 2013.

R&D Program on sealing issues for in-service inspection and repair tools on ASTRID sodium prototype

K.Vulliez[a], L.Bruguière[a], L.Mirabel[a], A.Béziat[a], F.Baqué[c], M.Berger[d], B.Deschamps[a], J.F. Juliaa[b], F.Ledrappier[b], G.Rodriguez[c], B.Rouchouze[d]

[a] CEA, DEN, SDTC, Laboratoire d'Etanchéité Maestral, 30207, Bagnols Sur Cèze France.

[b] TECHNETICS Group France, Laboratoire d'Etanchéité maestral, 2 rue James Watt 26700 Pierrelatte.

[c] CEA, DEN, DTN, CEA Cadarache, 13108, Saint-Paul-lez-Durance France.

[d] TECHNETICS Group France, 90 rue de la roche du geai, 42029 Saint-Etienne

Presented by K.Vulliez

Abstract. The development of in-service inspection and repair tools for sodium cooled nuclear reactors is a challenging task. In present design, the tools regardless of their design and function are foreseen to be embedded inside a bell mounted on a remote handling device. Apart from the constraints inherent to the remote actuation and the docking of the system on the vessel structures, the high temperature sodium-tightness of the bell is a tedious issue to solve. This paper presents the R&D program conducted at CEA-Technetics sealing laboratory to address this matter. This program is divided along two axes, a characterization phase with radiation and sodium aging of several elastomer compounds, and the development of a full scale mock-up of a docking flange to qualify the sealing efficiency of different profiles. Advanced concepts of sealing systems and mechanical obturator for the inspection bell developed in the frame of this program are presented.

1. Introduction

In the framework of the ASTRID (Advanced Sodium Technological Reactor for Industrial Demonstration) project, innovative systems for In-Service Inspection and Repair (ISI&R) are under development [1][2]. The nuclear vessels environment with radiation and high temperature sodium where the ISI&R equipment will be deployed imply stringent technical constraints. The simplest and most straightforward way to limit the constraints on these systems is to keep them away from sodium (Na) exposure. The reference design option for most of the ISI&R tools foreseen is to embed them inside a sodium-tight diving bell. By the mean of a remote handling (RH) device, the bell will be moved in the nuclear vessel up to the structures requiring inspection or repair. Once docked and tightened on the chosen surface, a sealing system will be required to create of volume free of sodium where the ISI&R systems can operate. The development of the sealing system and the mechanism allowing the bell aperture and closure while immersed in sodium are therefore mandatory. The CEA-Technetics MAESTRAL sealing laboratory has been involved to provide its expertise to develop an integrated system to be interfaced on a Remotely Handled Inspection Bell (RHIB).

A dedicated R&D program was initiated hinged on two axes: a program to select and characterize proper sealing materials that include mechanical tests of samples exposed to sodium and radiation and the development of a test stand to qualify full scale mock-ups of sealing concepts. The description of these activities, their main results, and advanced concepts are presented here after.

2. Materials selection and characterization

The choice of a seal with a given technology and material among the large panel available is always the result of a compilation of requests specific to the foreseen application. In the case of ISI&R systems, with a sealing system immersed inside sodium, the constrains of the environment both thermally with temperature up to 220°C (the retained temperature during reactor shut-down), radiation, and chemical, strongly reduce the technical options. If the low pressure involved (below 3 bars) and the short duration of immersion (below 30 days) partly release the constraints, the uneven geometries of the vessel surfaces to inspect, together with the RH tooling specification are other matters to address. Two type of sealing technologies emerge from a first analysis: metallic seals, and seals made with silicone compounds.

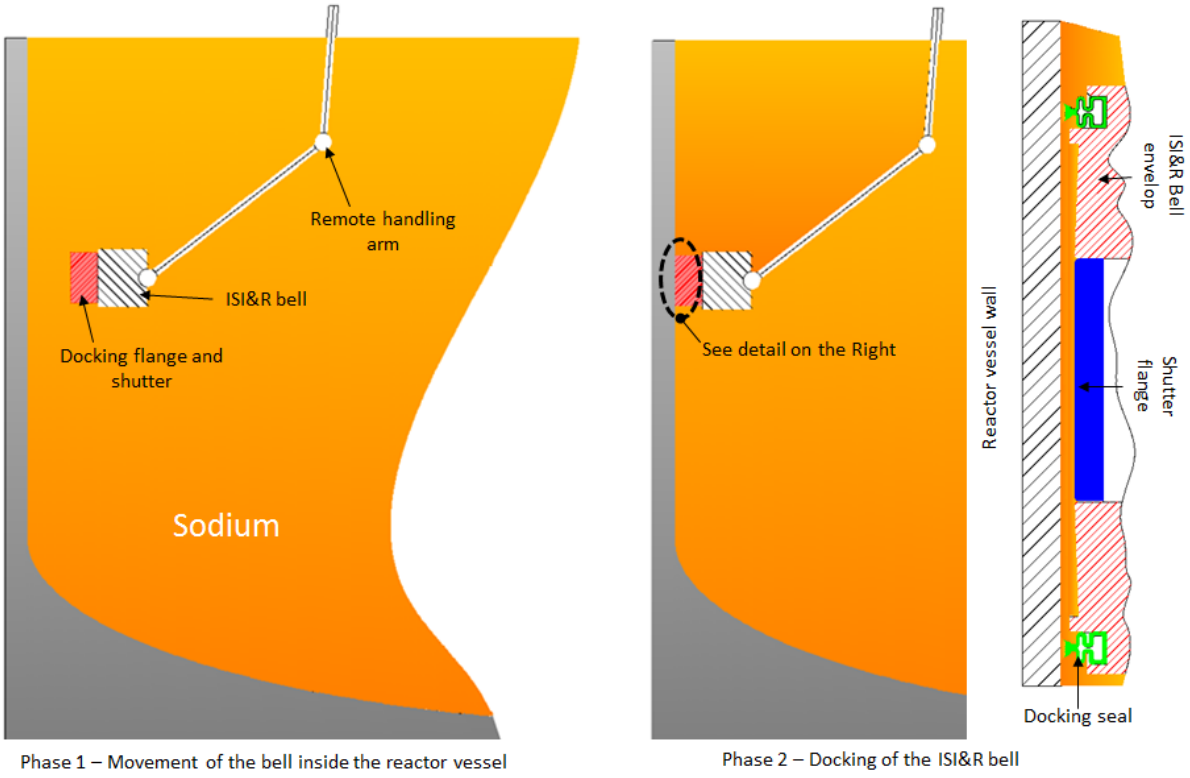

FIG. 1. Tests samples for mechanical characterization and sealing performance test

The metallic seals presents several advantages in terms of working temperature (featuring large margins for temperature below 250°C), and for most alloys a good sodium compatibility. In regards of the quasi-isothermal conditions, the purity of the sodium and the short-term immersion, the corrosion on steel and nickel base alloys will not be a concern [3]. However, the limited forces the RH systems (Fig.1) can transmit to the RHIB sealing-system during docking (estimated below 10kN) strongly limited the technical options. Indeed, a sealing-system is at some point constrained and designed in regards of the minimal force required to ensure the seals compression, and most of metallic seals require rather high compression forces. With a proper choice and shape of the seal together with a well-designed assembly this matter can be overcome. At first in the program, with a design of the RH component of the ISI&R still evolving, the metallic seals option was set aside. Solutions with this type of seals were only worked out on more advanced concepts.

Solution based on elastomer seals was the second option considered, thanks to the far lower compression forces they require to ensure sealing. But if the mechanical issues are lowered, the material compatibility with high temperature and sodium become a tricky concern. First, the range of 200°C offers little operating margins for elastomer, for the few materials compatible with high temperature the maximal allowable working temperature seldom exceed 250°C. Secondly, most

elastomer materials are disqualified for sodium use due to the presence of Fluor or Halogen elements, two elements commonly present in most of the high temperature compatible materials. Thanks to their chemical composition and thermo mechanical properties, some silicone based material can be considered for the RHIB.

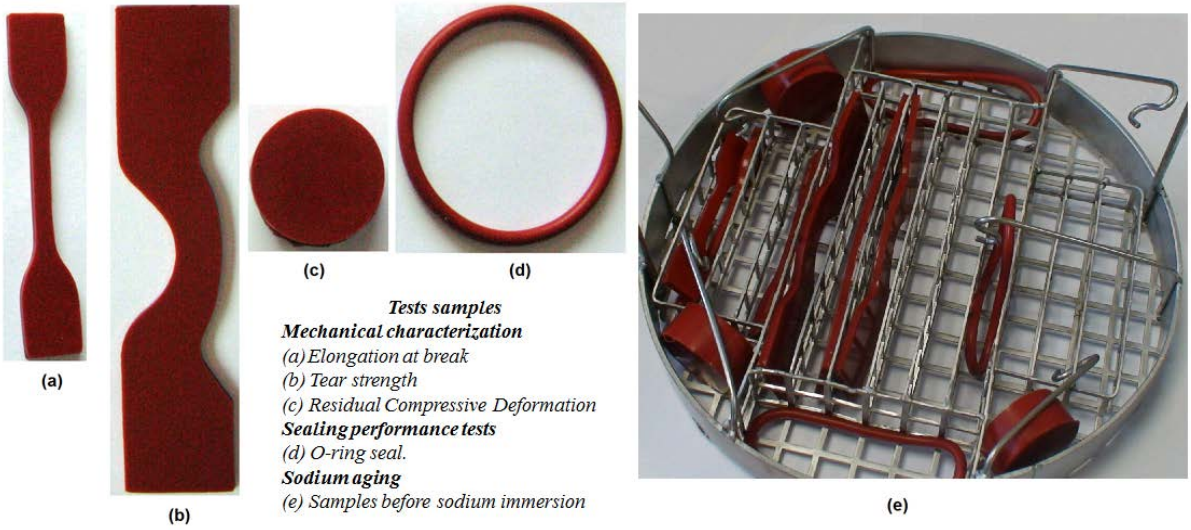

FIG. 2. Tests samples for mechanical characterization and sealing performance test

Many studies on sodium chemical compatibility with this type of elastomers have been conducted since the early sixties [5][6][7], and further tests were also performed later on during the PHENIX project[8]. All these experiments made on various types of silicone compounds, under a large span of constraints (temperature, geometries) demonstrate the compatibility of this type of materials for sodium use, with however some reservations regarding material aging. In the choice of a specific silicone, the quality and chemical composition (in particular the incorporated oxide rate) also appear to be important regarding the manner the material will behave in sodium.

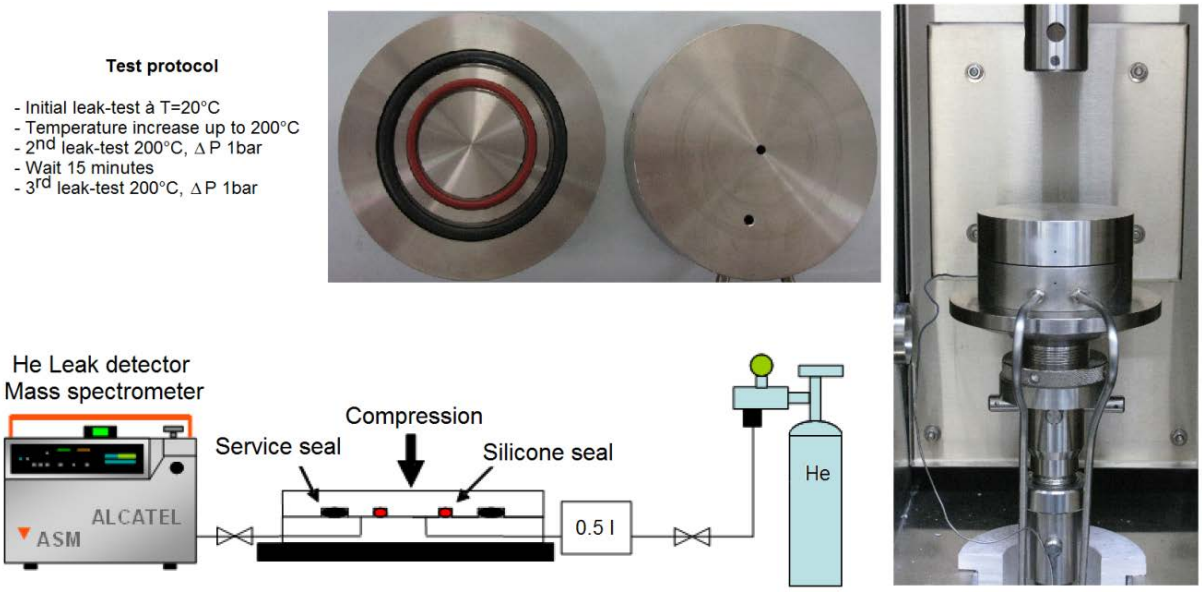

FIG. 3. Test stand for sealing performance characterization by vacuum leak detection.

Table 1. Mechanical characteristics of silicone C85MC6/60 under several test conditions.

Test conditions	**Duration or CD[a]**	***Hardness[b]***	***Ultimate strength* (MPa)**	**Tear strength (kN/mm)**	**RCD[c]**	**Leak rate[d]**	
						20°C	200°C
20°C Air	30 days	59.1	9	43.3		$1.7\ 10^{-6}$	$3.5\ 10^{-5}$
200°C Air	30 days	60.3	7.9	37.1	12.5%	$2.2\ 10^{-6}$	$2.2\ 10^{-5}$
200°C Na	30 days	67	3.9	26.8	12.7%	$9\ 10^{-2}$	$1\ 10^{-5}$
11Gy/h	666Gy	60.6	7.4	38	10%	$1.2\ 10^{-6}$	$9.8\ 10^{-6}$
+ Na 200°C	15 days	65.6	4.8	25.3	9%	$9.5\ 10^{-2}$	$2.6\ 10^{-2}$
71Gy/h	6117Gy	64.5	8	35	12%	$7.6\ 10^{-7}$	$9.5\ 10^{-6}$
+ Na 200°C	15 days	64.8	4.9	27.4	10%	$1\ 10^{-1}$	$7\ 10^{-2}$
397Gy/h	662Gy	61.5	8.5	43.3	9%	$9.8\ 10^{-8}$	$1.3\ 10^{-5}$

[a] Cumulative Dose in Gray.

[b] Shore A Hardness scale.

[c] Residual Compressive Deformation in percentage.

[d] Mean leak rate express in (mbar.liter.s^{-1}) for a ΔP=0.1MPa at T=20°C (after 15minutes) and 200°C (after 30 minutes).

Two different silicone based materials compatible with high temperature and with proper mechanical characteristics for sealing applications were selected. Test samples of different geometries (Fig.2) were produced to perform classical uniaxial traction tests, tearing strength and Residual Compressive Deformation (RCD) measurements. O-rings shaped samples were also made to validate by means of dedicated leak-tests (Fig.3) the sealing performances of the materials after aging.

Batches of samples were exposed to irradiation, with ambient gamma dose rate up to 400Gy/h and Cumulative Dose (CD) up to 10kGy. The samples were then immersed for 15 days in a sodium crucible maintained at 200°C. The other samples were exposed to radiation only, or aged in air at 200°C or in sodium at 200°C for duration ranging from 15 to 30 days. These different batches exposed to different conditions aim to verify the respective effects of environmental solicitations on the materials. Table I presents for all the different tests the results of the mechanical characterization and sealing performance tests performed on the most promising of the two silicone compounds tested.

The first observation that can be made from these tests is the relatively low influence of irradiation on the material (Table I); this point is to be confirmed with complementary tests at higher dose rate and CD. The effect of the sodium is however more significant and highly dependent on the silicone composition and test duration. The first compound featuring stronger degradation of its mechanical behavior (up to 30% higher than the one presented in Table I) had to be rejected. On the selected silicone, the degradation of the mechanical properties remains significant, but the losses (above 40%) do not jeopardize the use of material for sealing application. The hardening of the material and the surface degradation observed on the samples (Fig.4) are more bothersome as sealing is concerned.

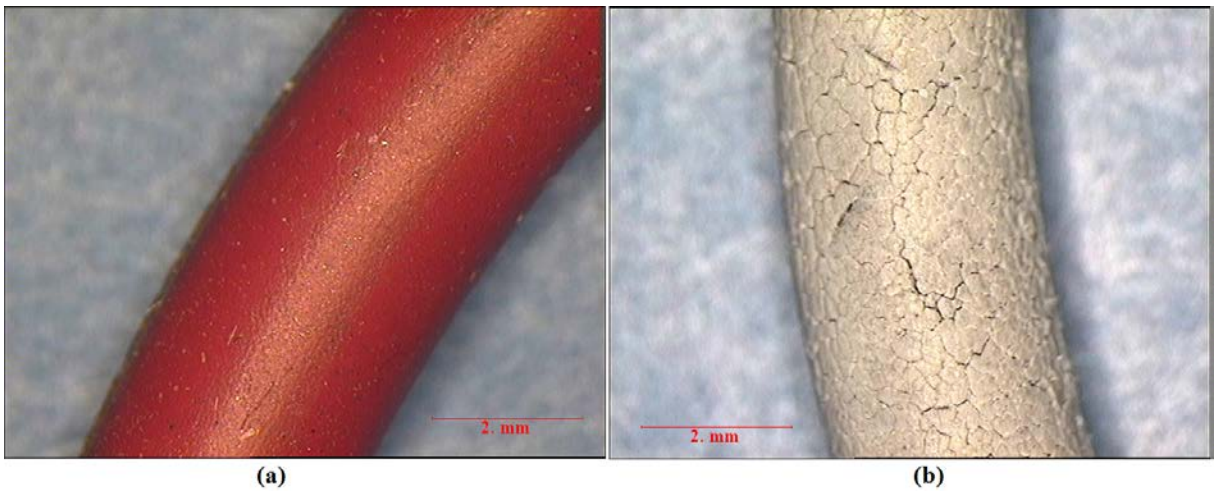

FIG. 4. Samples of O-ring made of C85MC6/60 silicone (table I): (a) After 30 days at 20°C in air (b) after30 days immersed in 200°C Na

After the aging and the mechanical characterization, the sealing performance was tested on the leak-test stand. A significant increase of the forces required to compress the seals was observed, in coherence with the previously observed hardening (link to bulk densification) and mass losses of the seals. And as expected, the degradation of the outer surface of the seal exposed to sodium, strongly affect the sealing performance (Table I). The surface cracks offering potential leak-paths all over the seal circumference.

The on-going program is now testing a new silicone compound developed for high temperature. Samples exposed to higher dose rate and CD will be tested, and some of the O-ring seals will be aged in sodium mounted between flanges. Indeed, it should be pointed out that the plain immersion of the sample in sodium strongly increase the surface exposed to chemical attack compared to a compression seal mounted in a groove in real assembly. The sealing-tracks created the seal compression between the two surfaces are kept sodium-free; therefore the formation of the leaking paths induced by the chemical attack will take longer in this configuration. Chemical analysis of the sodium and silicone after aging will also be performed to better understand the chemical reaction responsible of the silicone surface damages. The data collected from these analyses will be helpful to optimize the silicone composition or develop specific coatings for the seal outer surface.

3. Sealing system development and qualification

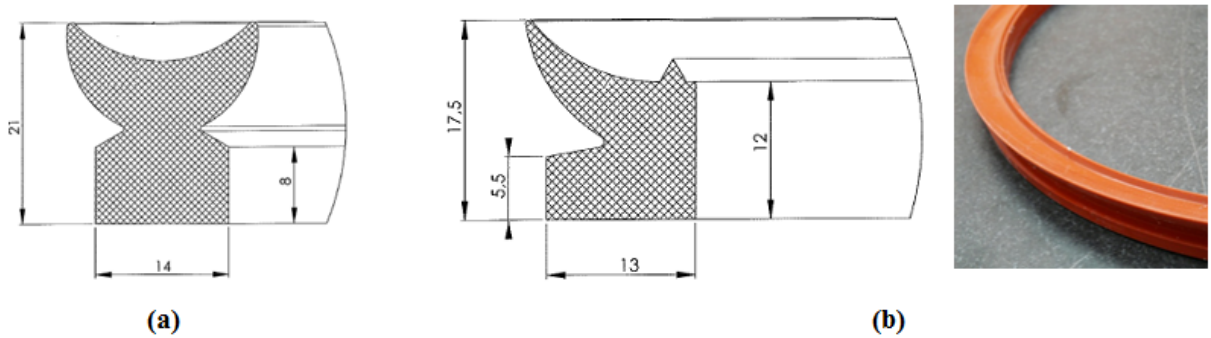

FIG. 5. Seal profiles: (a) double lip (b) simple lip with delta.

In parallel of the material selection and characterization, the mechanical design of the RHIB sealing system, a key component part of the ISI&R equipment, was studied. With rather low definition of the future systems to be embedded inside the RHIB, that can go from camera for inspection to complex repair tools, some hypothesis were taken to set around the design. A cylindrical geometry was chosen

with outer diameter not exceeding 350mm, with a minimal operating window (once docked on the vessel) for the ISI&R systems of Ø120mm. The maximal outer pressure was fixed at 3 bars, offering some margins in regards of the future operating conditions. Considering a seal of Ø350mm, the maximal planar default the seals shall accommodate is below 15mm, corresponding to a docking of the bell on a cylindrical surface of one meter radius. The design focused on the shape of the seal, trying to limit the required compressive forces needed to achieve a proper sealing. In collaboration with the CEA industrial partner Technetics Group France (a word leader in sealing technologies), several profiles of silicone seal were considered. A lip-shape concept (Fig.5) emerged among a large panel of designs. This type of shape allows a large contact surface and tolerates important geometrical defaults with only limited applied forces, thanks to the high flexibility of the lip.

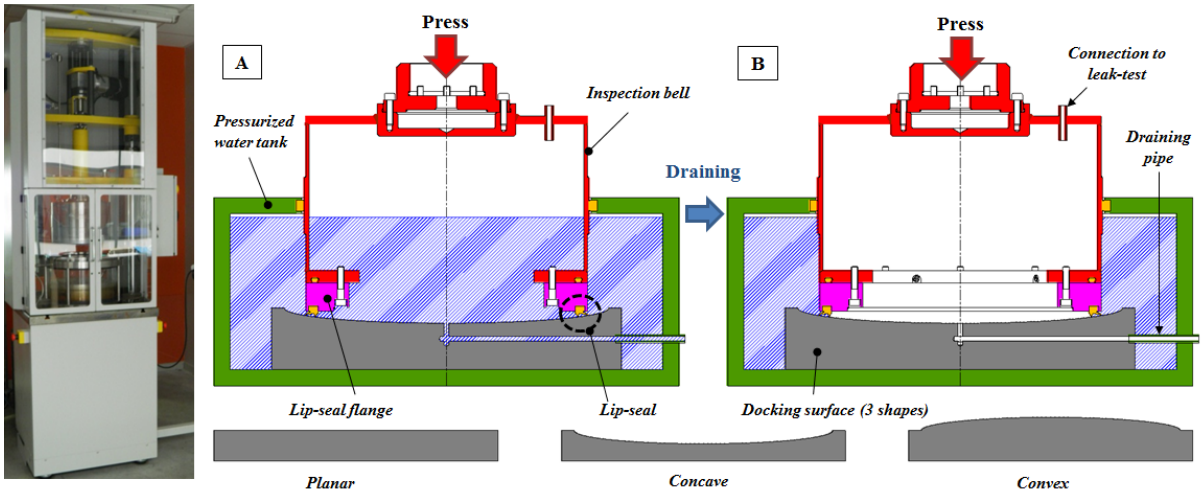

FIG. 6. MARIUS test facility. [A]Docking of the bell on the surface followed by a pressurization of the water tank [B] Draining of the bell leak test and visual survey.

To qualify the sealing efficiencies of seal-profiles and measure the corresponding applied forces, a dedicated test-device (Fig.6) was built. Named MARIUS (acronym for Modular Assembly for Repair and Inspection Under Sodium), this test facility consists of an Electromechanical force driven press connected to a cylindrical bell immersed inside a pressurized water tank. The bottom of the bell is equipped with modular flanges on which seals can be mounted in a groove. In front of the seal, docking surfaces of various shapes (plane, concave or convex) can be installed. The principle of the test is to immerse the bell inside the water, and then the tank is pressurized to a given pressure. The water can be used to mimic sodium thanks to its rather similar hydraulics properties of concern regarding sealing, such as viscosity, density or silicone-wettability. Once the seal is docked on the surface, a pressure is applied on the bell with the press then the bell is drained of its water. Leak-test and visual survey of the inner part of the bell are made, while in the meantime, the force applied on the bell is decreased until a leak appears. Several prototypes of seal were made and tested on MARIUS. With the lip-seal profile (b) shown on Figure 5, the sealing was achieved with only 200N applied (seal Ø350mm). Thanks to the seal shape, the water pressure on the outer surface of the lip provides almost enough pressure to stick the seal on the surface. At 350N, the seal compression was sufficient to a watertight contact for the delta tip of the seal located behind the lip. With this double contact the sealing is improved and a better stability of the bell is ensured, especially on a surface with strong local defects. These results, demonstrating the efficiency of a silicone lip-seal to seal the front RHIB face with less than 500N of applied force, are encouraging and promote solutions based on a silicone seal. Indeed, this 500N have to be compared with the estimated compression force of 10kN than can be transferred to the RHIB by a robotic arm.

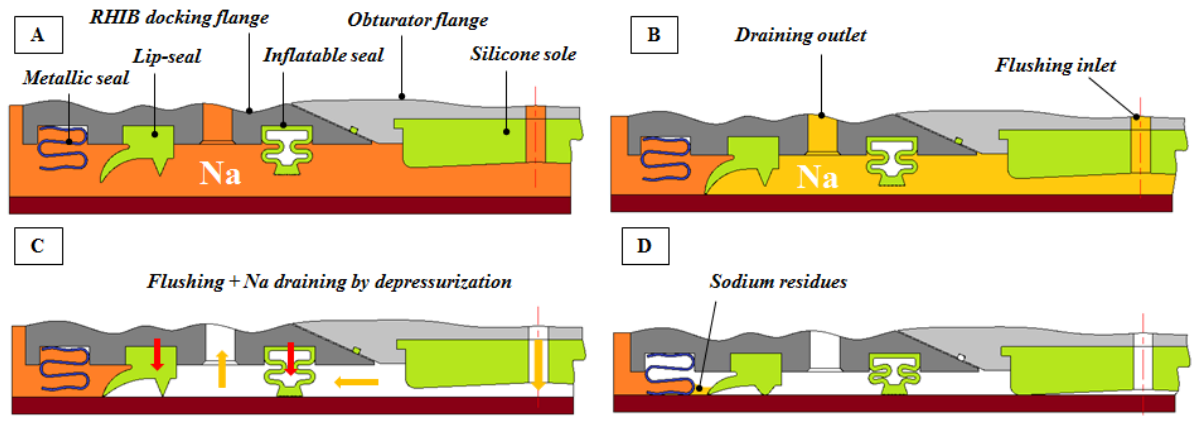

FIG. 7. Principle of the triple seals docking flange: [A] Flange approach [B] Docking of the silicone lip-seal, 1st compression [C] Flushing of Na from the middle of the RHIB followed by a draining by depressurization, 2nd compression of lip-seal and inner seal [D] The resulting suction effect lead to the compression of the metallic seal, the RIHB is maintained in depression with three sodium-thigh barriers.

In order to solve the issues raised by the aging tests and to cope with the degradation of the silicone immersed in sodium, an advanced concept is under consideration (Fig.7). The idea is to combine two silicone seals to form a closed volume which will be depressurized to generate a suction effect, providing extra-force to compress a metallic seal. Protected behind a metallic barrier, the silicone seals will be only exposed to un-drained sodium residues and therefore will be less exposed to chemical degradation. The metallic seal shall be carefully chosen to feature a low compressive stress, even though the suction effect can generate high forces proportional to the surface of the enclosed volume. The metallic and silicone seal-shapes also need to be designed to help the flushing of the sodium during the second compression phase. If the lip of the outer seal, despite a higher compression, is leaking, the sealed enclosed volume and therefore the suction effect will be maintained (and even increased) by the inner silicone seal and outer metallic seal. The extra-force generated by the suction will also be of some interest to release constraints on the RH system to counteract the torque and forces of repair tools (such as mechanical washing brush).

The next challenge of the RHIB is the design of the bell shutter required to seal the bell before its docking. The sealing system of the obturator must allow the bell opening flushing the residual sodium in front of the working window, and once the operation completed the bell closure and sealing before the undocking. If the sealing between the shutter and the RHIB flanges is not an issue, the flushing and draining of the sodium, trapped in front of the bell after the docking, remains a tricky problem to solve. Indeed, most ISI&R tools will not accommodate a thick sodium film after docking, and sticking residues on the shutter or bell flanges may strongly impact the sealing efficiency.

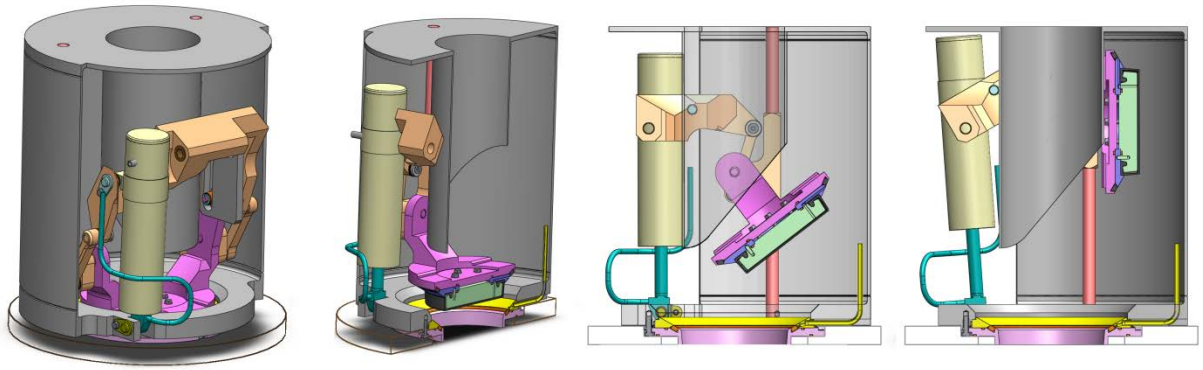

FIG. 8. Conceptual RHIB shutter system

Added to these functional constraints and the very restricted volume of the RHIB, the design of this system was conducted with the idea to conceive of a simple system with as few interfaces as possible. Indeed, the impact on the design of the future ISI&R systems (still to be defined) mounted on top of the RHIB have to be strictly limited. With the assumption of Ø120 circular working aperture and a bell outer diameter below 350mm, a conceptual design of an obturator with its subsystem was conceived. The chosen design consist of a robust mechanical system (Fig.7) based on simple mechanical cams transferring the movement of linear actuators (located on the side) to a rotatable shutter lid pressed against the bell closure flange. Pneumatic actuators were preferred to others mechanical or electrical systems. In this solution, inlet and outlet gas pipes are the only mechanical interfaces required, and they are used both for the actuation and the sodium flushing and draining. A flushing pipe with a non-return valve is connected to the center of the shutter flange, to allow an argon blow after docking. On the shutter flange a thick and smooth silicone sole (possibly hollow or inflatable) is mounted to limit the volume of sodium trapped between the seals. Another pipe located near the external lip-seal is used to drain the remains of sodium after flushing, and ensure the suction effect described above once the two elastomers are compressed. Further analysis and mechanical calculations are on-going to improve the system to the mature stage. The next step will be the development of a full scale prototype to be tested in the MARIUS facility.

4. Conclusions

Ensuring the dynamic and static sealing of a remotely handled system inside a nuclear vessel filled with sodium at 220°C is a real challenge. The choice of a proper sealing material is probably the hardest issue. Confident in the possibility that silicone base compound can be used providing a limited exposure of the seal to sodium (time and exposed surface), new compositions of silicone are under study. More severe aging under radiation and surface coatings are foreseen.

In this R&D program the study of preliminary concepts has been an opportunity to address several technical options and to compile a list of pertinent features for very specific mechanical system such as the RHIB. On the sealing system operating during the docking phase, an efficient seal profile has been designed and successfully tested. The concept of concentric seals used to drain the residual sodium, and attach the bell by suction to the surface is a promising and innovative idea. The proposed obturator associated with this sealing system form an integrated system fulfilling the requirement. The detailed definition of the system to be followed by its test in MARIUS is the next step of the program.

The integration of the obturator and sealing system with the embedded ISI&R tools will be another task on its own. The development of specific systems allowing for the inspection and repair of complex geometries will be from the sealing point of view a very challenging task. The RHIB concept presented in this paper is a rather universal concept that might be adapted depending on the reactor zone to inspect or repair.

ACKNOWLEDGEMENTS

The authors would like to thanks all the colleagues at CEA, Technetics group and EDF who provided us with fruitful information, guidance and technical insight. We would like to quote the work of the CEA Cadarache team of DTN/STPA/LIET which operates the sodium crucible facility PENELOPE for their availability.

REFERENCES

[1] F. JADOT, F. BAQUE, J.Ph. JEANNOT, J.M. AUGEM, J. SIBILO ASTRID, Sodium cooled Prototype : program for improving In Service Inspection and Repair, ANIMMA 2011 Int. conference, Paper 3-37.

[2] F.BAQUE,F.REVERDY,J.M. AUGEM, J.SIBILO, Development of Tools, Instrumentation and Codes for Improving Periodic Examination and Repair of SFRs, Hindawi Publishing Corp., Science and Technology of Nuclear Installation, Vol 2012, Article ID 7 18034,

(2012).

[3] J. DAVIOT et V. GRABON – FRAMATOME, Studies of liquid metal interaction with materials, Science Forum Vols 251-254,pp 671-678(1997).

[4] J.R WEEKS, H.S. ISAACS, Corrosion and deposition of steel and nickel base alloy in liquid sodium, Advanced in corrosion Science and technology Vol.3 Plenum Press (1973).

[5] R.H. JONES – Test memorandum N°4 – Atomic Power Development associates – December 1958 - Compatibility of rubber and elastic materials in Sodium and sodium vapour

[6] L. ROSENBLUM, H. PUTRE – NASA TN-D-1284 – 1962 - Compatibility of several Plastics and Elastomers with Sodium, Potassium, and Rubidium

[7] E. F. ANTAL, compatibility with liquid sodium at 450°F, technical report of Hanford Engineering Development Laboratory, US Atomic Energy commission, June 1971.

[8] JF. SAUVAGE, “Phénix 30 years of history: the heart of a reactor”, Ed. CEA, France (2004).

IAEA-CN-199
Paris, France, 4-7 March 2013
Paper CN-199-126

Sodium-Water Reaction approach and mastering for ASTRID Steam Generator design

Manuel SAEZ[1], Sylvain MENOU[2], Alexandre ALLOU[1], François BEAUCHAMP[1], Carole BERTRAND[1], Gilles RODRIGUEZ[1], Gérard PRELE[3]
[1]: CEA, DEN, 13108 Saint-Paul lez Durance Cedex, France
[2]: AREVA NP, 10 rue Juliette Récamier 69456 Lyon Cedex 06, France
[3]: EDF SEPTEN, 12-14 avenue Dutrievoz, F-69628 Villeurbanne Cedex, France
Contact author: Manuel SAEZ, +33442253465, manuel.saez@cea.fr

Abstract. The Steam Generator Unit (SGU) is one of the key components in the Sodium-cooled Fast Reactor system for it provides an interface between sodium and water. The objective for the SGU is related to the elimination or to the improvement of mastering of Sodium-Water Reaction (SWR).
A first measure of prevention is the presence of the intermediate sodium circuit to separate chemical risk and radiological risk and to avoid pressure loadings inside the primary circuit in case of SWR.
Modular SGU concept is selected, which limits the mechanical consequences on the secondary loop and on the intermediate heat exchanger of a postulated large SWR characterised by simultaneous guillotine failure of all the tubes of an SGU module (accidental envelope case). In addition, protection against large SWR is ensured by passive fast draining of the sodium loop using rupture disks.
The redundancy and performance of the leak detection systems is reinforced.
Supporting work includes SWR studies (modelling, pressure loading in the SGU, in the secondary loop and in the intermediate heat exchanger). SGU concepts are reviewed.

1. Introduction

Fast Reactors have a unique capability as sustainable energy source in terms of both utilisation of fissile material for energy production and minimisation of the nuclear wastes, due to hard neutron spectrum. As a result of a screening review of candidate technologies and in the framework of the international forum Generation IV, Sodium Fast Reactors (SFRs) are among the selected systems to address the sustainability issues with a coherent set of innovative requirements. Guidelines for the definition of such innovative requirements are the Generation IV goals with significant improvements on economy, safety, environment, waste management and proliferation resistance as promising milestones towards sustainable nuclear energy.

In terms of sustainability, Generation IV systems shall make the best use of Uranium resource, be able to multi-recycle plutonium, and have the capability to perform transmutation of certain minor actinides. This calls for fast neutron reactors and a closed fuel cycle.

In terms of safety, improved and robust safety demonstration with regard to former fast reactors is expected: enhanced prevention of whole core melting accidents, prevention and mitigation of risks due to sodium chemical reactivity, and robustness to external hazards. The level of safety must be at least equivalent to Generation III reactors. Lessons learned from the Fukushima accident will also be taken into account.

In terms of economy, Generation IV systems shall be competitive, for the same overall performance, compared to other sources of energy at the time they will be put into operation. This means a lot of effort will focus on investment costs but also to availability and operation costs.

Proliferation resistance applies not only to the reactor, but also to the whole fuel cycle.

A June 2006 French law on sustainable management of radioactive materials and wastes requests that, concerning transmutation of long-lived radioactive elements, studies and investigations shall be conducted in order to provide by 2012 an assessment of the industrial prospects of those systems. Fast reactor strategy was confirmed in May 2008 at Ministry level, and in September 2010, an agreement was published between CEA and French Government in order to conduct design studies of the ASTRID prototype and associated R&D facilities [1].

ASTRID is an acronym for Advanced Sodium Technological Reactor for Industrial Demonstration. The essential objective of the ASTRID prototype is to demonstrate advances on an industrial scale by testing innovative options in areas earmarked for improvement (in particular safety, operability and inspection and repair). ASTRID will also be capable of carrying out radioactive waste transmutation in order to demonstrate the industrial scale feasibility of this technology for reducing the volume of end waste and lifetime of ultimate waste. Furthermore, ASTRID should be capable of carrying out experimental irradiations in a fast neutron spectrum.

ASTRID is a 1500 MWth reactor (about 600 MWe). Characteristics should be extrapolable to future high-powered industrial Sodium-cooled Fast Reactors.

A first phase of the Preliminary Design Project is being conducted from mid 2010 to the end of 2012. The pre-conceptual design delivered by the end of 2012 considers some open options. Innovation and technological breakthroughs have been favoured, while maintaining risk at an acceptable level. On completion of this phase it will be possible to obtain, for the important deadline set by the June 2006 law, the first investment cost estimation. During the pre-conceptual design phase, interactions started with the Safety Authorities on safety orientations. The conceptual design should be delivered by the end of 2014. During the conceptual design phase, the ASTRID design choices will be finalized and the Safety Option File will be submitted. Then from 2014 onwards, the basic design phase will start. ASTRID demonstration prototype is to be commissioned in the 2020 decade [2].

At this stage of the ASTRID studies, two Power Conversion Systems (PCS) are evaluated (steam water versus gas). Although the Rankine steam cycle is a well developed technology, the design and licensing safety evaluation must deal with the SWR and the secondary sodium fire issues. Potential SWR leads to hydrogen gas formation and exothermic energy release. As an alternative to the classical steam cycle for the thermodynamic transformations, a substantial effort is performed providing both significant expertise and original work in order to investigate the interest in using a gas based PCS; in this case, SGU is replaced by sodium-gas heat exchanger.

This paper addresses the Rankine steam cycle for power conversion. SWR studies are presented (phenomenology and modelling, impact on SGU, intermediate loop and intermediate heat exchanger). The paper presents also a status of the ASTRID Steam Generator design, with details on SUPERPHENIX, EFR (European Fast Reactor), PFBR (Prototype Fast Breeder Reactor), and BOR-60 SGUs.

2. Sodium-Water Reaction

This section addresses the sodium-water reaction. Chemical reaction, origins, effects, protection and detection systems are discussed; phenomenology and modelling are also presented.

2.1. Chemical reaction

SWR is a violent and exothermal chemical reaction, characterized by three reactions (a main reaction, and two secondary reactions).

- The main reaction is a complete, quasi-instantaneous and irreversible reaction:
  - $Na + H_2O \rightarrow NaOH + ½ H_2 + 162$ kJ/water mole
- Secondary reactions are the following:
  - (1) $2Na + NaOH \leftrightarrow Na_2O + NaH$
  - (2) $Na + ½ H_2 \leftrightarrow NaH$

2.2. SWR origins and effects

Normal operation of the SG may induce damage to the heat exchange tubes. SWR origins are given hereafter:

- Tube corrosion: loss of tube wall thickness due to generalized corrosion or stress corrosion cracking (mainly in welded zones) in case of aggressive chemical conditions.
- Thermal shocks: when under-saturated water is injected at the superheater inlet, inducing thermal fatigue.
- Restraint tube expansion: buckling.
- Tube bundle vibrations: hydraulic effect of sodium flow, inducing tube wear.

SWR effects are:

- Chemical effects: generalized corrosion due to oxides (superficial corrosion) and stress corrosion cracking due to NaOH (very high at high temperature), and local erosion / corrosion (wastage) due to propagation to surrounding structures.
- Mechanical effects due to large water leaks (>100 g/s), leading to rapid overpressure (due to pressure wave propagation), or low overpressure (due to mass transfer associated with a massive water inlet in the sodium side).
- Overheating effects due to large water leak effects on tubes: deformation, swelling, bursting.

2.3. SWR wastage and overheating effects

The origin is an initiating defect (mainly in welded zones) leading to a crack, then a leak, plus a SWR leading to a reaction jet. The effects are the growth of the leak orifice (self-wastage), and the damage of the neighbouring tubes or wall by removal of material. Consequences are the perforation of adjacent tubes leading to secondary leaks. Under effects of the very hot reaction products, tubes strongly become strained (swelling of tens of %) and can burst in tens of seconds by creating important breaks.

2.4. SGU protection and detection

The SG and the secondary circuit are protected against a SWR event by two ways: protection and detection systems [4].

- The protection system is used to minimize SWR effects in the secondary loop after a water leak into sodium. Protection systems are integrated in the design against corrosion risk (for example, draining or not and purification of polluted sodium), against wastage risk (protection of tube welds), and against overheating and overpressure risks (bursting disks on sodium side). Detection systems are active systems.
- The detection of small leak is done by detecting the hydrogen produced by the SWR, dissolved in sodium or dispersed in the cover gas. Different ways can be used: permeation of hydrogen through thin nickel membranes, electro-chemical flow meters and acoustic detection in complement of hydrogen detection. The detection of the rupture of the membranes (detection of presence of sodium) initiates the “active” system of isolation and blow down of the steam side of the SG and the shutdown of the reactor.

2.5. SWR modelling

Figure 1 presents stages of SWR evolution in the SGU. Four classes of leaks are defined:

- Micro-leak (water leaks below 0.1 g/s), with self-wastage evolution: reaction products are formed so slowly that they do not damage other tubes and the leak is so small that it could be not detected.
- Initiation of a small leak (from 0.1 to 50 g/s) by self-wastage that leads to a reactive jet causing wastage on the direct adjacent tube or wall: the neighbouring tube can be perforated by wastage if the leak is not detected before leading to a secondary leak (intermediate leaks).
- Intermediate leak (from 50 g/s to 200 g/s): many other tubes are damaged by wastage. An intermediate leak could be due also to the bursting of one tube after overheating. It will produce significant excess pressures in the secondary circuit. There is a significant risk of failures of many tubes and propagation towards large leaks if the leak is not detected beforehand.
- Large leak (from 200 g/s to several kg/s) with mechanical effects with firstly a shockwave and secondly a mass transfer correlated to massive hydrogen production: the affected SGU is isolated and depressurized if the leak is detected or by the detection of the rupture of the bursting disks. To be noted that the pressurized nitrogen is also introduced within the tubes when the steam pressure decreases to avoid sodium ingress in the water steam system. If the disk bursts, it initiates the fast draining of the SG sodium side.

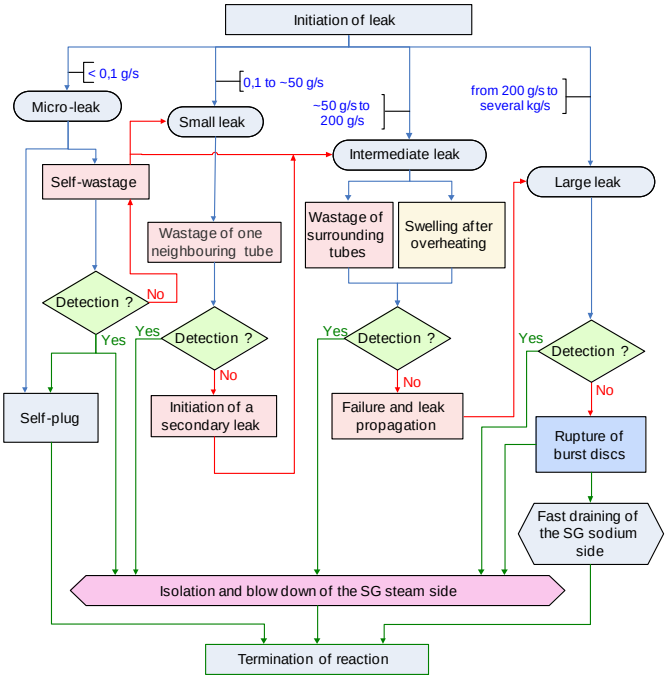

FIG. 1. Stages of SWR evolution in SGU

Codes are used for SWR modelling to assess SWR consequences on the SG and the secondary circuit.

- PROPANA for self evolution calculation, wastage modelling (PERCEVAL), and response time of the hydrogen detection system (HYDET).
- CALHYPSO for modelling of SWR products evolution and transport, hydrogen detection response modelling according to leak characteristics.
- MECTUB for thermo-mechanical behaviour of SG tubes submitted to overheating effects.
- EUROPLEXUS for pressure waves propagation and effects on secondary sodium circuit.
- REACNOV for long term pressure fluctuation effects on secondary sodium circuit.
- GVNOV for thermal-hydraulic conditions for transient states such as during a water leak event.

3. Steam generator design

There is a variety of tube types in the worldwide experience on FBR SGU, i.e., straight, U-tube, hairpin, bayonet, helical coil, and serpentine [3].

The majority of operating or in project sodium steam generators produce superheated steam after a single pass through the component (once through). The component may consist of a unique module or of separated economiser-evaporator and then a super-heater (plus sometimes a re-heater).

In order to limit the risks of SWR and its consequences, special care is taken for the material choice and the tube bundle design. The choice criteria are: the mechanical properties at temperature (fatigue, creep,…), the manufacturing aspects (tube fabrication, welding), the SGU capital cost, the corrosion strength on water-steam side and on sodium side in normal and incidental operating conditions, and the wastage behaviour in case of SWR.

In the following paragraphs, several steam generators are presented (SUPERPHENIX, EFR, PFBR, BOR-60 and ASTRID).

3.1. SUPERPHENIX

The SUPERPHENIX SG are 750 MWth once through units with three heat transfer zones (economiser, evaporator and super-heater) located along the same tube. The principal design characteristics are:

- Once through Steam Generator; single body vessel, sodium topped by a gas blanket.
- Downward sodium flow, upward water-steam flow, water and sodium completely drainable.
- Use of only one tube material with good corrosion resistance and sufficient mechanical properties. This material is a nickel-chromium-iron alloy-type, alloy 800.
- A small number of relatively long tubes to minimise the number of welds. Multi-helix bundle.
- Exclusive use of butt welds for all tube joints in contact with both sodium and water-steam. Such welds are the most reliable and the easiest to inspect.
- Water and steam boxes or headers located outside the unit.

Each SGU comprises a tube bundle helically wound around a vertical tube and inserted in a vertical cylindrical shell. The SGU is approximately 23 m long and 3 m in diameter. It is closed at both ends and penetrated by two upper lateral, diametrically opposed sodium inlet nozzles. The unit is supported on a cylindrical skirt. Each Steam Generator weights 180 tons. All shell structural parts are made of stainless steel. Tubes are made of Alloy 800.

The hot sodium entering each steam generator is collected in an inner distribution plenum from which it flows down around the helical tubes. The sodium level within the distribution plenum is allowed to vary freely to absorb pressure waves due to the SWR. The sodium flowing down past the tube bundle is divided into eight parallel streams by the tube supporting devices.

The tube bundle comprises 17 concentric layers of tubes wound round the central tube. The lower ends of the tubes individually enter the lower section of the steam generator through thermal sleeves and are welded to the tube-plates of the four water inlet boxes. Expansion bends connect the helically wound tubes to their thermal sleeves. The upper ends individually pass through the outer shell, below the sodium free level, again by thermal sleeves and are welded to the external steam headers. The tubes associated with each of the four water boxes are divided between the four steam headers, with the result that the heat exchange bundle is divided into 16 groups of tubes.

During start-up and power ascension, steam-water before to have production of super-heated steam, pass through a steam-water separator which is installed at the outlet of the steam generator in parallel with the steam outlet line. It is put out of service at about 12.5% of the load when the steam temperature overruns the saturation temperature, and inversely it is automatically put in service during the stop phases of the nuclear island when the steam temperature decreases under about 400°C.

Each SGU is equipped with a water steam fast depressurisation system. These valves open/close in a time of 3 seconds (an operating time of 6 seconds is still acceptable). The water steam depressurisation system is activated automatically in case of a SWR by the hydrogen detection system thresholds, by the breaking of the bursting disks or by the operator if needed. Large leaks induce a pressure increase in the secondary circuits which are filled each with about 320 tons of sodium. To limit these pressure increases, the secondary circuits are fitted near the steam generator with rupture disks placed in an effluent line connected to a drain tank and a stack: the rupture of these disks empties the Steam Generator from sodium and stops the SWR. Another effect is the "opening" of the secondary circuit to the atmosphere at the stack top limiting any pressure increase. Such a protection is efficient for large leaks enabled by the breaking of rupture disks. Such a system protects the plant against large leaks. Each Steam Generator is fitted with one double disk assembly (in series). This assembly is placed in a sodium discharge pipe (with a diameter of 750 mm) located at about four meters from the outlet of the Steam Generator. The distance between the SGU and the rupture disks is short to increase the efficiency of the system but has to be long enough to protect the disk from thermal stresses. A small pipe is set up to connect the gas space between the two disks and the gas downstream space of the pipe between the secondary disks and the dump tank. A sodium detector is set up in the gas space between the two disks to detect a leak of the first disk and to raise an alarm. Three sodium detectors are placed between the secondary disk and the dump tank to trip automatic actions. Each SGU has two in sodium hydrogen detection systems; these systems are independent.

3.2. EFR

The development of a straight tube Steam Generator design was launched at the beginning of the EFR project because there was a lack of an exhaustive SUPERPHENIX steam generator feedback and because preliminary economic estimations had shown that the straight tube SGU design was cheaper than the helical one and was more adapted to in line production.

The SGUs proposed for EFR are once through straight tube units using modified 9Cr1MoVNb (grade 91) ferritic-martensitic steel. The reference design is the purely straight tube (stiff tube, bellows on shell concept) and the preferred unit size is 600 MWth leading to six units per station. The tubes are arranged in a circular pitch between two tube-plates. There is no weld in the tubes other than the one at each end required to attach the tubes to the tube-plates. Between the tube-plates, the tubes are restrained by a series of grid plates which are supported by brackets to the shell. At the top of the unit, the shell diameter increases to form the sodium inlet annulus and carries a single sodium inlet nozzle. The sodium inlet flow enters the unit between the shell and the internal cylinder before being directed by a suitable baffling into the active section of the bundle. At the bottom of the unit, the shell diameter similarly increases to form the sodium outlet annulus and carries a single sodium outlet nozzle. A semi-stagnant sodium region is provided adjacent to the lower tube-plate to mitigate the thermal shocks. High integrity forgings are used for both tube-plates, into which are welded the steam and water headers forming together spherical headers. Expansion bellows on the main shell above the lower tube-plate provide a large flexibility to compensate for tube bundle-shell differential thermal expansion. Wastage due to upper and lower tube welds leaks is minimised by the adoption of a gas space at the top weld, and a thick anti-wastage plate at the bottom weld. The SGU support system consists of a conical support skirt above sodium outlet collector and a radial guide, under sodium inlet collector. The external surface of the SGU can be used as a heat sink for removing heat from the secondary sodium.

3.3. PFBR

The Steam Generator is a once through integrated type design using straight tubes and an expansion bend in each tube.

Based on overall engineering judgement from manufacturing schedule and leak rate to be lower than BN-600 of about $2x10^{-5}$ welds/year, four Steam Generators per loop are selected. Based on ASTM Gr 91 (modified 9Cr–1Mo) as Steam Generator material and optimization studies, the steam parameters at turbine stop valve have been set to 16.6 MPa and 490°C. Steam Generator tube leaks are detected by a leak detector (hydrogen in sodium) provided at the outlet of each SG module and an additional detector provided in the common outlet header. Two “hydrogen in argon” detectors are installed in the cover gas space of the surge tank. Acoustic leak detectors are also installed at various locations on the outer shell of the steam generator.

3.4. BOR-60

BOR-60 experimental reactor serves as a facility for tests and development of various SG designs. Five steam generators have been tested on BOR-60 reactor during previous time. First, two of them were designed in Russia, the other three in Czech Republic; they were: the SGU 1 and SG2 prototype for BN-600 power plant, the prototype of the BN-350 modular steam generator, and the inverted steam generators (where secondary sodium is flowing inside tubes and water-steam outside). The inverted design proves to be very preferable from the leakage viewpoint because the evaluation of the tube wall damage is slower and qualitatively different to the steam generator types where water flows inside the tubes. Two steam generators of the inverse type have been developed, the first, a Micro Module Inverse Steam Generator (MMISG) and the second, a Module Inverse Steam Generator (MISG). The MMISG and MISG are being tested at the BOR-60 facility.

3.5. ASTRID

Improving Sodium-Water-Air Reaction risk management is one of the key safety issues for ASTRID. This is why studies dealing with Sodium-Water Reaction, including Sodium-Water-Air Reaction, are considered of prime importance in view of a Steam-Water Energy Conversion System. Studies include both prevention and mitigation aspects, with dedicated tools to be developed through R&D.

Potential benefit of a modular SG with respect to the robustness of the safety demonstration is evaluated. Several modular SG designs (with power ranging from 94 to 150 MWth) are studied with regard to their potential benefit from a safety point of view. The particular concern is the capability to build a very robust demonstration showing that the consequences of bounding scenarios of SG tubes failures can be limited. In that respect, calculations have been performed to study the consequences of the bounding case of an simultaneous and instantaneous rupture of all tubes of an SG module, and evaluate whether integrity of the secondary system can be maintained (at intermediate heat exchanger level, at sodium loop level, and also at steam generator level). It is emphasized that such an accident should have a very low occurrence frequency and, should it be considered in the safety demonstration, would be considered as a design extension condition. In terms of safety, consideration of such an accident should contribute to the robustness of the demonstration as it would ensure avoidance of any cliff edge effect which might be linked to the assumptions regarding the number of tube failures or to the kinetics of the phenomena leading to the failure of several tubes.

The objective for the ASTRID SGU is related to the elimination or better mastering of SWR.

Concerning practical elimination of large SWR by leaks propagation, investigations are focused on alternative concepts including an inverted concept with sodium inside the tubes and water outside. This concept can meet the objective to minimize consequences of small water leaks. It features intrinsic limitations on the evolution of a water leak by wastage to the affected tube (no propagation to the surrounding tubes) due to small volume of sodium that can react with water and hydraulic blockage phenomena. Major issues are the SWR modelling, and in service inspection.

Concerning intrinsic limitation of the magnitude of the largest SWR, a straight tube ferritic-martensitic steel (modified 9Cr–1Mo) 125 MWth concept was found an appropriate design in terms of economy.

The helical SGU design can be favourably considered for ASTRID. A design adapted to a compact secondary loop with hot and cold legs connected at the bottom part of the SG is also under investigation.

3.6. Design comparison

The steam generators are compared on the following items: material, design, and protection system.

- Material: ferritic-martensitic steels are very sensitive to generalized corrosion and present an important wastage and leak auto-evolution rates. The austenitic alloys have a better behaviour towards the above phenomena, but are sensitive to the stress corrosion in the presence of sodium hydroxides. It can be outlined that 9%Cr presents good mechanical properties at high temperatures.
- Design: the straight tubes design with bellows on the shell is more difficult to justify towards thermo-mechanical behaviour than tubes with expansion bends designs. The straight tubes design with expansion bends on the tubes allows for higher flexibility to accommodate differential thermal expansions, especially between the tubes. On the other hand, due to the bend on the tubes, the manufacturing sequence and the tube supporting system need to be adapted accordingly.
- Protection system: the protection systems are designed to detect water in a sodium leak. The worse behaviour of ferritic-martensitic steels towards leak auto-evolution and wastage than the alloy 800 alloy leads to require acoustic detection in addition to the conventional chemical detection system.

4. Sodium-Water Reaction calculations

4.1. SWR studies in support to ASTRID SG design

Wastage and overheating models, from respectively PROPANA and MECTUB codes, are very strongly correlated with the type of the SG tubes material and with its intrinsic behaviour. These models were elaborate and validated for alloy 800 and helical tubes of SUPERPHENIX SG. An evolution towards straight SG tubes made of ferritic-martensitic steel (grade 91) would require improved knowledge in the following fields: influence on the kinetic of evolution of the leak and on the wastage rate and behaviour towards the overheating and bursting effects in the field of the high temperatures (up to 1200°C). Studies are underway to adapt the models and to qualify the codes for this material. R&D actions are based on experimental programs: wastage tests performed on the SWAT-1R facility at the JAEA/O'Arai research centre [5], and bursting tests of SG tubes in the SQUAT bench at the CEA/Cadarache research centre.

4.2. Wastage propagation calculations

For steam leak rates in the range from 0.5 to 20 g/s, the calculation of penetration times of the SG tubes by impingement wastage using the following PROPANA code highlights:

- The helical tube alloy 800 design seams more suitable than the straight tube ferritic-martensitic steel 9%Cr concept because penetration times are twice to 6 times longer. In sodium hydrogen detection systems are sufficiently effective to detect any kind of leak before the initiation of a secondary leak in the helical SG concept.
- The inverted SG design is the best one on the wastage point of view. Indeed, tube penetration is 3 to 100 times longer than in the other traditional concepts.

PROPANA is also used to evaluate the penetration time of the external ring of the SGU if the SWR jet is directed towards the internal wall of the ring. The key point is the existence of a second external ring, inside of the main one. This additional barrel increases the distance between the leaking tube and the target wall, which involves a strong decrease in the wastage rate.

The inverted Steam Generator is not affected by this phenomenon because the direction of the pressure gradient in the SGU keeps the SWR jet inside of the leaking tube. It is obvious that there is no leak propagation from one tube to the other tubes by wastage in the inverted SG design.

4.3. SWR pressure calculations for ASTRID secondary loop

The first system investigated is hydrogen detection by means of permeation through a very sensitive nickel membrane, but fabrication and operation is complicated, and response time must be optimized. The second system is an electro-chemical flow meter tested recently in PHENIX; the system is simple, with a possible optimization of response time. Then, study of a diversified detection method based on acoustic principle is in progress. Their advantage is the short response time due to the absence of transit time like those for hydrogen detection.

The main goal of this modelling is the assessment of the mechanical consequences of large water leaks, especially bounding scenarios of one to several “Double Ended Guillotine Failures” (DEGF) instantaneous Steam Generator tubes failures, in very short times: 1 millisecond for water leak build-up time, several tens to hundreds of milliseconds for characteristic times for the sound wave.

Elements of the loop can be affected by the pressure loadings, particularly integrity of the intermediate heat exchanger (as an element of the secondary containment barrier) must be maintained to withstand pressures of all water leaks covered by the envelope scenario.

Calculations are performed for design and safety studies to demonstrate that consequences of steam generator tube ruptures can be limited [4].
The loop configuration studied has discharge lines: three (four in the loop configuration with inverted SG) DN400 cold discharge lines in the lower part of each SG module, one DN700 cold discharge line in the cold pipe and one DN700 hot discharge line in the hot pipe.
Three configurations are calculated with EUROPLEXUS code; each one corresponds to an ASTRID SGU concept (straight tubes, helical tubes, inverted tubes). EUROPLEXUS calculations consider the bounding case of a simultaneous and instantaneous rupture (< 1 millisecond) of all tubes of a SG module.

- In case of a secondary loop with 3 SG of 125 MW (straight tubes) the calculation corresponds to 468 DEGF in the lower part of one of the 3 SG modules (calculations are done for each module). The maximum pressure in the steam generator is 163 bar, under the allowable pressure of 210 bar (category 4). The maximum pressure in the pipes is 123 bar, the maximum plastic deformation is lower than 5%, which is acceptable considering the good ductility of the material of the piping (austenitic steel 316). The pressure obtained in the IHX is 20 bar, under the allowable pressure of 55bar (category 4).

- In case of a secondary loop with 3 SG of 125 MW (helical tubes) the calculation corresponds to 84 DEGF in the lower part of one of the 3 SG modules (done for each module). The maximum pressure in the pipes is 122 bar; the maximum plastic deformation is lower than 5%. The pressure obtained in the IHX is 32 bar, under the allowable pressure of 55 bar (category 4).
- The cold discharge line at the outlet of each of the SG modules allows for the reduction in pressures in the nearby modules. Moreover, the addition of a DN700 cold discharge line (in addition to the DN700 hot discharge line), as a complement to the cold discharge lines at the outlet of each module, considerably decreases the pressures in the IHX and in the main pipes, where the category 4 criteria are now verified with good margins, except for the inverted Steam Generator.

5. Conclusions

The modular steam generator concept is selected for ASTRID. It brings flexibility for the expertise of failed modules after their removal. Another advantage of modular units is to intrinsically limit the mechanical consequences of a postulated large SWR.
Sodium water air reaction studies will include both prevention and mitigation aspects, with dedicated tools to be developed through R&D.
Regarding safety analysis, the possibility to move from the scenario of instantaneous failure of the whole steam generator tube bundle toward a scenario with sequenced failure needs to be investigated.

NOMENCLATURE

ASTRID	Advanced Sodium Technological Reactor for Industrial Demonstration
DEGF	Double Ended Guillotine Failures
EFR	European Fast Reactor
IHX	Intermediate Heat eXchanger
MMISG	Micro Module Inverse Steam Generator
MISG	Module Inverse Steam Generator
PCS	Power Conversion System
PFBR	Prototype Fast Breeder Reactor
SFR	Sodium-cooled Fast Reactor
SG	Steam Generator
SGU	Steam Generator Unit
SWR	Sodium Water Reaction

REFERENCES

[1] F. Gauché; The French Prototype of 4th Generation Reactor: ASTRID; Annual meeting on nuclear technology, Berlin, May 17-18, 2011.
[2] P. Le Coz *et al.*; Sodium-cooled Fast Reactors: the ASTRID plant project; Proceedings of ICAPP'11, Nice France, May 2-5, 2011; Paper 11249.
[3] Y. Chikazawa *et al.*; Technology gap analysis on sodium-heated Steam Generators supporting advanced burner reactor development; Nuclear Technology, vol. 164, pp.410-432; 2008.
[4] A. Gerber *et al.*; Safety improvement research to design a Sodium Fast Reactor Steam Generator with regard to sodium-water reaction risk; Proceedings of ICAPP-2010; San Diego, USA, June 13-17 2010; Paper 10067.
[5] F. Beauchamp *et al.*; Cooperation on impingement wastage experiment of Mod. 9Cr-1Mo steel using SWAT-1R sodium-water reaction test facility; Proceedings of IAEA FR13 meeting, 2013.

Set-up of a Sodium Loop at the SAPHIR Facility

R. Coulon[a], F. Carrel[a], M. Bakkali[a], F. Lainé[a], S. Normand[a], H. Hamrita[a]

a CEA LIST, Laboratoire Capteurs et Architectures Electroniques, F-91191 Gif-sur-Yvette, France

Abstract. Electron accelerator enables high energy photons to be produced by bremsstrahlung interactions into a conversion target. Photons above 6 MeV can induce photo-fissions into uranium 238 nuclei. A neutron flux with a fast spectrum can be driven by an electron accelerator. Using this property an irradiation experiment could be conducted in order to study the sodium coolant activation into a fast neutron flux.
This paper presents a preliminary study of a sodium loop set-up at the SAPHIR facility. The specifications are the capability to perform tests in order to validate coolant activation model for sodium cooled fast reactors.
These experiments will allow validation and optimization of power monitoring method using activation product measurement by high resolution gamma spectroscopy.

1. Introduction

Activation products could be used in Generation IV sodium cooled fast reactors (SFR) as power tagging agents. The fluorine 20 is very suitable for this application thanks to its decay period of 11 s which is about 10 times lower than the mean coolant cycle time avoiding all build-up effects and its fast spectrum representativeness thanks to the $^{23}Na(n,\alpha)$ reaction threshold at 7 MeV. Feasibility of such measurement has been demonstrated during the ultimate testing program of the PHENIX reactor in 2009 (CEA Marcoule) [1]. The ADONIS prototype has been installed close to the delayed neutron detecting system in order to measure the primary sodium circulating into it [2]. During the first power increase the fluorine 20 signal has appeared in the energy channel of 1664 keV (see Fig. 1).

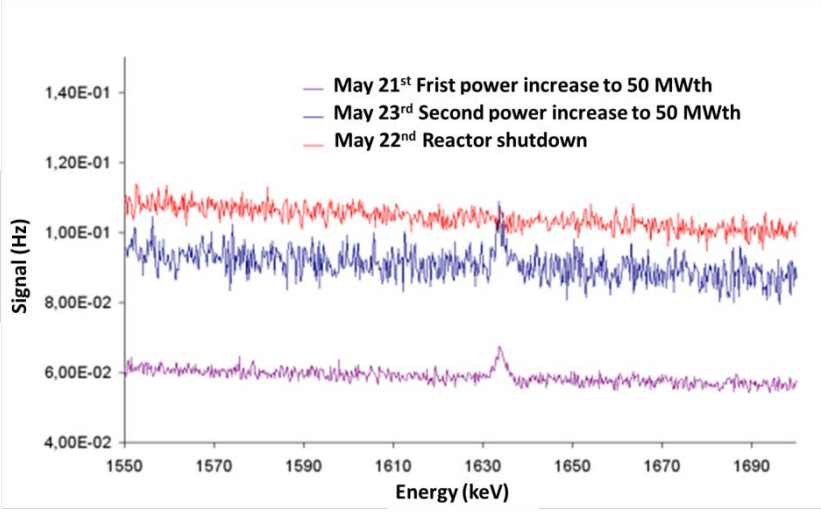

Fig. 1 : First observation of the fluorine 20 signal (behavior with reactor status)

The Fig. 2 presents a comparison between the ^{20}F signal and the heat balance power measurements. A linearity within a range of uncertainty of 20 % and the absence of build-up effect has been observed.

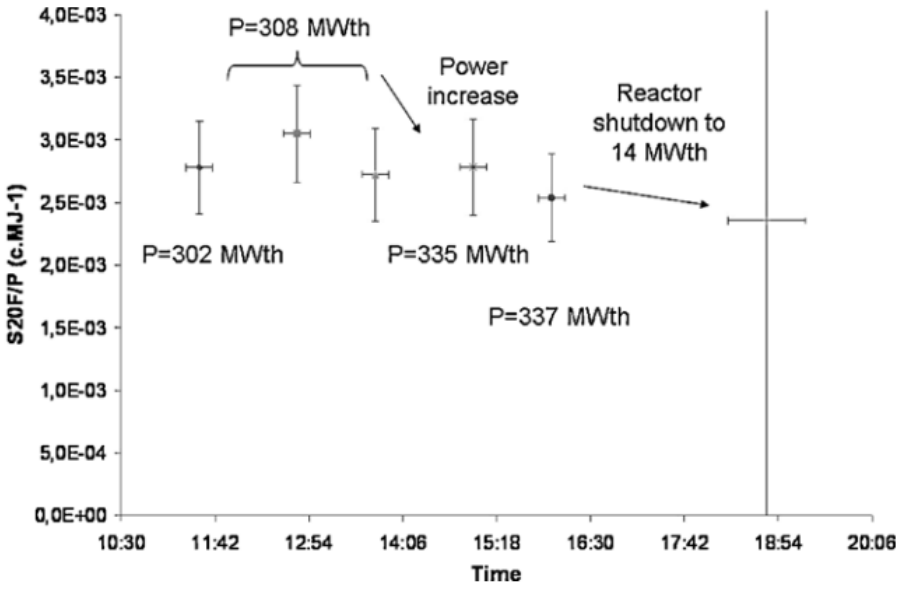

Fig. 2: ^{20}F signal to released power ratio at the reference power measurement points

A power measurement based on gamma spectroscopy needs a transfer function to be calculated. This calibration uses a model based on the nuclear balance conservation equation estimated using nuclear data and a discretization of the core geometry. The activation products concentration N_j is calculated by the Eq.1.

$$\frac{\partial N_j}{\partial t} + div\left(N_j \vec{v}\right) = N_i \int_E \sigma_j \varphi(E) dE - \lambda_j N_j \qquad \text{(Eq. 1)}$$

Where N_i is the nuclear concentration of the target nucleus i, N_j is the nuclear concentration of activation product j, σ_j is the reaction cross-section producing the activation product j, λ_j is the decay constant of the activation product j, $\vec{v}$ is the velocity field of the sodium coolant, and $\varphi(E)$ is the neutron flux.

In order to validate parameters influences of this model (as the nuclear data, nuclear concentration, coolant velocity…) an experimental set-up using a linear accelerator is presented in the next chapter.

3. Methods

The SAPHIR facility (CEA LIST) houses a linear electron accelerator using radiofrequency cavities (shown in Fig. 3). Electrons could achieve a kinetic energy up to 18 MeV and a conversion target (in a dense material like tungsten or tantalum) produces high energy photons by bremsstrahlung reactions. The SAPHIR facility enabled to develop photon activation analysis methods. Indeed, high energy photons above 6 MeV could produce photo-fission (γ,f) into a waste package. Delayed neutrons or delayed gamma-rays could then be measured in order to quantify fissile and fertile materials contained into it [3].

Fig. 3 : SAPHIR accelerator beam-line

The accelerator also produces photoneutrons by photonuclear reactions (γ,xn) into the conversion target. Current works are carried out in order to use the linear electron accelerator as a multi-device enabling to conduct active neutron interrogation in addition to active photon interrogation and high energy imaging [4]. It has been notably demonstrated that the target could be optimized in order to reach average emission intensity of the photoneutron flux close to 10^{11} $n.s^{-1}$ (two decades higher than the neutron flux delivered by traditional d-t generators). The fast photoneutron spectrum is illustrated in Fig. 4.

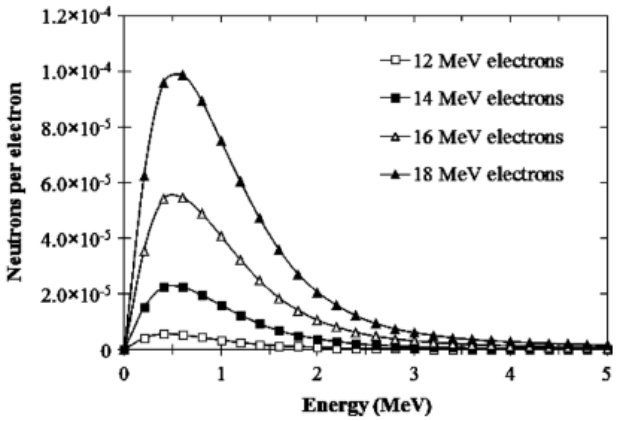

Fig. 4: Photoneutron energy spectra obtained with MCNPX and CNDC cross-sections for a 5 mm thick tungsten target (extract from [4]).

The possibility to use this fast neutron flux for reactors applications are currently under investigation. Using with a loop containing typical reactor coolant as water or sodium, the SAPHIR facility could be then an opportunity to validate coolant activation models. Compared to nuclear reactor, a linear accelerator constitutes a flexible facility to test coolant activation in different configurations of coolant temperature, coolant flow-rate, neutron spectrum, and axial flux distribution, etc.

Photoneutrons are mainly produced by evaporation process into giant dipolar resonance [5]. The shape of the spectrum is a Maxwell function with a maximum energy of 0.5 MeV and a mean energy about 1 MeV. A fission spectrum could be modeled by a Watt function with a maximum energy of 0.5 MeV and a mean energy about 2 MeV. The photoneutron spectrum is then smoother than fission spectrum and is not well adapted to simulate the fast part of a reactor neutron flux which contributes to the tagging agent productions (reaction thresholds above 5 MeV). An easy way is to add nuclear materials, like ^{238}U, close to the loops in order to produce prompt neutrons by photo-fission reactions.

3. Results

First experiments have been conducted using an air process circuit enabling to move a sample from the conversion target to the HPGe detectors in only a few seconds. The device set-up is presented in Fig. 5.

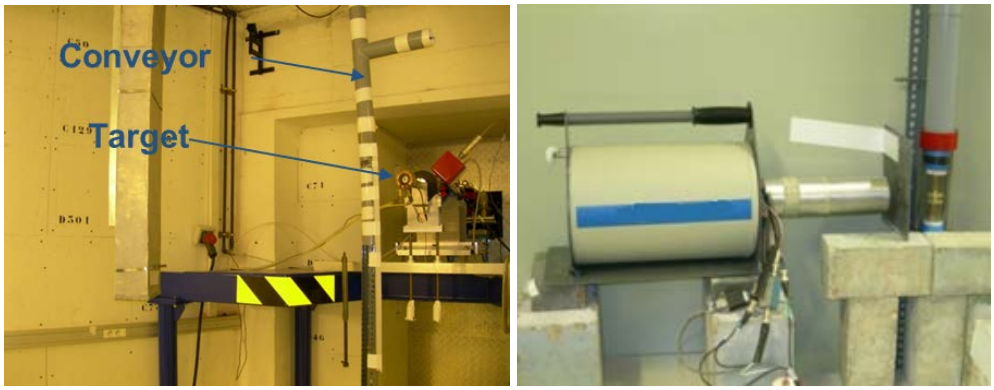

Fig. 5 : On the left: pneumatic conveyor in front of the conversion target. On the right: pneumatic conveyor in front of the HPGe detector.

Uranium oxide materials have been setup close to the conveyor position and in the field of the photon beam in order to produce neutrons from photo-fission on ^{238}U nuclei. Sodium hydroxide (NaOH) and sodium chloride (NaCl) samples have been irradiated under a photon flux produced by 18 MeV electrons. Delayed gamma spectra measured after two seconds of cooling time show that the sodium nuclei have been activated. A significant amount of fluorine 20 and neon 23 disintegrations has been measured (see Fig. 6 and Fig. 7).

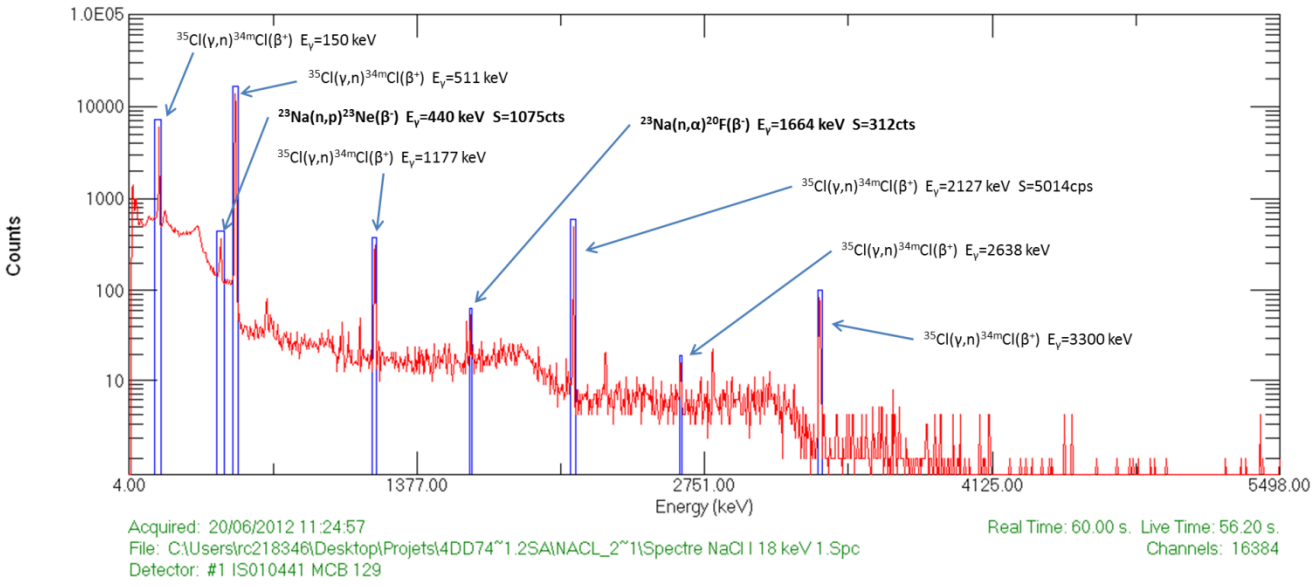

Fig. 6 : Gamma spectrum obtained after 1 minute irradiation of a sodium chloride (NaCl) sample

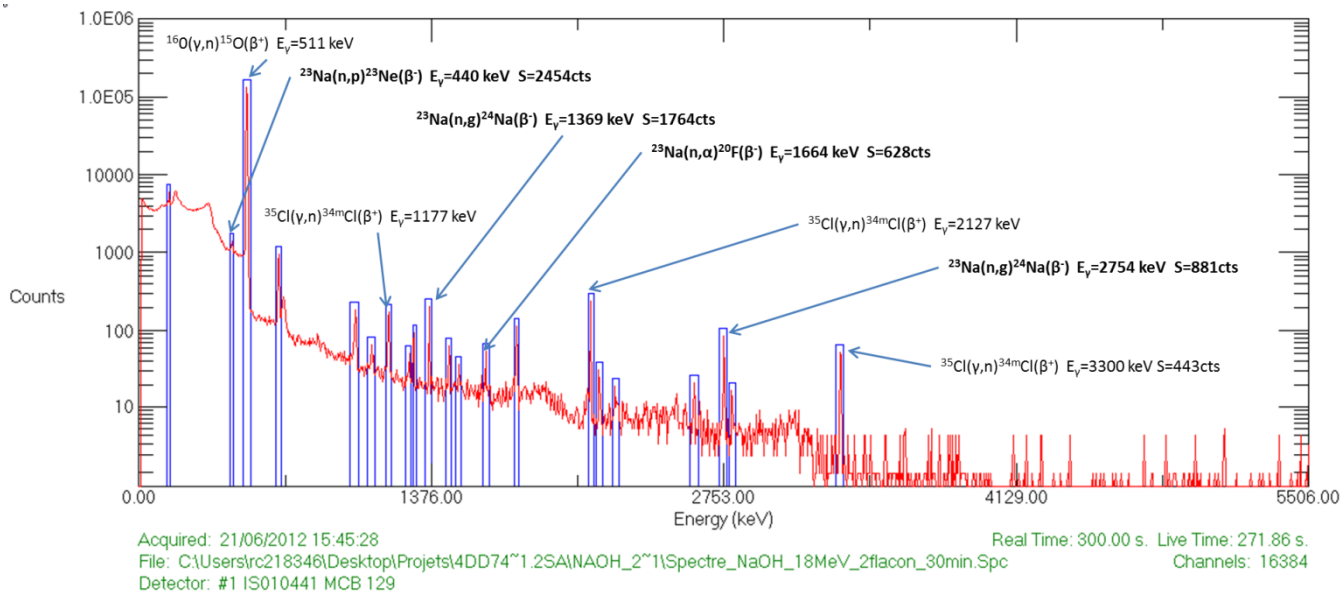

Fig. 7 : Gamma spectrum obtained after 30 minutes irradiation of a sodium hydroxide (NaOH) sample

These preliminary results show encouraging results to pursue investigations of coolant irradiation using SAPHIR linear accelerator.

6. Conclusion

The use of the linear accelerator SAPHIR is notably under investigation for studying the neutron activation of the sodium coolant. First tests using sodium chloride or sodium hydroxide have permitted to understand the way to design the sodium loop in order to conduct the activation study. The accelerator flux could not be directly used and needs to be associated with nuclear materials in order to achieve a representative neutron spectrum. The sensitivity of the activation is enough for the production of neon 23 or fluorine 20.

The next step will be the set-up of a sodium chloride loop during 2013.

REFERENCES

[1] R. Coulon, S. Normand, G. Ban, E. Barat, T. Montagu, T. Dautremer, H.P. Brau, V. Dumarcher, M. Michel, L. Barbot, T. Domenech, J-M. Bourbotte, P. Jousset, G. Barouch, S. Ravaux, F. Carrel, N. Saurel, A-M. Frelin-Labalme, H. Hamrita, and V. Kondrasovs. Delayed Gamma Power Measurement for Sodium-cooled Fast Reactors. *Nuclear Engineering and Design*, 241:339–348, 2011.

[2] E. Barat, T. Dautremer, T. Montagu, and J.C. Trama. A Bimodal Kalman Smoother for Nuclear Spectrometry. *Nuclear Instruments and Methods in Physics Research A*, A 567:350–352, 2006.

[3] F. Carrel, M. Agelou, M. Gmar, and F. Lainé. Detection of high-energy delayed gammas for nuclear waste packages characterization. *Nuclear Instruments and Methods in Physics Research A*, A 652:137–139, 2011.

[4] A. Sari, F. Carrel, M. Gmar, F. Lainé, A. Lyoussi, and S. Normand. Detection of Actinides with an Electron Accelerator by Active Photoneutron Interrogation Measurements. *IEEE Transactions on Nuclear Science*, 59(3):605–611, 2012.

[5] G. S. Mutchler. *The angular distributions and energy spectra of photoneutrons from heavy elements*. PhD thesis, Massachusetts Institute of Technology, 1966.

The Hydrogen Detection Technique for SG Protection System

Lv Mingyu[?], Pei zhiyong[?], Yu Huajin[?]

China Institute of Atomic Energy,Beijing,China

Abstract. SG that is pressure boundary between secondary loop and triple loop is the key equipment of fast reactor, in which heat in secondary loop is transferred to water or steam in triple loop. According to data from IAEA, SG is the highest failure rate equipment in fast reactor, especially because of failure of heat transfer tube. In order to monitor failure of heat transfer tube, Fast Reactor Engineering Department develops diffusion type hydrogen detection system, which is used to detect sodium-water reaction in time. This paper firstly introduces experimental research scheme and results of this hydrogen detection technique; Subsequently, it is described that how this technique can be engineering realized in CEFR; Moreover, through developing a series of calibration tests and hydrogen injection tests, it is obtained that sensitivity, response time and calibration curse for hydrogen detection system of CEFR.

1. Introduction

Fast reactor in China started in the 60s of the last century and developed in the 1990s, but eventually harvested fruit in the beginning of this century. On July 21, 2010, China Experimental Fast Reactor (CEFR) reached the critical for the first time, and then CEFR succeeded in generating power on July 21, 2011,. China has become the eighth country in the world to master fast reactor technology. This series of achievement embodies several generations of Chinese fast reactor researchers unremittingly pursuit and exploration for science and career.

A large number of key technologies were domestically researched and applied during design, construction, installation, commissioning and trial operation of CEFR, and diffusion-type hydrogen detection technology is the most representative one of them.

Like many other fast reactors in the world, CEFR adopts sodium - sodium - water triple circuit structure. Steam generator (SG) is pressure boundary between secondary circuit and triple circuit in which heat in secondary circuit is transferred to water or steam in triple circuit. High-temperature and low-pressure sodium flows in the shell, while high-temperature and high-pressure water or water vapor passes in the tube. They exchange heat through the heat transfer tubes of SG. According to data from the International Atomic Energy Agency (IAEA), the large leakage accident resulting from small leakage in the heat transfer tubes of sodium-water steam generator has already happened quite frequently in the countries possessing fast reactor. For example, more than 18 times leakage in BH-350 reactor took place in the past 20 years; 15 leakage occurred in BH-600 during 12 years; Femi reactor in U.S. ceased because of SG' leakage; France Phoenix reactor once leaked; Leakage accident happened in British PFR SG just after trial operation, etc. [1,2]. These examples illustrate that it is very difficult to completely avoid leaking in the expected lifetime, although we have taken a series of measures in each stage of SG, such as designing, manufacturing, selecting material and so on.

[?] Xinzhen, Fangshan District, Beijing, China
[?] Xinzhen, Fangshan District, Beijing, China
[?] Xinzhen, Fangshan District, Beijing, China

Therefore, it is necessary to prevent occurrence and expansion of the sodium-water reaction through setting a variety of methods to detect early leakage of SG.

CEFR adopts diffusion-type hydrogen detection system, pulse-noise detector and cover gas pressure gauge as leakage detection methods of SG. Furthermore, diffusion-type hydrogen detection system that is used to detect early leakage of SG, that is a main means of small leakage detection has the highest detection sensitivity. This paper will introduce engineering implementation and calibration test of diffusion-type hydrogen detection technology.

2. The engineering implementation of diffusion-type hydrogen detection technology

The diffusion-type hydrogen detection technology in engineering implementation is diffusion-type hydrogen meter which comprises sampling branch system, ion pump high vacuum system and measurement and control system. The sampling branch system is composed by nickel tube sensor, sodium valves, sodium flowmeter, regenerator, heater, electromagnetism pumps and pipes. The installation on site shown in Figs 1, its main function is that draw out sodium from the main pipe and make hydrogen in sodium through nickel tube sensor into the vacuum system. That is the whole process of hydrogen in sodium sampling. The high vacuum pump group, middle vacuum meter, safety shut-off valve and other components constitute ion pump high vacuum system. The measurement and control system includes worksite control cabinet, host computer, remote control cabinets, etc.

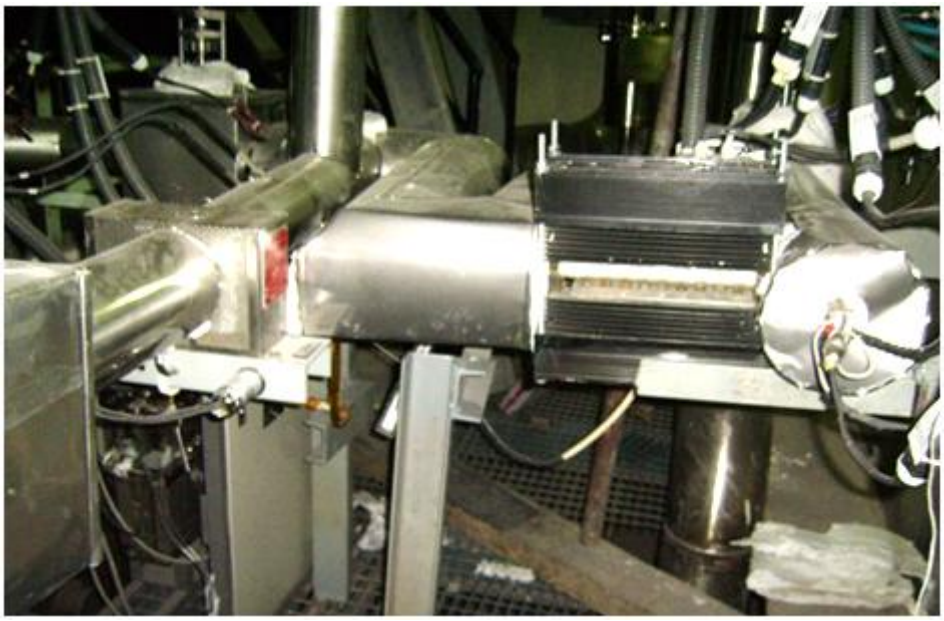

FIG. 1. Installation drawing of sodium sampling branch on site.

The secondary system of CEFR includes two loops and each loop consist a SG, a sodium buffer tank and four diffusion-type hydrogen meters. Furthermore, a set of large diffusion-type hydrogen meter used in sodium is installed in the outlet pipe of evaporator and a set of small diffusion-type hydrogen meter used in sodium is installed in the overflow pipe of evaporator and superheater respectively. A set of small diffusion-type hydrogen meter used in argon gas is installed in the gas chamber of sodium buffer tank top. The specific installation position and number of each hydrogen meter are shown in Table 1. The measurement point layout of single-loop hydrogen meter is shown in Figs 2.

Table 1. Number and installation position of hydrogen meter

Sequence number	Number of hydrogen meter	Installation position of hydrogen meter	Type of hydrogen meter

1	No.1 hydrogen meter	Evaporator port in I loop	Large hydrogen meter (sodium)
2	No.2 hydrogen meter	Evaporator port in II loop	Large hydrogen meter (sodium)
3	No.3 hydrogen meter	Overflow pipe of evaporator in I loop	Small hydrogen meter (sodium)
4	No.4 hydrogen meter	Overflow pipe of evaporator in II loop	Small hydrogen meter (sodium)
5	No.5 hydrogen meter	Overflow pipe of superheater in I loop	Small hydrogen meter (sodium)
6	No.6 hydrogen meter	Overflow pipe of superheater in II loop	Small hydrogen meter (sodium)
7	No.7 hydrogen meter	Top of buffer tank in I loop	Small hydrogen meter (argon)
8	No.8 hydrogen meter	Top of buffer tank in II loop	Small hydrogen meter (argon)

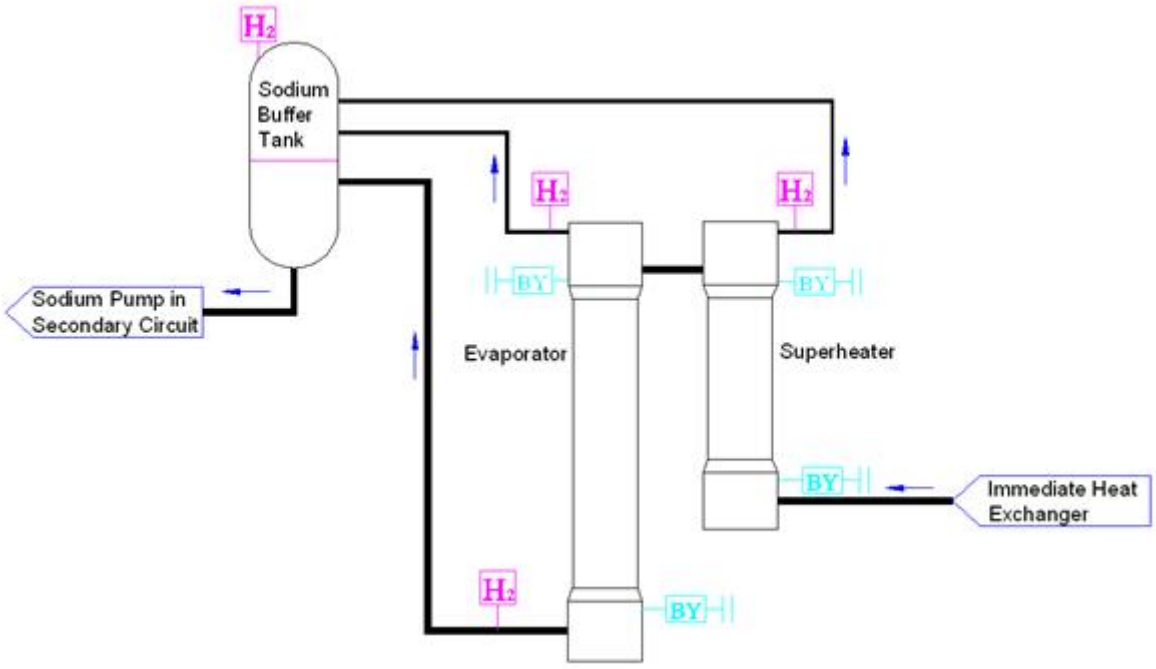

FIG. 2. Schematic diagram for single loop hydrogen meter layout.

3. Calibration teat for diffusion-type hydrogen meter

3.1. Description of calibration test

Sweep injection hydrogen pipe with argon before injecting hydrogen. At the same time, open injection hydrogen port in evaporator or superheater, which makes sure injection hydrogen loop expedite.

Turn on mass flow controller after hydrogen injection is beginning. When instantaneous flow appears, open ball valve in inlet of injection hydrogen capillary, which makes hydrogen injected into SG until accumulative flow reaches enactment value. Then turn off mass flow controller, and injection hydrogen is over. Sweep injection hydrogen pipe with high-purity argon to make rudimental hydrogen in injection hydrogen pipe enter into SG. Record output of diffusion-type hydrogen meter as soon as ball valve is open, until 60mins later.

Hold temperature of nickel tube at 450 degree. Conduct injection hydrogen test when it is confirmed that hydrogen concentration in sodium is just equal to solubility at cold trap temperature.

Working condition of I loop in the secondary circuit is: sodium temperature 300~310℃ and sodium pump speed 950 r/min. Totally conduct 4 injection hydrogen tests, which includes the bottom of superheater(2 times), the top of evaporator(1 time) and the bottom of evaporator(1 time). Make sure that hydrogen injected in last test has spread homogeneously or interval time is long enough before each injection hydrogen test.

3.2. Result of calibration test

Figs 3 and 4 show response curse of No.1 and No.5 hydrogen meter during injection hydrogen test. In addition, response data of diffusion-type hydrogen meter in I loop is list in table 2.

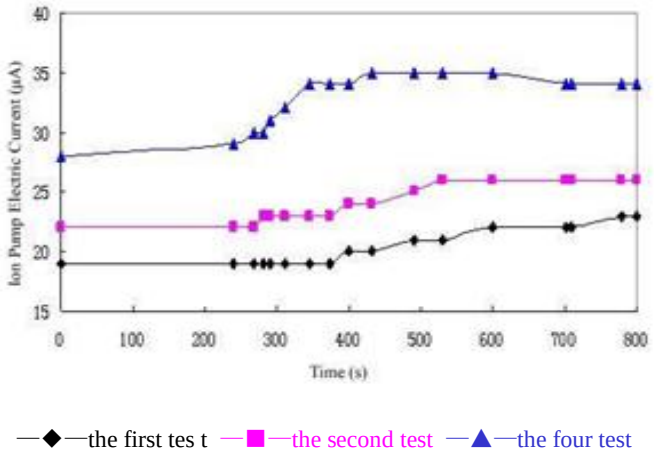

FIG. 3. Response process of No.1 hydrogen meter.

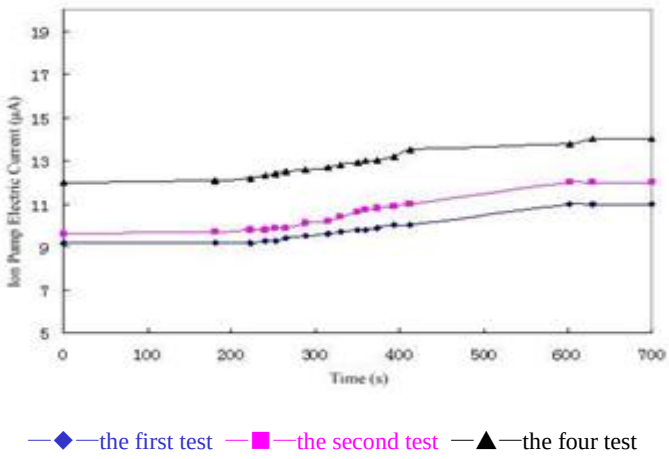

FIG. 4. Response process of No.5 hydrogen mete.

Table 2. Response of hydrogen meters in I loop during injection hydrogen test

Sequence number of injection hydrogen test		1		2		3		4
Test stage		before	after	before	after	before	after	after
Injection time / (s)		——	420	——	420	——	480	450
Injection volume / (l)		——	3	——	3	——	3	3
Accumulative volume / (l)		——	3	——	3	——	6	9
Hydrogen concentration in sodium / (μg/g)		0.0375	0.0475	0.045	0.052	0.052	0.055	0.085
Ion pump electric current / (μA)	No.1 hydrogen meter	19	23	22	26	26	28	35
	No.5 hydrogen meter	9.2	11	9.6	12	11	12	14
	No.7 hydrogen meter	64	98	40	79	73	92	190

Annotation: Because temperature of sodium is lower that makes solubility of hydrogen in sodium lower, response of hydrogen meter in argon gas is huge.

Figs 5 and 6 show calibration curse on response of No.1 and No.5 hydrogen meter relative to hydrogen concentration in sodium.

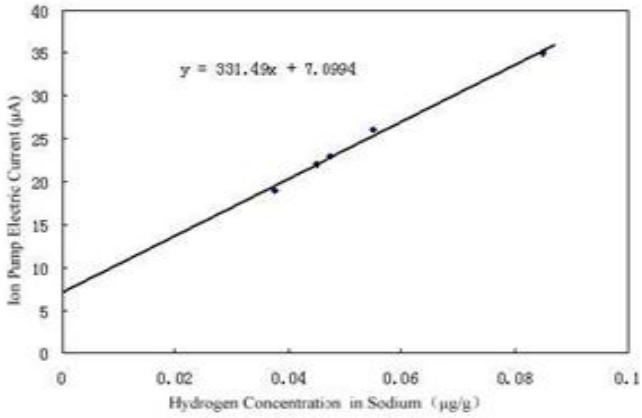

FIG. 5. Calibration curse of No.1 hydrogen meter (nickel tube sensor temperature 450 ℃).

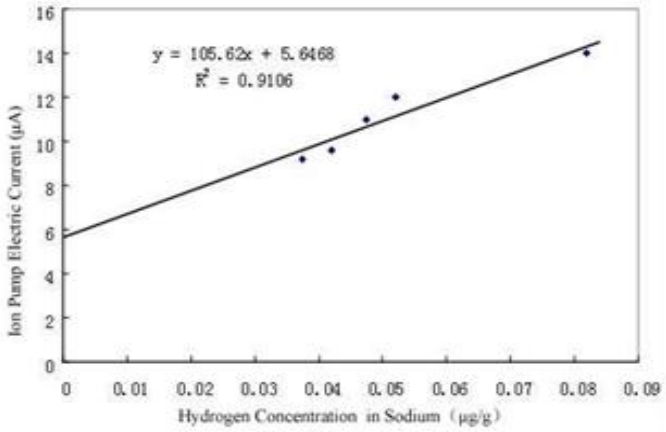

FIG. 6. Calibration curse of No.5 hydrogen meter (nickel tube sensor temperature 450 ℃).

In the same way, it is obtained that calibration curse of diffusion-type hydrogen meter in II loop, which is shown in figs 7 and 8. Just because calibration test of II loop is conducted in working condition of sodium pump speed 500r/min, resulting in spreading rate of hydrogen slower, it is lower that background of diffusion-type hydrogen meter. The purpose that conduct injection hydrogen test in this working condition is comparing response of diffusion-type hydrogen meter with different sodium pump speed.

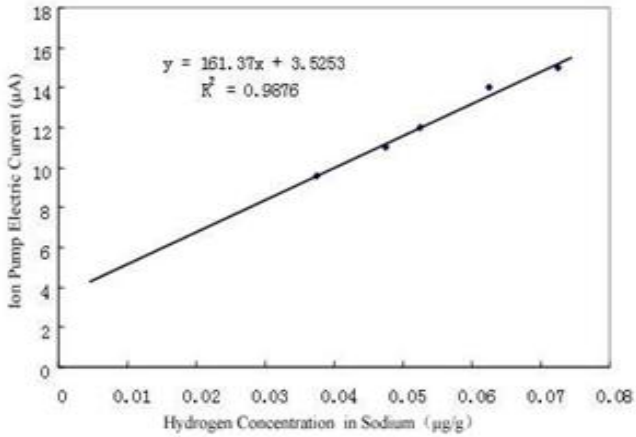

FIG. 7. Calibration curse of No.2 hydrogen meter (nickel tube sensor temperature 450 ℃).

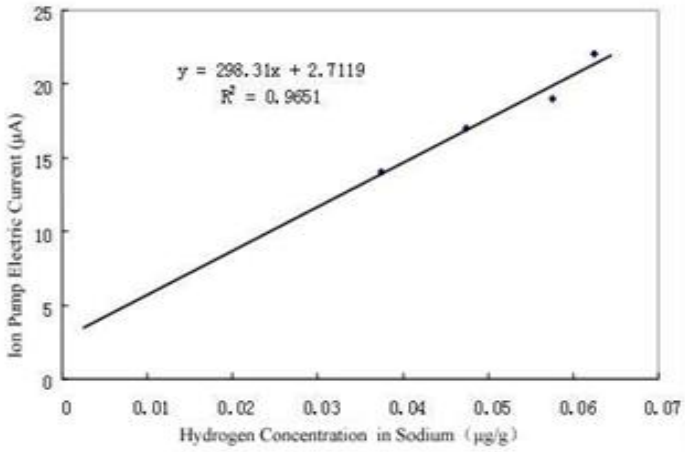

FIG. 8. Calibration curse of No.6 hydrogen meter (nickel tube sensor temperature 450 ℃).

4. Time response characteristics of diffusion-type hydrogen meter for CEFR

Hydrogen injection test can be realized by injection port in evaporator or superheater. Figs 9 shows a schematic diagram about pipeline of hydrogen injection. Due to pipeline of hydrogen injection being long and large volume, response time of diffusion-type hydrogen meter is delay.

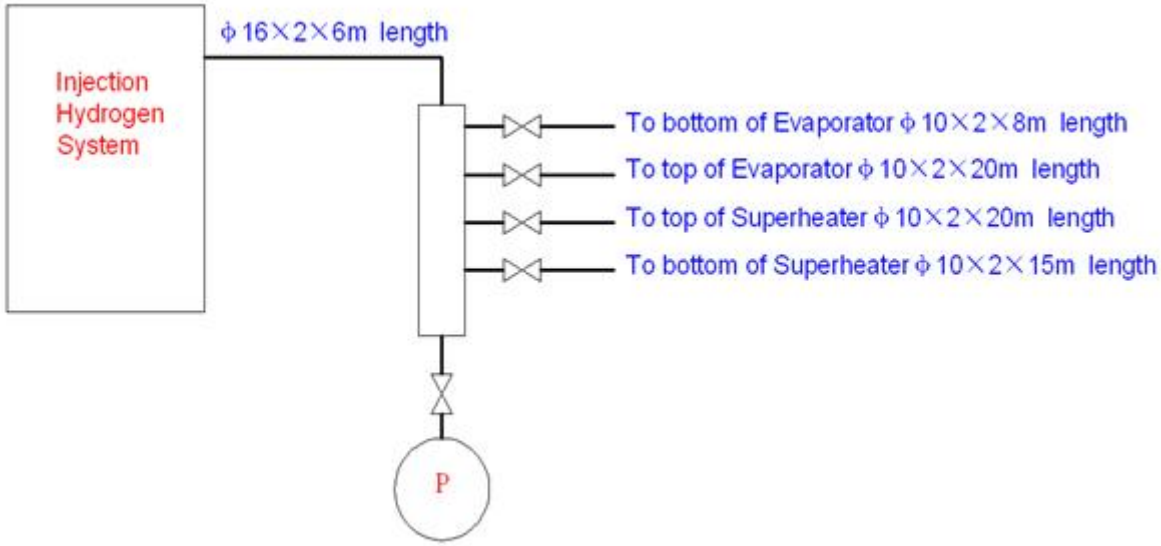

FIG. 9. Schematic diagram for injection hydrogen pipe.

4.1. Response characteristics of diffusion-type hydrogen meter when sodium pump being high speed

Through hydrogen injection test, it is realized that not only calibrating relation between hydrogen concentration and response of hydrogen meter, but also investigating hydrogen propagation in SG and even the whole secondary circuit. That is an important link which influences detection performance of hydrogen meter or hydrogen meter group. Especially, it is judged that size and approximate position of leakage according to response of each hydrogen meter.

When hydrogen injection test is beginning, response of all hydrogen meter should be recorded， which will last about 20 mins. Figs 10 shows response of each hydrogen meter after the first and the second hydrogen injection test. As shown in figs 10, there exists huge difference for response speed of

diffusion-type hydrogen meter, which is due to different argon flow used in hydrogen injection test. Different argon flow results in different delay time that hydrogen resort in pipeline, which is main reason for delay of response of hydrogen meter.

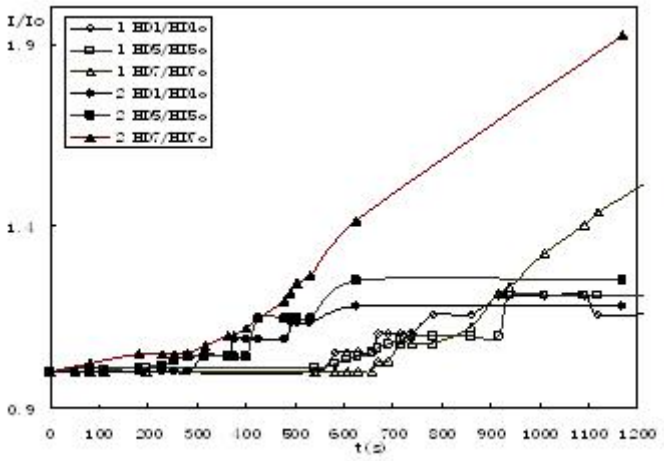

FIG. 10. Response process of hydrogen meter during the first and second test when sodium pump speed is at 950r/min.

is at 950r/min

4.2. Response characteristics of diffusion-type hydrogen meter when sodium pump being low speed

It is obviously different that flow behavior of sodium in secondary circuit when speed of sodium pump is low compared with design condition. Except for low velocity, even lower than floatation speed of hydrogen bubble, there is no flow in overflow pipe of evaporator and superheater, which makes hydrogen meter in overflow pipe all in non-working condition.

In this case, injecting hydrogen or hydrogen-argon mixed gas is not flowing with sodium flow, but lifts to top of superheater or evaporator, which influences detection of hydrogen meter seriously.

Although there is no flow in overflow pipe, sodium flow still exists in sampling branch of hydrogen meter in overflow pipe of superheater. That is only local circulation flow between sampling branch and overflow pipe. Hydrogen injected by bottom of superheater, hydrogen bubble lifts along superheater, possibly into overflow pipe, which may cause huge response of hydrogen meter in overflow pipe. Electric current of ion pump increases from 14μA to 130μA, that means hydrogen concentration increasing from 0.03μg/g to 0.3μg/g. Because of hydrogen accumulating in the top, hydrogen meter in outlet of evaporator is unresponsive for long time.

Likewise, hydrogen bubble can’t enter into buffer tank through overflow pipe or outlet of evaporator, which makes output of hydrogen meter in argon unchanged obviously during hydrogen injection test.

5. Conclusion

(1) Sensitivity

As shown from calibration curse of hydrogen meter, output of hydrogen meter exists about 2~3 μA response when increment of hydrogen concentration is 0.01μg/g. It is totally satisfied that sensitivity of hydrogen meter for 0.1μg/g alarm value of SG accident protection system in CEFR.

(2) Time response characteristic

Response time of diffusion-type hydrogen meter is about 35s obtained from hydrogen injection test, but most of which is that hydrogen spreads in injection loop. Response time of each hydrogen meter is different to different injection hydrogen positions. It can be used to predict approximate position of leakage point. The time shown in injection hydrogen response curse is total response time of hydrogen meter, which we can make use of to estimate spreading time of hydrogen in sodium by subtracting resorting time of hydrogen in injection loop. Morever, resorting time not only takes up most of response time, but also influnces hydrogen concentration seriously, which results in estimating spreading time of hydrogen in SG inaccurately.

Table 3. Spreading time of hydrogen in sodium

Injection point	Response time of No.1 hydrogen meter/(s)	Response time of No.5 hydrogen meter/(s)	Response time of hydrogen meter/(s)
Bottom of superheater	300	25	30
Top of evaporator	350	410	450
Bottom of evaporator	80	260	20

As shown from table 3, it takes some time to dissolve hydrogen into sodium at low temperature, and spreading time of hydrogen is longer when hydrogen is injected at top of evaporator because hydrogen bubble lifts contrary with sodium flow. Furthermore, hydrogen accumulates in the top of evaporator when sodium pump speed is at 500r/min, which makes hydrogen spread in sodium difficultly. As a result, hydrogen meter is unresponsive for long time.

According to layout of the secondary circuit system, it is obtained that spreading time of hydrogen in secondary circuit is 10~20s. Besides, total response time of diffusion-type hydrogen meter includes spreading time in sampling branch and diffusing time in nickel pipe sensor. So the total response time of diffusion-type hydrogen meter is about 60~70s at normal condition of reactor.

REFERENCES

[1] Su zhuting, Ye changyuan, Yan fengwen, etc. Sodium-cooling Fast Bread Reactor. Beijing: Atomic Energy Press, 1991.

[2] 《Fast Reactor Research》 compiler group. Design Pandect for Fast Reactor Engineering.

T1-CN-199/165

In-Service Inspection and Repair for the ASTRID Project: Main Stakes and Feasible Solutions.

F. Jadot[1], F. Baqué[2], J. Sibilo[3], JM Augem[4], V. Delalande[5], J.L. Arlaud[6]

[1] CEA, DEN, Cadarache, CPA , Bât. 155, 13108 St Paul lez Durance CEDEX, France

[2] CEA, DEN, Cadarache, DTN , Bât. 202, 13108 St Paul lez Durance CEDEX, France

[3] AREVA NP, 10 rue Juliette Récamier 69456 Lyon CEDEX 06, France

[4] EDF SEPTEN, 12-14 avenue Dutriévoz, 69628 Villeurbanne CEDEX, France

[5]EDF R&D, 6 quai Wattier 78400 Chatou, France

[6]COMEX NUCLEAIRE, 10 avenue Francis Perrin, ZAC Rourabeau 13115 St Paul lez Durance, France

Abstract : For the future ASTRID prototype, the improvement of in-service inspection and repair (ISI&R) capabilities was identified as a major issue. The aim is to overcome one of the drawbacks of sodium, namely its opacity, by developing defect detection and characterisation means, as well as the means to implement them by simplifying access and providing carriers adapted to each situation, as presented in this paper.

The ASTRID project, in collaboration with the French SFR R&D project, has mobilised a number of complementary teams both within CEA and with its partners, specifically AREVA, EDF and COMEX Nucleaire. Joint efforts are focusing on developing and qualifying all the necessary means needed to guarantee a level of inspection and repair so ASTRID meets the Generation IV requirements.

Introduction

ASTRID is the future integrated technology prototype designed for the industrial-scale demonstration of Generation IV sodium-cooled fast reactor safety and operation. To satisfy the requirements of this 4th generation in terms of safety, reliability, availability and energy savings, ASTRID will need to achieve a higher level of performance than that of previous fast reactors.
In this respect, improving in-service inspection and repair (ISI&R) will be a major focus area in the ASTRID project.
Liquid metal sodium is the reference coolant for this type of reactor as it is perfectly adapted to the operating conditions of a fast reactor due to its neutron and thermal properties. This is why it has been chosen as the coolant for ASTRID.
However, its opacity is a significant drawback particularly for in-service inspection, but ultrasonic methods can help to overcome this issue.
Even though it has always been possible *a posteriori* to satisfy “on demand” inspection requirements in the former French SFRs, one of ASTRID’s main objectives is to extend the means of inspection either for programmed maintenance or exceptional operations. The repair means must also be considered.
To minimise the consequences of this opacity, the approach involves integrating ISI&R requirements into the design phase to facilitate access, to develop methods for detecting and characterising potential defects, and to design associated robotics that provide access to the areas to be inspected or repaired.

Definition of ISI&R for ASTRID

Within the framework of this project, ISI&R refers to all the measures required to:

- Check that the operating conditions to which the structures are subjected are in line with the design assumptions,
- Guarantee that there will be no defects that are incompatible with the safe operation of the facility,
- Enable the implementation of additional comprehensive examinations,
- Guarantee investment protection thanks to the possibility of being able to repair local defects.

In order to meet the ISI&R objectives defined below, a 5-level classification has been proposed [1].

Level 0 involves taking into account ISI&R requirements from the design phase.
One of the objectives for the ASTRID project is to consider from reactor design:
1) how to reduce the inspection requirements by means of a design which limits the areas to be inspected, and
2) how to enable - and simplify where possible - access to the reactor block, specifically the areas where access is the most difficult.

Level 1 refers to continuous monitoring. It integrates all the instrumentation needed to monitor the reactor in operation, including the instrumentation needed for core monitoring and protection against abnormal events. The instrumentation requirements and recent developments in this field are the subject of the document in references [2] and [3], and will not be developed here.

Levels 2 and 3 involve in-service inspection [4]. Level 2 refers to the periodic inspections which are conducted in compliance with regulatory requirements, while Level 3 refers to exceptional inspections which are conducted in the case of a doubt or consecutive to abnormal operation. The latter involve either extending the inspected area (weld length, surface area, number of components) or, for example, implementing more efficient methods of characterisation than those used for detection. These inspections are mainly performed with the reactor shut down.

Lastly, level 4 refers to repairs. In so far as possible, the removal or replacement of components will be prioritised over *in situ* repairs. Nevertheless, within the scope of investment protection, the ASTRID project must assess situations which could necessitate *in situ* repairs so as to limit them as much as possible and, ultimately, to study the means of solving them in order to provide investors, future operators and the safety authority with a risk assessment that is exhaustive and that reduces the risks as much as possible.

Certain repairs and even certain checks may necessitate very heavy operations such as complete core unloading and/or total or partial draining of the primary sodium. Every effort will be made to avoid such situations but they nonetheless must be covered.
Therefore, specific means must be integrated into the design, such as external fuel storage which is compatible with complete core unloading, and sodium storage tanks with a sufficient total capacity in the case of complete draining of the primary sodium.
The associated operational means must nevertheless be studied.

Whether for inspection or repairs, all potential defects must be identified, including their location, the detection means, the means for repair and requalification if necessary.

Strategy: iteration and complementarity between methods, sensors, carriers and design

The main difficulties are to be found in the reactor block where the majority of structures are immersed in sodium, an opaque metal, at relatively high temperatures (approximately 200°C with the reactor shut down).

In order to reach the ambitious target of inspecting nearly all the structures and specifically those which are important from a safety point of view, the ASTRID project has called on skills and means in all the relevant fields. This not only concerns specialised research teams (R&D) but also industrialists who are either partners in the project or under contract, both in France and overseas, with the goal of finding solutions that are adapted to the Nuclear Power Plant design and that take into account the manufacturing methods, from the sensors to the carriers.

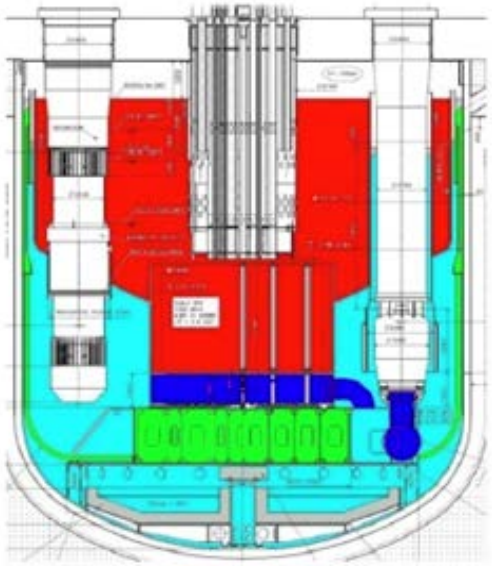

Figure 1: ASTRID reactor block

Measurement methods and sensors

Generally speaking, the R&D actions for in-sodium inspection mainly involve the development of associated sensors and methods available under sodium, specifically ultrasonic methods: high-temperature ultrasonic transducers (TUSHT,TUCCS) or electromagnetic acoustic transducers (EMAT).

Within the framework of the tripartite R&D agreement between AREVA, EDF and CEA, these actions are steered by the SFR R&D project at CEA.

The main breakthroughs in this field are discussed in the document in reference [4].

TUSHT TUCSS EMAT

Fig. 2: Ultrasonic transducers available under sodium.

Transducers developments have led to the manufacture of efficient new mono-element sensors which can be tested in sodium. These ultrasonic sensors are used to detect and/or characterise defects. They can also be used to rebuild an image which makes it possible to visualize objects in sodium. In order to do this, a scanning device or phased-array sensors are necessary for this 3D application. The current R&D actions aim to use this type of sensor in the near future. They will then be tested in water and in sodium.
The CIVA software was developed to design these sensors and to optimise the measurement parameters. It is still evolving as it has to integrate all the needs and applications for the inspection of structures in sodium.

To carry out these inspections, sensors are necessary but are not sufficient on their own. Whether in sodium or gas environments, it is necessary to get near the areas to be inspected using carriers. These can be a simple vertical pole, an articulated arm, a remotely operated vehicle (ROV) or a robot.

Inspection carriers and robots

There are a number of different inspections and operations to be carried out. It is not possible to consider one type of carrier alone for all these operations.

As partners in the project, CEA, AREVA, EDF and COMEX Nucléaire are currently working on this complex subject of carrier and robot development.

Inspections from outside the vessel are preferable whenever possible.

The implementation conditions of the methods of inspection are actually less restrictive in the space between vessels than in the vessel itself:

- Gas rather than sodium environment
- Lower temperatures (120-150°C rather than 200-250°C)
- Possible additional visual methods (endoscopes, cameras, positioning support system, reading of coordinates)
- Limited risk of pollution or deterioration of the reactor as a result of limited maintenance
- Possibility of accessing the core support structure at the bottom of the vessel.

By introducing a carrier into the space between vessels (between the main vessel and the safety vessel) [4], it is possible to inspect not only the vessels themselves, and particularly the welds, but also the state of the core support shell using ultrasounds.

Current studies aim at demonstrating that it would moreover be possible to inspect certain core support structural welds using structures as waveguides (Figure 3).

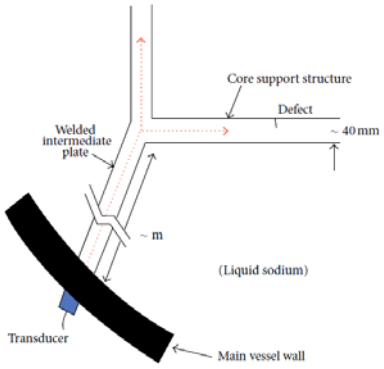

Figure 3: Inspection of structures used as wave guides.

Other studies carried out in particular by the LCND[1] laboratory associated with the latest developments in the CIVA code, show that it may even be possible to detect a defect through one or even two walls separated by sodium (figure 4) [5]. Current parametric studies are still needed to check the feasibility of this method through the primary vessel (40 to 50 mm thick) and the impact on the sensitivity of the factors method, such as the sodium flow between these walls and their geometry.

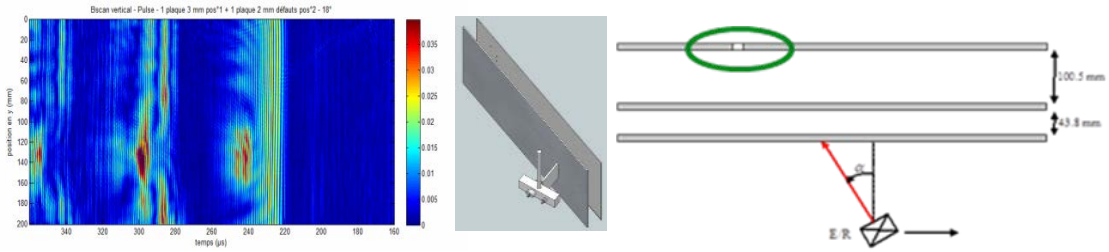

Figure 4: Inspection through two walls

Even if these development efforts make it possible to improve the detection of defects or the performance of characterisation from outside the main vessel, the reactor dimensions (height 18 m, diameter 15 m) and the complex internal structure architecture leaves no doubt as to the need for additional maintenance from inside the vessel.

As the power plant designer, AREVA has then focused some of its actions on the access requirements for the ISI&R of the whole reactor block.

The access to the most sensitive or difficult points are addressed, for instance:

- Core support in the cold pool; specifically the inner core support structures,
- Above core structure which holds the instrumentation positioned at the core outlet.

[1] *Laboratoire de Caractérisation Non Destructive* (laboratory for non-destructive examinations) at the University of Aix-Marseille

To access the cold pool, it has been planned to implement 3 dedicated internal vessel ducts at 120° apart, corresponding to the three slab penetrations. Two other accesses are planned in the large and small rotating plugs respectively, which allows an azimuthal degree of freedom.

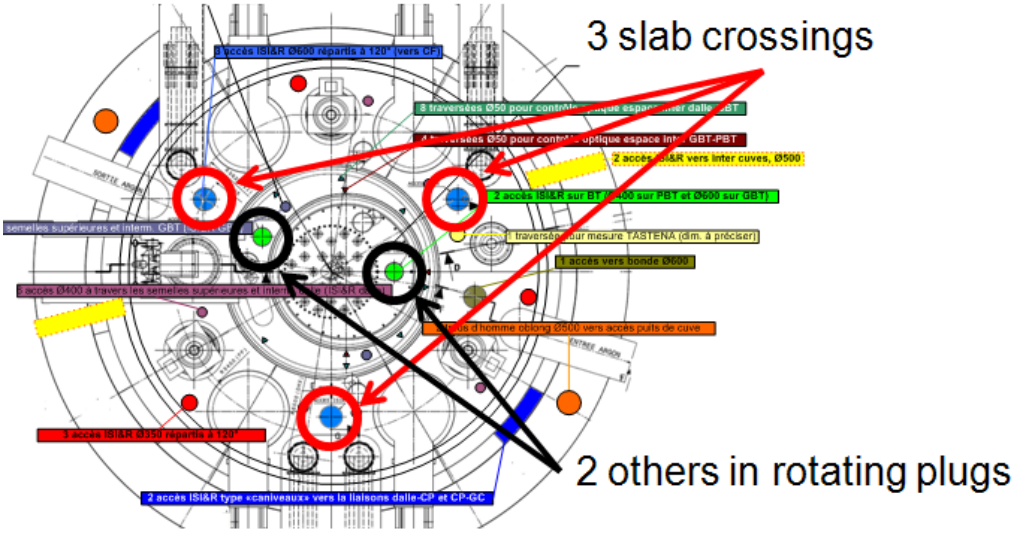

Figure 5: Dedicated accesses for ISI&R

The alignment of the slab penetrations, the internal vessel ducts and the holes in the inner core support structures allows for access to the inner core support structures from above but also from below.

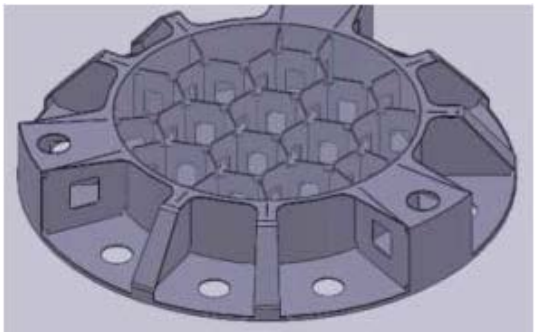

Figure 6: The inner core support structure

The core support structures have been arranged in such a way as to use their walls to perform ultrasonic examinations by guided mode. The inspections could also be carried out from underneath the core support structures using either a robot or a push-pull chain.
Furthermore, the welds inside the core support structures between the walls could be inspected using specific ISI holes in the crossing of the stiffeners.

AREVA is also working on the access to the space between vessels, closely linked to the design options of the reactor pit.

In addition to the ISI&R access improvement, AREVA designs also the suitable carriers. It concerns two complimentary works with very high interactions, enabling to optimise the carrier design as well as the access implementation.

So far, the ISI&R carriers designed by AREVA are:

1. Inter vessel vehicle
2. Roof slab examination vehicle
3. Roof and vessel support structure examination vehicle
4. In-vessel examination mast (with telescopic arm) for the central part of the core support structure
5. In-vessel examination mast (with push-pull chain) for the underneath part of the core support structure
6. In-vessel examination mast (with push-pull chain) for the peripheral part of the core support structure

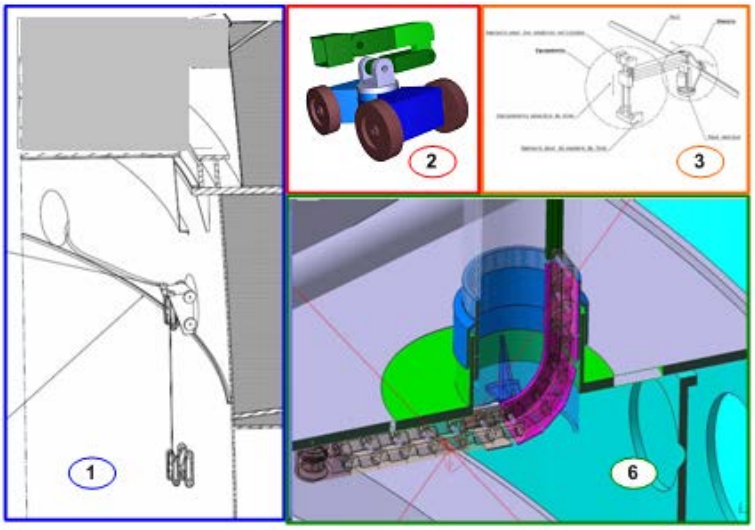

Figure 7: ISI&R carriers designed by AREVA

The next carriers to be designed by AREVA will be those dedicated to the examination of the ACS (Above Core Structure).

In the same time, COMEX Nucleaire has conducted an exhaustive study of the different types of carriers for both inside and outside the vessel. For the second phase of the partnership, this preliminary study has led to the more in-depth study of the design and the corresponding safety assessment for:

1. Two additional in-vessel carriers:

- A poly-articulated arm which has the advantage of being able to access the largest possible surface and areas of which inspection is not only periodic but can also be exceptional.
- An arm and a trolley which would be placed on a rail set up for this purpose at the design stage, in this case, for inspections planned from the outset.

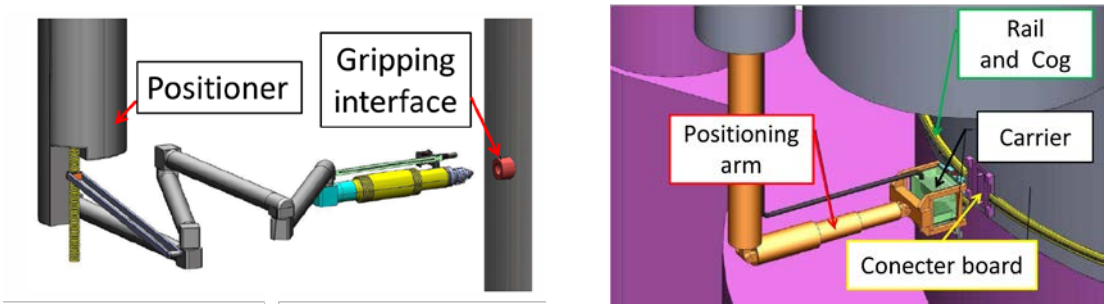

Figure 8: Articulated arms designed by COMEX Nucleaire

The basic design studies and iteration with the power plant design studies still remains to be done in order to determine the structures likely to support such a rail.

2. Several inter-vessel carrier solutions:

- A self-driven vehicle
- A carrier chain
- A push-pull chain

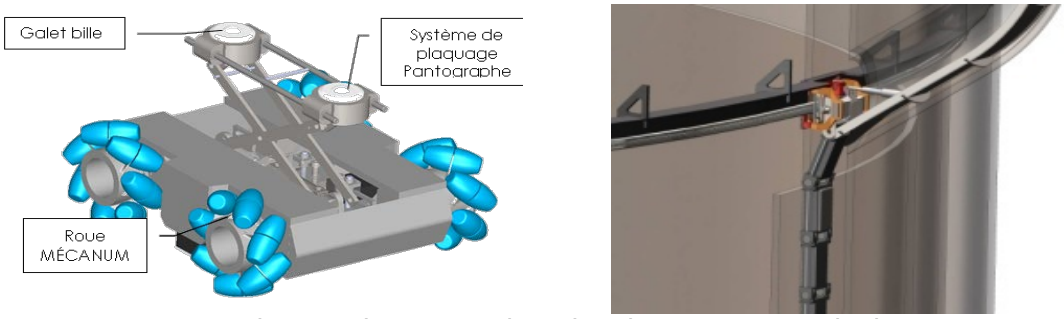

Figure 9: inter-vessel carriers by COMEX Nucleaire

Here too, studies must be continued to remove any uncertainties and guarantee the compatibility of the solutions proposed with the design, manufacturing and safety requirements.

In addition to this, CEA R&D is studying a very promising and innovative hexapod-type carrier design, and associated technological improvements.

EDF has focused its R&D studies more on adapting existing robots for applications in sodium. Based on industrial robots (STAUBLI, Snake Arm concept, etc.), the aim is to develop a leaktight casing compatible with sodium and a thermal or cooling insulation system according to the needs.

Repairs

Initial studies have confirmed the difficulty of carrying out *in situ* repairs.
Complete core unloading and total or partial sodium draining are complex, long and therefore costly operations. They must be taken into account but mainly impact the reactor design.
These operations may be avoided in some cases, provided that fairly simple repairs can be carried out *in situ* in sodium.
As the welding operations cannot be performed in a sodium environment, pre-conceptual studies of leaktight cavities (bells) have been conducted in order to obtain an estimate of overall dimensions and mass. These studies lead to more in-depth studies on leaktight seals

in sodium (temperature and irradiation) and on the means of cleaning the surface (sweeping of sodium), machining and reloading.
Tests on design, resistance to radiation, resistance in temperature and in sodium of specific seals are currently being conducted at CEA. The first tests have resulted in streamlined seals and specific silicone-type materials which will be tested on the MARIUS test bench [6].
Recent progress in the field of LASERS makes it possible to consider the use of a single LASER for all 3 applications: cleaning, machining and welding. A parametric optimisation programme should be carried out to obtain a tool adapted to specific ASTRID requirements.

Qualification and tests

These examples of developments clearly illustrate the complementarity which is necessary between the reactor design, the performances of the inspection and repair methods and the associated carriers.
Once they have been designed during detailed studies, achieving the targets for each of these solutions must be demonstrated first by tests in water and finally in sodium.
In order to do this, CEA has been equipped with a test platform (VESQUO): a framework and positioner capable of testing both CEA (hexapods) poly-articulated arm terminal devices and those proposed by the partners.

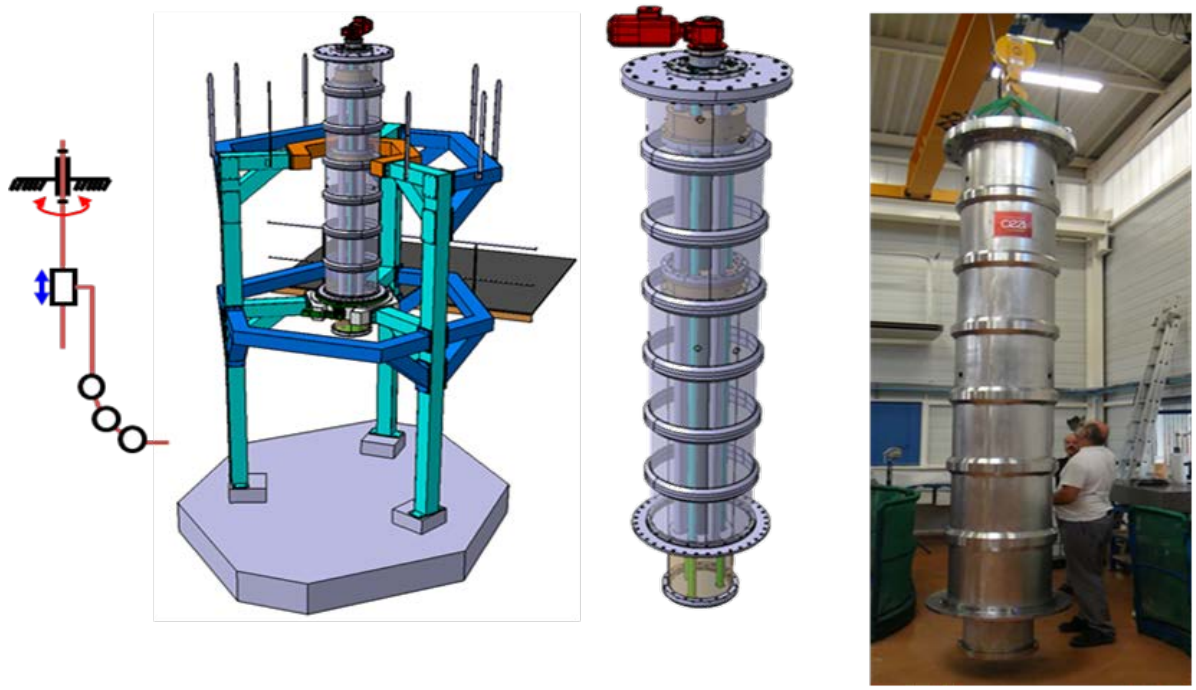

Figure 10: CEA test platform VESQUO

Conclusion

ISI&R is one of the major stakes of the ASTRID project.
The aim is to overcome one of the drawbacks of sodium, namely its opacity, by developing defect detection and characterisation means, as well as the means to implement them by simplifying access and providing carriers adapted to each situation.

The ASTRID project, in collaboration with the French SFR R&D project, has mobilised a number of complementary teams both within CEA and with its partners, specifically AREVA, EDF and COMEX Nucleaire. Joint efforts are focusing on developing and qualifying all the necessary means needed to guarantee a level of inspection and repair so ASTRID meets the Generation IV requirements.

During the first phase of the pre-conceptual design of ASTRID, the constant objective to limit the needs for inspection by design has led AREVA to eliminate high-risk areas or welds which are difficult to inspect. Taking into account the access requirements in all the areas of the reactor block also makes it possible to have a sufficient number of dedicated accesses to be able to consider directly or indirectly accessing a large majority of structures. The considerable design efforts relative to the core support have led to real breakthroughs from the point of view of inspectability.

The ASTRID design is by definition still evolving and the very encouraging results obtained during this first phase highlight the need for permanent iteration between the reactor design and ISI&R so that all the means developed remain coherent with the ISI&R requirements of ASTRID.

ACKNOWLEDGEMENTS

The authors would like to thanks all the colleagues at CEA, AREVA, EDF and COMEX Nucleaire who provided us with fruitful information, guidance and technical insight.

References

[1] F. Jadot F. Baqué F. Jeannot J.Ph. Augem J.M. Sibilo J., “ASTRID Sodium cooled Prototype : program for improving In Service Inspection and Repair”, ANIMMA Int. Conf., Ghent, Belgium, 6-9 June 2011, Paper 3-37

[2] JP. Jeannot, G. Rodriguez, C. Jammes, B. Bernardin, JL. Portier, F. Jadot, S. Maire, D. Verrier, F. Loisy, G. Prele, “R&D program for core instrumentation improvements devoted to French Sodium Fast Reactor”, ANIMMA Conf., Ghent, Belgium, 6-9 June 2011

[3] F. Jadot et al, “Instrumentation in the ASTRID project : Main Stakes and Feasible Solutions”,.FR’13, ref. T1-CN-199/274,

[4] F.Baqué et al, “ASTRID In Service Inspection and Repair: review of R&D program and associated results”, FR’13, ref. **Error! Unknown document property name.**337,

[5] G. Corneloup, MA. Ploix, JF. Chaix, I. Lillamand, F. Baque, “Potential of ultrasounds for NDT of a structure located behind parallel immersed plates”, QNDE 2010, San Diego, California, USA, July 18-23, 2010

[6] K.Vulliez et al, “R&D Program on sealing issues for in-service inspection and repair tools on ASTRID sodium prototype”, FR’13, ref. **Error! Unknown document property name.**,

Enhancing safety in Nuclear Power Plants with Optical Fiber Sensors

P. Ferdinand, S. Magne and G. Laffont

CEA LIST, Laboratoire de Mesures Optiques, Gif-sur-Yvette, F-91191, France

Abstract. The Fukushima disaster showed that safety must prevail in nuclear industry. Innovations are needed to strengthen instrumentation capabilities, which went out-of-order at Fukushima due to loss of power supply. Improvements concern materials and structures, which could be remotely monitored with Optical Fiber Sensors providing reliable measurements of many parameters. So, `quasi-distributed' Fiber Bragg Gratings sensors are considered up to high temperature for sodium-cooled fast reactor monitoring. Moreover, `distributed' sensing, allowing heavy multiplexing, conveys large safety improvements: no need for power supply, remote measurement, multi-kilometric range, no risk-to-people, and no common failure mode with other technologies. Radiation-hard fibers deployed within the containment vessel and the concrete containment would greatly enhance safety of retrofitted or future NPPs. In operation, OFS would monitor the temperature of spent fuel pools, leakages along pipes, fire detection and radiation monitoring, and be helpful for supervising a nuclear accident, detecting reactor breakthrough, corium advancement through the concrete floor, H_2 concentration...

1. Introduction: OFS advantages to enhance the nuclear installation's safety

We claim that to strengthen safety of existing or new Nuclear Power Plants (NPPs), both designers and plant operators can now take advantage of the potential of Optical Fiber Sensors (OFS) coming from 30 years of applied research in both instrumentation and telecommunications [1, 2]. These technologies are now made reliable, standardized, amortized on a mass market (telecoms), and are increasingly used in several industrial sectors (oil & gas, fire monitoring, civil engineering...). The (quasi-) distributed OFS sensing technologies make it possible to remotely perform reliable sensing of many parameters (temp., strain, radiation dose ...). In addition, OFS has no equivalent as it allows a wide multiplexing (one fiber can be equivalent to thousands of sensors), and so offers new features.

In the field of nuclear safety, a wide panel of advantages finds all their interests: *i)* Passive sensor (no need for local power), *ii)* Electromagnetic immunity, *iii)* Remote sensing (reduced risks for workers), *iv)* Redundancy (several fibers and cables deployed over several paths, ability to query both ends of (the) fiber (s), looped for the occasion), *v)* Multiplexing many points on a single optical cable (up to tens of thousands), *vi)* Contribution to diversification (no common failure mode with all other measurement technologies already deployed), *vii)* Good resistance to harsh environments (tolerance to ionizing radiations), *viii)* With the Reflectometry: ability to identify (with sub-meter accuracy), the fiber break if a cable has been destroyed somewhere, so precisely locate the event, etc.

It should be noted that many optical cables (telecom standards) are already installed in NPPs. They often contain spare optical fibers, available, which may be used to remote the optical sensing instrumentations. In addition, optical feedthroughs are manufactured by several companies (*e.g.* IST-Conax-Auxitrol) in order to interface the optical sensors installed inside the nuclear building.

2 Applications for which OFS sensing may enhance power plants' safety

To determine these topics, we may have a look to the first study for the U.S. nuclear safety authority dealing with the safety and nuclear reactor risks. It was driven from 1972 to 1975 (before the TMI

accident) by Norman C. Rasmussen from the MIT [3]. We can also read what was written, more recently, while designing the EPR reactor. In europe, the Permanent Working Group in charge of nuclear reactors (GPR), thanks to the joint work carried out by the IRSN, GRS (Germany) and the German RSK Safety Commission, wrote almost ten years ago a paper entitled "*Preliminary Report safety of the EPR Flamanville 3*" [4], which was unveiled at the public debate that took place from Oct. 2005 to Feb. 2006. *The good way, is to deduce the design of new tranches of existing evolutionary manner*, the GPR said. Their report noted that a significant improvement in the safety of new units is required, as follows: *i)* The efficiency of the sealing of the nuclear shield (low leakage of the inner wall), *ii)* Protection against external hazards (earthquake, aircraft crash, external explosion, lightning and EMI, groundwater, weather and extreme floods, ice, toxic, corrosive, flammable..., *iii)* Protection against internal failure of components subject to pressure, internal floods, fires, explosions internal projectiles (missiles effects), falling loads... *iv)* Prevention of hydrogen detonations, *v)* Prevention of fusion in the spent fuel pool, *vi)* Instrumentation...

Of course, these recommendations were then taken into account in the design of the EPR. However, it is clear that several issues raised by these working groups are still valid after the Fukushima accident. Such risks relate to all NPPs, but are depending on the type of reactors and buildings. Finally, it would be worthwhile to consider two types of situations to improve the NPPs' safety (Fig. 1), namely:

1 / In service: *i)* Nuclear building monitoring, *ii)* Thermal monitoring of pipes, pools, transformers, fire...

2 / During an accident or in post-accidental situation (PA): *i)* Detection of reactor breakthrough, corium casting, monitoring the erosion of the concrete floor, *ii)* Nuclear building monitoring, *iii)* Monitoring of spent fuel pools, steam pipes, *iv)* Fire detection, *v)* Hydrogen Risk, *vi)* Radiation monitoring (dosimetry).

Clearly accidental and PA situations are those for which the panel of topics involved is the most extensive. Moreover, we can notice that several of the applications dealing with safety are related to temperature sensing. In the next section, we present the most relevant techniques.

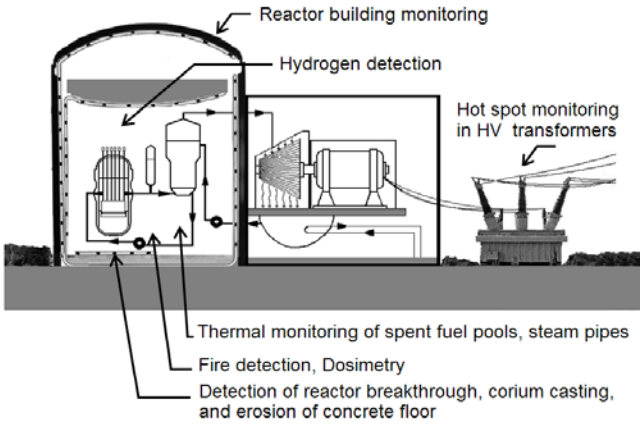

Figure 1: Artist view describing some applications for which OFS may provide a gain in safety

Last, in december 2011, based on NPPs' stress tests, the French Nuclear Authority (*Autorité de Sureté Nucléaire*, ASN) confirmed that the safety of existing French NPPs is good but should be enhanced on several aspects, and so the ASN requires important modifications to operators [5-6].

2.1. Continuous temperature measurement – Raman Distributed Temperature Sensing (DTS)

The DTS principle, is based on the Raman backscattering in the fiber core analysed by Optical Time Domain Reflectometry (the OTDR is somehow a guided optics Radar), *i.e*. a process of spatial localization along the fiber, based on the spatio-temporal duality (temporal analysis is equivalent to a spatial scaling since the light velocity c/n is known). OTDRs are widely used in optical telecommunications, as they help ensure the availability of the distribution network (detection of any changes in the fiber attenuation profile, location of specific problems like bending, breakage or bad connexion...). Many OTDRs are commercially available and used by operators in this sector.

Traditional OTDRs use the elastic Rayleigh backscattering in the fiber core. However, the Rayleigh effect is not the only one in fibers, Raman and Brillouin effects are also usefull. In case of Raman scattering, there is interest in the light having undergone a wavelength shift of a few tens of nm from the excitation wavelength (about 40 nm at 1 µm in wavelength): The inelastic scattering mechanism (photon energy is partially exchange with the scattering fiber core molecules, *i.e.* the silica) leads to generate two symmétrical frequencies (two spectral lines) with respect to the laser excitation (Fig. 2). The respectively called ν_0 Stokes line ($\nu_S = \nu_0 - \nu_B$) and anti-Stokes line ($\nu_{AS} = \nu_0 + \nu_B$), ν_B denotes the characteristic vibration frequency of the fiber core. Since I_{AS} the signal corresponding to the anti-Stokes line comes from an energy level higher than the fondamental one, it is strongly temperature dependent according to the Boltzmann statistics: $\exp(-h\nu_B/kT)$. The Stokes signal I_S, coming from the fundamnetal energy level, is free from temperature influence. The ratio $R = I_{AS}/I_S$ is defined by: $R(T) = (\lambda_S / \lambda_{AS})^4 \exp(-h\upsilon_B / kT)$ where h and k are respectively the Planck and Boltzman constants. Such a relation is only function of the temperature and vibrational characteristics of the fiber. So, a very selective temperature sensing is obtained. Thus, any influence of variations in the transfer function of the DTS instrument (power source, detector sensitivity, amplifier gain...) is removed by the normalization of these two intensities. In turn, the main advantage of the Raman technique lies in the fact that the result does not depend on the local value of the intensity of the initial pulses, and has a high insensitivity to mechanical perturbations applied to the fiber, as well as to local or distributed fiber losses. This technique, in addition to OTDR features used, provides a means to determine the temperature profile all along the fiber under test. Since many years, several DTS instruments are commercially available.

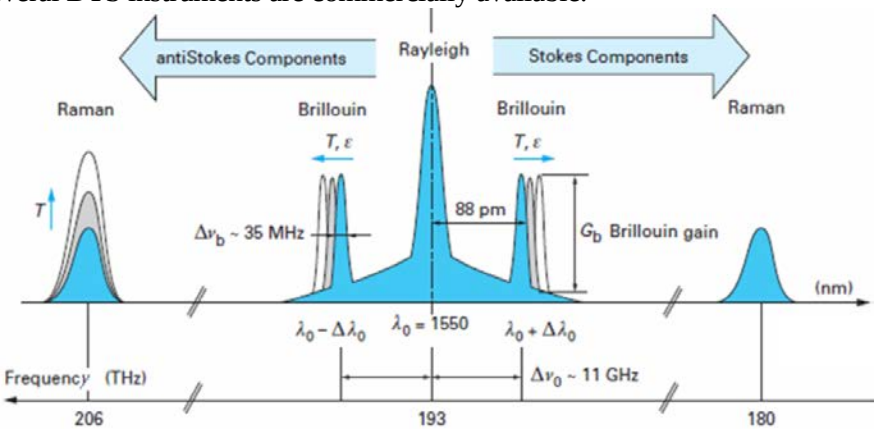

Figure 2: Rayleigh, Raman and Brillouin scattering intensity in silica fibers (excitation at 1.55 µm)

These instruments would therefore, when used in the nuclear building or in any NPP area, provide the temperature profile of any equipment/structure on, or in which, the fiber optic cables have been deployed. That is to say offer a remote thermal monitoring and fire detection on thousands of points, without any need for local power supply. The Fukushima event have shown that such feature could be very important in case of severe accident. It may becomes clearly crutial in case of reactor core fusion associated to reactor vessel perforation leading to corium release. Extra needs concern thermal monitoring of spent fuel pools, detection of leakages on primary steam pipes.

2.2. Reactor breakthrough and corium casting detection

In case of accident leading to the fusion of the reactor core, and to the vessel breakthrough, the corium flows on the concrete floor (thickness varies with NPP). In 1979 when the accident take place at Three Mile Island (TMI), a conjunction of incidents led to a partial melting of the reactor core, but without piercing the vessel. After hours, a partial core reflooding avoided the worst. At Chernobyl, the authorities were scared by a potential concrete breakthrough by the corium. In this case an explosion would took place. So, the basement was flooded; after cooling attempts by firemen. Authorities asked ten thousand miners to dig a tunnel 200 m long and 900 m² room located under the reactor to place a cryogenic cooling system. But, the corium cooled and finally stabilised itself, so that this cooling system was not installed, and the cavity filled with concrete. Regarding Fukushima, the information available is too few and accurate to conclude anything to date on the concrete status under the reactors.

So, concrete erosion by the corium is a strong matter of concern in case of severe accident. Concerning the EPR (Generation III), several improvements have been made to the concept of Pressurized Water Reactor (PWR, generation II, *i.e.* the main French reactors). On the one hand, it has been thickened (4 m) and, on the other hand, the lower part of the building has a specific room made of sacrificial concrete where the corium may spread. This room is followed by an optimized recovery area, which consists in a metallic structure of large surface able to passively cool the corium. In addition, a suitable refractory material (zirconia) is arranged on the lower walls to protect the building during the corium casting. Finally, solidification is achieved in a few days by flooding. But, this concerns the EPR only. Around the world, today's NPPs are not designed that way.

Also, in order to increase the information provided to the operators, and to the authorities, about the reactor breakthrough in case of a serious accident, we propose that NPPs be equipped with optical sensing cables, forming a grid below the reactor (into the concrete, in order to be protected againt the corium). This fiber mesh could then be interrogated remotely, securely, with a fiber optic instrumentation, even in case of total loss of control, or lack of electricity in the power plant. Of course fibers used in such application may be radhard to sustain the ionizing radiations over 40 years (*i.e.* 250 kGy with a mean dose rate ~ 0,7 Gy/h) plus those corresponding to the accident (600 kGy dose corresponding to 1 kGy/h dose rate; Standard NF M 64-001). From our opinion, this is now possible with modern radhard fibers designed for reduced sensitivity to radiation effects.

2.3. Temperature sensing in nuclear reactors

Tiny diffraction gratings photowritten inside the core of single mode optical fiber, Fiber Bragg Gratings (FBGs) are used for many years in sensing applications for numerous industrial fields. Reflecting a narrow spectral line called the Bragg wavelength, these transducers encode any measurand (temperature, strain, pressure, refractive index) in the form of a wavelength-shift of the Bragg wavelength. Therefore FBG-based sensing is insensitive to fluctuations of the optical signal's amplitude, as could occur in harsh environments, especially in the case of deployment for nuclear applications with radiation induced attenuation of optical fibers. FBGs feature key advantages for sensing in hostile environments: electromagnetic immunity, low intrusivity, low power consumption, excellent metrological properties, remote interrogation capabilities and wavelength-encoded measurement information. Moreover, FBGs sensors benefit from the wavelength multiplexing technology as used for telecommunications. Several tens of FBG sensors can be distributed over a single optical fiber (or using even more complex routing topology) as each sensor is identified through its own Bragg wavelength, defined during the photo-writing step. Conventional silica FBGs are usually limited for long-term use in high temperature environments. Through thermal engineering of such gratings, FBGs transducers are now made highly resistant even for temperature reaching 900°C during several thousands of hours. The so-called regenerated FBG transducers exhibit considerable improvements of their thermal stability with respect to their conventional counterpart.

The deployment of ultra-stable FBG temperature sensing arrays in extreme temperature environment is becoming a reality. Such sensors are promising candidates especially for nuclear environments. Ultra-stable regenerated FBG withstand operating temperatures well beyond 500°C as expected in several fourth generation nuclear core designs. This is especially the case of Sodium-cooled Fast Reactors (SFR) in which the coolant reaches 550°C. Their extremely high core's operating temperature pose challenging developments in order to ensure their safety and integrity. Health monitoring systems and specific sensing technology have to be developed to address the issue of high temperature continuous monitoring. Multiplexed and ultra-stable regenerated FBG sensors have levelled the challenge of long-term temperature stability. Their deployment as temperature sensing arrays within the core of SFR reactor needs now to progress regarding their qualification *versus* ionising radiation hardness. Once their behaviour under combined high temperature and high energy neutron flux assessed, FBG sensing could provide fruitful insight in order to accurately monitor temperature profiles within liquid Sodium coolant but also in order to improve SFR's core health and improve safety. FBG transducers could address measurements needs well beyond the basic but unvaluable multiplexed temperature sensing: innovative packaging and mounting procedures will trigger their use as strain and pressure sensors.

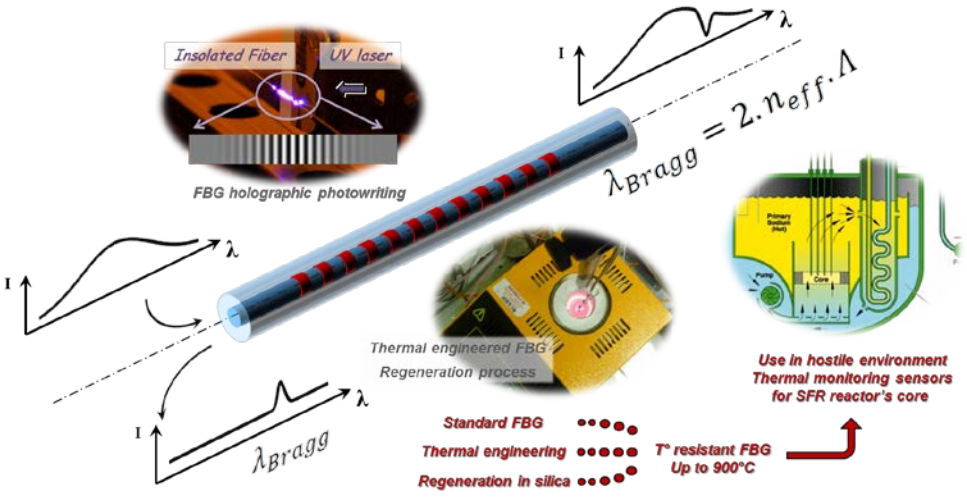

Figure 3: Regenerated FBGs: A technological breakthrough to achieve long-term temperature sensing up to 900°C even in hostile environment such as the next generation nuclear core of Sodium-cooled Fast Reactor.

Regenerated FBG temperature sensing heads have been recently evaluated to assess their compatibility with liquid Sodium heated up to 500°C and to confirm low response time below 200 ms above 200°C. These tests have been conducted in the Penelope glove box at CEA Cadarache [7]. Recent results and detailed explanation about regenerated FBG-based temperature sensing are presented in our second paper presented at the Fast Reactor 2013 conference (paper AIEA-CN-199/176).

2.4. Steam pipe monitoring

Primary circuits of PWR plants operate under high pressure and high temperature (155 bar; 325°C) in a relatively complex system (tank, pump, steam generator, pressurizer) including a large number welds. In case of failure, *e.g.* due to thermomechanical aging, steam leaks can lead to a loss of coolant accident (LOCA, Loss Of Coolant Accident). Thus, each NPP is equipped with an automatic emergency shutdown system. Moreover, in the case of a steam leak in the reactor building, due to a primary circuit crack, spray cooling systems are activated to condense the steam and prevent concrete building cracking due to overpressure.

In order to improve the monitoring of heat exchangers and main pipes (primary and secondary circuits), it may be useful to detect and localize any leak steam, including those which could lead to cracks. Such detection is therefore included in the concept so-called "leak detection before break" retained by the EPR. Some experiments, relatively older, conducted by the CEA on an experimental loop showed that a water leak of 100 l/h under standard pressure induce elevations of 40°C to 100°C on the inner face of the pipes insulation. The rise time of the phenomenon depends on the sensor location (1 s above the pipe, up to 30 s under the pipe). Practically, a steam or hot water leakage (up to 230 l/h) induces heating (primary circuit: 100°C; secondary circuit: 140°C) at the outer insulation. Traditional methods able to detect leaks already exist, but they are global (total quantity of water balance, dose level...) and therefore can not localise the leaks. Detection can also be based on local temperature sensing (*e.g.* thermosensitive cable, IR thermography...), but the cabling complexity in case of a large number of sensors become huge. Moreover, all of them require electrical power to operate, and frequent maintenance (emissivity recalibration for IR cameras), cameras which are not able to detect hot spots in presence of steam along the line of sight.

In such a context, the deployment of optical cables all along the pipes (under the insulation) and their interrogation with a remote DTS Raman system may become very convenient to accurately detect any hot spot, due to a steam leak, before it becomes a significant pipe break. Such fibers could also specifically control the elbows, valves and critical equipments. In France, this kind of monitoring has already been proposed more than two decades ago [8]. But, the idea had been considered as too far from industrial objectives. This point-of-view should be reconsidered today, given the significant advances in the technology since then.

2.5. Thermal monitoring of spent fuel pools

At Fukushima, the cooling of spent fuel, stored in the pools, quickly became a problem as pumps stopped. Various solutions (helicopters dropping water, high power water pumps) were used. In fact, for many days, TEPCO ignored the water level in pools, or even if the water was boiling and evaporating. These used fuel pools are located in different places within the NPP depending on their design (in France, they are confined in a concrete building able to withstand an earthquake). Measuring the temperature would be very useful to know if the water boils and evaporates or not. For this need, as for steam pipes, we recommend the use of optical cables and a remote Raman DTS.

2.6. Fire detection

Fire detection within the reactor and auxiliary buildings is an important issue as related to safety and availability of the NPPs. It is classified "Important For Safety" by regulators. Currently, this monitoring is done by conventional smoke and flames sensors, connected in series along loops. In France, these systems have been retrofitted a decade ago. But, such technologies were not able to prevent every fires. It was for instance the case in 2011 at The Tricastin (Drôme, France) or at Saint-Alban (Isère, France). While these incidents have caused no injuries and had no effect on safety, analyzes are underway to determine their origins. More generally, it should be noted that today, globally, with more than 400 reactors in service, we may count thirty serious fires per year. So, as consequences of a major fire would induce damage to the production means, a loss of electricity production for a long period of time, and a possible degradation of the plant safety, the fire detection remains an important topic.

To be efficient, a fire detection system must be redundant, without common mode... Moreover, selectivity of the measurement must be guaranteed in order to limit the consequences of a false alarm, with consequences on the electricity production (*e.g.* emergency reactor shutdown in case of fire in a primary pump casemate). A PWR reactor building is divided into 27 elementary zones to be monitored. Classically, a fire detection network is made of about 300 sensors distributed along loops, including 15 detectors each. Any primary pump casemate remains the priority area, insofar as the presence of a large amount of oil (~ 6 m^3) for lubrication during lifting and maintenance, remains the main risk of fire. A second one is related to electric cables, likely to release chlorinated products.

Usually, fire generates combustion gases, aerosols, radiation, and thermal energy. Each of these events can be detected by a dedicated method. Traditionally, fire monitoring systems are based on smoke or flames sensors. Indeed, the increase in temperature is sometimes considered a non-essential parameter to monitor due to its later appearance. In addition, conventional thermo-velocimetric, suffer from complex and recurent maintenance. This lack of reliability means that these point sensors for detecting temperature variations are not popular, and the temperature sensing alone is often unsuccessful. Nevertheless, today, the availability of distributed temperature sensors able to provide temperature profiles along a single fiber leads us to revisit this approach. It seems useful to consider using DTS-Raman sensing (1 measuring point per meter), of course in reactor building, but also wherever narrowness makes it difficult to detect fire near close from risk factors: in the casemates, around power cables which sometimes tend to heat up, as inserted in confined spaces,"hot spots" in transformers, etc.

2.7. Containment building monitoring by optical cables and Brillouin sensing

The civil engineering plays an important role in NPP safety since it ensures the confinement. For forty years, design techniques and construction rules, as well as the formulation of concrete, have gradually improved. So the EPR (Flamanville) concrete has very little to do with those Fessenheim (casting in April 1977) or Bugey (in May 1978). The containment building remains the ultimate barrier, it is designed to withstand a hypothetical risk of H_2 explosion. The ultimate pressure is 12 bar for 900 MW and 9 bar for both 1300 MW and 1450 MW reactors. Although a pressure integrity test is performed every decade, a complementary approach based on a monitoring system able to provide the operator with local, accurate and continuous information would improve safety and reduce maintenance costs.

Several years ago, the GPR has formulated some recommandations for the construction of the EPR: *"The inner wall of the containment building should be equipped with adequate instrumentation to accurately follow the prestress loss over time"*. In such context, in 2007 EDF has investigated the use, during the Flamanville concrete building casting, of fiber cables to measure strains by Brillouin sensing. However, in 2007, Brillouin optical cables available was not able to provide the required performances for such an application, in terms of transduction (lack of reliable qualification tests available). To our knowledge, such experiments have been suspended, but motivations remain.

However, since that time, the situation has evolved positively. Today, the cable manufacturer ACOME offers innovative products, namely optical fiber cables dedicated to distributed sensing: Rayleigh (OTDR and OFDR), Brillouin (BOTDR, BOTDA) or Raman (DTS). One of the sensing cables manufactured by ACOME is called "3D" (Fig. 4), [9]. It provides simultaneously a plurality of information about the structure under test (strain [traction and compression], bending, plane of curvature and temperature) at each measurement point defined by the interrogation system, *i.e.* every meter with a Brillouin-based instrument. The use of such cable embedded in a concrete containment building, or attached to the surface of existing buildings, may allow the operator to monitor, in real time and remotely (the instrument can be installed in an auxiliary building, even a long distance), the behavior of the structure *versus* time, to detect loss of prestress, and so to increase the safety level.

As a reminder, measurement systems based on the Brillouin effect are a variant of distributed sensors that implements a mechanism described as an inelastic interaction of the light wave propagating in the fiber core with acoustic phonons. The metrological interest lies in the dependence of this shift with temperature (~ 1 MHz /°C) and strain (1 MHz/20µstrain). The R&D led to the development of two Brillouin techniques, usually designated by the letters BOTDR (Brillouin Optical Time Domain Reflectometry) and BOTDA (A standing for Analysis). The main advantage of the BOTDR method, is that it does not need to have access to both fiber ends. Its drawback is the low efficiency of diffusion leading to long measurement times. The advantage of the BOTDA lies to a better signal-to-noise ratio, but the fiber must be looped on the instrument. Due to Brillouin amplification, the BOTDA provides useful signals whose intensity exceeds two orders of magnitude than the Rayleigh backscattering. The spatial resolution obtained today with commercial systems are: 30 km range (up to 80 km recently); 1 m resolution (or even beter), while the Brillouin frequency shift resolution remains about 1 MHz, equivalent to ± 1°C in temperature and ± 10 µm/m in strain. So far half a dozen manufacturers offers Brillouin instruments. Functionalities and performances differ on how to separate the strain measurement from temperature influence, but also in terms of spatial resolutions, measurement time, without forgetting the ergonomy.

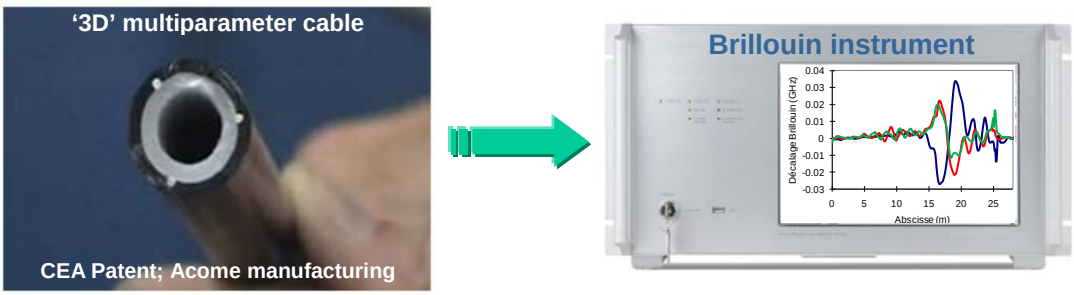

Figure 4 : Left : "3D" cable (3 fibers at 120°) to measure profiles of strain, curvature, plane of curvature and temperature ; Right: A Brillouin instrument with the measurement of the 3 sensing fibers, while the cable is bent.

2.8. Dosimetry based on fiber remote Optically Stimulated Luminescence (OSL)

Online fiber remote OSL dosimetery finds electronuclear applications such as radiation protection, recycling and dismantling operations, long-term nuclear storage. Basics of OSL are described in many papers and will not be reviewed here [10]. The readout unit is placed away in safe location and dose and dose rate data are remotely recorded online *via* an optical fiber link (no sensor disconnection for readout) by laser stimulation. The integral (over time) of the OSL signal is proportional to the dose absorbed by the dosimeter between two successive stimulations. The average dose rate is then estimated taking into

account the time elapsed between two successive stimulations (called the integration time). The reset time ranges between some 100 ms to some minutes and the acquisition rate may vary from some minutes up to several hours, days or more. Several OSL materials are used depending on applications. Radiation protection requires highly sensitive, low-Z materials to provide a tissue-equivalent dose measurement. The OSL detector may be inserted inside compensation packages (metallic filters) that provide both angular and energy compensations (to comply with standardization bodies, *e.g.* CEI 61066) [11]. Dosimetric-grade alumina crystals (Al_2O_3:C) is a low-cost, leading material for this purpose.

In electronuclear applications, the energy spectrum is often known and stable during exploitation. In this respect, energy compensation may not be required (relative measurements). In that case, it is worth using high-Z dosimetric materials such as usual photostimulable phosphors (e.g. BaFBr:Eu) or rare-earth (RE)-doped Alkaline-Earth Sulfides (AES, *e.g.* BaS:Eu,Sm) in order to increase dose sensitivity. Besides, stimulation and emission spectra of these materials are often red-shifted compared to that of alumina which enables long-range detection (up to some kilometers). Two generations of OSL/FO (OSL/Fiber Optics) systems have been developed by CEA LIST in the purpose of a remote OSL dosimetry *via* an optical fibre link [10]. The OSL1 systems were developed under contract by AREVA NC for dismantling applications and relies on RE-doped AES and operates in the Near Infra-Red spectrum. This readout unit was integrated into an industrial PC as a single channel version (Range [1 mGy -10 Gy]). Several units were sold to CEA and AREVA NC for use in the dismantling of installations in Marcoule, France. OSL/FO dosimetry enables low dose rate monitoring due to its passive mode of operation (a trade-off exists between response time and resolution in dose rate). AREVA used day-long integration times in order to improve the resolution in dose rate (below 50 µGy/h), taking advantage of the long cleanup process (weeks to months).

Figure 5. Left: Multichannel OSL/FO dosimeter [MAESTRO project for medical applications (CEA /C. DUPONT)] Right: 1-D multichannel sensor [INTRADOSE project for intracavitary in-vivo dosimetry].

The second generation OSL system (Fig. 5, left) is an improved version of the latter that relies on dosimetric-grade alumina crystals (Landauer Inc.). We have shown that the dose resolution is well below 50 µGy [11]. Therefore, it is possible to measure an average dose rate as low as 50 µGy/h for an integration time of 1 h, or 2 µGy/h with 1 day an integration time. This estimation is based on preliminary results [10] that are likely to be improved in the future by using high-power laser pulses instead of low power DPSS laser. The OSL2 system is a CW multichannel reader (16 outputs) built in a 19-inch enclosure that includes a diode-pumped solid-state laser (532 nm), a 16-channel optical fibre switch. It is linked to a laptop by an USB connection and handled through dedicated software written in LabView®. It was designed for radiation protection and medicine (*in vivo* dosimetry of patients treated by radiation therapy) within the European Project MAESTRO (2004-2007). OSL sensors were tested with photon, electron and proton beams. Several sensors were designed and tested: single sensors and multichannel sensor forming a sensing cable (1-D sensor, Fig. 5 right). This multichannel fiber optic sensor was designed and tested by the CEA LIST in the framework of a French ANR funded INTRADOSE Project for intracavitary *in vivo* dosimetry (Fig. 5, Ø = 3 mm) [12]. It is composed of 7 PMMA fibers and incorporate tiny alumina crystals (Landauer, 0.3 x 0.3 x 1 mm^3) inserted into fiber tips. This 1-D dosimeter concept associated to the multichannel readout may be used for dismantling applications as well. A multi-sensor cable might incorporate a plurality of detectors placed along, depending on installations and dose gradients). Such a sensing cable would be deployed and let in place during dismantling operations (for months to years) so as to provide online check-up of the remaining activity during the course of the cleanup.

2.9. Hydrogen risk

In case of LOCA, the melting of the nuclear core releases a large amount of H_2 due to both oxidation of zirconium sheaths (protecting nuclear fuel rods) and eventually concrete-corium interaction. Depending on air-H_2 and water vapour concentration, a spark or local heating may initiate a deflagration or a detonation that may endanger structure safety (Tchernobyl, Fukushima). Three zones (safety, deflagration risk, detonation risk) are depicted onto the Shapiro's diagram. Gas analysis within a nuclear containment is not expected to be trivial though. Firstly, H_2 concentration is not homogenous within containment and in some parts, it may accumulate, thus leading to local zones where detonation is likely to occur although no risk would have been identified on the whole structure. Distributed measurements are much pertinent than averaged one. Secondly, main measurements are done by extracting part of the gas out from the containment where it is analyzed by conventional methods (conductance, fuel cells, catalytic oxidation). However, sampling is not satisfactory because gas accumulate along the tubes leading to delayed and biased estimation. Finally, it is whorthwhile reminding that most analytical methods require a local power supply that may run out of order (Fukushima). Remote sensing is thus an added value for safety as far as the instrumentation is placed away, in safe location.

The aim of the H_2 risk assessment is therefore to provide reactor supervisors with an instrumentation able to correlate every critical location in the containment building with its situation on the Shapiro's diagram so as to account for heterogeneities in gas concentrations at each step of the accident.
Fiber optic technology provides distributed measurements inside the containment building with the help of passive rad-hard gas cells that operate without sampling. Each gas cell provides a local sensing of all gases of interest for post-accidental supervision (H_2, O_2, N_2, H_2O, CO and CO_2). The basic principle relies upon Raman spectroscopy, widely used in chemical, physical, biological and medical sciences. Fiber Remote Raman Spectrometry can be used for industrial analytical applications in a cost-effective design and more particularly for real-time monitoring of nuclear accidents (H_2 risk).

Raman spectroscopy is a very selective and versatile method (each gas molecule is identified by a line shape (Stokes line) in the optical spectrum and the amplitude of each one is proportional to both gas concentration and its interaction cross-section. The lightest molecule (H_2) provides the greatest Stokes shift (4161 cm^{-1}), *i.e.* 140 nm under green excitation (514 nm). Therefore, if another unexpected gas is present, it is detected since its lineshape will fall within this spectral range. This is an added value for safety and supervision of a potential accident, compared to selective sensors (*e.g.* Pd-coated sensors). Furthermore, only one instrumentation is necessary (multi-elementary) for the whole sensor network which simplifies both cabling and deployement. The basics of Raman spectroscopy may be found in many paper books and will not be described here. Preliminary tests in CEA LIST are also described in an earlier book chapter [2]. The response time of the detection system should be of the same order than that of the H_2 production rate (related to the number of oxided zirconium sheaths) and also compatible with the delay for action (typically several minutes).

Finally, two important constraints remain. The first one is radiation-induced degradation of fiber transmission combined with aerosols projection over sensor interface. Protection from aerosols is expected with a sintered metallic or ceramic filter mounted within a mechanical housing. Dedicated fibers were investigated for use in nuclear hostile environments, *e.g.* fluorine-doped silica fiber. Furthermore, the best spectral window lies in the near infrared (around 1 µm) where reliable sources and detectors are commercially available. Indeed, the measurement system must remain in "stand-by" during reactor lifetime (40 years or so) and be operational in the above hostile conditions. The fiber network would be arranged in parallel to reduce the exposed fiber length. Even in worst conditions (an hypothetical accident 40 years after reactor commissioning), fiber transmission is preserved.

The second constraint is due to regulatory requirement regarding the implementation of Optical Penetration Assemblies (OPA, the optical equivalent of Electrical Penetration Assemblies (EPA)). Such implementation should be anticipated very early in the reactor design. Otherwise, it requires derogation (old reactors) and necessitates to program another containment tightness test (pressure test). Nuclear operators (*e.g.* EDF in France) are therefore reluctant in installing such OPAs unless they are being forced to by nuclear authorities (*Autorité de Sureté Nucléaire* (ASN) in France).

3. Conclusion and perspectives

The nuclear disaster at Fukushima-Daiichi showed that the need for safety must always prevail. In this paper we have analyzed the advantages of Optical Fiber Sensing for remote monitoring, to improve the Nuclear Power Plants' safety, both in service (PWR, Pressurized Water Reactors), for the EPR (European Power Reactor) and for the future generations of reactors. During the accident of Fukushima, the loss of electricity power supplies had quickly lead traditional instrumentations to be inoperative and the operator TEPCO blind. To overcome these important drawbacks, we propose to take advantage of the considerable potential of distributed and quasi-distributed sensing technologies based on optical fibers, to strengthen both monitoring and Nuclear Power Plants' safety. Sensing technologies spatially continuous, *i.e.* those based on reflectometry and backscattering phenomena in silica fibers (Raman, Brillouin, and Rayleigh), namely the Distributed Fiber Optic Sensors are the best candidates for such objectives. Sensing arrays of multiplexed and temperature resistant Fiber Bragg Gratings (quasi-distributed sensors) are promising candidates for in-core continuous thermal monitoring in order to improve health and safety. Benefiting both from wavelength multiplexing technology and long-term stability even under hostile environment, they may be deployed in the form of dense and reliable sensing arrays in nuclear facilities, especially the next generation and high operating temperature nuclear reactor cores. R&D needs to be pursued intensively focusing especially on testing and qualification for nuclear environment operation. From the standpoint of safety, the benefits are many: no need for local power supply, remote instrumentations up to several kilometers, redundancy (multiple fibers and cables connected from different paths to the instrumentation units), diversification (no common mode failure with other measurement technologies)... Thus, optical fibers (some of them selected for their resistance to ionizing radiation), judiciously deployed in the power plant, may provide this monitoring, on real time or on demand, in nominal situation as well as in accident and post-accidental situations.

ACKNOWLEDGEMENTS

The authors want to thanks L. Ayrault, G. Rodriguez and J.-Ph. Jeannot from the CEA DEN for their support.

REFERENCES

[1] **P. Ferdinand, J.C. Gaucher, S. Magne, C. Martinez, V. Marty, L. Pichon, O. Roy, S. Rougeault**, *Potential applications for Optical Fiber Sensors and networks within the nuclear power industry*, in "Optical Sensors", Ch. 8, J.-M. Lopez-Higuera editor, Universidad de Cantabria, ISBN 84-8102-197-0, 1998.

[2] **P. Ferdinand and S. Magne**, *Applications of optical fiber sensors for nuclear power industry*, in Handbook on Optical Fiber Sensing Techn. Principle and Applications, Ch. 6, Edit. by J.-M. Lopez-Higuera, ISBN 0 471 82053 9, John Wiley and Sons, Ltd., 2001

[3] **N. C. Rasmussen, *et al.*** *Reactor safety study. An assessment of accident risks in U. S. commercial nuclear power plants*, Technical report n°*WASH-1400 (*Nuclear Regulatory Commission *NUREG-75/014)*, Oct. 1975. http://www.osti.gov/energycitations/product.biblio.jsp?query_id=6&page=0&osti_id=7134131

[4] EPR-European Pressurized water Reactor, Rapport Préliminaire de Sûreté de Flamanville 3, EDF 2006

[5] Evaluations complémentaires de Sûreté. Rapport de l'Autorité de Sûreté Nucléaires, déc. 2011

[6] Avis n° 2012-AV-0139 de l'ASN du 3 janvier 2012 sur les évaluations complémentaires de la sûreté des installations nucléaires prioritaires au regard de l'accident survenu à la centrale nucléaire de Fukushima Daiichi

[7] **G. Laffont, R. Cotillard and P. Ferdinand**, *Multiplexed regenerated Fiber Bragg Gratings for high temperature measurements*, 22nd Int. Conf. on Optical Fiber Sensors, OFS-22, 17-22 october, Beijing, China, 2012

[8] **P. Ferdinand, Y. Denayrolles *et al***., *The potential for distributed sensors and optical fibre sensor networks in the electric power industry*, Meas. Sci. Technol., vol. 1, 1990, pp. 908-916

[9] **J.-C. Da Rocha, A. Poulain, V. Dewynter, M. Giuseffi, S. Magne, L. Maurin, S. Rougeault, et P. Ferdinand**, *Câbles-Capteurs à Fibres Optiques pour les mesures réparties Brillouin, Raman et Rayleigh dédiées à la surveillance des structures*, Conférence CMOI, 21-25 nov. 2011, Lille

[10] **S. Magne, P. Ferdinand**, *Fiber Optic remote gamma Dosimeters based on Optically Stimulated Luminescence: State-of-the Art at CEA, IRPA 11 Conference*, Madrid (2004)

[11] **G. Ranchoux, S. Magne, J.P. Bouvet, P. Ferdinand**, *Fibre Remote Optoelectronic gamma dosimetry based on Optically Stimulated Luminescence of Al_2O_3:C, Radiat. Prot. Dosim.*, vol. 100, pp. 255-260, October 2002

[12] **E. Spasic, S. Magne, I. Aubineau-Lanièce, L. de Carlan, C. Malet, C. Ginestet, P. Ferdinand**, *Intracavitary in vivo dosimetry based on multichannel fiber-coupled radioluminescence and optically stimulated luminescence of Al_2O_3:C*, 2nd Intern. Conf. on Advancements in Nuclear Instrumentation Measurement Methods and their Applications (ANIMMA), Ghent, 6-9 June 2011, DOI: 10.1109/ANIMMA.2011.6172964.

Regenerated Fiber Bragg Grating sensors for high temperature monitoring in Sodium-cooled Fast Reactor

G. Laffont[a], R. Cotillard[a], P. Ferdinand[a], G. Blevin[c], J.Ph. Jeannot[c], G. Rodriguez[b]

[a] CEA LIST, Laboratoire de Mesures Optiques, Gif-sur-Yvette, F-91191, France

[b] CEA Cadarache DEN CAD/DTN/DIR, Saint Paul lez Durance, F-13108, France

[c] CEA Cadarache, DEN CAD/DTN/STPA, Saint Paul lez Durance, F-13108, France

Abstract. Optical Fiber Sensors relying on high temperature resistant and spectrally multiplexed Fiber Bragg Gratings transducers are proposed for remote multi-points temperature monitoring in fourth-generation reactors such as Sodium-cooled Fast Reactors. FBGs are well-established transducers finding applications in many industrial fields. Their use is usually limited to temperature up to 400°C in continuous use. Thanks to innovative thermal engineering methods of glass at the nanometer scale, FBGs operating lifetime in high temperature environments (up to 900°C) is significantly increased, opening the way for a wide range of applications for the nuclear industry. This paper will present the thermal regeneration process used to stabilize FBGs transducers. Long-term annealing experiments up to 890°C illustrate the relevant improvments of their stability. Multiplexed regenerated FBGs have also been tested in liquid sodium up to 500°C in order to investigate their compatibility, their response time and to show potential for high temperature gradient mapping.

1. Introduction

Expected increase in world electricity demand in the coming decades together with need for sustainable energy sources have triggered the design and development of new generation nuclear reactors. Merged under the Generation IV initiative, the most promising technologies for next generation nuclear reactors mainly feature fast reactor spectrum. Using the R&D development performed within the CEA, EDF and AREVA coordinated research program on Sodium-cooled Fast Reactors (SFR), the ASTRID prototype project has been launched in 2010. Standing for Advanced Sodium Technological Reactor for Industrial Demonstration, the ASTRID prototype is considered as a precursor to assess the technological choices in the scope of an industrial grade SFR reactor. Among the various R&D topics studied, progress In Service Instrumentation and continuous Monitoring (ISIM) of the nuclear core integrity during reactor operation is a major issue. The very high operating temperature of next generation nuclear cores is a great challenge facing all new sensing technologies. Sensors able to resist sustained periods at temperature up to 550°C in harsh environments as it is the case within the liquid Sodium-based coolant of SFR reactors require specific developments and lifetime evaluation.

Among Optical Fiber Sensors (OFS), Fiber Bragg Gratings (FBGs) are promising candidates for the instrumentation of next generation nuclear core. Used for decades mainly as strain, pressure, chemical and temperature transducers in numerous and demanding industrial fields, they are an alternative to traditional sensing techniques in harsh environments. Featuring key advantages such as: electromagnetic (EM) immunity, low intrusivity, low power consumption, excellent metrological properties, remote interrogation, multiplexing capabilities and wavelength-encoded measurement information. Benefiting from the exceptional transmission properties of modern singlemode optical

fibers (attenuation below 0.2 dB/km), FBGs transducers can be distributed over a network of sensing optical lines meshing any complex structures and remotely interrogated.

FBGs use in harsh environment, especially in case of continuous monitoring under very high temperature, was until recently limited due to ageing of their main optical characteristics (Bragg wavelength drift, decrease in reflectivity). So, long term use of FBGs transducers at operating temperature of 550°C was requested to instrument SFR nuclear core for in service continuous monitoring of temperature require to develop a new generation of FBGs transducers.

In this paper, we present an overview of FBG-based sensing technology. Then we describe in detail how thermal engineering methods of glass through a so-called regeneration process has increased the operating temperature of FBGs up to 900°C. Results from a long-term annealing of multiplexed and regenerated FBGs are presented. Then we describe the deployment of such high temperature resistant FBGs into testing facilities for immersion in high temperature liquid Sodium. Compatibility tests with such a reducing environment and response time in temperature are shown.

2. Fiber Bragg Grating sensing technology

Fiber Bragg Gratings (FBGs) have existed since photosensitivity in optical fibers was discovered in 1978 [1]. They are now well-characterized and are used in a variety of high-performance communication and sensing devices. In the field of sensing, standard FBGs are usually employed to detect physical and/or chemical parameters such as temperature, strain, pressure and refractive index[2][3]. A Fiber Bragg Grating is a periodic or aperiodic perturbation of the effective refractive index of the guiding core of an optical waveguide, such as single mode optical fibers. This modulation is obtained through inscribing of the photosensitive fiber's core using UV laser light. A Fiber Bragg Grating reflects a narrow spectral band located at the Bragg wavelength according to the following relationship between n_{eff} the fundamental mode refractive index and Λ the grating's pitch:

$$\lambda_{Bragg} = 2 \times n_{eff} \times \Lambda$$

By simply changing the grating's pitch, one can easily change the Bragg wavelength from one FBG to another written at a different location along the same optical fiber. This is the basic principle of spectral multiplexing applied to FBG transducer. Each FBG sensor is identified by its Bragg wavelength. Any change of the measurand (temperature, strain and/or pressure for instance) observed by a given FBG induces a spectral shift of its Bragg wavelength. The measurand is spectrally encoded in the form of a spectral shift while the sensor identity is given by the absolute Bragg wavelength. Taking advantage of the low attenuation of single mode optical fiber in the near infra-red spectral window, FBGs are usually photowritten in order to get a Bragg wavelength in the 1,55 µm window.

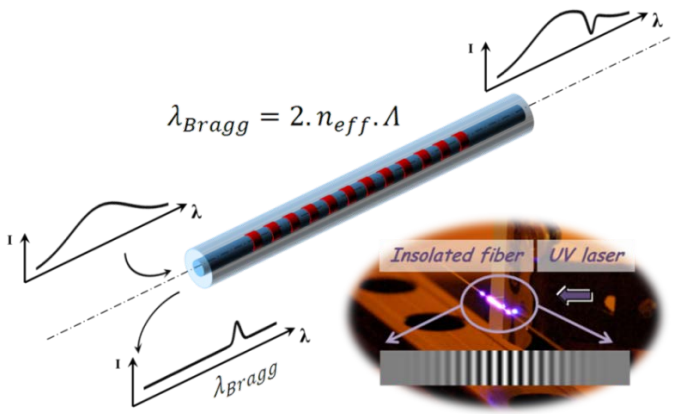

Figure 1: Spectral response of a standard FBG photowritten in a single mode optical fiber together with a picture showing a portion of fiber inscribed using a periodic interference pattern in UV laser light. The observed light at the insolation point stands for luminescence in the blue spectral window.

2.1. Fiber Bragg Gratings as temperature transducers

Any change of the temperature of a FBG transducer induces a spectral shift of its Bragg wavelength. This phenomenom is related mainly to the thermo-optic effect but also to the glass dilatation. At 1550 nm and over a limited range of temperature (let say 0°C to 200°C), the thermal sensitivity of a FBG temperature sensor is roughly constant and equals to:

$$\frac{\Delta\lambda_{Bragg}}{\Delta T}[1550\ nm] \backsimeq 11{,}3\ pm/°C$$

Over a broader range of temperature, the thermo-optic coefficient of silica changes non linearly with temperature. Thus it is necessary to calibrate the sensor using a polynomial fitting curve in order to keep precision to several tenths of a degree Celsius.

2.2. Wavelength multiplexing of FBG sensors

Each FBG transducer is identified through its own Bragg wavelength which is user defined at the photowriting step thanks to accurate control of the grating's pitch. Both the spatial position of each FBG on a single optical fiber and the spectral window containing its Bragg peak are known at the sensing line fabrication step. The Bragg wavelength not only indentifies the transducer but it also contains the measurand information: the parameter to be measured by each FBG transducer is spectrally encoded in the form of a Bragg wavelength shift. Using a calibration protocol, the absolute value of any measurand is retrieved from the Bragg wavelength shift and from the corresponding transducer's sensitivity, for instance *versus* temperature.

As the Bragg wavelengths allow transducers identification in the spectral domain, one can easily multiplex several FBG tranducers on a single optical fiber. But care has to be taken in order to prevent spectral crossing of adjacent FBGs: thus end users allocate a specific spectral window to each FBG based on the *a priori* knowledge of its expected wavelength shift. Figure 2 shows an example of spectral allocation table for FBG sensors dispatch over 6 different optica fibre channels. Each FBG is allocated to a pre-defined spectral window preventing spectral crossing with adjacent sensors. The maximum number of FBG sensors depends not only on the instrumentation used to interrogate the sensors but also on the expected wavelength shift and on gradient between adjacent sensors. Higher density of sensors can be reached in case of low gradient situation, for instance. Thus typical FBG monitoring system may interrogate from several up to tens of sensors depending on the application.

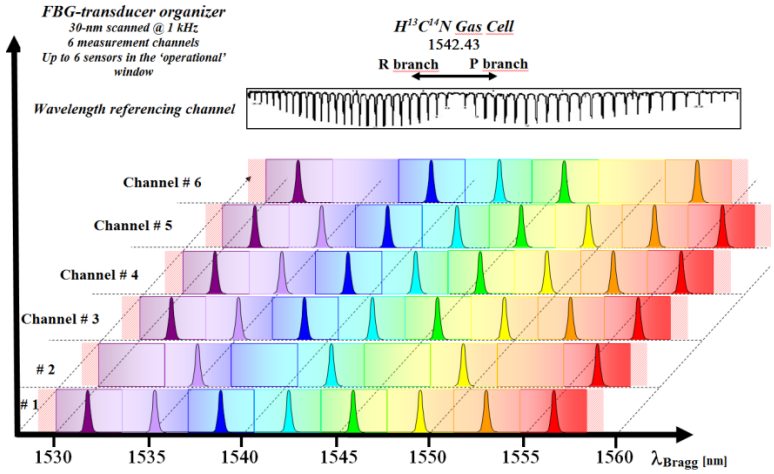

Figure 2: FBG transducers typical spectral allocation table to prevent spectral crossing. The sensor number is indicative: several tens of sensors may be easily interrogated depending on the measurand dynamic. Also shown at the top: a wavelength reference channel based on a gas cell providing absolute spectral calibration in real time of the monitoring system.

For instance, in case of a temperature sensor dedicated to measure temperature changes from 0°C to 600°C as could be expected in the case of SFR nuclear core monitoring, the maximum wavelength shift is expected to be roughly 8 nm and 13 nm over a 900°C wide range. Figure 3 shows a typical calibration curve obtained for five FBGs studied from ambient temperature up to 900°C. The non-linear behaviour of the Bragg wavelength with temperature is clearly visible while the evolution of the thermo-optic coefficient with the Bragg wavelength explains the difference between each FBG.

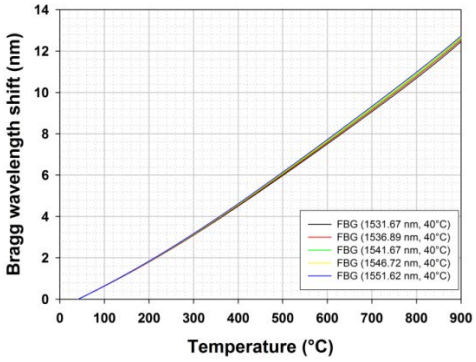

Figure 3: Bragg wavelength shift with temperature up to 900°C for five FBG transducer.

2.3. Overview of main industrial applications of FBG sensors

There is a wide diversity of scientific and industrial applications for FBG sensing technology [2]. FBG sensors are not limited to research and laboratories testing: they are now widely used in many industrial fields and have gain in maturity through two decades of field tests by numerous international teams. Starting from the main parameter addressed by a single FBG transducer (temperature, strain, pressure and refractive index), one can also measure a diversity of physical and chemical parameters thanks to appropriate packaging. Thus a non-exhausive list of available FBG-based sensor comprises: temperature sensor, strain gauge, pressure sensor, refractometer, extensometer, inclinometer, mono and/or multi-axes accelerometer, chemical and biochemical agents detection … This diversity of addressable measurand together with the excellent metrological properties of FBG sensors explain the corresponding diversity of industrial application fields: Civil Engineering, Materials, Composite materials, Railway and Sea Transport, Aeronautic, Space, Defense, and Nuclear.

3. Regenerated Fiber Bragg Gratings

FBG use in severe environment, such as for continuous monitoring under high temperature, is limited due to ageing of their main optical characteristics (Bragg wavelength drift, decrease in reflectivity). Improving the FBG long-term stability under high temperature is a major research topic. Increasing operating lifetime of high temperature FBG transducers has been addressed through several approaches: optimizing optical fiber's chemical composition, high temperature annealing to erase the unstable photowritten refractive index pattern, writing of damaged FBGs thanks to multiphoton excitation of silica. Among the various solutions considered to develop temperature resistant FBGs, the regeneration process of type I seed FBGs photowritten in standard single mode fiber is a fruitful approach. The so-called regenerated FBGs not only exhibit excellent stability of their reflectivity up to temperature of 1295°C [4] but also present spectral shape of the Bragg peak similar to that of type I gratings, thus preserving the spectral accuracy desirable to get transducers with appropriate metrological performances.

3.1. Erasing of standard FBG under high temperature

Figure 4 shows the typical erasing curve of a standard FBG photowritten in a single mode optical fiber. After almost seven days at a constant temperature of 586°C, 70% of the initial Bragg peak reflectivity has been erased. Moreover the decay in reflectivity will go on until total erasure of the grating. From a metrological point of view, this constant decay means that the signal to noise ratio is

also decreasing continuously. Thus the precision degrades in time down to a level preventing any measurement.

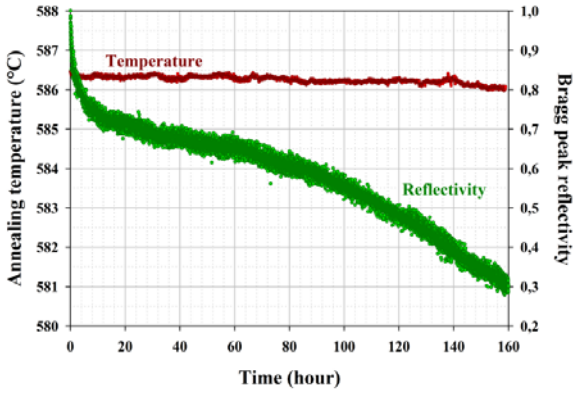

Figure 4: Evolution of a standard FBG reflectivity *vs* time at a temperature of 586°C. Reflectivity decreases by 70% over 6.6 days; decrease is continuous until total erasure of the photowritten pattern.

3.2. Regeneration process for temperature stabilization of seed grating

Regeneration is an exciting and attractive approach dramatically increasing the operating lifetime of FBGs employed in high temperature environment, thanks to glass material thermal engineering at the nanometer scale. Regenerated FBGs are a technological breakthrough for high temperature sensing opening the way to many applications. From a practical point of view, it consists in annealing a standard saturated FBG, the seed grating, at different temperatures or using a temperature ramp (depending on the selected protocol). Whatever the protocol used, the seed FBG is erased through an annealing at temperature closed to 900°C. At this step, instead of stopping the experiment and declaring the grating's erasure, one has to pursue the heating experiement: then a new Bragg peak appears on the spectrum, roughly at the same Bragg wavelength than that of the seed grating. Its reflectivity increases gradually up to a maximum level depending on the annealing protocol, on the seed grating initial reflectivity and on the fiber's composition and fabrication process. Stopping the annealing at this step gives rise to a so-called regenerated FBG. Figure 5 shows the typical evolution of the reflectivity during such a regeneration process. The obtained gratings are stable at temperature up to 900°C, namely that of the regeneration process (see section 4.2).

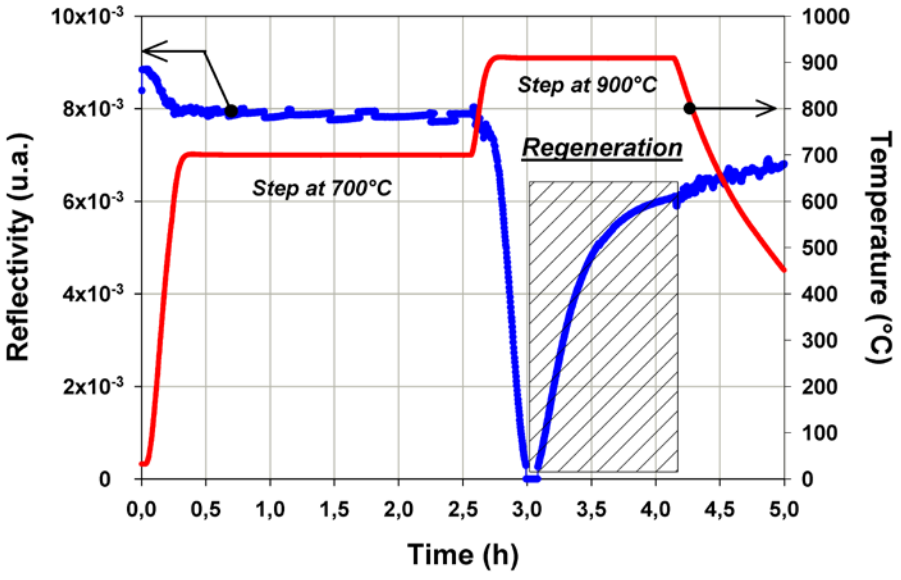

Figure 5: Evolution of the seed FBG reflectivity *vs* time during the regeneration process.

3.3. Regeneration of multiplexed FBGs sensing line

Many high temperature applications require the use of densely multiplexed sensing line, either to map a large structure or to get temperature profiles without moving the temperature probe. This would be the case of a SFR nuclear core: temperature resistant FBG have added values regarding standard sensors (thermocouples typically) in case of a dense array of transducers is deployed to monitor continuously the core's temperature while a single optical cable is used to remotely interrogate this sensing array. The sensor array's topology may be complex while routing to the remote system may preserve simplicity without requiring many hermetically sealed feedthrough.

As an illustration to the realization of multiplexed and high temperature resistant sensing line based on the regeneration process, we have demonstrated the regeneration of sensing lines with transducers spaced by only a few millimeter along a single fiber (see Figure 6): each seed FBG is 2 mm long and two consecutive FBGs are spectrally spaced by 5 nm to avoid spectral overlapping during temperature gradient characterization. In order to increase the reflectivity of multiplexed regenerated FBGs very close to each other and thus to get an optimal signal-to-noise ratio for the Bragg wavelengths measurement, we have chosen to photowrite strong seed gratings using a conventional interferometric setup (instead of draw tower gratings) and then to simultaneously regenerate all the gratings. A horizontal tubular furnace is used to anneal ten FBGs introduced in the tubular furnace having a temperature homogeneity of 3°C, at an average temperature of 913°C, over the fiber's sensitive length. In regeneration experiment, a type N thermocouple is adjacent to the central seed FBG in order to control the temperature within the furnace. The horizontal temperature profile has been determined previously. The spectral response of the seed FBGs is analyzed in reflection using a spectrometer and normalized with regard to the optical source profile.

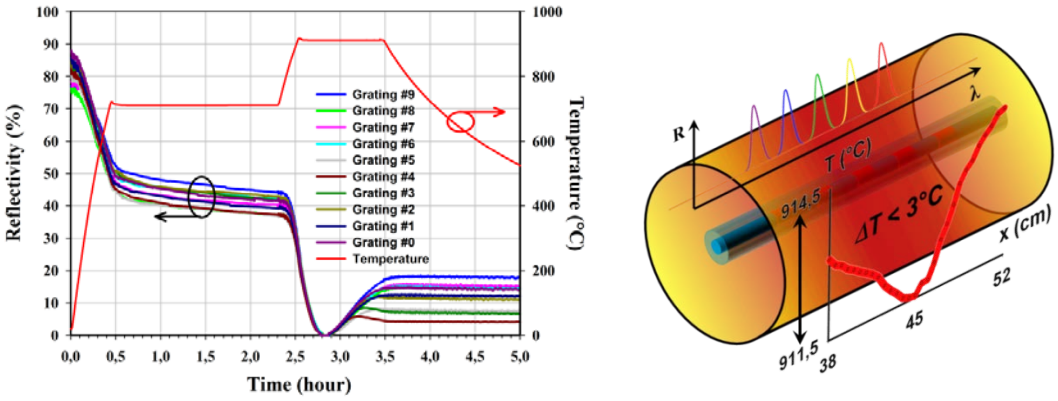

Figure 6: Evolution of the reflectivity of ten seed FBGs during the regeneration process (left) and scheme of the furnace together with the FBG spots and the temerature profile.

The regeneration process is highly sensitive to the annealing temperatures. In that experiment, even a small heterogeneity of 3°C in horizontal temperature profile is enough to induce significantly different regeneration ratio (see Figure 6). Better control of the regenerated FBG reflectivity is of importance in order to get the same signal to noise ratio for the whole sensing line. This can be achiever either by reducing the temperature gradient along the seed FBGs or by compensating for the regeneration ratio.

4. Stability of regenerated FBGs for use in high temperature environment

4.1. High temperature annealing setup

In order to assess the stability of regenerated FBG at high temperature, a long-term annealing setup has been implemented. Four regenerated FBGs have been inserted in a vertical tubular furnace. Each regenerated grating is located at a different position along the furnace in order to take benefit from its temperature gradient. Thus each grating is tested at a different temperature over 2000 hours in continuous: 760°C, 810°C, 860°C and 890°C.

4.2. Long-term stability of regenerated FBGs

Blanks in the data points stand for period of time with the spectral acquisition being stopped (spectrometer used for other experiments) while the heating has never been interrupted. The evolution of the reflectivity for each regenerated FBG is shown on Figure 7.

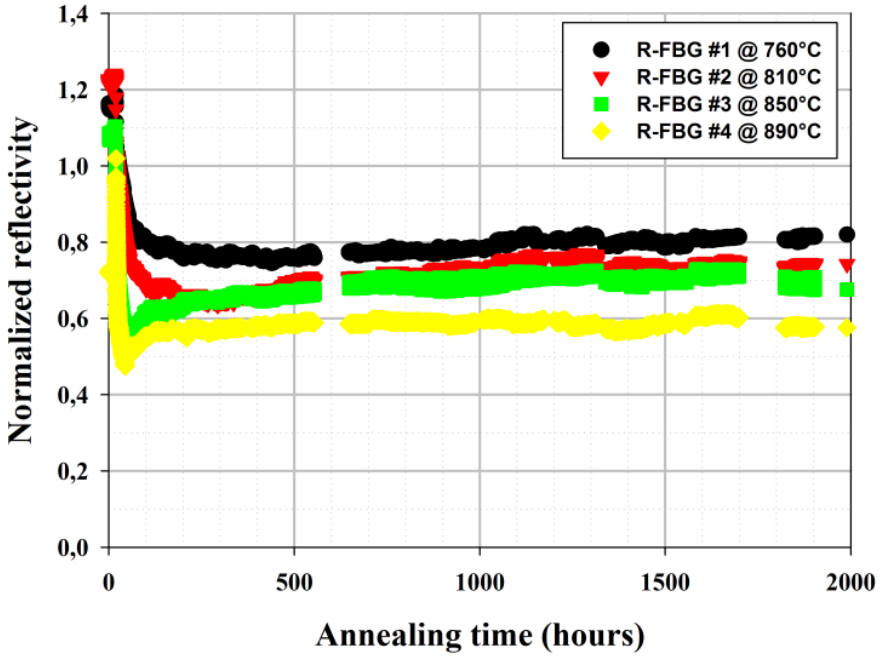

Figure 7: Long term and continuous annealing of four regenerated FBGs over 2000 hours and at distinct temperatures of 760°C, 810°C, 850°C and 890°C.

A rapid decrease is observed during the first 200 hours of annealing at the lowest temperature of 760°C before reflectivity stabilization to occur. At 890°C, this initial decrease in reflectivity is observed during 50 hours before stabilization. At 890°C, the initial drop in reflectivity reaches 50% and only 30% at 760°C. Once intial burn-in is achieved, the reflectivity's stability is better than +/-5% and no subsequent decrease is observed, even at the highest annealing temperature. Such a result clearly indicated that regenerated FBGs are temperature resistant. No model can be applied to predict lifetime, except going on with this experimental annealing test. Standard modelling methods for temperature erasable FBGs, such as the *master curve* formalism used in telecom, has been implemented but it does not work on gratings that cannot be erased.

5. Regenerated FBGs sensors in liquid Sodium

Once their stability with temperature well beyond 600°C has been assessed, experiments for the evaluation of regenerated FBGs in liquid Sodium have been conducted. These tests aim to clarify the compatibility with high temperature (550°C) liquid sodium of packaged optical fiber temperature probes relying of the regenerated FBG technology. The response time of a regenerated FBG-based temperature probe has been characterized together with the ability to measure temperature gradients in a hot glove box compatible with liquid sodium.

5.1. Penelope glove box for testing in liquid sodium

All the tests in liquid sodium are conducted in the Penelope glove box operated at CEA Cadarache (see Figure 8). This box allows to safely heat liquid sodium up to 550°C and thus to realize the tests in immersion of materials, sensors and/or instrumentation prototypes.

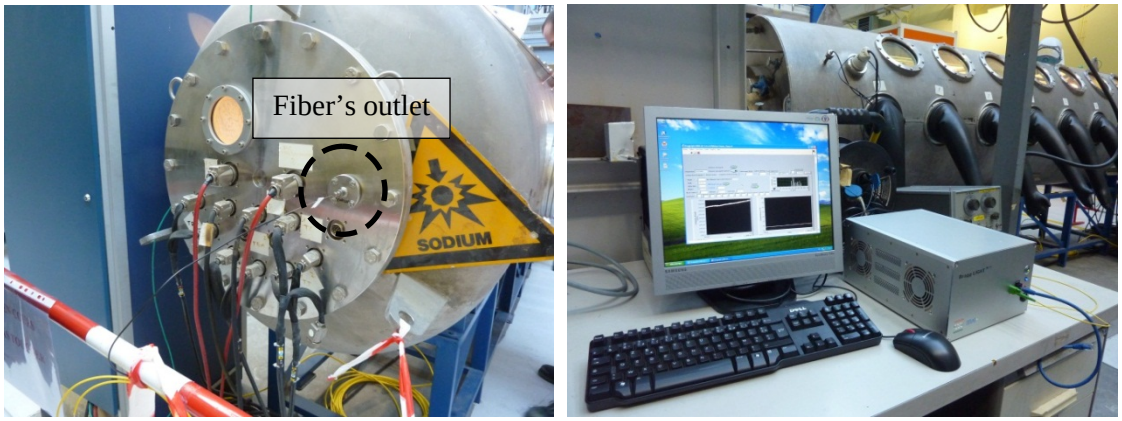

Figure 8: On the left, the CEA/Penelope glove box for testing of sensors in heated liquid sodium and on the right CEA LIST proprietary FBG monitoring system deployed nearby the Penelope facility located at CEA/Cadarache research centre.

5.2. FBG sensors packaging

For testing, we have realized a sensing line comprising five regenerated FBGs. The gratings are 2 mm in length and spaced by 3 mm. The sensing optical fiber is inserted in a metallic capillary made of Inconel 600. The extremity of the capillary inserted in sodium was sealed. A Swagelok seal fitting is used for the capillary outlet.

5.3. FBG monitoring unit for sensors demultiplexing

A proprietary interrogation system is located nearby the Penelope box (see Figure 8) and is used to demultiplex the FBGs at a rate of 1 kHz and a precision of 1 picometer. The system relies on a client/server approach. The opto-electronic unit can be remotely positioned with respect to the sensor (connected to the opto-electronic unit thanks to outdoor optical fiber cables) and its continuous operation controlled thanks to a client software interfaced through an Ethernet link to the unit (thus a remotely installed computer may controlled one or several opto-electronic units positioned in a dedicated cabinet). Thus one can control and/or process measurement data in real time without any impact on the main unit operation.

5.4. High temperature gradient measurement in a heated sodium box

A specific liquid sodium box was constructed and inserted into the Penelope facility in order to realize measurements in hot sodium and to characterize gradients of temperature. Thus the box is heated from its bottom. The sensors are inserted from the top as shown on Figure 9. Three thermocouples are also immersed in sodium at a close vicinity from the optical sensors. They are assembled all together thanks to a main metallic body also plunged into sodium. Stability of the sensing head during immersion in sodium at 500°C demonstrates the compatibility of the packaging with liquid sodium. As shown on Figure 9, a single capillary of 1 mm in outer diameter is enough to insert five high temperature resistant FBG sensors and to send the optical signal back to a remote monitoring system. With the same intrusivity, a sensing line with several tens of FBG sensors multiplexed on a single fiber is straightforward to implement. Thus the routing of the FBG temperature probe is easier than the routing of several thermocouples. During the 2.5 hours-long immersion in sodium, we do not observe any significant evolution of the Bragg wavelength and of the reflectivity. Initial evolution stands for stabilization of temperature inside the box. The observed ripple is due to the regulation of the heating system. With a typical temperature thermal sensitivity of 15 pm/°C at 500°C, the observed ripple of +/-2.5 pm corresponds to oscillation of +/-0.2°C in temperature. Ripple is also observed on the reflectivity due to the spectral dependance of the optical power density and the lack of normalization for the reflected Bragg peak.

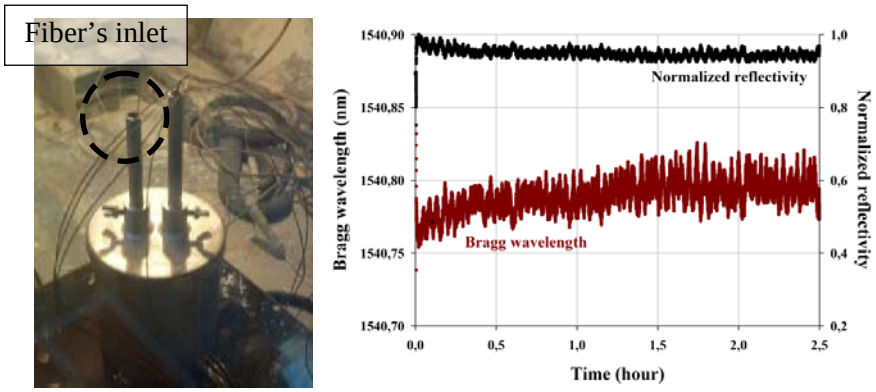

Figure 9: Sodium box installed in the Penelope facility and heated from the bottom (left). The fiber's inlet is highlighted: a single capillary is enough to position 5 multiplexed regenerated FBGs; the other inlet is for three thermocouples. On the right, stability of a regenerated FBG in hot sodium (500°C).

5.5. Regenerated FBG response time in liquid sodium

With regard to thermocouples, the use of regenerated FBG for nuclear core continuous monitoring have considerable advantages not only in term of sensor multiplexing but also in term of response time with regard to temperature changes. With a monitoring system operating at a rate of 1 kHz, the response time of a FBG-based temperature sensor is limited by the thermal inertia of the sensing head itself: temperature changes have to diffuse through the metallic capillary itself (Inconel 600, outer diameter of 1 mm, inner diameter of 300 µm), through the residual air film between the optical fiber and the inner wall of the capillary, and through the polymer and silica claddings of the fiber itself. The FBG is located in the optical silica core which is roughly 10 µm in diameter. The response time of the regenerated FBG-based temperature probe has been tested through quick but manual immersion of the probe inside the liquid sodium heated up at different temperature. Therefore the measured response time of the probe is greater than the diffusion-limited value due to the delay induced by the manual immersion. Figure 10 shows a typical increase of the Bragg wavelength during immersion in sodium, with a change in temperature from 47°C (temperature inside the Penelope box) and 500°C (temperature of the sodium).

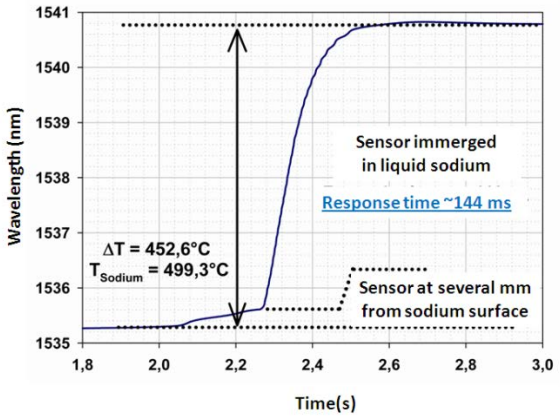

Figure 10: Bragg wavelength increasing during rapid immersion of the regenerated FBG-based temperature probe in sodium ($T_{Penelope}$ = 46.7°C; T_{sodium} = 499.3°C).

A slight increase in temperature is observed first when the probe is positioned close to the sodium surface. Then the probe is immersed in sodium: the observed rising time (10-90% step height) is equal to 144 ms. Repeated immersion experiments have been conducted according to different sodium temperatures.

Repeated experiments at low sodium temperature showed greater rising time as shown on Figure 12. The minimal observed value is between 300 ms and 700 ms, except two values above 1000 ms due to a too slow immersion. Reduced rising time is observed for sodium temperature increased up to 150°C: the rising time then decreases down to around 250 ms. We thus expected these high rising time values to be related to a poor wetting of the outer metallic capillary wall by liquid sodium at low temperature. Similar experiments are conducted on a second regenerated FBG-based temperature probe packaged in an identical Inconel 600 capillary as shown on Figure 11 (right graph). For sodium temperature higher than 200°C, the rising time is lower than 200 ms. Once the capillary has been immersed in sodium heated up to 400°C, the rising time stays within 220-250 ms even at low liquid sodium temperature (below 200°C). These results comfort the hypothesis that the high values observed at low temperature in our first experiment (left graph on Figure 11) may be imparted to a poor capillary wetting.

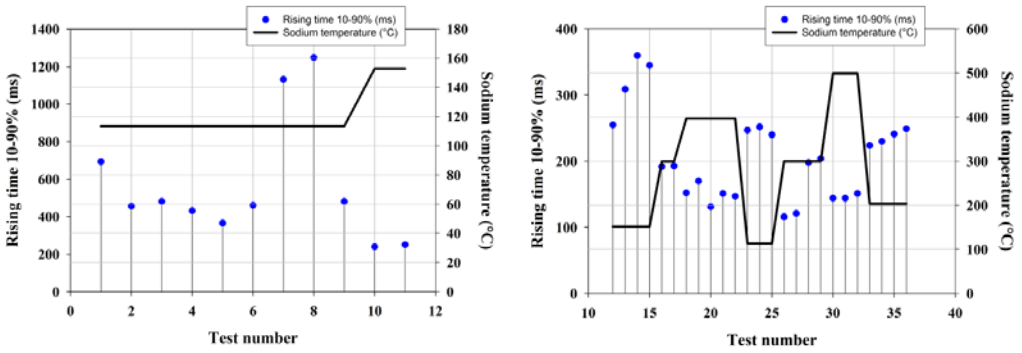

Figure 11: Analysis of regenerated FBG-based optical fiber temperature probe response time during immersion in liquid sodium heated at different temperatures.

6. Conclusion and Perspectives

Thermal annealing of Fiber Bragg Grating realized in conventional single mode optical fiber, the so-called regeneration process, opens the way to a rich and innovative fields of applications dealing with harsh environment, especially those involving extreme and high temperatures up to 900°C. Continuous temperature monitoring inside high temperature nuclear core is a typical target application for complex arrays of regenerated FBG-based temperature probes. Regenerated FBG sensing technology could contribute significantly to the continuous integrity monitoring of Generation IV nuclear core such as those designed for Sodium-cooled Fast Reactor prototypes. In this context, we have developed and validated the use of multiplexed regenerated FBG-based temperature probes in liquid sodium heated up to 500°C. The immersion tests in liquid Sodium have emphasized both the compatibility with hot and liquid sodium but also very short response time (typical rise time of 150 ms at sodium temperatures above 200°C). Forthcoming evaluation of the regenerated FBG-based sensing technology will focus on the realization of higher density sensing lines and on its use for temperature profile mapping within hot liquid Sodium or at the sodium/cover gas tidal zone. Emerging as promising candidate for instrumentation of fourth generation nuclear reactor, regenerated FBG sensing technology needs now to be qualified regarding radiation tolerance, especially under high energy neutron flux, this qualification is in progress.

REFERENCES

[1] K.O. Hill et al., *Photosensitivity in optical fiber waveguides: application to reflection filter fabrication*, Appl. Phys. Lett., 32, pp. 647-649, 1978

[2] P. Ferdinand et al., *Optical Fiber Sensors from laboratory to field trials: Applications and trends at CEA LIST*, Fiber and Integrated Optics, 28 (1), pp. 81-107, 2009

[3] G. Laffont, *Study and development of tilted FBG-based transducers and measurement systems in single mode optical fiber*, PhD Thesis, Univ. of Lille, France (2001, n°2983)

[4] J. Canning et al., *Extreme silica optical fibre gratings*, Sensors, 8 (10), pp. 6448-6452, 2008

Development of a Mobile CZT Detector System for Burnup Measurement of Spent Fuel Assembly and On-Site Application

LI Jianhua, ZHAO Yonggang, LIU Hongbin, JIN Huimin, ZHU Liuchao, CHEN Yan, Zheng Yulai

China Institute of Atomic Energy,Beijing,PR China

Abstract. The advantages of mobile CdZnTe (CZT) detector for nuclear safeguard applications of spent fuel burnup inspection in assembly storage pond are compactness，low cost and ease of operations. In this work, a mobile detection system shield with tungsten alloy was designed and then performed on-site. Net count rate of the 662 keV line of ^{137}Cs was produced linearly with burnup as experimental data simulations shows, in which the deviation from linearity is smaller than 9%. As a result, the feasibility of the method using CZT detector to monitor spent nuclear fuel assembly burnup in a fuel pond was validated. The results calculated with Monte Carlo procedure Geant4 can provide a theoretical guide for the further burnup measurement.

1.INTRODUCTION

The International Atomic Energy Agency (IAEA) verifies spent fuel for safeguards purposes and proliferation resistance applications. The chemical (destructive) assay techniques of spent fuel burnup provide accurate estimation of fissile material depletion in reactor fuel, but this method is both complex and costly. Non-destructive methods provide a convenient and cost-effective means. Gamma spectrometry is a well-established technique of non-destructive burnup measurements. Its principal advantage lies in that the measurements are carried out without affecting the fuel integrity. The equipment used are usually handy, rugged, lightweight and portable, easily deployable for underwater application, and the measurement times easily manageable【1】.

The instrument should have adequate energy resolution to resolve and separate the major gamma lines of nuclear material. It is concluded that for the application of safeguards small-sized CZT detectors are the best choice for characterizing irradiated fuel assemblies, for the reason that HPGe detectors are not practical for use underwater and Nal detectors are very sensitive, require heavy shielding and for short cooled fuel their resolution is not adequate. CZT detectors can easily be shielded, collimated and brought close to the item to be verified, often allowing in-situ measurements, and their resolution is sufficient to resolve the fission product gamma lines of spectra taken from irradiated fuel assemblies with a cooling time of just a few days【2】. Room-temperature semiconductor detectors (RTSD) provide an excellent alternative to the traditional detector options. They do not require cooling and for spent fuel verification their small size (20-500mm^3) is not a disadvantage because the signal is strong.

2. EXPERIMENT AND METHOD

In this work, a suite of instruments in which the shield was fabricated from a tungsten alloy (95% W by weight) was designed and then performed on-site.

The structure of the CZT Detector System for Burnup Measurement of Spent Fuel Assembly is shown in Figure 1. The cylindrical tungsten alloy shield and collimator included with wall thickness of 7 cm for the front face, 6 cm for the side and rear, which contains the CZT detector, were housed in a stainless steel watertight canister with wall thickness of 0.8 cm and outside diameter of 18 cm and length of about 44 cm.

For mitigating scattered X-rays and low-energy γ-rays，the detector was wrapped in 0.4 mm copper foil and shielded with 1 mm cadmium plate.

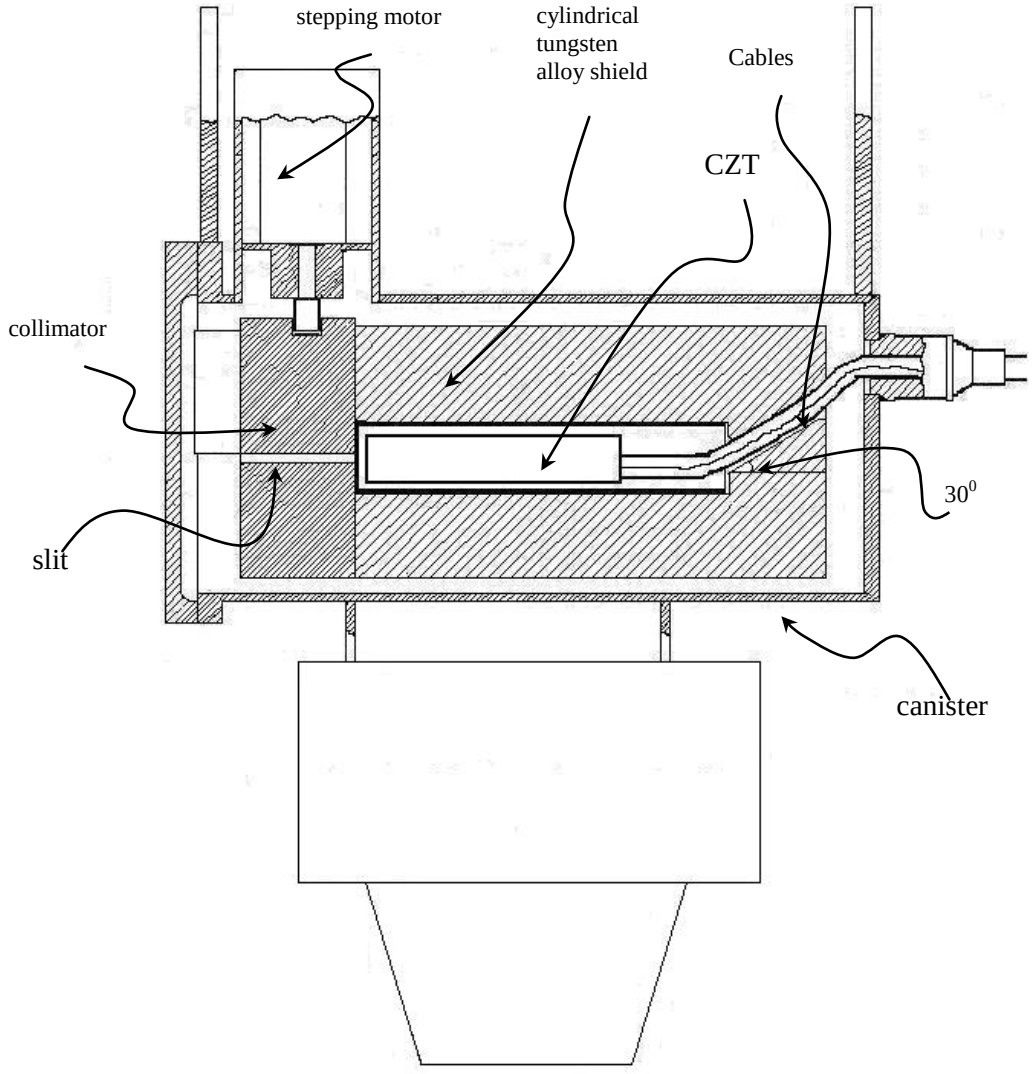

Figure1. Schematic view of the CZT Detector System for Burnup Measurement

For reducing counting loss and statistical errors from bad peak shapes caused by a high count rate, the collimator slit width is adjusted from 0 to 5mm as required by moving a tungsten alloy block of which the position could be controlled by a stepping motor through a threaded spindle and gear arrangement. So that the CZT detector with its collimator could measure a narrow section of the fuel. The carrier could fit in the racks and be transported by the plant's crane.

The CZT detector used for these experiments was a large-size detector 15×15×7.5mm3 (Co-Planar Grid (CPG) Detector, purchased from eV products，USA). Its full width at half-maximum is about 1.8% at 662 keV. It was connected to a portable Multichannel Analyzer（Inspector2000 from CANBERRA，USA）.

Essentially, gamma spectrometric method measures activity of a given fission product or fission products in a section of the fuel volume. This volume is defined by the dimensions of the instrument collimator and its distance from the fuel surface. The relative contents of fission products in an individual fuel assembly depend upon the irradiation history, type of fuel and cooling time of that particular element.

^{137}Cs is the most widely accepted indicator of fuel burnup because its neutron absorption cross section is negligible, its yield from both ^{235}U and ^{239}Pu are approximately the same, and its 30-yr half-life makes a correction for reactor power history unnecessary. The ^{137}Cs buildup is approximately linear over the entire range of bumup. Past experience with the ^{137}Cs burnup monitor shows that the absolute ^{137}Cs activity can determine burnup to an accuracy of 1 to 4% for individual fuel rods.【3】

In this work, the first assembly measurement data with calculated burnup value was used to determine the calibration factors, and the axial burn-up profiles of the fuel assemblies was also built, the duration of every measurement was about 30 minutes.

3. Results and Discussion

Net count rate of the 662 keV line of ^{137}Cs is produced linearly with burnup as experimental data simulations show, in which the deviation from linearity is smaller than 9%. As a result, the feasibility of spent nuclear fuel assembly burnup monitoring by using a CZT detector in the fuel pond was validated.

The spent nuclear fuel burnup measurement using the net count rate ratio of ^{134}Cs /^{137}Cs was also tested, in which spectra interpretation is not accurate enough and the deviation from linearity is about 25%, as the cooling time is too long (more than 10 a) and the background radiation level is too high on-site.

The energy depending dead-time correction factors were obtained from an experiment in this laboratory, for it is difficult to get a reference material which was similar to spent fuel assembly in lab ，and then be applied to all the experimental data on-site. The correction is very effective for the results measuring with a dead time above 10% , but almost has no effect for the data obtained as dead time is less.

The applicability of commercial available software Genie2000(from CANBERRA，USA) in this work was studied, and the results revealed total peak area method of Genie2000 was appropriate for calculation when the peak shape was bad. The best choice is to develop a special software to decisively interpret the gamma spectra【4】.

The shielding of tungsten alloy is effective. By changing the geometrical positioning (such as the size of collimator aperture), the precision is not significantly changed.

The CZT detector full energy peak efficiency as different size of collimator aperture is calculated with Geant4 in this work. The Direction Biasing Sample method of source particle is used to increase calculation efficiency. The calculated ratio of net count rate of the 662 keV line of ^{137}Cs of two different size of collimator aperture is agree very well with on-site measurements. The calculation will provide some theoretical reference for the further redesign of instrument for burnup measurement.

4.Conclusion

The feasibility of the method of spent nuclear fuel assembly burnup monitoring by using CZT detector on-site was validated. Net count rate of the 662keV line of ^{137}Cs is produced linearly with burnup as experimental data simulations shows. The deviation from linearity is 9%. The dead-time correction factors were obtained from an experiment in this laboratory, and then applied to all the experimental data on-site. This correction is effective for the result measuring with a dead time above 10%, but almost of no effect for the data obtained as dead time is less. Measuring spent nuclear fuel burnup by using the intensity ratio $^{134}Cs/^{137}Cs$ is restricted by the low measurement statistic for which the cooling time is long and the background radiation level is high on-site.

The further work for achieving a better precision is to improve shielding redesign and reduce the count rate of the spectrometer due to decreased dead time as the preamplifier has insufficient throughput for the high count rate on site.

ACKNOWLEDGEMENTS

The authors wish to acknowledge professor Dong Mingli and professor Gu Zhongmao of China Institute of Atomic Energy for their valuable help.

REFERENCES

[1] S.A. Ansari and et al，Burnup studies of spent fuels of varying types and enrichment，Annals of Nuclear Energy 34 (2007) 641－651

[2] K.H. Czock*, R. Arlt，“Use of CdZnTe detectors to analyze gamma emission of safeguards samples in the field”，Nuclear Instruments and Methods in Physics Research A 458 (2001) 175}182

[3] J. R. Phillips，Irradiated Fuel A4easuremenls，Passive Nondestructive Assay of Nuclear Materia，NUREG/CR-5550 LA-UR-90-732

[4] J. Brutscher, R. Arlt, K.H. Czock, Isotope identification software for Gamma spectra taken with CdZnTe detectors，Nucl. Instr. and Meth. A 458 (2001) 189

Modeling of the chemical behavior of sodium fire aerosols during atmospheric dispersion

T. Gilardi[1], A. Chassery[1], C. Perrais[1], C. Latgé[2], R. Baskaran[3], V. Subramanian[3]

1- CEA, DEN, Cadarache DTN/STPA/LIPC, F-13108 Saint-Paul-Lez-Durance, France
2- CEA, DEN, Cadarache DTN, F-13108 Saint-Paul-Lez-Durance, France
3- IGCAR, Safety Group, Radiological Safety Division, Kalpakkam-603 102, India

Abstract

The use of liquid sodium, as a coolant in the Sodium Fast Reactor (SFR) circuits, requires studying the consequences of a sodium fire for safety analysis, and particularly the production of sodium fire aerosols and its chemical evolution during atmospheric dispersion. The sodium fire aerosols initially composed of sodium oxides (Na_2O and Na_2O_2) are quickly converted into sodium hydroxide (NaOH) by hydration with moisture, and then into sodium carbonate (Na_2CO_3) with atmospheric CO_2.

A kinetic model was developed to calculate the chemical conversion from NaOH to Na_2CO_3 during atmospheric dispersion. This model is supposed to be coupled with atmospheric dispersion codes in order to assess the chemical impact of sodium aerosols at several distances. The limiting step of this reaction mechanism was identified thanks to a non-dimensional criteria analysis. The model was also compared to several experimental measurements reported in the literature and to recent experiments performed in IGCAR's Aerosol Test Facility (ATF).

Keywords: SFR, sodium fire, aerosols, carbonation, kinetic, modeling

1 Introduction

The development of Sodium cooled Fast Reactors (SFR) for future electric power generation is strongly dependant on the safety of the system in nominal and accidental conditions. The physical and chemical properties of the sodium coolant have to be considered for safety analysis in case of accidental scenarios. If due to a leak, hot liquid sodium (between 550°C and 280°C in secondary pipes) will contact air, the hot sodium can initiate a sodium fire. As a consequence, a large amount of aerosols may be produced from the combustion of sodium with oxygen. The sodium fire aerosols, initially composed of sodium oxides (Na_2O or higher oxide Na_2O_2 depending on oxygen concentration), are quickly converted into sodium hydroxide (NaOH) by hydration with airborne moisture. The presence of CO_2 in atmosphere is then responsible for a further chemical reaction with NaOH leading to the formation of sodium carbonate (Na_2CO_3). The kinetics of this former reaction is generally slower than the hydration step, and depends on aerosol particle characteristics (diameter, density, porosity). Because of the different toxicity of these substances (indeed NaOH is a corrosive compound while Na_2CO_3 is a weak irritant), the composition of sodium fire aerosols and its evolution during atmospheric dispersion must be determined in order to evaluate the environmental and human impact in case of an accidental release outside the building. Indeed, the description of aerosol conversion to less harmful sodium carbonate is of major interest for safety analysis of future SFR and more generally for sodium handling and experimental facilities.

Several experimental studies were carried out on sodium fire consequences in different conditions (sodium amount, local volume or outside atmospheric conditions, pool or spray fire) in different facilities such as Esmeralda in France [1], Containment Systems Test Facility (CSTF) in United States [2], FAUNA in Germany [3], and Aerosol Test Facility (ATF) at the Indira Ghandi Center for Atomic Research

(IGCAR) in India [4]. These studies provided a description of the sodium fire phenomenon as well as physical and chemical data about sodium aerosol behavior. A few theoretical studies about chemical transformation of sodium fire aerosols were also carried out to predict their chemical evolution. In 1970, Clough and Garland [5] proposed a theoretical description of the sodium aerosols size and the particle physical state (liquid or solid) in equilibrium with atmospheric relative humidity. They also proposed simple kinetic models of NaOH carbonation rate based on a control by CO_2 diffusion, either in the gas phase at the droplet surface, or in the liquid phase of the droplet. In 1980, Cooper [6] extended the analysis of Clough and Garland to study the transformation rates from the sodium oxides to sodium hydroxide and from the hydroxide to sodium carbonate. Assuming a mass transfer limitation, either in gas phase, or in liquid or solid (dense particles or agglomerates) particles, this study provided an estimation of the duration time of the preliminary transient phase before the steady state behavior. In order to assess the influence of initial particle size on these kinetic parameters, Cooper proposed a new correlation to determine directly the radius of the NaOH droplet in equilibrium with atmospheric humidity as a function of the radius of initial dry NaOH particle:

$$\frac{R_0}{R_i} = \frac{0{,}87}{(1 - HR)^{1/3}} \quad \textbf{(1)}$$

where R_0: is the radius of the NaOH droplet in equilibrium with atmospheric humidity
R_i: is the radius of the initial dry NaOH particle

This expression is coherent with the determination of aerosol size proposed by Clough and Garland, and is applicable for relative humidity between: $0.35 < HR < 0.99$. It will be used as the initial value of particle size (before carbonation reaction with CO_2) in the kinetic model developed in this work.

Using this parameter, Cooper studied the reaction rate of sodium fire aerosols with water vapor and with CO_2. He calculated the reaction time required for steady-state flux controlling aerosol transformation (Na_2O_2 hydration, NaOH carbonation), depending on particle diameter (varying from 0.1 to 10 µm) and on the evaluation of the diffusivities of gaseous reactants (water vapor and CO_2) through the different phases (gaseous atmosphere, liquid or solid particle) to the unreacted sodium aerosol. Particularly, in the case of a relative humidity above 35% for which initial NaOH particles are aqueous solution droplets, the carbonation of sodium fire aerosols is considered to be controlled by the CO_2 diffusion through a solid carbonate shell forming at the droplet surface. Using an expression of the diffusion flux through this solid product shell based on the shrinking core model, an order of magnitude of the half conversion time is given for a CO_2 diffusivity in Na_2CO_3 assumed to be 10^{-9} $cm^2.s^{-1}$. This study also approached the influence of particle porosity, in case of low humidity, leading to the formation of agglomerates. Indeed, the measurement of average particle density performed by Hinds [7] on sodium fire aerosols (assumed to be mainly under the carbonate form) revealed a lower value than the density of dense Na_2CO_3 material. The porosity was then estimated between 45% and 68% depending on the exact hydration level of Na_2CO_3 particles, and an effective diffusivity in agglomerates was evaluated based on the diffusivity in air and on the agglomerate porosity.

A theoretical study of NaOH aerosol carbonation was carried out by Ramsdale [8] who used also a kinetic model based on the shrinking core description and obtained results in good agreement with experimental measurements of Cherdron et al. [3].

Moreover, different experimental data are available for modeling development and validation. Cherdron et al. studied the behavior of sodium aerosols generated by a pool fire in the FAUNA facility [3] and their measurements showed the enhancing influence of relative humidity (in particular between conditions under 3% of relative humidity and conditions above 20%) on the carbonation rate. Hofmann et al. [9] studied sodium aerosols behavior generated from a spray fire in an experimental loop under 40% and 70% relative humidity conditions. The study of very small aerosol particles (particle sizes from 0.2 to 0.35 µm) highlighted the influence of this parameter on the carbonation kinetic rate which is faster when initial particles are smaller. More recently, Subramanian et al. [10] studied the chemical behavior of

sodium pool fire aerosols within a 1 m^3 aerosol chamber, in the Aerosol Test Facility (ATF), under different relative humidity conditions. They developed a specific methodology using a high-resolution conductometric tritration able to provide sodium aerosol speciation of samples collected (on filter paper) every 100 s. Tests performed under 50% and 65% of relative humidity and in the presence of CO_2 concentration around 300 ppm, showed a complete conversion of NaOH into Na_2CO_3 after 500 s from the onset of fire.

On the base of these previous studies, a new kinetic model was developed in CEA in order to calculate the conversion rate from NaOH to Na_2CO_3 occurring in sodium fire aerosols during the atmospheric transport of these particles. The analysis of both the theoretical approach and experimental results available in literature confirms that the shrinking core model is a relevant base for the development of a new modeling tool taking into account atmospheric conditions such as relative humidity (and its influence on initial size and physical state of NaOH aerosols), and devoted to be coupled with atmospheric dispersion simulation code. After a description of the physical and chemical phenomena, this paper presents the modeling correlations selected to calculate the kinetics evolution of NaOH aerosol carbonation. Then, an evaluation of this modeling tool is proposed with a sensitivity study to main parameters and with a comparison to experimental data.

2 Physical and chemical phenomenon involved in sodium aerosol behavior

Above its ignition temperature and depending on environmental conditions (oxygen concentration, heat exchange with atmosphere), hot liquid sodium burns with air (oxygen) and gives rise to a large amount of sodium oxide aerosols. Close to the flame, the aerosols generated are mainly composed of sodium monoxide, Na_2O. When dispersed at further distance from the flame, a higher oxidation rate may occur and the monoxide converts into sodium peroxide Na_2O_2 if the oxygen content remains close to air composition (≈ 20%) and if the gas temperature is below its decomposition limit (≈ 657°C). The formation of superoxide, NaO_2, is also possible at higher levels of oxygen content or high gas pressure, but is usually neglected.

Then, these oxides are further converted into sodium hydroxide, NaOH, by hydration with water vapor present in atmosphere:

$$Na_2O\ (s) + H_2O\ (g) \rightarrow 2\ NaOH\ (s) \quad \textbf{(2)}$$

$$Na_2O_2\ (s) + H_2O\ (g) \rightarrow 2\ NaOH\ (s) + ½\ O_2\ (g) \quad \textbf{(3)}$$

The humidity present in the atmosphere is generally in sufficient concentration (for instance ≈ 0,4 $mol.m^{-3}$ for 30% relative humidity at 25°C ambient temperature) and we assume that its concentration is not limiting the conversion into NaOH. In preliminary approach, the kinetics of this hydration is supposed to be very fast, as well as, the water vapor transport to the aerosol surface. Indeed, the diffusion time for external transport was evaluated less than 3.10^{-2} s by Cooper [6] under 30% relative humidity and 25°C for particles diameters under 10 µm. This is why we consider in our model that sodium aerosols are totally converted into NaOH as soon as they are released outside the building in case of a sodium fire occuring with accidental circuit leakage.

Consequently, we focused our study on the carbonation of NaOH aerosols during their atmospheric dispersion outside the building. This reaction is a heterogeneous reaction between a gas (CO_2) and a particle (NaOH liquid or solid depending on its hydration level). Such a gas/particle reaction can be generally described by a succession of several steps also involved in heterogeneous catalysis (granular catalyst):

a) The external diffusion of the reactive gas through the diffusion limit layer formed around the particle: the thickness of this limit layer depends on the hydrodynamic conditions of the atmosphere around aerosol particles

b) If a solid reaction product is formed and develops a solid shell on the superficial layer around the particle, the reactive gas will have to diffuse through this product layer to reach the unreacted core and carry on the chemical conversion.
c) The chemical reaction between the gas reactant and the unreacted core is another step of the heterogeneous reaction and has its own kinetics also.
d) If gaseous products are formed, their backward diffusion through the solid product shell and then through the external diffusion layer should also be considered, but this is not the case for NaOH carbonation.

In fact, because of the mechanistic complexity of fluid/solid reactions, different other kinetic models were also developed to be suitable to various kinetic conditions (transport limitation or chemical reaction limitation) or particle morphology (uniform or heterogeneous structure). Since the shrinking core model was already selected in previous studies [6, 8] to describe the carbonation of NaOH, it can be considered as the most relevant approach to investigate for further development. In the following part, the selection of the shrinking core model is discussed thanks to the analysis of non-dimensional criteria and complementary modeling improvements are proposed to take into account the influence of parameters such as the initial size of aerosol particles as well as their density evolution during chemical transformation.

3 Modeling of chemical transformation of sodium hydroxide aerosols during atmospheric dispersion

The shrinking core model is built for a heterogeneous reaction between a fluid reactant A and a solid particle of reactant B, leading to the formation of a solid product C and possibly other fluid products D.

$$A + \nu.B\ (s) \rightarrow C\ (s) + D \qquad \textbf{(4)}$$

The carbonation of sodium hydroxide involves a gaseous reactant A (g) = CO_2 (g), and a NaOH particle as reactant B which may be either solid or liquid depending on the relative humidity in atmosphere. The solid product C (s) is Na_2CO_3 and the fluid product D is H_2O which is in liquid form. In the case of solid NaOH particles, the chemical reaction can be written as follows.

$$2\ NaOH\ (s) + CO_2\ (g) \rightarrow Na_2CO_3\ (s) + H_2O\ (l) \qquad \textbf{(5)}$$

Assuming spherical NaOH particles (particularly in the case of liquid NaOH droplets) the concentration profile of the reactant gas CO_2 can be represented as showed on Figure 1.

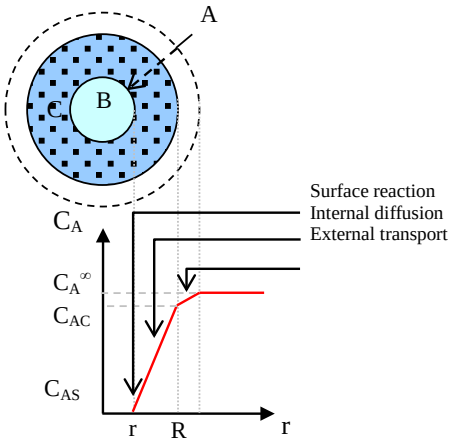

Figure 1: Profile concentration of CO_2 gas in a particle of NaOH during carbonation

C_A^∞ [mol.m^{-3}]: mean concentration of gaseous reactant A in atmosphere

C_{AC} [mol.m^{-3}]: concentration of gas A at the particle surface (external surface of solid product C)
C_{AS} [mol.m^{-3}]: concentration of gas A absorbed in the particle and located at the interface (spherical interface with the core radius "r") between the particle core of residual reactant B (NaOH) and the layer of product C (Na_2CO_3) (in the case of a kinetics governed by internal diffusion in the product layer, this concentration can be assumed as zero).

As shown in Figure 1, three steps can be distinguished in the mechanism of this heterogeneous reaction. Each one is characterized by an expression of the material flux of the gaseous reactant, involving different transfer resistances as well as concentration differences:

- External transport : $J_A = 4\pi R^2 . k_D . \left(C_A^\infty - C_{AC}\right)$ **(6)**
- Internal diffusion : $J_A = 4\pi rRD_e \dfrac{\left(C_{AC} - C_{AS}\right)}{\left(R - r\right)}$ **(7)**
- Surface reaction (1st order kinetics with A) : $J_A = 4\pi r^2 . k_r . C_{AS}$ **(8)**

J_A [mol.s^{-1}]: molar material flux (transfer or reaction flux) of reactant A (CO_2 gas)
k_D [m.s^{-1}]: external material transfer coefficient in the laminar limit layer of the atmosphere flow (relative to the particle)
k_r [m.s^{-1}]: chemical reaction kinetic constant
D_e [m^2.s^{-1}]: effective diffusivity of gas A in the external layer of solid product C

If we consider the cumulative influence of the three resistances in series, the conservative material flux can be written as a function of the atmospheric CO_2 concentration:

$$J_A = \frac{1}{\left(\dfrac{1}{4\pi R^2 k_D} + \dfrac{R-r}{4\pi rR D_e} + \dfrac{1}{4\pi r^2 k_R}\right)} \cdot C_A^\infty \qquad \textbf{(9)}$$

Since the material fluxes of the two reactants are related by the reaction stoichiometry:

$$\nu \cdot J_A = J_B = -\frac{\rho_B}{M_B} 4\pi r^2 \frac{dr}{dt} \qquad \textbf{(10)}$$

The combination of equations (9) and (10) can be integrated in the volume of the product layer, from the initial radius R of the particle to the time dependent r(t) radius of the remaining NaOH core. The general expression of the "shrinking core" kinetic model is given below:

$$t = t_0 - \frac{\rho_B}{\nu M_B C_A}\left[\frac{r^3}{3k_D R^2} + \frac{1}{D_e}\left(\frac{r^2}{2} - \frac{r^3}{3R}\right) + \frac{r}{k_R}\right] \qquad \textbf{(11)}$$

with $t_0 = t_{0D} + t_{0i} + t_{0c}$ representing the required time for a total chemical reaction (total conversion of B reactant) in the case of equivalent transfer resistances for the three mechanism steps that must be cumulated in series. The total conversion times for a kinetic control by each mechanism step are given by the expressions:

$$t_{0D} = \frac{\rho_B R}{3\nu M_B k_D C_A^\infty} \; ; \qquad t_{0i} = \frac{\rho_B R^2}{6\nu M_B D_e C_A^\infty} \; ; \qquad t_{0c} = \frac{\rho_B R}{\nu M_B k_R C_A^\infty}$$

The conversion rate can be defined for the NaOH carbonation by the following expression as a function of the radius "r" of the NaOH core inside the particle:

$$X_B = -\frac{dn_B}{n_B^0} = 1 - \left(\frac{r}{R}\right)^3 \quad \textbf{(12)}$$

The experimental studies performed by Cherdron et al. [3] showed that the transformation rate of NaOH particles to Na_2CO_3 depends strongly on relative humidity and was found to be slower than predicted by theoretical studies [5, 6] considering a kinetic control by CO_2 diffusion in liquid NaOH droplets. They invoked the assumption of the formation of a solid carbonate layer on the NaOH particle surface to explain these results and the fact that the kinetics slows down with the conversion progress. On the basis of these observations, Ramsdale [8] proposed a model taking into account a kinetic control by the CO_2 diffusion through a carbonate crust, and that is equivalent to the shrinking core model with a kinetic control by internal diffusion. This is why the development of our model was based on the same approach, but a theoretical justification of the kinetic limiting step was also carried out using mean conditions of sodium fire aerosols behavior during atmospheric dispersion.

Indeed, different non-dimensional criteria can be used to compare the kinetics of each step of the reaction mechanism.

- the Thiele's module: $\varphi_s^2 = \frac{r_s.L^2}{D_e.C_{AC}}$ compares the chemical reaction rate (r_s) with the internal diffusion flux.

Here, L is the characteristic particle dimension (volume / surface area): $L = \frac{d_p}{6}$ for spherical particles

The Thiele's module was evaluated for different particle diameters (cf. Table 1) , using the kinetics constant of Pohorecki et al. [11] measured for the reaction rate of CO_2 with NaOH aqueous solutions, and the effective diffusivity ($D_e \approx 10^{-10}$ m.s^{-1}) through solid carbonate estimated by confrontation of our model with Cherdron experimental results [3].

d_p [µm]	0.1	0.5	1.0	5.0	10.0
φ_s^2 [-]	1.06	26.4	106	2 639	10 554

Table 1: Evaluation of Thiele's module for different particle sizes

Since the size of sodium fire aerosols is generally around a few microns (at least 1 µm), it can be assumed that the Thiele's module φ_s^2 is greater than 1 for reaction with NaOH liquid droplets.

- The Biot number: $Bi_m = \frac{k_D.L}{D_e}$ compares the flux of external transfer (in gas phase limit layer) with the internal diffusion flux.

Here, k_D is the material transfer coefficient calculated from Ranz and Levenspiel correlation of the Sherwood number applicable for material transport in the fluid phase in contact with spherical grains:

$$Sh = \frac{k_D.d_p}{D} = 2{,}0 + 1{,}8\,\mathrm{Re}^{1/2}\,Sc^{1/3} \quad \textbf{(13)}$$

Where D is the CO_2 diffusivity in air ($D \approx 1.5.10^{-5}$ m².s^{-1}) and Re and Sc are respectively the Reynolds and Schmidt numbers. For very small particles, the Reynolds number is close to zero and the Sherwood number Sh ≈ 2. The minimal value of the Biot number can be estimated for the carbonation of NaOH aerosols during atmospheric dispersion:

$$Bi_m = \frac{k_D.L}{D_e} = \frac{k_D.d_p}{6 \cdot D_e} = \frac{Sh \cdot D}{6 \cdot D_e} \approx 5.10^4$$

This evaluation shows that for $Bi_m >> 1$, the external transport of CO_2 in atmosphere to the particle surface is much more rapid than the CO_2 diffusion through the sodium carbonate layer.

Consequently, the analysis of these non-dimensional criteria confirms that the carbonation of sodium fire aerosols during atmospheric dispersion is controlled by the CO_2 diffusion in the Na_2CO_3 layer surrounding the particle, which can be assumed as the kinetic limiting step for the average conditions of particle sizes and atmospheric humidity.

Because of density difference between initial NaOH particle and the solid reaction product Na_2CO_3, we have to take into account the volume contraction in the product layer due to the higher Na_2CO_3 density. Indeed in the case of initial solid NaOH particles (for very low humidity in atmosphere) the density increases slightly from $\rho(NaOH_{(s)}) = \rho_B = 2100$ kg.m^{-3} to $\rho(Na_2CO_{3(s)}) = \rho_C = 2500$ kg.m^{-3}, and in the case of NaOH droplets (for higher atmospheric humidity) the initial density is even lower. For instance if we consider a 85% relative humidity in atmosphere, the density of NaOH initial droplets can be estimated at a lower value $\rho_B = 1400$ kg.m^{-3} assuming a 1 µm initial droplet diameter in equilibrium with this relative humidity condition and using the sodium content in the droplet estimated by Clough and Garland [5].

Using the expression (6) of the conversion rate $X_B(t)$, the core radius r(t) and the global particle radius R(t) can be described by the following expressions in function of the initial radius of NaOH in equilibrium with atmospheric relative humidity :

$$r = R_0\left(1 - X_B\right)^{1/3} \quad \textbf{(14)}$$

and $$R = R_0\left[1 + \left(\frac{\rho_B M_C}{2\rho_C M_B} - 1\right) X_B\right]^{1/3}$$ respectively. **(15)**

A volume factor $z = \frac{v_C}{v_B} = \frac{\rho_B.M_C}{\rho_C.M_B}$ is then introduced and also a related parameter $\alpha = \frac{z}{2} - 1$.

On the assumption of a kinetic control by CO_2 diffusion in the surrounding product layer, the general model given in equation (11) can be simplified and transformed as a function of the conversion rate X_B. Taking into account the volume factor discussed above, the kinetic model adopted to describe the carbonation of NaOH aerosols generated from a sodium fire, can be finally presented by the following expression:

$$t = \frac{\rho_B.R_0^2}{4.M_B.D_e.C_A^\infty}\left[1 - \left(1 - X_B\right)^{2/3} + \frac{1 - \left(1 + \alpha.X_B\right)^{2/3}}{\alpha}\right] \quad \textbf{(16)}$$

In this model, several parameters are likely to change with atmospheric conditions and with sodium fire conditions:

- The atmospheric relative humidity determines the hydration level of NaOH particles produced from sodium oxide aerosols and consequently the initial radius R_0 of NaOH aerosols but also the physical state (liquid aqueous solution or solid particle) and the initial aerosol density (ρ_B).
- The CO_2 atmospheric concentration (C_A^∞) is also likely to vary from average conditions but in a very limited extent usually.
- The sodium fire conditions (pool or spray fire, sodium temperature and ejection velocity) are also determinant for the initial size of sodium oxides aerosols and so for the initial radius R_0 of NaOH aerosols.

The CO_2 diffusivity in solid Na_2CO_3 (D_e) is not a well-known parameter and was only estimated by the confrontation of modeling results with experimental data from Cherdron [3]. With a similar approach,

Ramsdale used a higher value of this diffusivity ($D_e = 10^{-9}$ $m^2.s^{-1}$) with good agreement with his model [8]. But this parameter will have to be consolidated in further studies because of its importance in the model.

4 Sensitivity study of major modeling parameters

The influence on model results of the main parameters was studied. In particular, sensivity studies were carried out on two parameters: the initial particle size and the atmospheric relative humidity.

4.1 Influence of the initial particle size

Two sets of calculations were carried out. One with a version of the model applied to solid NaOH particles (for lower relative humidity RH% < 35 %) and another one with a version applied to NaOH liquid droplets (for high relative humidity RH% > 35 %). Different values of the initial particle radius were studied in the range of sodium fire aerosols sizes between 0.2 and 10 µm.

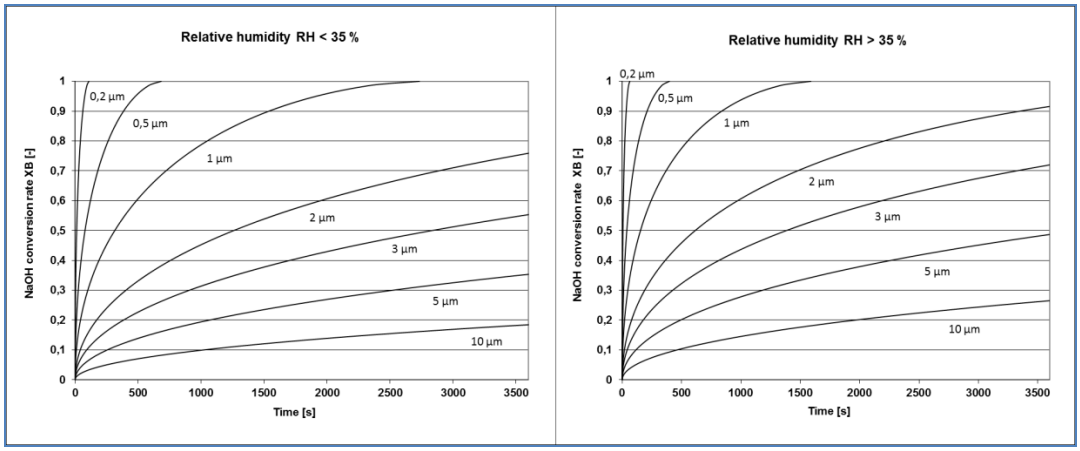

Figure 2: Conversion of NaOH aerosols with different initial radius R_0

This sensitivity study shows that the conversion rate is enhanced in the case of smaller particles, in agreement with Cherdron experimental observations [3]

4.2 Influence of atmosphere relative humidity

Atmosphere humidity has a direct influence on the physical state of NaOH particle and consequently on its density. For different values of relative humidity, the initial radius R_0 of NaOH aerosol was calculated (from equation (1) and for an initial radius of the dry particle R_i = 1 µm). The time required for total carbonation was calculated and represented in Figure 3.

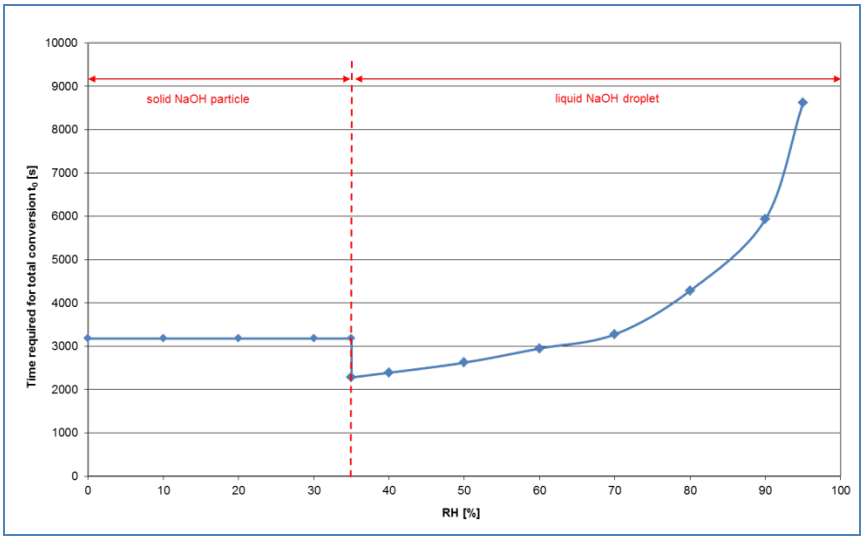

Figure 3: Time required for total carbonation of NaOH aerosols (radius of dry particle R_i = 1 µm)

In the case of liquid NaOH droplet in equilibrium with atmosphere humidity, the phase change of NaOH particle from solid to liquid (and the density decrease) reduces the carbonation time for medium relative humidity (lower than 70%). But with increasing droplet size (at higher relative humidity), the total carbonation time rises up to longer durations.

5 Comparison of modeling calculations with experimental measurement

The kinetic model developed for the carbonation of NaOH aerosols was used for the comparison of modeling calculations with different experimental studies.

A first comparison was carried out with Cherdron et al. study [3] on the behavior of sodium aerosols generated from a pool fire in the FAUNA facility. For coherent calculations with experimental conditions, the initial size of sodium fire aerosols was settled at R_i = 0.5 µm (particle diameters were around 1 µm in the first seconds of the experiment). Three conditions of atmospheric humidity were studied during the experiments: RH ≤ 3%, RH = 20%, RH > 50%. The modeling results presented in Figure 4 show a good coherence with experimental measurements of carbonation conversion rate evolution for the experiments with higher relative humidity. Nevertheless, under very low humidity (RH ≤ 3%), the modeling results are not representative of experimental results: in this case a change of kinetic limitation may occur in favour of a possible chemical limiting step rather than an internal diffusion kinetic control. Moreover the quantitative hydration of sodium oxide aerosols into NaOH is likely to be limited, under very low water partial pressures, as well as the formation of sodium carbonate.

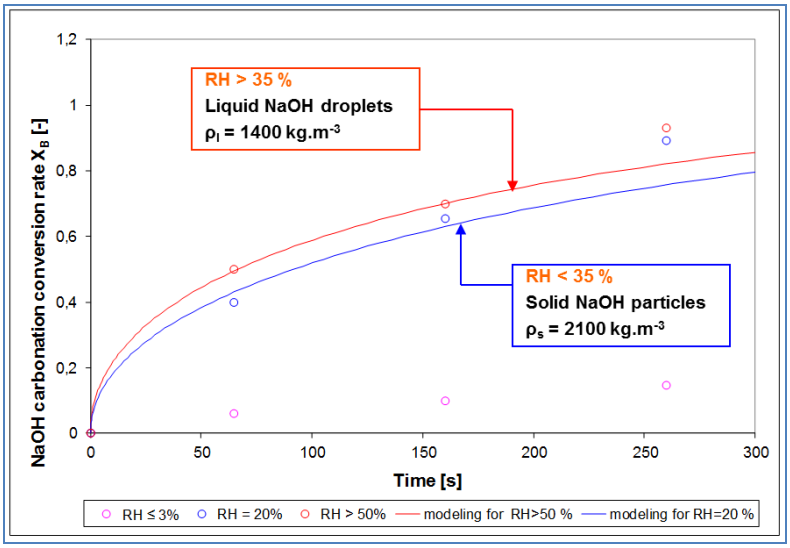

Figure 4: Comparison of modeling results with experimental data from Cherdron [3]

A second comparison was carried out with sodium spray fire experiments performed by Hofmann et al. [9] under two humidity conditions RH = 40% and RH = 70%. The mean aerosol diameters measured in these experiments d_p = 0.20 µm and d_p = 0.35 µm respectively, were directly used as modeling data for the evaluation of NaOH aerosols initial size (R_0).

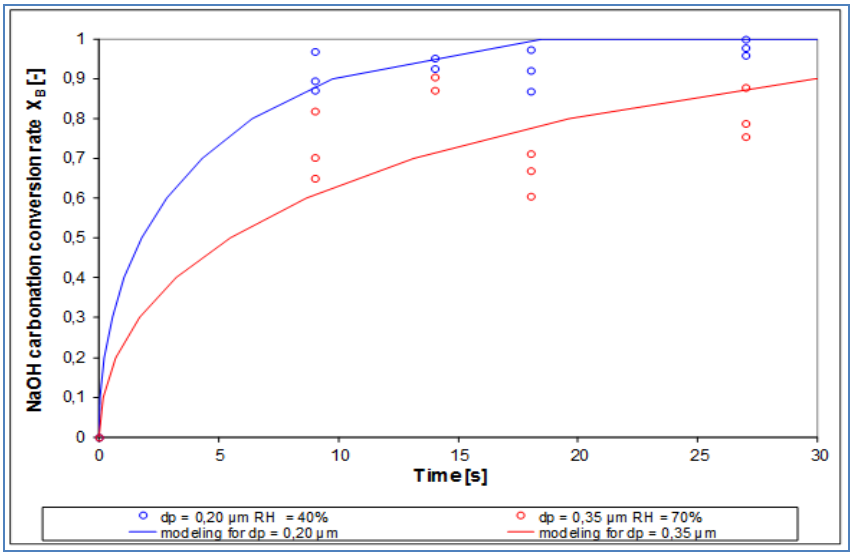

Figure 5: Comparison of modeling results with experimental data from Hofmann et al. [9]

The modeling results presented in Figure 5 show a good correspondence with the order of magnitude of experimental measurements though the particle sizes are especially small in this study.

Another comparison was carried out with more recent experiments performed by Subramanian et al. [10] in the ATF facility. The behavior of aerosols generated from a sodium pool fire was studied under two relative humidity conditions, RH = 50 % and RH = 65 %. An initial size of sodium fire aerosols around R_i = 0.5 µm was considered to be representative of the mean conditions of these experiments (the initial sizes estimated for NaOH droplets are R_0 = 0.61 µm et R_0 = 0.68 µm respectively for the two humidity conditions).

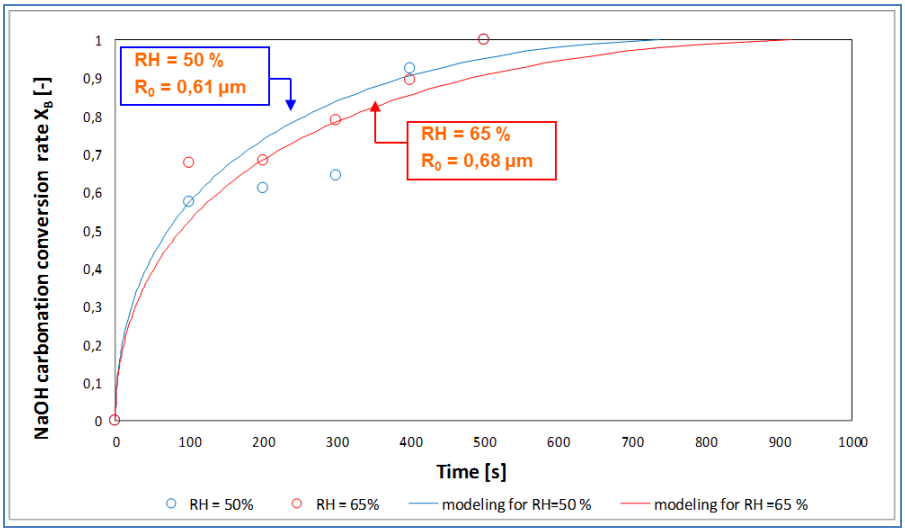

Figure 6: Comparison of modeling results with experimental data from Subramanian et al. [10]

The modeling results presented in Figure 6 show a good agreement with the order of magnitude of these experimental measurements. In a further research program, new sodium fire experiments will be carried out in the IGCAR-ATF facility to study a wider range of relative humidity conditions (from RH = 20 % to 90%) and with a higher sampling frequency at the experiment beginning. Thanks to the diverse measurements techniques instrumenting this facility, a more exhaustive validation of this modeling tool is expected as well as a better comprehension of sodium aerosols behavior.

6 Conclusions

A first version of a kinetic model was developed in order to predict the chemical evolution of sodium fire aerosols during their transport in atmosphere. The development focused on the modeling of NaOH aerosols carbonation with atmospheric CO_2 taking into account the influence of major parameters such as the initial size of aerosols in equilibrium with atmosphere relative humidity, the particle density depending on its hydration level and the corresponding physical state (solid or liquid) of NaOH aerosols.

The “shrinking core model” was used as the base of our study and the selection of modeling correlations was discussed and justified in regards with previous theoretical and experimental studies available in the literature. In a wide range of experimental conditions, the CO_2 diffusion through the Na_2CO_3 product layer surrounding the aerosol particles controls the kinetics of NaOH carbonation. The analysis of non-dimensional criteria was carried out in order to justify the choice of this limiting step for the kinetic model.

An evaluation of this model was carried out by a sensitivity study to main parameters and by a comparison of calculations with experimental data. In particular, the influence of the initial aerosol size and of the atmospheric relative humidity on carbonation kinetics was illustrated. The comparison with experimental measurements performed in several studies showed a good agreement with available data. Nevertheless, a complementary validation is still necessary with a wider range of experimental conditions, and particularly with larger particle sizes (a few micrometers) for which modeling extrapolation may have to be improved.

Moreover, different paths for development can be considered for future improvement of this modeling such as a more precise determination of CO_2 diffusivity in sodium carbonate, or the influence of aerosol particles porosity on material transfer properties and consequently on the carbonation kinetics. Moreover, the behavior of sodium fire aerosols under very low levels of atmosphere humidity has to be studied experimentally and further model development should be carried on to describe this particular condition range.

7 References

1 Y. SOPHY, M. LOUBRIAT, A. BENTZ, A. GEROSA, H. FRESLON, and U. PIATTI, “The ESMERALDA Project for Studying Extensive Sodium Fire,” *Proc. Topl. Mtg. Liquid Metal Fast Breeder Reactor Safety*, Lyon, France (1982)

2 R. K. HILLIARD, J. D. McCORMACK, and A. K. POSTMES, “Aerosol Behavior During Sodium Pool Fires in a Large Vessel CSTF—Tests AB1, AB2,” Hanford Engineering Development Laboratory (June 1979)

3 W. CHERDRON, S. JORDAN, and W. LINDNER, “Sodium Fire Particles—Chemical Transformation and Properties,” *Proc. Conf. Liquid Metal Engineering Technology*, London, United Kingdom, British Nuclear Energy Society (1984)

4 R. BASKARAN, T. S. SELVAKUMARAN, and V. SUBRAMANIAN, “Aerosol Test Facility for Fast Reactor Safety Studies,” *Indian J. Pure Appl. Phys.*, 42, 873 (2004)

5 W.S. CLOUGH, J.A. GARLAND, "The behaviour in the atmosphere of the aerosol from a sodium fire", *UKAEA Report, Atomic Energy Research Establishment, Harwell, AERE-R6460* (1970)

6 D.W. COOPER, "Prediction of the rates of chemical transformation of sodium fire aerosols", *Harvard School of Public Health, Boston, Massachusetts, USA* (1980)

7 W. HINDS, E. MALLOVE, M.W. FIRST, « Density and shape factor of sodium aerosol », Report to U.S. ERDA, Contract No. E(11-1)-2803, Harvard School of Public Health, Boston, MA (April 1977)

8 S.A. RAMSDALE, "The chemical conversion and dispersion of toxic sodium fire aerosols in the atmosphere", *J. Aerosol Sci.* Vol.20 No.8 pp.1401-1404 (1989)

9 CH. HOFMANN, S. JORDAN and W. LINDNER, "Chemical reactions of sodium fire aerosols in the free atmosphere", *The annual conference of the GAF* p.191 (1978)

10 V. SUBRAMANIAN, P. SAHOO, N. MALATHI, R. ANANTHANARAYANAN, R. BASKARAN, B. SAHA, "Studies on chemical speciation of sodium aerosols produced in sodium fire", *Nuclear Technology* Vol.165 pp.257-269 (2009)

11 POHORECKI R., MONIUK W., “Kinetics of reaction between carbon dioxide and hydroxyl ions in aqueous electrolyte solutions”, Chemical Engineering Science, Vol.43, pp.1677-1684 (1988)

Synthesis and characterization of yttria doped ceria powders and pellets with a view to develop oxygen sensors in sodium fast reactor

M. Gabard[a*], B. Tormos[a], L. Brissonneau[a], M. C. Steil[b], J. Fouletier[b]

[a] CEA Cadarache, DEN, DTN/STPA/LIPC Cadarache, F-13108 Saint-Paul-Lez-Durance, France

[b] Laboratoire d'Electrochimie et de Physico-chimie des Matériaux et des Interfaces de Grenoble (LEPMI), UMR 5631 CNRS, Grenoble-INP, Université Joseph Fourier, Université de Savoie, BP 75, F-38402 St Martin d'Hères, France

Abstract. In sodium fast reactors, oxygen must be carefully monitored as the corrosion rate of steel claddings is directly proportional to its content. A specific measuring device for oxygen, as an electrochemical cell with solid electrolytes, can helpfully complete the global monitoring insure by the plugging indicator. Yttria doped thoria is the reference material for the electrolyte, regarding to its electrochemical properties and its compatibility with sodium. Highly pure with small homogeneous size grain and dense sintered materials are required to obtain good mechanical and chemical properties. An improved process for fabrication of yttria doped thoria solid electrolyte has been studied. Yttria doped ceria was first elaborated to develop both preparation and sintering methods. This paper deals with the elaboration and the characterization of yttria doped ceria. The future objectives are to test the electrolyte in sodium.

1. Introduction

In sodium fast reactor (SFR), the measurement of the oxygen activity in liquid sodium is mandatory because this impurity affects the steel cladding corrosion rate. Then a low oxygen content is foreseen (lower than few ppm). Plugging indicator have been currently used in SFR for the monitoring of the oxygen in the primary system, but this device does not specifically respond to oxygen content. An electrochemical cell for measuring oxygen in sodium was proposed first in 1961 by Horsley [1] [2]. These sensors are based on the Nernst's law :

$$E_{EMF} = \Delta E^{0} + \frac{RT}{4F} ln\left(\frac{a_{O_{2réf}}}{a_{O_{2sodium}}}\right)$$

with R, constant of perfect gases (8.315 $J.mol^{-1}.K^{-1}$) ; T, temperature (K) ; F, Faraday constant (96500 $C.mol^{-1}$) and ΔE^{0}, potential in standard conditions. The measured electrical potential, called electromotrice force (E_{emf}), is induced by the difference between the oxygen activity in the sodium ($a_{O_{2sodium}}$) and the one of the reference electrode ($a_{O_{2réf}}$), which is generally set by using a gas with a determined oxygen content (e.g. air) or by an equilibrium between a metal and its oxide. The reference and the sodium are separated by an electrolyte, which properties have a great influence on the sensor quality response, first of them being its passivity against sodium corrosion.

Electrochemical oxygen-meters became commercially available in 1965[3] [4] and have received further developments. Indeed, in the 70s, industrial oxygen meters were elaborated by Westinghouse Electric Corporation (USA, 1968-1978) [3] and by Harwell (UK, 1975-1985, sensors MkIIA and MkIIB). The electrolyte form is a long tube of about 160 mm long which is partially immersed in the sodium (at 450°C). In other programs, the electrolyte is brased to the steel and totally immersed in the sodium. Such sensors were developed by Interatom (Germany, 1981) [5] and by EDF-CEA (France,

1986), which for, the solid electrolyte is a pellet (2.5 mm in thickness and 12 mm in diameter) or General Electric Company (USA, 1974) [6] [7] [8], Harwell (sensors MkIII) [9] and IGCAR more recently (India, 2004) [10] [11] which for the electrolyte is a thimble (about 20 mm long). Brased sensors can be immersed at low depth in the reactor and do not require a dedicated loop.

The electrolyte used in all this investigations consists of ThO_2 doped with 7 to 8 wt % Y_2O_3 (YDT) prepared by co-precipitation method (oxalic co-precipitation for Harwell or EDF-CEA meters) or by powder mixing (Westinghouse). Various sensors with different reference electrodes (e.g. air, Cu/Cu_2O, Sn/SnO_2, In/In_2O_3…) were tested in experimental loops or reactors. The feedback on these sensors is that they often experiment early loss or drift of the signal (in few days, weeks or month, when typical lifetime of more than one year would be required). Failures generally occur at the YDT ceramic/metal braze (seen in Interatom, Harwell MkIII and IGCAR sensors) or/and at the YDT ceramic fracture. In this last case, the main cause is the temperature gradient on the partially immersed long tube (Westinghouse and Harwell MkII). The causes of these failures are generally related to the electrolyte quality. It must be highly pure with small homogeneous grain size (less than one micron) and dense sintered (up to 99 %) to obtain good mechanical and chemical properties .

For the elaboration of electrolyte material, it's known that Harwell and EDF-CEA used oxalic co-precipitation. However, as for Westinghouse sensors, a sintering temperature of 1700-2000°C was necessary to reach the required density. In recent studies, this temperature has been reduced at 1550°C. In these researches [10] [12] [13] [14], the preparation is based on gel formation, using citric acid and ethylene glycol.

A program is developed by the CEA (French Alternative Energies and Atomic Energy Commission) in the framework of ASTRID reactor research program, to develop small, less fragile, oxygen sensors. One way is yttria doped thoria first in pellet form and after thimble form, taking into account the current process technologies. In particular, all elaboration process is reviewed by using low sintering temperature to obtain low grain size (but still high density) and by avoiding milling which can cause problems of pollution. In a first step, yttria doped ceria has been selected as a simulant to handle the most critical aspects of the process. CeO_2 as ThO_2 is an oxide of the fluorite structure. When it is doped with trivalent cations, CeO_2 or ThO_2 become ionic (oxygen) conductors. In a number of studies [15] [16], yttria doped ceria powders were prepared by the co-precipitation method. This material is developed as solid electrolyte for solid oxide fuel cell (SOFC) application.

This paper presents the work realized on yttria doped ceria, to highligth the main steps of the elaboration process and develop the characterization tehnics that will be used for the YDT electrolyte. In this work, $(CeO_2)_{1-x}$ $(YO_{1.5})_x$ (with x between 0 et 15 mol %, last corresponding to 7.5 % Y_2O_3, which generally exhibits the best ionic conductivity) solid solution was prepared by the oxalic co-precipitation technique. In all stages of process elaboration, the powders and the pellets are characterized. Influence of calcination temperature and of the dopant level of $YO_{1.5}$ on final properties as density, final grain sizes, or conductivity are analyzed.

2. Experimental

2.1. Pellets preparation

The yttria doped ceria powder is prepared by the oxalic co-precipitation method from nitrate precursors. The obtained oxalate have low solubility constants : 5.90×10^{-30} for cerium oxalate [17] and 5.34×10^{-29} for yttrium oxalate [18] at zero ionic strength.

$Ce(NO_3)_4$ in solution (Alfa Aesar) and $Y(NO_3)_3.4H_2O$ (99.9 % Sigma Aldrich) are used as precursor materials. First, a cerium and yttrium nitrate solution is added to an oxalic acid solution under ambient temperature. The resulting precipitate is centrifuged, washed with water and ethanol, dried at 90°C and milled in a mortar. Sample numbers and preparation parameters are listed in table 1. Then, the oxalate powder is calcined in air at 500°C or 700°C. The obtained oxide powder (~300 mg) were uniaxially

pressed under 350 or 500 Mpa and the pellets were sintered at 1500 or 1550°C for 8 or 6 hours, respectively in air. The final pellets dimensions are about 2 mm in thickness and 5 mm in diameter.

Table 1. Preparation parameters of different yttria doped ceria samples

Sample number	YDC1	YDC2	YDC3	YDC4
mol % $YO_{1.5}$	0	2	8	15

2.2. Characterization

X-Ray diffraction patterns (Bruker D5000) are obtained using a Cu Kα radiation in the 6-90° 2θ range. The crystallite size, t_{XRD}, is estimated by the Sherrer equation [19]. Density of the pellets, before sintering, the green density GD, is calculated by geometrical dimensions. The density after sintering is determined by geometrical dimensions, d_{GEO}, and by Archimedes (in ethanol) method, d_{ARC}.

The microstructure of the pellets are observed by Scanning Electron Microscopy (SEM) (Cambridge Stereoscan-360) in direct view or after polishing, and elementary analysis is simultaneously performed by Energy Dispersive Spectroscopy (EDS, Oxford Si-Li 7060 detector).

3. Results and discussion

Figure 1 shows the X-ray diffraction patterns of the powder YDC3 obtained after precipitation (oxalate) and figure 2 the powder YDC3 after calcination at 500°C and at 700°C. The behavior for the other samples is similare.

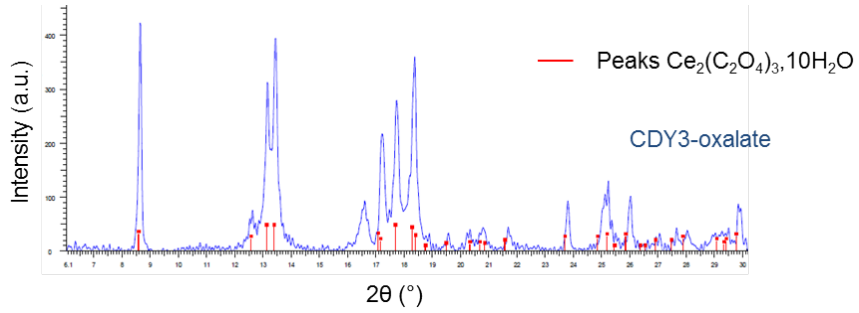

FIG. 1. X-ray diffraction patterns for oxalate powder YDC3.

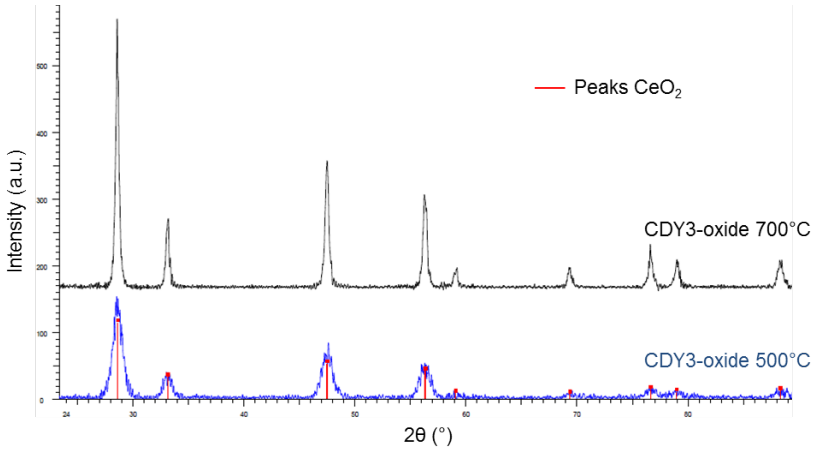

FIG. 2. X-ray diffraction patterns for oxide powder YDC3.

The presence of one phase in the X-ray diffraction patterns of oxide suggest that the solid solution is well formed. Similar results were obtained in previous study [15], this is clearly an advantage of the co-precipitation process, when no milling nor high calcination temperature are required to obtain intimate mixing of yttria and ceria.

Influence of pressing pressure

Sample YDC3 is pressed at 350 MPa and at 500 MPa. Results before and after sintering at 1550°C during 6 hours are shown in table 2.

Table 2. Green and sintered densities for YDC3 sample at the two pressures

Pressure	GD ($g.cm^{-3}$)	d_{GEO} ($g.cm^{-3}$)
350 MPa	3.73 ± 0.07	6.48 ± 0.08
500 MPa	3.72 ± 0.09	6.52 ± 0.01

About the same sintered densities are obtained for the two pressures. Nevertheless, 500 MPa is the chosen pressure for all the pellets preparation, because of a best mechanical strength of the green pellets.

Influence of calcination temperature

The diffraction peaks become sharper after calcination at 700°C, indicating an increase of the crystallite size. These sizes and the obtained densities after sintering at 1500°C during 8 hours are listed in table 3.

Table 3. Sample YDC3

Calcination temperature	t_{XRD} (nm)	GD ($g.cm^{-3}$)	d_{GEO} ($g.cm^{-3}$)	d_{ARC} ($g.cm^{-3}$)
500°C	9	3.5 ± 0.3	6.5 ± 0.2	6.86 ± 0.02
700°C	41	4.3 ± 0.2	6.6 ± 0.3	6.97 ± 0.03

The powder calcined at 700°C produced just a little denser YDC pellet.

The grain size of YDC3 sintered pellets (1500°C for 8 hours) exhibits a broad distribution, from 0,1 to 3 µm and from 0,1 to 6,5 µm for calcination temperature of 500 and 700°C respectively. Nevertheless, we can notice a little increase with temperature.

Influence of the concentration of $YO_{1.5}$

The crystallite sizes determined from XRD are respectively 12 nm, 11 nm, 9 nm and 8 nm for YDC1, YDC2, YDC3 and YDC4 after calcination at 500°C during 6 hours. So, the values decrease with the percentage of $YO_{1,5}$.

Elementary analysis by EDS are made on sintered pellets containing a theoretical 8 molar % of $YO_{1.5}$ (from initial quantity) after coating and polishing. The results are shown in figure 3.

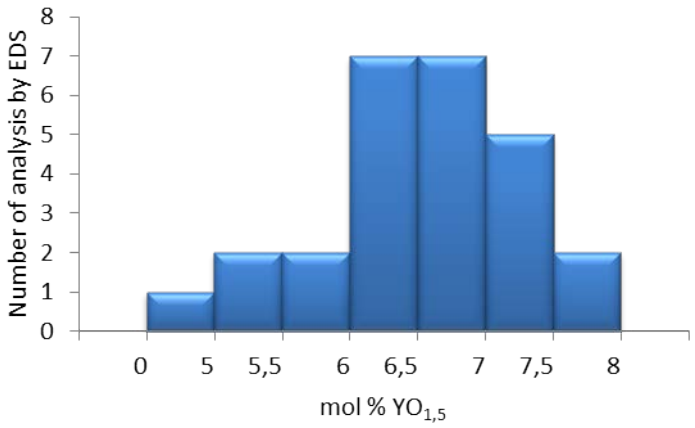

FIG. 3. Repartition of molar % $YO_{1.5}$ calculated by EDS analysis.

In pellets, the experimental percentage of $YO_{1.5}$ is 6.5 ± 1.5. So, precipitation of $YO_{1.5}$ is not quantitative, nor perfectly homogeneous.

Figure 4 shows the evolution of the densities with the foreseen molar percentage of $YO_{1.5}$ after calcination at 500°C during 6 hours and sintering at 1500°C during 8 hours.

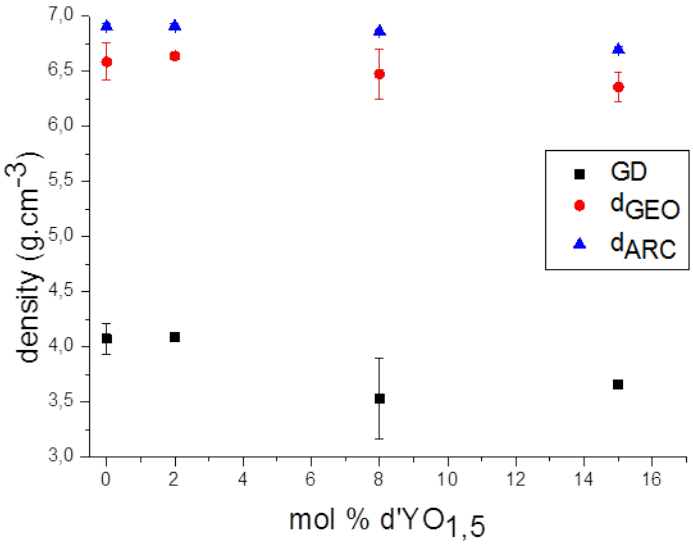

FIG. 4. Evolution of densities for different molar percentages of $YO_{1,5}$.

The densities values of compacts have a little decrease due to yttrium addition. So, the $YO_{1.5}$ content has no effect on the final densities. This result corroborates literature data [16].

SEM micrographs of pellets YDC2 and YDC3 after calcination at 500°C and sintering at 1550°C during 6 hours are presented on figure 5. The average equivalent particle diameters determined by image analysis on surface and in the bulk of the pellets are written on SEM micrographs.

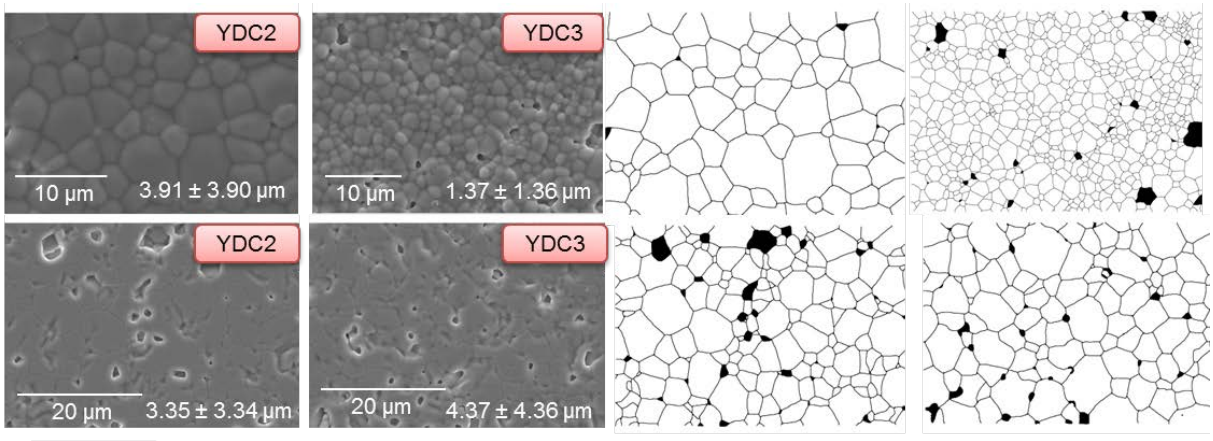

FIG. 5. SEM micrographs of pellets sintering at 1550°C for 6 hours at the surface (top) in the bulk (below).

Average grain size is about 4 µm (except for YDC3 on surface), however, the distribution is heterogeneous, as shown in figure 5. For YDC2, grains have similar average sizes at the surface or in the bulk. However, it's not the same for YDC3. Indeed, grains at surface are smaller (~1 µm) than in the bulk (~4 µm).

4. Conclusion

To obtain reliable oxygen sensors for sodium fast reactors, a fine grains dense electrolyte is needed. Obtaining a dense doped ceria ceramic by conventional solid techniques is difficult at sintering temperatures below 1650°C in air. Using chemical methods as co-precipitation and sol-gel allows to reduce this temperature. It is the case of the process presented in this paper. This process is based on the oxalic co-precipitation method and leads to the production of nanocrystalline (~10 nm) powders after calcination at 500°C. The calcination temperature (500 or 700°C) seems to have little effect on the final density. Dense pellets with average grain sizes of 4 µm are obtained after sintering at 1550°C. However, a difference between surface and bulk density is observed in some cases. Concerning the percentage of $YO_{1.5}$, it seems to have no influence on final densities of the samples sintered at 1500°C. All steps of this process to obtain dense materials are mastered and can be applied to yttria doped thoria ceramic.

AUTHOR INFORMATION

Corresponding Author

*E-mail : marie.gabard@cea.fr ; Phone : +33 4 42 25 20 78 ; Fax : +33 4 42 25 72 87

REFERENCES

[1] HORSLEY, G.W. A possible galvanic cell method for monitoring the activity of oxygen in a hot-trapped sodium coolant circuit, UKAEA Report AERE-R-3037 (1961).
[2] BORGSTEDT, H.U., MATHEWS C.K., Applied Chemistry of the alkali metals.
[3] MCKEE, J.M., et al., Calibration stability of oxygen meters for LMFBR sodium systems, Nuclear Technology 21 (1974).

[4] KOLODNEY, M., et al., Continuous Oxygen Monitor For Liquid Metals, United States Patent Office 3481855 (1969).
[5] HAUBOLD, W., et al., Monitoring and control of impurities in sodium systems.
[6] ROY, P., BUGBEE, B.E., Electrochemical oxygen sensor for measurement of oxygen in liquid sodium, Nuclear Technology 39 (1978).
[7] LICINA, G.J., et al., Continuous monitoring of oxygen activity in liquid sodium with an electrochemical oxygen sensor.
[8] ROY, P., LICINA, G.J., Dispositif électrochimique pour la mesure de la concentration en oxygène d'un métal alcalin en fusion (1975).
[9] TAYLOR, R.G., THOMPSON, R., The Harwell MkIII electrochemical oxygen sensor - testing and performance in liquid sodium, AERE R 12177 (1987).
[10] GANESAN, R., et al., Novel approach for the bulk synthesis of nanocrystalline yttria doped thoria powders via polymeric precursor routes, Journal of Nuclear Materials 325 (2004).
[11] GANESAN, R., et al., Development of Sensors for On-Line Monitoring of Nonmetallic Impurities in Liquid Sodium, Journal of Nuclear Science and Technology 48 (2011).
[12] ARUL ANTONY, S., et al., Preparation of 15 mol% YO1,5-doped ThO2 disk electrolytes by a polymeric gel-combustion method, Journal of Nuclear Materials 295 (2001).
[13] CONSENTINO, I.C., MUCCILLO, R., Powder synthesis and sintering of high density thoria-yttria ceramics, Journal of Nuclear Materials 304 (2002).
[14] CONSENTINO, I.C., MUCCILLO, R., Properties of thoria-yttria solid electrolytes prepared by the citrate technique, Materials Letters 32 (1997).
[15] TADOKORO, S.K., et al., Synthesis, sintering and impedance spectroscopy of 8 mol% yttria-doped ceria solid electrolyte, Journal of Power Sources 130 (2004).
[16] VAN HERLE, J., et al., Sintering Behaviour and Ionic Conductivity of Yttria-Doped Ceria, Journal of the European Ceramic Society 16 (1996).
[17] CHUNG, D.Y., et al., Precipitation Equilibrium of Cerium Oxalate in Nitric Acid and Oxalic Acid Media, J. of Korean Ind. and Eng. Chemistry 6 (1995).
[18] FEIBUSH, A.M., et al., Solubility of Yttrium Oxalate, Analytical Chemistry 30 (1958).
[19] DEGALLAIX, S., ILSCHNER, B., Caractérisation expérimentale des matériaux : propriétés physiques, thermiques et mécaniques, Traité des Matériaux : Tome 2 (2007).

R&D and Design Studies for the ASTRID Core-Catcher

F. SERRE, P. ALLEGRE, F. BERTRAND, C. JOURNEAU, J-C ROBIN, C. SUTEAU

CEA Cadarache -CEA/DEN/CAD/DER
Blg 212, 13108 St Paul lez Durance - FRANCE
frederic.serre@cea.fr,

J. CHAMPIGNY, C. VIALA
AREVA
10, rue Juliette Récamier F-69456 Lyon CEDEX 06

Abstract

The reinforcement of safety requirements for new sodium fast reactors leads to take into account whole core melting situations during the reactor design phase. In order to mitigate the consequences of a hypothetical core melting in ASTRID, a core-catcher will be implemented.
Its main requirements are to fit the whole material core-inventory, to insure the sub-criticality and cooling of the corium during the accidental and post-accidental phases.
Two options of core-catcher designs are studied: one implemented in the primary vessel ('in-vessel'), one located outside the primary vessel ('ex-vessel').
To support the core-catcher development, a large R&D program is underway regarding the molten core progression (characteristics of the corium arriving on the core-catcher), protective materials to limit the thermo-mechanical loads of the core-catcher, corium behavior and cooling on the core-catcher – all being supported by experimental programs.

1. INTRODUCTION AND CONTEXT

The ASTRID reactor (Advanced Sodium Technological Reactor for Industrial Demonstration) [1] developed by the CEA with its industrial partners, will be used for demonstration of the safety and operability, at the industrial scale, of sodium fast reactors of the 4th generation [2]. Among the goals fixed to ASTRID, one is to improve the safety and the reliability of such reactor (compared to previous built sodium-cooled fast reactors), and to lower the likehood and degree of reactor core damage. The WENRA (Western European Nuclear Regulators Association), in line with the continuous improvement of nuclear safety, proposes to extend, at the design stage of new reactor, 'the design beyond traditional design basis, in the area of core melt prevention and mitigation'; this means that severe accident sequences have to be considered as a fourth level of defense in depth. It is specified that for accident with core melt, 'design provisions have to be taken so that only limited protective measures in area and time are needed for the public' [3].
In the ASTRID project, the safety objectives are to prevent the core melting in particular by the development of an innovative core, and to enhance the reactor resistance to severe accident by design. To mitigate the consequences of hypothetical core melting situations, specific dispositions or mitigation devices will be added to the core and to the reactor.
The strategy is to study natural (inherent) behaviors of the core and of the reactor under severe accident conditions, and to add mitigation dispositions if necessary to meet acceptable consequences for the public.
A new safety approach is proposed for ASTRID: the mitigation devices will be designed with the best efficiency achievable at acceptable cost, and it will be verified that situations which could lead to loadings higher than the design capabilities might be eliminated.
At the beginning of the ASTRID project, it was decided that a core catcher will have to be implemented in order to mitigate the consequences of severe accidents, by ensuring the confinement of the radionuclides by the protection of the containment structures.
In the ASTRID organization led by CEA, the core catcher as well as the decay heat removal and cooling systems are designed by AREVA NP which is the industrial partner in charge of the nuclear island design. The CEA is carrying out, in support of AREVA NP, specific R&D for the core catcher development, and is in charge of the severe accident studies (it must be pointed out that the CEA is also responsible of the core design).

In this paper, the work related to the development of the core catcher, performed by CEA and AREVA NP during the ASTRID pre-conceptual design phase (2010-2012), will be presented.

2. EXISTING DESIGNS of CORE CATCHERS

For first Sodium Fast Reactors (such as Phenix in France [4]), under severe accident conditions it was expected to have a limited corium propagation due to the various structures existing in the lower part of the core and the reactor (lower axial fertile blankets, core supporting structures).
However, the safety demonstrations were rather limited, so for the next generation of SFRs, some systems were proposed to catch the corium and to insure its cooling. The core catcher was located either inside the primary vessel of the reactor (in-vessel core catcher), or outside the reactor vessel (ex-vessel core catcher).

In-vessel core catcher

For Superphénix reactor, the core catcher was located below the diagrid and the core supporting structure, inside the main vessel [5]. It is composed of double annular steel plates with a chimney at its center. The first plate acts as a thermal shield. The cooling of the debris tray is ensured by sodium natural convection flow through the chimney up to the decay heat removal systems implemented in the hot pool (RUR).

In the EFR project, a whole core meltdown accident was taken into account; an in-vessel core catcher was implemented able to ensure the subcriticality of the corium, and its coolability by sodium natural convection flow. The core catcher was derived from the Superphénix one (with a larger capacity). It must be point out that, contrary to studies performed for Superphénix, the formation of a molten pool on the core catcher was expected.

Other reactors as BN-800 [6], CDFR, DFR [7], PFBR [8], or new reactor projects as JSFR [9] and CFBR [10] have in-vessel core catcher. They will be not described here.

Ex-Vessel core catcher

The SNR-300 reactor [11] was equipped with a double containment. A ‘retention pond of mobile core material with distribution device’ was located outside the reactor vessel and the guard vessel, and inside the inner containment. This core catcher had the capability to fit the whole core inventory, was designed to avoid any critical situation (using the ‘distribution device’), and had a thermal insulation made of depleted uranium bricks. Its bottom was cooled by a NaK cooling system, with a Nitrogen back-up system. The sodium from the primary circuit was collected in a ‘sodium retention pond’. The temperature of the concrete inner containment was controlled by a thermal insulation and a Nitrogen cooling system.

3. The ASTRID CORE CATCHER SPECIFICATIONS

3.1 Functional Specifications

The main specifications of the core catcher and the associated systems of the ASTRID reactor are:
- to collect the whole core inventory in case of an hypothetical core melting sequence, the corium being formed by solid debris or molten materials,
- to maintain this corium in a sub-critical state,
- to evacuate the corium residual power and guaranty its coolability on the long term.

So, the core catcher will guaranty that the containment will not be jeopardized by the melt progression in order to avoid any ground or atmosphere contamination.
Also, its periodic controls, and possible maintenance work have to be taken into account. Its recycling with minimization of the waste, during the dismantling phase of the reactor, is also to be considered.
Last, but not the least, the core catcher cost must be acceptable.
One reminds that the core catcher must:

- be designed in order to sustain the mechanical energy potentially released during a severe accident,
- be designed to resist to any operating conditions and hazards (e.g., earthquake),
- be chemically compatible with its environment (especially with Na),
- and not disturb the normal operation of the reactor.

3.2 Work Hypothesis for the preconception design of the ASTRID core catcher

In order to design the ASTRID core catcher, at the level of the pre-conceptual design phase, some hypotheses have to be taken. Some of these hypotheses are based on simplified calculations, on knowledge drawn from the existing experimental data base, or on some expert judgments; furthermore, some reactor options are not frozen yet, so additional hypothesis have to be made.
It is recalled that, the objectives of the core catcher pre-conceptual design studies are to evaluate the feasibility of different options, the need of further R&D, their cost and schedule. Based on these studies, the core catcher design for ASTRID will be chosen.

According to the safety approach defined for ASTRID, the core catcher design will not be adjusted on a reference scenario of a core melting sequence. It must fulfill its requirements for various initial states of core degradation, whatever is the initiator of the accident.
For the pre-conceptual design, it is supposed that during the secondary phase of the accident a molten pool was formed in the core region, delimited by a solid crust. It is supposed that the reactor decay heat removal systems are available and the core is subcritical (if necessary by adding neutronic absorbents). The molten pool is supposed not reaching the boiling temperature and not pressurized: its temperature is supposed to be fuel melting temperature (2850°C).
It is then supposed that the corium propagates either axially through mitigation devices such as corium ducts, either radially in the core; in this latest situation, at the periphery of the core, by design or with dedicated devices, the corium should flow down toward the bottom part of the vessel (i.e., on the core catcher in case of in-vessel option).
It is supposed that the iron content of the corium and its temperature depends on the melt progression path. It is then supposed that the length between the outlet of the corium duct and the core catcher is such that a jet of corium may impinge the core catcher. This hypothesis leads to require protecting the core catcher with sacrificial materials. Therefore, the mixing of the core materials with sacrificial materials has to be taken into account.

For the design of the core catcher, it is supposed that the ASTRID core is the low sodium worth core named CFV core [12]. The mass of corium is in the range of 350-370t, leading to around 60m^3 of debris.

4. CORE-CATCHER DESIGN OPTIONS

Two main options of core catchers have been studied in the frame of the ASTRID pre-conceptual design phase. They are defined by their location in the reactor either at the bottom of the main vessel where is localized the reactor core, or outside the main vessel under it. These two types of options are respectively called “in-vessel” or “ex-vessel” core catchers. These designations are consistent with the design concepts of previous reactor projects as presented in section 2 above.
As a general description, the core catcher is made of metallic structures composed of a debris tray which receives the melting core and of a support structure. As presented previously, the debris tray must be covered by one or more material layers of various natures to protect the structure and spread the corium for limiting thermal loading (transient and steady states thermal loads) and achieving subcriticality. The constitutive materials and protection materials have to be selected to be compatible with the environment in normal operation but also in post-accidental conditions (sodium, gas, and corium).
The size of the core catcher should allow to sufficiently spread the corium and the core debris.
The core catcher design studies performed during the pre-conceptual design phase allowed bringing to light the main issues of both options. The present section will propose to set out key features of the different concepts and the current status of studies performed on each type.

4.1 In-vessel core catcher

The in-vessel (or internal) core catcher studied for ASTRID is located into the cold plenum, under the core and its support structure (see Fig. 1). It protects the main vessel boundary in severe accident (even though the main vessel leak-tightness can be lost due to Core Disruptive Accident – CDA). This option is well adapted to a pool type reactor as the primary vessel is larger than in a loop type design concept. It offers the possibility to implement a core catcher with a significant corium spreading area under the core.
The debris-tray is welded to its support structure and both are designed to contribute to sodium natural convection in post-accident conditions and should not impact the forced convection in normal and

accident operating conditions (e.g. support structure made of openwork stiffeners). A central chimney protected by a 'hat' favors also the sodium convection around the structure for its cooling. The tray is inclined so as to prevent the sodium steam bubbles for stagnating and also favor natural convection.
Due to its location in main vessel, the structure is permanently immersed in sodium which implies materials compatible with sodium over at least 60 years lifetime. The core catcher is designed to accommodate a sufficient thickness of protection materials; in this way, a large spectrum of corium jet impinging the core catcher is taken into account.
For ASTRID, the decay heat removal is ensured by decay heat removal systems in vessel. These systems in vessel have to be available after the severe accident. An additional system outside the main vessel is investigated for mitigation of possible failures of in-vessel systems. Sodium natural convection around the core catcher allows decay heat transfer to the heat sink, and ensures also the structure cool down. Preliminary thermo-hydraulic studies have been performed and show that natural convection takes place around the core catcher and within the whole primary circuit. In parallel thermal studies estimated decay heat removal performance to reach acceptable temperature in the tray and support structure taking into account the mixing of the corium with sacrificial materials.

4.2 Ex-vessel core catcher

The ex-vessel core catcher is an alternative solution to the in-vessel one which has also been examined for ASTRID. The location of the core catcher behind the main vessel depends on the reactor pit layout. It can be set up just behind the main vessel, between the main vessel and the safety-vessel (inter-vessel core catcher – innovative concept) or behind the safety vessel in the reactor pit (external core catcher). Fig. 1 below shows the different options of core catchers investigated in ASTRID and both solutions of ex-vessel core catcher (inter-vessel type) depending on cooling mode.

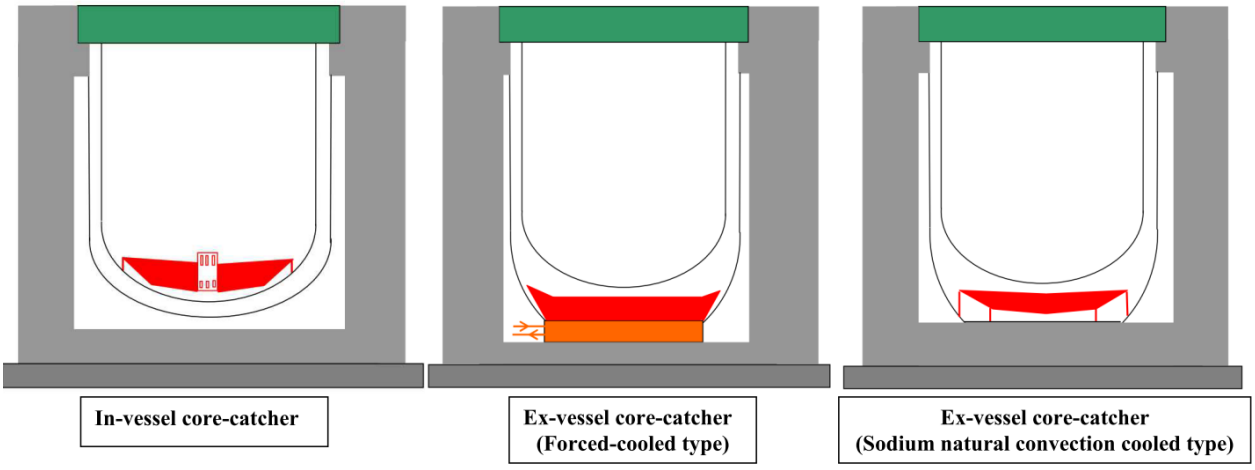

FIGURE 1: Options of core catcher depending on its location and cooling type

Due to its location, the ex-vessel core-catcher may offer a larger area for corium catching and more space for material protection. This concept eliminates drawbacks associated to long time residence in sodium. The implementation of material is less complex (possible inert atmosphere instead of sodium) and may offer a larger selection of materials than for in-vessel type. The dimensions of the core catcher should however be defined in order to minimize impact on the reactor building.
To manage thermal transients during post-accidental situation, two ways have been investigated for ex-vessel core catcher: cooling insured by sodium natural convection around the structure, or direct cooling through a dedicated system (forced cooling).
The first solution is based on the same passive cooling approach as for in-vessel core-catcher: sodium natural convection around the structure. This inter-vessel core catcher concept with layers of sacrificial materials led to a CEA patent [13]. Preliminary mechanical and thermal studies have been carried out on such concept; in particular one shows that, the sodium levels in the primary and safety vessels after the primary vessel failure are sufficient to avoid the core uncovery and for achieving the coolability of the corium located on the core catcher.

In the forced-cooled type the dedicated cooling system is designed to evacuate the bottom heat flux due to corium presence on the tray. It is integrated in the support structure of the debris-tray and constitutes a massive disk covered by protection material layers. Preliminary sizing of such a system has been performed with thermal calculations to estimate the temperature range in the structure of the core catcher during post-accidental conditions. Results show satisfactory values.
As for in-vessel core-catcher, the decay heat removal is ensured by DHR systems within and outside the main vessel.
Further studies in the conceptual design phase should concentrate on support structures of such core catcher concepts under seismic loads.

4.3 Foreseen studies and choice of the core catcher options

In summary, different concepts of core catchers are still under investigation and selection process is still underway. All concepts require further design studies together with specific R&D actions to confirm assumptions taken at this stage of the design.

5. EXPERIMENTAL PROGRAMS for the CORE CATCHER DEVELOPMENT and QUALIFICATION

Although a large experimental database exists from the times of Superphénix related R&D, experimental programs have been launched in support of the development of ASTRID core catcher in order to answer new issues as the selection and characterization of sacrificial materials that will be installed on the core-catcher tray. A thermal hydraulic experimental program is to be performed to assess the heat transfers to the core-catcher (debris bed or molten pool) and from the corium to the decay heat removal system. Finally, experimental programs are needed to determine the initial condition of the corium arriving on the core catcher.
The first experiments related to ASTRID core catcher have been conducted in the VITI facility of the PLINIUS platform [14] and were dedicated at the study of mixing of UO_2 with candidate sacrificial materials [15]. Powders of UO_2 and of materials as B_4C, Al_2O_3, HfO_2, Hf, Eu_2O_3 have been mixed and heated up to melting (FIG. 2). Results from these experiments serve to improve our knowledge on molten core-sacrificial material chemical thermodynamics. A corrosion experimental program has been launched at the CORRONA facility [16]. It started with an analysis of the corrosion of alumina. Further studies will be dedicated to the compatibility of candidate ceramic materials with sodium.

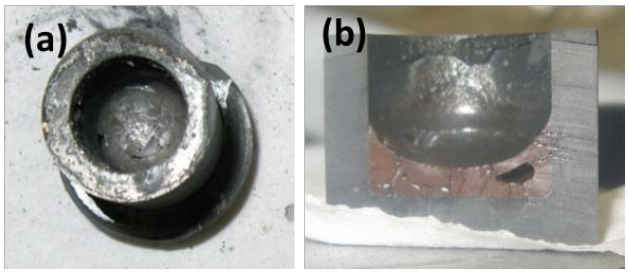

FIG. 2: Crucible with 52 wt% Al_2O_3- 48% UO_2 molten in the VITI facility

There exists a large experimental database on debris cooling (e.g. [17-19]). The convective heat transfer in a molten pool still requires some experimental data, especially in case of dissolution of a sacrificial material layer. Simulant material experiments shall be built to analyze with low temperature simulant the heat fluxes during transient thermal dissolution, and to evaluate heat flux distributions in stratified configurations. For this last issue, it is planned to adapt the CLARA facility currently used for LWR severe accident studies [20]. These simulant material tests shall complement experiments with prototypic (UO_2-containing) material in the VULCANO facility [21]. In these tests, 30-40 kg of molten material will interact, with decay heat simulated by induction, with sacrificial materials. Larger scale integral tests are planned in the future FOURNAISE facility [22]. Knowing the heat fluxes at the core-catcher boundaries, experiments will be necessary to validate the proper natural convection heat transfer from the core catcher to the decay heat removal systems. The PATH experiment [23] at IGCAR can be adapted to ASTRID geometry and used if the in-vessel core catcher is selected. Another facility may be needed for ex-vessel core catcher.

Finally, an experimental program is also planned to study the arrival of corium in the core catcher, which will provide initial conditions to the post accidental phase and assess the risk of sacrificial ablation by a corium jet. Corium jet experiment shall be conducted as it has been demonstrated that different fragmentation behaviors are observed with aluminum oxide, the classical simulant of corium [24]. Currently, a fuel coolant interaction experimental program, SOFI, is starting at IGCAR [25] and first exchanges with CEA took place in the frame of a CEA-IGCAR collaboration agreement. Nevertheless larger scale tests would be needed in the to-be-built FOURNAISE facility. Finally, some configurations including the operation of Corium Discharge Channel will require out-of pile tests in FOURNAISE and possibly complementary in-pile tests to EAGLE1&2 programs [26], conducted in the Kazakhstani Impulse Graphite Reactor for JAEA.

6. CODE DEVELOPMENT for the CORE CATCHER DESIGN

Simulation of severe accident scenarios of sodium-cooled fast neutron reactors (SFRs) is a complex issue because it involves subsequently or simultaneously various and numerous phenomena. To do so, CEA is developing and validating a reference set of codes [27]. Its objective is to permit best-estimate calculations of all the phenomena involved in any scenario. The reference set includes existing codes, adaptation of existing codes and new developments. The simulation of corium behavior on the core catcher is part of the issues that the reference set must address.

Mitigation devices located in the core, such as Corium Discharge Channels, produce corium jets moving downwards. Depending on the conditions of corium progression towards the core catcher, corium forms a molten pool or a debris bed. If, during the corium progression, corium-sodium interaction is not highly energetic, SIMMER-III [28] and SIMMER-IV [29] codes have the capabilities for simulating the corium spreading on the core catcher.

If energetic corium sodium interaction occurs, a code dedicated to Fuel Coolant Interaction (FCI) must be used. There is no up-to-date FCI code dedicated to sodium coolant available. FCI codes couple jet fragmentation model and models of heat exchange between fragments and coolant. CEA plans to implement specific sodium models into existing FCI codes dedicated to light water reactors. Hence, the future adapted code benefits from existing jet fragmentation model. The future adapted code will be validated on existing experimental results such as FARO-THERMOS [30], CORECT II [31], MFTF-B05, or MFTF-B06 [32]. A review of existing experimental data shows that experiments with larger mass of corium and sodium are needed. To complement the existing experimental database, CEA will use the FOURNAISE facility.

If the corium jets have important fragmentation during the corium progression, corium forms a debris bed on the core catcher. The coolability of the debris bed depends on the fragment size, the porosity and the layers thickness. In the past, CEA simulated debris bed cooling with LIDEB code that is no longer maintained. CEA will make a review about debris bed cooling in order to choose a simulation strategy.

On the core catcher, the corium jets may form corium pools that ablate the sacrificial material layer. Codes simulating this ablation do not exist but the phenomenon has similarities with concrete ablation by corium simulated by molten corium concrete interaction codes such as TOLBIAC-ICB [33]. TOLBIAC-ICB is based on the phase segregation model where the corium is modeled by three liquid phases (liquid oxide phase, liquid metallic phase and the gaseous phase) and where the solid phase is located at the corium pool boundaries as a solid crust composed of refractory oxides. In the model, corium pool contains no solid. Under the hypothesis of homogeneity, the corium pool is described by a punctual model (zero dimension). The interfacial temperature between the crust and the pool is at the liquidus temperature calculated with the composition of the pool. The interaction between thermal hydraulics (mass and energy balances) and physical chemistry (liquidus temperature, crust composition, chemical reaction) is modeled through a coupling between TOLBIAC-ICB and GEMINI2 [34].The CEA is adapting TOLBIAC-ICB to the SFR core catcher. Due to the specific geometry and location of SFR core catchers, the geometry capabilities of TOLBIAC-ICB must be improved. The second adaptation is the addition of sacrificial material physical characteristics (density, thermal conductivity…) in TOLBIAC and phase diagram in the GEMINI2 database. For SFR core catcher, corium pools are not boiling (no gaseous phase) if spreading is sufficient, and have an axial temperature distribution. So, the 0D discretization of the pool must be replaced by an axial 1D discretization. Finally, the heat exchange between the pool and the crust must be adapted to non-boiling pool and the core catcher geometries.

The assessment of this adapted version, TOLBIAC-SFR, needs experimental data that does not exist yet. A program dedicated to core catcher sacrificial material interaction with corium will be performed in VULCANO and FOURNAISE as described in section 5.

8. CONCLUSIONS

Severe accident situations with whole core melting sequences are taken into account in the ASTRID design since the pre-conceptual design phase. In particular first studies of core catcher design have been performed. The objectives of these studies are to evaluate the feasibility of different options and the need of further R&D.

A review of core catcher characteristics and designs in existing, or under project, Sodium Fast Reactors has been carried out. As well the functional specifications of the ASTRID core catcher have been given, with in particular the objective to guaranty the safety of the reactor during the different phases of the hypothetic whole core melting sequences (including the long term phase). It must be pointed out that the core catcher must fit the whole core-inventory and in this condition, insure the sub-criticality of the fissile material lying on its tray and its coolability.

Derived from the core-catcher review and the ASTRID core catcher functional specifications, two main options of core catcher designs (in-vessel or ex-vessel types), have been studied during the ASTRID pre-conceptual phase design. The objectives of these options studies are to show their feasibility and to define the R&D needs for the next design step.

In parallel to the core-catcher design studies, an experimental program has been launched for selecting the sacrificial materials which will be used to protect the ASTRID core catcher (devoted to the studies of the mixture of UO_2 and the candidate materials, and of the behavior of those materials in Sodium environment)

Complementary experimental programs with simulant materials or with prototypic UO_2, at small or large scales are foreseen to study the interaction between the corium and the sacrificial materials, the thermal behavior of the molten pool made of mixed materials, and the cooling of the core catcher.

As well, a review of existing codes to calculate phenomena taking place on or around the core catcher, necessary for its design, is under way. Already some needs for model developments or adaptations have been pointed-out (Fuel Coolant Interactions, corium-sacrificial materials interactions); also the existing experimental data-base to assess the models has been review, and the needs for its extension have to be defined.

ACKNOWLEDMENTS

Many people are involved in this vast program and it was not possible to put all of them as co-authors. Nevertheless authors would like to thanks them.

REFERENCES

[1] P. LE COZ, et al., “Sodium-Cooled Fast Reactors: the ASTRID Plant Project” – Proceedings of ICAPP 2011, Nice, France, May 2-5, 2011

[2] US DOE Nuclear Energy Research Advisory Committee (2002). *A Technology Roadmap for Generation IV Nuclear Energy Systems*, Dec. 2002

[3] : WENRA Reactor Harmonisation Working Group, ‘Safety Objectives for New Power Reactors’, Dec. 1 2009

[4]: L. MARTIN et al., “Phénix: 35 Years’ Operation 1974-2009’, Revue Générale Nucléaire, Année 2009, N°1

[5] C. LE RIGOLEUR et al., “The Internal Core Catcher in Super Phenix 1”, Actes de la Conférence de Lyon, Proceedings of the LMFBR Safety Topical Meeting, 19 –23/07/1982

[6]: G.N. VLASICHEV, N.G. KUZAVKOV, “Computational Analysis of Heat Removal from the Core Melt Catcher in BN-800 Vessel in the Case of a Serious Unanticipated Accident”, Atomic Energy, vol. 92, n°2, 100-108, 2002

[7] S.C. CHETAL et al., “The design of the Prototype Fast Breeder Reactor”, Nuclear Engineering and Design 236 (2006) 852–860

[8]:D. BROADLEY et al. “The Evolution and Validation of Internal Core Debris Retention in the UK LMFR’S.” – Proceeding of the LMFFBR Safety Topical meeting, Vol. 3, July 19-23, Lyon, 1982.

[9] : KAZUYA KOYAMA et al., "Development of Severe Accident Evaluation Technology (Level 2 PSA) for Sodium cooled Fast Reactors (4) Identification of Dominant Factors in Core Material Relocation and Heat Removal Phases", Paper 9126, Proceedings of ICAPP '09, Tokyo, Japan, May 10-14, 2009
[10]: P. CHELLAPANDI, "Development of Innovative Reactor Assembly Components towards Commercialization of Future FBRs", Asian Nuclear Prospects 2010
[11] : GRS, "Risk-Oriented Analysis of the SNR-300", GRS-56', April 1984
[12] F.VARAINE et al., "Pre-conceptual design study of ASTRID core" – Paper 432757, Proceedings of ICAPP 2012, Chicago, USA, June 24-28, 2012
[13]: P. LO PINTO and P. ALLEGRE, "Dispositif Récupérateur de Corium dans l'intercuve d'un Réacteur Nucléaire et Réacteur Nucléaire Mettant en Œuvre un tel Dispositif », Demande de Brevet Français, N° 1150870, Bureau de Paris, 2011.
[14] : C.JOURNEAU, C. SUTEAU, L. TROTTIGNON, G. WILLERMOZ, J.M. RUGGIERI, F. SERRE, "Experimental programs and facilities for ASTRID development related to the SA Issue", Fast Reactors 2013, Paris, 4-7/3/2013.
[15] : K. PLEVACOVA, "Etude des matériaux sacrificiels absorbants et diluants pour le contrôle de la réactivité dans le cas d'un accident hypothétique de fusion du Coeur de réacteurs de 4^{ième} generation", PhD thesis, University of Orléans, 2010.

[16] : G. RODRIGUEZ, L. AYRAULT, J. DUMESNIL, E. SANSEIGNE, F. DUJET, B. COLLARD, F. SERRE, C. JOURNEAU, "Development of experimental facility platform in support of the ASTRID program", Fast Reactors 2013, Paris, 4-7/3/2013.
[17] : J.D. GABOR, E.S. SOWA, L. BAKER, J.C. CASSULO, "Studies and experiments on heat removal from fuel debris in sodium", ANS Fast reactor Safety Mtg, Beverly Hills, 1974.
[18] : J.B. IVARD, "In reactor experiments on the cooling of fast reactor debris", Nucl. Technol., 46, 344-349, 1979.
[19] : C.A. OTTINGER, G.W. MITCHELL, R.J. LIPINSKI, J.E. KELLY, "The D9 experiment: Heat removal from Stratified UO_2 Debris", Sandia Nat. Lab. Report, NUREG/CR 2951, SAND84-1834, 1985.
[20] : M. AMIZIC, E. GUYEZ, J.M. SEILER, "Experimental Investigation on Heat Transfer for Two-Phase Flow under Natural Convection - First CLARA Test Results", ICONE20, Anaheim, 2012.
[21] : C. JOURNEAU, P. PILUSO, J.F. HAQUET, E. BOCCACCIO, V. SALDO, J.M. BONNET, S. MALAVAL, L. CARÉNINI, L. BRISSONNEAU, "Two-dimensional interaction of oxidic corium with concretes: The VULCANO VB test series", Ann. Nucl. Energ. 36 (2008), 1597-1613.
[22] C. JOURNEAU, J.M. RUGGIERI, P. PILUSO, "Plans for a new large scale facility at CEA Cadarache: the FOURNAISE project", European Review Meeting on Severe Accident Research (ERMSAR 2012), Cologne, Germany, 2012.
[23] : L. GNANADAS, A.K. SHARMA, B. MALARVIZHI, S.S. MURTHY, E. H. RAO, M. KUMARESAN, S.S. RAMESH, J. HARVEY, B.K. NASHINE, P. CHELLAPANDI, S.C. CHETAL, "PATH – An experimental facility for natural heat circulation heat transfer studies related to Post Accident Thermal Hydraulics", Nucl. Eng. Des., 241 (2011)3839-3850.
[24] : I. HUHTINIEMI, D. MAGALLON, H. HOOHMANN, "Results of recent KROTOS FCI tests: alumina versus corium melts", Nucl. Eng. Des., 189 (199) 379-389.
[25] : P. CHELLAPANDI, "Experimental studies towards SFR Safety", IAEA-GIF Workshop on Operational and Safety Aspects of Sodium Cooled Fast Reactors, Vienna, 2010.
[26] : Yu.S. VASSILIEV, A.D. VURIM, V.A. GAIDACHUK, A.A. KOLODESHNIKOV, V.A PAKHNITS, A.V. PAHNITS, A.S. MARININ, G.V. SHAPOVALOV, JV. LOGACHEV, K. KONISHI, J.I. SATO, S. KUBO, S. KOTABE, K. KOYAMA, "Research on problems of safety of Nuclear Power Reactors in the IGR Reactor: the Results of Medium-Scale Experiments Realised under the Eagle Project", 13th Int. Conf on Radiation Physics and Chemistry of Inorganic Materials, Tomsk, 2006.
[27] : C. SUTEAU, F. SERRE, J.-M. RUGGIERI, F. BERTRAND, "Code strategy for simulating Severe Accident Scenario", submitted to FR13 conference, Paris, France, March 4-7, 2013
[28] : KONDO, S., et al., "SIMMER-III: An Advanced Computer Program for LMFBR Severe Accident", ANP'92, Tokyo, Japan (1992) Oct. 25-29, No 40-5

[29] : YAMANO, H., et al., “Development of a three-dimensional CDA analysis code: SIMMER-IV and its first application to reactor case”, Nuclear Engineering and Design, Volume 238, Issue 1, 2 October 1984, 381-391
[30] : MAGALLON D., HOHMANN H., SCHINS H. "Pouring of 100-kg-scale molten UO2 into sodium", Nucl. Techn., 98, 1992
[31] : BERTHOUD G., "Synthèse des études concernant l'interaction combustible-réfrigérant dans les réacteurs à neutrons rapides", STR/LML/92-92 – Décembre 1992
[32] : LE RIGOLEUR C., "Présentation des rapports techniques britanniques concernant les essais effectués dans l'installation d'essais sur les matériaux fondus "Molten Fuel Test Facility" à WINFRITH", Note Technique-DER-PAC-97-01, 1997
[33] : SPINDLER B., et al., “Simulation of MCCI with the TOLBIAC-ICB code based on the phase segregation model “ Nuclear Engineering and Design, Volume 236, Issues 19–21, October 2006, p. 2264-2277
[34] : CHEYNET, B., et al., « Thermosuite », Calphad, 26 (2) (2002), p. 167

Safeguards in Prototype Fast Breeder Reactor Monju

E.UMEBAYASHI[a], Y.YAMAGUCHI[a], M.MATSUGUCHI[a], S.USAMI[a], S.YOSHIMOTO[b], S.YATSU[c]

[a] Japan Atomic Energy Agency, Tsuruga, Fukui, Japan

[b] FBR Technology Engineering Services Company, Tsuruga, Fukui, Japan

[c] Ministry of Education, Culture, Sports, Science and Technology, Tokyo, Japan

Abstract. The assemblies loaded in the core and stored in the ex-vessel storage tank (EVST) are in liquid sodium in the Japanese prototype fast breeder reactor (FBR) Monju. Since it is difficult to apply a direct verification procedure for the fuel assemblies in these areas, a dual containment and surveillance system consisting of two monitoring devices such as surveillance camera and radiation monitor that are functionally independent has been applied. In addition, the Monju Remote Monitoring System was developed to strengthen the continuous surveillance and to reduce the load of the inspection activities. Furthermore, the ex-vessel transfer machine radiation monitor (EVRM) and the exit gate monitor (EXGM) were upgraded to strengthen the monitoring of spent blanket fuel assemblies and to improve the reliability of distinguishing between fuel assemblies and non-fuel items. As the result, the integrated safeguards was introduced in November 2009, and the effective safeguards activities have been implemented in Monju.

1. Introduction

Monju, a 280 MWe prototype FBR located at the Shiraki site on the Tsuruga Peninsula of Fukui Prefecture, is a predominant R&D facility for the FBR development in Japan. The operating experience of Monju will be invaluable for the improvement of plant reliability of FBRs and will contribute to the establishment of real operating techniques, including safeguards activities. Since plutonium is contained in the core fuel assemblies (mixed oxide fuel) and the burnt blanket fuel assemblies (depleted uranium fuel), the flows of fuel assemblies on all the fuel handling routes are required to be verified using the surveillance cameras, the radiation monitors and the seal systems, and frequent inspections are needed. In addition, the assemblies loaded in the core and stored in the ex- vessel storage tank (EVST) are in a difficult-to-access area filled with liquid sodium in Monju, thus a dual containment and surveillance system has been applied. Furthermore, the development of the Monju Remote Monitoring System was carried out to reinforce the continuous surveillance and to reduce the load of inspection activities, and the radiation monitors were upgraded to improve the reliability of monitoring. The present paper describes the fuel transfers in the Monju facilities, their verification through the safeguards equipment as well as the introduction of the integrated safeguards to Monju.

2. Plant Description

Monju is a sodium-cooled loop-type fast breeder reactor with an output of 280MWe (714MWt) fueled with mixed oxides of plutonium and uranium. The principal data on plant design and performance is shown in Table 1.The former Power Reactor and Nuclear Fuel Development Corporation (PNC), now a part of JAEA, started the construction of Monju in 1985, completed equipment installation in 1991, began the system startup test (SST) in 1992. The first criticality was attained in April 1994. Then Monju sent electricity to the grid in August 1995 and operated at the 40% electric power in October. On December 8, 1995, a sodium leakage occurred from the secondary circuit, and then Monju suspended its operation for 14 years and 5 months. After refueling with 84 core fuel assemblies, Monju restarted its system startup test (SST) and reached criticality on May 8, 2010. The SST is planned to be conducted in the three steps: Core Confirmation Test (CCT), 40%-power Confirmation Test and Power Rising Test. The CCT, which is the first step of SST, was carried out at a very low reactor power for 78 days and completed on July 22, 2010 in order to confirm core characteristics and functions of the primary and secondary sodium circuit. After refueling succeeding to the CCT, 40%-power Confirmation Test will be conducted at the minimum electricity output of 40% in order to check the soundness of the water/steam system and the turbine/generator system after its long-term layup. After another refueling, a Power Rising Test will be carried out in order to check the performance of the whole plant in the output ranges to 100%. After finishing these steps, the full power operation will start.

Table 1 principal design and performance data of Monju

Reactor type	Sodium cooled loop type	Cladding material	Type 316 stainless steel
Thermal power / Electrical power	714 / 280 MW	Breeding ratio	Approx.1.2
Fuel	Plutonium-uranium mixed oxide	Primary sodium temperature (Reactor inlet/outlet)	397 / 529℃
Core dimensions:			
Equivalent diameter / Height / Volume	Approx. 180cm / 93cm / 2,340liters	Second. sodium temperature (IHX inlet/outlet)	325 / 505℃
Blanket thickness (Upper / lower / radial)	30 / 35 / 30cm	Number of loops	3
Plutonium fissile enrichment	(Inner core/Outer core)	Dimensions of reactor vessel (Height/diameter)	18 / 7m
Fuel of initial core: Type1, Type2, Type3	15/20, 16/21, 16/21wt%		
Fuel of equilibrium core	16/21wt%	Interval of refueling	Approx. 6 months
Fuel inventory:		Refueling system	Single rotating plug with fixed arm fuel handling machine
Core(U+Pu+Am-241 metal) / Blanket (U metal)	5.9 / 17.5 t		
Average fuel burn up	Approx. 80,000 MWd/t		

2.1.Reactor core and fuel assembly

The Monju reactor core consists of 198 core fuel assemblies surrounded by 172 radial blanket fuel assemblies. The top and bottom parts of the core fuel assemblies contain depleted uranium, forming axial blankets to the core. All fuel assemblies are of identical overall size and have a hexagonal outer shape; they weigh 200 kg each and are 4.2 m long. Core fuel assemblies contain 169 pins and blanket fuel assemblies contain 61 pins. Pins are filled with pellets of mixed oxide (MOX) and depleted uranium oxide, respectively. The core configuration and fuel assembly are shown in Figs 1 and 2, respectively. To flatten the power distribution, the core is divided into two radial zones with different plutonium enrichment, 16% and 21% Pu-fissile/(Pu+U) for the inner and outer zone, respectively, in the equilibrium cycle. The design average core fuel burnup in the equilibrium core is 80,000 MWd/t.

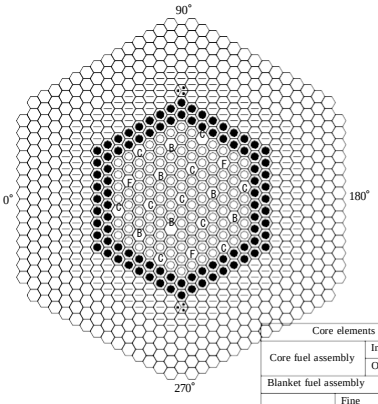

Core elements		Symbol	Number
Core fuel assembly	Inner core		108
	Outer core		90
Blanket fuel assembly			172
Control rod	Fine	F	3
	Coarse	C	10
	Back-up	B	6
Neutron source			2
Neutron shield assembly			316
Surveillance assembly			8

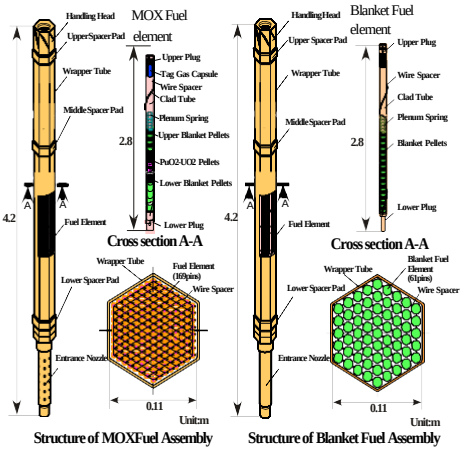

IAEA-CN-199
Paris, France, 4-7 March 2013
Paper CN-199-262

ASTRID power conversion system: assessment on steam and gas options

Guy LAFFONT[1], Lionel CACHON[2], Vincent JOURDAIN[3], Jean Marie FAUQUE[4]

[1]: CEA Cadarache, DEN/DER/CPA, 13108 Saint-Paul lez Durance Cedex, France
[2] : CEA Cadarache, DEN/DTN/STPA, 13108 Saint-Paul lez Durance Cedex, France
[3]: Alstom Thermal Power, 3 Avenue André Malraux 92300 Levallois Perret, France
[4]: AREVA NP, 10 rue Juliette Récamier 69456 Lyon Cedex 06, France
Contact author: Guy LAFFONT, +33442256644, guy.laffont@cea.fr

Abstract. Within the framework of the French SFR prototype project called ASTRID (Advanced Sodium Technological Reactor for Industrial Demonstration), two options for the Power Conversion System (PCS) are being investigated:

- a steam solution based on the Rankine cycle, similar to the solution implemented in the past in France, in the Phenix and Super-Phenix Sodium Fast Reactors (SFRs), and is also being implemented in other SFRs in construction around the world (Russia, India, China).
- a gas solution based on the Brayton cycle, which has never been implemented in any sodium reactor but has been investigated for high temperature reactors (HTR).

The steam PCS option is the most mature option. As the conversion system for all SFRs up to now, it benefits from a worldwide experience amounting to tens of unit-operating years. Nevertheless, the always present sodium-water reaction risk is a strong design and operation constraint to be overcome. The closed Brayton gas PCS option is generally considered as the likely choice for High Temperature Reactors where it provides the best cycle efficiency. Its application for a sodium cooled fast reactor is very innovative, and is mainly justified by safety and acceptance considerations in inherently eliminating the sodium-water reaction risk existing with a Rankine cycle. Pure nitrogen at 180 bars has been selected as the reference gas for the ASTRID gas PCS. Based on a conceptual design study of the two PCSs, this paper discusses the general assessment of both ASTRID PCS options in terms of performance, safety approach, operability and balance of plant (BOP).
.

1. Introduction

The Sodium-cooled Fast Reactors (SFR) is one of the Generation IV reactor concepts selected to secure the nuclear fuel resources and to manage radioactive waste. Within the framework of the June 2006 act on the sustainable management of radioactive material and waste, the French Government asked CEA to conduct design studies for the Advanced Sodium Technological Reactor for Industrial Demonstration (ASTRID) project [1] in collaboration with industrial partners. Collaboration agreements were signed at the beginning of the project: with EDF as an experienced operator of SFRs, with AREVA which is in charge of the nuclear island engineering, and with Alstom which is in charge of the power conversion system engineering.

ASTRID will be an integrated technology prototype designed for industrial-scale demonstration of 4th-generation sodium-cooled fast reactor (SFR) safety and operation aimed at improving safety, operability and robustness levels against external hazards compared with previous SFRs.

The pre-conceptual design phase – conducted from mid-2010 to the end of 2012 – has been focusing on innovation and technological breakthroughs, while maintaining risk at an acceptable level. The ASTRID

pre-conceptual design is based on a sodium-cooled pool reactor of 1500 MWth with an intermediate circuit in sodium generating about 600 MWe. The target lifetime for ASTRID is 60 years.
Among the numerous open options investigated during the pre-conceptual design phase, two Power Conversion Systems (PCS) were studied in parallel, one based on a Rankine steam cycle and one based on a Brayton gas cycle.
The steam PCS option is the most mature option. As the conversion system for all SFRs up to now, it benefits from a large experience and tens of unit-operating years. For this option, conventional 180b/500°C steam cycle conditions have been selected. Nevertheless, the always present sodium-water reaction risk is a strong design and operation constraint to be overcome.
The closed Brayton gas PCS option is generally considered as the likely choice for high temperature reactors (HTR), where it provides the best cycle efficiency. Its application for a sodium cooled fast reactor is very innovative, and is mainly justified for safety and acceptance considerations by inherently eliminating the sodium-water reaction risk existing in a Rankine cycle.
Based on the ASTRID pre-conceptual design studies, this paper discusses the general assessment of both ASTRID PCS options in terms of performance levels, safety approach, operability and balance of plant (BOP).

2. ASTRID Steam Power Conversion System

2.1. Cycle performance

The main boundary conditions for the thermodynamic steam cycle calculations are the following:

- Thermal power delivered to the steam cycle: 1502 MWth
- Steam generator outlet temperature: 500°C
- Steam generator outlet pressure: 180 bar
- Final feedwater line temperature: 245°C
- Cooling water inlet temperature: 21°C
- Condenser design vacuum: 60 mbar

In the course of the pre-conceptual study, several cycle variants have been investigated corresponding to different PCS configurations and turbine and equipment dimensioning. In effect, the main steam conditions are quite close to what can typically be achieved for a fossil-fired steam turbine power plant of the same output for instance, but the concept of reheat is quite different. A steam plant of this size would always include (at least) one reheat loop, where steam expanded in the HP turbine is returned to the boiler for reheating before entering the IP and LP turbines for further expansion and condensation. Such a concept has not been deemed practicable (additional SWR in a sodium/steam reheater), and a reheating concept based on the condensation of higher pressure level steam, similar to what is done by the moisture separator reheaters (MSRs) in present water reactors has been selected (it was already the Super-Phenix choice).

Based on the fixed main boundary conditions, an optimisation phase of the PCS has taken place, defining the turbine intermediate pressures, the position of the dryer, reheater, reheater drain recovery configuration, etc.. This has given rise to several cycle variants which have been evaluated and ranked on efficiency and technology maturity. Some of them are based on a cycle with a separator and reheat process located upstream the intermediate pressure (IP) turbine. For this first set of options (re-heating process upstream of the IP turbine), the heating steam is the main steam that is taken just upstream the turbine inlet valves. As a consequence, the re-heater condensates temperature is close to 356°C and this value is

far above the feedwater outlet temperature (245°C). The recovery of such drains at the appropriate level is thus the key to the unit efficiency.
However, the re-heaters will be non-standard components and should be specifically developed. One of the major concerns is the operating pressures and temperatures, close to the limit of the existing market equipment.

Other cycle options based on a moisture separator (with or without a reheating stage) located downstream of the IP turbine were also investigated. Such a cycle reduces the erosion and corrosion risks within the LP turbine modules and solves the technology issue concerning the high temperature and high pressure re-heater.

The selected steam cycle for the ASTRID cycle is a saturated steam cycle with steam reheating and feedwater reheating. The MSRs are located downstream from the intermediate pressure turbine. This cycle presents the main benefit of using only standard equipment, both for the steam turbine and for the MSR, with all used in their nominal operating range. No technical risks associated with long time behaviour of newly introduced technologies are to be expected. The expected net efficiency of the reactor plant is above 42 %.

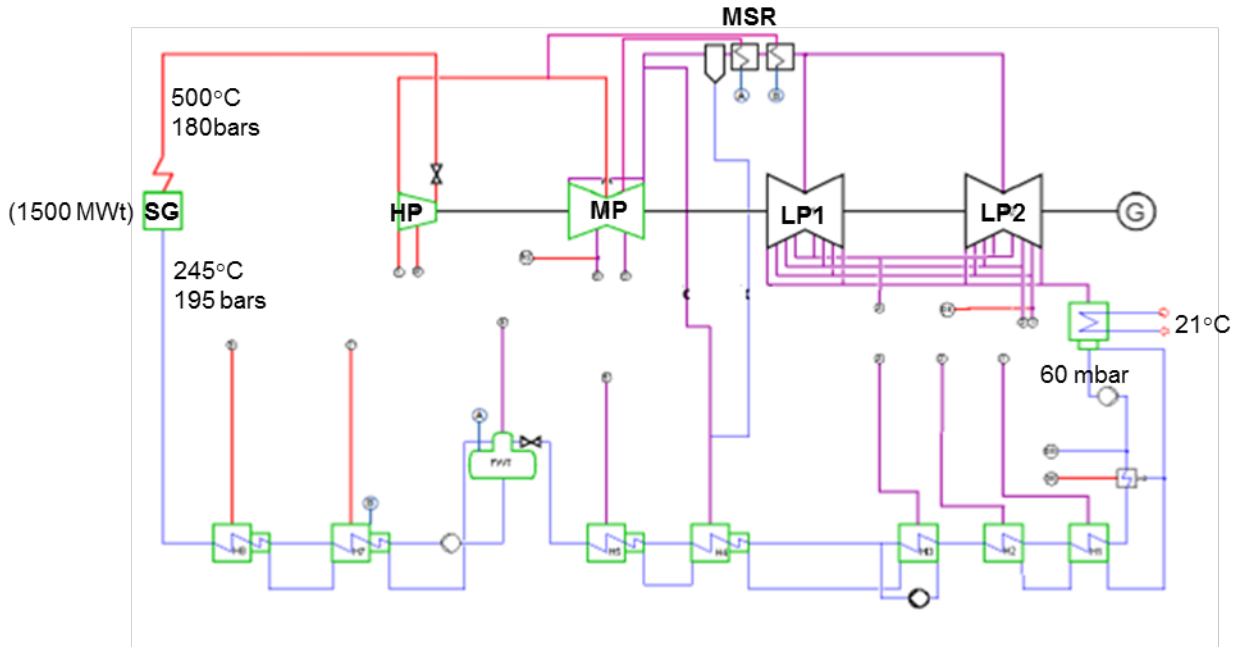

FIG.1. Schematic architecture of the selected steam cycle with an MSR process

2.2. Turbomachinery

The turbine is a 3000 rpm multistage impulse type with horizontal centerline associated with a cycle including moisture separation and intermediate reheating.
It is composed of:

- one single flow High Pressure (HP) module,
- one double flow Intermediate Pressure (IP) module,
- two double-flow Low Pressure (LP) modules.

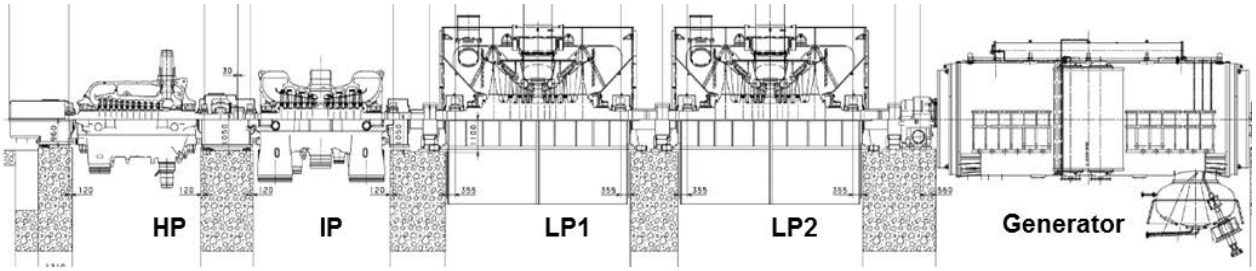

FIG.2. Turbo-generator general layout

The proposed generator is a GIGATOP 2-pole turbogenerator with a fast-acting excitation system. The stator and the rotor are cooled with pressurised hydrogen gas in a closed circuit.

The total length of the shaft line is 48.5 meters. To prevent shaft bending when the unit is not in operation, the turbine generator shaft line is rotated at low speeds by an AC motor-driven turning gear. Operation of the turning gear is fully automatic.

2.3. Steam generator

One of the objectives for the ASTRID reactor is related to a better mastering of sodium-water reaction (SWR) [2]. Although the Rankine steam cycle is a well developed technology, the design and licensing safety evaluation must deal with the SWR and the sodium-water-air reaction. Studies related to steam generator design aim to the elimination of large size SWR, or to be able to mitigate the consequences of such a reaction. A modular steam generator concept (several components of limited power in place of a large component) is selected for ASTRID, as it intrinsically limits the mechanical consequences of a postulated large SWR by limiting the sodium available in a single module for reaction. It also makes easier the failed module removal for expertise.

Two main SG technologies [3] are investigated both comprising a tube bundle enclosed in a vessel: classical design (helical or straight tubes) where sodium flows in the vessel while water circulates inside the tube bundle and an inverted design where sodium is flowing inside the tube bundle. Although we don’t have any experience on fabrication and operation of inverted steam generator, this steam generator type is expected to be preferable from the leakage viewpoint because the evolution of the tube wall damage is slower. Steam generator technical solutions considered in this study are presented in figure 3.

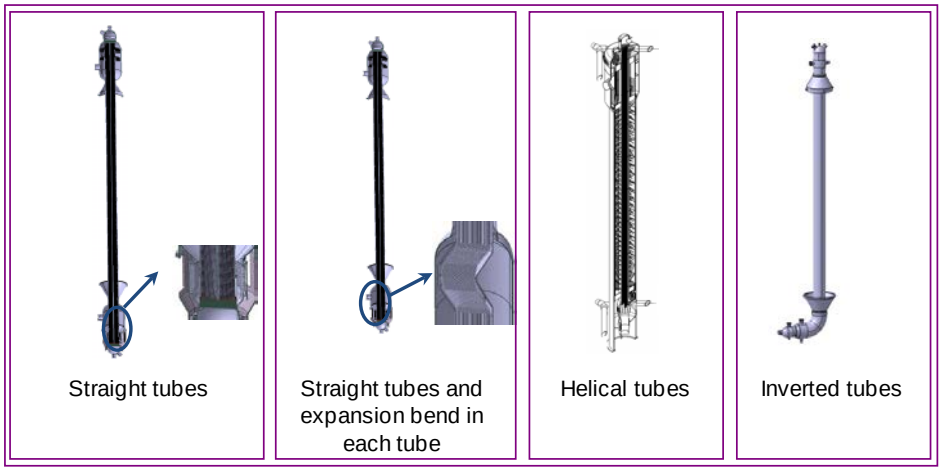

FIG.3. Steam Generator concepts

3. ASTRID gas power conversion system

3.1. Choice of gas

One solution to prevent SWR is the use of an alternative inert coolant with sodium to feed the turbine. For ASTRID, the alternative solution investigated during conceptual design studies is the Brayton gas cycle. Several perfect gases and mixtures of gases were envisaged [4] and a performance sensitivity study was carried out in a preliminary phase. The best compromise between heat transfer, compression work, pressure level and simplicity of cycle operation led to the adoption of nitrogen gas at 180 bars as the reference coolant for the ASTRID Brayton cycle.

3.2. Cycle performance

The main boundary conditions for the thermodynamic gas cycle calculations are the following:

- Thermal power delivered to the steam cycle: 1502 MWth
- Sodium gas heat exchanger outlet temperature: 515°C
- Sodium gas heat exchanger outlet pressure: 180 bar
- Sodium gas heat exchanger inlet temperature: 330°C
- Outlet cooler temperature : 27°C

Several constraints have to be taken into account to fulfil the project requirements. First of all, the 1500 MWth heat duty of the industrial prototype represents a nitrogen mass flow of 7200kg/s to be heated by 185 K. Secondly, the high pressure is set to 180 bars which means the pipes must be relatively thick. A maximum gas pipe diameter of one meter has been set for mechanical and on-site fabrication reasons (mainly welding and post-weld heat treatment). Finally, the study demonstrated that the gas velocity must be limited to about 20m/s in order to minimize pressure losses and maximize the performance of the system. This clearly indicates that multiple pipes in parallel will be required for the gas PCS architecture.
A parametric study on the cycle's main parameters has shown that the turbomachinery performance and the pressure losses are the most sensitive parameters. Several layouts were investigated in order to reduce pressure losses in the ducts, in the headers, and in both the inlet and outlet of the turbomachinery.

Finally, the net efficiency is above 37.5%, taking into account cooling requirements, sodium pumps and auxiliary power.

.

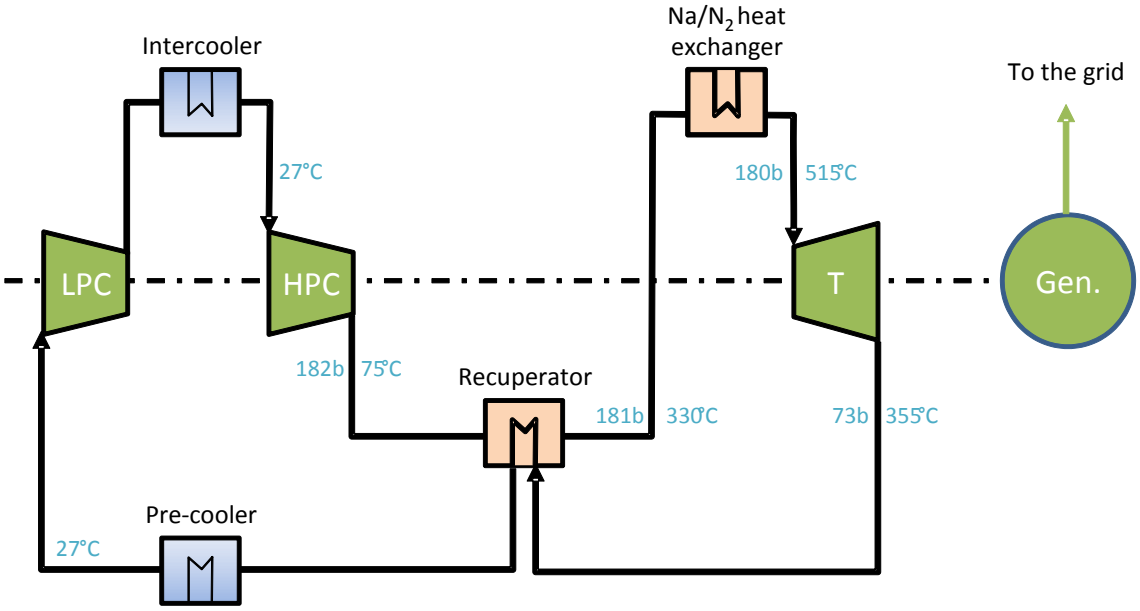

FIG.4. Brayton cycle of the reference case

3.3. Turbomachinery

In a conventional single shaft gas turbine, the axial loads generated in the compressor are, to a great extent, balanced by the axial loads generated in the turbine. The residual thrust can then be balanced by means of a balance piston, but the corresponding hot gas bypass is a loss of performance. For ASTRID, because of the high level of individual thrust involved, it has been decided to balance the thrust on the turbine and on the compressors separately so that the axial load is not supported by the shaft. Therefore, the turbine design will use a split flow configuration. The axial technology has been preferred for the ASTRID turbine. The turbine isentropic efficiency is estimated at 94%. In order to reduce the size of the casings, transition ducts designed for diffusion have been used instead of traditional volutes. This permits to maintain casings below 5 m in diameter, which is beneficial for manufacture and transportation.

Because of the relatively low compression ratio, both radial and axial compressor technologies can be used and can achieve a similar efficiency. The radial technology is selected because it offers the advantage of being much simpler and more robust, together with the fact that no stage-matching test is required. The compressors are implemented face-to-face to reduce the thrust on the shaft. The compressor efficiency for both high pressure and low pressure units is estimated at 91%.

Other aspects closely related to the turbomachinery have been investigated: overall shaft line configuration and torsional behaviour, bearings, sealing system and thrust balance. If the turbomachinery remains a technical challenge, no obvious show-stopper has been identified.

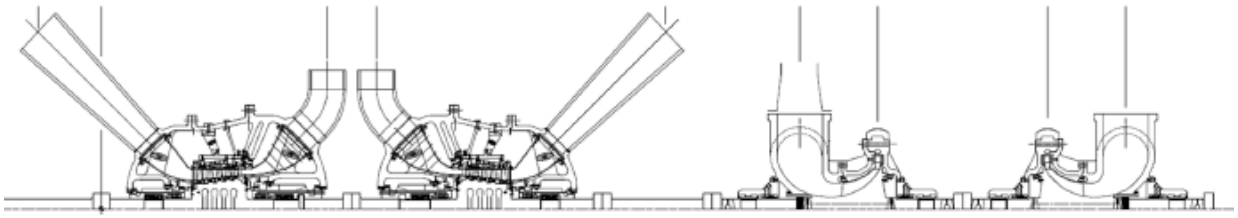

FIG.5. Overview of the shaft line

The turbines are located between the compressors and the generator. In this configuration, only a partial torque is transmitted to the compressors and to the generator. As for the steam cycle, the adapted generator is an Alstom GIGATOP 2-pole turbogenerator with a fast-acting excitation system.
The total length of the shaft line is 45 meters.

3.4. Sodium/gas heat exchangers

The other main technological challenge for the gas PCS option is the development of the key component where heat is transferred from the secondary sodium to the gas: the sodium-gas heat exchanger. Several technical solutions are being considered for this component.

The “compact heat exchanger” concept is based on a stack of corrugated plates where the fluids flow through micro-channels. The most common PMHE (Plate Machined Heat Exchanger) is the PCHE (Printed Circuit Heat Exchanger) concept developed by the HEATRIC Company, where the plates are assembled by uni-axial diffusion bonding. This type of heat exchanger presents high potential in terms of performance, safety, economics and operability.

The compact PMHE has been selected as the reference design for ASTRID. The sodium and nitrogen flow through narrow channels in the plate thickness. The stacks of plates are placed in a pressure vessel which acts as the gas collector and the second barrier for sodium. The corrugations are machined (classical, chemical etching…) and the diversity of feasible heat transfer patterns is very large: classical micro-channels of different cross-section areas up to grooves which can be machined in the plates. The reference material for the plates is SS 316LN.

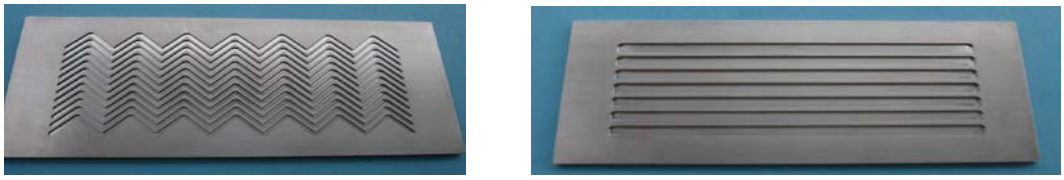

FIG.6. Machined plates for compact heat exchanger : gas pattern (left) – sodium pattern (right),

High isostatic pressure diffusion bonding (HIP-DB) has been selected as the assembly process to obtain a junction quality compatible with that of a nuclear component. The key points for successfully using this process are the plate surface finishing and the adjustment of the diffusion bonding parameters

(temperature, pressure, holding time) to control the grain growth for an acceptable microstructure and a the good quality of the plate junctions.
Apart from the fact that the design rules and standards require specific development of the French code RCC-MRx, the studies of the sodium-gas heat exchanger must incorporate constraints associated with fabrication control and regular in-service inspection while retaining the component compactness. A methodology and technologies for controlling this process are currently being developed.
The reference design of the sodium-gas heat exchanger for ASTRID is based on PMHE technology, with a vertical arrangement of plate stacks for gravitational sodium draining. The unit power of the sodium gas heat exchanger is 125MWth, and three components per intermediate loop are required.

More classical concepts are based on shell-and-tube heat exchanger designs. In these concepts, the gas flows inside the tubes. One of the main restrictions of these technologies is the limited thickness of the tubular plate because of manufacturing aspects with respect to design parameters (180bar, 530°C). Two options are currently being investigated :

- a classical "U shape tube" concept in which the mechanical resistance of the classical disc shaped tubular plates limits the unit power to around 22 MWth,
- an "annular concept" of straight tubes in which an original design of the tubular plates (ring shaped) makes it possible to increase the unit power to 80 MWth.

These concepts are more robust options and are considered as a back-up option for ASTRID, since they are easier in terms of manufacturing and inspection. Nevertheless, this concept leads to heavy components and large floor space requirements (5 to 17 components per loop). Their feasibility and integration also remain to be assessed in greater detail.

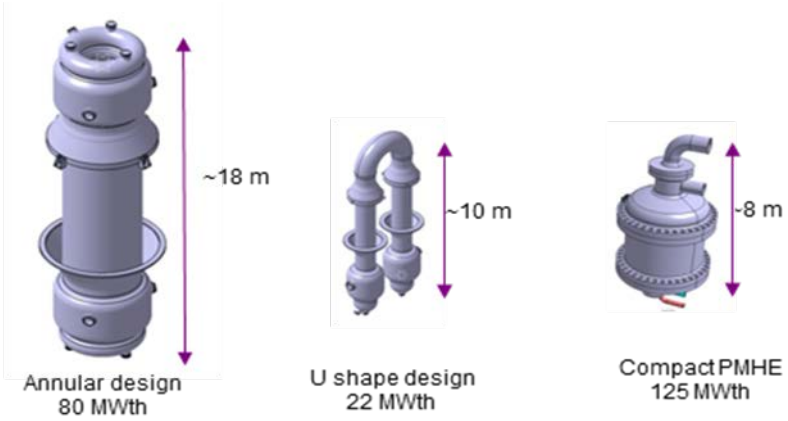

FIG.7. Heat exchanger concepts

4. Reactor layout

4.1. Reactor layout with Steam PCS

The main requirements to be taken into account for the Nuclear Island architecture are:

- the general architecture of the reactor block and its ancillary systems,
- the reactor building containment,
- the reduction of shell damage risks, in particular due to sodium leaks, sodium fires and sodium-water-air reactions,
- the seismic and airplane crash protection,
- the geographic segregation of safety systems and independency of in-depth defence lines,
- the feasibility and the complexity of civil engineered structures,

- the operability and the availability.

Among several architectural options (cross-shaped, rectangular or circular), the cross-shaped architecture has been selected as the reference for the reactor layout. This architecture fulfils the fundamental requirements taken into account at this stage relatively well and seems to be robust and flexible enough to be compatible with different civil work design options (simple or double shell, internal and external loadings, etc.).

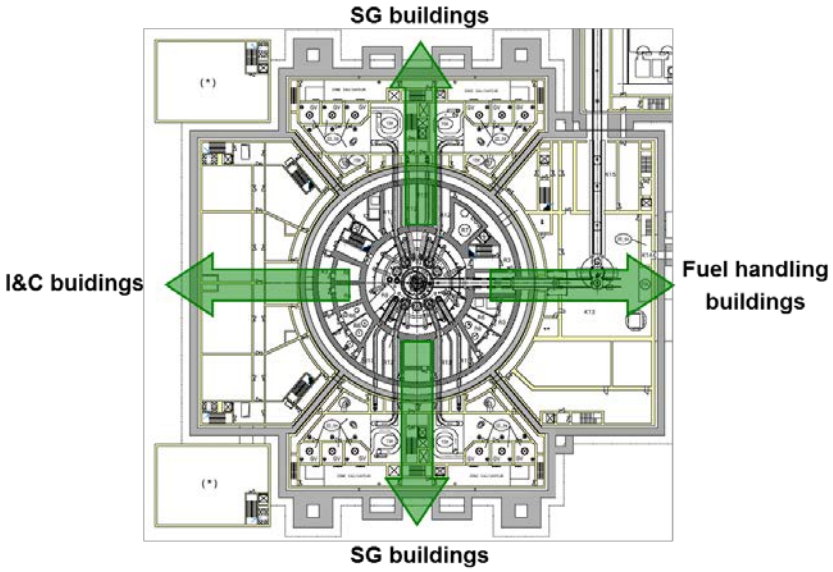

FIG.8. Cross-shaped architecture of the Nuclear Island

4.2. Reactor layout with Gas PCS

Concerning the reactor layout with a gas PCS, the main requirements for the Nuclear Island remains the same. Nevertheless, several options can be envisaged: the sodium/gas heat exchanger could be located inside or outside the reactor containment, and on or off the common seismic foundation raft. The objective is to choose the most suitable configuration for gas system.
The cross-shaped architecture is still well adapted to the main requirements of the Nuclear Island. The main drawback of this option is the length of the gas lines. An alternative option - the frontal configuration - aiming at locating the sodium/gas heat exchanger close to the turbine hall has been proposed. This option is favorable for the gas inventory and pipe lengths but it increases the sodium line complexity and footprint. This option requires a new arrangement of the Nuclear Island general architecture.
Improvements have to be made to find an optimized configuration for the reactor layout with the gas PCS.

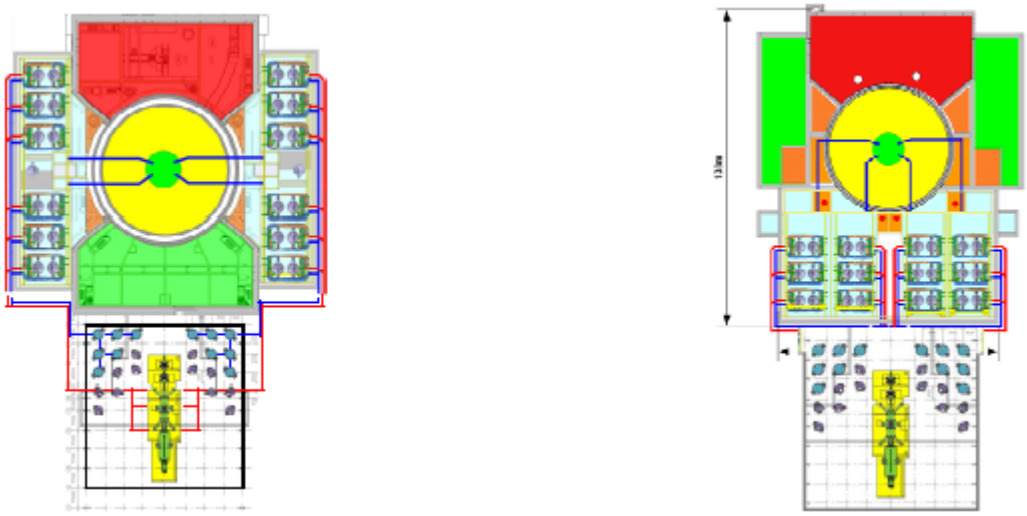

FIG.8. Cross-shaped and frontal architecture of the Nuclear Island with a gas PCS

5. General assessment

5.1. Performance

It terms of the net plant efficiency, the Rankine steam cycle is clearly much better than the Brayton gas cycle. The expected performance of the selected steam cycle for ASTRID is above 42% while the expected performance of the selected gas cycle is closer to 37.5%. The lower performance of the gas cycle is mainly due to the large power required to recompress the gas up to 180 bar. The difference in terms of net electrical power production is more than 10% in favour of the steam cycle.

5.2.General safety approach

The main difference in the safety approach between both the PCS is related to the SWR risk and the sodium-water-air reaction (SWAR) management and their consequences. The steam generators have to be placed in a separate building from the reactor containment on a common seismic foundation raft and under a protective shell against airplane crashes.
The gas PCS makes it possible to eliminate the SWR risk and the specific associated systems (hydrogen detection, management of reaction products). It also makes possible to eliminate the sodium-water-air reaction in case of the SGHE external vessel failure. Then, it is possible to envisage locating the SGHE inside or outside the reactor containment and/or off the common raft which would greatly simplify the civil work.
Then, specific risks related to the gas PCS have to be taken into consideration such as a leakage of the SGHE in the secondary loop (the integrity of the intermediate heat exchanger has to be guaranteed) or the rupture of a large gas pipe (risk of reactor building pressurisation) have to be considered.

5.3. Operability

A preliminary Reliability, Availability and Maintainability (RAM) analysis concludes with very similar forced outage factors for the turbine hall equipment for both the steam and gas systems. During normal

operations, the gas system seems to be simpler than the water/steam system (conditioning of water and filling constraints of SG with water) in terms of start-up and stop operational requirements. There is no requirement of high-quality nitrogen gas and industrial gas with impurities such as hydrogen or oxygen could be favourable in forming a protective layer against corrosion or nitriding. Concerning inspection requirements, steam generators must be inspected every 18 months. Following the European Pressure Equipment Directive, the periodicity for gas equipment checks is every 40 months. Nevertheless, the gas system inspection strategy and the contribution of the gas PCS to the heat removal[1] during reactor normal outages have to be defined.

5.4. Balance of plant

Concerning the balance of plant, the main specificities of the steam system are the required water polishing system and the auxiliary steam source for preconditioning. The electric power required in the steam turbine hall (27MWe) is about ten times more than for the gas turbine hall. The main reason of the difference is that all the gas pumping is done by compressors driven by the turbine of the Brayton cycle, when the return of condensate water to the steam generator is insured by electric driven pumps in a Rankine cycle.

The gas inventory management is a crucial issue for the gas PCS. Two concepts are envisaged for filling and emptying the gas circuit : a passive system by the pressure difference which requires storage tanks for a total volume of 61,000 m^3 or an active system with compressors which is more flexible, and requires a smaller total storage volume of 21,000m^3.

6. Conclusions

Two power conversion systems have been investigated for the ASTRID prototype. The most effective and the most mature system is the classical steam PCS. Although the Rankine steam cycle is a well-developed technology, the design and licensing safety assessment of a SFR must deal with the SWR risk. Studies on steam generator designs and leak detection systems are being carried out with the aim of reducing the risk of large SWRs and of limiting the consequences of a hypothetic violent reaction. The gas PCS presents the strong advantage as it inherently eliminates the SWR risk. However, this system is a very innovative option for which the feasibility and its viability have to be demonstrated.

NOMENCLATURE

ASTRID	Advanced Sodium Technological Reactor for Industrial Demonstration
BOP	Balance of Plant
CEA	Commissariat à l'Energie Atomique et aux Energies Alternatives
EDF	Electricité de France
GENIV	Generation IV initiative
HIP-DB	High Isostatic Pressure Diffusion Bonding

[1] It is possible to limit the transfer of tritium to the gas PCS by controlling the hydrogen concentration in the secondary sodium loop and trapping tritium in the secondary loop.

HP	High Pressure
HTR	High Temperature Reactor
IP	intermediate pressure
LP	Low Pressure
MSR	Moisture Separator Reheater
PCHE	Printed Circuit Heat Exchanger
PMHE	Plates Machined Heat Exchanger
PCS	Power Conversion system
RAM	Reliability Availability Maintainability
RCC-MRx	Règles de Conception et de Construction des Matériels Mécaniques des Installations Nucléaires – Réacteurs Rapides et Réacteurs Expérimentaux (in French) – Design and Construction Rules applicable to equipment of Fast Reactors and Experimental Reactors
SFR	Sodium-cooled Fast Reactor
SG	Steam Generator
SGHE	Sodium Gas Heat Exchanger
SWAR	Sodium-Water-Air Reaction
SWR	Sodium-Water Reaction

REFERENCES

[1] F. Gauché; The French Prototype of 4th Generation Reactor: ASTRID; Annual meeting on nuclear technology, Berlin, May 17&18th; 2011.

[2] M. Saez *et al.*; Sodium-Water Reaction approach and mastering for ASTRID Steam Generator design; Proceedings of FR13, Paris France 4-7 March 2013; Paper CN-199-126

[3] M. Saez *et al.*; Status of ASTRID nuclear island pre-conceptual design; Proceedings of FR13, Paris France 4-7 March 2013; Paper CN-199-127.

[4] L. Cachon *et al.*; Innovative conversion system for the French SFR prototype ASTRID; Proceedings of ICAPP'12, Chicago United-States, June 24-28, 2012.

IAEA-CN-199
Paris, France, 4-7 March 2013
Paper CN-199-263

Large electro-magnetic pump design for application in the ASTRID sodium-cooled fast reactor

Guy LAFFONT[1], Frédéric REY[2], Rie AIZAWA[3], Tetsu SUZUKI[3]

[1]: CEA Cadarache, DEN/DER/CPA, 13108 Saint-Paul lez Durance Cedex, France
[2] : CEA Cadarache, DEN/DTN/STPA, 13108 Saint-Paul lez Durance Cedex, France
[3]: TOSHIBA Corporation, 1-1, Shibaura 1-chome, Minato-ku, Tokyo 105-8001, Japan
Contact author: Guy LAFFONT, +33442256644, guy.laffont@cea.fr

Abstract. Within the framework of the French SFR prototype called ASTRID (Advanced Sodium Technological Reactor for Industrial Demonstration) aiming at demonstrating the progress made in Sodium Fast Reactor (SFR) technology on an industrial scale, it is foreseen to implement Large capacity Electro-Magnetic Pumps (LEMP) in place of mechanical pumps on the intermediate sodium circuits. The use of LEMPs is justified by several advantages in the reactor design, operation and maintenance. Due to the specific operating conditions, an annular linear induction pump (ALIP) type is the most promising technology for such an application. Nevertheless, some theoretical and technological developments have to be carried out in order to validate the design tools by taking into account Magneto Hydro Dynamic (MHD) phenomena and the applicability of the LEMP to ASTRID steady state and transient operating conditions. In this aim, a collaboration agreement between the CEA and TOSHIBA Corporation came into force in April 2012 to carry out a joint work program on the ASTRID EMP design and development. This paper discusses the dedicated design studies and experimental activities for the LEMP development within the framework of the CEA-TOSHIBA collaboration.

1. Introduction

The Sodium-cooled Fast Reactor (SFR) is one of the Generation IV reactor concepts selected to secure the nuclear fuel resources and to manage radioactive waste. Within the framework of the June 2006 act on the sustainable management of radioactive material and waste, the French Government asked the CEA to conduct the design studies for the ASTRID Advanced Sodium Technological Reactor for Industrial Demonstration) prototype [1] in collaboration with industrial partners.
ASTRID will be an industrial prototype of a GENIV system integrating French and international Fast Reactors feedback and aiming at improving safety, operability and robustness against external hazards compared with previous SFRs.
The ASTRID pre-conceptual design is based on a sodium-cooled pool type reactor of 1500 MWth with an intermediate circuit in sodium and generating about 600 MWe. The target lifetime for ASTRID is 60 years. The pre-conceptual design phase, conducted from mid-2010 to the end of 2012, has been focusing on innovation and technological breakthroughs, while maintaining risk at an acceptable level. Among the numerous open options investigated during the pre-conceptual design phase, it has been decided to implement LEMPs in place of mechanical pumps on the intermediate sodium circuits. The use of LEMP is justified by several advantages in the reactor design, operation and maintenance. During the conceptual design phase, the ASTRID design choices will be consolidated and finalised by end of 2014. Due to the specific operating conditions, an annular linear induction pump type is the most promising technology for such an application. Nevertheless, some theoretical and technological developments have to be carried out in order to validate the design tools by taking into account MHD phenomena and the applicability of the LEMP to ASTRID steady state and transient operating conditions. In this aim, a collaboration agreement between the CEA and TOSHIBA Corporation came into force in April 2012 to carry out a joint work

program on the ASTRID EMP design and development. This paper discusses the dedicated design studies and experimental activities for the LEMP development within the scope of the CEA-TOSHIBA collaboration.

2. Relevance of large EMP for ASTRID

Investigating the use of large EMPs on the intermediate loop of an SFR is motivated by several potential advantages that may be gained in the SFR design and maintenance. Generally speaking, the use of EMPs would provide a better balance-of-plant (BOP). It is worth underlining the following points in particular:

- An EMP has the advantage of being a simpler technology as it does not require the same auxiliaries as a mechanical pump, e.g. reduction gear, mechanical seals, lubricating oil system and pump over-flow system to cover sodium leakage on the rotating shaft.
- Installing an EMP on the intermediate loops would simplify the loop design itself. This would make it possible to reduce the piping length and sodium volume, therefore resulting in a simplified intermediate loop implementation (improved BOP).
- In comparison with mechanical pumps, it is possible to design EMPs with a sufficiently low internal pressure drop to initiate natural convection inside the intermediate sodium circuit in case of electrical power supply loss (relevant to safety).
- Finally, an EMP has several decisive technological advantages: no moving parts, no penetration through the sodium vessel, no lubricant loop, low flow velocity favourable for noise reduction, and reduced maintenance. The EMP maintenance time is estimated to be ten times lower than for mechanical pumps.

To fully benefit from the EMP advantages, this component has to be self-cooled, which means it has no auxiliary cooling system in sodium or gas.

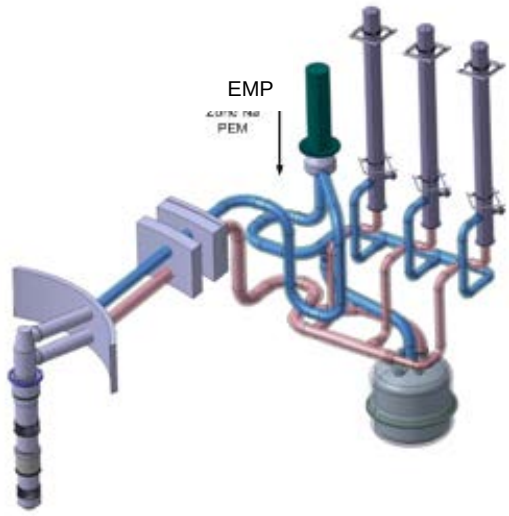

FIG.1. Example of a compact intermediate sodium loop with an EMP on the cold leg.

3. TOSHIBA feed-back on the design of large EMPs

An electromagnetic pump as shown in figure 1 is an annular linear induction pump (ALIP) which can reach self-cooling. This requires high temperature electric insulation as developed by Toshiba and allows

to immerse the pump into sodium. The heat power transferred to the surrounding sodium is recovered by the turbine generator as electricity. A LEMP was developed for application to the main circulation pumps of FBR [2]. This LEMP was designed, manufactured and then tested on a sodium test facility. The pump efficiency that exceeded 40% at the rating ($160m^3$/min, 0.28MPa) was confirmed. Toshiba performed magnetic field measurements in air and many sodium tests over 2550 hours which satisfied the design target. The applicability of the LEMP for FBRs was confirmed on the basis of the test results and post-test inspections.

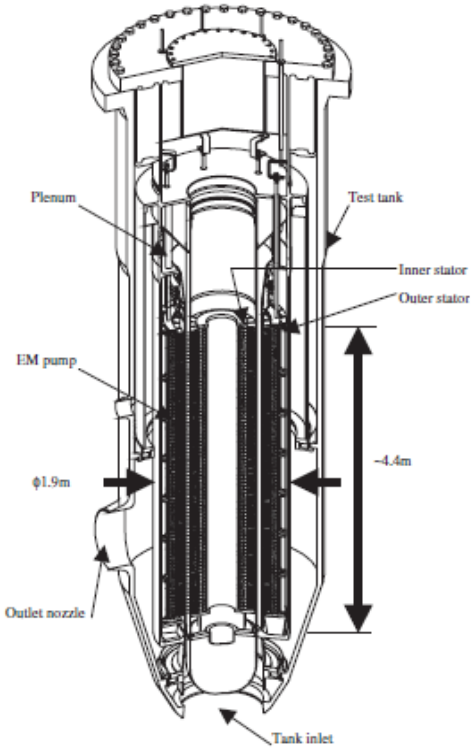

FIG.2. Bird-eye view of the LEMP [2]

4. ASTRID EMP design specifications

4.1. Nominal operation

In the ASTRID reference reactor layout, there are four intermediate sodium loops from the Intermediate Heat exchanger (IHX) to the Steam Generators (SG) or the Sodium-Gas Heat Exchanger demending on the power conversion system. Each sodium loop is equipped with an EMP. The EMPs are located on the cold legs of the intermediate sodium loops (see figure 2).
In nominal operation conditions, the EMP design requirements are the following: the sodium flow rate must be 1.98 m^3/s with a pressure head of 0.37 MPa at a sodium temperature of 345°C. During the reactor start-up tests, the sodium temperature may reach 425°C for several tens of hours. The nominal design pressure of the EMP piping is 0.8 MPa.

4.2. Transient conditions

The most severe transient conditions for the EMP are the loss of SG feeding water with the SG drying. The scenario is as follows : in case of feeding water loss leading to SG drying, the Automatic Reactor Shut Down occurs when the sodium temperature reaches 380°C at the SG outlet. At the same time, the secondary sodium mass flow rate is reduced from 100% to 15 % of EMP's nominal flow rate in 9 seconds. The consequences are a fast temperature increase at the SG outlet up to 540°C in 200 seconds and the propagation of a hot shock in the secondary loop cold leg. This type of transient is expected to occur 150 times during the reactor's 60-year lifetime.

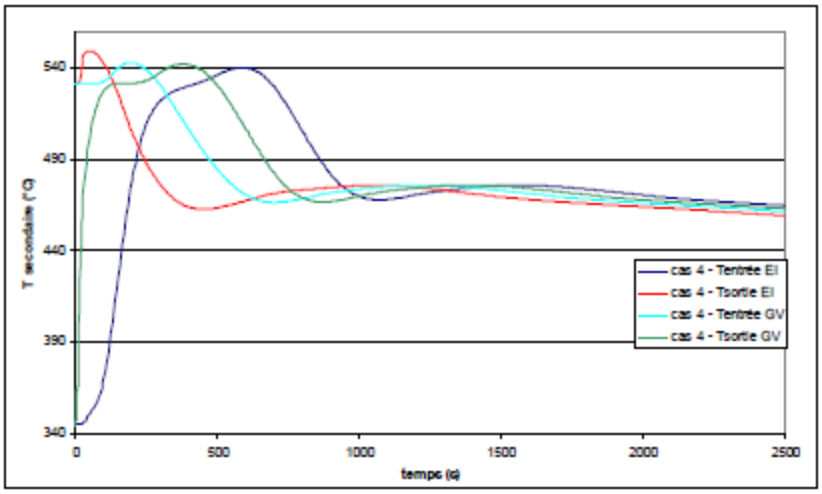

FIG.3. Thermal transient in the intermediate sodium loop

5. ASTRID EMP design

5.1. CEA

Computer tools are used to define the operating points of an EMP [6]. They provide both the flow rate versus pressure curve of the component and the different post-processing quantities that are directly used to define the technical design of the component. The design code for EMP currently used by the CEA is the commercial code COMSOL Multiphysics® based on finite-element method. This model is used to solve uncoupled MHD equations (Maxwell's equations and Ohm's law) by means of a frequency harmonics method.
The calculated EMP has a cylindrical shape with two concentric stator windings, with one stator on each side of the sodium channel [6]. The stator coils are placed in a ferromagnetic yoke. The electrical arrangement of each stator is composed of two coils per pole and per phase. The sodium flow path is located between two non-magnetic concentric stainless steel tubes.

By solving equations with an appropriate geometry, the main characteristics of the EMP operation can be achieved through suitable post-processing: flow vs pressure curve, optimized frequency, magnetic field distribution and potential magnetic saturation areas, current density, power balance, etc.

A preliminary design of the double stator LEMP for the ASTRID secondary loop led to the following results:

Characteristics of the EMP for the ASTRID intermediate loop			
Geometry		**General characteristics**	
Stator active length	4575 mm	Electric power	1.74 MW
Fluid channel mean diameter	800 mm	Sodium flow rate	1.88 m3/s
Sodium channel width	75 mm	Pressure head	0.34MPa
Thickness of pump pipes	10 mm	Sodium temperature	350°C
Number of poles	14	Frequency	20 Hz
Number of phases	3	Efficiency	38%
Number of coils	84	Rm*slip	1.42

Table 1 : Main preliminary characteristics of the ASTRID EMP calculated with COMSOL

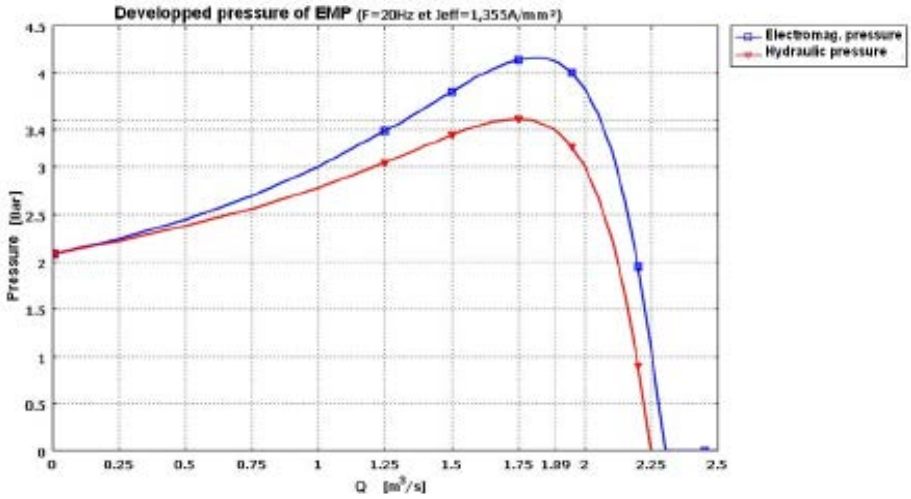

FIG.4. Effective pressure as a function of the flow rate

5.2. TOSHIBA

TOSHIBA performed an electromagnetic fluid analysis to define the pumping function and the electromagnetic characteristics for the LEMP design of the ASTRID secondary loop. The electromagnetic fluid analysis code was performed with the code named EAGLE developed by TOSHIBA. EAGLE is a code that solves coupled equations of the electromagnetism (Maxwell's equations) and the fluid dynamics (Navier-Stokes equation) in a two-dimensional model. The electromagnetic fluid analysis provides the Q-H (flow rate vs pressure) characteristic, the electromagnetic force distribution, the magnetic field in the inner and outer iron cores.

The analysed axi-symmetrical model takes into consideration the sodium channel, the concentric sodium channel walls, the inner and outer iron cores, the coils and the casing.

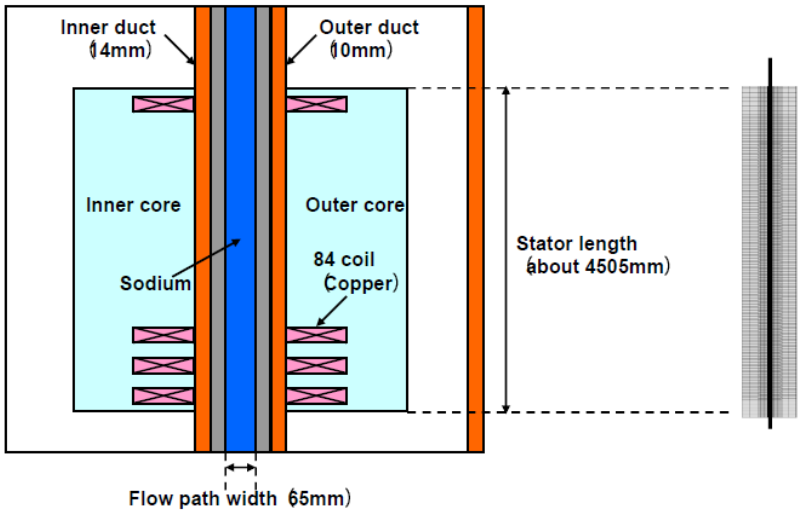

FIG.5. Geometrical model

The Q-H characteristics for the nominal sodium temperature of 345°C are shown figure 6 for a constant V/f ratio. The pressure reached at the nominal flow rate of 119 m³/min fully satisfied the specified 0.37 MPa in a stable control-of-flow area.

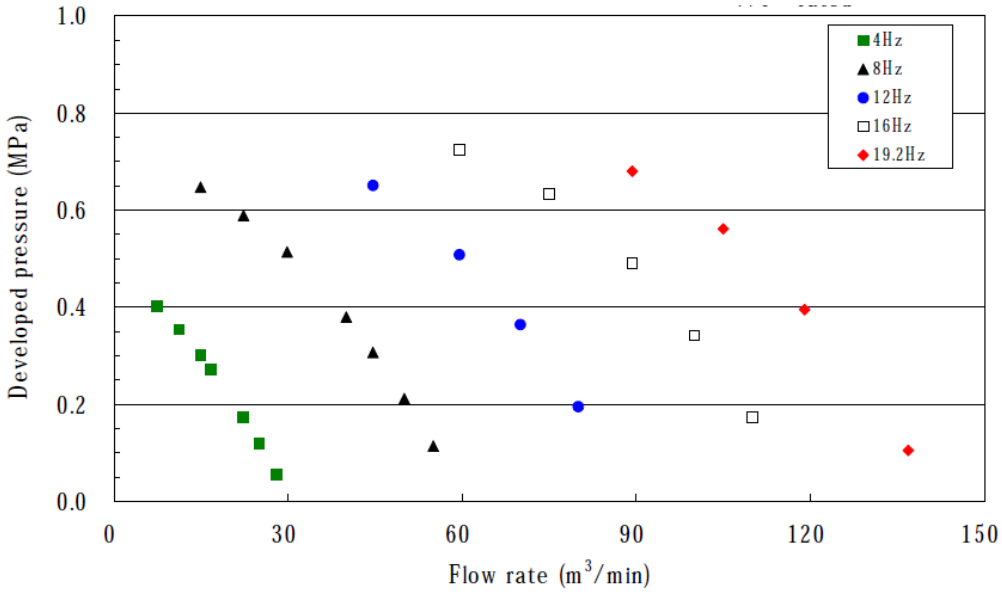

FIG.6. Q-H characteristic

The analysis of the electromagnetic force distribution in the annular sodium channel is shown figure 7. The negative thrust near 0.4 m and 4.7m in the axial direction of the LEMP is the consequence of the classical end effect of the stator. Therefore, this negative effect remains small compared with the electromagnetic force developed in the sodium channel of the stator and the

impact on the pump performance remains limited. The main characteristics of the ASTRID EMP are summarised in table 2.

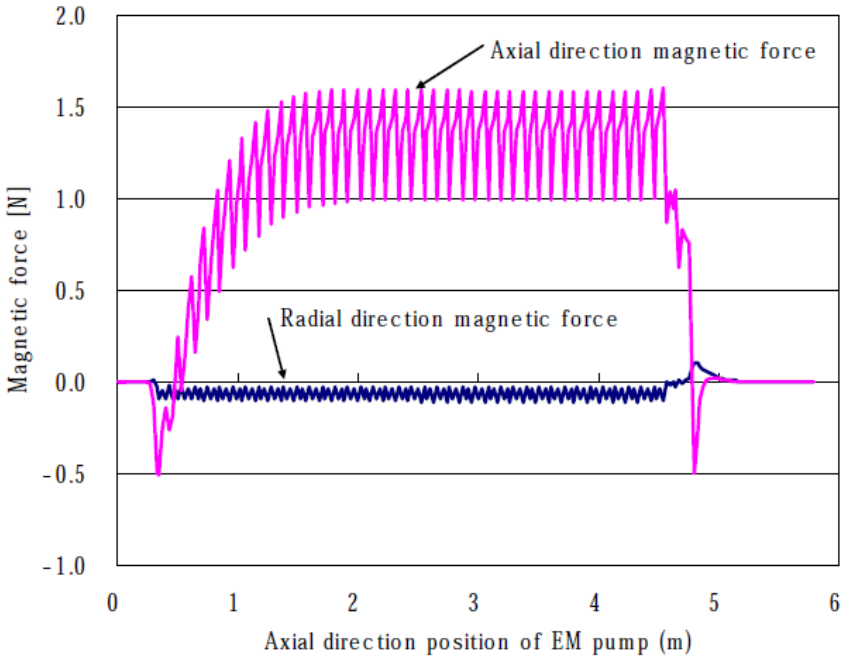

FIG.7. Electromagnetic force distribution in the annular sodium channel

Item	Specification	Unit
Type	ALIP / **Double** stator	-
Sodium flow rate	119	m3/min
Pressure head	0.37	MPa
Sodium temperature	345	°C
Electric Power	1.94	MW
Frequency	19.2	Hz
Efficiency	40	%
Rm*s	0.99	-
Sodium channel width	65	mm
Sodium channel mean diameter	1030	mm
Number of coils	84	pieces
Number of poles	14	poles
Stator active length	4500	mm
Outside diameter of casing	1800	mm

Table 2: Main preliminary characteristics of the ASTRID EMP calculated with EAGLE

A preliminary design of the ASTRID EMP was proposed as a basis for the thermal and thermo-mechanical analysis (see figure 8).

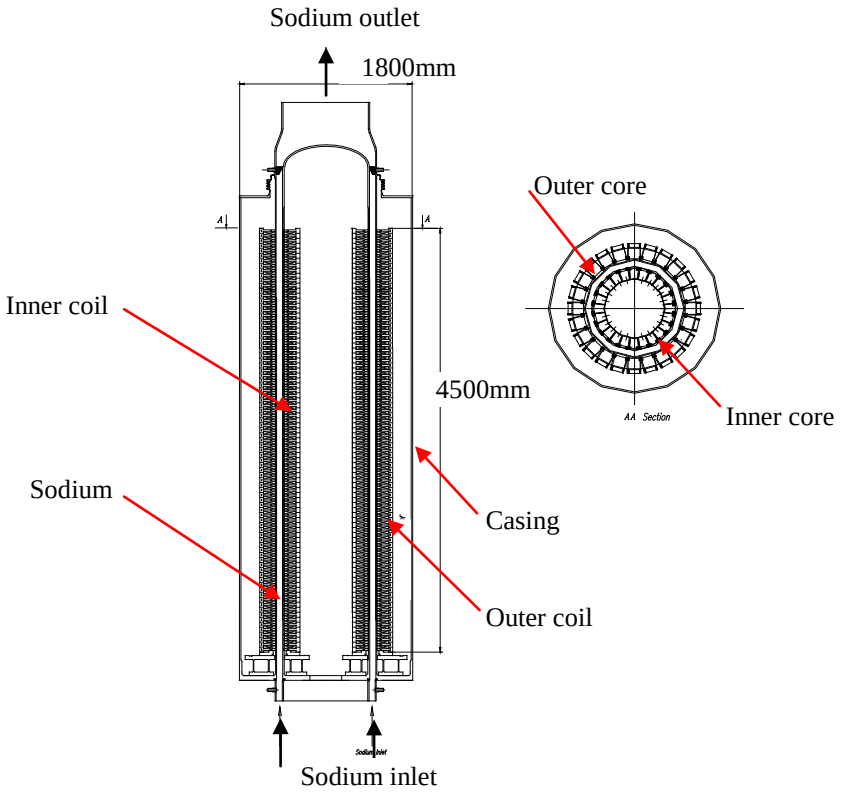

FIG.8. Main geometrical dimensions of the ASTRID EMP

6. Qualification tool development

6.1. Theoretical global analysis

There has been much research on the development of large-scale annular linear induction pumps (ALIP) [2-4]. The main objective of this theoretical analysis is gain a better understanding of this type of pump and to quantify any additional effects which influence both the pump efficiency and operation. Among such effects, there are the so-called instabilities due to various phenomena, like the entry or end effects, the internal three dimensional flow, and turbulence generated by the magnetic field heterogeneity.
Several parameters take into account the occurrence of instabilities, e.g. 1) the Hartmann number, the interaction parameter defined as the ratio between the flow transit time along the duct axis and the electromagnetic time, 2) the Yamamura criterion [5] for the end effects, and 3) the magnetic Reynolds number multiplied by the slip Rm*s [4].

This analysis intends to compute both the magnetic field inside the EMP gap and the turbulent flow field. The feedback influence of the flow on the magnetic field in the Ohm's law will be taken into account. First computations with an enhanced constant viscosity using the commercial code COMSOL indicate that coupling may be achieved. Preliminary coupling between the commercial software FLUX3D (for electromagnetic computations) and the FLUENT CFD code indicates that this approach is realistic [6]. However, the mesh refinement in the Hartmann layers is obviously an issue. Furthermore, it will be necessary to investigate the effects of the magnetic field on the turbulence since the interaction parameter

based on turbulence could be around the unity. Special attention should also be paid to the turbulence near the wall which will affect the wall function currently used in standard turbulence model closures.

6.2. Experimental validation

An EMP model is currently being built by the CEA to support these theoretical developments [6]. This model consists of a middle-size annular EMP. The liquid metal is sodium. The expected dimensions are :

- active length : 1 to 2 m,
- gap thickness : 0.02 to 0.05 m,
- frequency : f = 10 to 20 Hz,
- typical value of the magnetic field : from 0.05 to 0.1 T,
- flow velocity : up to 10 $m.s^{-1}$,
- magnetic Reynolds number : higher than 10,
- operating temperature : around 120°C.

In the current design, the Hartmann number is about 240, which is quite high. The presence of the conducting walls is therefore of primary importance. The interaction parameter is about 5, which means that the velocity profile may be established. Concerning the end effects, the Yamamura criterion is equal to 2.3 for f = 20 Hz. According to this criterion, instabilities could be observed in the experiments. The magnetic Reynolds number multiplied by the slip Rm*s is about 2.8 for a slip equal to 0.2. The latter value has been chosen quite high in order to promote possible instabilities in the EMP.

The tests will consist of magnetic field measurements and overall electromagnetic ones, such as electrical resistance and power losses. Considering hydrodynamics, except the pressure drop and flow rate measurements, the flow velocity inside the gap will also be determined. In order to carry out these tests, the EMP will be implemented in the facility called PEMDYN which is currently being built at the CEA Cadarache Centre. It is a closed loop in sodium together with an EMP, heat exchangers and a regulating valve all connected in series.

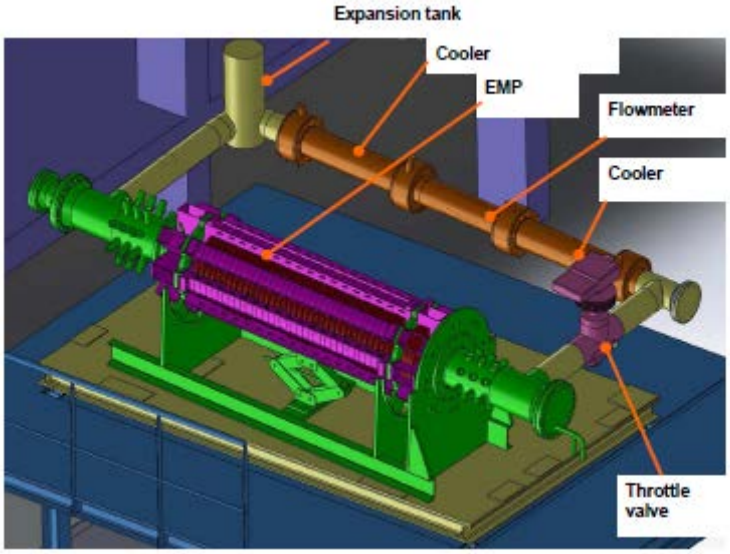

FIG.9. Schematic view of the PEMDYN facility

.

7. Conclusions

The use of a LEMP is justified by several advantages in terms of the reactor design, operation and maintenance. A collaboration agreement between the CEA and TOSHIBA Corporation came into force in April 2012 to carry out a joint work program on the ASTRID EMP design and development. During the ASTRID pre-conceptual design phase, preliminary LEMP calculations were carried out by the CEA and TOSHIBA using dedicated numerical tools. These pre-conceptual design results are in good agreement on the main characteristics of the LEMP and provide a good confidence in the feasibility of the annular LEMP for the ASTRID intermediate sodium loop.
With the aim to improve the numerical tools, theoretical and experimental investigations are currently underway at the CEA so as to identify and characterise the instability phenomena and their impact on the EMP performance.
In parallel, the ASTRID EMP conceptual design studies are ongoing at TOSHIBA. This includes thermal and thermo-mechanical analyses to demonstrate the LEMP self-cooling, the structural analysis of the casing, the supporting legs and the mechanical interfaces, the definition of the power supply unit, the instrumentation and the remote control procedure.
This program is aiming to consolide the ASTRID EMP conceptual design report by end of 2014 and to support the design option choice for the ASTRID basic design.

NOMENCLATURE

ALIP	Annular linear induction pump
ASTRID	Advanced Sodium Technological Reactor for Industrial Demonstration
BOP	Balance of Plant
CEA	Commissariat à l'Energie Atomique et aux Energies Alternatives
CFD	Computational Fluid Dynamics
EFR	European Fast Reactor
EMP	Electro Magnetic Pumps
FBR	Fast Breeder Reactor
GENIV	Generation IV initiative
IHX	Intermediate Heat Exchanger
LEMP	Large Electro Magnetic Pump
MHD	Magneto Hydro Dynamics
SFR	Sodium-cooled Fast Reactor
SG	Steam Generator
SGHE	Sodium Gas Heat Exchanger
SWAR	Sodium-Water-Air Reaction
SWR	Sodium-Water Reaction

REFERENCES

[1] F. Gauché; The French Prototype of 4th Generation Reactor: ASTRID; Annual meeting on nuclear technology, Berlin, May 17&18th; 2011.
[2] H. Ota *et al.*; Development of 160m^3/min Large Capacity Sodium-Immersed Self-Cooled Electromagnetic Pump; Journal of Science and technology, Vol 41,N°4, p.511-523, April 2004. Paper CN-199-126
[3] B. Karasev *et al.*; 3500 m^3/h MHD pump for fast breeder reactor, IUTAM Symp. On Liquid Metal Magnetohydrodynamics, Riga (Russia), May 16-18 (1988).

[4] H. Araseki *et al.;* Double-supply-frequency pressure pulsation in annular linear induction pump. Part I: Measurement and Numerical analysis, Nuclear Eng. and Design, Vol. 195, p. 85-100 (2000).

[5] S. Yamamura; Theory of linear induction motors, University of Tokyo Press, Tokyo (1972). ISBN 0470265833.

[6] F. Rey *et al.* ; Development of large flow ALIP EMP for application in ASTRID sodium cooled fast reactor and future power plant reactors, 8th PAMIR International Conference, Vol. 1 paper B2_18, p. 551-556, September 5-9, 2011, Borgo, Corsica, France,

Safety orientations, general recommendations and preliminary architecture of the ASTRID I&C

M.TREVISIOL[a], B.CARLUEC[b], P.MARTINET[b]

[a] CEA

[b] AREVA NP

Abstract. The overall architecture of Astrid I&C (Instrumentation and Control) has to be compliant with safety and operability requirements for ASTRID. It has to be also compliant with requirements coming from reactor operations principles, human and organizational factors considerations and maintenance strategy.
From the safety point of view, it contributes to the defense in depth and the physical and functional segregation of the components involved in a safety function.
I&C design achieving safety functions is based on the independence of the functions and has to be compliant with the single failure criterion even during maintenance operations.
I&C architecture is divided within three different levels, from the signal acquisition to the information processing to help the operator in normal conditions and in crisis situations.
This paper presents the current status of I&C architecture and gives examples of technological solutions which could be implemented.

Main Text.

This presentation provides the main principles used for defining I&C (Instrumentation and Control) overall architecture and gives examples of technological solutions which could be implemented.

The overall architecture of Astrid I&C is based on high level requirements defined by considering:

- application of the most recent international standards
- defense in depth strategy with high principles of independence between the levels of defense in depth
- up to date consideration of reactor operations
- optimized maintenance strategy
- human and organizational factors considerations

The reference normative system for Astrid I&C is directly constructed from the international standards of the IAEA (International Atomic Energy Agency), Wenra (Western European Nuclear Regulators Association), IEC (International Electrotechnical Commission) and from the French standard RCCE issued by AFCEN.

The overall I&C architecture is based on the methodology used on the ASTRID safety demonstration which consists on the establishment of lines of defense regarding an accidental situation. In particular, a goal is to be able to demonstrate that the severe accident is sufficiently unlikely.

For each event which can lead to the severe accident, at least two strong lines of defense (high reliabity, high safety classification) so-called LDDa and one medium line noted LDDb have to be implemented.

Additionally, according to defense in depth strategy, as expressed by IAEA and Wenra, there is one line so-called “severe accident mitigation line (LDM)” in order to manage and control the severe accident situations.

The design of I&C systems in support to the systems achieving the LDDa is based on the following requirements:

- full independence (physical, electrical, functional) and diversity of the systems achieving the two LDDas, and for all functions necessary for achieving the safety function performed by these LDDa,
- compliance with the single failure criterion for each system achieving a LDDa.

Each I&C system performing Cat. A functions according to the CEI 61226 (C1 in the ASTRID safety classification) has the appropriate redundancy to meet the single failure criterion even during preventive maintenance, periodic testing, inspection or repair, if the function is required.

In the overall I&C architecture, a high level of diversity (functional and technological diversity) is required between the two strong lines of defense (LDDa) to cope with the common cause failure.

According to these requirements, the reference configuration for I&C necessary for achieving a strong line of defense (LDDa) is:

- 3x acquisition channels
- 2x actuators trains with their own majority voting actuation module (2-out-of-3 voter)

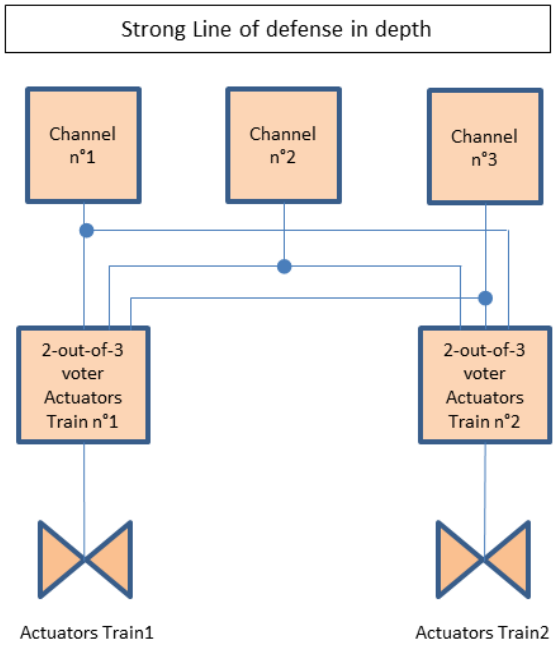

FIG. 1.

To cope with the internal and external hazards, the different parts of I&C systems are located in different divisions. A division is a geographic area of the nuclear island protected physically from the other divisions and usually power supplied individually. Physical separations can be carried out by structures, spacing or barriers or a combination of these means according to postulated events (fires, explosions…) for which they must protect.

As usually, I&C architecture is divided within three different levels:

- Level 0: includes the sensors with their signals conditioning modules,
- Level 1: includes electronics acquisition and treatment modules, programmable controllers, automation systems,
- Level 2: Human Machine Interface (HMI) to monitor and operate the reactor.

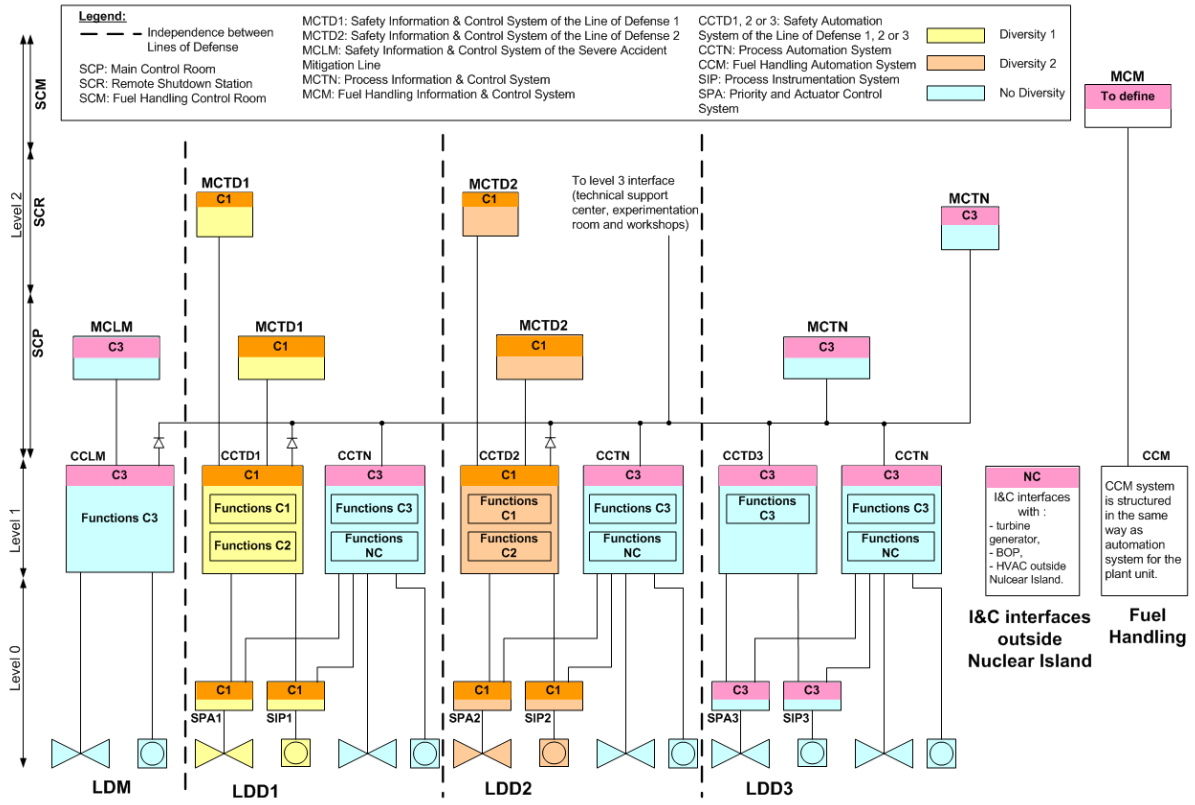

FIG. 2.

Most of I&C systems are foreseen to be implemented in Digital I&C platforms, for diversity reasons some I&C systems are implemented in a non-computerized technology (analog electronic, ASIC, or one shot programmable digital component).

I&C systems, performing high classified functions of one the two LDDa, will be implemented in the AREVA's TELEPERM® XS. TELEPERM® XS has been especially developed by AREVA to implement safety functions and/or functions with a fast response time. TELEPERM® XS is already fully used in a lot of Nuclear Power Plants (new build or modernization plants) and have received the licensing agreement in a lot of countries.

Diversified I&C of the other LDDa system architecture could be implemented in the AREVA's UNICORN platform developed for UK EPR project. Safety functions are implementing on modules with basics components like discrete electronic (transistor, operational amplifier …) or logic gate electronic component (and, or, not, nand…).

Perspectives and improvements for Astrid I&C definition:

One way to improve Astrid I&C is to manage technological diversification with a robust electronic using analog electronic or non-computerized digital electronic or mixed electronic, while keeping a high level of integration.

The goal is to have a robust protection against common mode failures of programmable systems, malicious acts, parameterization and coding errors, while minimizing the volume occupied by these systems.

Opportunities for signal processing (thresholds detection, alarms, and algorithms) embedded closer to the instrumentation have to be studied in order to reduce the wiring and the number of cabinets.

Instrumentation in the ASTRID Project: Main Stakes and Feasible Solutions

F. Jadot[1], JP. Jeannot[2], C. Jammes[3], J. Sibilo[4], F. Loisy[5], JM Augem[6]

[1] CEA, DEN, Cadarache, DER/CPA, 13108 St Paul lez Durance CEDEX, France

[2] CEA, DEN, Cadarache, DTN, Bât. 202, 13108 St Paul lez Durance CEDEX, France

[3] CEA, DEN, Cadarache, DER, Bât. 238, 13108 St Paul lez Durance CEDEX, France

[4] AREVA NP, 10 rue Juliette Récamier, 69456 Lyon CEDEX 06, France

[5] EDF R&D, 6 quai Wattier, 78400 Chatou, France

[6] EDF SEPTEN, 12-14 avenue Dutriévoz, 69628 Villeurbanne CEDEX, France

Abstract. The ASTRID project was launched in 2010. Improving the instrumentation of this future prototype has been identified as a major issue. The key roles of this instrumentation will be the continuous in-service monitoring and protection against accidents for the whole plant. The safety objective for the ASTRID project is threefold: a) a level of safety that it is at least equivalent to the last GEN III reactors, b) integration of the defence-in-depth principle and c) a better safety demonstration than those of Phenix and Superphenix. Considering the safety objective as the main issue in this paper, the related instrumentation requirements are first analysed. The instrumentation developments currently in progress are then broadly reviewed. Within the framework of the CEA-EDF-AREVA coordinated research programm for the development of Generation IV sodium-cooled fast reactors (SFR), the main developments aim to enhance the performance levels of sensors (responsiveness and sensitivity).

1. Introduction

ASTRID is the future integrated technology prototype designed for the industrial-scale demonstration of Generation IV sodium cooled fast reactor safety and operation. To meet the requirements of this 4th generation in terms of safety, reliability, availability and energy savings, ASTRID will need to achieve a higher level of performance than that of previous fast reactors.

In this respect, improving in-service inspection and repair (ISI&R) – including instrumentation – will be a major stake in the ASTRID project.

Within the framework of this project, ISI&R refers to all the measures required to:

• Check that the operating conditions to which the structures are subjected comply with the design assumptions,

• Guarantee that there will be no defect that is incompatible with the safe operation of the facility,

• Enable the implementation of additional comprehensive examinations,

• Guarantee investment protection thanks to the possibility of being able to repair local defects.

In order to meet the ISI&R objectives defined for ASTRID, a 4-level classification has been proposed [1]; the CEA added level 0 to highlight ISI&R in the design.

FIG. 1. Level of ISI&R

Level 1 refers to continuous monitoring. It integrates all the instrumentation needed to monitor the reactor in operation, including the instrumentation needed not only for core monitoring and protection against abnormal events, but also for monitoring during or after an accident, even in case of a severe accident. The instrumentation requirements and recent developments in this field are developed in this paper.

The other levels refer to in-service inspection and repair (ISI&R) which are discussed in paper [2]

This paper starts with a general overview and a description of the objectives for the continuous monitoring instrumentation (Level 1), focussing on studies for detecting total instantaneous blockage both in ASTRID and other SFRs. The instrumentation devoted to core monitoring and leak detection for both the water/steam power conversion system (steam PCS) and the gas power conversion system (gas PCS) are then detailed.

2. Instrumentation: Level 1 ISI&R for ASTRID

Level 1 ISI&R deals with continuous monitoring during reactor operation (including operation with the sodium temperature reaching 550°C). It is mainly based on checking the operating parameters (neutron flux, temperature, flow rate, pressure) with some global measurements indicating the state of the structure and components (leaks, mechanical deformation, vibratory or acoustic characteristics). Level 1 monitoring has to detect any parameter drifts or irregularities with regard to the operating range as early as possible. For this reason, the monitored parameters are continuously compared with the project values which were used for dimensioning and qualified by start-up tests. Several calculators continuously check that the operating parameters do not exceed the safety thresholds in order to prevent an accident. Level 1 instrumentation has to be diversified in order to comply with the safety requirements and to prevent accidents.

The major incidents that have to be detected are: total instantaneous blockage or loss of the cold source, fuel sub-assembly flow blockage, inadvertent withdrawal of one or more control rods, fuel handling errors, abnormal core movements, gas ingress into the core, clad failure, sodium leakage and sodium/water reactions. This probability of occurrence for these incidents ranges from 10^{-7} to 10^{-2} per year per plant.

Even though the various instrumentation systems specially designed for sodium reactors have provided satisfactory performance levels in the former French SFRs, it is necessary to improve the performance of sensors and to design new systems capable of detecting core accidents much earlier so as to meet the requirements of Generation IV sodium-cooled fast reactor safety. The operator's viewpoint and its impact on normal operation also have to be taken into account.

An exhaustive overview of the safety requirements and the R&D programme for detection and monitoring methods is given in paper [3].

The safety objectives for the SFR project are:

- A level of safety at least equivalent to that of the last GEN III reactors,

- Consolidation of the defence-in-depth principle,

- A more robust safety demonstration than those of the Phenix and Superphenix reactors.

These objectives must be applied to the three main types of transients: Loss Of Flow (LOF), Loss Of Heat Sink (LOHS), and Transient Over Power (TOP). A “Defence Line” (DL) approach, which is from the EFR project, is recommended within the scope of core meltdown prevention. Analysis has identified the accident conditions for which the safety demonstration and core meltdown accident prevention must be improved by developing better core monitoring systems (reinforcing the defence lines or adding an extra line of defence).

Total instantaneous blockage (ULOF-type local accident)

This hypothetical accident with fast dynamics corresponds to the total and instantaneous loss of the coolant flow in a fuel sub-assembly of a reactor at full power. The stages of the accident are: sodium boiling, cladding meltdown, fuel meltdown and then propagation to nearby sub-assemblies in about ten seconds. The physical phenomena, which may help to detect such events, are:

- before perforation of an hexagonal tube: heating of the nearby sub-assemblies, loss of sodium flow in the sub-assembly, acoustic noise representative of sodium boiling, release of fission products emitting delayed neutrons from the damaged sub-assembly,
- after perforation of a hexagonal tube of neighbouring sub-assemblies: detection of fission products emitting delayed neutrons.

Though it remains difficult to detect the physical phenomena occurring before perforation of the hexagonal tube due to their weak transfer into the sodium above the blocked sub-assembly, efforts to improve detection are not only focussing on the feasibility of acoustic detection and a design suitable for delayed neutron detection so to reduce the response time, but also on the loss-of-flow detection with Eddy current flow meters.

In parallel with other innovative programmes on this subject, specific sensors are being developed and thermohydraulic calculations are being performed to assess how to detect a loss of flow directly at the outlet of each fuel sub-assembly.

Currently, an unobstructed gap between the outlet of the fuel sub-assembly and the above-core structure bottom is necessary during fuel handling operations so the ultrasonic vision system can be used to check that there is nothing preventing the movement of the rotating plugs.

The severity of the operating conditions (higher temperature, higher flow rate and strong neutron flux) increases as the distance of the sensors from the fuel sub-assembly outlet decreases, but better (shorter) detection times can be achieved in this manner.

The aim is therefore to find the right balance between the operating restrictions and the required performance of this instrumentation.

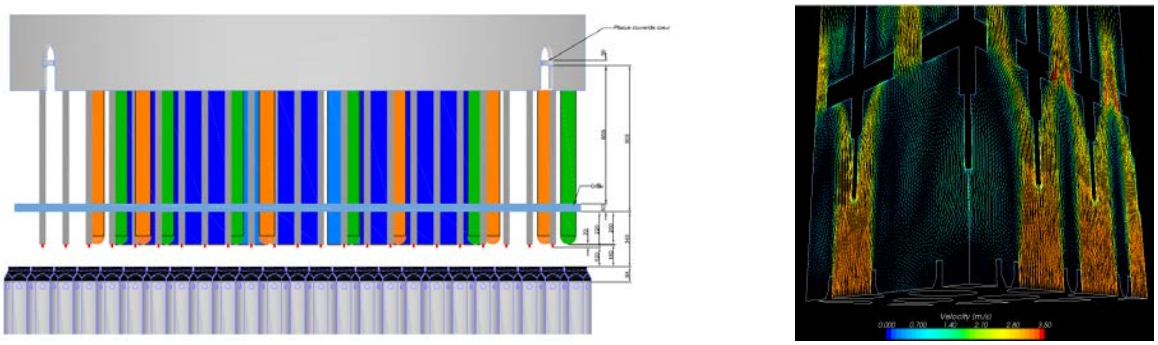

FIG. 2. Bottom of the Above-Core Structure (ACS)/ preliminary calculation results in case of loss of flow

Though the preliminary results which cover only a small fraction of the core (two crowns) show a significant drop in the flow rate, the calculations need to be extended to cover the entire core and all conditions in order to take into the potential account crosswise flow.

While more technological studies and calculations still have to be made, a pending experimental programme in a mock-up should confirm the results of the calculation step.

3. Core instrumentation

The core instrumentation is designed to monitor the different core parameters so the reactor can operate correctly and to detect any incident or accident events affecting the core. Part of instrumentation is supported by the above core structure (see Figure 2); studies for the ASTRID project have focused on nuclear, thermohydraulic and acoustic monitoring.

3.1.Nuclear monitoring

Development actions have focused on fission chambers based on the observation that they were the most suitable detectors for a range of different situations, see Figure 3 [4]. The intention to install some of these fission chambers in the core, which reaches 550°C at full power, requires pursuing their development so they can be adapted to these conditions (performance, lifespan). The development actions focus on:

1. designing and manufacturing a wide range of fission chambers to cover almost the entire range,
2. experimentally qualifying these chambers,
3. their self-diagnostic function,
4. studying their optimal location,
5. monitoring reactivity levels [5].

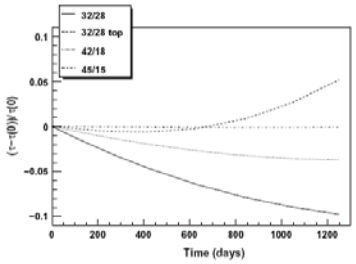

FIG. 3. Pu242 fission chamber in 4 core locations [5].

The definition of requirements for the ASTRID neutron control and monitoring system (including the safety orientations, among others) has essentially been used to select the most relevant in-vessel locations. This selection was made using five performance criteria for neutron detection:

- neutron response (dynamic level),
- linearity of the response as a function of power (which may be reduced by the effect of the sodium expansion or disturbed by the presence of an absorbent in the vicinity),
- local monitoring of the neutron power (against the risk of deforming the power distribution by an initiating event, such as the inadvertent control rod withdrawal which can lead to local melting),
- operating conditions (temperature and gamma irradiation level),
- technological aspects, taking into account the ease of integration (crossing thimble) or continuous service during shutdown states for handling.

Based on the results of thermal-neutron calculations, as well as on the ambient temperature and gamma radiation, two locations have been selected at this stage of pre-conceptual design (of the aim1 CFV-1500-V1 core). The first location is in the cold pool behind the inner shell facing a neutron guide through the neutron shields and positioned axially on the median plane of the core. Both the ambient temperature of 400°C and the required fissile mass of several dozen milligrams mean that standard fission chambers can be used. The second location, which is less ranked, is in the lower part of above-core structure. It has two disadvantages compared with the previous: (a) development of specific fission chambers, (b) discontinuous service handling phase.

The results of this study, which have to be completed, provide new input data for the design of high-temperature fission chambers and their qualification in reactor conditions. It is also important to note that the conditions for starting a new core have yet to be investigated and that they may require the use of specific neutron instrumentation located in the centre of the core. Finally, the installation of ex-vessel neutron detectors cannot be excluded since this would meet a requirement of monitoring the core conditions during the mitigation of a severe accident (i.e. in post-accident).

3.2.Thermohydraulic monitoring

Thermohydraulic monitoring – especially the core outlet temperature – was ensured in Phénix and Superphénix by a thimble containing several thermocouples above the sub-assembly (around 100 mm at operating power), see Figure 4. For ASTRID, the CEA is working on a thimble containing three thermocouples, an Optical Fibre Bragg Grating (OFBG) and an Eddy Current Flowmeter (ECF).

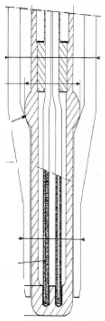

FIG. 4. Superphenix thimble with 2 Cr-Al thermocouples and 1 Na-SS thermocouple

Detecting accident conditions (particularly control rod withdrawal and cooling failure) and monitoring the temperature of fuel sub-assemblies will be ensured by K-type thermocouples. The objective of the studies is to improve the response time. For this purpose, the thimble design has been optimised.

The OFBG will be placed in the thimble to be qualified for SFRs. The objective is to monitor the temperature with in the same objectives as those for the thermocouples. Research on optical fibres by the CEA Technology Research Department since 2009 has made it possible to manufacture high-temperature resistant sensors and spectrally multiplexable sensors [6]. The use of optical fibre in sodium heated to 500°C was validated with multiplexed regenerated OFBGs. A response time was assessed in a hot sodium for an OFBG in a 1 mm Inconel 600 capillary to 150 ms. It is foreseen to qualify this sensor in terms of its radiation tolerance, especially under a high-energy neutron flux.

The main objective of the Eddy current flowmeter (Figure 5) is to detect the hypothetical total instantaneous blockage accident. The advantages of the ECF are its small size, together with its ability to withstand temperatures up to 600°C and radiation. Feedback on their use showed a measurement range from 0 to 7 m/s with an accuracy of ±5 or ±10%. The ECF was tested in the primary pump of Superphenix while its end-of-life test was performed in Phenix. An ECF simulation was performed by IGCAR (India) in reference [7].

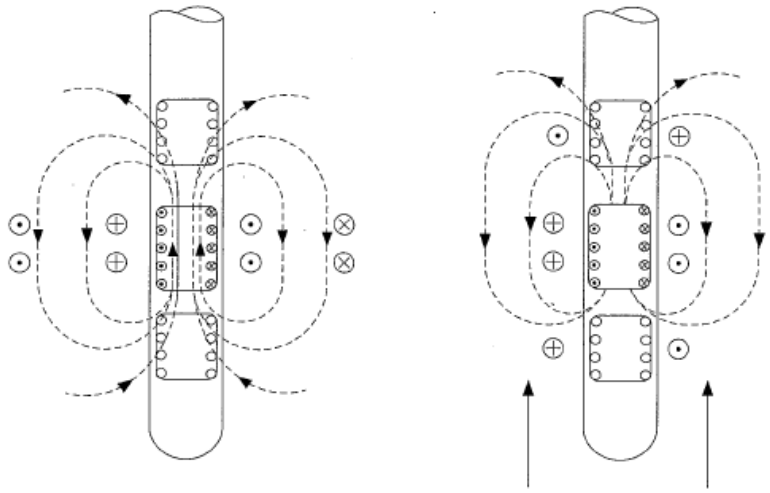

FIG. 5. Schematic diagram of an eddy current flowmeter (three coils are in a thimble). Left: sodium is stagnant and the magnetic field emitted by the central coil is not deflected. Right: the sodium flows upwards (two upward arrows) and the magnetic field is deflected upward.

3.3.Acoustic monitoring

The acoustic monitoring is based on the use of high-temperature ultrasonic transducers (TUSHT[1]) manufactured by the CEA, see Figure 6 [8].

Error! Objects cannot be created from editing field codes.

FIG. 6. TUSHT general architecture

Between 1970 and 1980, these sensors were the subject of loop tests which made it possible to qualify its use in static sodium at a temperature around 550°C and under thermal transient conditions (thermal shocks, 550°C-400°C, -20°C/s). Furthermore, additional tests in a furnace were performed at a temperature of 600°C. A test showed that this type of sensor was capable of operating at temperatures around 900°C.

The acoustic characteristics of the TUSHT are: a frequency response covering a range from 0.7 MHz to 4.5 MHz and a leading edge of the ultrasonic signal around 5 to 15 µs depending on the frequency.

One of the limits of this transducer is the loss of oxygen that occurs in the NL crystal at high temperature, making the transducer inoperative. To overcome this problem, the inner part of the box is

[1] French abbreviation for *traducteur à ultrasons à haute température*

pre-oxidised and the vent tubes maintain a partial inner oxygen pressure at a stable level. Other solutions have been tested in the past or are still being investigated.

In 2011, TUSHTs were manufactured once again according to a procedure identical to that of the previous models. The first tests performed in water and in sodium showed satisfactory operation, though these results remain to be confirmed.

The use of TUSHTs in Phénix involved a sonar rod which was designed to identify any movement in the Phénix core sub-assemblies. Such movement in the past may have provoked the four negative reactivity trips which occurred in Phénix in the early 90s. The sonar rod was operated in Phénix for 18 years (1991 to 2009) without any signal degradation. However, following its installation, no negative reactivity shutdowns occurred during the periods of reactor operation, which meant it was not possible to validate the detection of core movement by the sonar rod.

The use of TUSHT sensors is planned for all acoustic monitoring in ASTRID during power operation.

In addition to the telemetry application (Phenix sonar), the possibility of characterising the continuous gassing of sodium has also been investigated. The main sources of gassing are due to dissolution and then nucleation (gas dissolution occurs in certain areas of the reactor and particularly at the sodium/cover gas interface). The gas fraction in the Superphenix cold pool was estimated to be $2.56.10^{-6}$ with an accuracy of a factor of 2 by a ^{41}Ar measurement method.

A thesis by the CEA between 2007 and 2010 [9] made it possible to develop an acoustic method to characterise the sodium void fraction; the method involves mixing acoustic frequencies to prove bubble resonance, with the analysis of the non-linear result of the acoustic signal being used to determine the histograms of the micro-bubble radiuses and the void fraction. Another acoustic technique, which is relatively simple but only makes it possible to trace back to the void fraction is called a low-frequency sound velocimeter. This corresponds to the linear acoustics based on Wood's model which associates wave velocity with the gas rates in a two-phase environment, and it is currently the reference option for the ASTRID prototype. Its applicability in sodium is currently being investigated. Its operation in water with acoustic transducers that are compatible with sodium (TUSHT) will first be validated.

4. Power conversion system (PCS) instrumentation

4.1.Sodium leak detection for steam/water PCS

The principle of offset thermal insulation is based on detecting leaks in the sodium pipes. There are different types of detector systems based on this principle: electrical beaded wire detectors, sandwich detectors and preheating wires. The studies for ASTRID are focussing on improving these last detector systems, as well as on the research of industrial methods which could be used for sodium leak detection.

A patent application was filed for a sandwich detector improvement (Figure 7). This detector comprises a layer of thermal insulation with an electrical conductor between two layers comprising thermal and electrical insulation. This so-called “multilayer sandwich detector” surrounds the sodium pipe. When a sodium leak occurs, the first layer is permeable to the sodium and an electrical contact appears between the pipe and the conductor layer. This principle should avoid spurious alarms, which are one of the main disadvantages of sandwich detectors.

After having checked the compatibility between the different materials and the sodium, the best thickness for the layers was calculated. The first tests demonstrated the good behaviour of the detector. At present, the work is focussing on the evaluation tests for this innovative detector. The objective is to conduct the qualification campaigns to evaluate the whole performance of this multilayer sandwich detector in real operating conditions

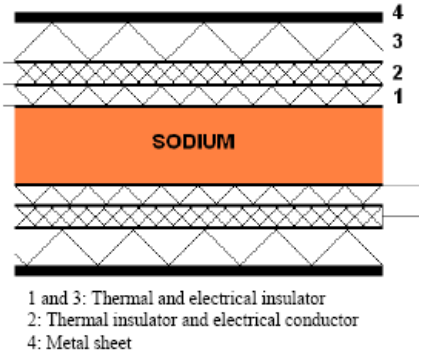

FIG.7. Schematic diagram of the multilayer sandwich detector

4.2.Leak detection for gas PCS

A preliminary study for the monitoring and protection against nitrogen leakage in sodium for the gas PCS was performed. The goal is to detect and locate a gas leak at a stage where there is still no impact on safety, before it reaches a significant level of severity. This study was limited to small leaks. The study of the detection means is based on the parameters characterising the leak:

- The leakage rate,

- The presence of argon dissolved in sodium during transient thermal degassing could be confused with a nitrogen leak,

- Characterisation of the population of nitrogen bubbles and its variation after a sodium leak.

- A number of techniques have been assessed without studying their implementation. Thus, it appears that ultrasonic techniques are promising for monitoring in terms of detecting, locating and characterising a gas leak in the heat exchanger. A 0.4 g/s leak inducing a void ratio of 8.10^{-5} can be detected by a method measuring the celerimetry of the ultrasonic wave in the liquid sodium. In addition, other complementary techniques were also assessed, e.g. gas chromatography for the detection of leaks. The latter method could be implemented only from sampling in the argon cover gas exchanger with the need to differentiate between argon and nitrogen stress on the response time. On-going studies on the characterisation of the gaseous primary liquid sodium certainly provide short-term transferable techniques for detecting/ characterising leaks in the gas PCS, especially for the above-mentioned ultrasonic techniques, but also for electromagnetic techniques. Experiments in water or sodium will be necessary to remove some uncertainty from these early studies.

4.3.Detection of sodium-water reactions

Depending on the flow rate of the water leak, different types of instrumentation must be studied for detection purposes. For flow rates below 100 g/s, hydrogen detectors were used in Phenix and Superphenix. For higher flow rates, the progress of the leak can be very fast which means that instrumentation with a very short response time (some seconds) is required; the system tested up until now was acoustic detection with an accelerometer, but it had never operated as a safety system in French reactors. At present, the work on the detection of sodium-water reactions for ASTRID is based on both types of instrumentation.

- Hydrogen detector: two hydrogen meter concepts have been studied. The first uses a conventional technology with nickel membranes used both in the Phenix [10] and Superphenix [11] reactors, which must now be updated and improved. The second is an electrochemical hydrogen meter (ECHM), recently developed by IGCAR (India), which demonstrates attractive properties [12]. Comparative tests of both different technologies were performed in the Phenix reactor during the first half of 2009 in real operating conditions at nominal power [10, 13]. The test results showed a good correlation between the various signals; the ECHM exhibited good behaviour except in response to thermal transients, while the intrinsic response time of the ECHM was slightly shorter (a few seconds) than for other systems. Further tests are planned for 2012-13 on the CEA Cadarache site using a dedicated sodium loop with both systems (a new ECHM provided by IGCAR) as part of collaboration between IGCAR and the CEA. It should then be possible to confirm the above results and the study will be particularly thorough in terms of temperature dependence and behaviour at various stress levels (sodium freeze, thermal shocks, etc.). The choice of instrumentation has not been made, but the ECHM exhibits advantages such easy operation, low cost and reliability.

- Acoustic detector: this type of instrumentation was tested in Phenix and Superphenix but never connected to the automatic safety actions. The main issue was to avoid spurious alarms. The present study for ASTRID is based on a thesis on the acoustic detection of defects or leaks inside a cylindrical fluid loaded shell, representing a defect or a leak on the secondary loop or steam generator of sodium fast reactors [14]. The use of the beamforming technique is investigated in this work to detect the position of an acoustic monopole inside a cylindrical elastic shell, from shell vibration measurements. In order to study the effect of the fluid-structure interactions and the distance of the source to the array on the beamforming, a vibro-acoustic model of the fluid-loaded shell is considered for numerical experiments. The beamforming technique is then applied to the radial velocities of the shell calculated with the model. Different parameters such as the distance between sensors, the radial source position, and the damping loss factor of the shell and the fluid can be easily considered. Analysing different results makes it possible to highlight the influence of the fluid-loaded shell behaviour on detection.

5. Conclusion and perspectives

Even though the various instrumentation systems specially designed for sodium reactors have provided satisfactory performance levels in the former French SFRs, the instrumentation for ASTRID monitoring, especially for core monitoring, has to be significantly improved to meet GEN IV requirements.

Major studies are being performed within the framework of the CEA-EDF-AREVA coordinated research programme for the development of Generation IV sodium-cooled fast reactors.

The aim is to be able to prevent any major incident by using efficient monitoring instrumentation.

Focused research on flowmeters is underway due to their ability to improve the detection of total instantaneous blockages.

The results of studies on high temperature fission chambers are very encouraging, even though they have to be completed by in-reactor qualification.

Studies on a multilayer sandwich detector for sodium leakage are also being carried out. Qualification tests have to be continued.

Finally, the use of TUSHT sensors is planned for all acoustic monitoring in the ASTRID reactor during power and handling operations.

In the case of the gas power conversion system (gas PCS), ultrasound techniques are promising for in-service monitoring in terms of detecting, locating and characterising a gas leak in the heat exchanger.

ACKNOWLEDGEMENTS

The authors would like to thanks all their colleagues at the CEA, AREVA and EDF who provided a wealth of information, guidance and technical insight, especially D. Haubensack, Ph. Filliatre, Ch. Lhuillier, K. Paumel, P. Taraud, J.S. Bailly, M. Cavaro, S. Albaladejo, D. Cambet, J. Moriot.

REFERENCES

[1] JADOT, F., and al., Astrid sodium cooled fast reactor: program for improving in service inspection and repair, Animma Inter. Conf., Ghent, Belgium 6-9 June 2011
[2] JADOT, F., and al., In-Service Inspection and Repair for the ASTRID Project: Main Stakes and Feasible Solutions, FR13, Paris, France 4-8 March 2013
[3] JEANNOT, JPH., and al., R&D Program for Core Instrumentation Improvements Devoted for French Sodium Fast Reactor, Animma Inter. Conf., Ghent, Belgium 6-9 June 2011
[4] FILLIATRE, Ph., and al., In vessel neutron instrumentation for sodium-cooled fast reactors: type, lifetime and location, ANE 37, 2010
[5] JAMMES, C., and al., Assessment of the high temperature fission chamber technology for the French fast reactor program, Animma Inter. Conf., Ghent, Belgium 6-9 June 2011
[6] LAFFONT, G., and al., Regenerated Fiber Bragg Grating sensors for high temperature monitoring in Sodium-cooled Fast Reactor, FR13, Paris, France 4-8 March 2013
[7] SHARMA, P., and al., Development, computer simulation and performance testing in sodium of an eddy current flowmeter, Annals of Nuclear Energy 37, 332–338, 2010.
[8] JEANNOT, JPh., and al., Acoustic Waves: A Route to Enhance Sodium Fast Reactor Safety, FR13, Paris, France 4-8 March 2013
[9] CAVARO, M., Contribution of nonlinear acoustic to the characterization of microbubbles clouds in liquid sodium application to the Generation IV nuclear reactors, PhD Thesis, University of Mediterrannea Aix-Maseilles II, Aix-en-provence (2010) (in French).
[10] JEANNOT, JPH., and al., In-Sodium Hydrogen Detection in the Steam Generator of PHENIX Fast Reactor : A Comparison Between Two Detection Methods, Conference ANIMMA, Marseille, France, June 7-10 2009 (2009).
[11] CASTELNAU, L., and al., SUPER PHENIX 1-steam generators protecting devices, Proceedings of the L.M.F.B.R. Safety Topical Meeting, Lyon Ecully, France, July 19-23 1982, 4, pp. 603-10 (1982).
[12] SRIDHARAN, R., and al., An electrochemical hydrogen meter for measuring hydrogen in sodium using a ternary electrolyte mixture, Journal of Nuclear Materials, 312, pp. 10-15 (2003).
[13] PAUMEL, K., and al., Comparative tests of two hydrogen-meter technologies in the Phenix reactor, Conference NPIC & HMIT 2012, July 22-26, 2012 San Diego, California US.
[14] MORIOT, J., and al., Use of beamforming for detecting an acoustic source inside a cylindrical shell filled with a heavy fluid., Mechanical Systems and signal processing, on-going review process

Development of Under-Sodium Inspection Technique Using Ultrasonic Waveguide Sensor

Y.S. JOO, J.H. BAE, C.G. PARK, J.B. KIM

Korea Atomic Energy Research Institute

Daedeok-daero 989-111, Yuseong-gu, Daejeon, Rep. of Korea

*E-mail address of main author:**Error! Unknown document property name.** ysjoo@kaeri.re.kr*

Abstract

The under-sodium inspection technique using ultrasonic waveguide sensor has been developed for the in-service inspection of a reactor core and in-vessel structures in the sodium-cooled fast reactor. The 10 m long prototype ultrasonic waveguide sensor modules have been designed and manufactured for the applications of under-sodium viewing and ranging. The real-scale test facility with a 13 m H-beam structure was constructed for the feasibility tests of the prototype ultrasonic waveguide sensor modules. The inspection program has been developed for the under-sodium inspection using the prototype ultrasonic waveguide sensor modules. The performance of the ultrasonic waveguide sensor modules has been successfully demonstrated in water. A novel under-sodium ultrasonic waveguide sensor with beryllium and nickel coating layers is suggested for the enhancement of the radiation and wetting performance of ultrasonic waveguide sensor in sodium. The sodium test facility with a glove box system and a sodium tank has been designed and fabricated to carry out the performance test of under-sodium ultrasonic waveguide sensor in sodium environment condition. The sensitivity and C-scan imaging tests have been carried out in sodium for evaluating performance of the under-sodium ultrasonic waveguide sensor.

1. Introduction

The sodium-cooled fast reactor (SFR) uses liquid sodium as a coolant which can provide thermal inertia with its high thermal conductivity. While the liquid sodium has additional advantages such as not causing corrosion in reactor structures, one of its disadvantages in an inspection viewpoint is that it is optically opaque so that the direct visual inspection of the reactor core and in-vessel structures through the coolant medium is not possible. The liquid sodium pool is kept at a high temperature (between 200-550^{o}C) and at a high level of radiation during the reactor's operation. This also makes the applications of many of the existing inspection techniques difficult. On the other hands, since the SFR operates at a low pressure in the primary circuit, the reactor vessel and structures are constructed with relatively thin and ductile stainless steel. For this reason, visual inspections based on instrumented viewing/visualization and continuous monitoring are required inspection methods for the in-service inspection of the SFR (e.g. according to ASME code, Section XI. Div. 3 [1]). Therefore, at present it is highly in demand to develop a reliable and sustainable technique that enables viewing/inspecting the reactor core and in-vessel structures in the under-sodium environment.

A few techniques based on the use of ultrasound have been developed for viewing and/or visualization of the reactor core and structures submerged in the liquid sodium pool [2-8]. These techniques are classified into two categories: techniques based on immersion ultrasonic transducers [2-4], and the other ones based on remote ultrasonic waveguide sensors [5-8]. In the first kind of techniques, a single focus ultrasonic transducer or an array of ultrasonic transducers are immersed in the liquid sodium pool. The piezoelectric elements in the transducer housing are exposed to the high temperature and high radioactive environment. These hostile environmental conditions make the

otherwise simple immersion techniques unfeasible. The lifetime of typical piezoelectric materials in liquid sodium is known to be on the order of several hundred hours. In the waveguide sensor techniques, the ultrasonic (piezoelectric) sensors are located outside the reactor and the probing ultrasonic signals are transmitted and received through a long waveguide. Recently, a plate-type ultrasonic waveguide sensor has been developed [8]. This plate-type ultrasonic waveguide sensor transmits A_0 mode Lamb wave signals from the outside of the vessel structure through an approximately 10 m long waveguide steel strip and measures signals reflected from targets in the liquid sodium pool. The plate ultrasonic waveguide sensor can thus be applied to the under-sodium inspection of SFR. Figure 1 shows the concept of the under-sodium inspection of reactor core and in-vessel structures in SFR using the plate ultrasonic waveguide sensor.

In this work, the 10 m long prototype ultrasonic waveguide sensor modules have been designed and manufactured for the application of the ultrasonic waveguide sensor to the under-sodium inspection of in-vessel structures in SFR. The experimental facility with 13 m long H-beam structure has been designed and constructed to verify the performance of the prototype ultrasonic waveguide sensor modules. And the inspection programs are developed for the control of ultrasonic waveguide sensor modules and the C-scan imaging visualization by using a LabVIEW graphical programming language [16]. The new under-sodium ultrasonic waveguide sensor with a layered-structured plate is suggested. for the the effective generation of a leaky wave in liquid sodium. The sodium test facility with a glove box system and sodium tanks is designed and manufactured. The performance of ultrasonic waveguide sensor have been verfied in sodium environment condition

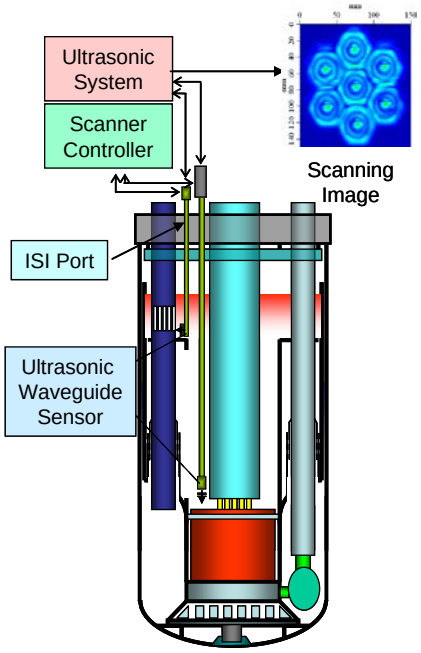

FIG.1. Application concept of the ultrasonic waveguide sensor to the under-sodium inspection of in-vessel structures in SFR.

2. Plate-type Ultrasonic Waveguide Sensor

The plate-type ultrasonic waveguide sensor consists of a thin strip plate, a wedge, and an ultrasonic transducer, as shown in Fig. 2. The liquid wedge is clamped to the top of the waveguide. The A_0-mode Lamb wave is generated in a plate by an excitation from the transducer where the compression wave is impinging at an angle α within the wedge. The generated Lamb wave at the top of the plate propagates toward theplate. If the plate is in contact with a liquid, the Lamb waves become leaky Lamb waves because the energy of the Lamb wave leaks from the solid plate to the liquid in the longitudinal wave. The normal component of a Lamb wave in a plate creates a local disturbance within a liquid, and thus the acoustic energy is lost to the liquid by the mode conversion.

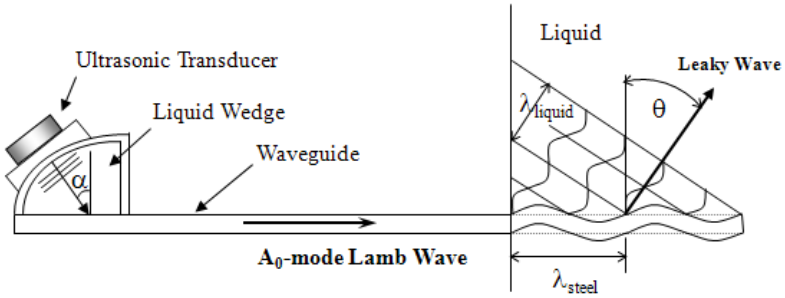

FIG.2. Plate waveguide sensor and leaky Lamb wave propagation

The radiation beam resulting from the mode conversion is emitted at an angle θ to the waveguide normal, given as

$$Sin\theta(fd) = \frac{V_L}{C_p(fd)} \tag{1}$$

where V_L is the longitudinal wave velocity in a liquid and C_p is the phase velocity of the Lamb wave in a plate

Figure 3 shows both the phase and group velocity dispersion curves of the A_0 mode in a SS304 stainless steel plate. A wedge filled with a liquid couplant or water (V_L = 1480 m/s) is used for a generation of the A_0 mode in the dispersive region (fd < 2). In the dispersive region where the products of the frequency and the thickness of the plate (fd) are below 3.5, the phase velocity depends strongly on the frequency so that a fine frequency tuning of the excitation pulse causes a change in the phase velocity. As shown in Eq. (1), the beam radiation angle θ of a leaky wave can be changed by the phase velocity of the A_0 mode. For efficient radiation beam steering in a liquid, it is important to choose the proper frequency range because the ultrasonic beam cannot be formed when the phase velocity C_p of the A_0 mode in a waveguide is equal to or less than the compressional wave velocity of a liquid, shown in Fig. 2. In the design of a waveguide sensor, the way to increase the energy loss is to enclose one side of the plate so that the liquid is in contact with only one face. The energy will then be radiated from the one face contacting with the liquid. Thus a single beam is generated from the one emission face and the radiating energy becomes double. The ultrasonic radiation beam is reflected from the object in a liquid and the reflected ultrasonic waves are received via the face of the impinging plate surface by the reciprocal mode-conversion process.

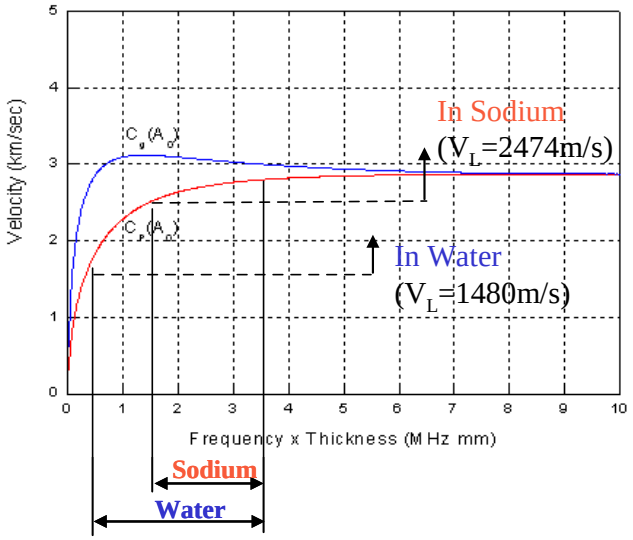

FIG.3. Dispersion curves of the A_0-mode Lamb wave in an SS304 plate

3. Feasibility Test of Waveguide Sensor in Water

3.1 Proto-type waveguide sensor module

Two prototype ultrasonic waveguide sensor modules were developed for the potential applications to the under-sodium inspection, which were designed so that it can be inserted into the ISI access port in the rotating plugs of SFR. One is the single waveguide sensor module and the other is the dual waveguide sensor module. Figure 4(a) shows the schematic design drawing of the 10 m long prototype waveguide sensor modules. The prototype ultrasonic waveguide sensor modules are comprised of the the upper head unit, the ultrasonic waveguide senors and the multistage guide tube. The single and dual waveguide sensor modules have been developed for the under-sodium viewing and ranging of one and two channel waveguide sensor, respectively. The dual waveguide sensor module can be applied to in the localized access area of the ISI port. In the upper head unit of the dual waveguide sensor module, the double rotation scanners and the stepping motors are installed for the rotation and vertical movement of the ultrasonic waveguide sensor. The dual waveguide sensor module which has the two channel waveguide sensor and the double rotation scanner can be applied for the loose part detection and identification by the self double rotation scanning. Figure 4(b) shows the manufactured 10 m long waveguide sensor modules and real-scale experimental facility. The real-scale experimental facility is composed of a 13 m long H-beam frame, a XYZ scanner, a scanner driving module, and ultrasonic C-scan system. The 13 m long H-beam frame structure was constructed to install the 10 m long prototype ultrasonic waveguide sensor modules in the vertical state. The ultrasonic C-scan system is composed of a scanning driver module, a multi-channel high power ultrasonic pulser/receiver (RITEC RAM-5000-3C), a digital oscilloscope, an A/D convert board and a personal computer.

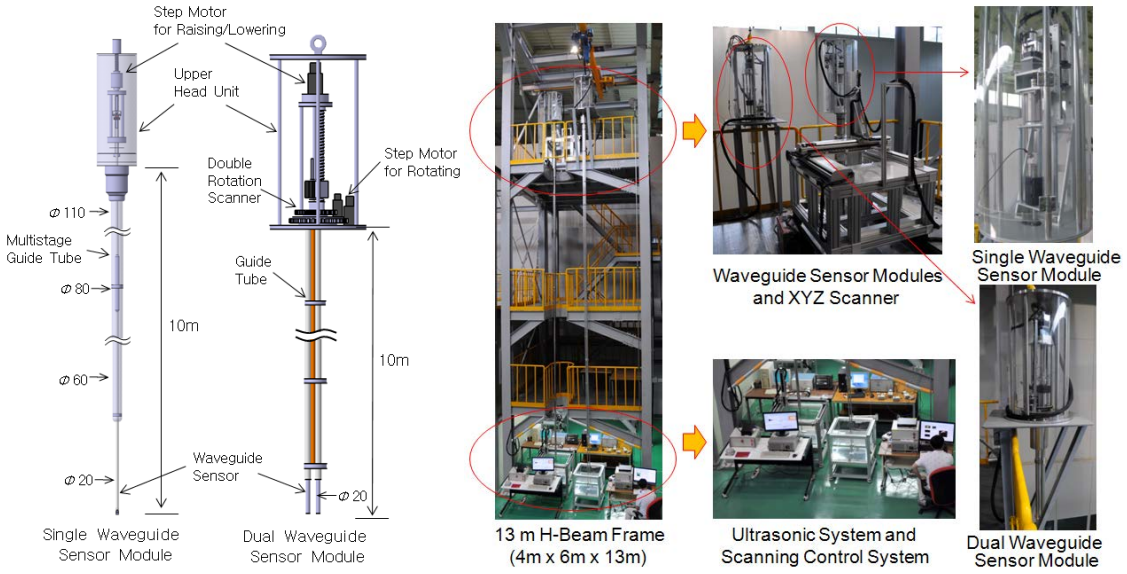

(a) Proto-type waveguide sensor modules *(b) Feasibility test facility*

FIG.4. Schematic design of proto-type waveguide sensor modules and experimental facility for feasibility test of proto-type waveguide sensor modules

3.2 Feasibility test in water

The 10 m long single waveguide sensor module was installed on the external XYZ scanner for the C-scan resolution test. The visualization imaging resolution of the single waveguide sensor module was evaluated by a C-scan test of various targets in water. The test targets are a reactor core mock-up, loose part pins and surface slit flaws on the block. The reactor core mockup and loose part pins were clearly identified in the C-scan images and the slit flaws could be resolved in the C-scan image, as

shown in Fig. 5. It was verified that a spatial resolution of the C-scan image for the detection of a surface flaw is about 0.8 mm in water.

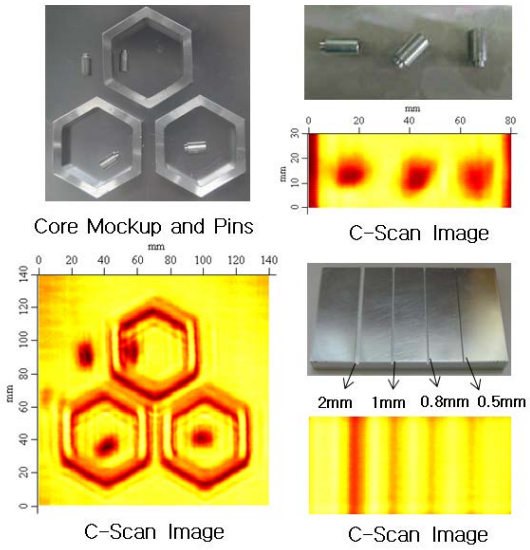

FIG.5. Visualization image of reactor core mock-up, loose parts and slits by the single waveguide sensor module

In the dual waveguide sensor module, the first channel of the waveguide sensors provide the 0 degree vertical beam and the second channel provide the 45 degree angle beam. The dual waveguide sensor module can be applied for the vizualization and identification of the missing loose parts which one waveguide sensor emitting the 0 degree vertical beam is used for the C-scan vizualization and the other one radiating a 45 degree angle beam is used for the identification.

The under-sodium visualization program which is named as Under-Sodium MultiView (US-MultiView) has been developed to control the double rotation scanner, the acquisition of ultrasonic signals and the mapping of the scanning images by using LabVIEW software. The performance test was performed for the C-scan imaging and loose part identification using the dual waveguide senor modules and US-MultiView program. The C-scan mapping and radiation pattern mapping of a loose part pin were achieved by the internal double rotation scanning in the ultrasonic waveguide sensor module at the localized area. The loose part pin can be detected and clearly identified, as shown in Fig. 6.

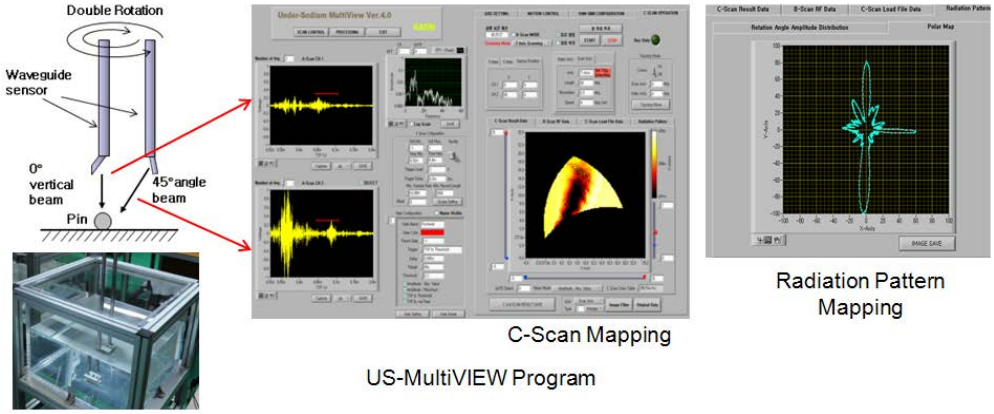

FIG.6. US-MultiView program : C-scan visualization image of loose part pin by using the dual waveguide sensor module

4. Performance Test of Waveguide Sensor in Sodium

4.1 Under-sodium waveguide sensor

To apply the ultrasonic waveguide sensor to under-sodium inspection, the phase velocity of the A_0-mode Lamb wave should be faster than the longitudinal wave velocity V_L (2.474 m/ms) of liquid sodium. Then, the A_0-mode Lamb wave is mode-converted into a leaky longitudinal wave and an ultrasonic beam can be radiated through the radiation face of the waveguide sensor. The novel under-sodium ultrasonic waveguide sensor formed of an SS304 stainless steel plate provided with beryllium (Be) coating layers was developed for the effective generation of a longitudinal leaky wave in liquid sodium [9]. The beryllium (Be) is a material of which the ultrasonic velocity is fastest among materials that exist in nature. The longitudinal wave velocity of beryllium (Be) is 12890 m/s and is twice as fast as the longitudinal velocity (5790 m/s) of a SS304 stainless steel plate. When the waveguides are formed of an SS304 stainless steel plate with the coating layers made of beryllium (Be), the phase velocities of the A_0-mode Lamb wave propagated through the waveguides are remarkably increased as compared with those of the A_0-mode Lamb wave propagated through the SS304 waveguide plate provided with no coating layer as shown in Fig. 7. Therefore, the ultrasonic beam of a leaky longitudinal wave could be radiated through the radiation face of the beryllium-coated waveguide sensor in liquid sodium with the wider range of the radiation beam angle.

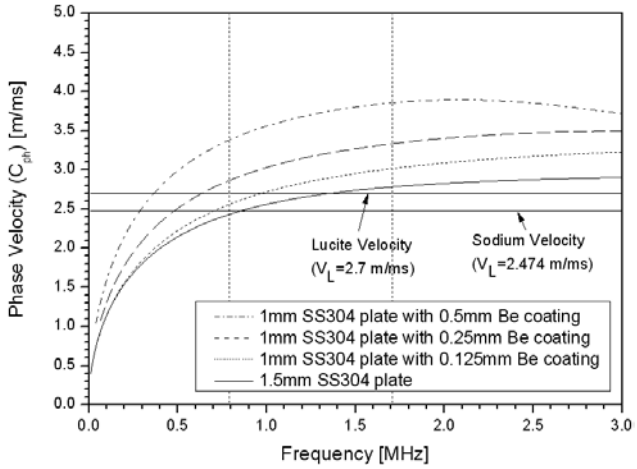

FIG.7. Dispersion curves of the A_0-mode Lamb wave of Be-coated SS304 plates

4.2 Sodium test facility

The sodium test facility was designed and manufactured to carry out the performance test of ultrasonic waveguide sensor in sodium environment condition. Figure 8 shows the photograph of the sodium test facility. The sodium test facility consists of a glove box with an anti-chamber, an open-type sodium test tank with a volume of 30 liters, a sodium drain tank with a volume of around 70 liters, an electric resistance heater, a heater control unit, an Ar circulation and cooling system, a XYZ scanning system and an under-sodium ultrasonic waveguide sensor. The XYZ scanning system is comprised of the XYZ scanner and the scanning control and mapping system. All components of the test device in contact with sodium or sodium vapor were made of SS304 austenitic stainless steel. The sodium test tank for conducting the under-sodium scanning tests is enclosed in a glove box system providing a volume of 1200 mm x 800 mm x 1000 mm. The sodium test tank is a vertical cylindrical vessel, whose dimensions were 30 cm in diameter and 55 cm in height. In the glove box system, an argon gas is used as an inert cover gas. The argon gas is circulated to provide the cooling of the glove box system. A cover gas purification system was installed on the glove box, and the glove box should be maintained an atmospheric purity of 1 ppm of oxygen and 0.1 ppm of moisture during the sodium experiments. The XYZ scanner is installed in the glove box. The scanner is driven by stepping motors. The test specimen is mounted on the XYZ scanner. The test specimen is put into the pool of sodium tank. The scanner is capable of moving an area of 150 by 150 mm. The scanning control and mapping

system consists of the industrial computer, the motor control board, and ultrasonic A/D board. The Winspect C-scan software program will be used for the control of scanner and the C-scan image mapping.

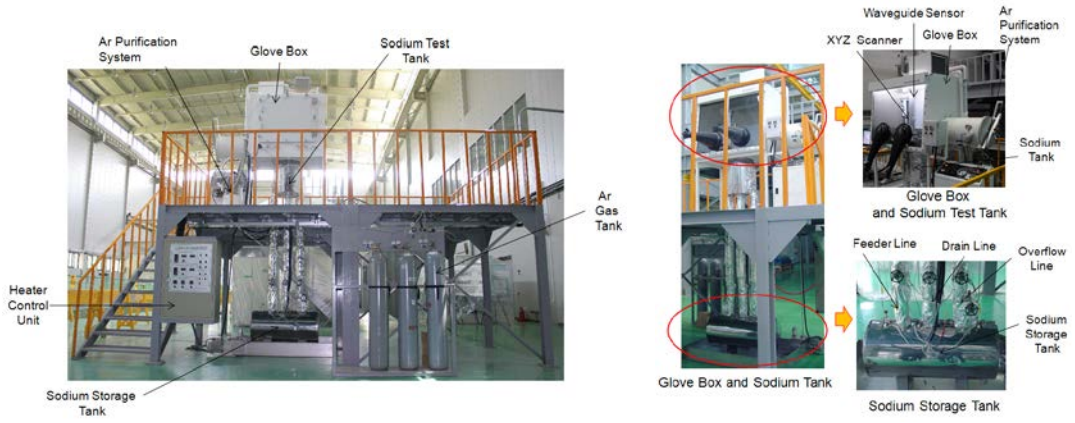

FIG.8. Photograph of sodium experimental facility for the under-sodium performance test of ultrasonic waveguide sensor

4.3 Performance test in sodium

The 1.7 m and 10 m long under-sodium ultrasonic waveguide sensors have been designed and manufactured. Figure 9 shows the schematic drawing and photograph of the under-sodium ultrasonic waveguide sensors. The waveguide (WG) sensors consist of an ultrasonic transducer, a Teflon wedge, a waveguide strip plate, an acoustical shielding tube, and a bellows as shown in Fig. 9 (a). A commercial PZT transducer (1 MHz, 0.5" diameter) is used. A Teflon wedge is designed to launch an A_0 mode Lamb wave in the plate strip since the longitudinal velocity in Teflon (1270 m/s) is lower than the phase velocity of the A_0 lamb wave in the operating frequency range. The 1.7 m and 10 m long strip plate of the waveguide sensor is 15 mm wide and 1.5 mm thick SS304 stainless steel plate. The acoustical shielding tube is a 19 mm diameter, 1 mm thick SS304 stainless steel tube. In the design for the beam radiation part of the waveguide sensor submerged in liquid sodium, only the front face of the strip plate is exposed to be in contact with the liquid sodium thus providing one radiation face. The bending angle of the beam emission face at the tube end section is determined so that the emerging beam is vertically directed. The bellows is installed in the middle of the shielding tube for the adjustment of the vertical direction of the under-sodium waveguide sensor. An argon (Ar) gas is injected into the shielding tube to prevent the sodium-water reaction in the leak-break accident of the under-sodium waveguide sensor. In the inside surface of radiation end section, a beryllium is coated with the thickness of 0.25 mm to decrease the radiation angle in sodium. On the outside surface of radiation end section, a nickel with the thickness of 0.1 mm is coated and micro-polished to improve the sodium wetting capability.

The under-sodium ultrasonic waveguide sensor mounted with a flange is installed throughout the roof of the glove box and inserted in the sodium test tank. The radiation section of the waveguide sensor is submerged into the sodium pool of the sodium tank, as shown in Fig. 10. The under-sodium ultrasonic wave propagation test has been carried out in the sodium test tank using the under-sodium ultrasonic waveguide sensor. The sensitivity of the 10 m under-sodium ultrasonic waveguide sensor is evaluated by a measurement of the received ultrasonic signal from a flat reflector in sodium. Figure 11 (a) shows the typical ultrasonic pulse-echo signal which has the initial pulse, the reflection signals from the top end and radiation end sections of under-sodium waveguide sensor. Figure 31 (b) shows the enlarged reflection signal from the radiation end section of the under-sodium waveguide sensor in the case of the installation of the test target (flat stainless steel block) in sodium test tank. The test target is placed in water a 50 mm away from the end section of the waveguide sensor. The reflection signal from the flat test target in sodium has the amplitude of 28 mV and the maximum amplitude of the background noise level in the transit ultrasonic signal has the amplitude of 8 mV. So, the signal-to-noise (S/N) ratio of the reflection echo signal from a test target in sodium was measured as the level of

10 dB. C-scan imaging test was performed for the verification of under-sodium visualization performance of the 10 m long under-sodium ultrasonic waveguide sensor. Figure 12 shows the C-scan results of test target with protrude defects and loose parts by the under-sodium waveguide sensor module in sodium. The loose part reflectors were partially identified and also the protrude defects were clearly resolved in the image. Figure 12 (b) shows the C-scan results of the SFR character specimen with an engraved slit (width = 2 mm). The C-scan image of SFR character was clearly identified and resolved. These results manifest that the 10 m long under-sodium ultrasonic waveguide sensor has the performance to achieve the C-scan image in sodium.

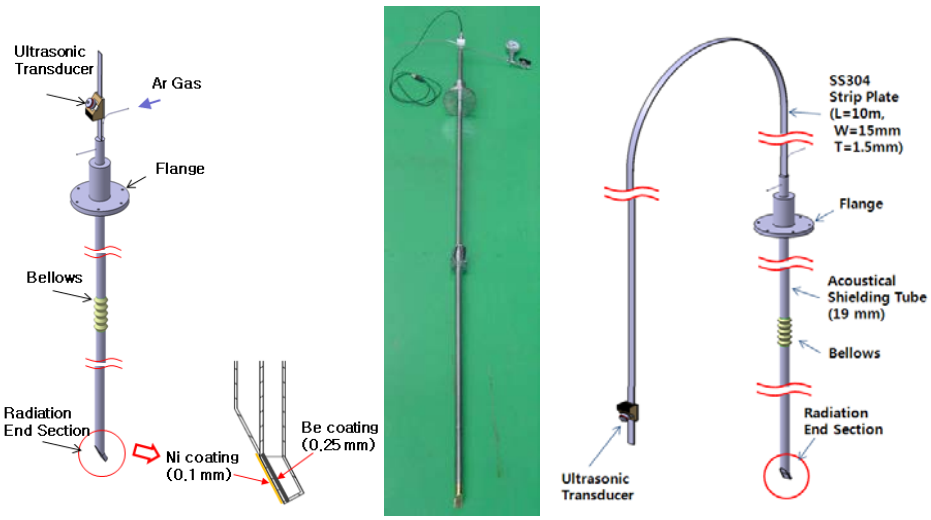

FIG.9. Schematic view and photograph of the 1.7 m and 10 m long under-sodium waveguide sensors

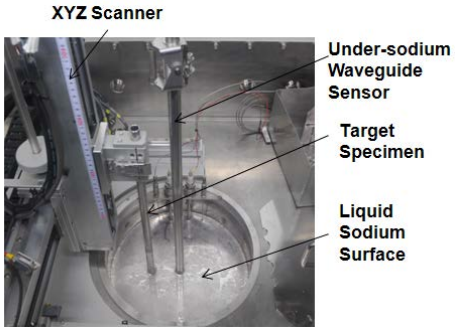

FIG. 10. Performance test of the under-sodium waveguide sensor in sodium

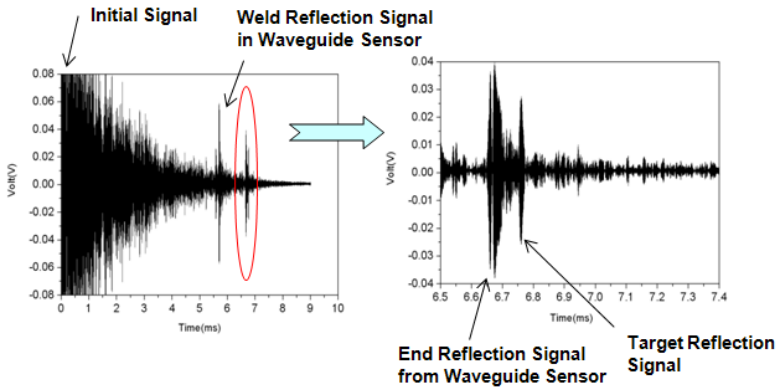

FIG.11. Typical ultrasonic pulse-echo signal obtained in a sensitivity test of the 1.7 m under-sodium waveguide sensor in sodium

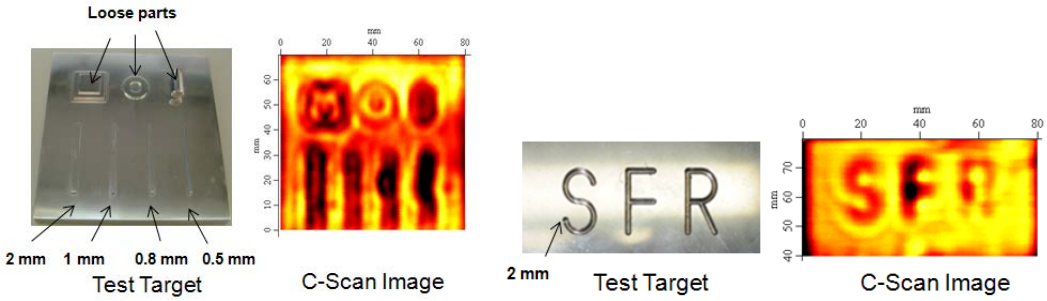

(a) Protruding defects *(b) Engraving defects*

FIG.12. C-scan test results of the 10 m under-sodium waveguide sensor in sodium

5. Conclusion

The plate-type ultrasonic waveguide sensor has been developed for the under-sodium inspection of a reactor core and in-vessel structures in the sodium-cooled fast reactor (SFR). The prototype 10 m long ultrasonic waveguide sensor modules have been developed for the under-sodium inspection of a reactor core and in-vessel structures in SFR. The test facility with H-beam structure has been designed and constructed for the feasibility tests of ultrasonic waveguide sensor modules. The feasibility of the ultrasonic waveguide sensor modules has been successfully demonstrated in water environment condition. The under-sodium ultrasonic waveguide sensor with a beryllium (Be) coating layer on the waveguide plate was suggested for the enhancement of the radiation performance in sodium. The sodium test facility with a glove box system, an argon purification system and a sodium tank has been designed and constructed. The under-sodium ultrasonic waveguide sensor modules with a beryllium coating layer was designed and manufactured. The basic performance tests, such as ultrasonic beam propagation test and C-scan imaging test have been carried out for evaluating performance of the under-sodium ultrasonic waveguide sensor in sodium environment condition. The visualization performance has been successfully demonstrated in liquid sodium environment.

ACKNOWLEDGEMENTS

This study was supported by the Ministry of Education, Science and Technology of Korea.

REFERENCES

[1] ASME B&PV Code, Section XI, Division 3, *Rules for In-service Inspection of Nuclear Power Plant Component*, (1992)

[2] J.P. Argous, M. Brunet, J. Baron, C. Lhuillier, J.L. Segui, "Immersed Acoustical Transducers and Their Potential Uses in LMFBR," *Int. Conf. on Liquid Metal Technology in Energy Production*, CEA-CONF 5257, (1980)

[3] R. Hans, E. Kranz and H. Weiss, "Under-Sodium Viewing – A Method to Identify Objects in an Opaque Medium," *Liquid Metal Engineering and Technology*, BNES, London, pp. 419~423 (1984)

[4] H. Karasawa, T. Susuki, S. Nagai, M. Izumi and T. Kobayashi, "Development of Under Sodium Inspection Techniques for FBR", *Proceedings of ICONE 4*, Vol. 1 Part B, pp. 605-613 (1996)

[5] R.D. Watkins, L.M. Barrett and J.A. McKnight, "Ultrasonic Waveguide for Use of the Sodium Coolant of Fast Reactors," *Nucl. Energy*, **27 (**2) , pp. 85-89 (1988)

[6] N. Lions, R. Berger, A. Bret, H. Buis and J. Barton, "Apparatus for Ultrasonic Visualization in Sodium (VISUS) and Acoustic Detection in the Phenix Reactor," ORNL-TR-4136, (1973)

[7] K.Wang, H.T. Chien, T.W. Elmer, W.P. Lawrence, D.M. Engel, and S.H. Sheen, "Development of Ultrasonic Waveguide Techniques for Under-Sodium Viewing", *NDT&E International* **49**, pp. 71-76 (2012)

[8] Y.S. Joo, C.G. Park, J.H. Lee, J.B. Kim, S.H. Lim, Development of Ultrasonic Waveguide Sensor for Under-Sodium Inspection in a Sodium-cooled Fast Reactor, *NDT&E International* **44**, pp. 239-246 (2011)
[9] Y. S. Joo, J. H. Bae, J. B. Kim and J. Y. Kim, "Effects of Beryllium Coating Layer on Performance of the Ultrasonic Waveguide Sensor," *Ultrasonics*, **53**, *2*, pp. 387-395 (2013)

Design Features of a Large-scale Sodium Thermal-hydraulic Test Facility: STELLA

J.H. EOH, H.Y. LEE, T.J. KIM, J.Y. JEONG, Y.B. LEE

Korea Atomic Energy Research Institute

Daedeok-daero 989-111, Yuseong-gu, Daejeon, Rep. of Korea

*E-mail address of main author:****Error! Unknown document property name.*** *jheoh@kaeri.re.kr*

Abstract

A large-scale sodium thermal-hydraulic test program called STELLA (Sodium Test Loop for Safety Simulation and Assessment) and its first test facility aiming at a performance demonstration of the major components and their design codes verification & validation (V&V) were introduced with the preliminary computational fluid dynamic (CFD) analysis results for assessing the thermal-hydraulic performance of the major test heat exchangers, e.g. DHX (sodium-to-sodium decay heat exchanger) and AHX (sodium-to-air heat exchanger). An integral effect test facility design simulating a pool-type sodium-cooled fast reactor(SFR) was also carried out on the basis of reasonable scaling approach. For the reduced height scale of 1/5, a similarity in heat transfer between solid and fluid were intensively discussed together with its distortion, and viable design parameters for the test facility were obtained. A one- and three-dimensional verification calculation were also made and showed good agreements for the key design parameters. This scaling approach in this study is expected to be used in an exact reproduction of transient behaviors in a prototype SFR system.

1. Introduction

According to the long-term fast reactor development plan of the Korean government, a prototype sodium-cooled fast reactor (SFR) will be constructed by 2028. The Korean prototype SFR is currently being developed along with basic key technologies of KAERI (Korea Atomic Energy Research Institute), which employs highly reliable safety-grade decay heat removal systems. In regard to the verification of decay heat removal performance, a large-scale sodium thermal-hydraulic test program is being developed by KAERI. This program is called STELLA (Sodium Test Loop for Safety Simulation and Assessment), and finally aims at the construction of an integral effect test facility subject to the prototype SFR. At the first step of the STELLA program, the first sodium test facility (hereafter called STELLA-1) was completed at the KAERI site, and it will be used for thermal-hydraulic testing of major components such as heat exchangers and mechanical sodium pump representative of the prototype SFR system.

The second step of the STELLA program includes an integral effect test is called STELLA-2, which will be constructed to demonstrate the plant safety and to support the specific design approval for the prototype SFR system in Korea. Starting with the conceptual design of the prototype in fiscal year 2012, the basic and detailed design of the test facility reflects the whole design features of the prototype system will be performed subsequently based on the design requirements of the integral effect test facility. The STELLA-2 facility is scheduled to be installed by the end of 2016. The main

experiments including the start-up tests will begin in 2017. The overall schedule of the STELLA program described above is summarized in Figure 1.

This study briefly introduces the overall design features of the STELLA-1 facility and provides the preliminary CFD analysis results to assess the thermal-hydraulic performance of the DHX and AHX test heat exchangers of DHX(sodium-to-sodium decay heat exchanger) and AHX (sodium-to-air heat exchanger). At the first step of the STELLA-2 design, scientific design parameters have been obtained by using proper scaling methodologies complying with the reduced-height scale of 1/5 . Some design restrictions imposed on the scaled components design and the scaling distortions of the prototype are discussed as well.

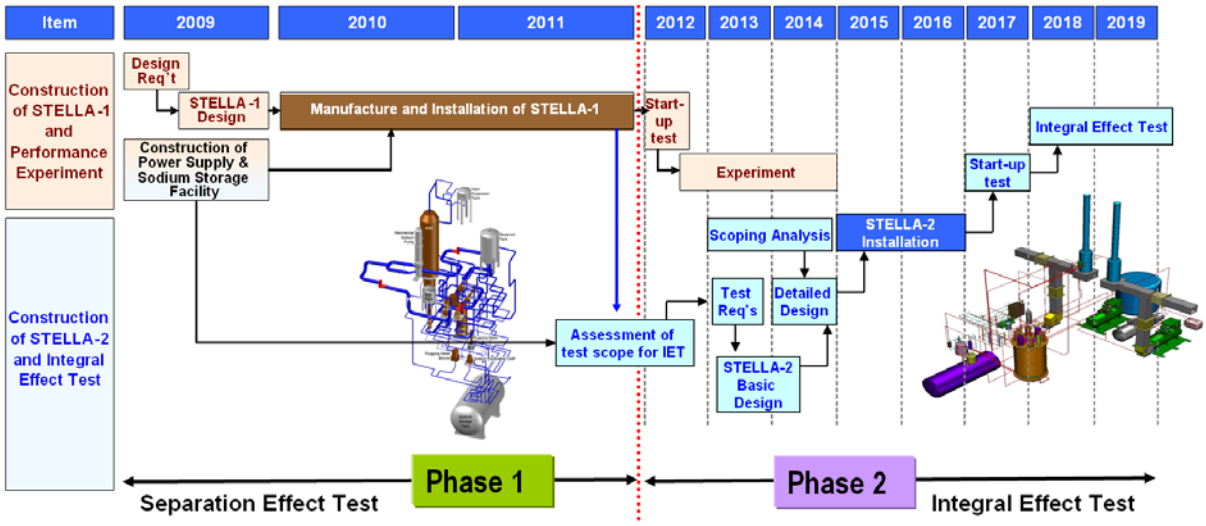

FIG.1. Overall schedule of the STELLA program

2. Design Features of the STELLA-1 facility

2.1 Loop constitution and test scope

STELLA-1 consists of a main test loop, a sodium purification system, and a gas supply and related auxiliary systems. The main components of this facility are a sodium-to-sodium heat exchangers, sodium-to-air heat exchanger, mechanical sodium pump, loop heaters, cold trap, plugging meter, electromagnetic pumps, flow meters, and a sodium storage tank. The general arrangement of the STELLA-1 facility is shown in Figure 2.

The maximum design temperature of the facility is 600^{o}C, and the designed power capacity of the main heat exchangers, such as the sodium-to-sodium and sodium-to-air heat exchanger, are 1MWt. The maximum electric power putting into the facility is around 2.5MWt, and the nominal liquid sodium flow rate supplying the test heat exchangers is designed to be less than 10 kg/sec. During the mechanical pump test, more than 120kg/sec of liquid sodium circulates along 10-inch diameter pipes.

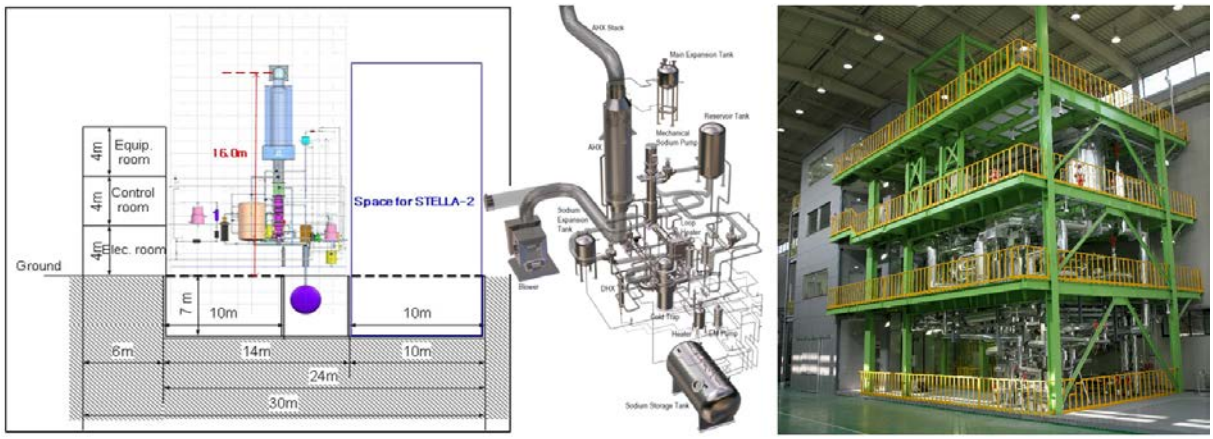

FIG.2. General arrangement of STELLA-1 facility with images of the structures

The sodium purification system consists of main equipment, such as a cold trap, tanks, an electromagnetic pump, and a closed loop piping system. In the purification system, liquid sodium is circulated by the electromagnetic pump and cooled down in the cold trap. The cold trap purifies the sodium by removing the impurities in the liquid sodium. The cold trap is composed of a trap, a mesh-packing, a heater, and a cooling blower. The impurities in liquid sodium are removed by capturing them at the mesh-packing in the cold trap after the temperature falls below their solubility level. Finally, the purified sodium returns to the main sodium loop. The plugging meter is an on-line measuring device for impurities contained in liquid sodium. It is designed to control the temperature of sodium in a cooling or heating pipe and extract sodium impurities by manipulating their saturated solubility. The plug temperature is measured at the point where the sodium flow rate decreases or goes down to zero.

A kind of separate effect test for assessing the performance of heat exchangers and the mechanical sodium pump has been planned. The sodium-to-sodium heat exchanger tests will be performed to investigate the rate of heat transfer through the tube wall by hot and cold sodium loop operation. In regard to the sodium-to-air heat exchanger tests, the heat transfer performance from liquid sodium flow inside the tubes to the air flow will be investigated by cooling the external tube surface with ambient air. To evaluate the heat removal capability in passive mode, a natural circulation flow inside a sodium loop piping is also investigated using a bypass of the electromagnetic pump. The mechanical sodium pump test will also be performed to simulate prototype pump performance. The test will be performed using the pump test loop of the STELLA-1 facility. The pump test loop consists of a reservoir, pipes, valves, and a vertical test pump unit, which is equipped with various sensors for measuring the flow rate, temperature, liquid sodium level, etc. The test will be performed to investigate the pump performance during normal operating conditions and during transient operations using a flywheel.

2.2 Design features of the test components

The reference design of the STELLA-1 test components is the demonstration SFR(600MWe capacity) developed by KAERI[1]. To reproduce both hydrodynamic and thermodynamic similarities to the prototype plant with a natural circulation flow, proper scaling methods to preserve the performance of each component have been implemented in the STELLA-1 design. According to the design requirements, the test heat exchangers were scaled and designed to preserve the overall heat transfer coefficient (U) and the log-mean temperature differences (LMTD) of the prototype. To verify the heat exchanger design codes, all scaled heat exchangers have an identical tube size, arrangement, and materials as those of the prototype, and the pressure drop, flow rate, and heat capacity are also determined complying with the overall scaling criteria.

FIG.3. Images of the test heat exchangers of STELLA-1

On the basis of the comparison results of the full-height and reduced-height scaling concept[1], the overall scale ratio of the test heat exchangers is determined to be unity for the height (or length) and 1/9 for power level (or volume). The electric power source supplied into the test facility and the space for its installation were also considered in the determination process. The material of the shell- and tube-side of the DHX and AHX unit are Mod.9Cr-1Mo steel (ASME Grade 91; Gr.91) and austenitic stainless steel type 316, respectively. The images of the test heat exchangers installed in the STELLA-1 loop are shown in Figure 3, and the general specifications of each scaled heat exchanger are summarized in Table 1[1].

TABLE 1. Design parameters of the test HXs

Parameters	Design value	
	DHX	AHX
Tube arrangement	Straight	Helical
No. of tubes(tube row)	42 (N/A)	36 (3)
Tube O.D / I.D (mm)	21.7 / 18.4	34.0 / 30.7
Tube thickness (mm)	1.65	1.65
Active tube length (m)	1.73	23.76
Tube material	M.9Cr-1Mo	STS316
Shroud I.D (m)	0.298	1.53
Shroud length (m)	2.456	5.66
Unit total mass (kg)	~275	~3,483

Based on the scaling consideration, the heat capacities of the scaled heat exchangers and the shell- and tube-side flow and temperature conditions were reasonably determined in accordance with the scaling ratio. The detailed component design, manufacturing and installation processes have been completed by considering the design features of each test heat exchanger, and preliminary CFD analyses were also made to check their thermal-hydraulic performance.

In the scaling process of the test pump, the similarities between the model and prototype pump, such as speed, developing head and capacity, were properly preserved to secure the performance of the test pump. These relationships can be arranged and represented as a single design parameter of the specific velocity. To this end, the scaling work has been carried out on the basis of the identical specific speed to preserve its performance. The scaled model pump has the same configurations to the prototype except the inlet and outlet duct or nozzle shape, which should be modified by considering the physical connection to the main test loop piping. Developing head, speed and capacity of the model pump were adjusted within the practical and feasible operation range to keep the same specific speed. In the preliminary component design of the model pump, the reasonable length scale of the prototype sodium pump was determined to be approximately 1/4. The design specifications of the model pump are summarized in Table 2, and its configuration is shown in Figure 4 with real images. The process of design,

TABLE 2. Design parameters of the model sodium pump

Parameters	Prototype (P)	Model (M)	Ratio (M/P)
Capacity (kg/sec)	4183	122.6	3 %
Head (m)	62.888	50.31	80 %
NPSH available (m)	14.702	11.76	-
Synchronous speed (rpm)	450	2235	497%
Impeller O.D.(mm)	1685	305.0	18 %
Pump speed (rpm)	433	2140	-
Specific speed (-)	330.3	330.3	-
WHP (kW)	2572.7	60.3	-
Pump efficiency (%)	80.0%	71.8%	-
Motor output (kW)	4000.0	110.0	-

manufacturing and installation have been already completed, and the main test of the model sodium pump will begin in 2013 fiscal year complying with the schedule of STELLA-1 operation.

2.3 CFD analysis for the scaled heat exchangers

In this section, the CFD analysis results for the test heat exchangers are provided to confirm the thermal-hydraulic performance at a complicated heat transfer tube arrangement. In general, the design of the test heat exchangers were completed by using a one-dimensional design approaches with reasonable heat transfer and pressure drop models based on various empirical formulas. The thermal sizing process of the heat exchangers is basically carried out for a single-tube system, and then the results are extended to an N-tube system complying with the methodical tube arrangement. Hence, three-dimensional CFD analyses for the designed heat exchangers need to be performed to confirm the multi-dimensional flow characteristics coming from a complicated heat transfer tube arrangement in a practical situation.

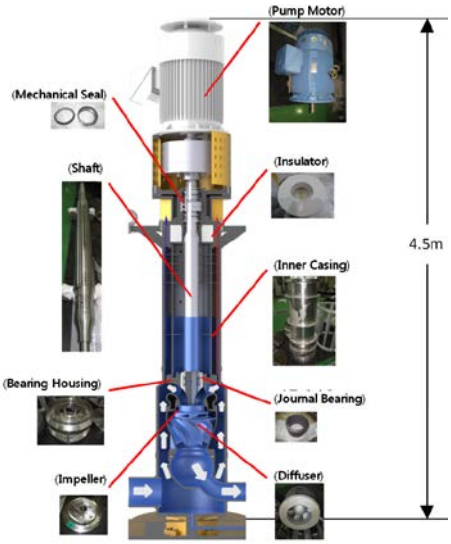

FIG.4. Shape of the model pump

Based on the thermal-sizing results of the scaled DHX, a CFD analysis for the full-shape unit was performed to assess the thermal-hydraulic performance of the scaled DHX by using STAR-CD[2]. One of the main concerns of the work was to investigate the nozzle effect at the inlet and outlet region connecting to the main test loop piping. Actually there are two grid-spacers in the DHX shell-side flow region, and one of them is installed just below the inlet nozzle part. This is to mitigate or remove an undesirable flow and temperature distribution in the shell-side DHX flow region due to the impractical nozzle connection. Figure 5 shows the results of CFD analysis for the scaled DHX unit. From the CFD analysis results, it was found that the temperature and velocity distributions of the DHX shell- and tube-side sodium flow seem to be reasonable along each flow direction. The difference of the calculated heat transfer rate between the one-dimensional approach and the CFD analysis was less than 5%, which means the one-dimensional approach is practicable to the thermal sizing and design work. It was also found that the anti-vibration grid spacer also contributes to the flow stabilization in the shell-side flow region.

Since the scaled AHX design is basically performed by using a one-dimensional design approach based on several empirical correlations regarding heat transfer and pressure drop, the multi-dimensional effect of air flow passing the helically-coiled tube bundle region needs to be evaluated to confirm the feasibility of thermal sizing and design methodology. On the shell-side AHX, the air flow is assumed to be a cross-flow across a tube bank composed of helically-coiled tube bundles. Therefore, to assess the thermal-hydraulic performance of the scaled AHX, a CFD analysis for the full-shape unit was performed also using STAR-CD[2].

Figure 6 shows the results of a CFD analysis for the scaled AHX unit, and it was found that the temperature and velocity distributions of the shell-side air and tube-side sodium flow seem to be reasonable along each flow direction. The difference of the calculated heat transfer rate between the one-dimensional approach and the CFD analysis was less than 5% when we use an alternating winding method for the helically-coiled tubing system. That is, two kinds of tube arrangements distinguished by the winding method of helical tubes were considered. One is based on the winding with an aligned direction for all tube rows, and the other is with alternating directions for every other tube row.

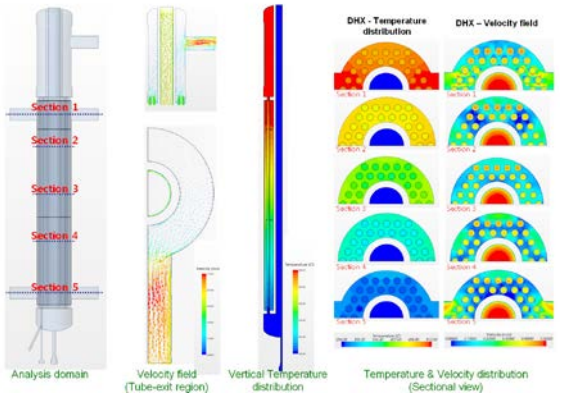

FIG.5. CFD analysis results of the scaled DHX

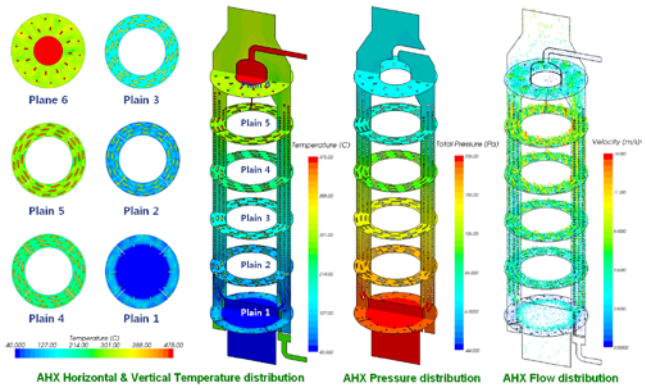

FIG.6. CFD analysis results of the scaled AHX

The results of a previous study[3] show that the air flow of the aligned winding model swirls over the helical tube bundle, and there is a rare turbulence effect caused by a cross-flow passing the horizontal tube bank. Hence, the alternate tube row arrangement contributes toward mitigating the flow separation around the rear surface of the heat transfer tubes across the flow direction. This means that the conventional AHX design with alternate winding method is feasible and has better performance in terms of heat transfer.

3. Design Features of the STELLA-2 facility

3.1 System description of the reference design

The reference design of the STELLA-2 facility is a demonstration SFR with 600MWe capacity[4]. The system employs a pool-type primary heat transport system (PHTS), a two-loop intermediate heat transport system (IHTS), a steam generator system (SGS) and a decay heat removal system (DHRS). The main thermal-hydraulic components of the system consist of steam generators (SGs), intermediate heat exchangers (IHXs), mechanical sodium pumps, and several types of heat exchangers for a DHR system, such as a sodium-to-sodium decay heat exchanger (DHX), a helically-coiled sodium-to-air heat exchanger (AHX), and a finned-tube sodium-to-air heat exchanger (FHX)[3]. Auxiliary systems including gas supply and a sodium purification system are also equipped to maintain the overall sodium coolant boundary.

The DHRS comprises two diverse decay heat removal loops composed of active and passive DHR paths, and both of them remove heat from the primary sodium inventory using DHXs, and reject the heat load to the environment using different types of sodium-to-air heat exchangers located on top of the reactor or auxiliary buildings[3]. DHRS provides a highly reliable heat rejection capability from the primary system in case of an unavailability of the main heat transport path from the PHTS to the water/steam system via the IHTS. Each system is able to fulfill the functional requirements for decay heat removal even in case of a complete loss of a single DHR loop. For the demonstration of short- and long-term decay heat removal capability by natural circulation in the safety-grade DHRS and the PHTS, a large-scale sodium thermal-hydraulic test facility called STELLA-2 has been preliminarily designed on the basis of the following design requirements for the test facility[3].

3.2 Facility design requirements

The scaled test facility should be designed in a way to preserve the overall system behavior and reproduce the major thermal-hydraulic phenomena in the conditions which correspond to the test objectives. Since the experimental facility should be designed so as to simulate the various thermal-hydraulic phenomena, as closely as possible, to be occurred in the reference reactor during the decay heat removal operation, the design characteristics of the reference plant were analyzed for drawing major constitutive elements to be simulated in the experimental facility. The priority of various thermal-hydraulic phenomena which should be considered in the design of the experimental facility was determined on the basis of PIRT(phenomena identification and ranking table) analyses for the reference plant, and the general design requirements for the experimental facility were established [4].

The STELLA-2 main test section is composed of the PHTS, IHTS and the DHR system, which covers the whole system except the feedwater system. Design basis events will be simulated under the real boundary conditions. The simulation capabilities of general transients during the design basis events should be assessed by considering several limitations such as cost and space. On the basis of the tentative evaluation results for the full-height and reduced height concept, the facility scale was determined to be 1/125 in volume and 1/5 in height. Maximum simulated core power is 7% of the scaled nominal power, and Electrical heater design should be practically possible to construct[3].

3.3 Scaled design of the system and components

In order to represent important thermal-hydraulic phenomena in the reference plant, the main test section should be designed complying with a proper scaling method for geometric, hydrodynamic and thermal similarities. In general, it is hardly possible to reproduce both hydrodynamic and thermodynamic similarity on any scaled system or equipment other than the prototype itself. Hence, model simulations for the heat transport paths have been based on hydrodynamic consideration only. However, since it is unreasonable to ignore heat transfer entirely in natural convection flow, both hydrodynamic and thermodynamic similarity in the scaled test facility should be considered even though both similarities cannot be achieved simultaneously. For this reason, various scaling methodologies have been considered by implementing mathematical identity of analogous physical features to the prototype system.

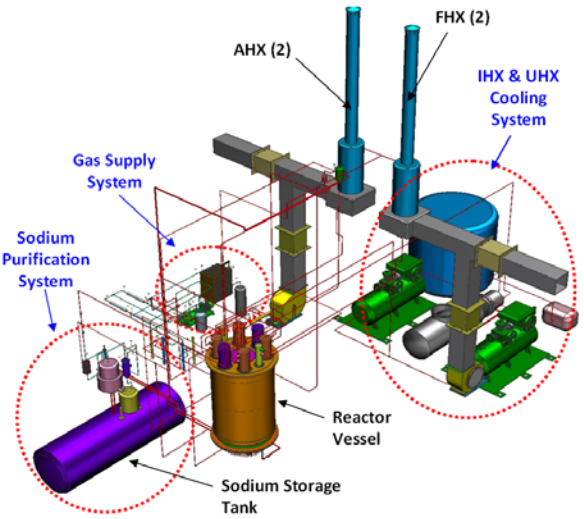

FIG.7. Preliminary layout of the STELLA-2 facility

TABLE 3. Key design requirements

Parameters	Scaling Law	Values
Length	l_R	1/5
Diameter	d_R	1/5
Area	$a_R\ (=d_R^2)$	1/25
Volume	$a_R\ l_R$	1/125
Temperature distribution	1	1
Time	$l_R^{1/2}$	1/2.24
Velocity	$l_R^{1/2}$	1/2.24
Power/volume	$1/\ l_R^{1/2}$	2.24
Core power	$a_R\ l_R^{1/2}$	1/55.9
Mass flow rate	$a_R\ l_R^{1/2}$	1/55.9
Pressure drop	l_R	1/5
Aspect ratio	$l_R\ /\ a_R^{1/2}$	1

The three-level scaling methodology of Ishii et al.[5] has been applied to the facility design, which consists of integral scaling, boundary flow scaling and local phenomena scaling. It is considered to be suitable for preserving the natural circulation phenomena in the reduced-height scale facility. The overall system design parameters are drawn by the integral scaling criteria which are produced based on the one-dimensional system balance equations of mass, momentum and energy, and the boundary condition at the interface between fluid and solid. Also, the important components such as the heat exchangers, the primary pump and the core simulator are designed by preserving the local thermal-hydraulic phenomena related with the corresponding components. The key scaled design requirements derived from the scaling criteria are summarized in Table 3.

According to the test requirements[3], the major concerns of the transient in the prototype plant are a total loss of flow accident (LOF, loss of low), loss of feedwater accident (LOHS, loss of heat sink), and PHTS pump discharge line break accident(pipe break). Therefore, the principal phenomena are the mass and energy inventory, heat transfer between solid and fluid, pump behaviors, and multidimensional phenomena, which have to be considered in a bottom-up approach.

3.3.1 Overall configuration of the test facility

The STELLA-2 facility is composed of the main test section and the auxiliary systems. The main test section includes all major components reflecting the realistic configuration. The PHTS mainly

consists of a reactor vessel with the same internal structures as the prototype plant, a core simulator, four intermediate heat exchangers (IHX) and two primary pumps. In the DHR system, there are four DHXs, two AHXs, two FHXs, a expansion tanks and the connecting pipes between DHX and AHX and/or FHX. Two ultimate heat exchangers (UHXs) are used to simulate the SGS and feed water system in the prototype plant, which is composed of a finned-tube sodium-to-air heat exchanger to provide enough heat sink capability to make the system heat balance and adequate boundary conditions. The capacity of the single UHX unit is basically scaled from the prototype SG by considering a forced-draft air cooling instead of a water/steam cooling process in the prototype. The auxiliary systems such as a sodium supply and purification system, a heat loss compensation system, a power supply system and a gas supply system are included in the experimental facility to provide the various environments for performing the experiments. The preliminary layout of the main test section is shown in Figure 7.

3.3.2 Reactor vessel and core simulator

The reactor vessel and the core simulator were designed to preserve the distribution of the temperature, pressure, coolant volume, flow, and flow area. Most of the design parameters are based on the integral scaling criteria. The configuration of the reactor vessel internals is identical with that of the prototype. Four IHXs, four DHXs, two primary pumps and a core simulator are located inside the reactor vessel. The height and outer diameter of the reactor vessel are 3.4 m and 2.4 m, respectively.

Since the experiment will be performed at the decay power level, the maximum electric heater power was set to be 1.9 MW, which corresponds to 7% of the scaled nominal power. To preserve multi-dimensional phenomena, the wall thickness of the simulated cladding should be scaled to length ratio rather than original ratio except for the fuel rods. Under this constrain key design parameters of the simulated core were obtained and their distortions were throughly discussed. A total of 124 electrical heaters are used to simulate the reactor core. The diameter of each electric heater rod was determined to be 36 mm by considering assembly arrangement, instrument space, commercial availability, flow area and cost. The simulated core is divided into 3 groups as in the core of the prototype.

3.3.3 Heat Exchangers and Pumps

A total of five sodium-to-sodium and sodium-to-air heat exchangers are considered for the scaling design of the STELLA-2 facility, which are IHX, DHX, AHX, FHX, and UHX. The schematics of the UHX unit are dipicted in Figure 8. Heat exchangers of the STELLA-2 facility have been designed to preserve the overall heat transfer coefficient (U) and the log-mean temperature differences (LMTD). The scaling ratio of the pressure drops, flow rates and heat capacities are also maintained as the general scaling criteria. All scaled heat exchangers of the test facility have the same configurations and tube materials as the prototype, and identical heat transfer tube diameters (ID/OD) to the prototype were also employed to verify the overall performance of each heat exchanger unit. The parameters of {UA}, log-mean temperature differences, heat transfer tube lengths and heat transfer surface areas for each scaled heat exchanger are well-preserved as the ideal scale ratio. The major dimensionless numbers such as Richardson, friction, modified Stanton, Biot and time ratio numbers have been considered in the local scaling processes, which were quantitatively evaluated to understand the scaling distortions for the scaled heat exchanger design parameters obtained in this work.

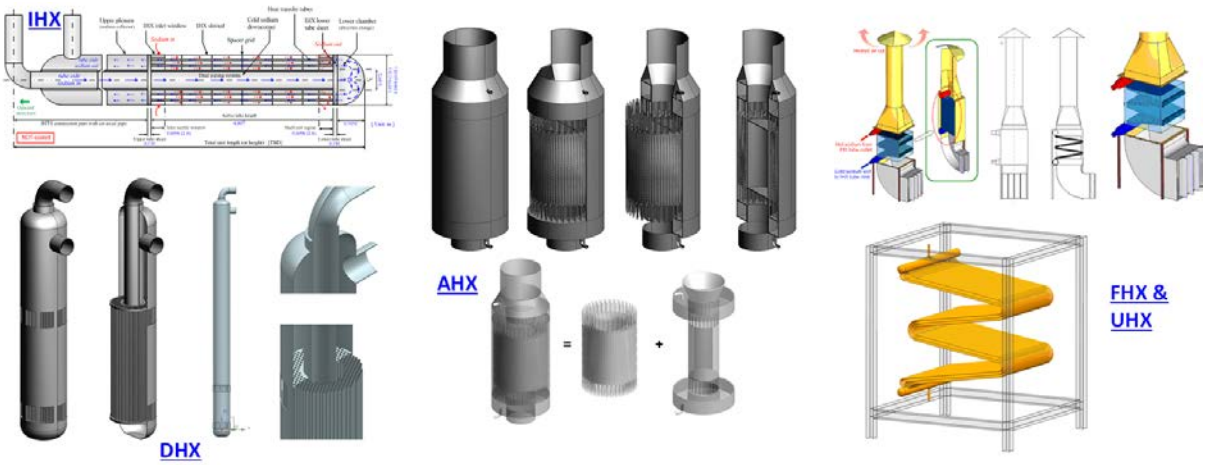

FIG.8. Schematic drawing of the heat exchangers in STELLA-2 facility

According to White[6], the geometrical similarity with a homologous curve as well as three non-dimensional parameters such as the specific velocity, specific flow, and specific head that determine the characteristics of the pump should be conserved between the prototype and scaled model. Hence the model sodium pumps of the STELLA-2 facility have designed to preserve the similarity of pump performance.

3.3.4 Pipings

The IHTS and DHRS include the main pipings connecting IHX-UHX and DHX-AHX, respectively. Since the pipe arrangements of both systems provide a natural circulation flow as well as a forced circulation flow path of the loop sodium coolant, the pressure drop through the piping and the elevation difference between the key heat exchangers were designed to satisfy 1/5 of those for prototype according the integral scaling criteria. A pressure drop similarity is obtained if only the friction number is conserved. The similarity of the sodium volume between the model and the prototype was also preserved to ensure a thermal effect of the scaled sodium inventory.

3.3.5 Auxiliary systems

The sodium supply/purification system controls the impurities of 17 tons of sodium, and it consists of a storage tank, cold trap, plugging meter, EM pump, etc. The heat loss compensation system compensates for the heat loss in the reduced scale facility. It controls the heat loss for 34 separate regions, and consists of heaters with a total capacity of 117 kW and insulation materials. The power supply system has 4.5 MW capacity, and the gas supply system provides service gases such as nitrogen and argon. The fire protection system is composed of 2-wire sodium leak detector, catch pan and fire extinguishing equipment.

3.4 Validation of the facility design

The validation of the STELLA-2 facility design was preliminarily performed by both multi-dimensional numerical incestigations using the commercial CFD package[2] and scoping analyses using the best-estimation code, MARS-LMR[7], which has been focused on the following points.

- Validation of the overall scalabilities for event scenarios (i.e. loss of flow, loss of heat sink, etc.)
- Validation of the local phenomena scalabilities for major thermal hydraulic phenomena
- Comparison of full-height and reduced-height scaling
- Identifiaction of the design parametric effects such as heat structure, design dependency, etc.

The similarities of multi-dimensional flow and temperature distributions inside the whole reactor vessel were investigated by using a 1/10 linear mock-up model for the reactor vessel[8] of KALIMER-600[9]. The boundary conditions for the 1/5 scale model were determined in accordance with the scaling ratio, and the results were compared as shown in Figure 9. This comparison shows that 1/5th scale model would well reproduce the multi-dimensional thermal-hydraulic behaviors in the reactor pool of the prototype.

The scaling approach used in this study was also assessed by using the MARS-LMR code which is a modified version of the MARS code[7] for an SFR system analysis and was developed by KAERI. The MARS-LMR nodalization model was scaled down with the global and local scaling ratio as mentioned previous sections. A transient capability of the scaling approach was assessed for the total Loss of Flow (LOF) caused by a failure of all PHTS pumps. It should be noted that the model used an electrical heaters for the fuel rod simulation with the derived scientific scaling ratios. As described in Figure 10, the model ideally scaled down from the prototype has sufficient capability to reproduce the integral thermal-hydraulic phenomena and behaviors shown in the prototype with a reasonable quantitative and qualitative similarity based on the scaling methodology employed in this study.

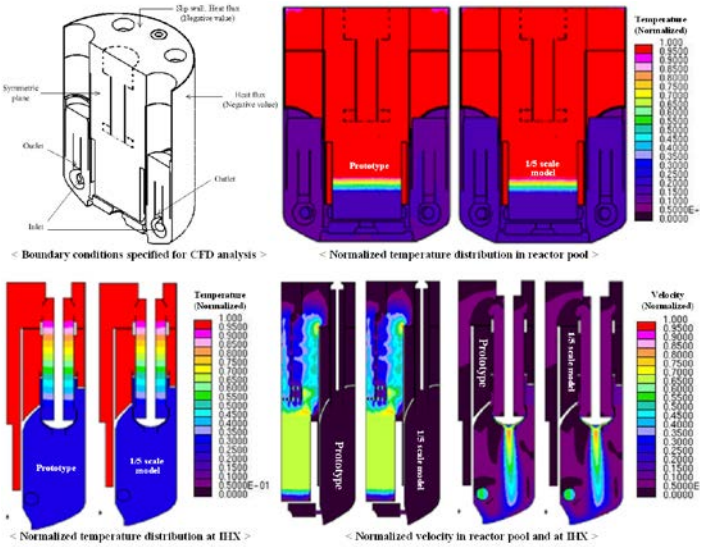

FIG.9. Comparison of 1/5 scale model with the prototype

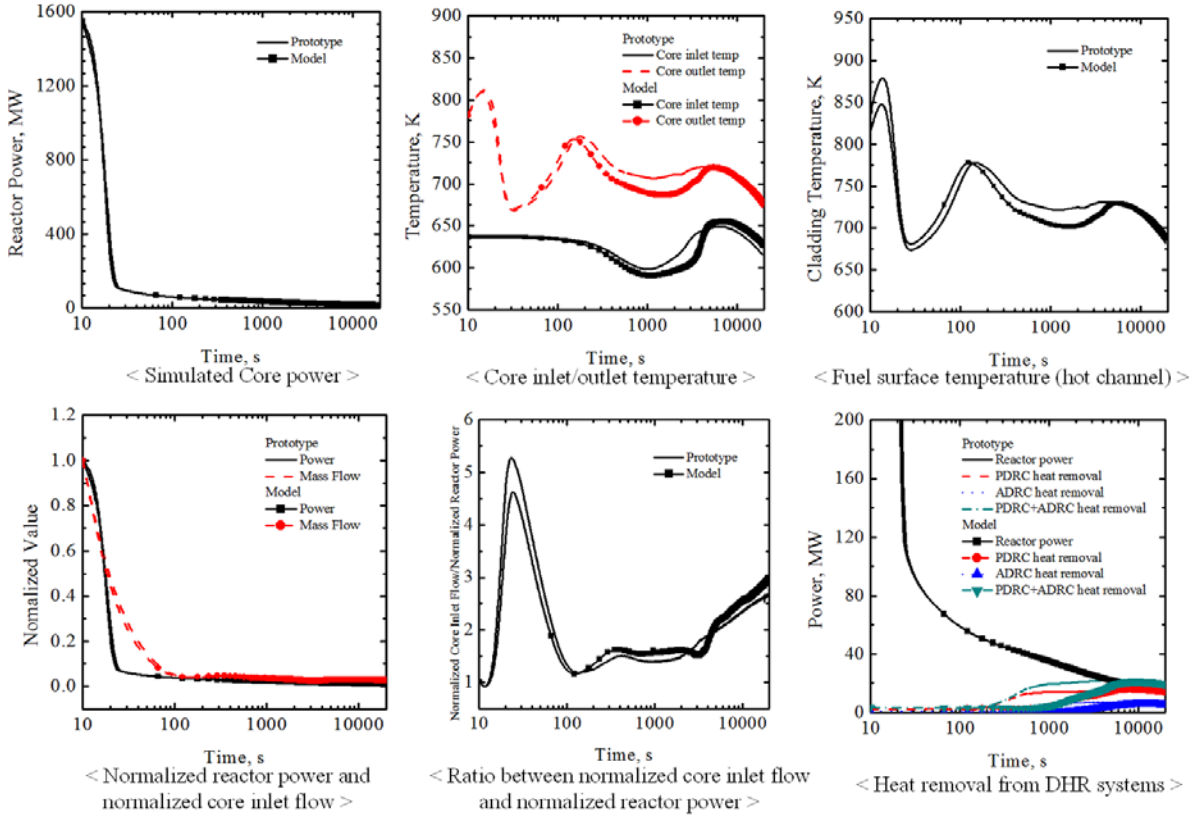

FIG.10. Scoping analysis results for comparison of 1/5 scale model with the prototype

4. Conclusion

In this study, a large-scale sodium thermal-hydraulic test program called STELLA were introduced and the design features of its first-phase test facility, called STELLA-1 were throughly described with the performance analysis results of the key test components, i.e. heat exchangers and mechanical sodium pump. The pre-test analysis for the main test components were made to confirm the multi-dimensional flow characteristics at a complicated heat transfer tube arrangement, and the feasibility of specific design methodologies of the test components were discussed as well. The integral effect test facility, called STELLA-2 has been designed from the view points of both global and local scaling,

based on Ishii et al.'s methodology. To assess the similarities in pressure, velocity, and temperature distributions of the 1/5 length scale model, thermal-hydraulic performance was analyzed by using a commercial CFD package and the results were compared to those of the prototype. For the scaled design, one-dimensional scoping analyses for the representative LOF scenario were also made and the results showed good agreement of transient behaviors for important parameters including fuel cladding temperature and coolant temperature distributions. It was found that the scaling approach proposed in this study is suitable for preserving the natural circulation phenomena in the reduced-height scale test facility.

ACKNOWLEDGEMENTS

This study was supported by the Ministry of Education, Science and Technology of Korea.

REFERENCES

[1] Eoh, J.H., Lee, T.H., Lee, H.Y., Han, J.W., Lee, Y.B., "Scaled Heat Exchanger Design of the Sodium Thermal-Hydraulic Experimental Facility; STELLA-1," Transactions of the KNS Spring Mtg., Jeju, Korea, October 21-22 (2010)
[2] STAR-CD, a commercial CFD code Users' manual, V4.06, CD-adapco (2010)
[3] Eoh, J.H., Kim, B.G., Lee, H.Y., Lee, Y.B., "Design and Evaluation of the Helical-coil Sodium-to-Air Heat Exchanger of STELLA-1," Proc. of the KNS Autumn Mtg., Gyeongju, Korea, October 27-28 (2011)
[4] Lee, T.H. et al., "Preliminary Test Requirements for the Performance Test of Passive Decay Heat Removal System of Sodium-Cooled Fast Reactor," KAERI/TR-3768/2009, Korea Atomic Energy Research Institute (2009)
[5] Ishii, M. et al., "The three Level Scaling Approach with Application to the Purdue University Multi-dimensional Integral Test Facility," Nuclear Engineering and Design, Vol.186, No.177 (1998)
[6] White, F.M., "Fluid Mechanics," 3rd Ed., McGraw-Hill, INC (1994)
[7] KAERI, "MARS Code Manual," Korea Atomic Energy Research Institute, KAERI/TR-2812/2004 (2004)
[8] Jeong, J.H., Hwang, S.W., Choi, K.S., "Local flow distribution analysis inside the reactor pools of KALIMER-600 and PDRC performance test facility," Korea Atomic Energy Research Institute, KAERI/CM-1276/2009 (2009)
[9] Hahn, D. et al., "KALIMER-600 Conceptual Design Report," Korea Atomic Energy Research Institute, KAERI/TR-3381/2007 (2007)

Development of Electrochemical Oxygen Sensors for Liquid Sodium

B.K. Nollet, M.G. Hvasta, M.H. Anderson

University of Wisconsin-Madison

Abstract. This paper focuses on the theory, design, and performance of galvanic cell oxygen concentration sensors for use in high temperature liquid sodium. These sensors are crucial both in the evaluation of high temperature materials being tested in liquid sodium and monitoring of advanced sodium cooled fast reactors. Performance of yttria stabilized zirconia (YSZ) as an electrolyte for the sensor is analyzed. Construction techniques are also presented to address difficulties encountered in the development of a galvanic cell. Response times and sensitivity to changes in oxygen concentration are analyzed with observed limiting factors to cell performance.

1. Introduction

The galvanic cell oxygen sensor is an on-line instrument that continuously measures the thermodynamic activity of the oxygen in sodium. The cell generates a voltage that is dependent on the ratio of the oxygen activity in sodium, C, to that of some reference, C_o. Unlike the plugging meter (PM), the galvanic cell is selective to oxygen, so only a change in *oxygen* concentration will result in a change in voltage, ΔV. For a sensor at constant temperature, a change in cell signal is related to a change in oxygen concentration by equation 1 [1]:

$$\ln\left(\frac{C}{C_o}\right) = K\,\Delta V \tag{1}$$

K in equation 1 is an experimentally determined constant.

These oxygen sensors have historically been made using yttria stabilized thoria (YST) as an electrolyte. However, this material is expensive and extremely difficult to acquire in the United States. This paper outlines the theory, previous work, and main problems encountered with these sensors. The development of a cost-effective prototype made out of yttria stabilized zirconia (YSZ) is then discussed, and the results of this prototype are presented. While the prototype was not tested for long-term durability in liquid sodium, ongoing tests are described which will provide data necessary to determine the longevity and accuracy of a YSZ oxygen sensor.

2. Sensor Theory

Galvanic cell design varies slightly from sensor to sensor, but several key components are common. The sensor is composed of an electrolyte barrier (usually a crucible) that serves as an ionic conductor for oxygen in liquid sodium. This barrier separates liquid sodium from an electrode that samples the oxygen activity (labeled *Reference electrode* in figure 1). The oxygen activity in sodium is then compared to the oxygen activity in a controlled environment (of known oxygen concentration); this difference in activity results in a measurable voltage.

Reference electrodes for galvanic cell oxygen sensors fall into two categories: a metal-air reference, or a metal-metal oxide reference. In the metal-air reference system, a porous metal catalyst (usually platinum) is attached directly to the ion conducting electrolyte, and air is supplied to the platinum. The air is assumed to be a constant, known oxygen activity, so the activity on the sodium side of the electrolyte can be determined. The metal-metal oxide reference system uses a metal (usually in

powder form [2]) in electrical contact with the electrolyte, and in a sealed container with some cover-gas. This sealed chamber then reaches an equilibrium oxygen partial pressure between the gas and the metal powder, and the oxygen activity is held constant. Liquid bismuth has been used as a metal-metal oxide reference electrode for liquid lead systems, and the chemistry of this system is identical to the powders [3].

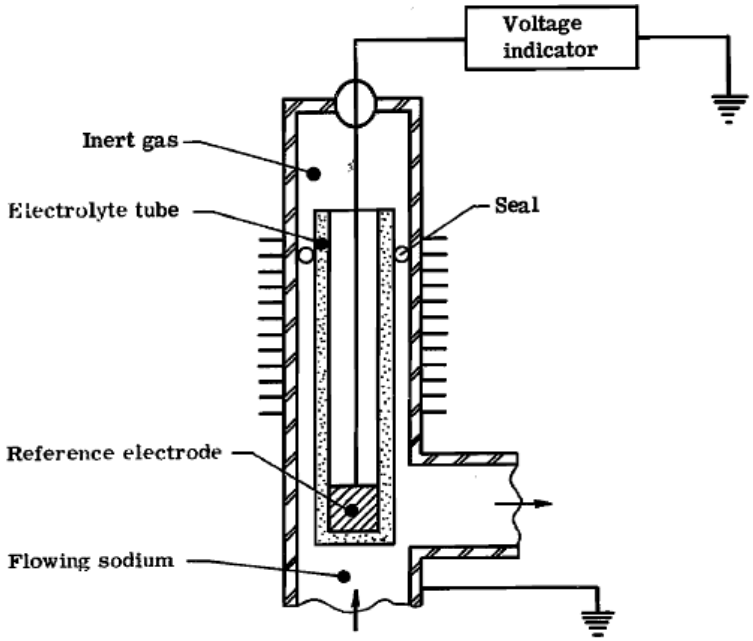

Figure 1 – A simple schematic of an electrochemical oxygen sensor by Minushkin and Kolodney [1]

2.1. Nernstian Potential

Electrochemical oxygen sensors follow a nernstian relationship, which can take many forms. For platinum-air reference electrode galvanic cell oxygen sensors, the Nernst equation is most commonly represented as:

$$E = E_o - \frac{RT}{2F}\log_{10}\left(\frac{[Na_2O(Na)]}{[O_2]^{1/2}}\right) \quad (2)$$

E is the voltage generated by the electrochemical reaction, or the electrochemical potential, E_o is the standard potential of the cell, T is the cell temperature, and the quantities in brackets are the activities of the respective components. R is the gas constant, and F is the Faraday constant. In the numerator of the logarithm, the quantity listed is the activity of sodium oxide in sodium solution (in parenthesis); the denominator is the activity of oxygen in the reference gas (in most cases, air).

For a metal-metal oxide reference electrode, equation 2 simplifies to the following [2,4]:

$$E = E_o - \frac{RT}{2F}\log_{10}([Na_2O(Na)]) \quad (3)$$

The second term in equations 2 and 3 show a logarithmic dependence on the ratio of oxygen in sodium to the oxygen in the reference. In addition, both terms are temperature dependent. The direct dependence on temperature is shown in the second term, and for E_o, the temperature effect is hidden in the underlying chemistry:

$$E_o = E_o(T) = \frac{\Delta G^o_{MO}(T) - \Delta G^o_{Na_2O}(T)}{2F} \quad (4)$$

$\Delta G^o_{MO}(T)$ and $\Delta G^o_{Na_2O}(T)$ represent the standard energy of formation of the metal-oxide in the reference electrode, and the sodium oxide dissolved in liquid sodium. These values must be evaluated at cell temperature. Knowing these values accurately is imperative to an accurate prediction of the cell output. The subscripts refer to metal-oxide (*MO*) and sodium oxide (Na_2O), respectively. Note that for a platinum-oxygen reference system (or sometimes palladium), the metal acts as a catalyst, not a reactant, so no platinum is actually consumed during operation. In this case, the standard cell potential simplifes to:

$$E_o = E_o(T) = -\frac{\Delta G^o_{Na_2O}(T)}{2F} \quad (5)$$

For all metal-metal oxide reference systems, both liquid and powder, equation 4 describes the system chemistry. Platinum-air and other catalyst-gas reference systems are described by equation 5.

2.2. Electrochemistry of Operation

The operation of a galvanic cell oxygen sensor requires a difference in oxygen concentration across a solid electrolyte. For the air-catalyst sensor, air (~20% oxygen) is supplied to one side of the electrolyte, while the liquid sodium with oxygen dissolved in solution contacts the other side. The oxygen gas (O_2) is not free to move through the electrolyte in molecular form, so a porous catalyst (usually platinum) is attached at the electrolyte-air interface. The porous structure of the platinum catalyst provides vacancies within which molecular oxygen can break into oxygen ions, and borrow electrons from the platinum (from now on referred to as the reference electrode). This process can be seen in the following equation:

$$O_2 + 4e^- \rightarrow 2O^{2-} \quad (6)$$

The oxygen ions then traverse the ionic conductor (electrolyte). They will be driven across by the concentration gradient, from high oxygen concentration (air) to low concentration (in sodium). Upon reaching the electrolyte-sodium interface, the sodium atoms will shed an electron and ionically bond with the newly arrived oxygen ions.

$$Na \rightarrow Na^+ e^- \quad (7)$$

$$Na^+ + O^{2-} \rightarrow Na_2O \quad (8)$$

The liberated electrons allow an electronic current to flow through the sodium and adjoining stainless steel walls (these metals are used as the second electrode) for the system. A high impedance voltmeter then completes the circuit when connected between the reference electrode and the liquid sodium. The signal generated on the multi-meter should resemble the Nernst equation described above (2).

The metal-metal oxide reference electrode does not require a catalyst. Rather, the ratio of metal to metal oxide will remain in equilibrium with the available oxygen in the cover gas as long as the cover gas is sealed (no leaking). Thus, the oxygen concentration on the reference side of this sensor is maintained at a constant value. The magnitude of this partial pressure can be looked up on an Ellingham diagram. As long as this partial pressure is still higher than that of liquid sodium, oxygen ions will continue to move in to the sodium through the electrolyte, and the reaction will be the same as for the air-catalyst sensor.

3. Oxygen Sensor Limitations & Common Problems

The greatest problem facing the galvanic cell oxygen sensor is the compatibility of the porous ceramic barrier with liquid sodium. Since sodium oxide is more chemically stable than most other oxides, the oxide of the conductive ceramic will preferentially move into sodium solution, thus corroding away the critical outer ceramic layer. Historically the best material for an outer conductive layer has been YST [5]. While the best thoria sensors have been shown to last in excess of 3000 hours, their cell-to-cell variation was found to be greater than 10% [6]. Furthermore, sensor lifetime and calibration time have been found to be much less consistent at temperatures above 340[C][6].

Cell-to-cell variation has been observed with these sensors as a result of an inconsistent ionic transport number of the electrolyte [2]. Example data of cell-to-cell variability is shown in figure 2 [7].

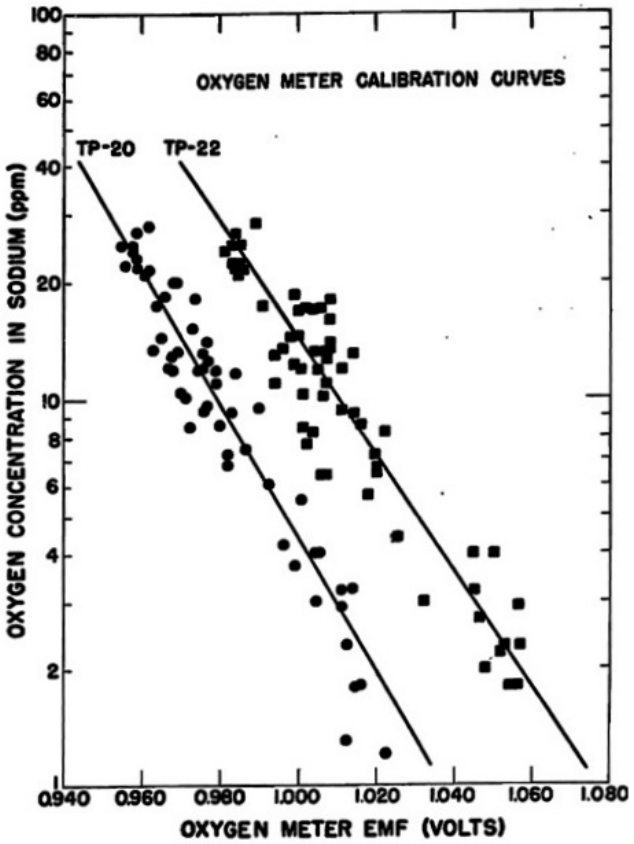

Figure 2 – This figure shows data from two identical eleectrochemical oxygen sensors and demonstrates the significance of cell-to-cell variability [7].

Possible variations in the heat of solution of sodium oxide have been cited as the cause for the observed difference between theoretical sensor behavior and actual data[8] (see figure 3). However, innaccuracy of the heat of solution of sodium oxide is not commonly accepted as an explanation for this phenomenon[9]. Indeed, a widely accepted explanation has not been found for the difference between expected and actual sensor voltage.

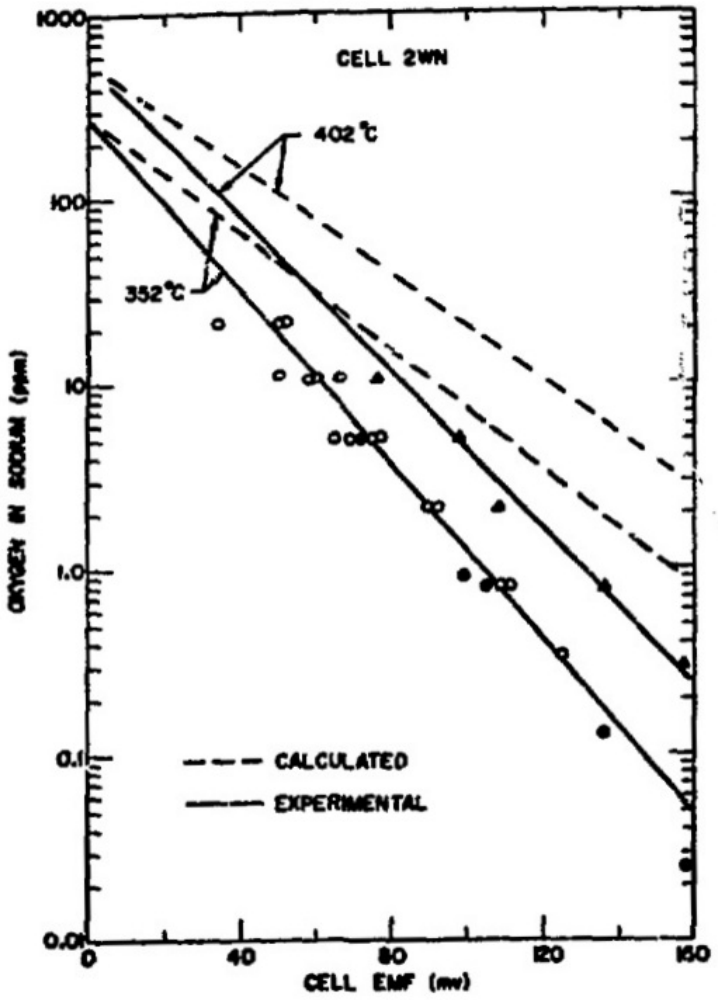

Figure 3 – This figure shows an oxygen sensor run at 352[C] and 402[C], examining the signal strength as a function of oxygen concentration. The signal was significantly offset from theory[8].

4. Oxygen Sensor Design & Experiment Setup

The goal of this research was to examine the feasibility of a cost-effective, easy to construct oxygen sensor using a cheaper material than YST. Knowing that zirconia is not as thermodynamically stabile in sodium as YST, it is not realistic to seek a permanent or extremely long-lived oxygen sensor using a zirconia based electrolyte. However, as the following data will show, this material can work for a limited time.

Yttria doping of a zirconia ceramic (YSZ) introduces oxygen vacancies in the ceramic lattice, and allows ionic conduction in the same method that YST does. The substitution of the yttrium ion (3+) for a zirconium ion (4+) does not conserve charge. In order to offset this, oxygen vacancies are introduced (2-) vacancies for every two yttrium ions introduced. As the number of these vacancies increases, so does the ionic conductivity of the material (until the vacancies begin to interact with each other and the structure of the ceramic changes). A commonly available yttria concentration was chosen for the experiments reported on in this paper.

Commercially available yttria stabilized zirconia (YSZ) crucibles were chosen for the electrolyte of the prototype sensor. This YSZ was stabilized with *10.5* weight-percent yttria, which should have an

excellent oxygen diffusion coefficient. The crucible was twelve inches long and *0.375* inches outer diameter, with a *0.25*-inch inner diameter.

The electrolyte was secured into an eleven-inch 316SS tube using a zirconia paste. The sensor was made this length to create a freeze seal before sodium could overflow into the reference electrode chamber. A first attempt with the zirconia paste was done with a six-inch crucible, and the hot sodium penetrated through the paste, and caused a leak. This likely occurred because the coefficients of thermal expansion (CTE) are substantially different between the 316 stainless steel sleeve, and the zirconia components (the CTE of 316SS is *2.5* times greater than that of zirconia). Thus, a longer sensor was made, and the thermal expansion at the cold end of the sensor was minimized. This design change fixed the leak problem. Figure 4 shows the sensor components described above.

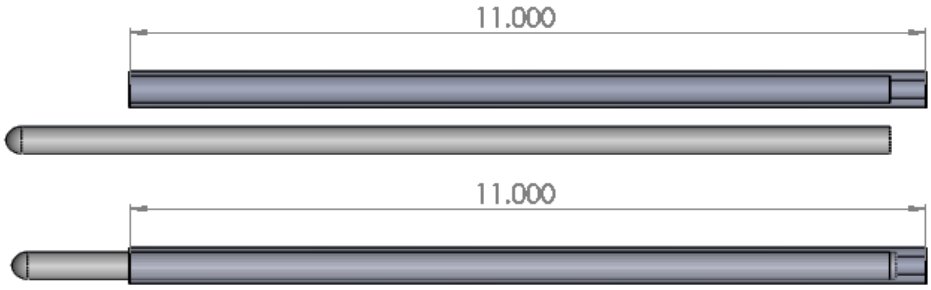

Figure 4 – This figure shows the 10.5% YSZ crucible and the 316SS sheath that housed the crucible. The 316SS is *0.5”* outside-diameter, and the zirconia ceramic is *0.375”* outside-diameter.

A 325 mesh (44 [μm]) copper powder was used as a reference electrode. Past experiments have shown that copper gives more reproducible results than other reference electrode metals [4,8]. Because the reference electrode is a metal powder, the sensor had to be mounted vertically. This restriction does not exist for platinum-air reference electrodes, and the next generation of sensors currently under development at UW-Madison eliminates this restriction. The reference chamber was then sealed to ensure there would be no leakage of the cover gas (nitrogen). Figure 5 shows an actual sensor as assembled, before insertion into the sodium loop.

Figure 5 – This figure shows the first YSZ prototype oxygen sensor tested in sodium at UW-Madison. This type of sensor was used for all of the data included in this report.

The sodium loop in which these prototype sensors were tested does not have a cold trap. The oxygen concentration was measured using a plugging meter, and as a result, no data points are quoted below *10*[wppm]. Obtaining accurate plugging measurements below *10*[wppm] was difficult, and inconsistent.

Varying the oxygen concentration in the loop was achieved by filling the loop with the sodium tank at different temperatures. Since the oxygen saturation of sodium is a strong function of temperature,

changing the fill temperature successfully changed the quantity of oxygen in the loop for that experiment. Once filled, the loop would operate until a uniform temperature had been achieved (*350*[C]), and plugging tests were conducted. Each plugging test is typically repeated five times, and the average of each series of measurements was taken and plotted.

5. Sensor Data & Analysis

For a copper-copper oxide reference electrode, the signal output should be described by equation 3:

$$E = E_o - \frac{RT}{2F}\log_{10}([Na_2O(Na)]) \tag{9}$$

The standard electrode potential, E_o for a copper system is determined from the following equation (acqured using *HSC 7 Chemistry* software by Outotec Research):

$$E_o(T) = -0.0003\,T + 1.2958\ [V] \tag{10}$$

All data was taken at a cell operating temperature of *350*[C] (~623.15[K]). Plugging in the appropriate constants: $F = 96485[C/mol]$, $R = 8.314J/(mol\,K)]$, yields equation 11. Equation 12 shows the general functional form with two fit paramters. The acquired data was fit to this functional form.

$$E([Na_2O(Na)]) = 1.109[V] - 0.0268\log_{10}[Na_2O(Na)] \tag{11}$$
$$E([Na_2O(Na)]) = \boldsymbol{A} - \boldsymbol{B}\log_{10}[Na_2O(Na)] \tag{12}$$

The data from the first two sensors is displayed in figure 7. This figure shows the data as it is comonly displayed in literature (see figures 2 and 3) with the oxygen concentration on a log-scale y-axis, and the signal voltage on the x-axis. On a semi-log-plot, the nernstian behavior should appear linear. At a glance, the data appears to follow a logarithmic trend and voltage decreases as oxygen increases, which is also expected according to equation 11 above. There is a substantial offset between the two sensors, and the slopes of the least-squares fits appear different from one-another.

Figure 6 displays the same data in a linear-scale, with the voltage on the y-axis and oxygen concentration on the x-axis (just as equation 11 is written). In addition, the theoretical sensor performance is shown in the red dashed line on top of figure 6. The prototype oxygen sensors are producing a signal significantly smaller than expected. The *change* in signal as a function of oxygen concentration appears to be even greater than expected, and the noise in the signal is on par with that shown in figures *2* and *3*.

These tests were short duration, each for ~*25*[hr] cumulative exposure. A new test section in a larger sodium loop is currently being tested, and allows for long-term testing of multiple sensors in parallel. Table 1 summarizes the results of these preliminary tests.

Table 1 – This table summarizes the least-squared fits for the oxygen snesor data from both prototypes. Two fit parameters were found, A & B, when the data was fit to equation 12.

	A	***B***	*Variable*
Theory	$1.109[V]$	-0.0268	$\log_{10}[Na_2O(Na)]$
Prototype 1	$0.979[V]$	-0.108	
Prototype 2	$1.17[V]$	-0.188	

It is felt that the noise level in the oxygen sensor data shown in figures 7 and 8 is due sediment layer buildup on the electrolyte, which is then quickly removed from the surface and dissolved into the sodium. Sodium oxide in the presence of zirconia will spontaneously undergo the following reaction:

$$ZrO_2 + Na_2O \rightarrow Na_2ZrO_3 \quad (12)$$

The above reaction has a negative change in gibbs energy of $\Delta G = -171[kJ/mol]$, which means that this reaction happens spontaneously. The formation of this compound will take place at the surface of the electrolyte before breaking free into the sodium. This continous process will effect sensor signal.

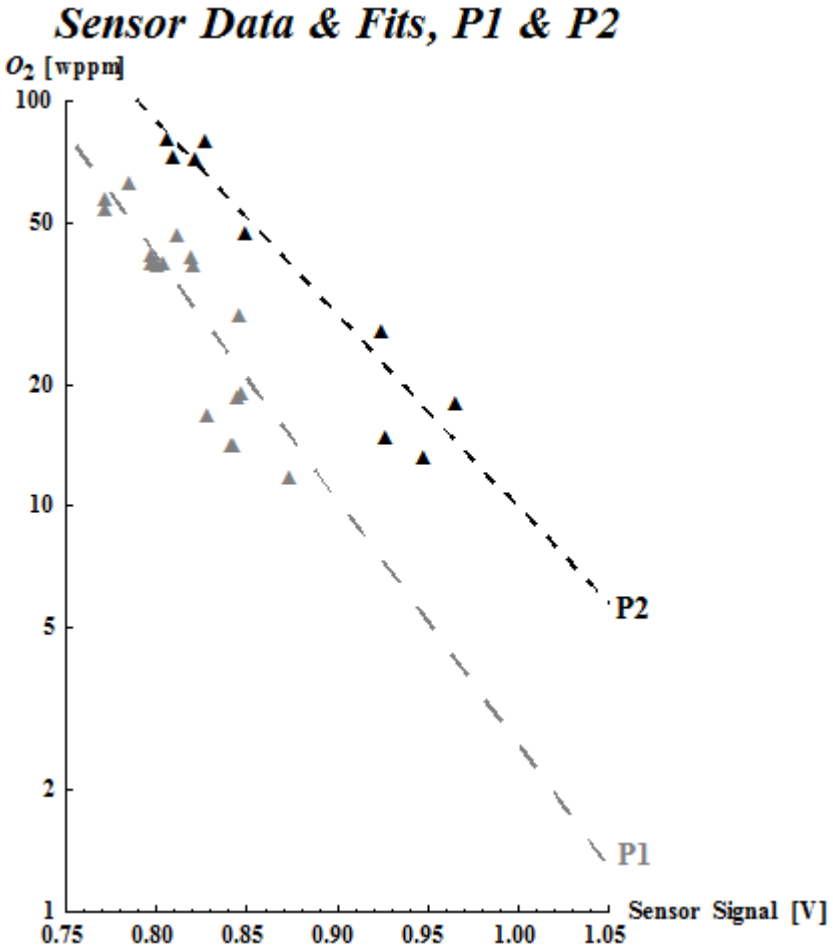

Figure 6 – This plot shows the data from two YSZ oxygen sensors in liquid sodium at *350*[C]. These sensors each ran for *25*[hr] without failure.

Additional sources of error in the signal could stem from impurities at the interface between the reference electrode (copper) and the electrolyte (YSZ). The cell voltage is determined by interactions at this interface rather than by properties of the bulk copper, which suggests that interface impurities could provide a deviation from theory. A possible solution to this problem in future experiments is to outgas the electrolyte at various temperatures before sodium immersion. Furthermore, using a liquid reference elctrode (like bismuth) would help eliminate contact resistance at the interface, and possibly help shift the signal closer to theory.

Any *electronic* conduction across the electrolyte would directly lead to a decrease in a current leak, and subsequent drop in voltage. This effect is minimized by using a ceramic with high ionic conductivity, like YSZ or YST, and therefore is not expected to be a substantial contributor to the difference between theory and data.

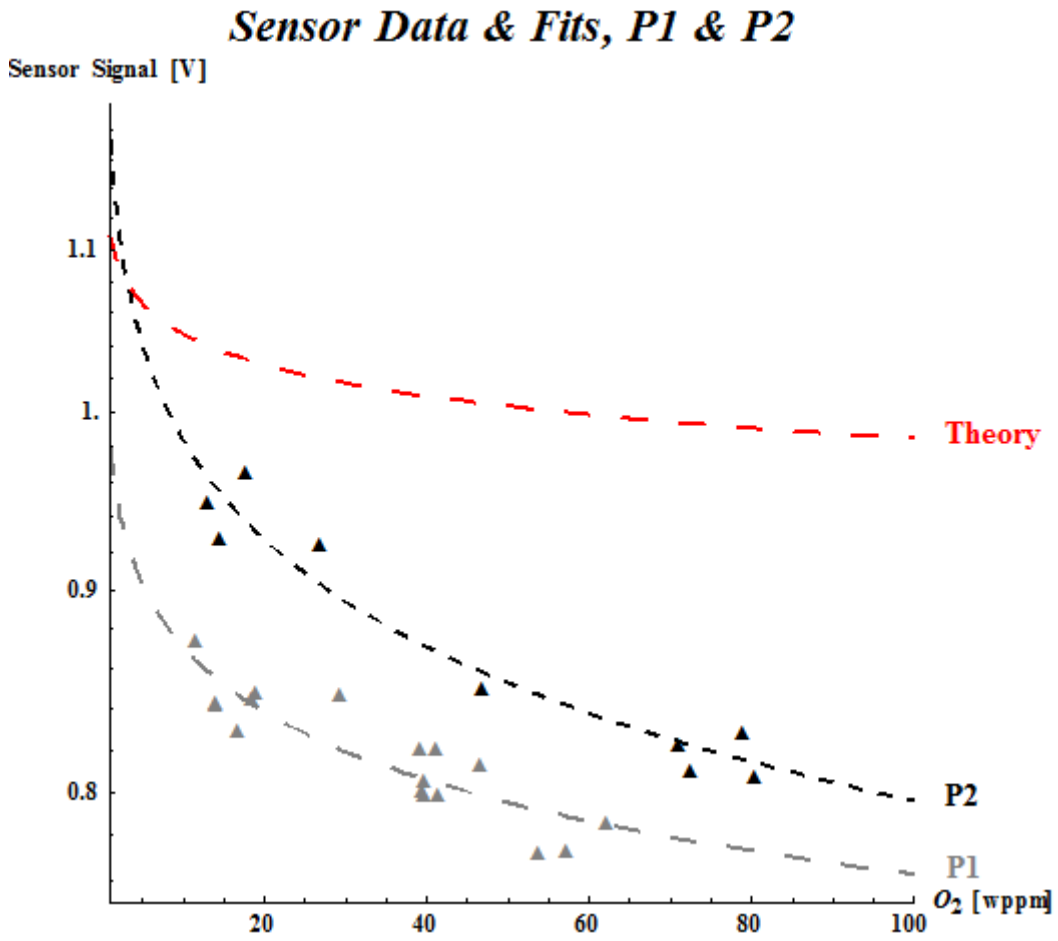

Figure 7 – This figure shows the data acquired from both prototype oxygen sensors on a linear plot. The theoretical output of these sensors is overlayed in red. The signal strength is significantly less than expected, but the oxygen dependence is stronger.

Investigation into the cause of the difference in slopes between the acquired data and theory is ongoing. The steeper experimental slope is consistent with past research, but an acceptable explanation has not yet been reached. Furthermore, the prototype sensors experienced up to ten hours of non-sensible data before they started to respond to oxygen changes appropriately. This observation is also consistent with past research, and again, a popularly accepted explanation has not been reached. Future investigation into both of these effects is outlined below.

Future tests will be conducted with a consistent quantity of copper powder reference electrode in each sensor. This quantity was not measured because none of the described thermodynamics suggested this quantity would matter. However, given the difference between the two slopes from the respective sensors, it is suspected that the different amounts of copper take different amounts of time to equilibrate with their enviornment (sealed nitrogen gas). This equilibration may effect the response of the sensor to oxygen concentration, and the time-response as well. When the reference electrode is sealed in the sensor, it is at equilibrium with its enviornment at that temperature. However, as the sensor is brought to operating temperature, the reference metal must reach a new equilibrium. This will depend on the diffusion coefficient of the copper powder and oxidation potentials of the copper, both of which are functions of temperature. The dynamics of this problem need to be aproximated to determine whether or not this process is having an effect.

6. Conclusion

Electrochemical oxygen sensor testing at UW-Madison has shown that YSZ could function as an appropriate electrolyte in liquid sodium for short durations. Longer duration tests are ongoing, but preliminary results show that sensor response to oxygen concentration changes and follows the theoretical trend, but would have to be calibrated against a cold-trap or plugging meter. Given the difficulty of acquiring YST electrolytes, YSZ is an attractive alternate.

The reasons for the difference between acquired data and theory are likely due to impurities in the electrolyte and at the reference electrode-electrolyte interface. Future work will be focused on different ionic conductivities of the electrolyte, and on different reference electrode materials. It is suspected that improvements can be made on the contact resistance between the reference electrode and the electrolyte wall by moving to a liquid reference system. Reducing this resistance may reduce the difference between the expected and acquired signal strength from the sensor.

The limiting factor with liquid sodium oxygen sensors is electrolyte corrosion in liquid sodium. This issue, while mentioned above, was not addressed in detail in this report. Corrosion studies are being conducted in parallel to this oxygen sensor research to determine the optimum material for an oxygen ion conducting electrlyte. It is anticipated that signal strength will be sacrificed in order to increase corrosion resistance as long as the sensor can still be calibrated against a cold trap or plugging meter.

7. Acknowledgements

The authors would like to thank Paul Brooks for his assistance in experiment design and construction, and Dr. Dane Morgan (UW-Madison) for his assistance with electrochemical analysis of the sensor systems. This research is being performed using funding received from the DOE Office of Nuclear Energy's Nuclear Energy University Programs.

REFERENCES

[1] B. Minushkin. *Electrochemical Oxygen Meter Operating Manual*. The United Nuclear Corporation, White Plains, New York, August 1965

[2] B. Minushkin & M. Kolodney. Development of a continuous electrochemical meter for oxygen in sodium. Technical report, Unitded Nuclear Corporation, 1967

[3] Ning Li, T.W. Darling. Oxygen concentration in liquid Pb-Bi eutectic. Technical report, Los Alamos National Laboratory, January 2001

[4] H. Steinmetz. Development of a continuous meter for oxygen in sodium. Technical Report, United Nuclear Corporation, White Plains, New York, January 1963

[5] O.J. Foust, editor. *Sodium-NaK Engineering Handbook*, volume 5. Liquid Metal Engineering Center, 1979

[6] B.Minushkin. The liquid metal oxygen meter. Technical report, United Nuclear Corporation, White Plains, New York, 1965. p.272-273

[7] C.C. McPheeters, J.M. Williams. A Comparison of Three Methods of Oxygegn Concentration Measurement in Sodium. Technical report, Los Alamos Scientific Laboratory, Los Alamos, New Mexico, 1966

[8] D.L. Smith. Monitoring and Measurement of Oxygen Concentrations in Liquid Sodium. Technical report, International Conference on Liquid Metal Technology in Energy Production, 1976

Challenges in Manufacturing of Large Dimensional Stainless Steel Vessels of PFBR

Mahendran Narayansamy[†], Azhagarason Boobendran[‡], Tarun Kumar Mitra[§], Prabhat Kumar[††]

Bharatiya Nabhikiya Vidyut Nigam Limited (BHAVINI)
Department of Atomic Energy,
Kalpakkam 603 102,
Tamilnadu, India

Presented by Mahendran Narayansamy

ABSTRACT

Prototype Fast Breeder Reactor (PFBR) is liquid sodium cooled, pool type reactor with generating capacity of 1250 MWt / 500MWe. Reactor assembly consists of many large dimensional vessels made of austenitic stainless steel material. The main vessel for PFBR contains the bulk of primary sodium and thereby serves as the primary boundary supporting the core support structure along with the other loads acting on it. The main vessel consists of a cylindrical shell (25 mm thick) portion at top end and torispherical dished end (30&40 mm thick) at the bottom portion made of SS316 LN material. The 12.9 m diameter, 12.8 m height vessel weighs approximately 135 MT with running weld length of 540m. Forming of dished end petals (39 nos.), welding of core support structure support shell at the transition region with matching holes for cooling pipes at thermal baffle end, overlay of weld on the inside surface of transition region to accommodate the profile on dished end and to facilitate core support structure support shell welding was a real challenging task during manufacture. Circumference matching between the cylindrical shells, cylindrical shell to dished portion was achieved within the tolerances specified. Due to limitations of transportation, large sized components like safety vessel, main vessel, inner vessel, thermal baffle were manufactured at PFBR site. This paper discusses the experiences gained during the manufacturing of such over dimensional components at PFBR site in meeting the stringent tolerances on various dimensions and NDE requirements.

1. Introduction

The Prototype Fast Breeder Reactor (PFBR) 1250 MW t / 500 MWe is presently under advance stage of construction at Kalpakkam site. Being a pool type reactor, it requires large diameter vessels. Reactor assembly of PFBR, consists of primary sodium circuit contained by a unique vessel called main vessel (MV) made of SS 316 LN material supported at the top with top shield containing roof slab, large and small rotatable plugs and control plug. The core subassemblies are supported on a grid plate and their collective load is transferred to main vessel through the core support structure (CSS). The safety vessel (SV) made of SS 304 LN with Ø13.5 m and 12.5 m height is positioned concentric and outside of the main vessel. The inner vessel (IV) separates the hot and cold pools of primary sodium and houses primary sodium pumps (PSP - 2 nos.) and intermediate heat exchangers (IHX - 4 nos.).

[†] Project Engineer - Procurement (Nuclear Systems)
[‡] Scientific Officer - D
[§] Director - Technical
[††] Chairman and Managing Director

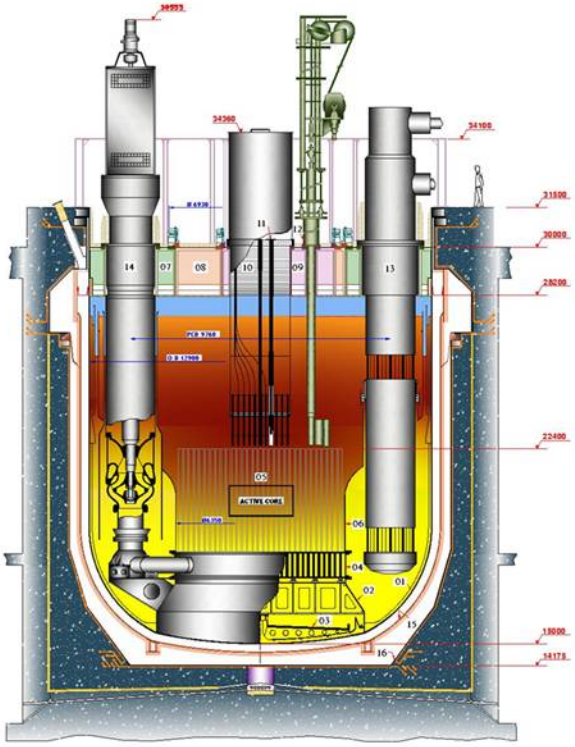

FIG. 1. Cross section of PFBR Reactor Assembly

Reactor assembly is housed in a concrete vault lined with carbon steel. The roof slab that supports the MVl is supported by a cylindrical support shell, which in turn is welded to an embedment provided in the reactor vault concrete. Fig. 1 shows the cross section of PFBR reactor assembly. Two thermal baffles, outer and inner, form a part of the main vessel cooling system and are welded concentric to inside of the MV at an optimum elevation. All together, the weight of components and sodium is carried by the MV. This paper discusses the in-house manufacturing experiences of such over dimensional components at PFBR site towards meeting the stringent tolerances on various dimensions and NDE requirements.

2. Component Description

2.1. Safety Vessel

The SV of the PFBR is concentrically located outside of the main vessel and in the unlikely event of leakage of sodium from MV, maintains the sodium level at an elevation such that continued decay heat removal is ensured. The principal material of construction is SS 304 LN. Also, The SV acts as a support along with main vessel for the passage of robotic vehicle in the inter-vessel space for in-service inspection of main vessel. There is a nominal gap of 300 mm between the safety vessel and main vessel, which has been arrived at based on the requirement for of in-service inspection vehicle movement. The overall diameter of the SV is Ø13.5m with a height 12.5m. The thickness on the shell region is 15 mm and 20 mm on the dished region in total weighing about 111 T.

2.2. Main Vessel

The main vessel is a cylindrical shell with a specially shaped torispherical dished end of 12.9 m diameter, 12.8 m height weighing approx. 135 t. Material for construction is SS 316 LN, chosen for its high temperature properties, weldability and compatibility with liquid sodium. Core loads, along with that of the grid plate, inner vessel, and core support structure, are transferred to the dished end torus –

sphere junction through the CSS. The junction has intended profile discontinuity, between torus and sphere, to reduce the compressive stress in the dished end torus region. The support shell of the CSS is welded at this junction and transmits the above mentioned load approx. 7.5 MN to the MV. The vessel contains ~1150t of sodium. The thickness of the cylindrical portion is chosen as 25 mm, dished end as 30 mm and thickness is further increased up to 40 mm locally near the CSS support shell junction.

The main vessel experiences a maximum temperature of 420ºC during normal operating conditions. The main vessel is cooled by cold sodium, through the annulus formed between MV and thermal baffles to minimise the effects of creep, thermal fatigue & embrittlement of the structure.

2.3. Inner Vessel

The inner vessel (material of construction is SS 316LN) separates the hot and cold pools of sodium (ΔT of 150^0C) and is supported on grid plate by bolting. It has an upper and a lower cylindrical shell with a conical shell in between. The junctions of the cylinder to the cone are through small toroidal knuckles. The OD of the lower and upper shells are 6.35 and 12.2 m respectively. A thickness of 15 mm for cylindrical shells and 20 mm for conical shells are selected to enhance the buckling resistance of the vessel under all operating conditions.

Standpipes are provided for the pump and IHX to enter from the hot pool to the cold pool. A mechanical seal, with rings designed to act as barriers against leakage, is provided at the penetration of the IHX to minimize leakage of sodium from the hot to the cold pool. Hard facing is provided at the interface surfaces of the seal.

2.4. Thermal Baffle

The thermal baffle has two large concentric cylindrical shells, inner and outer diameters of 12440mm (thickness 20,25mm) and 12670mm (thickness20, 25 and 50mm), respectively. The total height of the baffle is 4930mm. The principal construction material is AISI 316LN plate. The main purpose of the thermal baffle is to provide annular passage for the cold sodium, which is circulated to cool the main vessel. Leakage sodium from the bottom of the grid plate is fed to the annular space between the main vessel and the outer baffle through 24 pipes each of 88.9mm OD X 3.05mm thick X 7943mm length. The spillway has a special shape such that the overflowing sodium completely wets the inner surface with out any separation thereby avoiding any risk of gas carry over in to the sodium pool

3. Design features

Being high operating temperature system and use of sodium as coolant due to its good heat transfer property, stresses developed due to thermal transients are to be minimized by using thin walled structure. Sensitisation of stainless steel materials is to be kept low to avoid intergranular corrosion, pitting corrosion, intergranular stress corrosion cracking, and loss of ductility, etc. Distortion is to be kept to a minimum to avoid stress concentrations and to maintain dimensional stability. A minimum heat input is to be used during welding. Delta ferrite shall be maintained at the minimum level to avoid sigma phase formation during operation at high temperature. All of the above leads to specific requirements that are more stringent than those required for other thermal reactors.

3.1. Material Specification

The material chosen for construction is SS 316 LN (MV, IV & TB) for its high temperature strength and compatibility with sodium. Low carbon grade has been chosen to ensure freedom from sensitisation during welding of the components and hence to avoid risk of chloride stress corrosion cracking during storage in coastal sites. Since low carbon grades have lower strength than normal grades, nitrogen is specified as an alloying element to improve the mechanical properties so that the strength is comparable to that of SS 316. Although the SS 316 L (N) that is specified by ASME has nitrogen in the range of 0.10 to 0.16 wt%, for PFBR, the nitrogen content is limited to 0.08 wt% in

view of improved weldability, code data availability and for minimising scatter in mechanical properties.

Phosphorus, sulphur and silicon are treated as impurities, as they have adverse effects on weldability. Therefore, acceptable maximum limits are reduced to values that can be achieved in steel making practice. Considering the adverse effects of titanium, niobium, copper and boron on weldability, maximum permissible limits have been imposed. A minimum level has been specified for manganese to improve weldability.

Additional mechanical tests like impact strength at room temperature in solution annealed and embrittled condition, tensile test at elevated temperature, control of delta ferrite, stringent control over inclusion content etc., are specified.

3.2. Dimensional requirements

Thin walled vessels designed to withstand thermal stresses load due to usage of sodium as a coolant require tight tolerances on shells to provide rigidity against buckling. Major dimensional tolerances for cylindrical shells and dished ends such as form tolerance, local deviations for roundness, straightness, and contour were more stringent when compared to RCC – MR. Additional supplementary controls are also specified on straightness of the generatrix, weld mismatch, circumference control etc to control the deviations in forming of the shells.

3.3. Welding requirements

To ensure the soundness of the weld, design requirements on weld tolerances are stringent when compared to other codes. Major tolerances are detailed below:

3.3.1. For joints welded on both sides

The internal and external surface alignment tolerances between parts of identical thickness shall be t/4 mm max. for $t < 5$ mm, and t/10+1 with maximum of 4 mm for $t \geq 5$ mm.

3.3.2. For joints welded on a single side

For joints welded on a single side and inaccessible on the back side, for parts of identical thickness, the alignment tolerances for accessible surfaces shall be t/4 mm for $t < 5$ mm and t/20 + 1 mm with a maximum of 3 mm for $t \geq 5$ mm.

The slope on welding materials of different thickness shall be less than <1/4.

3.3.3. Distortion and Shrinkage

Distortion and shrinkage during welding is to be minimized for avoiding stress concentrations and to achieve dimensional accuracy. The following methods are used to minimize distortion and shrinkage;

- *Minimum heat input/unit length of weld.*
- *Welding on both sides wherever possible.*
- *Sequencing of welding.*
- *Simultaneous welding of two (or) more welders in case of large length welds and large dia pipes.*
- *Use of minimum bevel angles.*
- *Use of special fixtures wherever required.*
- *Limiting the number of repairs to two.*

3.3.4. Tests to be carried on production test coupons

The qualification production test coupons must undergo all the destructive and non destructive examinations applied in fabrication for the joints it qualifies and must satisfy the highest quality level requirements applicable to these joints. These requirements make the procedure qualification more difficult than that qualified by only tensile and bend tests required as per ASTM.

4. Manufacturing

Considering the complexities involved in manufacturing of large sized components to meet the design requirements, concrete procedure was developed for each stage of action involving the activity, its process, its inspection methodology, and the NDE requirements. A few stages of manufacture involving challenging works are discussed below.

4.1. Forming of Dished End & Conical Petals

The safety vessel dished end consists of knuckle and crown portions. Due to the inherent size of the vessel, the knuckle portion of radius (IR of 4815mm) is divided into two halves in the meridional direction and a total of 22 petals in the longitudinal direction. The crown of radius (IR of 19650mm) is divided into two halves in meridional direction and a total of 7 petals in the longitudinal direction constituting overall total of 29 petals for the dished end. The main vessel has 39 petals (2 tiers of crown region having 7 petals of 30 mm thick, 1 tier of transition region having 10 petals of 40 mm thick and 2 tiers of knuckle region having 22 petals of 30 mm thick). The inner vessel has 14 special shape conical petals with double curvature at the top and bottom end. The diameter at the top is 12200mm and at the bottom is 6350mm with an overall height of 3294mm. Redan petals are trial assembled at manufacturer works on a row-by-row basis without the closing petals. Full trial assembly is carried out, dismantled and then brought to site for reassembly and welding.

Prior to procedure qualification, a mock-up of the petal pressing was carried out using carbon steel material of 20 mm thick to check the feasibility of pressing without point pressing and thereby qualify the vendor. On successful completion of the mock-up testing, procedure qualification was carried out on SS material for typical regions of dished end petals. Further to template measurement, basket gauges were used for checking the profile of petals. Full size die and punch were deployed, incorporating the spring-back allowances for pressing since, point pressing was not recommended.

FIG. 2. Safety Vessel Dished end with Swing Arm Gauge

These large size petals are to be formed to very close tolerance by developing dies and punches. Profile inspection of these large sized petals requires a special technique of inspection by using templates and employing non contract method. Dduring assembly, a special inspection method, such as Swing Arm Gauge and Electronic Coordinate Determinate System are used for accurate inspection of these large dished end vessels. All the welds are ground flush with the base material or to required radius and are examined by visual, liquid penetrant inspection on weld edge preparation (before weld fit up), root pass, back gouge and on the finished weld. 100% of the weld length is examined by radiography inspection methods and helium leak tested under vacuum by jacket method.

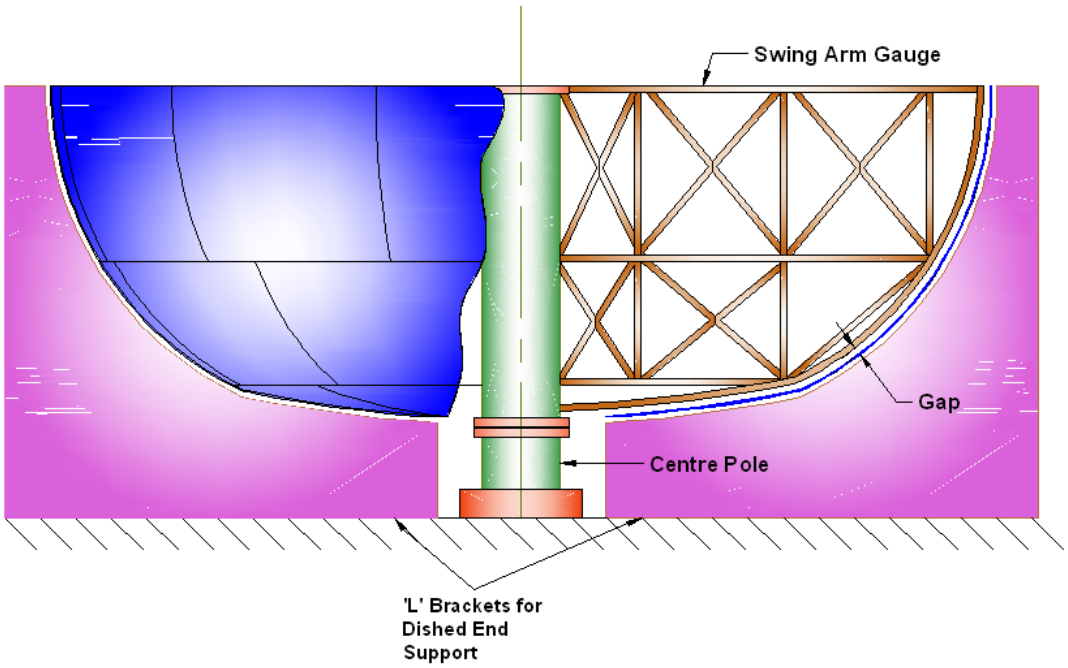

FIG. 3. Typical Swing Arm Gauge for Dished End

4.2. Circumference Matching

The cylindrical portion of the safety vessel, main vessel, and inner vessel consists of 3, 4 and 2 shell courses, respectively. Initially, shell segments were taken up for fit up and then welding was carried out with one shell segment space open. After completion of segments welding, the last closing segment is trimmed accordingly to maintain the circumference specified. Subsequently, the weld edge preparation for the last segment was made after fixing the length for meeting the required circumference considering the root gap and weld shrinkage and then welded to form the shell course. On completion of shell courses, shell course-1 and shell course-2 were welded circumferentially, followed by shell course-3.

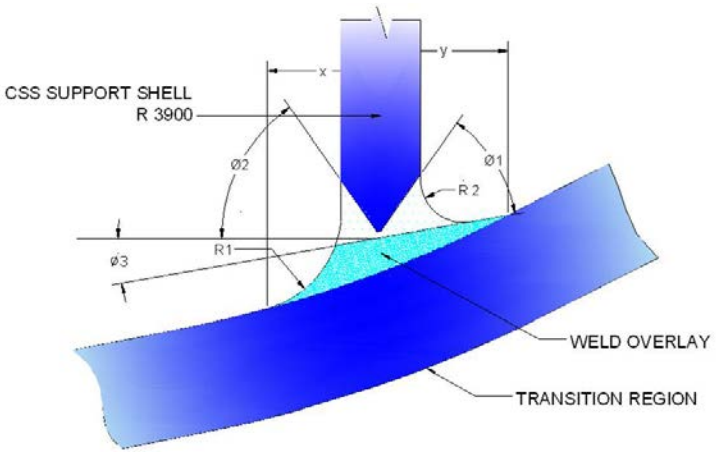

FIG. 4. Main Vessel Weld Overlay

4.3. Weld Overlay at Transition Region

To facilitate the weld between the core support structure support shell and the transition region, weld deposition was carried out on the inside surface of the transition region along the circumference. This 25 m circumferential weld deposit was carried out in a sequential manner by continuous monitoring on the heat input, interpass temperature and other weld parameters. The contour and profile were achieved as per drawing respecting the elevation requirements by grinding. The transition region was inspected by ultrasonic examination before and after overlay.

4.4. Welding of Core Support Structure Support Shell

The welding of the core support structure support shell on weld overlay was carried out in a phased manner. This support shell of 3900 mm radius and 30 mm thick consists of three segments. 24 holes were drilled on the circumference of the shell prior to welding to the transition region considering the root gap and shrinkage allowance. Circumference of shell, elevation of 24 holes and orientation of holes with respect to thermal baffle support plate were achieved within the tolerances specified. Utmost care was taken to maintain the circumference and verticality during welding of core catcher support plate inside the shell. This facilitated easy welding of the main vessel cooling pipes to the thermal baffle support.

4.5. Integration of the Thermal Baffle with the Main Vessel

Two concentric shells of diameter 12440 mm and 12670 mm with a total baffle height of 4930 mm was lifted with a suitable lifting spider and integrated with the main vessel. The requirement on horizontality of the thermal baffle was stringent due to its system requirements. The annular space between the thermal baffle and the main vessel was maintained by maintaining the horizontality of the baffles. Controlled heat input and sequencing of welding were key parameters to achieve the specified tolerances.

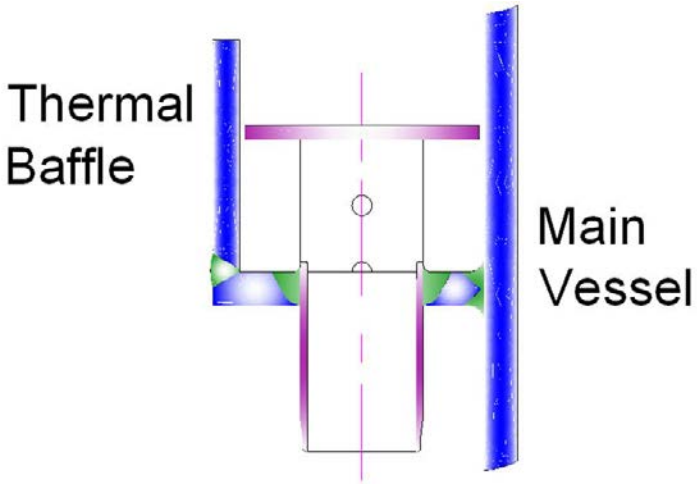

FIG. 5.

4.6. Hard facing of inner vessel standpipes

There are four hard faced standpipes in the inner vessel (Fig.6 and 7) through which intermediate heat exchangers pass through. These standpipes form part of the mechanical seals to minimise leakage of hot sodium into cold pool. After hard facing of the first standpipe, multiple cracks in the hard face deposit and large ovality in the standpipe were noticed. The cause behind this was critically analysed. The first standpipe was rejected and the following improvements were made in the hard facing of other standpipes. The hard facing groove configuration was modified. For preheating and post weld heat treatment, the cooling, heating and holding were rigorously controlled so as to be uniform throughout the standpipe, the insulation thickness and effectiveness were improved, rigid circumferential and longitudinal restraints were tack welded to the outside of the standpipes, deposition parameters were suitably modified etc. With these changes, number of cracks and the ovality issues were significantly reduced. The residual ovality was nullified by calculated and careful mechanical correction. The small number of cracks noticed was repaired by local grinding and re-deposition.

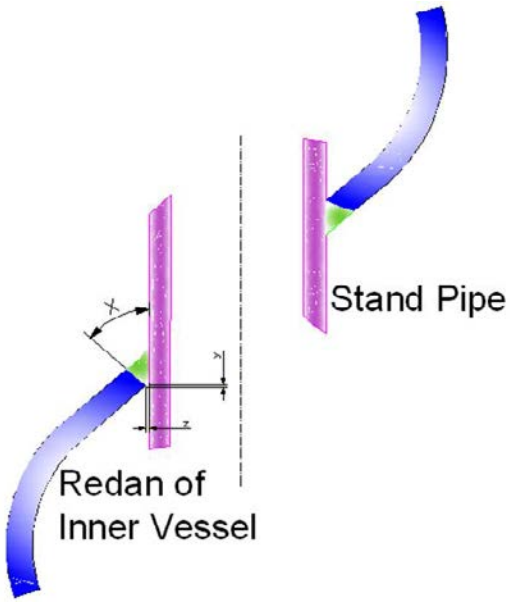

FIG. 6. Stand Pipe weld on Inner Vessel

4.7. Inner Vessel stiffener and stand pipes for pump, heat exchangers and level detectors

The upper shell is stiffened by a ring of 20 x 50 mm dimensions all along the circumference in order to: increase the dimensional stability of the cylindrical shell, enhance the buckling resistance of the shell to axial thermal gradients, provide vibrational stability against sodium free level fluctuations. The outer diameter of the upper shell (12200 mm) is arrived at by considering the minimum clearance required for welding of the IHX and PSP standpipes to the redan.

FIG. 7.top View of Inner Vessel with all stand pipes

Welding of a stiffener ring on the thin walled shell was carried out by sequential welding on both the sides of the shell. The OD, ID and flatness of the stiffener was achieved within specifications leaving the dimensions of the inner vessel shell undisturbed.

There are 8 penetrations in the redan; 2 for primary sodium pumps (PSP), 4 for Intermediate heat exchangers (IHX), 1 for cold pool level detector, and 1 for sodium purification & sodium fill and drain

lines. The stand pipes for all of the penetrations, except at the IHX, extend up to the cover gas space there-by isolating the hot pool from the cold pool.

The locations of these stand pipes were transferred from the roof slab to the inner vessel redan. The coordinates (X,Y) of stand pipe openings from roof slab were transferred to inner vessel with reactor centre as reference and the cut out on redan were made. The stand pipes were welded to the redan portion of the inner vessel. Verticality, location of stand pipes with respect to the inner vessel center was achieved within the tolerance limits.

The challenges faced in the manufacture of inner vessel were due to hard facing in the IHX standpipes, pressing and assembly of conical petals with toroidal ends to close dimensional tolerances, assembly of standpipes on the penetrations in conical shell with control on position and verticality of standpipes, and achieving the requirements on the bottom flange that has interface with the grid plate.

5. Quality Assurance

Quality assurance activities on these over dimensional vessels commenced from the procurement stage of raw material to the final dimensional inspection viz, non destructive examinations liquid penetration examination, ultrasonic examination, radiographic examination and Helium leak test for joints were carried out on these massive vessels. Apart from conventional dimensional measurements, electronic coordinate determination system of measurements were carried out on all the vessels.

6. Conclusions

The challenges in manufacture of over dimensional vessels of such large size ignited the Indian industry in tuning the manufacturing process. The experience in manufacturing of over dimensional components promises the indigenous development in Indian industries. The feedback of such experiences will be useful for the future FBR programme in India for reducing the construction time.

ACKNOWLEDGEMENTS

The authors are thankful to the Technology development team, M/s.L&T – Hazira and Kalpakkam site team, M/s.KRR-Chennai, NPCIL QS-Hazira & Chennai, Standing Task Force – 1 for reactor assembly components of PFBR comprising designers & Engineers from IGCAR & BHAVINI for their valuable contribution towards successful completion of the large sized vessels.

REFERENCES

[1] S.L.Mannan, S.C.Chetal, Baldev Raj and S.B.Bhoje; “Selection of Materials For Prototype Fast Breeder Reactor” J. Transactions of the Indian Institute of Metals 2003, vol. 56, pp. 155-178 [24 page(s) (article)].

[2] V.Balasubramaniyan, P.Puthiyavinayagam, P.Chellapandi, S.C.Chetal, “Experiences with Design and Manufacture of Reactor Assembly Components of PFBR”, abstract – 218, Proceedings of the International symposium on advances in stainless steel 2007, April 9 – 11, 2007, Chennai, India

DESIGN AND FABRICATION OF SERPENTINE TUBE TYPE SODIUM TO AIR HEAT EXCHANGERS FOR PFBR SGDHR CIRCUITS

ARAVINDA PAI[†], TARUN KUMAR MITRA[‡], T.LOGANATHAN[§], PRABHAT KUMAR[††]

Bharatiya Nabhikiya Vidyut Nigam Limited (BHAVINI)
Prototype Fast Breeder Reactor (PFBR) Project
Department of Atomic Energy
Kalpakkam - 603 102, India

Presented by ARAVINDA PAI

ABSTRACT

Prototype Fast Breeder Reactor (PFBR) is a 500MWe pool type, sodium cooled nuclear reactor which is in advanced stage of construction by BHAVINI at Kalpakkam, India. The sodium to air heat exchanger (AHX) in the safety grade decay heat removal (SGDHR) loop transfers heat from the intermediate circuit sodium to atmospheric air by natural convection. As the operating temperature is high and AHX forms part of reactor SGDHR system, the boundaries of the AHX must possess a high degree of reliability against failure. This is achieved by comprehensive design, precise material selection, high standard quality control and quality assurance during manufacturing. The major material of construction of AHX is Modified 9Cr-1Mo steel (N&T). AHX has straight sodium inlet and outlet headers with 116 nos. of hot formed pullouts on its surface having OD38.1mmX2.6mm thickness which are connected to a finned tube bundle. Due to the many hot formed pullouts on the headers and complex geometry, the welding sequence, heat treatment and non-destructive examinations of the welds is an extremely difficult and challenging task. Various special tooling and fixtures were designed and developed for the manufacture of the AHXs. This paper provides details of the salient design aspects, challenges, innovations and success achieved during hot forming, welding and fabrication activities of the serpentine tube type AHXs for 500MWe Prototype Fast Breeder Reactor.

1. INTRODUCTION:

Safety and reliability are of prime and supreme importance when it is referred to nuclear power plant. Nuclear decay heat generated in the core after reactor shutdown has to be removed to avoid core meltdown and maintain the structural integrity of reactor components. Therefore, a highly reliable SGDHR system is provided in PFBR. The SGDHR (Figure-1) system mainly consists of four independent loops each the 8MWt heat removal capacity. Each loop consists of one sodium to air heat exchanger (AHX) and one decay heat exchanger (DHX) which work on the principle of natural convection. Each AHX and DHX in two SGDHR loops are having one type of design concept and remaining two nos. of AHX and DHX in other two SGDHR loops are of different design concept to avoid common cause failure during reactor operation. Decay Heat Exchangers transfers heat from the primary radioactive hot pool sodium to the intermediate circuit sodium. AHX transfers heat from the intermediate circuit sodium to the atmospheric air by natural convection. Ambient air is induced

[†] Scientific Officer (Long Range Planning and Strategies), BHAVINI, Kalpakkam, India
[‡] Director (Technical), BHAVINI, Kalpakkam, India
[§] Project Engineer (QA and NDE), BHAVINI, Kalpakkam, India
[††] Chairman and Managing Director, BHAVINI, Kalpakkam, India

through AHX tube banks by a natural draft in the stack. Inlet and outlet air dampers are provided in AHX with diversity in damper drives to enhance the reliability of circuit activation.

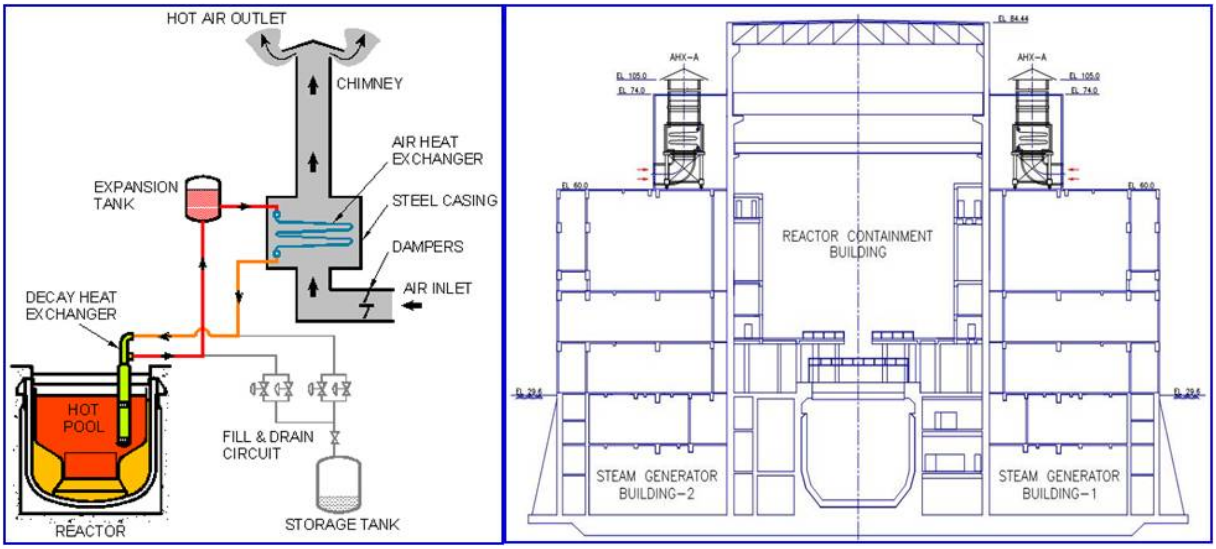

FIG. 1. Safety Grade Decay Heat Removal System Circuit diagram

The AHX (Figure-2) is a cross flow type finned tube heat exchanger. Modified 9Cr-1Mo ferritic steel (N&T) is selected for the major AHX components and are procured as per PFBR specification with stringent acceptance criteria. The AHX has straight sodium inlet and outlet headers. Each header has 116 hot formed pullouts which are connected to the serpentine tube bundle in 3 rows arranged in 4 banks. There are 116 modified 9Cr-1Mo tubes of size OD38.1X2.6mm wall thickness containing SS409 fins on its surface. The tube bundle is supported at two locations in an unfinned portion in the vicinity of the U bends. The integrated tube bundle along with the headers are placed inside the carbon steel casing. The inlet and outlet sodium headers are supported at three locations and supports are finally connected to the casing. Bonded mineral wool insulation is provided on the inner surface of the steel casing.

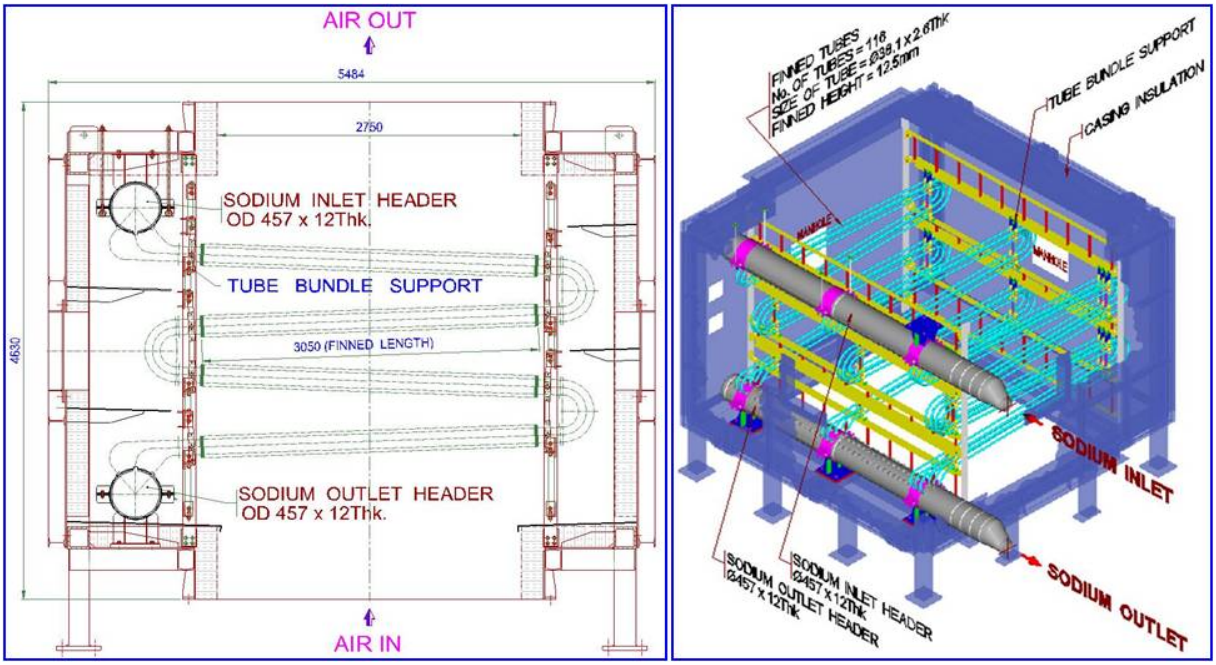

FIG. 2. Sodium to Air Heat Exchanger

Design, manufacture and quality assurance for AHXs are of prime importance from a safety and reliability point of view. Therefore, a highly conservative design was made and specifications requirements for manufacture is kept very stringent compared to the specification of other industrial applications[1]. Optimized design, correct material selection, high standard quality control and quality assurance during manufacture has given confidence on the reliability of the AHX for the design service life of 40 years.

2. DESCRIPTION OF FABRICATION AND MAIN CONSIDERATIONS:

Tubes, headers, pullouts and tube weld joints are identified as the most critical items during the design and manufacture of the AHX. Specification requirements are stringent, as they play a vital role while evaluating the tube bundle integrity. The tubes are produced by electric arc melting technique followed by electro slag refining (ESR) with tight control on inclusion content. Ultrasonic and eddy current testing is done on the entire tube length in accordance with ASME SEC III Class I. Ultrasonic examination is done for detection of both longitudinal and transverse defects. Each tube is subjected to a hydrostatic test with demineralized water. Modified 9Cr-1Mo plates for the headers are procured in normalized and tempered condition as per PFBR specification with stringent acceptance criteria. During material procurement, all plates were subjected to a thorough visual examination/liquid penetrant examination (LPE) and 100% ultrasonic examination (UE) scanning with overlapping of at least 10% of the previous scan to ensure soundness of plate. During plate and tube procurement, tensile testing at high temperature is carried out in addition to ambient temperature on plate and tube specimens to evaluate and ascertain the properties for service conditions. In addition, specimens of tubes and plates were procured with simulated heat treated condition meeting mechanical properties.

The top inlet header and bottom outlet header is connected to the heat exchanger tubes through header pullout to tube weld joints. The header pullout region is extremely sensitive where maximum stress is anticipated during reactor operation due to its geometry (Figure-3). The welds as well as heat affected zone (HAZ) being the weak regions are desired to be located away from the highly stressed zones. The hot formed integral pullout concept on the headers is envisaged in the design to ensure that the tube-to-header weld joints are away from the region of geometrical discontinuity where stress concentration are high. In addition, the straight portion in the pullouts facilitates 100% radiography of critical weld joints between pullouts and tubes for evaluating the quality during fabrication.

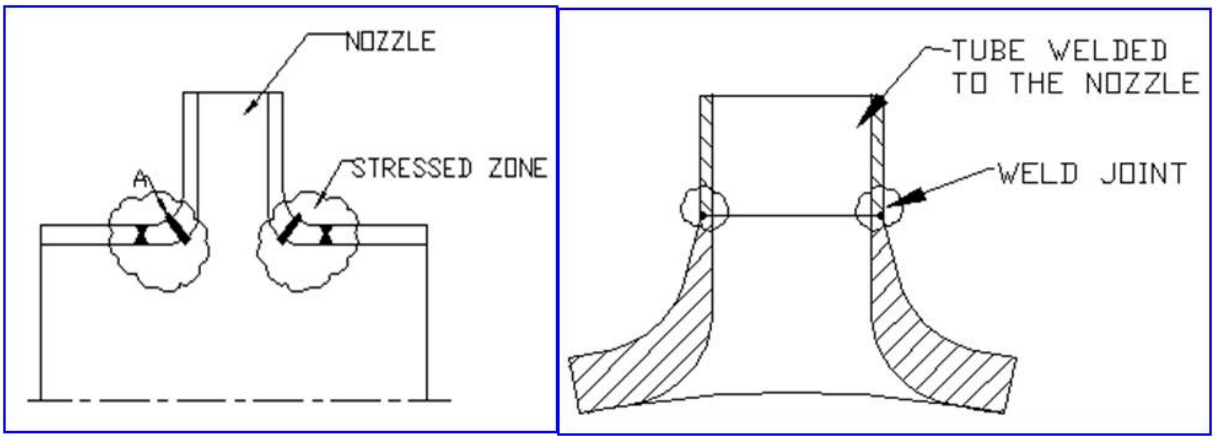

FIG. 3. Conventional nozzle concept and pullout concept

The alternative option of forming integral nozzle pullouts on headers by machining from higher thickness plate is not considered due to the high material/machining cost involved. As header pullouts are part of tube weld joints, it is very much essential to form the highest quality pullouts on the headers to achieve sound weld joint between the header pullout and the tube.

3. HOT FORMING OF PULLOUTS ON HEADERS AND PROCEDURE QUALIFICATION:

The AHX has straight inlet and outlet headers having an outer diameter of 457.2mmX12mm thickness and length of about 6 meters. The half cylindrical segment of inlet and outlet header is formed by rolling process. Each header has 116 hot formed pullouts on its surface (Figure-4). The forming of the pullout is carried out at 900-1100^{0}C followed by die and punch pressing.

FIG. 4. Machining of hot formed pullouts on the header segment

The header pullout forming qualification is a concentrated effort. The forming of pullouts on modified 9Cr-1Mo material is a difficult and challenging task due to the poor ductility of the material[2]. As the material possesses a tendency toward higher cracking during forming, enormous trials were conducted to optimize the process parameters to get high quality pullouts meeting the specification requirements. Heating of the entire header segment inside the furnace followed by forming of pullouts individually by die and punch pressing in conventional method in various stages is not recommended for the selected material (Modified 9Cr-1Mo) as the material is expected to undergo a repeated heating and cooling cycle which may deteriorate the material properties. The forming of pullouts in a group is practically not possible as the angular orientation is not the same for all pullouts and varies depending on the cylindrical profile. The above metallurgical and practical limitations required for development of a special die and punching tools and heating arrangements for hot forming of individual pullouts. Many trials were conducted to establish the size of the die and punch and also to decide the required volume of material for achieving the required dimensions and profile of pullouts at the specified forming temperature. The forming of the pullout is carried out by heating the local area of header shell segment using an induction heating process followed by die and punch pressing. A radiation type pyrometer is used for monitoring the temperature during induction heating. The headers after pullout forming undergoes normalizing at 1050-1090^{0}C followed by tempering at 780±10^{0}C to restore the original material properties.

Initially, a small diameter pilot hole is made at the pullout location to ensure accurate punch contact with header segment during forming. The material flow during forming and dimensions of pullouts are influenced by these pilot holes. Various pullout forming trials were conducted with different pilot hole diameters on header shell to get the required material flow, profile and dimensions. The trials conducted with smaller diameter pilot holes have shown cracks during visual examination and the profile was not smooth due to the higher material flow and improper punch contact. The bigger diameter pilot holes have shown crack free pullouts with an acceptable smooth profile with reduced pullout height and diameter due to insufficient material availability during forming. Finally, forming

trials carried out with optimized 6mm diameter pilot hole is meeting the pullout dimensions and formed surface showed good workmanship and the pullout was free from dents and cracks.

The forming process for header pullouts is qualified with 6 nos. of pullouts on qualification header segment simulating the actual job conditions. During qualification, dimensional check, thorough visual examination, liquid penetrant examination (LPE) of entire formed surface, in-situ metallography, tensile test at room temperature and elevated temperature and impact test is carried out after heat treatment of pullouts. “No indication” is the acceptance criteria for LPE. The mechanical properties of pullouts are met as per the original plate requirements. The actual job header pullouts are subjected to a thorough visual examination, dimensional inspection and LPE for the entire formed surfaces.

4. TUBE BENDING AND PROCEDURE QUALIFICATION:

The AHX tube bundle consists of various types of bend tubes of OD38.1X2.6mm wall thickness. Three tubes having minimum bend radius is qualified in the bending procedure before bending on actual job tubes. During procedure qualification, thorough visual examination, LPE of the entire bent surfaces, dimensional and lay out check for profile is carried out. In addition, sections are cut from each bend for verification of thickness and ovality. Visual examination specifies good workmanship and formed surfaces are to be free of dents and cracks. “No indication” is the acceptance criteria for LPE. The wall thinning allowance and ovality for the bend is restricted to a maximum of 12.5% and 8% respectively. The process parameters finalized during procedure qualification are adapted during bending of actual job tubes. The job bend tube undergoes a thorough visual examination, LPE and dimensional inspection after stress relieving at 760±10^{o}C for a minimum 30 minute soaking time.

5. HEADER WELDING AND FABRICATION:

After pullout forming, the longitudinal (figure-5) and circumferential seam welding of header segments is carried out to form a complete cylindrical header. Before welding, all modified 9Cr-1Mo joints are preheated at 200-250^{0}C and interpass temperature is maintained at 200-250^{0}C. After welding, post heating is carried out at 200^{0}C for 2 hours. One of the major problems associated with welding of modified 9Cr-1Mo steel is poor toughness of weld metal produced from any of the processes that involves use of flux. Data available in literature indicates that the toughness of weld metal produced by using these processes is far inferior (in the range of 40–100J) while that of the weld metal produced by Gas Tungsten Arc Welding (GTAW) process (typically 200J). Even though Shielded Metal Arc Welding (SMAW) process is permitted as per PFBR specification, 100% GTAW process alone is adapted to meet impact properties. In addition, GTAW process also ensures clean and quality welds for component during fabrication.

FIG. 5. Header longitudinal seam welding in the shop

Global purging of high purity argon gas is done to the entire inside volume of the headers during root and subsequent pass of GTAW process, as local purging from inside is ruled out due to very small access. Initially, argon gas flushing is done to evacuate the oxygen content available inside the volume

of header assembly to ensure availability of high purity argon gas during root and subsequent pass of GTAW process.

The welding procedure is qualified with stringent destructive and non-destructive examinations and testing before welding on the actual job. The qualification test coupons are subjected to all non-destructive examinations applied in fabrication of actual job. During qualification, weld joints are subjected to thorough a visual examination, LPE, radiography examination (RE), longitudinal tensile test at ambient temperature, transverse tensile test at ambient temperature and high temperature, bend tests, Charpy V notch impact test, hardness survey and metallographic examination at 200X magnification for the complete transverse section of weld. Each production weld joint undergoes a thorough visual examination, LPE and RE as per PFBR specification with stringent acceptance criteria. If RE is not possible, the soundness of welds is evaluated by ultrasonic examination (UE). After completion of Post Weld Heat Treatment (PWHT), a thorough visual examination, LPE and RE/UE is repeated on each weld.

The welding and fabrication of 12mm thick slender header shells having outer diameter of 457.2mm is a challenging and tricky task. Maximum 1% ovality is allowed during fabrication of cylindrical headers. Minimum ovality is desirable which reduces the bending stresses on headers during service. The distortion tendency for the header shell is less due to a smaller diameter and existence of formed pullouts, which will resist the material flow and distortion during welding. Even then, utmost care is inevitable during welding to avoid distortion and dimensional deviations. Due to the small inside diameter, the internal fixtures/spiders cannot be used at many locations for distortion control during welding. Due to many formed pullouts on the outer surface, fixtures/spiders cannot be placed directly on the headers during welding. Re-rolling after welding is not permitted as per PFBR specification, which may induce stresses on weld joints and may cause crack/failure of weld joints in thermal transient conditions during reactor operation. Due to all these limitations, it was inevitable to continually improve the processes, techniques and practices to reduce ovality in headers during the welding process itself. Many welding trials were conducted to understand the behavior of shells to meet the specified dimensions. Tremendous effort was expended to achieve less than 1% ovality during the welding process.

FIG. 6. Header circumferential seam machining and welding in the shop

Header fabrication involves welding of both longitudinal seams as well as circumferential seams to cover the entire length. As there is no sufficient access from inside of the header shells, the welding is carried out only from the outside. Due to this limitation; the shell joint weld edge preparation (WEP) has only a single V type WEP. The sequence of performing welding on the header assembly plays an important role in determining the quality. The longitudinal seams are welded first and then adjacent circumferential seams are welded to avoid stresses on longitudinal seams. Figure-6 shows WEP machining and welding of the circumferential seam of the header.

During shell fabrication, it is not advisable to stop welding after a single pass, as thickness of the weld is around 2mm which may not take the shrinkage stresses. There was a concern regarding the root pass weld cracking because of the high hardness (typically greater than 440 VHN) of deposited weld metal and shrinkage stresses. Therefore, welding is stopped for performing NDE after two layer welding (4-5 mm thickness of weld). Many trials were conducted on mock ups to examine defects for the root thickness of 4mm by hot MPE and ultrasonic examination. The trials were not successful for detecting the defects. As welds are subjected to preheating, it is not advisable to carry out LPE for the root run, in which case weld is to be cooled and preheating is to be done again before start of subsequent passes. Due to all these reasons, it was decided to carry out thorough visual examination at higher magnification in hot condition after completion of welding for the root run (4-5 mm thickness of weld). After completion of welding process for the complete thickness, welds are smoothly merged with base material to avoid abrupt geometrical discontinuity which may act as stress risers during reactor operation. In addition, smooth merging helps in performing effective and efficient ultrasonic examination of weld joints during fabrication of component and also during in-service inspection. The handling of headers before PWHT is done without direct lifting using belts and crane to the extent possible to avoid cracking of welds due to the very high as-welded hardness of modified 9Cr-1Mo welds.

6. TUBE BUNDLE FABRICATION AND CHALLENGES:

The tube bundle fabrication of AHX mainly consists of fin welding on modified 9Cr-1Mo tubes, header pullout to bend tube welding, serpentine M tube fabrication and integration of M tubes with bend tubes.

6.1. SS409 Fin welding on modified 9Cr-1Mo tubes:

SS409 fins are helically wound on modified 9Cr-1Mo tubes for increasing the surface area for heat transfer and are welded using a high frequency resistance welding process. The fin welding process is qualified as per ASME section IX. The process qualification requires that a minimum of 12 nos. of cross section through the weld zone shall be examined at 5X minimum magnification. There shall be no cracks in the base metal/weld and weld penetration shall be limited to a maximum of 20% of the nominal tube wall thickness. In addition, a tension test is carried out by radial pulling of fins and tensile strength value is reported.

6.2. Header to bend tube welding and Serpentine M tube fabrication:

Tube bundle activities of the AHX are carried out in separate nuclear clean hall conditions as per class-1 component requirements of PFBR to ensure the quality. The header pullout to bend tube welding (Figure-7) is carried out by manual GTAW process using ER 90S B-9 filler wire. The single V butt type of weld joint design is chosen for header pullout to bend tube welds. Due to very limited access and constraints, header pullout to bend tube welding requires highly skilled welders. Special fixtures were used for distortion control during the manual welding process.

There are three tube-to-tube joints to be welded in the AHX to form a single serpentine M shaped tube. Tube-to-tube welding (Figure-8) for M tube fabrication is carried out by automatic pulsed GTAW process in 5G position using ER 90S B-9 filler wire. The square butt type of joint design is selected and welding is carried out in two passes. LPE is carried out for WEP before setup of tubes to examine the surface indications if any. Each tube-to-tube joint undergoes preheating at 200-250^{o}C (Figure 8) and PWHT at 760±10^{o}C.

The final integration of the M tubes with header bend tubes is carried out after keeping both inlet and outlet headers in a horizontal condition inside the structural casing as shown in Figure 7. The final integration welding of M tubes with header bend tubes is carried out by automatic GTAW process in 2G position in two passes. The first pass is carried out by autogenous welding process and second pass by automatic welding process using ER 90S B-9 filler wire. The WEP, preheating, and PWHT requirements for integration tube-to-tube weld joints is similar to that of M tube to tube weld joints.

A separate welding procedure qualification is required to be carried out for header pullout to tube welding process and tube-to-tube welding processes with stringent destructive and non-destructive examinations and testing before welding on the actual job. During qualification, weld joints are subjected to a thorough visual examination, LPE, RE, transverse tensile test at ambient temperature and high temperature, bend tests, hardness survey and metallographic examination. Each job weld joint is subjected to a thorough visual examination, LPE, RE, pneumatic test and helium leak test (HLT) as per PFBR specification. HLT for tube-to-tube weld joints is carried out at M tube stage (Figure-8) in addition to final assembly stage (Figure-7) as a precautionary measure. The acceptance criteria for all these examinations are stringent compared to the acceptance criteria of ASME or other codes.

FIG. 7. Header pullout to tube welding and final integration in the shop

Production Test Coupons (PTCs) are welded for every 15 tube to pullout/tube production welds adapting same process parameters of the job welds to ascertain and control the quality of welds during production. The PTCs undergo all the destructive and non-destructive examination and testing carried out during procedure qualification.

FIG. 8. Preheating, welding and HLT for tube to tube joints of M tube

7. POST WELD HEAT TREATMENT (PWHT) AND CHALLENGES:

It is very important during material procurement to procure the materials (base and weld material) with simulated heat treatment and tested condition with additional soaking hours to ensure minimum required material properties. The additional soaking hours during simulated heat treatment is essential if PWHT of complete fabricated component is proposed to carry out in different heat treatment cycles or in case repair of any of the weld joints after PWHT (in which case re-PWHT is required after

repair) or stabilization heat treatment of the base material if carried out for dimensional stability during welding.

7.1. Difficulties in PWHT of headers and pullout to tube weld joints:

After fabrication, headers are subjected to PWHT at 760±10^{o}C to relieve the welding stresses and to get a homogenous tempered martensite structure. A dedicated calibrated electrical furnace is used for heat treatment with a controlled heating and cooling rate to avoid thermal shocks and distortion of components. The complete cylindrical header is divided into eight zones during PWHT. 100% redundancy thermocouples were kept along the headers at various locations to monitor and maintain the temperature difference in a narrow band. Nitrogen gas purging is done on the complete inside volume of the headers during PWHT to avoid oxidation of inaccessible inside surfaces. Special arrangements were made to take care of thermal expansion of the complete header assembly during PWHT. Mechanical rollers which can sustain high temperature were kept beneath the saddle supports of headers at various locations to take care of the thermal expansion during heat treatment.

Due to complex constructional features of AHX, the PWHT is an extremely challenging task. The PWHT of individual tube-to-tube weld joints are carried out by electrical resistance method using a metallic split cartridge (Figure-9). An enormous number of trials were conducted to establish the procedure for local PWHT of header pullout to tube weld joints using metallic split cartridge. The temperature control was extremely difficult due to the asymmetric shape and the non-uniform mass of pullouts. As local PWHT trials were not successful, it was decided to carry out PWHT of the header pullout to tube weld joints along with PWHT of the 12mm thick header weld joints in different charges; as such heat treatment methodology is acceptable as per ASME.

After fabrication of complete cylindrical header, PWHT is carried out at 760±10^{o}C for two hours soaking time for 12mm thick longitudinal and circumferential weld joints. After clearing the NDEs for joints, welding of the middle row header pullout to tube joint is carried out and complete header assembly is again heat treated at 760±10^{o}C for one hour soaking time, during which 12mm thick weld joints undergoes PWHT for a total of three hours and middle row pullout to tube weld joints undergoes heat treatment for one hour soaking time. After clearing NDEs for the weld joints, inner and outer row header pullout to tube welding is carried out. Subsequently, the complete header assembly is again subjected to heat treatment for another one hour soaking time, during which time the 12mm thick weld joints undergoes heat treatment for a total of four hours. The middle row header pullout to tube weld joint undergoes heat treatment for a total of two hours. The inner and outer row header pullout to tube welds undergoes heat treatment for a total of one hour soaking time.

Special fixtures were required to be used for bend the tubes (which are welded on headers) to avoid distortion at high temperatures during heat treatment. At each of the above stages, the RE is performed before PWHT to avoid repair of the weld joint if any after PWHT, in which case additional qualification is required for weld properties with additional soaking hours during heat treatment. In addition, the quality of each weld joint is ensured by various non-destructive examinations after each heat treatment cycle. The base materials (plate and tube) and weld materials are qualified for their properties with additional heat treatment cycles before going ahead with such heat treatment procedure on the actual job.

7.2. Challenges in PWHT of integration weld joints between M tubes and header bend tubes:

After integration of M tubes with header bend tubes, the local PWHT is carried out using a metallic split cartridge method similar to PWHT of tube-to-tube joints of M assembly. As headers are kept in a horizontal condition for facilitating integration activities, there was a concern of load (~75 kg) of M tube acting on 2.6mm thin integration tube weld joints during heat treatment. Therefore, various PWHT trials were conducted using ~75 kg load on the trial tube weld joints during heat treatment (Figure-9). During trials, it was found that no deformation was observed on or near tube weld joints either during PWHT or after PWHT. Even though trials are successful, it is always advisable to carry

out PWHT in free condition. Due to the critical nature of the tube-to-tube weld joints, it was decided to give an equal and opposite reaction load (~75 kg) using support channels and hydrualic jack at the bottom of each M tube to doubly ensure that the PWHT of integration tube weld joints is carried out in a free condition.

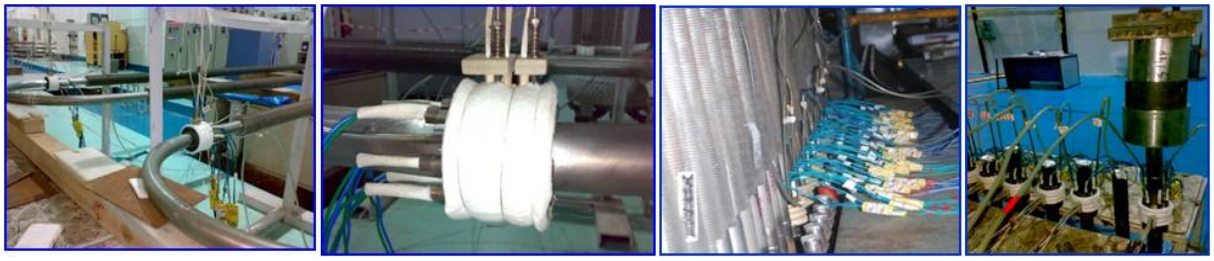

FIG. 9. Local PWHT of tube to tube weld joints and trials conducted for local PWHT

8. PNEUMATIC TEST, SURFACE TREATMENT AND HELIUM LEAK TEST AFTER COMPLETE FABRICATION:

On completion of the AHX fabrication, the tube side is subjected to a pneumatic test at 8 bars gauge pressure for a minimum of 30 minutes hold time to check the integrity of the component. Neither a drop in pressure nor leakage/deformation is acceptable during the test. The AHX casing is tested at a pressure of 50 mbar (gauge) and pressure is maintained for 10 minutes. After the pneumatic test, surface treatment is carried out on the tube side to remove oxides/grease/oil from the surfaces. Surface treatment involves degreasing and pickling followed by passivation. Degreasing is carried out by circulation of indigenously developed alkali solution (DK 9.5)by heating the solution to 55 ± 5^{0}C. The pickling is carried out at ambient temperature by circulation of a mixture of 15% by volume of 70% concentrated HNO_3 and 0.05% by volume of 40% concentrated HF solution. Finally, passivation is carried out by circulation of 20% by volume of 70% concentrated HNO_3 at ambient temperature. After surface treatment, the AHX is presumed to be dry when 1mm of mercury vacuum is maintained for 30 minutes without pumping. Subsequent to surface treatment, the tube side is subjected to a helium leak test during which the global leak rate shall not be more than $6.66X10^{-9}$ Pa-m^3/s and local leak rate shall not be more than $2.66X10^{-9}$ Pa-m^3/s. Helium leak test is done after surface treatment which also ensures complete dryness of the component, as the test is done in vacuum mode.

9. CONCLUSION:

The design and manufacture of components should employ proven techniques and it should be possible to conduct analysis of the design as may be necessary for the purpose of demonstrating adequate integrity at any specified time throughout the plant life. The important fabrication rules are use of high standard materials, use of high quality welding during all the stages of manufacture supported by a quality assurance program. Very high standard quality control and quality assurance during design, raw material procurement, welding, fabrication, handling, inspection and testing has given confidence on trouble free service from the AHXs for the design service life of 40 years.

ACKNOWLEDGEMENTS

The authors are thankful for the fruitful discussion provided by the project team at M/s L&T, Powai, Mumbai, India.

REFERENCES

[1] Baldev Raj and T. Jayakumar, “Challenges in meeting reliability requirements in welding”, A book on “Welding metallurgy for Engineers” Indira Gandhi Centre for Atomic Research, Kalpakkam.

[2] Aravinda Pai, T.K.Mitra and Prabhat Kumar, “Challenges in the hot forming of modified 9Cr-1Mo header pullouts for PFBR Sodium to Air Heat Exchangers”, INSAC-2009, Chennai, India.

INNOVATIONS IN EQUIPMENT ERECTION OF PROTOTYPE FAST BREEDER REACTOR (PFBR)

S.Sreekanth, Dr.Prabhat Kumar

Bharatiya Nabhikiya Vidyut Nigam Limited (BHAVINI)

Department of Atomic Energy (DAE), Kalpakkam-603102

Kancheepuram (Dt), Tamilnadu, India

Fax No. 044 27480978, Email: skanth_bhavini@igcar.gov.in

Abstract. Prototype Fast Breeder Reactor (PFBR) is sodium cooled, pool type reactor with generating capacity of 1250 MWt/500 MWe. Reactor assembly consists of large dimensional vessels like Safety vessel (13.54 m diameter, 12.8 m height and weight approximately 155 MT) and Main vessel (12.9 m diameter, 12.94 m height and weight approximately 202 MT including core catcher, core support structure and cooling pipes) and Steam generator (26 m length, 1.5 m diameter, and weight approximately 35 MT). PFBR reactor equipment erection was a challenging task where thin walled vessels had transported and handled with utmost precaution to avoid radial forces on the vessels which could buckle the vessels. There was a real challenge in lifting the vessels without swing, placement of large size and heavy vessel at a distance of 57 m where the crane operator had no line of site to the equipment being erected. To handle such over dimensional reactor components many mock-up tests had been carried out before erection and gained lot of confidence. Lot of care had been taken during lifting, handling and erection of thin walled over dimensional reactor components with innovative methods used for lifting fixtures, guiding arrangements, alignment fixtures and achieved the stringent erection tolerances. This paper discusses the first ever experiences gained during the handling and erection of such thin walled, over dimensional reactor components at PFBR site.

1.0 Acknowledgement: The author acknowledges the contribution made by the designers of Indira Gandhi Center for Atomic Research, Kalpakkam, Reactor Equipment Erection group, Quality Assurance group and Industrial Safety group in BHAVINI (Bharatiya Nabhikiya Vidyut Nigam Limited), Kalpakkam during execution of the reactor component erection activities which are described in this paper.

The author also acknowledges the Atomic Energy Regulatory Board, Mumbai for guidance during finalization of erection procedures for erection of reactor components.

2.0 Introduction of PFBR

Prototype Fast Breeder Reactor (PFBR) is a sodium cooled, pool type, Mixed oxide fuelled (PuO_2-UO_2) fast reactor of capacity 1250MWt / 500 MWe. The reactor is having three main heat transport circuits namely primary sodium, secondary sodium and steam water system. The heat is generated in the reactor core is removed by circulating primary sodium through the core. The primary sodium then transfers its heat to the secondary sodium in intermediate heat exchangers (IHX). The secondary sodium heats up water in the steam generators to raise steam for running steam turbine to produce electric power.

The reactor assembly (RA) consists of Safety Vessel (SV), Main Vessel (MV), Core Catcher (CC), Core Support Structure (CSS), Inner Vessel (IV), Thermal Baffle (TB), Grid Plate (GP), Roof Slab (RS), Large & Small Rotatable Plugs (LRP & SRP), Control Plug (CP) and Absorber Rod Drive Mechanisms (ARDM). The vertical section view of reactor assembly is shown below. The reactor assembly is housed in a concrete vault lined with carbon steel called reactor vault. The roof slab is supported on a cylindrical support shell, which in turn is

welded to an embedment in the reactor vault. The roof slab supports the main components like MV, LRP, SRP, Intermediate Heat Exchangers (IHX), Primary Sodium Pump (PSP), Decay Heat Exchangers (DHX) and Delayed Neutron Detectors (DND). All reactor internals including core and primary sodium circuit is contained in a single vessel called main vessel. The main vessel contains about 1150 MT of primary sodium and is supported from top by welding to the outer shell of roof slab and is free to expand downwards. The MV is surrounded by a concentric vessel called safety vessel and ensures safe level of sodium in the main vessel even in the case of unlikely leak in main vessel. The safety vessel supported directly on the reactor vault independent of the support for main vessel. On outer surface of SV, metallic insulation of 150 mm thickness is provided to limit the heat transfer to the reactor vault. The sodium pool is divided in two parts as hot pool and cold pool by the Inner Vessel.

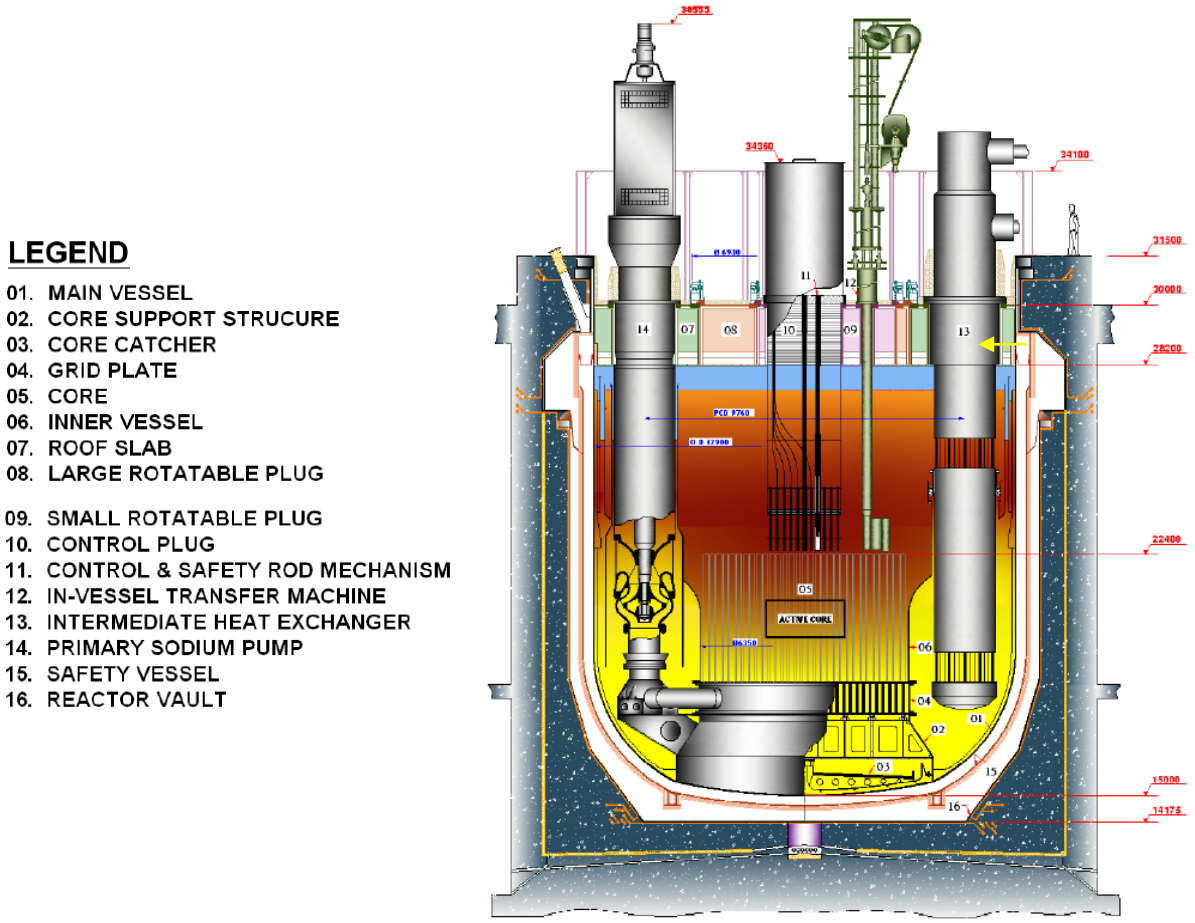

Fig.1. Vertical section view of reactor assembly

1.1 Site Layout details

The Prototype Fast Breeder Reactor (PFBR) site broadly divided into three parts. They are Site Assembly Shop (SAS) area, Nuclear Island (NI) and Power Island (PI). The site assembly shop is situated towards north side of Nuclear Island buildings. In Nuclear Island area, there are 17 buildings, out of that, 8 buildings (Reactor Containment Building (RCB), Steam Generator Building (SGB-1, SGB-2,), Electrical Building (EB-1, EB-2), Control Building (CB), Fuel Building (FB) and Rad waste Building (RWB)) are constructed on a single raft and they are called Nuclear Island Connected Buildings (NICB). The third part of the site is Power Island, in the Power Island Turbine building and Switch yard. The Power Island is situated towards south side of Nuclear Island.

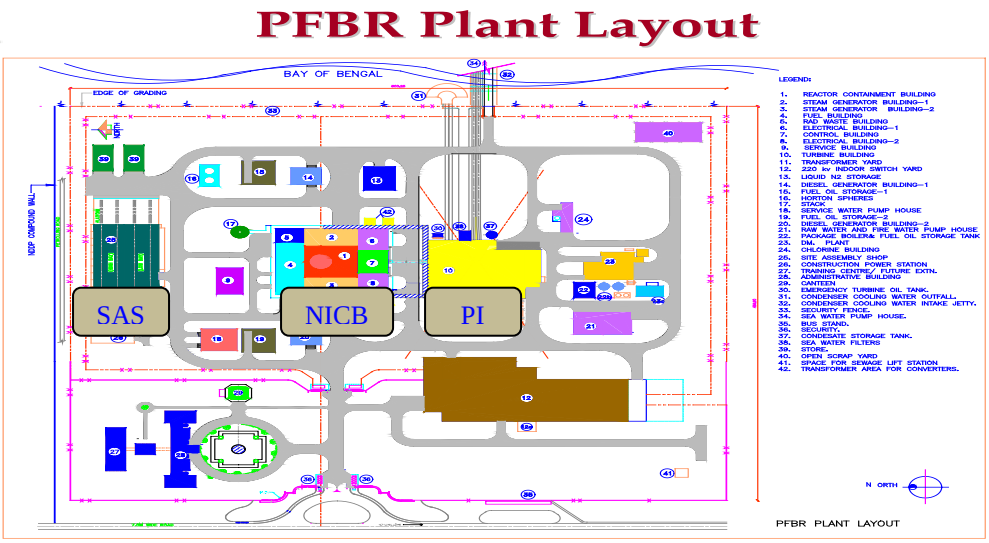

Fig.2. PFBR Plant Layout

3.0 Shifting and erection of safety vessel inside reactor vault

The Safety vessel is a large vessel made up of SS 304 LN material with a cylindrical shell of diameter 13.54 m with a special dished end at the bottom. The total height of SV is 12.8 m and thickness varying from 15 to 20mm. The outer diameter of the support flange of SV is 14.96 m. The SV support flange was welded to SV support embedment which was embedded in the reactor vault lower lateral portion at EL 26715 mm. SV contain the sodium that may leak from main vessel in the unlikely event and to ensure a safe level of sodium in the main vessel. On outer surface of SV, metallic insulation (each 0.1 mm thick sheet) of 150 mm thickness is provided to limit the heat transfer to the reactor vault concrete in order to maintain the temperature of concrete within permissible design limit. These SS insulation is a fragile sheet and nearly impossible to repair any defects occur on the same. The total weight of the SV including thermal insulation was 155 MT. Hence, handling of SV during the erection was a very challenging task.

Error! Objects cannot be created from editing field codes.

Fig.3. Safety Vessel with thermal insulation panels

3.1 Various mock-up tests and load tests conducted before erection of Safety vessel (SV)

SV

To handle such a huge over dimensional component, there was a requirement of conducting load test and mock-up tests before erection of SV. Hence, few load tests and two mock-up tests were carried out before erection SV into reactor vault and gained a lot of confidence. As part of the load testing a test base frame of size 16 m X 16 m was fabricated and placed a dummy load of 1.25 times of actual SV weight (i.e 194 MT). This test base frame had been transported from SAS on two sets of broad gauge rails by fixing the 4 nos. of self propelled trolleys to the bottom of test base frame at four locations and shifted towards the crane parking area. This base frame with load was lifted with Heavy duty crawler crane at the 57 meter working radius for SV erection. This exercise has validated the SV erection scheme and load tested for base frame, crane, rails, trolleys, and hydraulic jacks were qualified to handle the actual SV for erection.

Fig.4. Load testing of test base frame, rails, trolleys

3.1.1 Mock-up test for estimating wind load acting on SV

Mock-up test conducted for estimating the wind load acting on the SV during erection by fabrication of 13.54 meter x 12.8 meter cruciform structure simulating the SV dimensions (dia. & height). The dummy load had been placed on the structure and lifted, shifted towards the reactor vault. This mock-up was conducted for simulating the wind load acting on the structure during shifting and the procedure for Safety Vessel erection validated.

Fig. 5&6. Mock-up test for estimation of wind load acting on SV during shifting towards RV

3.1.2 Mock-up test for smooth passage of SV inside RV

Mock-up test conducted to check the smooth passage of SV into RV, by fabricating a structure simulating the SV diameter. This was fabricated of cylindrical shell of dia. 6 mtr and welding of additional frame to get 13.54 dia at the top. This cylindrical structure had been shifted towards reactor vault and lowered into the reactor vault opening. This mock-up was conducted and smooth passage of SV into RV was ensured before erection.

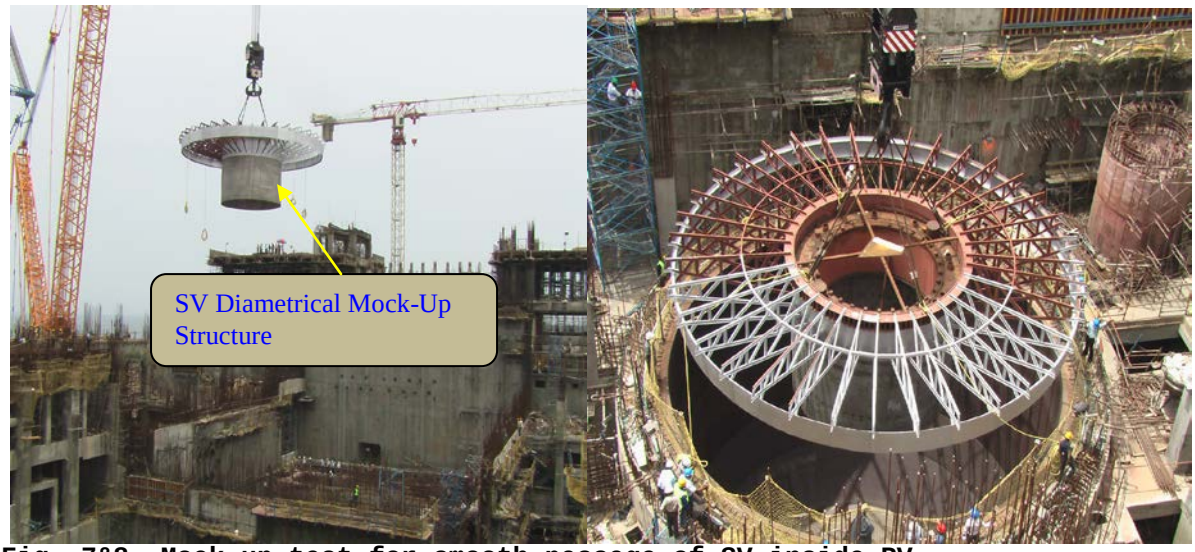

Fig. 7&8. Mock-up test for smooth passage of SV inside RV

3.2 Shifting and erection of Safety Vessel inside reactor vault

After validating the SV procedure by conducting above said mock-up tests, The Safety Vessel had been shifted from Site Assembly Shop with base frame (16 m X 16 m in size on two sets of broad gauge rails by fixing the 4 nos. of self propelled trolleys to the bottom of base frame at four locations) towards the crane parking area. The lifting gear had been connected between the SV and Crane, lifted, shifted towards the reactor vault and lowered inside the reactor vault. The precise alignment had been achieved and Safety vessel support flange had been welded with safety vessel support embedment of reactor vault.

Fig. 9&10. Lifting and erection SV inside RV

3.3 Challenges faced during SV erection into reactor vault

i) Lifting of the vessel without swing, placement of large size and heavy vessel at a distance of 57 m where the crane operator had no line of site to the equipment being erected.

ii) Avoid radial forces on the vessels which could buckle the vessels by lifting through innovative lifting spider.

iii) Lifting & handling of such huge cylindrical shell (13.54 m dia x 12.8 m height) and maintaining the same horizontally at top by adjusting turn buckles.

iv) Safely lowered into Reactor Vault without any damage on SV thermal insulation which was fixed outer surface of the SV.
v) Successfully lowered within the small radial clearance between the SV and RV during erection.
vi) Achieved the requirements within the erection tolerances

4.0 Shifting and erection of main vessel (MV) inside reactor vault

Main vessel (MV) is a large cylindrical vessel made of SS 316 LN material of dia 12.9 meter and height 12.94meter with self-weight of 202MT (including weight of Core Catcher, Core Support Structure and MV cooling pipes) and thickness varying from 25 to 30mm. Main vessel is a very important reactor component which is holding all the reactor components, core along with coolant (sodium) and supports the Core Catcher, Core Support Structure, Grid Plate, Inner Vessel and active core. The Core catcher (CC) and Core support structure (CSS) and MV cooling pipes were assembled before erection of MV at RV. To handle such huge over dimensional component vessel, a special lifting gear was used. The lifting gears are i) connecting rods – 4 nos. ii) ring spider with arms.

4.1 Mock-up test and load test conducted before erection of Main vessel (MV):

Mock-up test and load test similar to SV erection were conducted and MV erection procedure was validated and lifting gear was qualified to handle the MV for erection

Fig. 11&12. Load testing of MV Lifting gear and lifting of MV

4.2 Shifting and erection of Main Vessel inside reactor vault

After validating the MV procedure by conducting above said mock-up tests, The Main Vessel had been shifted from SAS with base frame towards the crane parking area. The CSS (which was integral part of MV) was provided with 4 lifting lugs for connecting the ring spider through the connecting rods; the MV was lifted with heavy duty crawler crane and taken to the top of the reactor vault. Before further lowering of MV, there is a requirement of checking and aligning the concentricity, angular axis of MV w.r.t SV and horizontality. The radial clearance

between the SV & MV is 25 mm only. Hence, it is required to achieve the above requirements within the same clearance. Innovative fixtures are fabricated for radial alignment of MV (for getting concentricity), angular alignment to match required angular orientation and horizontality maintained and the MV lowered precisely into Safety Vessel.

Fig.13. Lowering of MV with ring spider inside the SV

4.2.1. Radial guiding system for radial alignment of MV during erection

There are two set of radial guiding systems placed on reactor vault, the first set (12 nos. equally spaced) was placed on Roof Slab Support Embedment at 30 mtr elevation and second set (12 nos. equally spaced) is on 26.9 meter elevation. The radial alignment of MV is done through the screw system with Teflon rollers fixed at the end for smooth movement of MV. By rotating the one end of screw, the roller fixed on the screw can be moved forward and backward as per the site requirement. The roller facilitate to locate and radially lock MV at the designed position inside RV when the MV is hanging on the crane hook and at the same time facilitate in lowering MV in RV/SV in the radially locked condition. This way MV was erected successfully with in the design tolerances.

4.2.2. Angular guiding system for angular alignment of MV during erection

There is a requirement of matching the MV angular orientations (i.e 0^{o} - 90^{o} -180^{o} - 270^{o}) with angular orientations of SV. To achieve the above requirement, angular guiding system was used during MV erection. The MV was lifted with ring spider which is having 24 nos. arms and 4 lugs at 90^{o} spacing at the top face. These 24 nos. arms of the ring spider were seated on stools installed on RSSE. On the top of the stools, 4 nos. angular guiding system were installed at 90^{o} spacing to each other for locking the arms of the ring spider. The arms of the ring spider which align the angular guiding system has anti-rotation plates, which were provided at the respective arms location to prevent the arms of the ring spider from rotation.

Before lowering of MV, the jaws of the angular guiding system will be moved such that the gap between the jaws of angular guiding system is in line with arms of the ring spider. The MV was aligned to the required angular orientation by operating the jaws of angular guiding system and arms are locked of ring spider between the jaws with maximum gap of 0.5 mm. This way MV was arrested successfully to achieve the angular orientation of MV w.r.t SV.

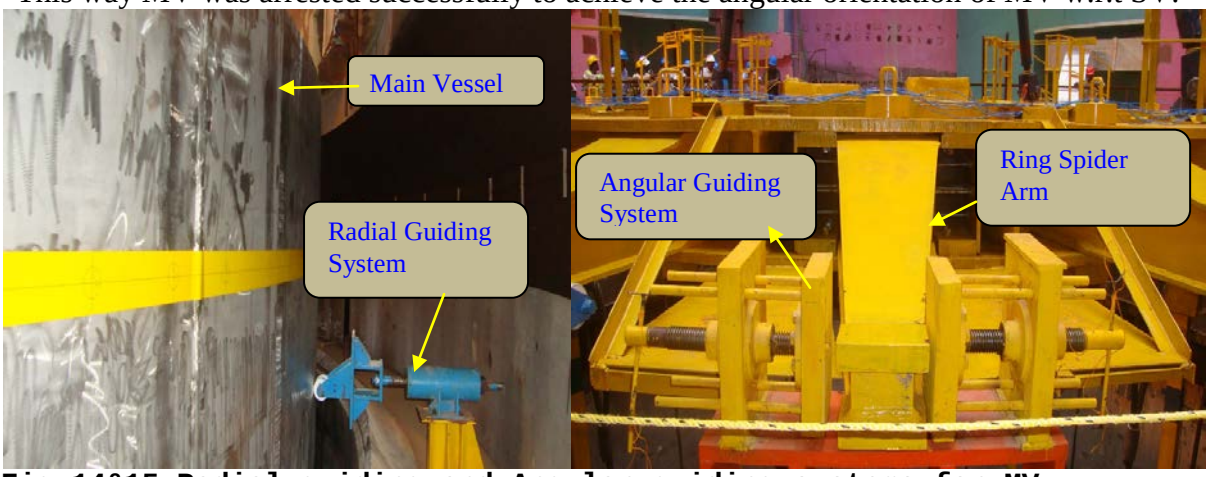

Fig.14&15 Radial guiding and Angular guiding systems for MV

4.3 Advantages by using of connecting rods for MV erection instead of slings

i) 4 nos. of connecting rods were designed for MV load and fabricated to achieve an uniform length, to avoid tilting of MV during handling/erection.

ii) Main vessel (MV) was lifted from below the center of gravity (CG) point, (i.e lifting points of main vessel are below centre of gravity point). To avoid the toppling of vessel, 4 nos. of connecting rods were used for MV handling.

iii) The connection between lifting spider and the component is a rigid connection through the connecting rods. Since connecting rods can take tensile and compressive loads and the clearance between the OD of pin and lug hole will be 1 mm which will ensure that tilting of MV will be minimal.

iv) 4 nos. of lifting lugs have been welded on CSS such a way that, it is radially towards the center of vessel to avoid dangling of MV during handling of the same.

v) Precise alignment of MV at reactor vault to achieve the erection requirements needs rigid structure (i.e connecting rods).

4.4 Challenges faced during during MV erection

i) Lifting of Main vessel was from the below of center of gravity (CG) point.

ii) Lifting of the main vessel without swing and dangling.

iii) Avoid radial forces on the vessels which could buckle the vessels

iv) Lifting & handling of such huge cylindrical shell (12.9 m dia.x 12.94 m height) and maintaining the same horizontally at top.

v) Lowering of the MV without any mechanical hindrance with in the small radial clearance and achieved the concentricity of the MV w.r.t SV

vi) Precise alignment of MV at reactor vault to achieve the designed erection requirements

5. Shifting, lifting and erection of Steam generators (SG) inside SG Building

The Steam Generator (SG) is a vertical, counter current, shell and tube type heat exchanger with sodium on shell side flowing from top to bottom and water/steam on tube side. The main function of SG is to transfer the heat from secondary sodium system to feed water thereby generating superheated steam. PFBR is having the two secondary loops, each loop consists of 4 nos. of SGs (i.e total 8 nos.of SGs). The total number of tubes in each SG is 547, OD of each tube is 17.2 mm and wall thickness of each tube is 2.3 mm. The total length of each SG

is 26 meters, with 1.5 meter diameter and weight of 35 MT. As the SGs were very slender, these were securely packed in transportation structure and delivered in horizontal condition to PFBR site. To handle such slender component in horizontal condition, making horizontal to vertical position and erecting the same in vertical position was very challenging task.

5.1. Mock-up test conducted before erection of Steam Generator (SG)

To handle such a slender component, there was a requirement of conducting mock-up test before erection of SG. Hence, a full scale mock-up test was carried out before erection of SG into SG Building to gain confidence during actual erection of SG. As part of the mock up test, full scale dummy SG structure of size 26 m in length, 1.5 m diameter and weight of 45 MT was fabricated. This dummy SG structure was kept in horizontal condition by horizontal handling beam, properly locked with skirts inside the transportation structure. The dummy SG structure was made vertical along with transportation structure by tilting beam using pivot point. After the assembly was made vertical, it locked with SG support structure which was a 30 meter tall structure mounted on wall of SG Building. The dummy SG was taken out by vertical handing beam through the dis-mantling of transportation structure. The dummy SG structure was lifted, shifted and lowered into respective position inside SGB. This exercise has validated the SG erection scheme and load tested for handling beams, lifting gear, transportation structure and the same were qualified for actual SG erection.

Fig.16&17. Mock-up test with dummy SG structure for SG erection

5.2. Handling and erection of Steam Generator into SG Building

After validating the SG erection procedure by conducting above said mock-up test, the actual Steam Generator with transportation structure had been lifted by horizontal handling beam and connected transportation lugs with pivot point on the ground. The SG transportation structure assembly was lifted by adjusting the crane working radius such that the assembly gets lifted at pivot point. After making the assembly in vertical, disconnected with pivot point and shifted the assembly towards SG support structure. The SG support structure was a 30 meter tall structure mounted on east side wall of SG Building-1, having dimensions slightly higher than the SG transportation structure. This SG support structure had in-built access platform, ladders to reach various elevations of SG transportation structure when it was vertical condition to remove the transportation structure skirts which were holding the SG. The SG with transportation structure assembly had been locked with SG support structure with bolting arrangement and dismantled the transportation structure by removing the skirts

around the SG. The Steam Generator was lifted alone by vertical lifting beam and shifted towards the SG Building top for lowering. The SG had been lowered precisely through the respective opening and integrated with SG support flange by bolting arrangement.

Fig.15&16.Horizontal handling and vertical lifting of SG for erection

5.3 Challenges faced during SG erection

i) Making of the Steam Generator horizontal to vertical position without damaging.
ii) Lifting of SG alone in horizontal condition due to non-uniform mass

REFERENCES

[1] PFBR Preliminary Safety Analysis Report, Chapter 1 General description of plant
[2] PFBR Preliminary Safety Analysis Report, Chapter 5.3 Reactor Assembly
[3] Safety Vessel Approved GA and As Built Drawings, Erection Procedures and QA Inspection Reports
[4] Main Vessel Approved GA and As Built Drawings, Erection Procedures and QA Inspection Reports
[5] Reactor vault Approved GA and As Built Drawings and QA Inspection Reports
[6] PFBR Final Safety Analysis Report, Chapter 6 Heat Transport Sodium Circuits
[7] Steam Generator Approved GA and As Built Drawings, Erection Procedures and QA Inspection Reports

Study on High Sensitive FFDL Technique for Monju and next generation SFR Using Laser Resonance Ionization Mass Spectrometry*

Takafumi Aoyama[a,b], Takashi Ishikawa[b], Yoshihiro Iwata[b], Chikara Ito[b], Yuko Morohashi[c], Toshikazu Takeda[a]

[a] Research Institute of Nuclear Engineering, University of Fukui

[b] Experimental Fast Reactor Department, Oarai R&D center, JAEA

[c] Engineering Department, Fast Breeder Reactor Research and Development Center, JAEA

Abstract. The high sensitivity and reliable Failed Fuel Detection and Location (FFDL) technique for Sodium Cooled Fast Reactor (SFR) has been developed using the Laser Resonance Ionization Mass Spectrometry (RIMS) method. The RIMS is suitable for the isotope analysis of elements at ultra-trace levels, since there is no increase of the background by interfering ion and isobaric interference except for measuring element in principle, because the measuring element is selectively ionized. The RIMS method was demonstrated by measuring the artificially blended xenon (Xe) and krypton (Kr) gas (tag gas) which was used for the pressurized steel capsule of in-pile creep rupture experiment in the experimental fast reactor Joyo. The measured isotopic ratio of Xe collected from the Joyo reactor cover gas by means of RIMS could successfully identify the ruptured capsule of which tag gas was contained. The RIMS was then applied for the proto type fast breeder reactor Monju, which uses tag gas as an FFDL method for driver fuels. Based on the experiences obtained at Joyo, the RIMS system for Monju FFDL was then proposed. The RIMS system can also detect stable Xe nuclides and radioactive ^{133}Xe in the collected from the Joyo reactor cover gas during the fuel failure simulation test, implying that the RIMS can apply to assume the burn-up of the failed fuel subassembly by using the ratio of stable and radioactive Xe isotopes. This result indicates that the RIMS can also be applied for the future SFR of which number of driver fuel subassemblies more than several hundred. As a result of this study, the RIMS is found to be a promising innovative instrumentation technique to detect the trace amount of Xe and Kr tag gas diluted in the argon cover gas and the RIMS is useful to enhance the safety and reliability of SFR.

1. INTRODUCTION

An early detection of fuel failure event and subsequent precise identification of the failed fuel subassemblies are essential and important for operational safety of SFR. This helps to prevent radioactive contamination by the fission products released from the failed fuel pins in the primary cooling system, to reduce the personnel radiation dose and also to improve the plant availability factor. The artificially blended tag gas is used as FFDL of Monju where the tag gas with different isotopic ratios is enclosed in each Monju fuel cladding tube and is measured by means of mass spectrometry in the event of fuel failure. Since the tag gas released in the argon cover gas region is eventually diluted to under the ppb level, it needs to be concentrated using a cryogenic charcoal bed which requires an elaborate operation and time[1]

The FFDL techniques are proposed some effective methods including the sipping method used in KNK-II (Karlsruher, Germany), Joyo and the selector valve method in Phenix (CEA, France), among

* A part of this study is the result of "Development of a Laser Optical System for Precise Tag Gas Analysis Using Resonance Ionization Mass Spectrometry" carried out under the Strategic Promotion Program for Basic Nuclear Research by the Ministry of Education, Culture, Sports, Science and Technology of Japan. Present study includes the result of "Core R&D program for commercialization of the fast breeder reactor by utilizing Monju" entrusted to University of Fukui by the Ministry of Education, Culture, Sports, Science and Technology of Japan (MEXT).

which the gas tagging method is currently employed in EBR-II (DOE, USA)[2], and Monju in Japan. The general principle of this method shown in Fig. 1 is summarized as follows:

(a) Kr and Xe noble gases of different isotopic compositions are loaded into fuel pins of as many as several hundred different fuel assemblies. Fuel pins in the same assembly have the same isotope abundance of Kr and Xe.

(b) In case of fuel failure, a partial amount of leaked Kr and Xe tag gas, together with FP gas arising from fuel burning, quickly moves into the argon (Ar) cover gas region without any reaction with liquid sodium.

(c) Isotope analysis of Kr and Xe in the cover gas makes it possible to identify the assembly including the failed pin.

Although dependent on the cover gas volume and other conditions of fast reactors, typically the isotope analysis of Kr and Xe is required with the concentration of as low as an order of parts-per-trillion (ppt) in Ar. The precision of the isotope analysis is needed to be an order of percent or better to discriminate several hundred kinds of fuel assemblies with different mixture ratios of Kr and Xe isotopes.

2. LASER RESONANCE IONIZATION MASS SPECTROMETRY SYSTEM FOR FFDL

The characteristics of RIMS are to obtain high signal-to-noise (S/N) ratio by selective photoionization of a specific element and to permit direct measurement of ppt level Kr and Xe tag gas with high accuracy. Compared to other methods like that adopted in Monju to increase the tag gas concentration up to an order of parts-per-million (ppm) followed by double-focusing mass spectrometry, the fact that additional procedures are not needed in RIMS method results in reduction of the required measurement time as well as system simplification. The high sensitive FFDL system has been developed using the RIMS method. The RIMS concept is illustrated in Fig. 2. The RIMS is suitable for the isotope analysis of an element at ultra-trace levels, since there is no increase of the background by interfering ions and no isobaric interference except for the measured element, because the measured element is selectively ionized.

The developed RIMS system as shown in Fig. 3 and Fig. 4 consists of the variable wavelength laser system with pulsed optical parametric oscillator and reflectron type time of flight mass spectrometer (RE-TOFMS). Employing a pulsed supersonic valve for sample gas injection enhanced the sensitivity. The RIMS system is then modified by employing the neutralization apparatus and Brewster window to reduce the amount of photoelectron. The electrode used in the center part of the ion chamber was changed to a slit-type hole from a circular hole to limit the generated Ar^+ and $Ar_2{}^+$ ions reaching the MCP detector without any loss of Kr^+ and Xe^+ ion signals. For the purpose of decreasing the adverse effects of these ions, the following two methods are considered for application in terms of reducing the amount of photoelectron and limiting these ions to reach the detector[2], [3].

2.1 Neutralization apparatus and Brewster window

Application of a set of a neutralization apparatus and a Brewster window, as shown in Fig. 3, is effective for the decrease of the amount of photoelectron. The neutralization apparatus placed before laser irra- diation in vacuum removes any charged dust on the viewport window by producing positive and negative ions to neutralize it. The Brewster window mounted at the exit of the vacuum tube in the laser ir- radiation direction utilizes a window tilted at Brewster's angle θ_B to prevent reflection of p polarized light. It is made of quart, whose in- dex of refraction n_q is 1.459, so the Brewster's angle is approximately $\theta_B = \tan^{-1}(n_q) \simeq 56°$. These charged dust and reflected p polarized light can otherwise cause the generation of photoelectron.

2.2 Electrode with a slit-type hole

An electrode with a slit-type hole instead of a circle one is proposed as the center of the ion acceleration electrodes to limit the generated Ar^+ and $Ar_2{}^+$ ions to reach the detector without any loss of Kr^+ and Xe^+ ion signals. Though the center electrode has a circle hole in the typical TOF-MS to extract as many ions as possible, a slit-type hole is much more suited to the RIMS setup because Kr^+ and Xe^+ resonant ions are created within the laser irradiation region, but Ar^+ and $Ar_2{}^+$ non- resonant ions can be generated away from the laser path as illustrated in Fig. 5. In this work, the size of the slit-type hole is determined to be 1 mm × 10 mm taking into account the fact that the electrode we have used so far has a circle hole of 12.7 mm in diameter and the laser spot diameter is sufficiently smaller than 1 mm.

Further modification included utilizing the YAG laser beam for photo ionization from the excited state. As a result, the ionization efficiency is significantly improved[4].

3. EXPERIMENTS OF MARICO

The principle of RIMS for FFDL in SFR was demonstrated by the tag gas release test which was conducted in Joyo using the irradiation test device MAterial testing RIg with temperature Control (MARICO).

3.1. MARICO overview

The main purpose of the MARICO is to evaluate the creep rupture strength of fuel cladding materials in the fast neutron irradiation environment. The creep rupture strength is an important fuel design parameter that determines the maximum fuel burn-up, and it depends closely on the temperature. Therefore, the MARICO was developed to carry out in-pile testing in Joyo with high temperature accuracy[5]. To determine by identifying the ruptured specimen, the following two methods were employed in the MARICO-2[6]:

(a) Two Chromium/Aluminum (C/A) thermocouples were installed inside each capsule containing the ODS irradiation specimens. One is located at the center of the capsule for temperature control, in the same manner as the MARICO-1, and the other is newly installed at the upper end of the MARICO-2 capsule to measure the temperature change due to the change of the thermal conductivity when the coolant in the capsule is replaced by the released gas.

(b) A few cm^3 of a unique blend of stable Xe and Kr tag gas is contained in each specimen together with the filled helium gas. The MARICO-2 test assembly had 4 capsules for creep rupture experiment, each containing 6 ODS specimens with different isotopic ratio of tag gas. In the event of a specimen rupture, the gases are released into the coolant sodium and transferred to the argon cover gas region as illustrated in Fig. 6. The cover gas is then measured by means of gamma-ray spectrometry using the OLGM and the new RIMS device. The OLGM monitors the activated tag gas nuclides produced by (n, γ) reactions every 30 minutes using a high purity germanium semiconductor detector. The RIMS, which has ultra high sensitivity to measure the Xe and Kr gases diluted in the cover gas volume to a level as low as a few ppb, was originally developed for the purpose of failed fuel detection and location and is now also applied to the MARICO tag gas identification. The RIMS system, consists of a variable wavelength laser system and time-of-flight mass spectrometer. There is no increase of the background ion and isobaric interference because only Xe or Kr atoms are selectively excited resonantly and ionized.

3.2. Creep rupture detection

Both the temperature change in each capsule and the gamma-ray spectrometry of the cover gas have detected creep rupture events successfully. Fourteen creep rupture events were detected during irradiation. The temperature change more than 10 ℃ using thermocouples at the upper end of each capsule indicates the capsule which contains the ruptured specimen as shown in Fig. 7 and Fig. 8. The OLGM successfully measured the gamma-rays emitted from ^{125}Xe, ^{127}Xe, ^{129m}Xe, etc., which were the activated tag gas nuclides used to detect the creep rupture of specimens as shown in Fig. 9. Eleven creep rupture events were observed by means of both the thermocouples and the gamma-ray spectrometry in the MK-III core 3-2 operational cycle from June to July, 2006. A little rise of radioactivity was observed between event No. 6 and No. 7 in Fig. 9. The radioactivity change shows that the residual gas in No. 6 ruptured specimen was released because of temperature change of the same capsule and the same kind of tag gas that ruptured at No. 6 event. Radioactivity changes after No. 11 event were the same case as the event between No. 6 and No. 7.

3.3. Identification of ruptured specimen

A 300 cm^3 sample was taken from the reactor vessel cover gas when a creep rupture was detected. The sampled cover gas, containing released tag gas which was diluted to isotopic ratios of $10^0 \sim 10^2$ ppb, was measured by means of the RIMS to obtain isotopic ratios of Xe tag gas. An example of the measured mass spectra is shown in Fig. 10. It was compared with the 6 kinds of as-blended tag gas isotopic ratios. The isotopic ratios measured by the RIMS identified the tag gas corresponding to the ruptured specimen. The test result for the first tag gas release event in the MARICO-2 on June 12^{th}, 2006, is shown in Table 1. The events of No. 7 and No. 8 shown in Fig. 9 indicated that two specimens contained the same capsule ware ruptured at a time because the temperature in the capsule only was changed more than other events. The ruptured specimens were identified by comparison of the isotopic ratios measured by the RIMS with the isotopic ratios mixed 2 kinds of tag gases.

4. FUEL FAILURE SIMULATION TEST IN JOYO

Next, the application of RIMS to assume the burn-up of the failed fuel pin is carried out by means of the fuel failure simukation test conducted in Joyo.

4.1. Outline of the test

4.1.1. FFD, FFDL systems and fission gas traps

Figure 11 shows schematic diagram of the system in connection with the fuel failure simulation test[7]. The FFD consists of the delayed neutron monitoring system (FFD-DN) and the cover gas monitoring system. The FFD-DN is installed along the hot leg piping of each primary cooling system. Two kinds of neutron detectors, BF3 proportional counter and boron lined B-10 counter, are used to measure the delayed neutrons emitted from their precursors such as ^{87}Br, ^{89}Br and ^{137}I. These nuclides are released from the failed fuel pins into sodium and transferred to the primary piping. The cover gas monitoring system consists of two methods to measure the radioactivity of the argon cover gas in the primary cooling system. One is the cover gas precipitating system (Precipitator: FFD-CG) which detects ^{88}Rb and ^{138}Cs, the products by beta decay of ^{88}Kr and ^{138}Xe, released from the failed pins to the cover gas. The other is the on-line gamma-ray monitor (OLGM) which can identify the fission gas nuclides by means of gamma-ray spectrometry using germanium semiconductor detector. The sodium sipping method is employed for the Joyo FFDL system. Two types of FP trap have been installed in Joyo in order to reduce the radiation level in the primary cooling system and cover gas. One is the cesium trap equipped in the primary sodium purification system. Reticulated vitreous carbon (RVC) is used to selectively adsorb the cesium in sodium. The other trap is the cover gas clean-up system (CGCS) to collect and store noble fission gas in the cover gas. The cryogenic charcoal filter cooled by liquid nitrogen can adsorb Kr and Xe effectively.

4.1.2. Test fuel subassembly

The test fuel subassembly shown in Fig. 12 was loaded in the center position of Joyo MK-III core in November 2004 after the second duty operational cycle. Two test fuel pins each of which has an artificial slit filled with fusible alloy, and its sibling fuel pin without artificial slit were placed inside the test subassembly. The specification of the test fuel pins is the same as the MK-III driver fuel as shown in Table 1. The uranium and plutonium mixed oxide (MOX) was used for the fuel material and the cladding tube was made of modified 316 stainless steel. The slit was 0.1 mm width x 1.0 mm length at a gas plenum region through the cladding tube, and sealed with the fusible alloy melting about 300 degree-C. Therefore, the slit is opened to simulate the fuel failure when test fuel pin temperature exceeds 300 degree-C by the nuclear heating in the core.

4.1.3. Test flow

The test flow is as follows: The reactor power was increased until a noticeable signal increase of FFD was detected. The threshold level was set as twice the background counting rate corresponding to the reactor power.

The fuel failure event was confirmed in this test when the FFD signal reached twice the background counting rate and the fission gas nuclides were identified by OLGM. The reactor was then shut down. After the radioactivity in the cover gas was decreased by CGCS operation and cover gas purge, FFDL system was used to identify the failed fuel subassembly. The test subassembly was then discharged from the core and transferred to the Fuel Monitoring Facility (FMF) to conduct the Post Irradiation Examination (PIE). The cesium trap was operated to reduce the cesium concentration in the primary coolant sodium.

4.2. Test results

4.2.1. Reduction of fission gas nuclides

The CGCS was operated prior to the identification of failed fuel subassembly to decrease the radioactivity in the cover gas. At the CGCS operation, cover gas was fed into the cryogenic charcoal filter for 4 hours with 120 liters/min. flow rate and the collected noble gases including fission gas nuclides were transferred to the stainless steel cylinder to store them until the radioactivity decay. The volume of the cover gas which was fed to the charcoal filter of CGCS amounts to 28.8 m^3, and it is equal to 4.4 times of the total cover gas volume. As a result of the CGCS operation, the radioactive concentration of noble fission gas nuclides in the cover gas was reduced to 1/10 as shown in Fig. 13. After the CGCS operation, the cover gas purge with fresh argon gas was done for 2.3 hours. The volume of purged cover gas amounts to approximately 13 m^3. As a result, the radioactive concentration of noble fission gas in the cover gas was reduced to 1/10 as shown in Fig. 13. The operation procedure and performance of the CGCS and cover gas purge were confirmed.

4.2.2. Measured results using RIMS system

An ultra-trace analysis system for stable and radioactive fission gas nuclide has been developed using a laser resonance ionization mass spectrometry (RIMS). The RIMS selectively ionizes the

measuring element and can analyze isotope element of parts-per-trillion level, since there is no increase of the background by interfering ion and isobaric interference. During the sodium sipping operation, the sample of cover gas was taken into the stainless steel container and Xe nuclides were analyzed by the RIMS system. The measured result was shown in Fig. 14, indicating the RIMS system can detect stable Xe nuclides and ^{133}Xe of which absolute value was evaluated to be a few ppt using the germanium semiconductor detector. This is the first measured data of actual fission gas in the sodium cooled fast reactor plant, and it shows the applicability of the RIMS system for the future fuel failure detection designed for JSFR[9] using the stable radioactive Xe isotopes.

5. PROTOTYPE SODIUM-COOLED FAST BREEDER REACTOR MONJU

5.1. Monju overview

Monju is fueled by uranium-plutonium mixed oxide with a rated power of 280MWe (714MWt). The system startup test (SST) resumed in May 2010 after fourteen years and five months shutdown since the sodium leakage of the secondary heat transport system in December 1995. An example of core configuration of Monju is illustrated in Fig. 15.The reactor consists of core fuel assemblies, blanket fuel assemblies, control rods, core internals structure, upper core structure, shield plug, etc. The core is composed of 198 core fuel assemblies, each of 169 fuel pins.

5.2. Failed fuel detection & location systems in Monju

Monju has failed fuel detection (FFD) systems which consists of delayed neutron (DN) method FFD system, cover gas (CG) method FFD system similar to that of Joyo as illustrated in Fig. 11, and Monju employs the tagging gas method FFDL system and primary argon gas monitoring device of process monitoring system. The DN method FFD and the CG method FFD are used, together with the primary argon gas monitor, to watch the integrity of fuel assemblies continuously. In order to identify the location of the failed fuel, the tagging gas method FFDL is used. In case of the pin hole failure, the CG method FFD detects β-ray and γ-ray from noble FP gases that move into the argon cover gas. It gives fuel failure warning and automatic start signal of FFDL. The FFDL system collects tagging gas which migrates into the reactor cover gas from a failed pin. Because the isotopic composition of the tagging gas is specific to each assembly, the assembly containing a failed fuel pin in the reactor core can be identified by analyzing the isotopic composition. The tagging gas is made of stable isotopes of Kr and Xe. 270 types of isotopic composition are available using 15 types for Kr and 9 types for Xe. Therefore, the isotopic composition of the tagging gas can be made specific to each assembly. Concerning the design specification of the FFDL system, release of 5% of the tagging gas from the failed fuel pin is supposed. Tagging gas in the cover gas plenum is collected and condensed by about $10^4 \sim 10^5$ times. Then, the isotopic composition ratio is analyzed by the mass spectrometer. The failed fuel assembly can be identified within about 12 hours.

6. Measurement error of tag gas identification by RIMS

In order to confirm the accuracy of RIMS for the Monju FFDL condition in the order of less than sub ppb, the folowing test was conducted.

The standard Xe and Kr gas with their isotopic ratio the same as the natural abundance were diluted with argon gas to the order of ppt level, considering the specification of the Monju tag gas concentration in the actual primary argon cover gas[10]. An example of the measured isotopic ratio for Kr and Xe with its natural abundance is shown in Fig. 16. These standard gases were used for evaluating the measurement error by means of RIMS device. The isotopic ratio of the typical tag gas used in Monju such as ^{126}Xe/^{129}Xe was evaluated as 7.1 %, and that of ^{78}Kr/^{80}Kr was evaluated as 4.7 % for half hour (30 minutes) measuring intervals of each RIMS count. As a result, the RIMS is applicable for the Monju FFDL.

7. DESIGN OF THE FFDL SYSTEM USING RIMS FOR MONJU

The preliminary design of the primary cover gas introduction line and the system configuration of a Monju FFDL system using RIMS are investigated in this study. The RIMS system needs to be accommodated in the geometrical space available in the Monju FFDL instrumentation room and has to be operated in the actual argon cover gas temperature, pressure and flow rate conditions. The primary cover gas introduction and exhaust lines after the measurement will be connected to the new RIMS system so as not to influence the present function of both FFD and FFDL systems using the conventional electron impact ionization mass spectrometry. The RIMS is a highly sensitive device which is usually maintained in a well air conditioned room. In order to fit the RIMS system in the actual fast reactor environment, the laser equipments will be covered by an air-conditioned booth to keep the environmental temperature constant. A buffer tank of about 2 liters will be placed before the

entrance to the pulsed supersonic molecular beam valve (PSV) as shown in Fig. 17 in order to reduce the fluctuation of the cover gas temperature and pressure, and to feed the necessary cover gas volume to the PSV at higher than atmospheric pressure. The schematic diagram of the newly designed FFDL system for Monju is illustrated in Fig. 18. In or der to fit in the limited space in the present FFDL room, the configuration is reduced to a compact size.

8. CONCLUSION

The high sensitivity FFDL technique for SFR has been developed using the RIMS method. The RIMS is suitable for the isotope analysis of elements at ultra-trace levels, since there is no increase of the background by interfering ion and isobaric interference except for measuring element in principle, because the measuring element is selectively ionized. The RIMS method was demonstrated by measuring the artificially blended Xe and Kr tag gas which was used for the pressurized steel capsule of in-pile creep rupture experiment in the experimental fast reactor Joyo. The ptoto type FFDL system is proposed for Monju. This RIMS method is expected to improve the reliability of the FFDL for SFR and enhance the safety of SFR in the future.

REFERENCES

[1] J. D.B. Lambert et al., "Failed Fuel Identification Techniques for Liquid-Metal Cooled Fast Reactors," *Proc. of BNES Conference on Fuel Management and Fuel Handling*, Edinburgh, UK (1995)

[2] C. Ito et al., "Development of high sensitive and reliable FFD and sodium leak detection technique for fast reactor using RIMS," *Proc. of FR09*, Kyoto, Japan (2009).

[3] Y. Iwata et al., "Improvement of the resonance ionization mass spectrometer performance for precise isotope analysis of ppt level krypton and xenon in argon," *Int. J. Mass Spectrum,* **296**, 15 (2010).

[4] Harano, H., Ito, C., Watanabe, K., and Iguchi, T., Development of a RIMS-based FFDL system at the experimental fast reactor JOYO, 2001/2002, Int. J. Applied Electromagnetics and Mechanics, Vol. 14, pp. 307-310.

[5] Y. Iwata, et al, 'Upgrade of the Resonance Ionization Mass Spectrometer for Precise Identification of Failed Fuel in a Fast Reactor' AIP Conf. Proc. 1412, 295 (2011).

[6] Kataoka, H., Yasu, T., Takatsudo, H. and Miyakawa, S., Development of material irradiation rig with precision temperature control in experimental fast reactor JOYO, 1998, Journal of Nuclear Materials, Vol. 258-263, pp. 677-681.

[7] C. Ito et al., "Experimental method of in-pile creep rupture behavior of ODS cladding materials in the experimental fast reactor Joyo," *Journal of Power and Energy Systems* (2008).

[8] K. Ishida et al., "Fuel failure simulation test in the experimental fast reactor Joyo," *Proc. of GLOBAL 2005*, Tsukuba, Japan (2005).

[9] K.Aizawa et al., "Design study and comparative evaluation of JSFR failed fuel detection system," *Proc. of ICAPP'12*, Chicago, USA (2012).

[10] T. Aoyama et al., "Study on High Sensitive FFDL Technique for Monju Using Laser Resonance Ionization Mass Spectrometry," *Proc. of ANS annual meeting*, Chicago, USA (2012).

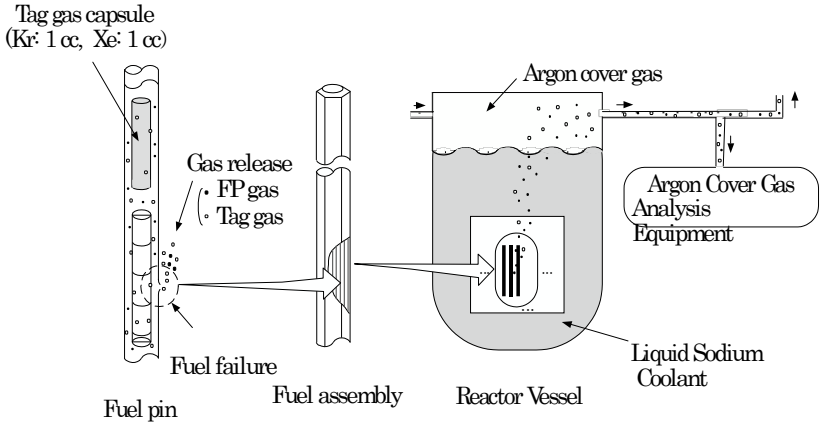

Fig. 1. Schematic diagram of the gas tagging method for FFDL system

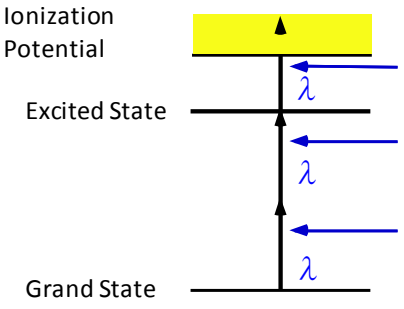

Fig. 2. Principle of resonance ionization

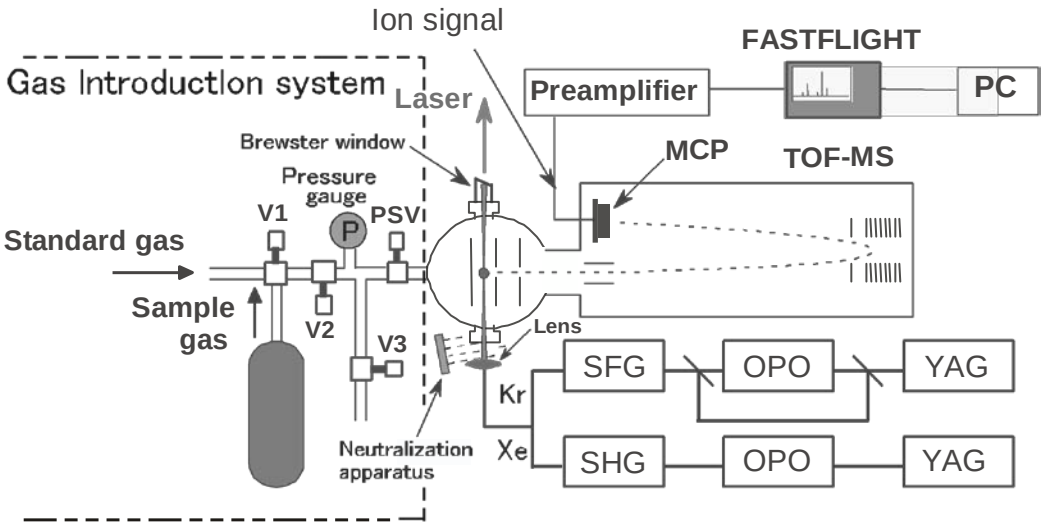

Fig. 3. Schematic diagram of the experimental apparatusof RIMS

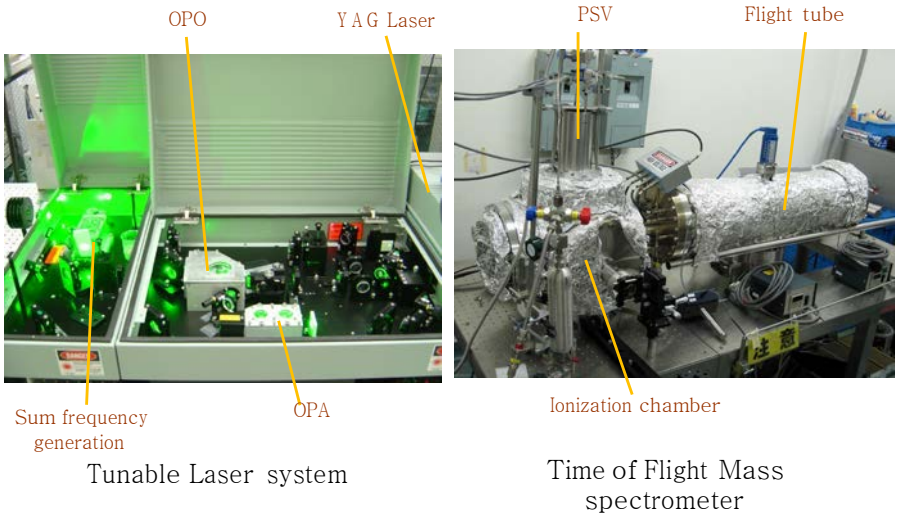

Fig. 4. Main parts of RIMS system

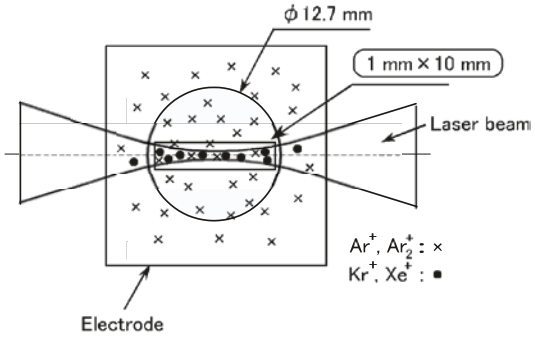

Fig. 5. Comparison of two types of electrode structures with a slit-type (1 mm×10 mm) hole and a circle (φ12.7 mm) hole.

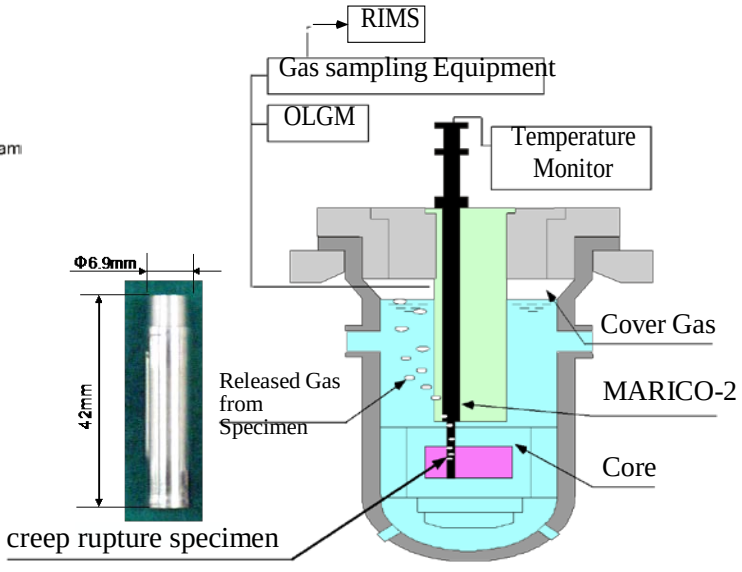

Fig. 6. Tag gas release into the Joyo reactor cover gas

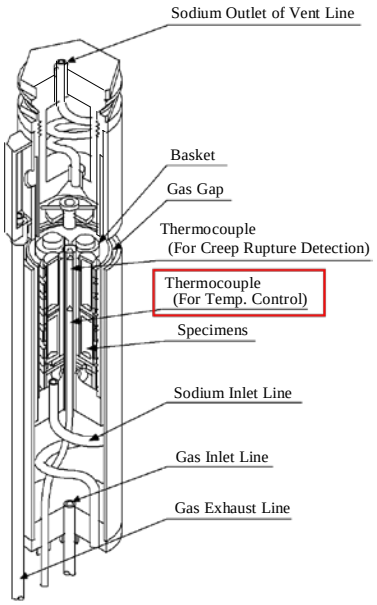

Fig. 7. Structure of temperature control type irradiation capsule (MARICO-2)

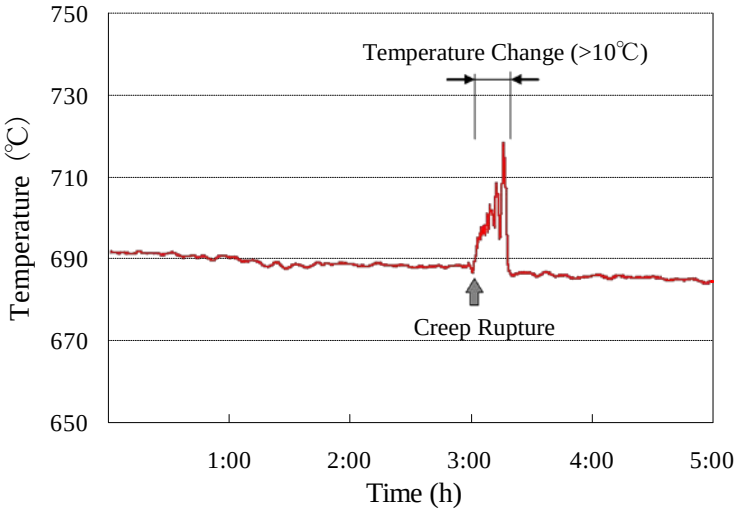

Fig. 8. Creep rupture detection by temperature change

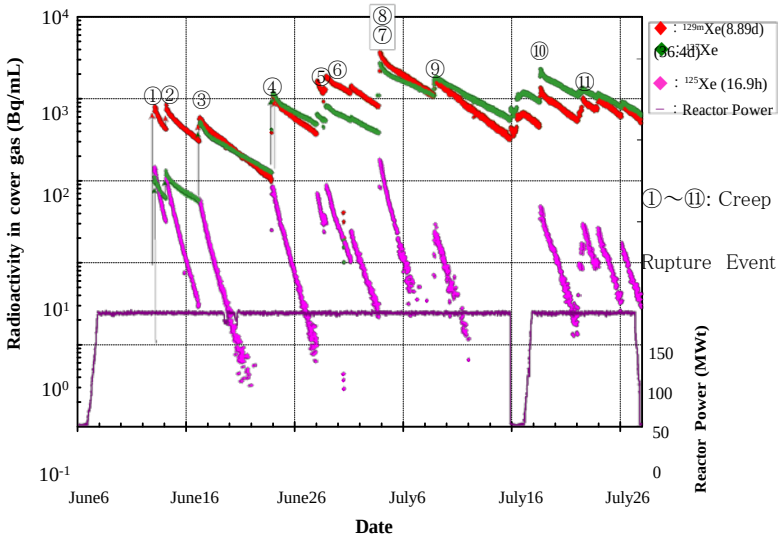

Fig. 9. Trend of radioactivity in reactor cover gas (OLGM measurement results)

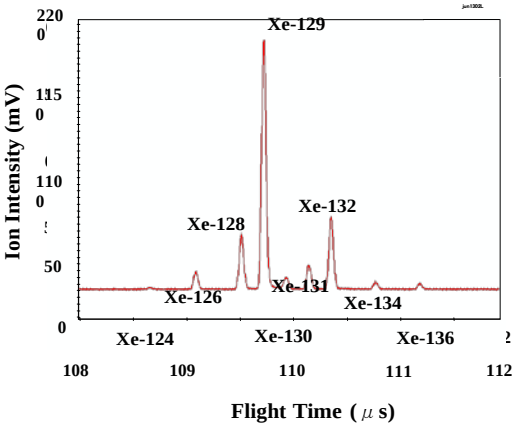

Fig. 10. Mass spectrum measured by RIMS

Table 1. Tag gas specification and measured result by RIMS (for the case of Fig. 9-① sampling gas)

Standard Gas No.	Xenon nuclides ratio to Xe-129		
	Xe-126	Xe-131	Xe-132
1	0.632	0.896	0.891
2	0.069	0.101	0.298
3	0.209	0.890	0.101
4	0.630	0.301	0.101
5	0.629	0.102	0.892
6	0.071	0.888	0.889
Measurement Result	**0.065**	**0.099**	**0.295**

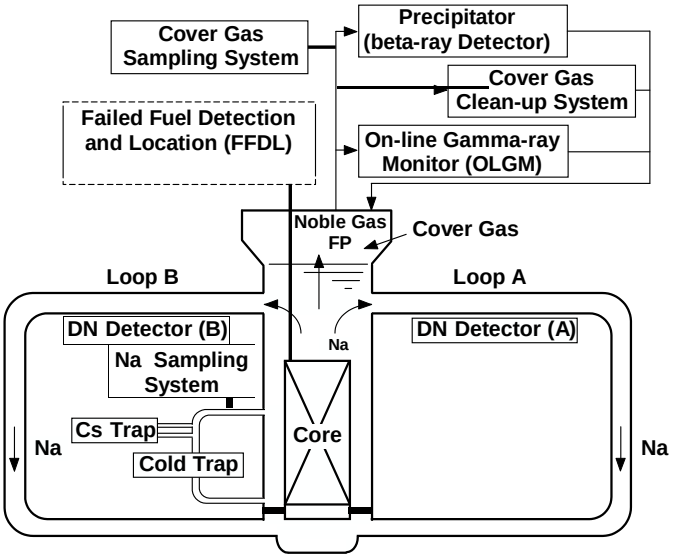

Fig. 11. Schematic diagram of the FFD and relating systems in Joyo

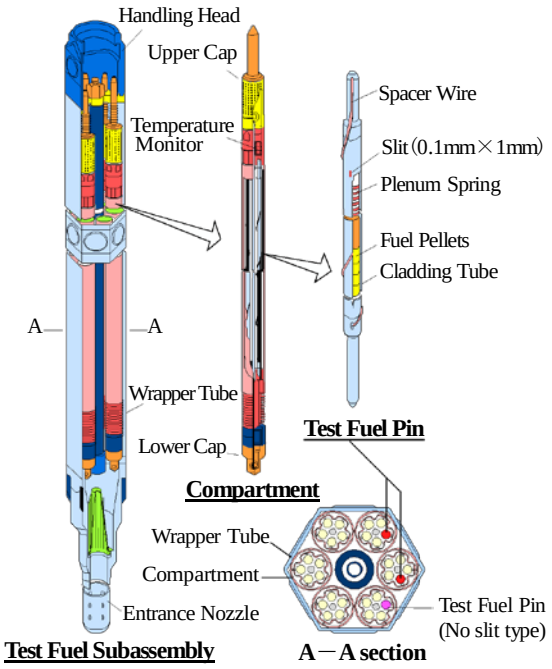

Fig. 12. Fuel failure simulation test subassembly

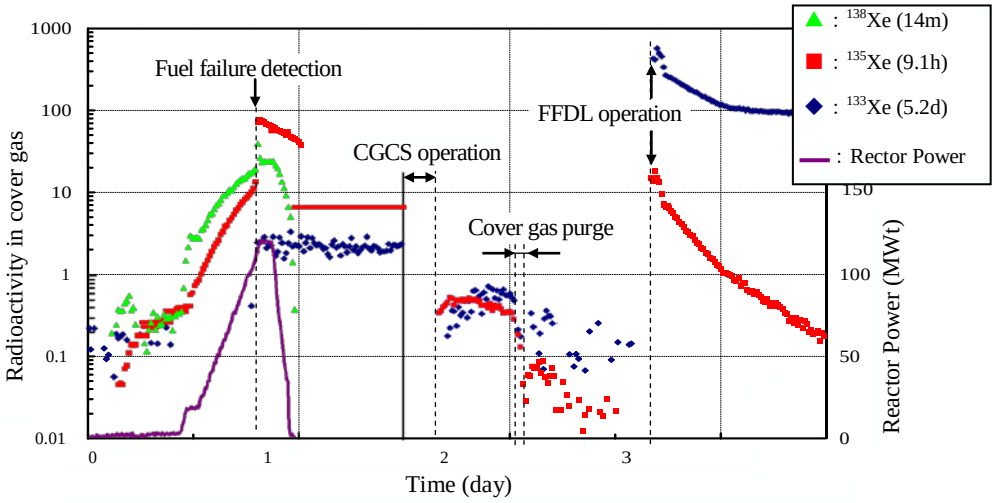

Fig. 13. Time history of radioactivity in reactor cover gas during the fuel failure simulation test in Joyo

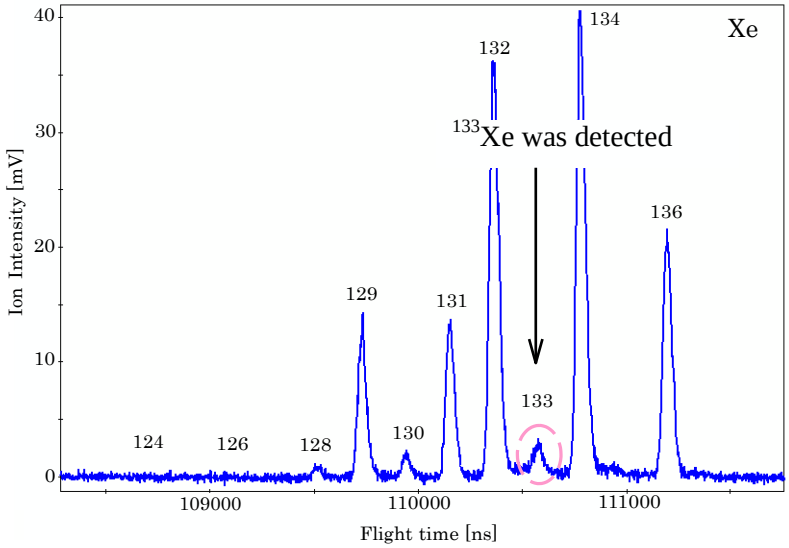

Fig. 14. Result of Xe nuclides analysis by the RIMS system

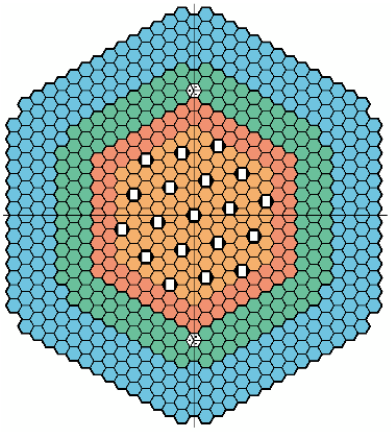

Core elements		Symbol	Number
Core fuel assembly	Inner core		108
	Outer core		90
Blanket fuel assembly			172
Control rod			19
Neutron source			2
Neutron shield assembly			316
Surveillance assembly			8

Fig. 15. Example of Monju core configuration

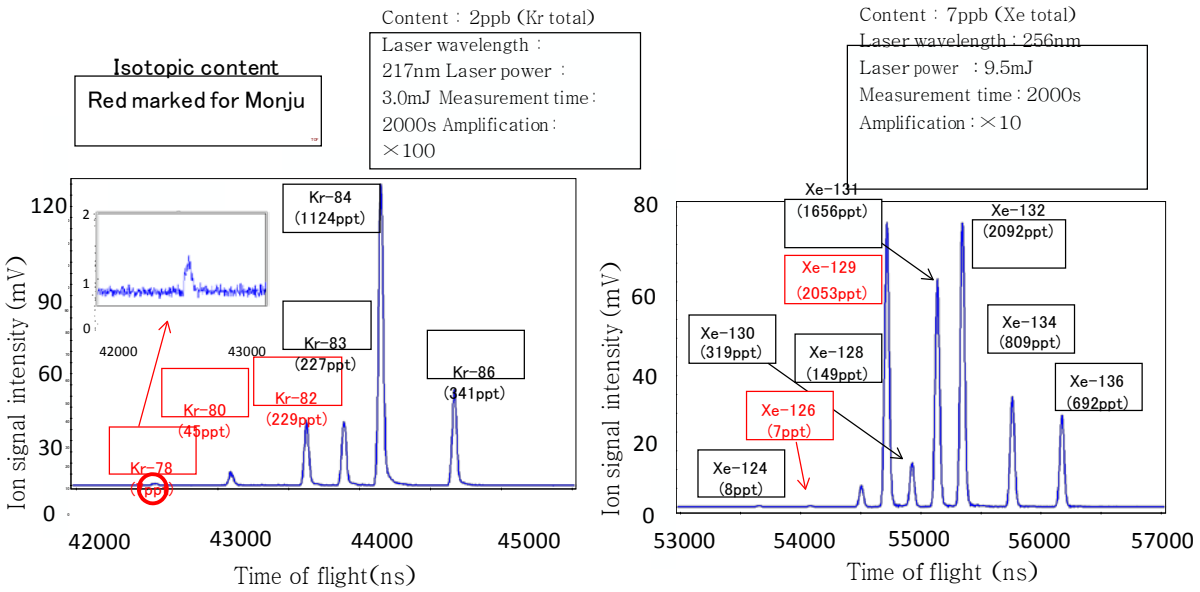

Fig. 16. Measured mass spectrum of natural Kr and Xe

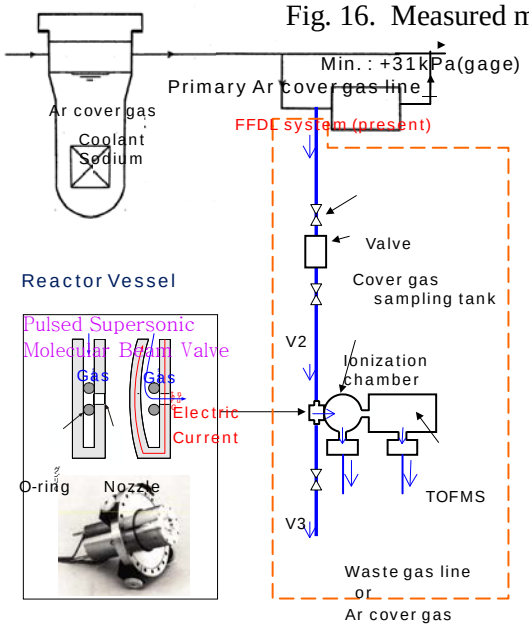

Fig. 17. Connection of RIMS to the Monju FFDL line

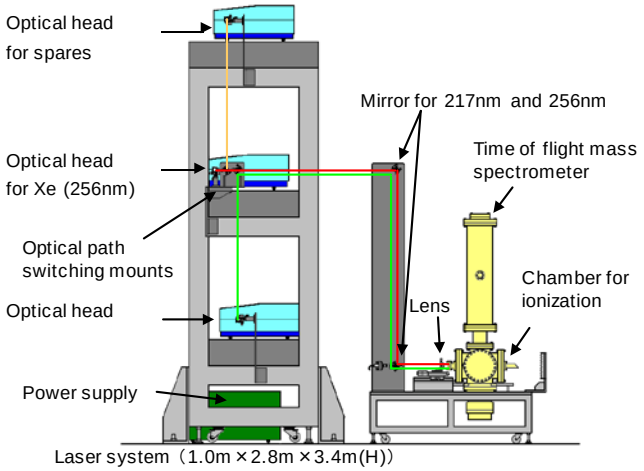

Fig. 18. Schematic diagram of the RIMS for Monju

Development of Electrochemical Oxygen Sensor and Experimental System for Materials Compatibility Test for Ultra-long Cycle Fast Reactor (UCFR)

S.H. Shin[1], J.J. Kim, J.A. Jung, K.J. Choi, S.I. Choi, J.H. Kim

Interdisciplinary School of Green Energy, Ulsan National Institute of Science and Technology (UNIST), Republic of Korea

Presented by S.H. Shin

Abstract. An electrochemical oxygen sensor has been developed for the use in high temperature liquid sodium environment. Gadolinia doped ceria (GDC) and yttria stabilized zirconia (YSZ) were used in this study as solid electrolytes for oxygen sensors that can be applied in sodium-cooled fast reactors. The rugged electrode design was calibrated to absolute metal-oxide equilibrium by using electrochemical impedance spectroscopy (EIS), which is a first principle of detecting pure metal-oxide transition. Also, the electrochemical potential was measured in the static and flowing sodium loop where dissolved oxygen concentration was administered by direct gas bubbling with N_2 + 50ppm O_2, N_2 + 100ppmO_2 and/or pure N_2. The result of measurement confirmed that the oxygen sensor developed in this study showed high degree of sensitivity and detectability for the high temperature sodium application. And, the developed sensor will be employed in the long term compatibility test of cladding and structural materials of fast reactors in high temperature sodium flowing loop facility.

On the other hand, the compatibility of ferritic-martensitic(FM) steel, austenitic steel and SiC coupon with sodium will be investigated in the sodium flowing loop system developed. Microstructral analysis of post exposure specimen by SEM, EDS, SIMS and TEM are ready. Electrochemical investigation, especially impedance spectroscopy, will be applied to a corrosion cell in order to characterize corrosion behavior of those specimens in sodium environment. Also, oxygen concentration is controlled and monitored by oxygen sensor and traps, respectively.

1.INTRODUCTION

Sodium is one of candidate coolants for advanced fast reactors that utilize spent fuels from light water reactor. One of goals of sodium-cooled fast reactor is to develop and qualify a nuclear fuel system that performs all of the functions of a conventional fast spectrum nuclear fuel while destroying recycled actinides. This will provide a mechanism for closure of the nuclear fuel cycle [1].

In this environment, the sodium behavior for a series of commercial austenitic alloys with a wide range of nickel content has been studied. However, the work has not shown the corrosion behavior at the intermediate periods [2-6]. The rate of corrosion of stainless steel is found to increase with the concentration of oxygen dissolved in the sodium. The effect can be either thermodynamic or kinetic. If the dissolved oxygen can form oxides, combined with sodium, the corrosion analysis based on the assumption that species dissolve as the element is incorrect. Dissolved oxygen can accelerate one of the steps in the corrosion process. It is

practically impossible to prevent the formation of sodium oxides,

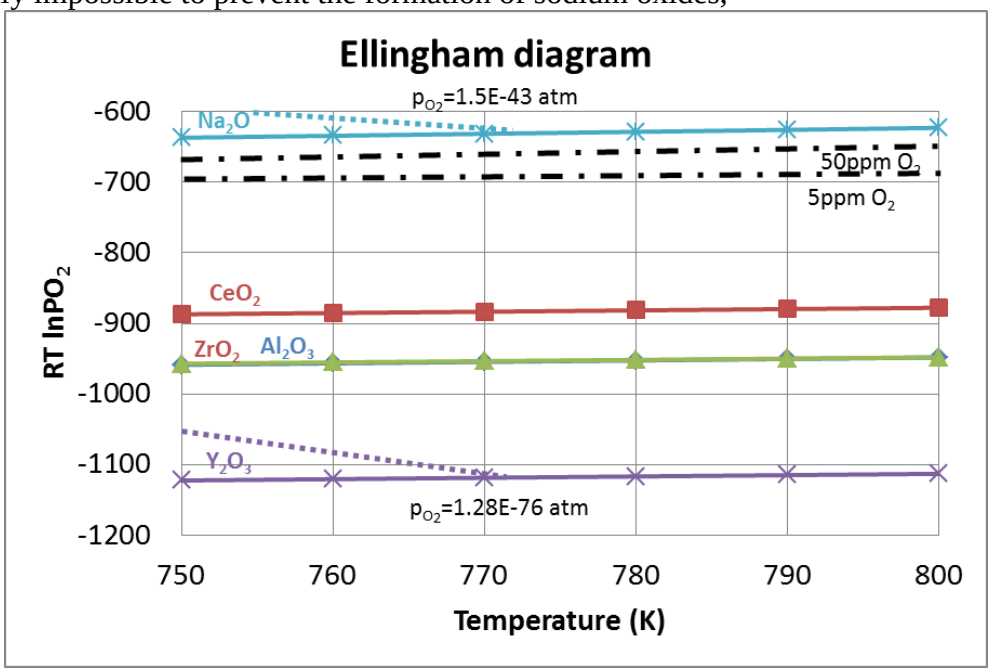

FIG. 1. Ellingham diagram of CeO_2, Gd_2O_3, Y_2O_3, ZrO_2, Al_2O_3 and Na_2O.

such as Na_2O and $NaCrO_2$, in sodium loop. However, the total quantity of chromium leached out of the material through the formation of Na2O and $NaCrO_2$ depends on the amount of oxygen that gains entry into the loop [7-10].

Therefore, the compatibility of cladding and structural materials with sodium has to be carefully investigated, as sodium could promote corrosion of cladding and structural materials in two ways. One is produced by the dissolution of alloy constituents into the sodium, and the other is produced through a chemical reaction with impurities (especially oxygen and carbon) in the sodium environment [11]. With the latter consideration, the concentration of dissolved oxygen in sodium has to be monitored and controlled during the operation of reactor. The need to monitor oxygen levels in the liquid sodium in fast reactor coolant circuits is well established [12-15].

Electrochemical oxygen sensors provide a sensitive means to measure the oxygen concentration in liquid sodium, and are capable of achieving the highly sensitive detection that is required in the operation of reactor system. Oxygen sensor mainly consists of solid oxide electrolyte, metal housing, reference electrode, insulating seal and lead wire.

Oxygen-ion-conducting solid oxide electrolytes are well known and their properties have been comprehensively reviewed [16-19]. The most common commercially available solid electrolyte materials are known as those based on zirconia (ZrO_2) and thoria (ThO_2) because of their thermochemical stability in liquid metals system. When these materials are doped with metal oxide, such as Y_2O_3, Gd_2O_3 and Sm_2O_3, having di- or tri-valent cations, oxygen ion vacancies are produced in the anion sublattice. The resulting increase in oxygen ion conductivity can lead to a situation where the electrical conductivity in the solid is essentially ionic, within certain ranges of temperatures and oxygen partial pressure [16].

The electrolyte based on ceria has been studied by some researchers because the ceria also exhibits a high ionic conductivity compared to zirconia- and thoria-based electrolyte. $Ce_{0.9}Gd_{0.1}O_{1.95}$ has an ionic lattice conductivity of 10^{-2} Scm^{-1} at 500°C, and the Gd^{3+} ion is the preferred dopant, compared to Sm^{3+} and Y^{3+}, at this temperature [17-19]. High electrical, thermal and sintering properties of ceria based solid electrolytes are reviewed in a number of sources [20-23]. However, thermochemical stability of both CeO_2 and its dopant Gd_2O_3 in

high temperature sodium are not widely studied.

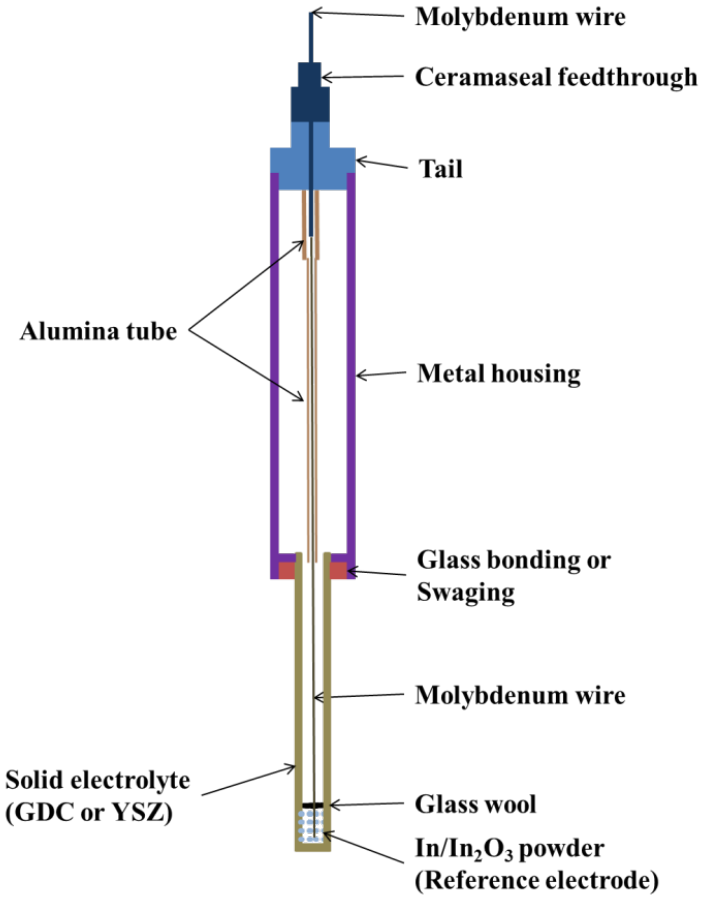

FIG. 2. Schematic of oxygen sensor which consists of solid electrolyte (GDC or YSZ), metal housing, In/In2O3 reference electrode, molybdenum lead wire and glass bonding.

Fig.1 shows the thermodynamic stability of selective oxides, CeO_2, Gd_2O_3, Y_2O_3, ZrO_2, Al_2O_3 and Na_2O, and oxygen concentrations controlled by bubbling 5ppm and 100ppm of oxygen in sodium environment. The threshold oxygen partial pressure of Na_2O and Y_2O_3 at 500°C is $1.5x10^{-43}$ atm and $1.28x10^{-76}$ atm, respectively.

In this study, emf signal calibration of both GDC and YSZ solid electrolyte based oxygen sensor has been performed and the thermochemical stability test of GDC as well as YSZ has been performed to develop highly sensitive oxygen sensor which is working at high temperature sodium environment for sodium fast reactor application.

2. EXPERIMENTAL

Each solid electrolyte was produced from Read-Ox consultancy by slip cast production. Gadolinia doped ceria, GDC-10, $(Ce_{0.90}Gd_{0.10})O_{1.95}$ (surface area: 30-40 m^2/gram) powder and yttria stabilized zirconia, YSZ-8, $(Y_2O_3)_{0.08}(ZrO_2)_{0.92}$ (surface area: 3-7 m^2/gram) powder are prepared from Fuel Cell Materials (FCM). GDC-10 powder is sintered in 1400°C air for 1 hour and YSZ-8 powder is sintered in 1500°C air for 2 hours.

At the upper open end of the tube, outer diameter (OD) is 6.0mm and inner diameter (ID) is 3.3mm, and at the lower closed end, the OD is 5.7mm and the ID is 3.0mm. The length is 100 mm. For all characterization studies that are discussed in the later section of this paper, subsamples were cut from these sintered solid electrolyte tubes with a low speed saw with a diamond saw blade.

The oxygen sensors used in this study were fabricated with both GDC and YSZ as a

solid electrolyte and In/In_2O_3 mixture as a reference electrode as shown in Fig. 2.

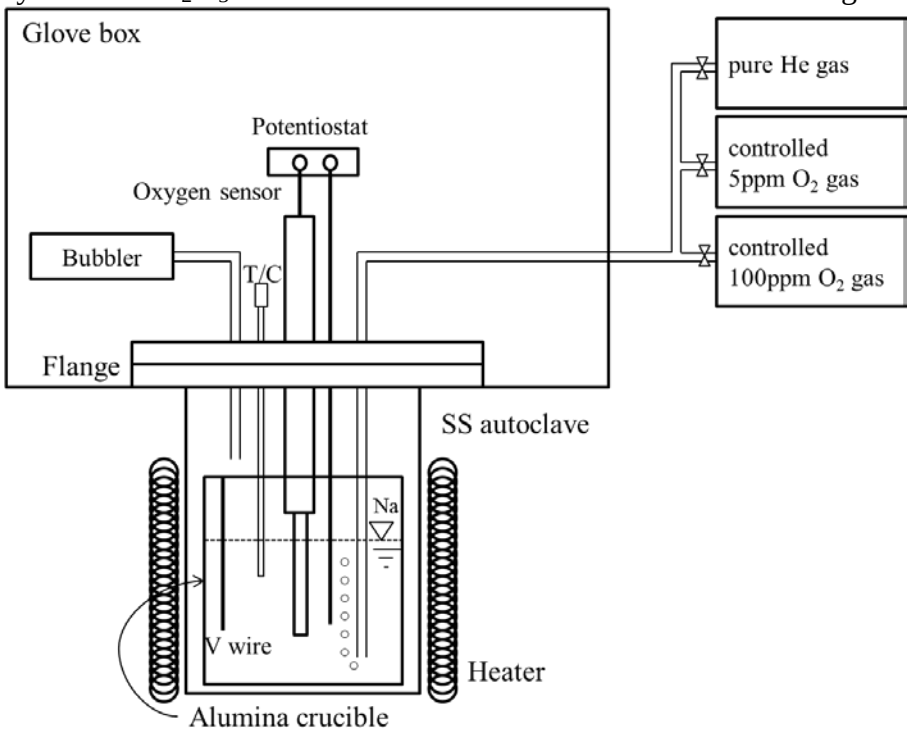

FIG. 3. a schematic of the experimental system.

The electrochemical galvanic cell between the oxygen sensor and sodium can be represented as follow:

In, In_2O_3 |GDC| Na,[O]
In, In_2O_3 |YSZ| Na,[O]

Emf signal measurements of both GDC and YSZ based oxygen sensors were performed by using open circuit potential technique with Solatron potentiostat 273A in liquid sodium at 500°C as shown in Fig. 3. Unknown emf signal of both GDC and YSZ based oxygen sensor with In/In2O3 mixture reference in sodium environment will be calibrated with controlled 5ppm and 100ppm O2 gas.

Scanning electron microscopy (SEM) was used to examine the microstructure of the s-sintered and post-exposed ceramics. Cut sample, ring shape, (6 mm OD, 3 mm ID) of YSZ-8 and GDC-10 were first ground on SiC paper (up to 1200 grit size) and then polished on a 3 lm grit diamond cloth. For SEM analyses, these samples were coated with a thin film of platinum (via physical vapor deposition). X-ray diffraction (XRD) was used to determine the crystal phase composition of the sintered ceramics.

In this study, high purity of helium gas, (which contains O_2 < 0.1 ppm, H_2O < 0.6 ppm, CO < 0.05 ppm, CO_2 < 0.05 ppm, CH_4 < 0.05 ppm and N_2 < 0.2 ppm), is bubbled for 3 hours before controlled oxygen gas is bubbled into liquid sodium.

To study the thermochemical stability of the sintered ceramics in oxygen saturated sodium, 2mm thick polished rings of the YSZ-8 and GDC-10 ceramics were exposed to sodium at 500°C. To check the oxygen concentration in the sodium, vanadium wire equilibration method that has been widely used in the similar studies [27-31], is adopted and used in this study. 0.5 mm diameter wire was electro-polished to remove any contamination that had occurred during handing, to remove the sodium.

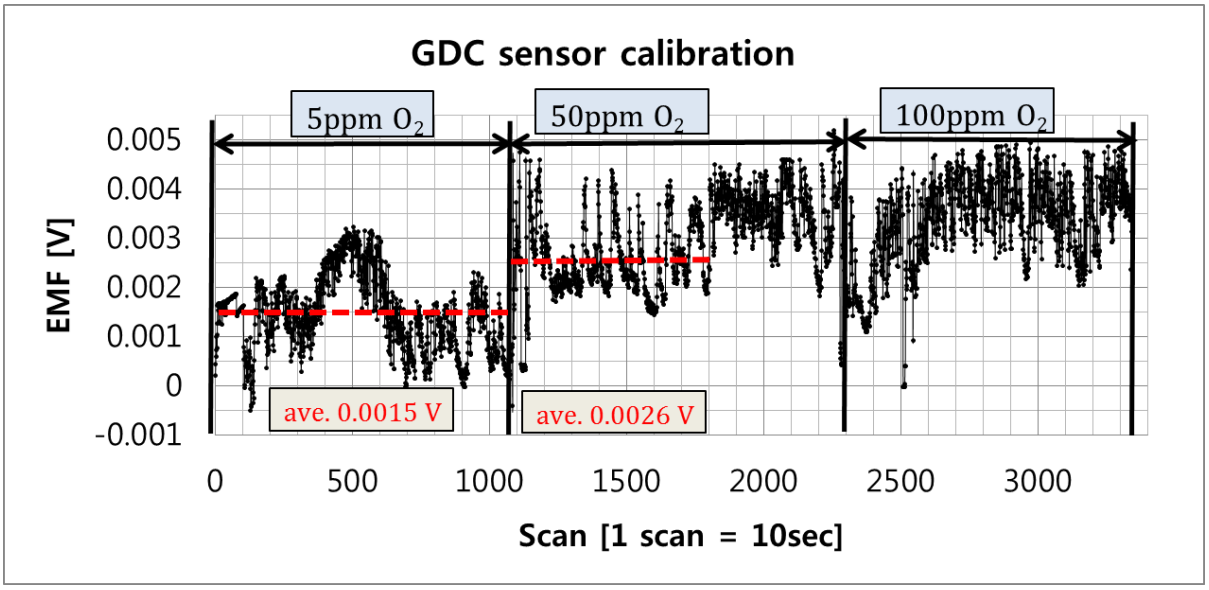

FIG. 4. Emf signal of GDC based oxygen sensor in liquid sodium environment at 500°C with controlled 5 ppm , 50ppm and 100 ppm oxygen gas.

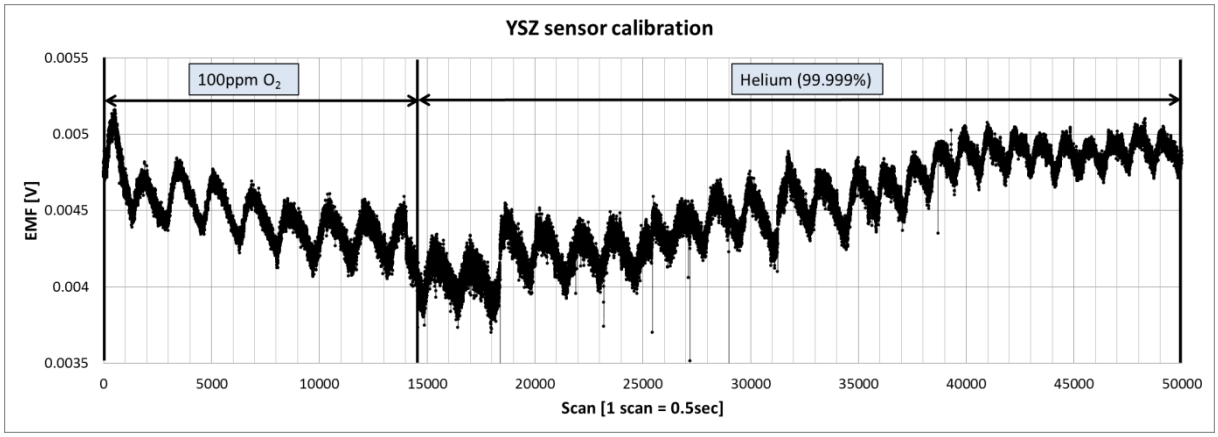

FIG. 5. Emf signal of YSZ based oxygen sensor in liquid sodium environment at 500°C with controlled 100ppm oxygen gas.

The sodium used in this study is 99.8% pure and produced by Alfa-Aesar.

After 5 and 10 days of exposure time, both the crystal phase composition of the ceramics and the microstructure of the surface layer that had been in contact with sodium were investigated by means of XRD and SEM. The rings of the ceramics were cleaned in ethanol with ultrasonic cleaning for 1 hour and in deionized water with ultrasonic cleaning for 1 hour to remove the sodium, prior to SEM and XRD analyses.

Electrical conductivity measurement was performed by using standard four-probe technique with a BioLogic Potentiostat in a temperature range between 400°C and 700°C with rectangular samples (10mm x 3.5mm x 1.5mm) of the sintered ceramics. Samples for conductivity measurement were prepared from sintered pellets (rectangular bars with Pt wire winding across the surface of the samples) and Ag paste was used as a contact adhesion. Platinum current leads were attached to the sample end surfaces, which were coated with Ag paste, and platinum voltage leads were wound around the sample in two circumferential grooves (of 0.3mm width and 0.2mm depth) at 2mm from the end surfaces. A constant current of 100 mA was supplied over the sample. The voltage difference over the voltage leads was measured with a BioLogic Potentiostat.

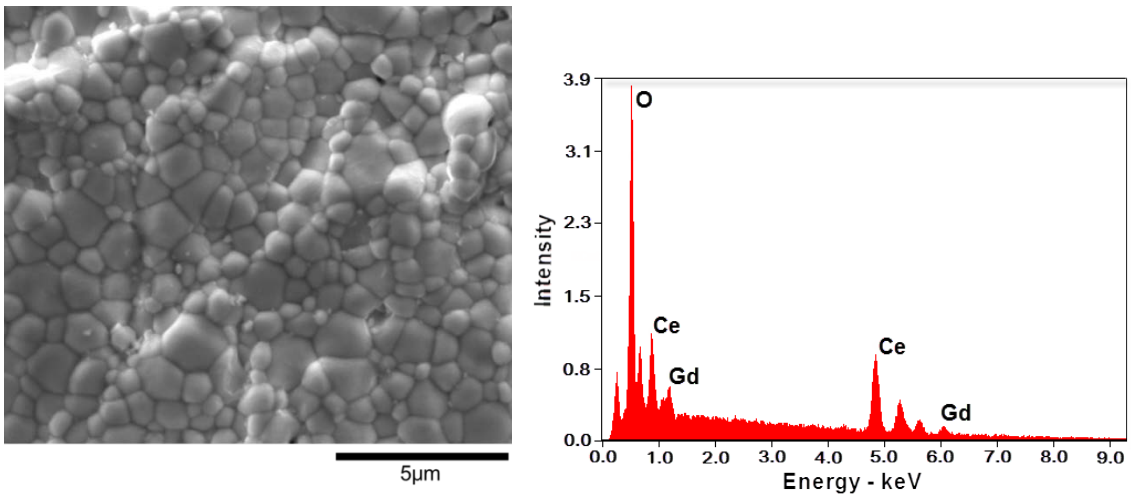

(a) (b)

FIG. 6. The microstructure of the as-sintered gadolinia doped ceria (GDC) tube (SEM image, x20,000 magnitudes) (a) and its EDS peak result (b).

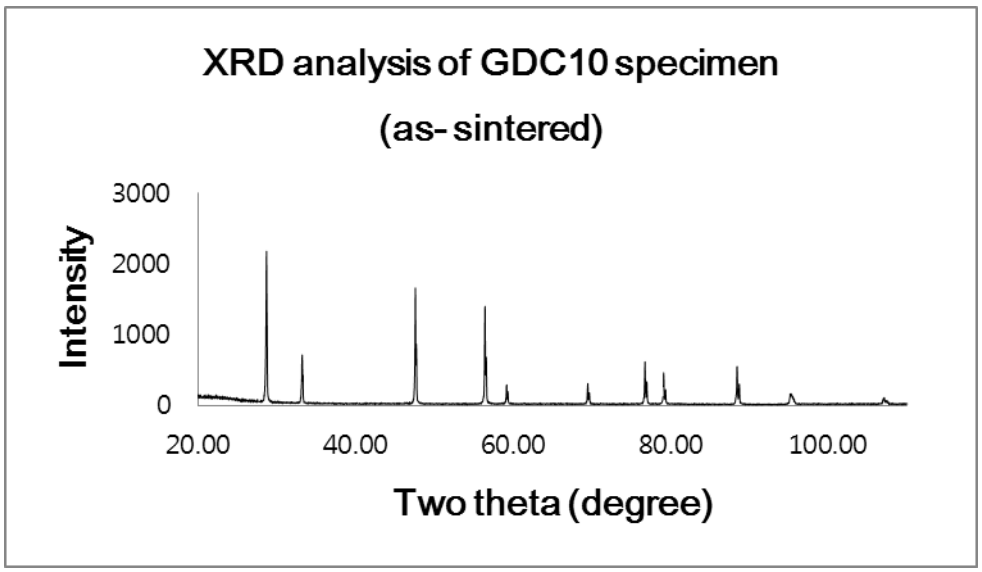

FIG. 7. XRD peak of as-received gadolinia doped ceria ($(Ce_{0.9}Gd_{0.1})O_{1.95}$) specimen.

3. RESULTS

3.1. EMF signal of both GDC and YSZ based oxygen sensors

Fig. 4 shows the emf signal of GDC based oxygen sensor in liquid sodium at 500°C with controlled 5 ppm, 50 ppm and 100 ppm oxygen gas. This result shows unstable emf signal during entire measurement. The average emf signal corresponding to 50ppm oxygen gas is 0.0026V, while emf signal corresponding to 5 ppm oxygen gas is 0.0015V. The average emf signal is proportional to oxygen concentration in sodium at 500°C. However, emf signal corresponding to 100 ppm oxygen gas is not proportional to the oxygen concentration.

3.2. Microstructure of the as-sintered ceramics

Fig.6 shows the grain size of the as-sintered gadolinia doped ceria sample (at 1400°C for 1 hour) is ~2 μm. These grain sizes are in good agreement with the crystallite sizes calculated from X-ray diffraction data as shown in Fig.7. Fig.6 (a) shows the scanning electron micrographs (SEM) of the surfaces of the GDC-10 samples sintered in 1400°C air for 1 hour. There are no open pores on the

surface, but 1~2 % of closed pores were observed on the surface. Fig.6 (b) shows that the energy dispersive spectroscopy (EDS) peaks. Cerium, gadolinium and oxygen peaks were clearly observed in these analyses. XRD analysis results proved that there are CeO_2 and Gd_2O_3 peaks, but no Ce2O3 in the crystals.

Fig.8 shows the grain size of the as-sintered (at 1500°C for 2 h) YSZ-8 sample is ~50 μm. These grain sizes are in good agreement with the crystallite sizes calculated from X-ray diffraction data as shown in Fig. 9. Fig. 8 (a) shows the SEM of the surfaces of the YSZ-8 samples sintered at 1500°C for 2 h. Fig. 8 (b) shows the EDS peaks, and zirconium, yttrium and oxygen can be clearly observed in the peaks. Further, no open pores are observed, although some closed pores are clearly visible.

3.3. Thermal and chemical stability in sodium

After 5 hours of exposure in sodium at 500°C, microstructural changes were observed in the SEM images of the YSZ-8 samples. However, the GDC-10 specimens had totally disintegrated after exposure to sodium at 500°C for 5 hours.

In the case of the YSZ-8 samples, the microstructure of the surface in contact with liquid sodium is visible in the SEM images in Fig. 10. The contact with sodium seems to have led to a disturbance of the microstructure, as clear differences can be observed between the microstructure of the surface in contact with sodium and the microstructure of the as-sintered ceramic, which had no contact with the sodium. A second observation is that the corrosion progressed along the grain boundary of the YSZ-8 samples. As shown in Fig. 10(a), the grain boundaries are clearly disintegrated, and the sodium peak was observed on the surface as shown in Fig. 10 (b). This means that zirconia or yttria reacts with sodium at this temperature, and there is a possibility of Zr-Na-O ternary compound formation on the surface of the YSZ-8 sample.

However, the XRD pattern of the YSZ-8 specimen that was exposed to sodium for 5 hours at 500°C shows no peaks on Na-Zr-O ternary compounds, and the peaks exactly matched with its original crystals.

In the case of the YSZ-8 specimen that was exposed to sodium at 500°C for 10 hours, the specimen was disintegrated for the most part. Analysis could not be conducted, as too small a specimen remained. Most of this specimen reacted with the sodium and the excess oxygen in the sodium at this temperature.

3.4. Total electrical conductivity measurement

The total electrical conductivity of the as-sintered YSZ-8 and Na exposed (for 5 hours) YSZ-8 samples was measured with a four-probe technique in air atmosphere environment (pO2=0.21 atm). Fig. 12 shows that the variation of total electrical conductivity with temperature for both as-sintered YSZ-8 and Na exposed YSZ-8 samples. All samples showed an increase electrical conductivity with increasing temperature and as-sintered YSZ-8 sample show higher conductivity than that of sodium exposed sample with 1 order of magnitude difference.

The electrical conductivities of polycrystalline materials are greatly influenced by their microstructure, i.e. the properties of grain and grain boundary. Grain boundaries are the crystallographic mismatch zones whose properties are determined by mismatch of the lattice, impurities (or second phase segregation), space charge, micro-cracks, or a combination of all of these.

3.5. Oxygen concentration measurement by vanadium wire equilibration method (VWEM)

0.5mm diameter vanadium wire was immersed in sodium at 500°C for 20 h. The surface analysis of the vanadium wire is shown in Fig. 13. The vanadium wire in equilibration with sodium in this study revealed that the oxygen concentration on the surface of vanadium wire is 72.31 at.%.
For the oxygen equilibration between sodium and vanadium, 0.5 mm dia. vanadium wire needs a minimum of 12 hours at 500°C. In this study, the vanadium was immersed in sodium for 20 hours at 500°C. The microstructure and EDS analysis of post-exposure vanadium wire show that it has 70 at.% of oxygen on the surface and the body became brittle.

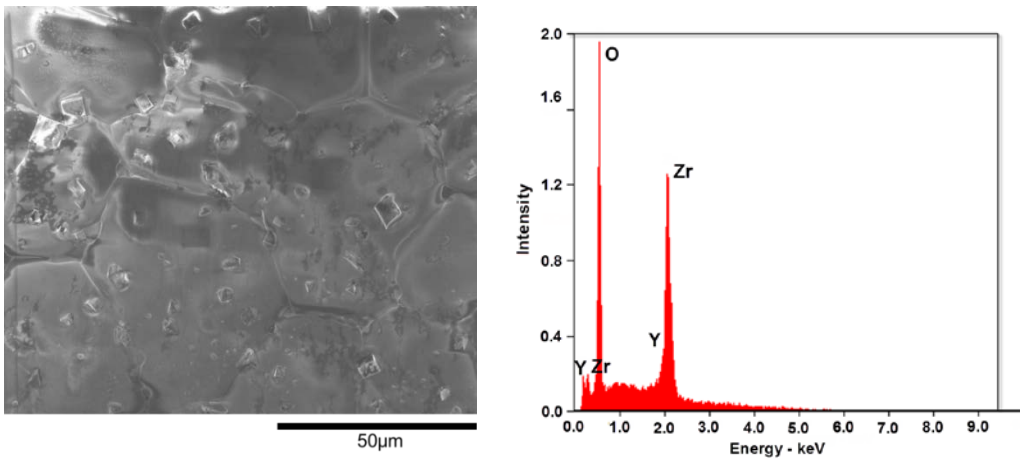

(a) (b)

FIG. 8. The microstructure of as-sintered yttria stabilized zirconia specimen (SEM image, x2,500 magnitudes) (a) and its EDS peak result (b).

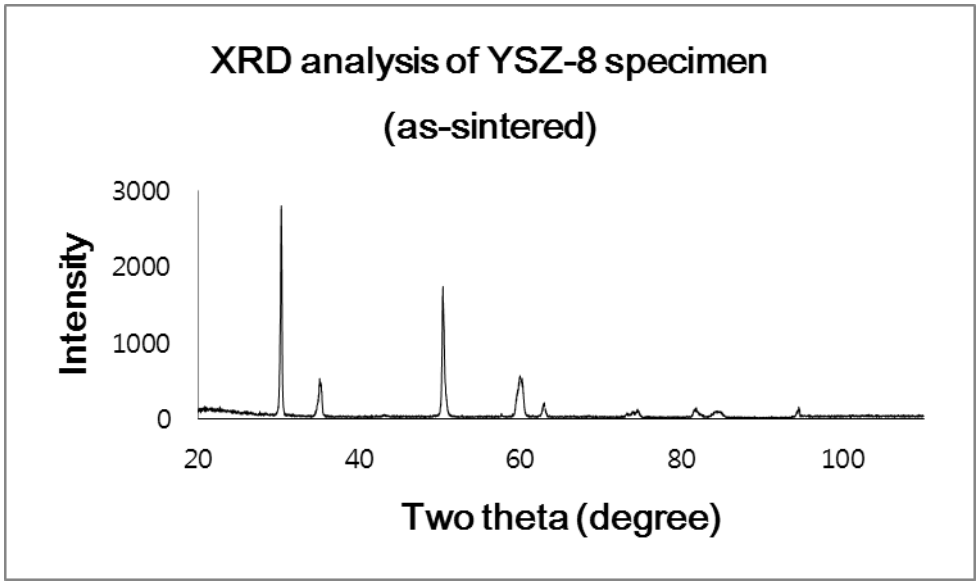

FIG. 9. XRD peak of as-received gadolinia doped ceria ($(Y_2O_3)_{0.08}(ZrO_2)_{0.92}$) specimen.

4.DISCUSSION

To prevent potential accidents, in which oxygen is introduced from a leaked heat exchanger or pipe, oxide based electrolytes have to be compatible, for long time, with the sodium which contains oxygen saturated conditions. As a result of potential leak at the heat exchanger or leak at pipe, sodium coolant in the secondary circuit can be saturated by oxygen. The solubility limit of oxygen in sodium at 500°C is 2153 ppm [24], 1181 ppm [25] and 661 ppm [26]. These values could be achievable within a few hours in a leak situation at heat exchanger. In this study, oxygen concentration in sodium is controlled by bubbling 5 ppm and 100 ppm oxygen gas for calibration of oxygen sensors in sodium at 500°C.

It is widely known that oxygen concentration in sodium increases, the corrosion rate of metals/alloys is also linearly increased [11]. However, oxides (solid electrolyte) which are known as to be compatible in sodium are not widely studied in oxygen saturated sodium environment. Solid electrolyte based oxygen sensor should work for long time even in oxygen saturated sodium condition due to its objectives to monitor oxygen concentration.

To investigate the initial corrosion state of GDC-10 and YSZ-8 samples in oxygen saturated sodium, GDC-10 and YSZ-8 ceramic samples were exposed to sodium at 500°C for 5 to 10 hours. As a result, the GDC-10 samples were totally disintegrated, because of excess of oxygen in the sodium at

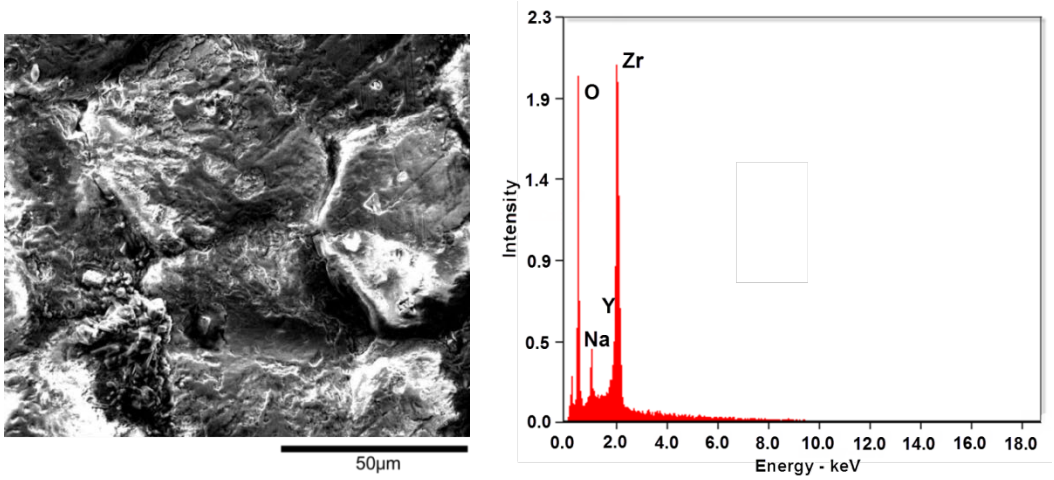

(a) (b)

FIG. 10. The microstructure of yttria stabilized zirconia specimen after exposure to sodium at 500°C for 5 hours (SEM image, x2,500 magnitudes) (a) and its energy dispersive spectroscopy peak result (b).

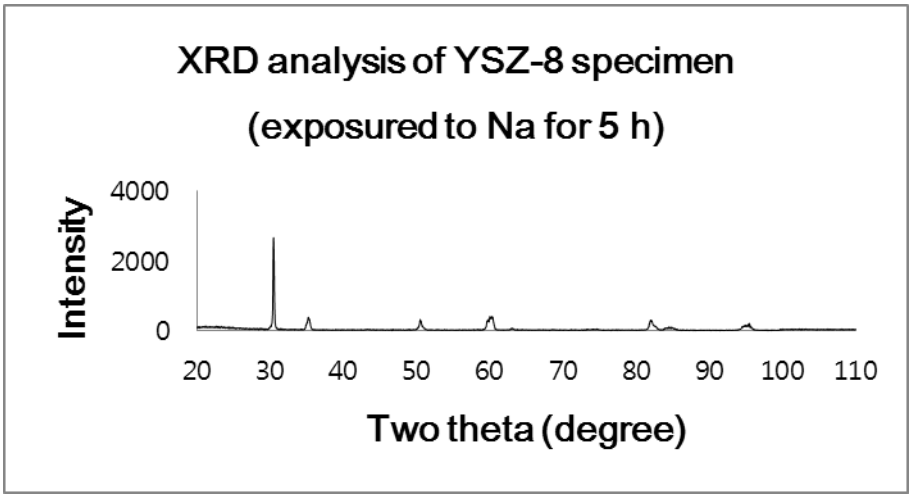

FIG. 11. XRD peak of yttria stabilized zirconia specimen after exposure to sodium at 500°C for 5 hours.

500°C. Cerium oxides (CeO_2 and Ce_2O_3) react with sodium oxides (Na_2O and Na_2O_2) and form compound products (Na_2CeO_3 and Na_2CeO_3, respectively) [33, 34]. The oxygen concentration threshold for these two compounds (Na_2CeO_3 and Na_2CeO_3) are calculated and shown in Table 1. In this study, the oxygen concentration in sodium at 500°C is about 5 ppm and 100 ppm. In the later oxygen concentration in sodium environment, ceria (CeO_2) easily reacts with sodium and sodium oxides, and easily produces ternary compounds with sodium oxides, proportional to the oxygen concentration increase that followed the reactions.

$$Na + CeO_2 \rightarrow NaCeO_2 \quad (1)$$

$$CeO_2 + Na_2O \rightarrow Na_2CeO_3 \quad (2)$$

$$NaCeO_2 + Na + \frac{1}{2}O_2 \rightarrow Na_2CeO_3 \quad (3)$$

In the case of the YSZ-8 sample exposed to sodium at 500°C for 5 hours, the samples were attacked along the grain boundary. In the literature, zirconia was known as compatible [36, 37] and it was exposed to sodium at 540°C for 300h. ZrO_2 is recorded to appear suitable for use in sodium, and show some discoloration on the surface [36]. The oxygen concentration in the sodium was not recorded in the literature.

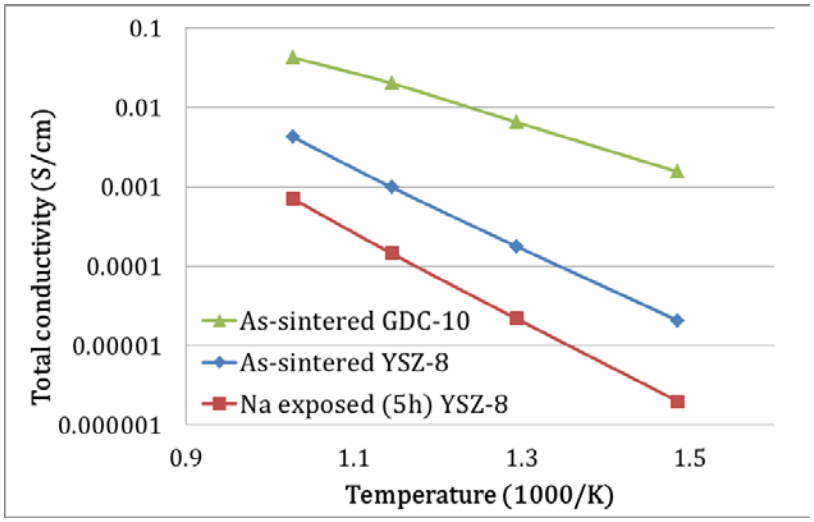

FIG. 12. Total conductivity of as-sintered GDC-10, as-sintered YSZ-8 and sodium exposed (for 5h) YSZ-8 specimens at air atmosphere (pO_2=0.21 atm) as function of temperature.

In the experimental in this study, the YSZ-8 specimens showed surface corrosion along the grain boundary after 5 hours exposure time, as shown in Fig. 10 (a), and a sodium peak was observed in Fig. 10 (b). These SEM and EDS analyses were conducted on the surface of the YSZ-8 specimen, and sodium penetration at depth was not observed. For the XRD peak analysis, the YSZ-8 specimens were powdered. In the XRD peak results, a sodium compound peak was not observed, as shown in Fig. 11. The XRD peak is precisely matched with the YSZ-8 crystals. This means that the specimen was attacked only on the surface along the grain boundaries, and not at depth. The reaction on the surface may be as below:

$$ZrO_2 + Na_2O \rightarrow Na_2ZrO_3 \qquad (4)$$

However after 10 hours of exposure in sodium at 500°C, the specimens had, for the most part, disintegrated in this study.

In Fig. 12 the measured total conductivity of YSZ-8 samples in air is compared with the conductivity. Decreased conductivity in sodium exposed YSZ-8 sample was observed. The observed temperature dependency of the conductivity is in agreement with the theory of oxygen ion conduction in solid electrolyte. Indeed, ionic conductivity is due to thermally activated ion hoping and can be expressed by the following equation:

$$\sigma_{ion} = \frac{A}{T}\exp\left(\frac{-E_a}{kT}\right) \qquad (5)$$

where σ_{ion} is the ionic conductivity (S/cm), T is the absolute temperature (K), A is a pre-exponential constant (K S/cm), k is the Boltzmann constant (1.38 x 10-23 J/K) and E_a is the activation energy (J). The activation energy represents the energy for the migration of oxygen vacancies, being the charge carries for oxygen ion transport in this kind of electrolyte [38, 39].

The electrical conductivities of polycrystalline materials are greatly influenced by their microstructure, i.e. the properties of grain and grain boundary. Grain boundaries are the crystallographic mismatch zones whose properties are determined by mismatch of the lattice, impurities (or second phase segregation), space charge, micro-cracks, or a combination of all of these. In many polycrystalline materials grain boundaries provide a region of relatively rapid mass transport compared to the bulk properties of the crystallites. However, in zirconia- or ceria-based electrolytes the grain boundaries have a lower effective charge carrier concentration and thus result in a highly resistive grain boundary phase [38]. In this study, the surface of sodium exposed YSZ-8 shown in Fig. 10 is disintegrated along the grain boundaries. For the determination of the oxygen concentration in sodium in this study, vanadium wire equilibration method (VWEM) was considered. This method is traditionally used to measure oxygen concentration in the sodium environment [24-31].

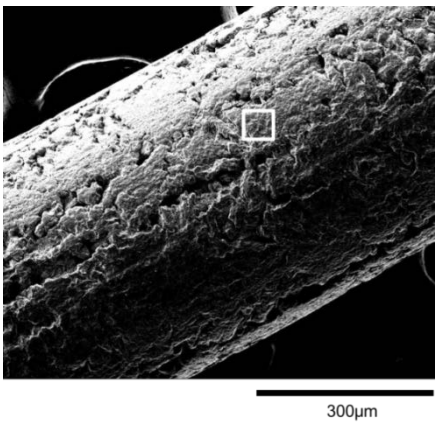

(a)

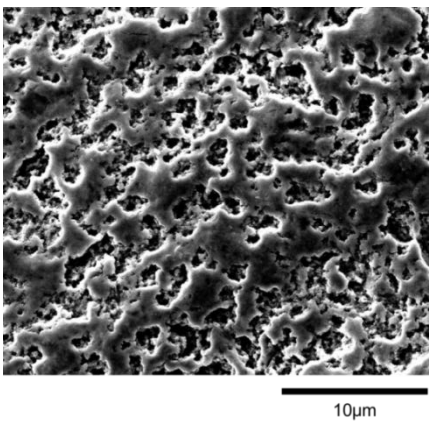

(b)

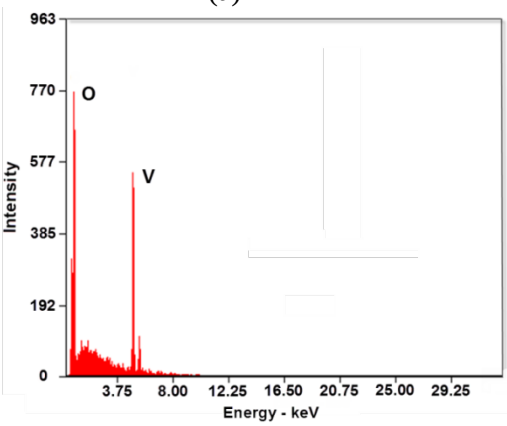

(c)

Element	Wt%	At%
OK	45.06	72.31
VK	54.94	27.69

(d)

FIG. 13. The microstructure of vanadium wire that was exposed to sodium at 500°C for 10 hours (a) x400, (b) x10,000 (c) energy dispersive spectroscopy peaks (x 10,000) and (d) chemical composition at the surface.

TABLE. 1. Oxygen concentration thresholds (wppm) for $NaCeO_2$ and Na_2CeO_3 calculated using the oxygen solubility data [23].

T (K)	**$NaCeO_2$**			**Na_2CeO_3**		
	a	**b**	**a**	**b**	**a**	**b**
700	11.7	7.6	4.9	10.9	7.1	4.6
800	13.9	7.8	3.9	41.4	23.1	11.5
900	16.0	7.9	3.2	117.4	58.3	23.7

For the oxygen equilibration between sodium and vanadium, 0.5 mm dia. vanadium wire needs a minimum of 12 hours at 500°C. In this study, the vanadium was immersed in sodium for 20 hours at 500°C. The microstructure and EDS analysis of post-exposure vanadium wire show that it has 70 at.% of oxygen on the surface and the body became brittle. The solubility limits of oxygen in vanadium are studied in [31], the analysis value in this study is over the solubility limit. This reveals that the sodium was saturated with oxygen.

5.SUMMARY AND CONCLUSION

For the development of solid electrolyte-based electrochemical oxygen sensor that works in high temperature sodium, oxide based electrolytes such as yttria stabilized zirconia (YSZ) and gadolinia doped ceria (GDC) were considered as candidate materials, due to their known oxygen ion conductivity and thermochemical stability tests has been conducted.

Ceria based specimens were entirely disintegrated after it was exposed to sodium at 500°C for 5 hours. In the case of zirconia based specimens, they also showed that the grain boundary was corroded after 5 hours, and the specimen was, for the most part, disintegrated after 10 hours of exposure.

ACKNOWLEDGEMENTS

This work was financially supported by the Human Resources Development Program of the Korea Institute of Energy Technology Evaluation and Planning (KETEP), funded by the Ministry of Knowledge Economy (MKE), and by the Korean Nuclear R&D program organized by the National Research Foundation (NRF) of Korea in support of the Ministry of Education, Science and Technology (MEST).

REFERENCES

[1] W.J. Carmack, D.L. Porter, Y.I. Chang, S.L. Hayes, M.K. Meyer, D.E. Burkes, C.B. Lee, T. Mizuno, F. Delage and J. Somers, J. Nucl. Mater. 392 (2009) 139-150
[2] T. Suzuki, I. Mutoh, T. Yagi and Y. Ikenaga, J. Nucl. Mater. 139 (1986) 97-105
[3] H.U. Borgstedt, J. Nucl. Mater. 317 (2003) 160-166
[4] D.W. Sandusky, J.S. Armijo and W.J. Wagner, J. Nucl. Mater. 46 (1973) 225-243
[5] S.P. Awasthi and H.U. Borgstedt, J. Nucl. Mater. 116 (1983) 103-111
[6] V. Ganesan and V. Ganesan and H.U. Borgstedt, J. Nucl. Mater. 312 (2003) 174-180
[7] V. Ganesan and V. Ganesan, J. Nucl. Mater. 256 (1998) 69-77
[8] S.R. Pillai, H.S. Khatak and J.B. Gnanamoorthy, J. Nucl. Mater. 224 (1995) 17-24
[9] T. Gnanasekaran and C.K. Mathews, J. Nucl. Mater. 140 (1986) 202-213
[10] D.R. Olander, Fundamental aspects of nuclear reactor fuel elements (US Dept. of Energy, 1976) Chap. 20.
[11] T. Furukawa, S. Kato and E. Yoshida, J. Nucl. Mater. 392 (2009) 249-254
[12] R.G. Taylor and R. Thompson, J. Nucl. Mater. 115 (1983) 25-38
[13] M.R. Hobdell and C.A. Smith, J. Nucl. Mater. 110 (1982) 125-139
[14] D. Jakes, J. Kral, J. Burda and M. Fresl, Solid State Ionics. 13 (1984) 165-173
[15] D. Jakes, J. Sebkova and L. Kubicke, J. Nucl. Mater. 132 (1985) 88-91
[16] T.H. Estell and S.N. Flengas, Chem. Rev. 70 (1970) 339-376
[17] B.C.H. Steele, Solid State Ionics. 129 (2000) 98-110
[18] J.E. Bauerle, J. Chem. Phys. 45 (1966) 4162-4166
[19] X.J. Chen, K.A. Khor, S.H. Chan and L.G. Yu, Mater. Sci. Eng. A-Struct. 335 (2002) 246-252
[20] H. Inaba and H. Tagawa, Solid State Ionics. 83 (1996) 1-16
[21] R.V. Mangalaraja, S. Ananthakumar, M. Paulraj, K. Uma, M. Lopez, C.P. Camurri and R.E. Avila, Process. Appl. Ceram. 3 (2009) 137-143
[22] K. Yasuda, K. Uemura and T. Shiota, J. Phys.: Conf. Ser. 339 (2012) 012006
[23] T. Kosaka and K. Sato, J. Nanomater. 2010 (2010) Article ID 935146
[24] D.L. Simth and R.H. Lee, ANL Report 7891 (1972)
[25] J.D. Noden, J. Br. Nucl. Energy Soc., 12 (1973) 57-62
[26] A.W. Thorley and A.C. Raine, Intern. Symp. on The Alkali metals, Nottingham (UK) (1966) - Special Publication No. 22, The Chemical Society, London (1967), p. 374
[27] A.J. Hooper and E.A. Trevillion, J. Nucl. Mater. 48 (1973) 216-222
[28] D.L. Simth, J. Nucl. Mater. 51 (1974) 280-282
[29] A.J. Hooper and E.A. Trevillion, J. Nucl. Mater. 52 (1974) 119-122
[30] B.R. Grundy, D.D. Durigon, J. Nucl. Mater. 55 (1975) 111-112
[31] D.L. Smith, J. Less-Common. Met. 31 (1973) 345-358
[32] K.R. Reddy and K. Karan, J ELECTROCERAM. 15 (2005) 45-56
[33] M.G. Baker, S.A. Frankham, P.G. Gadd. J. Nucl. Mater. 218 (1995) 256-260
[34] M.A. Mignanelli, P.E. Potter and M.G. Barker, J. Nucl. Mater. 97 (1981) 213-222
[35] F.E. Bowman and D.D. Cubicciotti, Alche. J. 2 (1956) 173-176
[36] W.D. Tuohig, J.T.A. Roberts and R.N. Singh, ANL-Conf-740414-1 (1974)
[37] J.H. Stang, E.M. Simons, J.A. DeMastry and J.M. Genco, DMIC report 227 (1966)
[38] S. Hui, J. Roller, S. Yick, X. Zhang, C. Deces-Petit, Y. Xie, R. Maric and D. Ghosh, J. Power Source. 172 (2007) 493-502
[39] V.V. Kharton, F.M.B. Marques and A. Atkinson, Solid State Ionics, 174 (2004) 135-149

ASTRID In Service Inspection and Repair: review of R&D program and associated results

F.Baqué[a], F. Jadot[b], F. le Bourdais[c], J. Sibilo[d], J.M. Augem[e], O. Gastaldi[a]

[a] CEA, DEN, DTN, CEA Cadarache, 13108, Saint-Paul-lez-Durance, France

[b] CEA, DEN, Cadarache, CPA , Bât. 155, 13108 St Paul lez Durance CEDEX, France

[c] CEA, DRT, Saclay, DISC , Bât. 611, 91191 Gif sur Yvette CEDEX, France

[d] AREVA NP, 10 rue Juliette Récamier 69456 Lyon CEDEX 06, France

[e] EDF SEPTEN, 12-14 avenue Dutriévoz, 69628 Villeurbanne CEDEX, France

Presented by K.Vulliez

Abstract. In the frame of the CEA / EDF / AREVA coordinated research program for the Generation IV sodium-cooled reactors, the improvement of in-service inspection and repair (ISI&R) capabilities was identified as a major issue. The future French demonstrator, ASTRID (Advanced Sodium Technological Reactor for Industrial Demonstration) is directly impacted. The Periodic Examination and Repair are looked at through the following main R&D axes: i) optimization of the plant structure design for easing periodic examination and repair, ii) development of inspection techniques (Non Destructive Testing tools and related simulation), iii) accessibility and associated robotics, and iv) development and validation of repair processes. The associated needs are being defined through an iterative work between designers and inspection specialists. They are mainly: adaptation of the Design to ISI&R capabilities and requirements, development of ultrasonic transducers and of some other NDT techniques (under sodium ultrasonic visualization) and of laser repair processes, and of robotic equipment. A review of the R&D efforts done in these fields is presented in this paper.

1. Introduction

Within the framework of the French Act, dated June 28th 2006, among the Generation IV systems, the sodium-cooled fast reactors seem to be the most mature technology to be developed for sustainable energy. Thus, since 2007, the CEA, EDF and AREVA French partners launched a coordinated research program on sodium cooled fast reactors (SFR) which is now being used for the next ASTRID (Advanced Sodium Technological Reactor for industrial Demonstration) prototype [1].

Reinforcement of In-Service Inspection and Repair (ISI&R) is a major transverse issue [2], as it is strongly linked to safety analysis (the three defense lines: checking the state of material and equipment during the reactor's life span, detection of premature failures, and in operation detection of significant failures), economic reliability (implementation delays), and investment protection (repair).

ISI&R for SFR has to firstly deal with high sodium chemical reactivity with air and water: this leads to monitor carefully the confinement and steam generators leakage, and to control the tightness during the interventions. Secondly, due to the risk of under stress caustic corrosion appearance, the sodium draining of reactor main vessel is only planned for exceptional interventions, and the current inspections and operations have then to be realized under sodium. Thirdly, the temperature corresponding to plant cold shutdown condition is about 200°C: thus, ISI&R devices have to work at these high temperature levels. Last but not least, the sodium being opaque, each intervention (inspection / repair) below the free sodium level cannot be performed / followed by optical devices, so, up to now the mostly used techniques are the ultrasonic ones.

On the basis of feedback experiences from former French sodium reactors (Rapsodie, Phenix and Superphenix [3]), this specific R&D program, which global objective is to increase ISI&R capabilities,

can be divided into four sections [4]: (1) Conceptual design optimization of the primary and secondary systems in order to reduce the number of structures and components to be surveyed, to locate sensitive zones in accessible areas from either the inside or outside, and to reduce the number and length of welds. (2) Development of measurement techniques and surveillance devices for continuous monitoring during reactor operation, and for periodic examinations during reactor shutdown. (3) Improvement of accessibility and development of remote controlled devices (robotics) with suitable carriers. (4) Identification, development and validation of repair processes (core discharge, sodium draining), as well as techniques for repair operations in sodium environment.

For ASTRID first criticality, it will be necessary to get a sufficient, available, efficient and qualified instrumentation. Moreover, it is planned to test in ASTRID during its operation, the instrumentation which has to be qualified for the future nuclear plants (Generation IV). The running program of research and development implies, on the one hand, usual and available devices to be improved, and, on the other hand, innovative ones to be developed, tested and qualified.

This paper focuses on the French developments undertaken for periodic examination and repair of reactor core vessel and associated internals. ISI&R of other components (such as Heat Exchangers like Steam Generator Units) are also looked at in the running program but are not described here.

2. Specifications for ISI&R Future SFRs

In service inspection for SFR must take part in the reactor integrity demonstration, by checking the structures insuring the three main safety functions (reactivity monitoring, decay heat removal, containment of hazardous products). The surveillance graduation applied to each structure is defined thanks to the “risk informed method”, which takes into account the damage probability all along plant life and the associated consequences. Repair ability is also an important specification for SFR, as it can save the overall investment.

ISI&R approach is now parted in five levels for SFR design (Figure 1.): a new Level 0 allows both to reduce ISI&R needs by design optimization and to take into account ISI&R requirements for design.

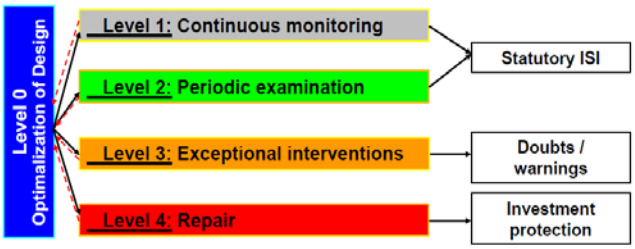

FIG. 1. ISI&R approach for future French SFRs

ISI&R level 1 deals with continuous monitoring during reactor operation (including in power operation with sodium temperature reaching 550°C). It is mainly based on the operating parameters checking (neutronics, temperatures, flow rates, pressure) with some global measurements reflecting the structure and component states (leaks, mechanical deformation, vibratory or acoustic characteristics). This item is out of the scope of the present paper.

During reactor cold shutdowns (sodium at about 200°C), ISI&R level 2 brings together tests and examinations in a statutory program (NDE purpose : Non Destructive Examinations). The periodic inspection program must provide the validation of the hypothesis and project values about the damaging mechanisms considered during the design studies. Moreover, ISI&R level 2 must look for the unforeseen damaging mechanisms, in order to check the material mechanical property degradation process, and the absence of corrosion-type mechanism. Mainly focused on safety related structures (core support structure, Above Core Structure ACS, reactor vessel), these checks may be also carried out on minor structures (inner vessel, various baffles). Even if some components can be inspected after their removal from the reactor (Primary Pump PP, Control Rod Drive Mechanisms) for maintenance, other parts of the reactor block need specific means for in situ inspection. Because they are easier and quicker, other inspections are preferentially performed from outside the main vessel, even for example using immersed structures as ultrasonic wave guides. Nevertheless, other inspections have to be

performed within the reactor block: the checks mainly consist in visual observation in the gas upper volume, but also in sodium telemetric positioning control, and volumetric non-destructive examinations of welded junctions.

ISI&R level 3 is the answer to abnormal situations, which may be consecutive to an operation warning or to an operation mistake. Considered as exceptional intervention for control (localization and characterization of any fault) at reactor shutdown conditions, the level 3 insures the entire range of associated operations: for this, it is necessary to provide the most extensive access to the internal structures. First, the design studies have to take this requirement into account. Then, the sodium immersed devices, including sensors and carriers (like for level 2), have to be available. Furthermore, if the needed operation requires a more accurate examination, or if it is sodium incompatible, core unloading and sodium draining have to be performed. These provisions are studied since the preliminary R&D phase. Main issues deal with draining without caustic stress corrosion risk and performing the entire operation (core unloading, draining, examination, reverse operations) within the duration target of one year maximum. In addition, the primary components withdrawal (Intermediate Heat Exchangers IHX, PP) may be necessary to get an improved access. The target duration for the associated removal and replacement is about one month per component (within the one year maximum duration for exceptional intervention). In this frame, only few technical solutions are available, then this justify to undertake a significant effort for innovation, specially for under sodium applications.

For SFRs, it is necessary to be able to guaranty the investment protection during the whole life span, even in case of unforeseen damage. That is why ISI&R specifications incorporate the repair ability for all the structures, and the replacement possibility for the primary components. These provisions are now insured by ISI&R level 4. Repair or replacement operations are performed in sodium environment: in the argon cover gas standard volume, under sodium with tight cavity, or in argon gas after sodium draining. To favor this ISI&R level 4 implementation, the reactor structures have to be simple and accessible. As far as possible, the high thermo mechanically loaded structures have to be designed as replaceable. Then, the ISI&R level 4 operations require repair tools to perform preliminary sodium local removing, machining and welding. The robotic carriers, which carry the tools, have to be suitable for sodium environment, but they have also to absorb machining forces, and to recover the produced wastes. Even if the main challenge deals with the reactor block system, the same approach is also applied to all other sodium devices and loops.

3. Design studies for ISI&R improving

Being a welded stainless steel manufacturing, operating at high temperatures (400-550°C), with significant thermal gradients, under neutron and gamma fluxes, during 60 year lifetime, future SFRs will undergo some significant loadings. These loadings may lead to failure modes such as excessive deformation, ratcheting, fatigue for the cold pool zones, creep-fatigue for the hot pool zones, buckling for thin structures in compression, thermal striping for zones subjected to high thermal gradient mixtures, irradiation damage for the structures near the core, corrosion, wear.

The risk reduction of the potential damage, which is an important issue for design studies, also allows minimizing surveillance, examination and repair needs. Thus, the reactor global design has to be selected, taking into account this requirement, and by collaborating with ISI&R specialists. The work mainly consists in proposing a robust design with significant margins. Therefore, the welds number has to be reduced and the remaining ones are to be located in low loaded areas. Moreover, geometrical singularities which may induce some stress concentrations or unusual operating ranges (cavitation wear, erosion, excessive vibrations) are to be avoided. Finally, this previous design work, which reduces ISI&R provision range, is being made for SFR design architecture (1500 MWth pool type) shown in Figure 2.

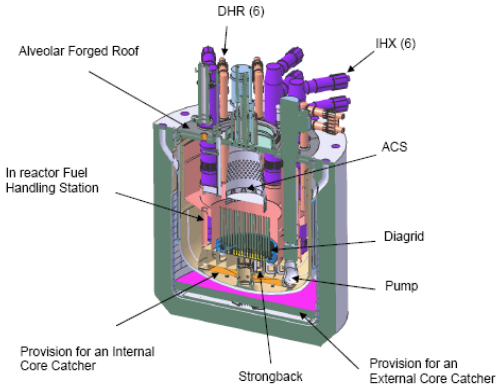

FIG. 2. Pre-conceptual Design for SFR reactor block

A related work is undertaken by the French partners for improving existing Design Rules: thus, RCC-MRx new code includes, in 2012 edition, NDE "good practice" information in order to ease/make them possible, through specific NDE recommendations for Designers. This is part of Level 0 item (see figure 1).

The reactor design has to favor ISI implementation with the help of sufficient accessibility and a suitable positioning of areas to be inspected.

The design has also to deal with repair operations by simplifying the structures and with replacement operations enabled by the removable component proposals. For pool type reactor, this leads to fewer and simpler internal structure design. The replacement operations have also to be foreseen since the design phase: for the PP and the IHX, some optimizations of the interfaces between the components and the slab have been proposed. Above Core Structure (ACS) is a highly thermo mechanically loaded structure, and so its replacement during reactor lifetime has to be considered too.

4. Technological Developments

Inspection simulation is performed with CIVA software for ultrasonic applications: telemetry measurement within primary sodium of the main vessel and Non Destructive Examination of internal structures and vessels. Two approaches are being followed: inside inspection where transducers are directly immersed in sodium coolant (considered as a static and homogneous fluid) and inspection from outside with transducers positioned along the wall of the main vessel (see figure 3 and hereafter). For both cases, acoustic bulk waves and guided/surface waves are looked at. Probe design and inspection performances can be predicted by using comprehensive models that can take into account the various variables of the problem: attenuation and deflection, transmission and reflection of ultrasounds, which depend on liquid sodium characteristics (mainly temperature and micro bubble fields), of immersed structures characteristics (mainly wetting at liquid/solid interface, thickness and shape).

Simulation of ultrasonic telemetry through screens, for examples with ultrasonic probes positioned outside the reactor along the main vessel wall, alow to estimate losses of energy at each interface.

Ultrasonic simulation tools have been developed and implemented in CIVA [5] [6]. A method based on a pencil approach allows the calculation of ultrasonic beam fields in heterogeneous media taking into account material attenuation and energy losses at interfaces between media of different acoustic properties. In order to validate these models for telemetric applications, experiments were carried out in water with two 40-mm thick stainless steel plates supposed to represent the main vessel wall and an internal structure were used. Transducers were positioned along one of the plates in a pulse/echo normal configuration and in a pitch and catch non-normal incidence configuration. For normal incidence application, CIVA predicts well the exponential decay of the ultrasonic energy reflecting back and forth in the plate supposed to represent the main vessel wall (Figure 4 left).

Multiple reflections still have significant energy by the time the echo off the front surface of plate 2 is detected, meaning that it can be difficult to interpret echoes coming from objects located close to the main vessel wall. Simulation can thus be used as a tool to predict the arrival times of the various echoes reflected off the internals. CIVA predicts correctly the amplitude of all the echoes, particularly the echo coming from the front of the surface of the second plate supposed to represent the surface of an internal structure.

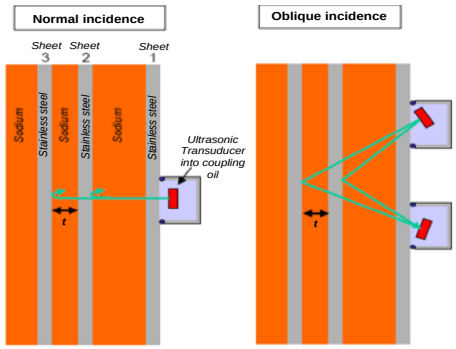

FIG. 3. Inspection through screens, for a normal incidence with a transducer working in pulse/echo mode (left) and non-normal incidence with a pitch-catch configuration (right)

For non-normal incidence application (pitch and catch configuration with ultrasonic waves propagating at 45° in the main vessel wall), the distance between the emitter and the receiver is adjusted to obtain an intersection of the emission and reception focal paths along the surface of plate 2. Non-normal configurations can be used to inspect internals that are not parallel to the main vessel wall and/or to decrease the duration of the multiple echoes inside the main vessel wall observed at normal incidence. When comparing experimental results and simulation calculated with CIVA (Figure 4 right), we observe multiples echoes early in the signals. They are coming from modes converted inside the main vessel wall; their time of flight allows analyzing each of them. The amplitude of the front surface echo off plate 2 is measured; reference is the mode conversion echo noted 3LT.

Validations performed for various frequencies and various angles of incidence confirm that CIVA can be used as a tool to predict telemetric applications for a quasi-static fluid. This will help determining which internal can be inspected from outside the main vessel wall according with design (thickness and spacing between immersed structures.

The need to propagate the maximum energy possible through bounded media orientated the study towards Lamb waves. Transfer matrix method is used in order to simulate the ultrasonic transmission through several immersed plates. In order to qualify this method, tests in water have begun investigating various influential parameters (frequency, pulse mode or wave trains; sheet thickness, spacing, number of plates and parallelism …). It can be seen that an artificial defect can be detected in a plate located behind one or two screens by generating Lamb waves in the last plate. Larger scale then in sodium test will be performed.

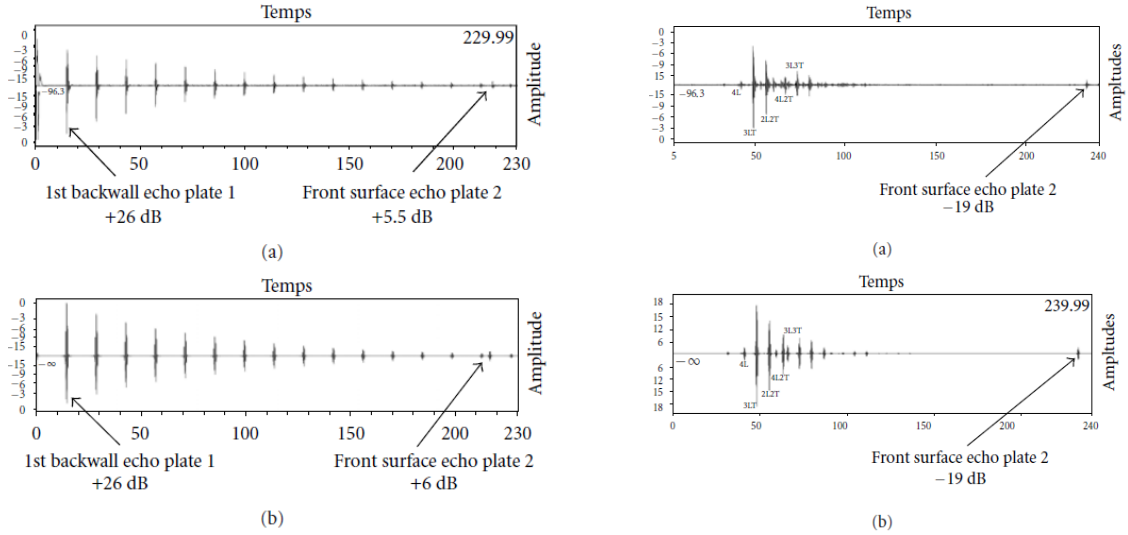

FIG. 4. Inspection through screens at 2.25 MHz,
Left: for a normal incidence configuration, experimental (top) and simulation (bottom)
Right: for a 45° configuration, experimental (top) and simulation (bottom)

Simulation of ultrasonic inspection with guided waves is devoted to examining of structures welded to the main vessel wall such as the core support, using guided waves. The goal is to generate guided waves from the main vessel external skin up to the inner vessel zone to control, by using intermediate plates as wave guides (Figure 5).

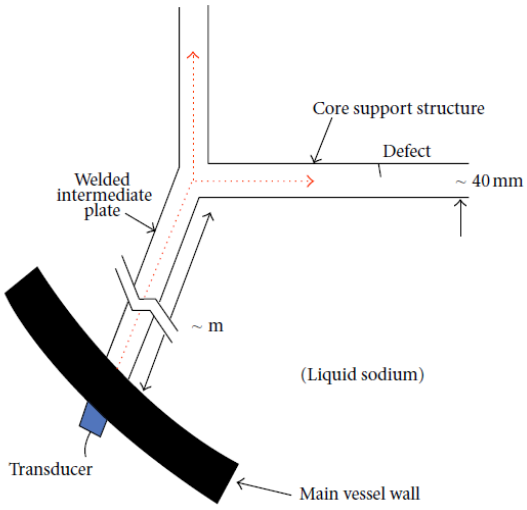

FIG. 5. Inspection of structures used as wave guides

The CEA has implemented in CIVA a model for the propagation of elastic guided waves using the semi-analytical finite element method (SAFE) [7] [8]. This method allows predicting the elastic field under the form of a modal decomposition for guides of complex section. It decomposes the solution into an analytical part for the propagation of the waves along the guide axis and a numerical approach using finite elements for the section of the guide. This method is however limited to guides that have a constant section along one extrusion plane and to defects that are contained along the section of the guide.To model the propagation of guided waves along the core support, we need to be able to deal with discontinuities such as the junctions between the various parts of the core support and defects of arbitrary shapes. One way to handle these problems is to use a finite element method around the areas presenting these discontinuities. Diffraction by a discontinuity or a defect is calculated using the finite element (FE) method to which we add transparent boundary conditions allowing to minimize the volume meshed (Figure 6).

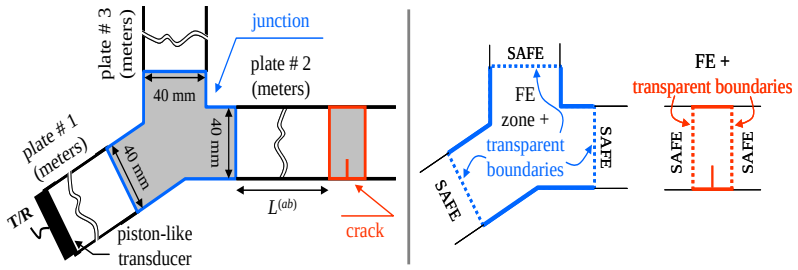

FIG. 6. Left: configuration of testing of plate #2 through a triple junction.
Right: the two phenomena of scattering (junction, crack) are computed independently by FE; guided propagations are computed by SAFE

Ultrasonic control with sodium immersed sensors for future SFRs, ultrasonic transducers working under sodium at about 200°C are required [9]. They are planned to be used for the telemetric and volumetric examinations of the internal structures, during periodic inspection phase. If needed, they also could be exceptionally used for the core support structure. These transducers must be able to measure distance of some meters with 100 µm accuracy and to detect cracks of about 200 mm x 10 mm. On the one hand, with regard to the high temperature transducers required for Level 1 monotoring and continuous inspection, these volumetric examination transducers are operated at a lower temperature and during a shorter duration. It implies a constraint reduction for the electro acoustic element choice. On the other hand, this kind of transducer use demands a better damping and efficiencies than high-temperature transducers, and easier focusing capacities. Furthermore the low temperatures (below 300°C) may cause some acoustic coupling deficiency, hence requiring a special treatment of the transducer active face. Available standard High Temperature UltraSonic Transducer (TUSHT) has been qualified by CEA in sodium and used in Phenix plant during 15 years (Figure 7): it is a multipurpose transducer, that was initially designed in order to be usable in a wide range of frequency (up to 5 MHz) and of applications, in the main vessel of sodium-cooled fast breeder reactors (and also PWR reactors), for all reactor conditions (shut-down, full power, transients).

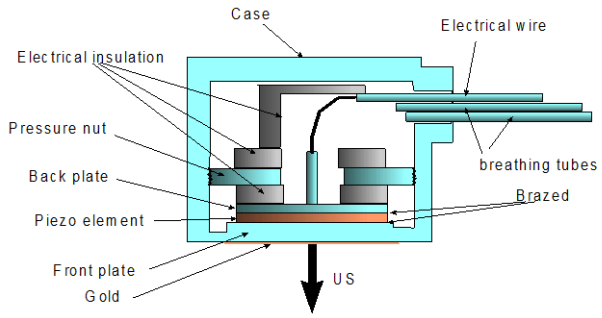

FIG. 7. TUSHT general architecture

The immersed TUSHT are, at the present time, reference transducers for use in the main vessel of sodium fast reactors, in all the possible operating conditions. The major current improvement studies aim at reducing the oxygen-loss causes and effects (it is why one can see on Figures 7 and 8 two so-called “breathing tubes” which allow continuous air supply within the casing), for use at full power conditions (550°C, long time operation), and to improve the bandwidth in pulse-echo applications, at least for use in inspection conditions (200°C, short time operation), with better damping and time resolution. Figure 8 also shows the first AREVA prototype which has been manufactured and tested under sodium. It integrates a piezo electric ceramic. The associated results are quite satisfying. AREVA-NDE Solutions was contracted to design and fabricate a transducer capable of performing NDE under liquid sodium with piezoelectric material for the generation of the ultrasonic pulse.

(a) TUSHT available CEA transducer (AISI 304L casing)

(b) TUCSS AREVA transducer (Nickel front face)

(c) EMAT CEA transducer (thin AISI 316L front face: here partially removed)

Fig. 8. Available under sodium transducers

As shown on Figure 8, the outside packaging of this transducer is entirely metallic to prevent any risk of inner part chemical degradation. Moreover, the front of the transducer is made of nickel and the emissive surface has been subject to a mirror-polished surface treatment. This solution allowed to obtain an immediate acoustic coupling into liquid sodium at temperature as low as 110°C (wetting by liquid sodium is also looked at but not reported here). For some applications, Electro Magnetic Acoustic Transducer (EMAT) is an interesting alternative to conventional piezoelectric transducers. The principle of an EMAT is to generate ultrasonic waves using the Lorentz Force [10]. Eddy Currents are induced into the inspected part thanks to a coil while magnets generate the required magnetic field. The interaction between these two fields creates the Lorentz Force, which produces ultrasonic waves. Reciprocally, the interaction of ultrasonic waves with a magnetic field induces currents in the receiving EMAT coil. A mono-element EMAT probe has been developed for in liquid sodium inspection at 200°C. First experimental results are promising. A full phased-array EMAT system is under development for sodium testing in 2012.

In order to qualify CIVA software, an experimental mock-up “MULTIREFLECTEUR” was specified for the study of ultrasonic diffractions and reflections in liquid sodium, and was successfully tested in 2010. It included a rotating high-temperature ultrasonic transducer TUSHT (firstly available for the test program), a fixed target, rotating targets and thermocouples (Figure 9). In order to reach the metrological objective, in air initial calibration at room temperature of all components was performed and led to a global uncertainty equal to ± 0,02 mm (20 µm) for their location and to ± 0,02° for their angular position. After under-water commissioning tests, the mock-up was used in a 1 m diameter pot in isothermal 200°C static sodium conditions: test parameters were TUSHT frequency and 6 target positions. Then, global uncertainty on ultrasonic distance measurement could be checked and is better than 100 µm.

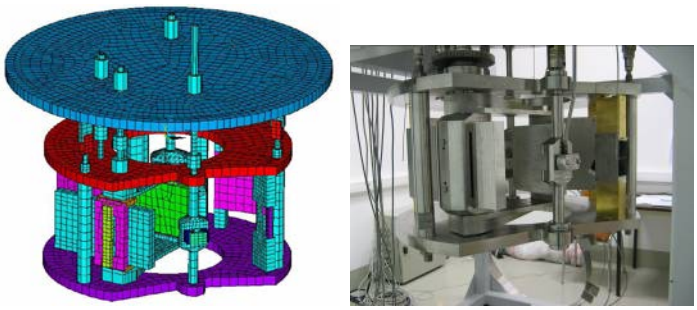

Fig. 9. MULTIREFLECTOR mock-up (1 m diameter) devoted to in sodium ultrasonic telemetry study

Extending telemetric measurement leads to the possibility of ultrasonic under sodium “vision”, also called « visualization », able to deal with different applications: surface mapping (imaging) of submerged structures/components, integrity inspection of structure/component surfaces (including the detection and sizing of opened cracks), determination/confirmation of robotic system positioning, fuel assembly identification, detection, localization and sizing of immersed objects (including migrating bodies). R&D program is beginning in 2012 and intends to compare all the

identified ultrasonic technologies available for surface telemetry options: orthogonal antenna (former CEA IMARSOD project: (see Figure 10), conventional or innovative SAFT (Synthetic Aperture Focusing Technique), 2D matrix with Full Matrix Capture for example (Figure 10)… Underwater tests will first be performed and then sodium tests will be carried out when ultrasonic corresponding sensors will become available.

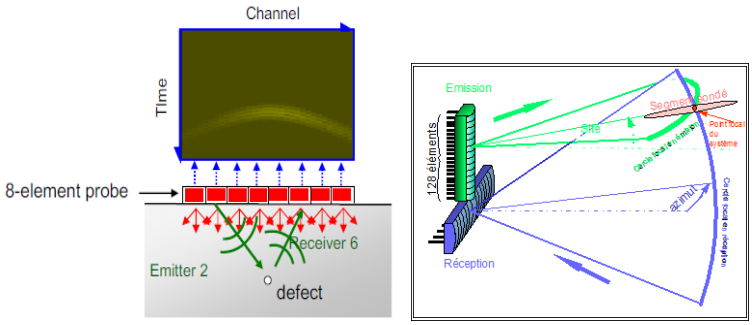

Fig. 10. Ultrasonic visualization techniques (examples)

Other ultrasonic techniques are also investigated, such as surface waves for thermal striping effect detection, especially in the ACS lower zone.

In Sodium Environment Repair for the non removable components will be performed in a gas environment: either in the upper dry zones of the reactor cover gas plenum, or in a gas-tight volume, if the faulty zone is located under the sodium free level. In that last case, the gas-tight system will have to contain the inspection and repair tools and protect them from the surrounding liquid sodium (Figure 11). Two concepts will be investigated: one in contact with the structures, having a seal formed by two flexible lips, and the other is a system that prevents liquid sodium penetration by using a gas pulsed screen, supplemented by a scraper seal. Specific seal material is being tested in 200°C liquid sodium: conventional PWR silicone material is being tested for in sodium qualification (Figure 11). Concerning the repair tools, the laser method has been selected for future SFRs, because it has the advantage of not generating any stress on the tool and because it is suitable for the various applications: indeed, the repair scenario for in sodium structures should be first removal of sodium (after bulk sodium draining), then machining and finally welding.

Robotics for in Sodium Examination and Repair has to be suitable with sodium environment: either in the cover gas plenum or in gas after sodium draining, or even under liquid sodium. Few in sodium carriers have been used in the past : it is why a specific R&D program has been initiated with the objective to have a prototype of robotic carrier for in sodium testing by 2014. This R&D program is parted in several axes: detailed definition for the SFR carrier needs, carrier architecture definition and specifications, carrier organ in sodium tightness, carrier material compatibility with sodium, temperature resistance (200°C), irradiation resistance (depending on location main vessel), intervention gas-tight bell for operation under liquid sodium, carrier positioning control in liquid sodium.

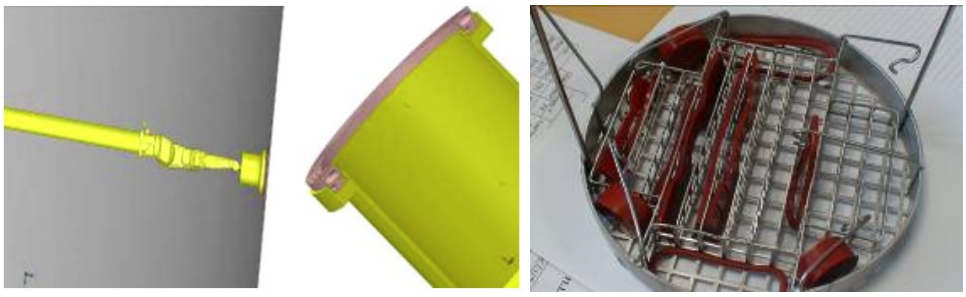

(a) In sodium robot concept: articulated arm with a bell

(b) Gas-tight bell design for Repair tools

(c) Silicone samples before sodium testing

Fig. 11. Tools for in sodium intervention

5. Conclusions

On the basis of available feedback and the new safety requirements, the ISI&R for next SFRs has been identified as a major task. The French R&D program launched in 2007 for Periodic Examination and Repair improvement is based on several aspects: ensuring a strong connection between the reactor designers and inspection specialists, and developing tools and techniques applicable in a sodium environment (inspection at 200°C). The key milestones (and main available results) of this ambitious R&D program are: validation for ultrasonic simulation (*achieved for isothermal sodium conditions*), validation of ultrasonic transducers (US telemetry and NDE sensors) under sodium conditions at 200°C (*procedures for manufacturing of available CEA designed TUSHT have been validated*), definition of key components of the robotic equipment for operation in sodium at 200°C (*in sodium seals and thermal isolation are being qualified*), validation of laser repair processes and techniques: sodium sweeping, structure machining and welding (*simulating zinc test are being performed*).

In the frame of this R&D activity, feasibility and qualification tests are performed, simulation of techniques (ultrasonic inspection and laser repair) are developed, inspection and repair tools are designed, manufactured and tested. ASTRID prototype project orientates these actions and will get large benefits from them.

ACKNOWLEDGEMENTS

The authors would like to thanks all the colleagues at CEA, AREVA and EDF who provided us with fruitful information, guidance and technical insight.

REFERENCES

[1] Jadot F. Baqué F. Jeannot J.Ph. Augem J.M. Sibilo J., “ASTRID Sodium cooled Prototype : program for improving In Service Inspection and Repair”, ANIMMA Int. Conf., Ghent, Belgium, 6-9 June 2011, Paper 3-37

[2] Baqué F. Rodriguez G. Jardin N.. Carpreau J.M Augem J.M. Sibilo J., “Generation IV Nuclear Reactors – R&D Program to Improve Sodium-Cooled Systems Inspection”, ANIMMA Int. Conf., Marseille, France, 7-10 June 2009, Paper 77

[3] Sauvage J.F., “Phénix 30 years of history: the heart of a reactor”, Ed. CEA, France, 2004

[4] Sibilo J. Breuil E. Baqué F. Augem J.M. “Generation IV Nuclear Reactors: Strategy and challenges of R&D Program for improving Inspection and Repair of Sodium Cooled Systems”, ICAPP 2010, San Diego, California, USA, June 13-17, 2010, Paper 8096

[5] Reverdy F. Baqué F. Lu B. Jezzine K. Dorval V. Augem J.M., “Simulation of ultrasonic inspection for sodium cooled reactors using CIVA”, ANIMMA Int. Conf., Ghent, Belgium, 6-9 June 2011, Paper 3-08

[6] Darmon M. Leymarie N. Chatillon S. Mahaut S., “Modelling of scattering of ultrasounds by flaws for NDT”, Ultrasonic Wave Propagation in Non Homogeneous Media, Springer Proceedings in Physics, Vol. 128, Springer Berlin, pp.61-71, 2009

[7] Jezzine K.and Lhemery A., “Simulation of Guided Wave Inspection Based on the Reciprocity Principle and the Semi-Analytical Finite Element Method,” in Review of Progress in QNDE, 26A, edited by D. O. Thompson and D. E. Chimenti, AIP Conf. Proc. vol. 894, pp. 39-46, American Institute of Physics, Melville, NY (2007)

[8] Lhemery A. Baronian V. Jezzine K. Bonnet-BenDhia A.-S., “Simulation of inspections of elastic waveguides of arbitrary section containing arbitrary local discontinuities or defects,” in Review of Progress in QNDE, 29A, AIP Conf. Proc. vol. 1211, pp. 145-152, American Institute of Physics, Melville, NY (2010)

[9] Lhuillier C. Descombin O. Baqué F. Marchand B. Saillant J.F. Augem J.M., “In sodium tests of ultrasonic transducers”, ANIMMA Int. Conf., Ghent, Belgium, 6-9 June 2011, Paper 3-06

[10] Frost H.M., “Electromagnetic-Ultrasound Transducers: Principles, Practice and Applications”, Physicals Acoustics Vol. XIV, pp 179-275, 1979

Acoustic Waves: A Route to Enhance Sodium Fast Reactor Safety

JPh. Jeannot, F. Baqué, M. Cavaro, O. Gastaldi, C. Lhuillier N. Massacret, J.Moriot, K. Paumel, M. Vanderheagen, G. Rodriguez

CEA, DEN, Cadarache, DTN , Lab. of Instrumentation and Technological Tests, 13108 St Paul lez Durance CEDEX,France

Abstract. The properties of sodium – both thermohydraulic and neutronic – offer a number of advantages when used as a coolant for fourth generation fast reactors. However, the opacity of sodium is a major drawback for the instrumentation. Acoustic waves could be an efficient means to sound this medium. An ultrasonic telemetry instrument called SONAR was used in the Phénix reactor to detect core movement, to check for missing objects and for sub-assembly handling. Acoustic methods were also used in Superphenix and considered for the EFR project as one of the monitoring solutions to detect anomalies. This paper focuses on the efforts made to develop acoustic techniques to meet the system protection and monitoring requirements. It covers various fields: the development of ultrasonic transducers such as the high-temperature ultrasonic transducer (TUSHT) which have recently been re-developed and manufactured, and current research on instrumentation methods using acoustic transducers for ASTRID. This paper discusses the development of acoustic-based instrument techniques as a means to strengthen the primary and secondary sodium system monitoring approach. In the case of TUSHTs, for example, the potential uses are: core monitoring during nominal operation, the detection of core meltdown accident initiators and fuel handling guidance.

1. Introduction

The safety and operating objectives for the SFR technology are even more demanding than for the Generation III reactors. Reliable and high-performance instrumentation is necessary to meet these objectives. The SFR operating constraints rule out the use of standard monitoring means. This led to the development of acoustic techniques which have been proving their worth in meeting the requirements since the 70s. The first section of this paper looks at the feedback that the CEA has accumulated on the development of high-temperature ultrasonic transducers (TUSHT), citing their potential applications where possible.

2. Development of high-temperature ultrasonic transducers

The temperature conditions of an SFR in operation (around 550°C in the hot pool) require developing special ultrasonic sensors. Development started in the middle of the 1970s and produced a high-temperature ultrasonic transducer (TUSHT). Between 1970 and 1980, these sensors were the subject of loop tests which made it possible to qualify its use in static sodium at a temperature around 550°C and under thermal transient conditions (thermal shocks, 550°C-400°C, -20°C/s). Furthermore, additional tests in a furnace were performed at a temperature of 600°C. A test showed that this type of sensor was capable of operating at temperatures around 900°C.

The standard TUSHT that was qualified in sodium and used in a reactor was initially designed to operate in a large frequency range (above 5 MHz) for applications in the primary sodium of a fast reactor and under all operating conditions (emergency shutdown, nominal power and transients).

It contains a piozoelectric element with a single crystal of lithium niobate ($LiNbO_3$ or NL) having an approximate Curie temperature of 1,150°C. The ^6Li in the NL crystal is specially depleted so as to improve its resistance against damage provoked by the flux of neutrons under the operating conditions at nominal power.

The box is composed of AISI 304L stainless steel. The acoustic wave transmission efficiency through the front side of the sensor is ensured by a specific brazing procedure developed by the CEA (in patenting). This brazing makes it possible to achieve transmission stability at high frequency (up to 5 MHz at least) and at high temperature (more than 550°C).

Two types of TUSHT were qualified: TUSHT 4540 (diameter of NL: 40 mm; outer diameter: 55 mm), and TUSHT 4515 (diameter of NL: 15 mm; outer diameter: 32 mm). The front side can have different shapes – flat or concave (spherical or cylindrical) depending on the acoustic wave focalisation. Figure (*FIG. 1*) shows a schematic diagram of a TUSHT 4540.

Error! Objects cannot be created from editing field codes.

FIG. 1. *TUSHT general architecture*

The thickness of the front side of the transducer is chosen so as to meet the 30-year life time requirement for the operating conditions in a reactor at nominal power. The acoustic characteristics of the TUSHT are:

- Frequency response covering a range from 0.7 MHz to 4.5 MHz (FIG. 2)
- Leading edge of the ultrasonic signal around 5 to 15 µs depending on the frequency.

One of the limits of this transducer is the loss of oxygen that occurs in the NL crystal at high temperature in favour of the inner metallic surfaces of the box, which increases its electrical conductivity. This provokes drift in the electrical signal transferred to the electronics progressively rendering the transducer inoperative. To eliminate this problem, the inner part of the box is pre-oxidised and the vent tubes making it possible maintain a partial internal oxygen pressure at a stable level. Other solutions have been tested in the past or are still being investigated.

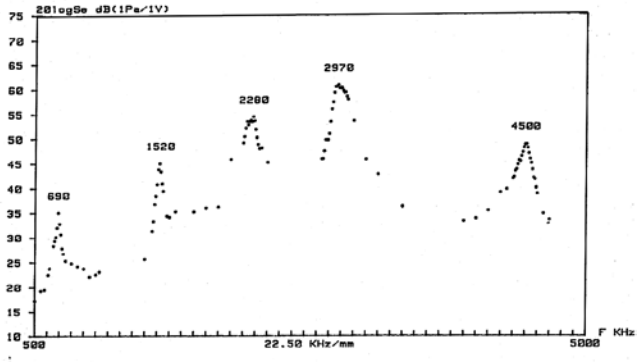

FIG. 2. TUSHT 4540. Sensitivity in emission (dB ref 1Pa/1V, 5 dB/div), Frequency (500 kHz – 5 MHz), in water, room conditions

In 2011, TUSHTs were manufactured once again according to a procedure identical to that of the previous models. The first tests performed in water and in sodium showed satisfactory operation, though these results remain to be confirmed.

3. Ultrasonic Telemetry

The most immediate use for TUSHTs is ultrasonic telemetry for the continuous monitoring of the displacement of parts in sodium. The application in the Phénix reactor involved the use of a sonar rod equipped with 4 TUSHTs with the objective of identifying any movement in the Phénix core sub-assemblies. This movement could have been explained by a scenario that could have provoked 4 trips for negative reactivity which occurred in Phénix in the early 90s.

Figure 3 shows a schematic diagram of the sonar rod. The latter is held by an access latch on the rotating plug on the edge of the core. The two main TUSHTs (C1 and C4) at the end of the rod take aim – with a 45° angle in relation to the vertical plane – at two different sub-assembly head so the time-of-flight of the ultrasounds can be measures (270 mm). A third transducer (C2) is positioned at the bottom the rod, aiming horizontally at the sheath holding the sonar rod, thereby making it possible to correct the effects of rod movement (vibration, expansion, etc.). The last transducer (C3) is aimed directly at the sub-assembly on a vertical plane to the sonar rod. It is used to measure vertical rod movement. Lastly, the rod can be positioned while the reactor is operating by making a manual adjustment on the reactor slab with a vertical displacement over a distance of 46 mm and a rotating angle of ±180° around the vertical axis.

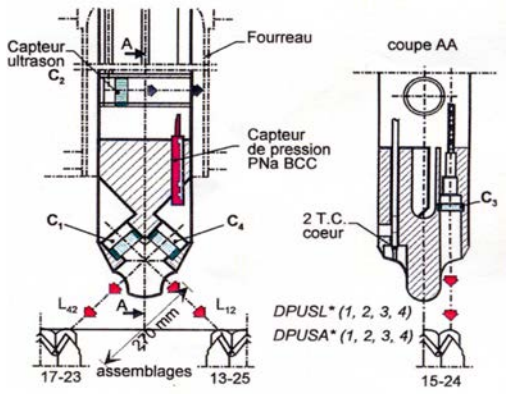

FIG. 3. Sonar rod in Phenix reactor. 17-23, 13-25 and 15-24 are sub-assembly heads. C1, C2, C4 are TUSHTs 4540. C3 is a TUSHT 4515

Concerning the sonar rod, the accuracy of the sub-assembly head displacement measurement depends on the accuracy of the flight-of-time measurement of the acoustic echo. Corrections by the C2 and C3 sensors make it possible to reach an accuracy of several microseconds. Therefore, the performance of the sonar rod have been assessed in Phénix by simulation: a 4 mm displacement of the sub-assembly heads was simulated with its impact on the sonar rod signal. This displacement is clearly visible (FIG. 4). This means that a displacement of 10 mm, which corresponds to that resulting from the scenario studies for negative reactivity trips, would have been observable. Furthermore, the background nose of the displacement measurement was estimated at 0.7 mm when the reactor is operating.

The sonar rod operated in Phénix for 18 years (1991 to 2009) without any signal degradation. However, during the periods of reactor operation following its installation, no negative reactivity shutdowns occurred, which meant that it was not possible to validate the detection of core movement by the sonar rod.

Feedback on this device is sufficiently positive for us to believe that the use of TUSHTs in a sonar rod type system could be used to identify millimetric movement in the sub-assembly heads. This movement could be provoked, for instance, by the flow of a gas bubble in the core which causes the sub-assembly heads to move apart. To improve ultrasonic telemetry for continuous monitoring (particularly in terms of signal stability, amplitude of displacement measurements and accuracy), studies are currently underway on the propagation of ultrasounds in high flow conditions with sodium at 550°C by means of both simulation and testing. To do this, the temperature and velocity maps were

simulated using computational fluid dynamics (CFD) in the design of the ASTRID prototype currently under investigation at the CEA; the next step will involve propagating the acoustic waves in this environment.

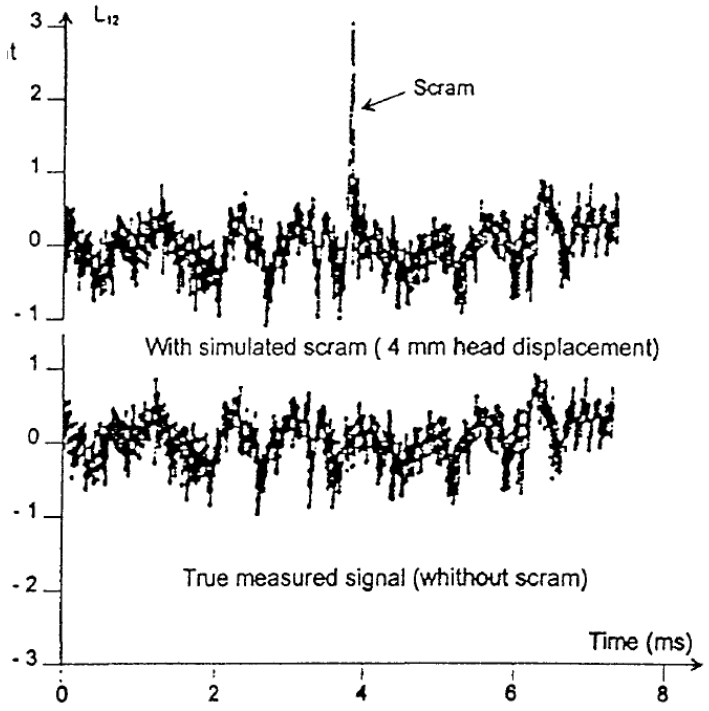

FIG. 4. Impact of a simulated scram (corresponding to 4 mm head displacement) on the SONAR signal

4. Bubble monitoring in a sodium

In the primary vessel of a SFR, the presence of a cover gas in the plenum (generally argon) is responsible for the continuous gassing of sodium in the form of free gas bubbles. Studies conducted for Phénix, Superphénix and the EFR project provide an inventory of the continuous gassing factors, which amount to 7 (FIG. 5), with the main factors being: dissolution and then nucleation (main source resulting from gas dissolution in certain areas of the reactor and particularly at the sodium/cover gas interface), entrainment via the thermal baffle (cascade effect), entrainment by the formation of vortexes, and entrainment by the pump shafts.

The main consequences of these bubbles in the primary sodium are: risk of accumulating gas which can have an impact on the core neutronics (in the case of a high void fraction), and modification of acoustic properties (celerity, attenuation, diffusion, etc.) capable of affect the acoustic-based monitoring means.

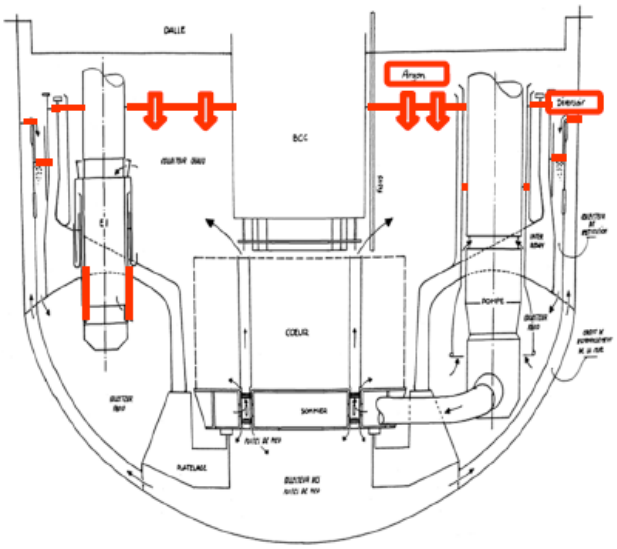

FIG. 5. Location of phenomena responsible for gas in the primary sodium

In 1996, the radioactive decay of ^{41}Ar in the Superphénix gas-cover plenum was measured following a fast shutdown, which was associated with a study on the transport of argon in the primary sodium. This helped to estimate the gas fraction in the cold pool at $2.56.10^{-6}$ with an accuracy of a factor of 2. The bubble size distribution was assessed for several bubble populations in relation to their origin, with bubble sizes ranging between 10 µm to several tens of µm.

The thesis research performed by the CEA between 2007 and 2012 [6] made it possible to develop an acoustic method to characterise the sodium void fraction; the method involves mixing acoustic frequencies to prove bubble resonance (FIG. 6), with the analysis of the non-linear result of the acoustic signal being used to determine the histograms of the micro-bubble radiuses and the void fraction.

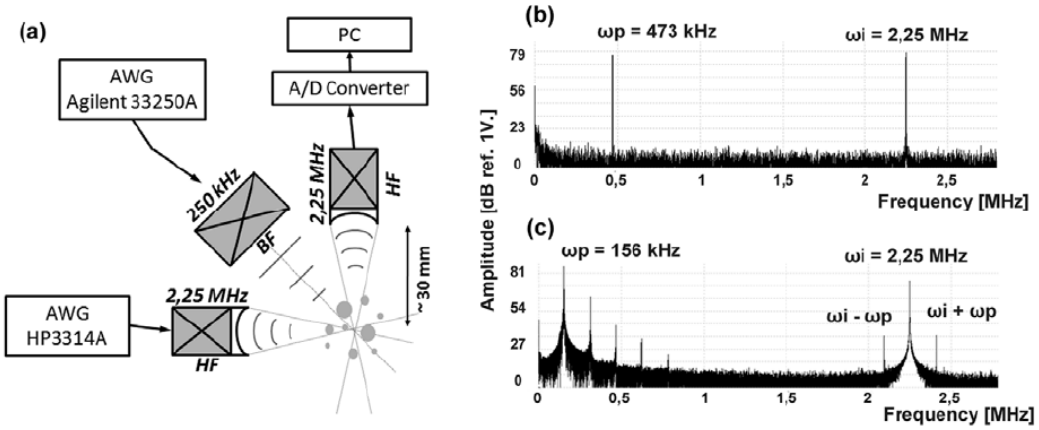

FIG. 6. Schematic diagram and frequency spectrum of mixing frequency techniques

Tests performed in water [6, 7] made it possible to validate the feasibility of the method and to plot a bubble histogram in agreement with that resulting from a reference optical method for a bubble population comparable to that assumed to exist in the reactor (FIG. 7).

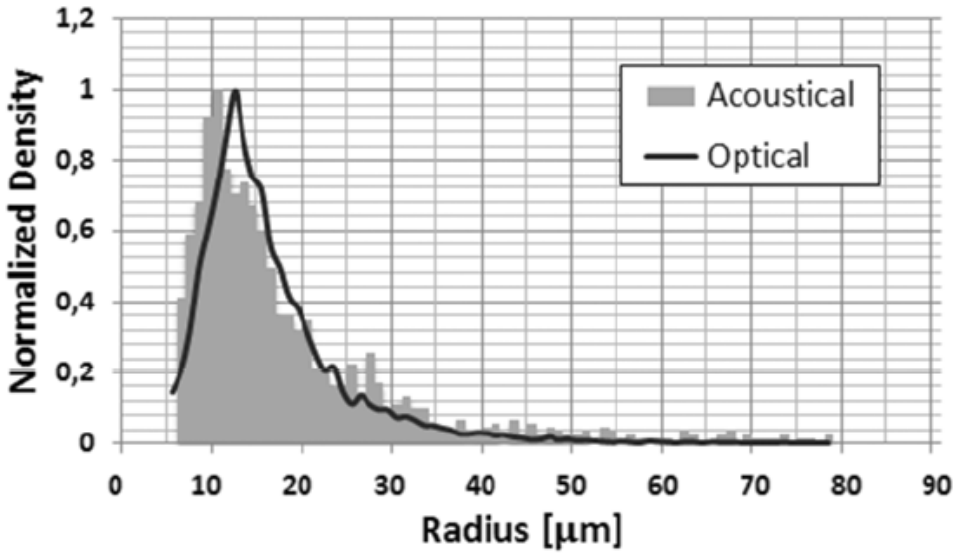

FIG. 7. Comparaison of micro-bubble caracterisation between mixing acoustic frequencies and optical method

Another acoustic technique which is relatively simple but only makes it possible to trace back to the void fraction is called a low-frequency sound velocimeter. This corresponds to the linear acoustics based on Wood's model which associates wave velocity with the gas rates in a two-phase environment, and it is currently the reference option for the ASTRID prototype. Its applicability in sodium is currently being investigated. Its operation in water with acoustic transducers that are compatible with sodium (TUSHT) will be first be validated.

By studying the possibility of using TUSHTs to implement the above-mentioned techniques, it will be possible to determine whether specific transducers need to be developed.

5. Core boiling detection

In the previous sections of this document, the two applications mentioned for acoustic monitoring are based on acoustic interrogation that we have decided to call "active acoustics". With the same type of method, it may be possible to detect ultrasonic beam attenuation (propagated between the outlet of the sub-assemblies and the bottom of the core cover plug) due to the presence of bubbles or pockets of vapour. Various acoustic tests performed in Phénix and Superphénix (depressurising the intermediate heat exchanger bell, injecting gas in the core via a primary pump) helped check the possibility of monitoring the flow of gas in the hot pool by monitoring the attenuation of the acoustic signal of the core acoustic detection. It has not, however, been demonstrated that the gas exiting a single sub-assembly attenuates the acoustic signal.

Implementing an acoustic system based on listening to ‘passive’ noise may also be worth studying. The following detection systems are worth mentioning:

- Local cavitation in the sub-assemblies in the pumps on the core inlet side,
- Abnormal mechanical noise in the main vessel: Migrating objects, rod drop defects, significant vibration of structural elements or mobile components, significant gaps, etc.,
- Checking that the pump-diagrid connection is leaktight during a programmed inspection,
- Sodium boiling during local melting inside the pin bundle or widespread melting of the sub-assembly.

Numerous CEA studies have focused on the last subject, as have many international studies.

The acoustic detection of sodium boiling by acoustic sensors located in the hot pool (or top plenum) requires knowledge on the acoustic source, the acoustic transmission, the reactor's parasitic acoustic background noise, the technology of the acoustic sensors, and optimal acoustic signal processing equipment.

Total instantaneous blockage is characterised by a specific boiling process that involves a fast transient; widespread boiling that lasts about 5 seconds represents the most 'accessible' boiling conditions in terms of detection. The acoustics of sodium boiling can be broken down into several acoustic signature processes. Among these processes, bubble implosion seems to be the major source of acoustic energy.

Experimental results show that conditions producing the most acoustic energy – particularly in the high frequency ranges (above 10 kHz) – are in decreasing order: start of widespread boiling, widespread boiling, local boiling and hot spots. All these conditions emit a broad frequency range; detection is optimal above 20 kHz under the considered experimental conditions [9].

Experiments conducted in the KNK II reactor show that acoustic propagation between the source and the sensors located in the top plenum are mainly liquid-based. Acoustic attenuation appears to be relatively constant but high (35 dB) from several kHz to 40 kHz [10].

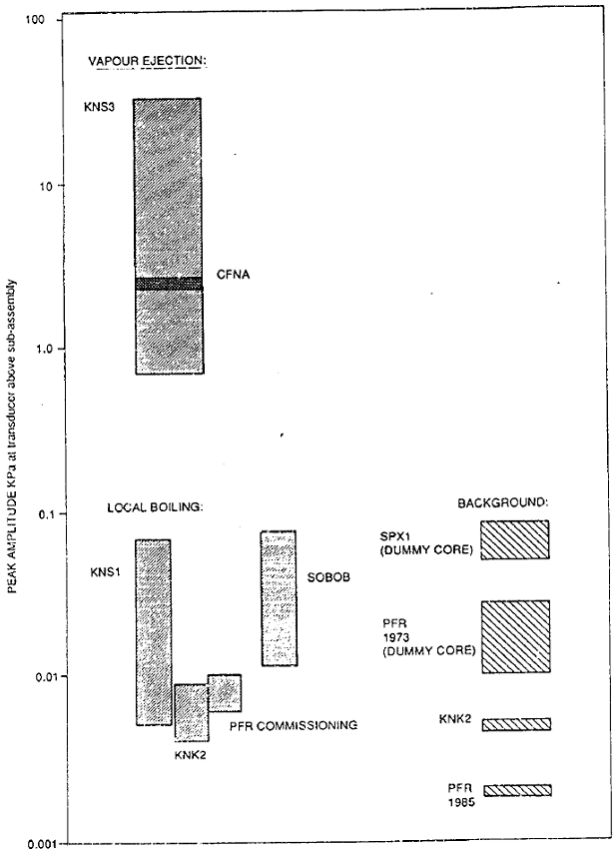

FIG. 8. Comparing the amplitudes of boiling signals and reactor background noise [9]

TUSHTs are considered to be interesting candidates for ensuring the passive acoustic detection of sodium boiling. As mentioned above, they offer a broad bandwidth (several kHz to 10 MHz), small overall dimensions (piezoelectric pellet diameter of 15 mm) and a response curve that reveals resonance though it remains continuous. Since its internal impedance is low, however, its use calls for suitable amplification electronics.

6. Perspectives

Strengthened by its experience in the field of sodium acoustics, the CEA launched three thesis studies in 2010:

- One on the phenomenology of sodium boiling and its acoustic production [11]. Based on an analysis of the vapour bubble dynamics during boiling, as mentioned in section 5, the implosion resulting from the condensation of a bubble in under-saturated sodium is the noisiest phenomenon. The implosion phenomenon is modelled and its similarity with other compounds besides sodium is investigated. Lastly, a test in boiling water is currently being studied.

- One on the feasibility of taking temperature measurements using an acoustic method at the outlet of the sub-assembly heads of the core, with the reactor in service [12]. This research first involved a theoretical study on the impact of thermohydraulic turbulence at the sub-assembly outlet (550°C and sodium velocity of several $m.s^{-1}$) on the propagation of ultrasounds. The second part of this research involves conducting tests - currently being prepared - to validate the models.

- One on acoustic detection of defects or leaks inside a cylindrical fluid loaded shell representing a defect or a leak on the secondary loop or steam generator of Sodium Fast Reactor. The use of the beamforming technique is investigated in this work to detect the position of an acoustic monopole inside a cylindrical elastic shell, from shell vibration measurements. In order to study the effect of the fluid-structure interaction and the distance of the source to the array on the beamforming, a vibro-acoustic model of the fluid loaded shell is considered for numerical experiments. Beamforming technique is then applied to the radial velocities of the shell calculated with the model. Different parameters such as the distance between sensors, the radial source position, and the damping loss factor of the shell and the fluid can be easily considered. Analysing different results allows us to highlight the influence of the fluid loaded shell behaviour on the detection.

The results already obtained on the issues discussed in this document give us an idea of the milestones achieved in the monitoring of certain operating characteristics of a SFR with acoustic methods. The TUSHTs are very good candidates for these different types of monitoring applications. Research is still on-going to optimise these transducers. Furthermore, knowledge of acoustic signatures is an essential stage, which means that phenomenological studies must therefore be developed. Lastly, the qualification of these methods in certain cases, e.g. telemetry or sound velocimetry, must be acquired in order to deploy these methods in the ASTRID prototype. Nonetheless, the latter could be used as a ‘qualification bench’ for the SFR technology, for example, in the case of acoustic monitoring.

REFERENCES

[1] JP. JEANNOT, JPH., and al., R&D Program for Core Instrumentation Improvements Devoted for French Sodium Fast Reactor, Animma Inter. Conf., Ghent, Belgium 6-9 June 2011

[2] JADOT, F., and al., Astrid sodium cooled fast reactor: program for improving in service inspection and repair, Animma Inter. Conf., Ghent, Belgium 6-9 June 2011

[3] LHUILLIER, C., In sodium tests of ultrasonic transducers, Inter. Conf., Ghent, Belgium 6-9 June 2011

[4] BAQUE, F., and al., Development of tools, instrumentation and codes for Improving Periodic Examination and Repair of SFR, Sci. Tech. Nuc. Inst. Journ., July 1, 2012

[5] BERTON, JL., and al., Continuous Monitoring of the position of two subassemblies heads of Phenix at 350 MWth and 550°C, SMORN VII, Avignon, 19-23 June 1995.

[6] CAVARO, M., Contribution of nonlinear acoustic to the characterization of microbubbles clouds in liquid sodium application to the Generation IV nuclear reactors, PhD Thesis, University of Mediterrannea Aix-Maseilles II, Aix-en-provence (2010) (in French).

[7] CAVARO, M., and al., Microbubbles cloud characterisation by nonlinear *frequency mixing*, J. Acoust. Soc.Am., Express Letters, 129(5), EL179-EL183, Mai 2011
[8] CAVARO, M., and al., Towards In-service Acoustic Characterization of Gaseous Microbubbles Applied to Liquid Sodium, Inter. Conf., Ghent, Belgium 6-9 June 2011
[9] LENNOX, T., and al., Application of acoustic instrumentation for use in liquid metal fast breeder reactors, Nucl. Energy, 32, No. 1, Feb. 29-40, 1993
[10] ABERLE, J., and al., Acoustic Measurements for Boiling Detection at KNK II, Experimental and Thermal Fluid Science, 4, 152-165, 1991.
[11] VANDERHAEGEN, M., and al., R&D, Program for French Sodium Fast Reactor: on the description and detection of sodium boiling phenomena during sub-assembly blockages, Animma Inter. Conf., Ghent, Belgium 6-9 June 2011
[12] MASSACRET, N., and al., Simplified modeling of liquid sodium medium with temperature and velocity gradient from thermohydraulic. Application to ultrasonic thermometry in Sodium Fast Reactor., QNDE, Denvers, Colorado, USA 15-20 July 2012
[13] MORIOT, J., and al., Use of beamforming for detecting an acoustic source inside a cylindrical shell filled with a heavy fluid., Mechanical Systems and signal processing, on going review process

Hydrodynamic stability analysis method of once-through sodium-heated steam generator with double-walled straight tube

Makoto Mito[a], N. Kisohara[b], Y. Yamada[a], K. Dozaki[c]

[a] Reactor plant design department,
Mitsubishi FBR System, Inc.,
Tokyo, Japan

[b] Advanced Nuclear System Research & Development Directorate,
Japan Atomic Energy Agency,
Ibaraki pref., Japan

[c] Research & Development department,
Japan Atomic Power Company,
Tokyo, Japan

Abstract. Since the once-through sodium-heated steam generator with double-walled straight tube (DWT-SG) adopted for Japan Sodium-cooled Fast Reactor (JSFR) has very thick tube wall due to high steam pressure of 19.2 MPa and high temperature of 497 degree-C, close attention should be paid to tube modeling from the perspective of hydrodynamic stability. This paper presents the methodology of DACS-DALMA computer code with a discussion on experimental verification. The DACS-DALMA computer code developed by MFBR and MHI is thermal hydraulic software intended for use as a design tool of a sodium-heated steam generator (SG) of a Fast Reactor. The DACS program (Design and analysis code for static thermal/hydraulic characteristics of sodium-heated SG) calculates the performance of sodium-heated SGs for steady state conditions and the DALMA program (Dynamic analysis estimating two-phase flow instability) evaluates the flow stability of SGs. The DALMA program solves the linearized partial differential conservation equations using Laplace transformation of the temporal terms and integration of the spatial variations. It employs frequency response techniques to develop the system transfer function. Stability criteria used in control system theory, Nyquist locus and D-partition locus, are then applied to determine flow oscillation inception. The DALMA program considers heating of the sodium fluid and the multi-lumped tube wall model for thick double-walled tube, specifying the pressure loss coefficient of the inlet orifice using the D-partition method and reliably predicting the inception conditions of dynamic instabilities. The experimental data of a 1 MW DWT-SG conducted by JAEA are in good agreement with the estimation by the DACS-DALMA computer code of the sodium temperature distribution along the SG and the inception conditions of dynamic instabilities.

1. INTRODUCTION

Dynamic instabilities are hazardous for a sodium-heated steam generator (SG), which is a crucial component of a Fast Reactor, since they induce flow maldistribution among the tubes or in the tubes, and thermal cyclings at the welds, at the upper tube plate and at the dryout location. The DACS-DALMA computer code developed by Mitsubishi is thermal hydraulic software intended for use as a design tool of a sodium-heated steam generator (SG) of a Fast Reactor. The DACS program (Design and analysis code for static thermal/hydraulic characteristics of sodium-heated SG) calculates the performance of sodium-heated SGs for steady state conditions and the DALMA program [1] (Dynamic analysis estimating two-phase flow instability) predicts the inception conditions of dynamic instabilities of the SG. It has been under development since 1974 for stability analysis of the Monju evaporator with helical-coiled tubes and downcomers and the No.1 Demonstration Fast Breeder Reactor (DFBR) SG. It has been qualified using a large number of

hydrodynamic stability tests on JAEA's design of 2 1/4 Cr-1 Mo SGs of 1 MW and 50 MW [2], and JAPC's design of Mod.9 Cr-1 Mo SGs of 0.5 MW and 1 MW, which are all helical-coiled and comparatively thin-walled tube type SGs.

The once-through sodium-heated steam generator with double-walled straight tube (DWT-SG) is adopted for Japan Sodium-cooled Fast Reactor (JSFR) of the Fast Reactor Cycle Technology Development Project (FaCT Project) because of high safety, no tube-to-tube welding and easier tube inspection while maintaining a competitive advantage of manufacture and economics as a large power unit. Since DWT-SG's base-line specifications are high steam pressure of 19.2 MPa and high temperature of 497 degree-C using steam with a high degree of superheating, the tube wall becomes very thick. The purpose of developing the DACS-DALMA computer code is to meet sodium-heated SG designers' demands, such as adopting thick double-walled tubes, specifying the pressure loss coefficient of the inlet orifice, employing various heat transfer coefficients and reliably predicting instabilities. This paper presents the methodology of the DACS-DALMA computer code and its verification using the flow stability tests for a 1MW DWT-SG [3] conducted by JAEA.

2. DACS PROGRAM

2.1. Outline

Before dynamic stability analysis, DACS is used to calculate the SG internal profile with sodium temperature, water-steam enthalpy, pressure and quality. There are two differences between helical-coiled tube and double-walled straight tube type SGs. First, the DWT-SG's wall consists of the inner and outer tubes and should consider the thermal resistance between them. Second, the DWT-SG adopts the film coefficient of heat transfer, which needs iteration to fix the film temperature. DACS comes complete with convenient options that satisfy the designer's needs.

2.2. DACS modeling

2.2.1. Water-steam and sodium fluid conservation equations

DACS solves conservation equations of mass, energy and momentum according to traditional procedures. It employs the Runge-Kutta-Merson method that is intended to improve precision by automatic control of the mesh length for the case of a discontinuous function.

2.2.2. Subsidiary equations

An overall heat transfer coefficient is defined as follows:

$$U = \frac{1}{\frac{1}{h_{NA}} + \frac{D_O}{2\lambda_t}\ell n\frac{D_O}{D_i} + \frac{D_O}{D_i}\left(\frac{1}{h_w} + \frac{1}{h_F}\right) + \frac{D_O}{D_{GAP}}\frac{1}{h_{\mathrm{GAP}}}} \tag{1}$$

where

U,	overall heat transfer coefficient at the outside surface of outer tube.
h_{NA},	heat transfer coefficient of sodium fluid.
h_w,	heat transfer coefficient of water-steam.
h_F,	equivalent heat transfer coefficient of inner wall fouling characteristic.
h_{GAP},	equivalent heat transfer coefficient of gap between inner and outer tubes.
λt,	thermal conductivity of tube.
Do,	outside diameter of outer tube.
Di,	inside diameter of inner tube.
D_{GAP},	outer diameter of inner tube.

The thermal conductivity of inner and outer tubes is supposed to be constant in the radial direction. The thermal resistance of the gap between inner and outer tubes is included as the equivalent heat transfer coefficient. Subcooled boiling is evaluated in the program. Two-phase pressure drop values are calculated using the Martinelli-Nelson two-phase friction factor (φ^2) and the friction coefficient is evaluated by means of Colebrook's formula.

3. DALMA PROGRAM

3.1. Outline

The DALMA program solves the linearized partial differential conservation equations using Laplace transformation of the temporal terms and integration of the spatial variations and has to use matrix equations due to countercurrent heat exchanger. It employs frequency response techniques to develop the system transfer function. Stability criteria used in control system theory, Nyquist locus and D-partition method [4][5][6], are then applied to determine inception of dynamic instabilities. The DALMA program features include considering heating of the sodium fluid and the multi-lumped tube wall model for thick double-walled tube, specifying the pressure loss coefficient of the inlet orifice using the D-partition method and reliably predicting the inception conditions of dynamic instabilities.

3.2. DWT-SG modeling

3.2.1. Conservation equations

3.2.1.1. Water-steam fluid

(a) Boiling region

The basic assumption is made that the fluid over any cross section of the tube is homogeneous, though the liquid and vapor phases in the boiling region may be moving at different velocities. According to A.B. Jones' derivation [7][8][9][10], variables indicated by a subscript wE as the boiling region, are normalized as follows:

$$\psi_{wE}(z,t) = \frac{P_{wE} \cdot g_c}{\rho_{wEf} \cdot L \cdot g} \tag{2}$$

$$y_{wE}(z,t) = \frac{W_{wE}}{W_{wE0}} \tag{3}$$

$$\beta(z,t) = \frac{A_{wEg}}{A_{wE}} \tag{4}$$

where

P_{wE},	static pressure.
g,	acceleration due to gravity.
gc,	mass acceleration/force conversion factor.
L,	tube length.
ρ_{wEf},	density of saturated liquid.
W_{wE},	water-steam mass flow rate.
W_{wE0},	water-steam mass flow rate in steady state.
A_{wE},	tube cross sectional area.
A_{wEg},	tube cross sectional area containing vapor in boiling region.

Normalized forms of mass, energy, momentum equations become as follows [7][8][9][10]:

$$\frac{\partial \beta}{\partial t} = \frac{u_{wE0}}{\eta} \cdot \frac{\partial y_{wE}}{\partial z} \tag{5}$$

$$\frac{\partial \left(y_{wE} \cdot \nu^{*} \right)}{\partial z} = \frac{\eta \cdot \varphi_{wE}}{(1-\eta) h_{wEfg} \cdot W_{wE0}} \tag{6}$$

$$-L \cdot \frac{\partial \psi_{wE}}{\partial z} = \cdot \frac{u_{wE0}}{g} \cdot \frac{\partial y_{wE}}{\partial t} + \frac{u_{wE0}^{2}}{g} \cdot \frac{\partial \left(B \cdot y_{wE}^{2} \right)}{\partial z} + F_{wE0} \cdot y_{wE}^{2-awE2} \varphi^{2} \Omega + (1 - \eta \cdot \beta) \cos\theta \tag{7}$$

where

$$\eta = 1 - \frac{\rho_{wEg}}{\rho_{wEf}} \tag{8}$$

$$u_{wE0} = \frac{W_{wE0}}{\rho_{wEf} \cdot A_{wE}} \tag{9}$$

$$\gamma = \frac{u_{wEg}}{u_{wEl}} \tag{10}$$

$$\nu^{*} = 1 - \xi + \frac{\eta}{1-\eta} \cdot X \tag{11}$$

$$\xi = \frac{P \cdot v_{wEg} \cdot g_{c}}{A \cdot h_{wEfg} \cdot g} \tag{12}$$

$$B = \frac{1 - \beta \left(1 - \gamma^{2} (1 - \eta) \right)}{\left[1 - \beta \left(1 - \gamma (1 - \eta) \right) \right]^{2}} \tag{13}$$

$$F_{wE0} = \frac{f_{wE0} \cdot u_{wE0}^{2}}{2 g D_{e}} \tag{14}$$

$$f_{wE0} = a_{wE1} (\mathrm{Re})_{0}^{-awE2} \tag{15}$$

ρ_{wEg}, density of saturated vapor.
u_{wEg}, vapor velocity in boiling region.
u_{wEl}, liquid velocity in boiling region.
φ_{wE}, heat input rate per unit length.
h_{wEfg}, heat of vaporization.
X, steam quality.
v_{wEg}, specific volume of saturated vapor.
A, mechanical equivalent of heat.
De, tube hydraulic diameter.
Re, Reynolds number.
a_{wE1}, friction coefficient in equation (15).
awE2, friction coefficient in equation (15).
φ^{2}, Martinelli-Nelson two-phase friction factor.
Ω, modified parameter to Martinelli-Nelson friction factor.
θ, tube inclination angle from vertical.

(b) Superheated region

The basic assumption is made that the fluid in the tube is single-phase and variable density, though sonic propagation of pressure waves (acoustic effects) are not considered. According to L. E. Efferding's derivation [11], variables indicated by a subscript wG as the superheated region, are normalized as follows:

$$\psi_{wG}(z,t) = \frac{P_{wG} \cdot g_c}{\rho_{wGf} \cdot L \cdot g} \tag{16}$$

$$y_{wG}(z,t) = \frac{W_{wG}}{W_{wG0}} \tag{17}$$

$$\sigma_{wG}(z,t) = \frac{\rho_{wG}}{\rho_{wGf}} \tag{18}$$

Normalized forms of mass, energy, momentum equations become as follows [11]:

$$\rho_{wGf} \cdot \frac{\partial \sigma_{wG}}{\partial t} + \frac{W_{wG0}}{A_{wG}} \cdot \frac{\partial y_{wG}}{\partial z} = 0 \tag{19}$$

$$A_{wG}\rho_{wGf} \cdot \sigma_{wG} \frac{\partial H_{wG}}{\partial t} + W_{wG0} y_{wG} \frac{\partial H_{wG}}{\partial z} = \varphi_{wG} \tag{20}$$

$$-L \cdot \frac{\partial \psi_{wG}}{\partial z} = \frac{u_{wG0}}{g} \cdot \frac{\partial y_{wG}}{\partial t} + \frac{u_{wG0}^2}{g} \cdot \frac{\partial}{\partial z}\left(\frac{y_{wG}^2}{\sigma_{wG}}\right) + F_{wG0} \cdot \frac{y_{wG}^{2-awG4}}{\sigma_{wG}} + \sigma_{wG}\cos\theta \tag{21}$$

where

$$F_{wG0} = \frac{f_{wG0} \cdot u_{wG0}^2}{2gD_e} \tag{22}$$

$$f_{wG0} = a_{wG3}(\mathrm{Re})_0^{-awG4} \tag{23}$$

ρ_{wGf}, density of satulated liquid.
ρ_{wG}, density of superheated steam.
H_{wG}, enthalpy of superheated steam.

(c) Subcooled region

The basic assumption is made that the fluid in the tube is single-phase and variable density even though the degree of temperature difference is small in the subcooled non boiling region. Similar to the super-heated region, variables indicated by a subscript wD as the no boiling region, are normalized as follows:

$$\psi_{wD}(z,t) = \frac{P_{wD} \cdot g_c}{\rho_{wDf} \cdot L \cdot g} \tag{24}$$

$$y_{wD}(z,t) = \frac{W_{wD}}{W_{wD0}} \tag{25}$$

$$\sigma_{wD}(z,t) = \frac{\rho_{wD}}{\rho_{wDf}} \tag{26}$$

Normalized forms of mass, energy, momentum equations become as follows:

$$\rho_{wDf} \cdot \frac{\partial \sigma_{wD}}{\partial t} + \frac{W_{wD0}}{A_{wD}} \cdot \frac{\partial y_{wD}}{\partial z} = 0 \tag{27}$$

$$A_{wD}\rho_{wDf} \cdot \sigma_{wD} \frac{\partial H_{wD}}{\partial t} + W_{wD0} y_{wD} \frac{\partial H_{wD}}{\partial z} = \varphi_{wD} \tag{28}$$

$$-L\cdot\frac{\partial\psi_{wD}}{\partial z}=\frac{u_{wD0}}{g}\cdot\frac{\partial y_{wD}}{\partial t}+\frac{u_{wD0}^2}{g}\cdot\frac{\partial}{\partial z}\left(\frac{y_{wD}^2}{\sigma_{wD}}\right)+F_{wD0}\cdot\frac{y_{wD}^{2-awD4}}{\sigma_{wD}}+\sigma_{wD}\cos\theta \tag{29}$$

where

$$F_{wD0}=\frac{f_{wD0}\cdot u_{wD0}^2}{2gD_e} \tag{30}$$

$$f_{wD0}=a_{wD3}(\mathrm{Re})_0^{-awD4} \tag{31}$$

ρ_{wD}, density of subcooled water.
H_{wD}, enthalpy of subcooled water.

The subcooled boiling under the negative quality is included considering both convection flow and boiling.

3.2.1.2. Sodium fluid

The basic assumption is made that the sodium fluid is single-phase and variable density even though the degree of temperature difference is small. Similar to the subcooled non boiling region, variables indicated by a subscript N as the sodium region, are normalized as follows:

$$y_N(z,t)=\frac{W_N}{W_{N0}} \tag{32}$$

$$\sigma_N(z,t)=\frac{\rho_N}{\rho_{Nr}} \tag{33}$$

Normalized forms of mass, energy equations become as follows :

$$\rho_{Nr}\cdot\frac{\partial\sigma_N}{\partial t}+\frac{W_{N0}}{A_N}\cdot\frac{\partial y_N}{\partial z}=0 \tag{34}$$

$$A_N\rho_N N_N\cdot\sigma_N\frac{\partial H_N}{\partial t}+W_{N0}y_N\frac{\partial H_N}{\partial z}=\varphi_N \tag{35}$$

ρ_{Nr}, representative density of sodium.
H_N, enthalpy of sodium.
φ_N, heat input rate per unit length.

Though the mass and energy equations of sodium have to be solved together with water-steam and tube side equations, the momentum equation of sodium is not solved together with them due to no limiting boundary conditions and is calculated just for pressure loss after solving the energy equation.

3.2.1.3. Tube thermal conduction and fluid heat transfer model

A single-walled tube is about 2.4 mm thick of 11.2 mm I.D. at a pressure of 20 MPa, while a double-walled tube will be about twice as thick, 4.6 mm under the same conditions. Therefore close attention should be paid to tube modeling from the perspective of hydrodynamic stability. Efferding's single-lumped tube wall model [11] is extended to a multi-lumped tube wall model, which could be divided into 20 nodes at most. Figure 1 shows the model and also visualizes the temperature profile. The correlation equations of energy become as follows:

$$\varphi_N=h'_{NA}\cdot\pi D_{t2}\cdot(T_N-T_{t2}) \tag{36}$$

$$\varphi_N = \varphi_{GAP} + \rho_t A_{t2} C_{pt} \cdot \frac{\partial T_{t2}}{\partial t} \tag{37}$$

$$\varphi_{GAP} = h'_{GAP} \cdot \pi D_{GAP} \cdot (T_{t2} - T_{t1}) \tag{38}$$

$$\varphi_{GAP} = \varphi_w + \rho_t A_{t1} C_{pt} \cdot \frac{\partial T_{t1}}{\partial t} \tag{39}$$

$$\varphi_w = h'_w \cdot \pi D_{t1} \cdot (T_{t1} - T_w) \tag{40}$$

where

$$h'_{NA} = \frac{1}{\frac{D_{t2}}{D_O} \cdot \frac{1}{h_{NA}} + \frac{D_{t2}}{2\lambda_t} \cdot \ln\left(\frac{D_O}{D_{t2}}\right)} \tag{41}$$

$$h'_{GAP} = \frac{1}{\frac{1}{h_{GAP}} + \frac{D_{GAP}}{2\lambda_t} \cdot \ln\left(\frac{D_{t2}}{D_{GAP}}\right) + \frac{D_{GAP}}{2\lambda_t} \cdot \ln\left(\frac{D_{GAP}}{D_{t1}}\right)} \tag{42}$$

$$h'_w = \frac{1}{\frac{D_{t1}}{D_i} \cdot \left(\frac{1}{h_w} + \frac{1}{h_F}\right) + \frac{D_{t1}}{2\lambda_t} \cdot \ln\left(\frac{D_{t1}}{D_i}\right)} \tag{43}$$

φ_{GAP},	heat rate per unit length through GAP interface.
ρ_t,	density of tube.
C_{pt},	specific heat of tube.
D_{t1},	center diameter of inner tube.
D_{t2},	center diameter of outer tube.
A_{t1},	cross sectional area of inner tube.
A_{t2},	cross sectional area of outer tube.
T_N,	temperature of sodium.
T_w,	temperature of water-steam.
T_{t1},	mean temperature of inner tube.
T_{t2},	mean temperature of outer tube.

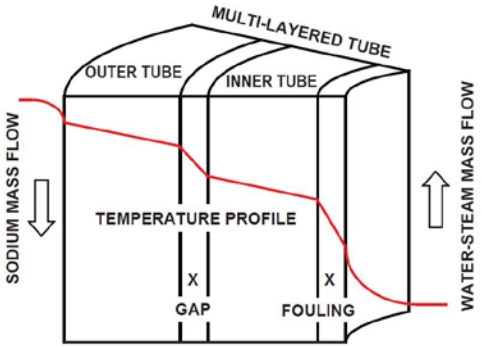

FIG. 1. Modeling of inner and outer tubes.

Since perturbation of the heat transfer coefficient depends on its pattern of equation (e.g. including Reynolds number or not, the number of index, etc.), the analytical procedure should be different for each heat transfer coefficient.

3.2.2. Boundary condition

The coupling equations of the inlet part, outlet part and the boundary between each region are derived and programmed.

3.2.3. Transfer function

The following is an open loop transfer function of the feedback system. The conventional Nyquist criterion can then be used to determine whether the specified system is stable or unstable.

$$1 + GH = 0 \tag{44}$$

According to Nakanishi [4] applying Yu.I. Neimark D-partition method [5][6] to the density-wave oscillation, a characteristic equation of a pressure loss coefficient K_{in} of inlet orifice becomes:

$$1 + GH + K_{in} \cdot \frac{u_{wD0}^2}{gL} \cdot \frac{\rho_{wDf}}{\rho_{wD0}} \cdot \overline{\delta y}_{wDin} = 0 \tag{45}$$

where

$$u_{wD0} = \frac{W_{wD0}}{\rho_{wDf} \cdot A_{wD}} \tag{46}$$

GH, open loop transfer function.

$\overline{\delta y}_{wDin}$, calculated perturbation of inlet water mass flow after Laplace transformation.

ρ_{wDf}, density of satulated liquid.

ρ_{wD0}, density of subcooled water.

If K_{in} of equation (45) is mapped onto the complex plane, a specified K_{in} value is predicted from the x-intercept. If the K_{in} value is positive, the system would be unstable and become stabilized with an inlet orifice of pressure loss coefficient of 33, as shown in FIG. 2.

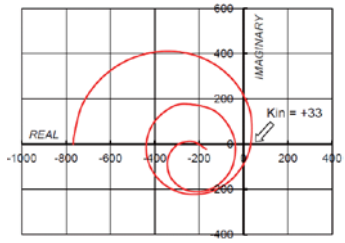

FIG. 2. Predicting a degree of dynamic instability by the D-partition method.

4. DWT-SG STABILITY TEST

4.1. Outline

Steady state thermal-hydraulic performance tests, Departure from Nucleate Boiling (DNB) tests, and dynamic stability tests [3] were performed using the 1 MW DWT-SG in the sodium test facility of the JAEA O-arai Research and Development Center shown in FIG. 3. The water-steam flows vertically upward in 10 tubes of 11.4 mm I.D. and 19 mm O.D., and is heated by sodium flowing downward around the tubes arranged inside a hexagonal cylindrical shell in an equi-triangular pattern of 36 mm pitch. The heated tube length is approximately 18 m and the total tube length between the tube plates is 20.6 m. The SG was manufactured from Mod.9 Cr-1 Mo ferritic steel. Best promising heat transfer coefficient equations derived by JAEA are adopted for estimation of the SG performance compared with experimental data. Figure 4 shows the calculated values with solid lines, and the measured values with points. The sharp inflection of the temperature profile caused by dryout phenomena was measured on the sodium side in good agreement with estimation.

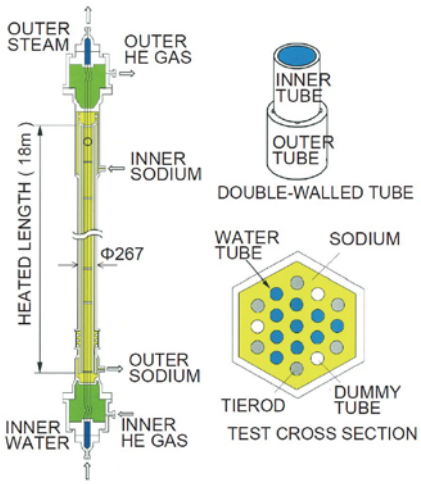

FIG. 3. 1 MW DWT-SG test model [3].

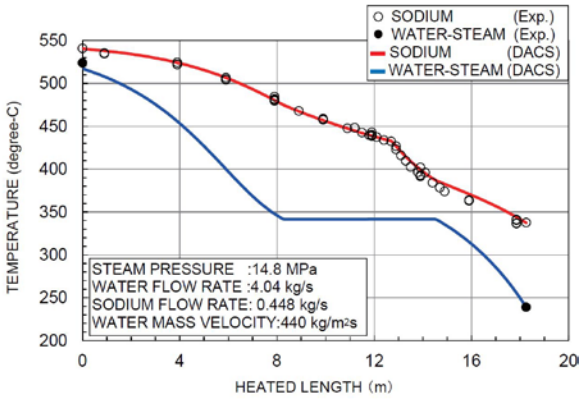

FIG. 4. Calculated and measured sodium temperature profile in steady state condition [3].

4.2. Flow stability test and prediction

Eighty-six dynamic stability tests were performed over a range of steam outlet pressure from 10 MPa through 15 MPa, a range of water mass flow from 120 to 730 kg/m^{2}s and a range of pressure loss coefficient of inlet orifice of 120 to 400, while the sodium inlet temperature was between 460 and 540 degree-C. The test procedure for the stability experiments was the following : starting from stable operational conditions the sodium flow rate was changed in small increments, while the total water mass flow, the sodium-inlet temperature, water-inlet temperature and steam-outlet pressure were kept constant. Figure 5 shows a typical example of density-wave oscillations. From the left to the right

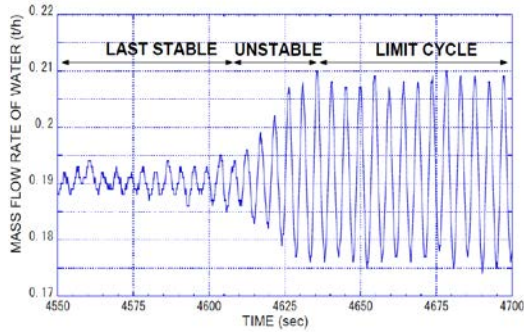

FIG. 5. Typical example of density-wave oscillations[3].

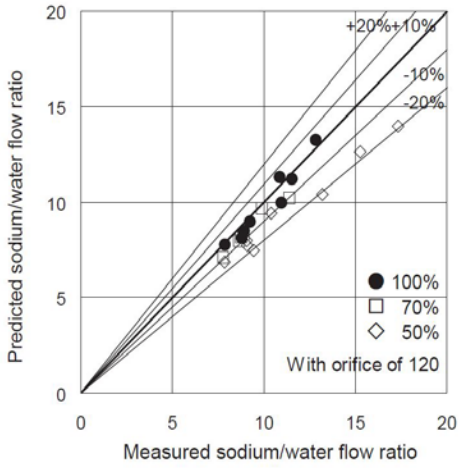

FIG. 6. Predicted and measured sodium/water mass flow ratio for inception of dynamic instability.

side, water-flowrates show the last stable, unstable and limit cycle. The process conditions of the last stable cycle just before the limit cycle oscillation are defined as the inception conditions of dynamic instabilities. The instabilities are evaluated by using the sodium/water mass flow ratios at their inceptions. Predicted and measured sodium/water mass flow ratios for inceptions of dynamic instabilities at the SG load of 100%, 70% and 50% are shown in FIG. 6. The experimental data were well accounted for by the DALMA program.

5. CONCLUSIONS

Responding to the JSFR-SG design needs, the DACS-DALMA computer code has been improved by considering iteration for decision of film temperature, subcooled boiling, the multi-lumped tube wall model for thick double-walled tube and the D-partition method for specifying the pressure loss coefficient of the inlet orifice. The instability test data of JAEA 1 MW DWT-SG were used for code verification, and the study confirms that the DALMA program predicts the inception conditions of dynamic instabilities of the sodium-heated SG. The details on the test data and the code verification will be presented shortly. The next step will be investigating the predicted and measured data under the same high pressure conditions of 20MPa as JSFR and evaluating design correlation equations. The Advanced Technology Experiment Sodium (Na) Facility (AtheNa) is planned to run dynamic stability tests in the near future.

ACKNOWLEDGEMENTS

We are very grateful to the members of JAEA, JAPC, MFBR and MHI for cooperation in this work. The DACS-DALMA computer code was developed by MFBR and MHI, stability tests were performed by JAEA and the verification study was conducted under the entrustment of the Japan Atomic Power Company (the representative of 9 electric utilities, Electric Power Development Co., Ltd. and JAPC).

REFERENCES

[1] M. MITO, S. OISHI, M. MIYAJIMA, M. HANAWA, Development of DALMA program for predicting the inception of dynamic instability taking into account sodium fluid in the sodium-heated steam generator , MAPI, AESJ annual report, No.1, pp.38, April, 1976.

[2] J. KUBOTA, T. TSUCHIYA et al., Hydrodynamic stability tests and analytical model development for once-through sodium heated steam generator, BNES, London, 1979.

[3] N. KISOHARA, S. NAKAI, H. SATO, T. YATABE, Evaluation of Hydrodynamic Instability Tests in 1 MWt Double-Wall-Tube Steam Generator, JAEA, AESJ annual report, No.2, pp.328, September, 1998.

[4] S. YAMAUCHI, S. NAKANISHI, S. ISHIGAI, Parametric study of density-wave oscillations in two-phase flow by means of D-partition method, Takamatsu Technical High School, No.16(1980), pp.47-57, March, 1981.

[5] М.А. АИЗЕРМАН, Теория автоматического регулирования, Наука, 141-223, 1966.

[6] A.A. FELJDBAUM, A.G. BUTKOVSKII, Metody teorii avtomaticheskogo upravleniya, Vol.6, pp.177-188, 1971.

[7] A.B. JONES, Hydrodynamic Stability of a Boiling Channel, KAPL-2170, October, 1961.

[8] A.B. JONES, and D.G. DIGHT, Hydrodynamic Stability of a Boiling Channel, Part 2, KAPL-2208, April, 1962.

[9] A.B. JONES, and D.G. DIGHT, Hydrodynamic Stability of a Boiling Channel, Part 3, KAPL-2290, June, 1963.

[10] A.B. JONES, Hydrodynamic Stability of a Boiling Channel, Part 4, KAPL-3070, August, 1964.

[11] L.E. EFFERDING, A Digital Computer Program for Study of the Dynamic Stability of Once-through Boiling Flow with Steam Superheat, GAMD-8656, June, 1968.

[12] J.R.S. TOM, W.M. WALKER, T.A. FALLON et al., Boiling in sub-cooled water during flow up heated tubes or annuli, Proc. Instn. Mech. Engrs. Vol. 180, Pt. 3C, pp.226, 1965-66.

[13] А.С. КОНЬКОВ, Experimental study of the conditions under which heat exchange deteriorates when a steam-water mixture flows in heated tubes, Thermal Engineers. Vol. 13, pp. 72-82, 1966.

Guidelines of elevated temperature structural design methods to realize compact reactor vessels

Naoto KASAHARA[a], Kazuyuki TSUKIMORI[b] and Kenichiro SATO[c], Nobuchika KAWASAKI[c]

[a] The University of Tokyo, Tokyo, Japan,

[b] Japan Atomic Energy Agency (JAEA), Ibaraki, Japan

[c] Mitsubishi FBR Systems, Inc.(MFBR), Tokyo, Japan

Abstract. Main loadings of reactor vessels in fast reactor plants are thermal stresses induced by fluid temperature change at transient operation. Structures respond to them with elastic plastic creep deformation under high temperature conditions. It can induce incremental deformation and creep fatigue crack at critical portions around the sodium surface, thermal stratification layer and core support structures. Those phenomena are so complex that design evaluation becomes sometimes too conservative. In order to achieve precise high temperature design for realizing compact reactor vessels of fast reactor plants, next guidelines were proposed for thermal load modeling, structural analysis and strength evaluation. This paper gives the summary of these guidelines.

GUIDELINES FOR THERMAL LOAD MODELING - Thermal hydraulic - structure total analysis with experimental design

GUIDELINES FOR INELASTIC DESIGN ANALYSIS - Design evaluation method based on recommended inelastic analysis

HIGH TEMPERATURE STRENGTH EVALUATION METHOD - Strain limit within negligible effects on creep-fatigue strength, Creep-fatigue damage evaluation method considering intermediate stress hold, aging and strain concentration

1. Introduction

In the FaCT(Fast reactor Cycle Technology development) project for realizing the Japanese Sodium Fast Reactor (JSFR) concept, feasibilities of innovative technologies were examined[1]. One of main issues among them is the compact reactor vessels with eliminating the thermal load mitigation devices which are installed inside the vessel (Figure 1).

Thermal loads may cause such failure modes on the reactor vessel as ratcheting deformation and creep-fatigue damage around the liquid sodium surface which moves up and downward cyclically with start-up and shut-down. Buckling is another failure mode of thin shell structure and its main cause is seismic load. To prevent this failure mode, the seismic isolation system is adopted[1]. To realize 60 years life period, longer time creep tests than 100,000 hours and thermal aging tests were achieved. If the existing design code[2] is applied, there is the possibility that the estimation of the strain amount becomes too conservative and exceeds the strain limit of the rule. Therefore new design guidelines were proposed to enable the compact reactor vessel [3] .

Figure 2 shows the expected failure mechanism of reactor vessels in JSFR. Origin of loadings is temperature distribution in vessels during start-up and shutdown. At start-up, the temperature of sodium goes up from 200 degree C to 550 degree C and liquid surface goes up more than 1000 mm, simultaneously. At manual trip, the temperature distribution change is more complicated. The liquid

temperature starts to descend from lower position, but the liquid near the surface cannot follow quickly, whose lead to temperature distribution. Consequently, during the thermal cycle, the maximum stress is generated at the position of the vessel near the liquid surface. Under high temperature condition, it induces elastic-plastic creep deformation. In the design this event is supposed to occur 300 times during the life, and such failure modes are concerned as the ratcheting phenomenon and creep-fatigue damage near the liquid surface, stratified layer and core support.

Elevated temperature structural design procedure has roughly three processes of (thermal) load modeling, structural analysis and strength evaluation. Taking above failure mechanism into account, design guidelines of reactor vessels were proposed for thermal modeling, inelastic analysis and strength evaluation as figure 3. A structural analysis program with new constitutive equations was also developed. These guidelines and programs were validated by the material and structural test database.

2. GUIDELINES FOR THERMAL LOAD MODELING

2.1 Difficulties of thermal load modeling

Sodium fast reactors are operated under low pressure and high temperature conditions. Since heat capacity of liquid metals is small, its temperature changes rapidly at transient operations of plant systems. In addition, because heat transfer coefficient of liquid metal is large, the temperature variation of the coolant efficiently transfers to components and pipes. Consequently large cyclic thermal stress is induced in them. One of typical thermal loads is system thermal transient loads. Origin of loads is temperature variation of coolant during transient operation. Structures respond to it and cause thermal stress by self constraint and stress concentration. Therefore, evaluations of both thermal-hydraulic and structure are required for thermal load modeling.

System thermal transient loads are affected by combination of various kinds of system parameters. Each parameter scatters in some range, and affects system thermal transient loads. For example, figure 4 shows system parameters and their scatter ranges in a sodium cooled reactor. The main difficulty of system thermal transient load modeling is how to envelop lots of influence parameters.

2.2 New thermal transient modeling method with Design of Experiments

For evaluation of thermal stress affected by many influence parameters, a lot of thermal-hydraulic-structure total analysis are required. In order to reduce these numbers within realistic calculation, new thermal transient modeling method with Design of Experiments was developed (Figure 5) [4]. The load is used to calculate the maximum thermal stress, and the structural integrity will then be evaluated by comparing the obtained thermal stress with the allowable stress in a failure mode. The thermal stress depends on plant operation conditions, thermal hydraulics and structure characteristics.

2.3 Validation of the thermal transient load modeling method by Monte Carlo simulation

Probabilistic analyses were conducted to validate the adequacy of the proposed modeling method[5]. An evaluation flow is shown in figure 6. It is firstly required to estimate the contribution to the thermal stress of each influence factor and its levels from the ANOVA program. Secondly, several dispersion patterns of each influence factor are assumed, and a large quantity of level value for an influence factor is generated by a Monte Carlo approach. Hereafter, the thermal stresses against the generated combinations of the influence factors are calculated. Then the distribution of thermal stress is compared with that obtained from the thermal transient load to check the reliability of the modeling method.

The proposed Design of Experiments method was applied to evaluate thermal loads of upper part of the reactor vessel of the JSFR. The maximum thermal stress estimated by the conventional method (multi-linear approximation) was 214.7 MPa and one by the Design of Experiments method was 176.0MPa. The probability density of the thermal stress as a function of the thermal stress for 10,000 combinations of the influence factors was obtained by the Monte Carlo simulation as in figure 7. It can be seen that the thermal stress reveals a normal distribution, and the thermal stress 176.0 MPa obtained from thermal transient load is situated away from the mean value of the normal distribution about 3.5

times of the standard deviation. It means that the proposed Design of Experiments method gives conservative and much rational results

3. GUIDELINES FOR INELASTIC DESIGN ANALYSIS

3.1 Basic policy and scope

One of the major difficulties for design use of inelastic analysis is the lack of definitive constitutive equations for describing elastic-plastic-creep behavior of materials. Furthermore, the detailed constitutive equations that were developed for the purpose of realistic modeling of inelastic behavior of materials can accurately simulate it, only when the material characteristics and load history are known. However, these conditions are not generally known in the design phase, which makes it difficult to place reliance on inelastic analysis. This is another major reason.

The basic policy of this inelastic design analysis method is to provide more rational evaluation results than those obtained by elastic analysis, and conservative ones in regard to design conditions, including essentially uncertain factors . Since inelastic analysis has many influencing factors on the results, it is difficult to maintain general conditions. Therefore, the applicable area of this method is limited by considering the features of materials and loading of reactor vessels in FBR plants. Material is restricted to the 316FR austenitic stainless steel. Loading conditions are limited to the ones with low primary stress typically seen in sodium components of FRs that receive basically displacement-controlled load. Failure modes to be evaluated are ratchet deformation and (creep) fatigue damage.

3.2 Development of new constitutive equations

To represent nonlinear stress-strain relation, the multi-linear kinematic hardening model proposed by Ohno and Wang [6] is employed. This model was extended to allow application to a varying temperature field (MK model)[7].

The, multi-linear Kinematic hardening model with Stress Reversal-on Resetting (figure8) was newly developed by incorporating a hardening reset procedure into the multi-linear kinematic hardening model at every stress reversal event. It is called the MK-SRR model[7]. The basic idea comes from the hardening reset procedure, or α-reset procedure, employed in the improved bilinear kinematic hardening model by ORNL [8].

The two-surface model which can simulate nonlinear stress-strain curves would be an ultimate multi-linear kinematic hardening model (figure 9). A two-surface cyclic plasticity model under isothermal condition was proposed by Iwata [9]. The model is constructed using a yield surface which moves kinematically in the deviatoric stress space, a limit surface which grows in an isotropic fashion whenever the yield surface comes into contact with it, and a plastic hardening modulus function which is defined consistently with fundamental stress-strain characteristic equations under monotonic and cyclic loadings. It is planned that the two-surface cyclic plasticity model will be extended to allow for temperature dependent analysis[10]. It would potentially be positioned closest to the target constitutive model of this project.

3.3 Experiments for verification and validation

For verification and validation, sets of experiments consist of three categories, i.e., uni-axial tests, basic structure element tests, and structure model tests were achieved[10].

The uni-axial tests consist of two series of tests, i.e., material property test and temperature dependency test. The former is used to mainly determine the parameters of constitutive models, and latter is used for basic verification of temperature dependency performance of constitutive models. The basic structure element tests consist of two kinds of simple ratcheting tests, i.e., three bar ratcheting test and bi-axial ratcheting test (figure 10). The former is based on the famous two bar ratcheting theory, while parallel three bar structures are used for symmetry. The latter was proposed considering the results of the preliminary analysis. The axial and circumferential components of stress and strain are dominant and they describe non-proportional hysteresis. In the structure model tests, similar phenomenon as the ratcheting in the reactor vessel is realized. Small cylinders are used as test

specimens and the movement of temperature distribution is generated by heater and water level control (figure 11).

4. High Temperature Strength Evaluation Method

4.1 Expected failure modes and their evaluation methods

Thermal loads may cause such failure modes on the reactor vessel as ratcheting deformation and creep-fatigue damage. When thermal loads become very large to induce both failure modes, they have possibilities to be interacted. From such point of view, criteria were determined within negligible area of their interaction. Load and environmental characteristics of reactor vessels were also taken into account such as loading patterns and thermal transient stress and aging effects during long term operation.

To understand the influence of ratchet on (creep) fatigue life in the operation conditions of FRs, ratcheting-fatigue tests were conducted to examine the influence of ratchet on fatigue strength [11]. In these tests, temperature is 550degree C, the same as operative temperature of hot leg of fast reactors. Furthermore new ratchet creep-fatigue tests were added with 600 degree C 1 hour hold time. The material is 316FR that is candidate for reactor vessels. Strain range is 0.5% or 0.7%, and strain rate is 0.1 %/s. Ratchet strains are valuable from 2% to 5%. They were superimposed on (creep) fatigue tests in the following way. From this results, authors judged that the ratchet strain lower than 2% has no influence on the fatigue and creep-fatigue lifetime when N0=1000. N0=1000 is a conservative condition compared with design conditions where the number of thermal transients is less than several hundreds. As the results, strain limit was determined as 2%. What about aging of welds and weldments?

Considering characteristics of operative conditions of reactor vessels, authors pay attention to such influence factors on creep-fatigue strength, as the intermediate stress holding, aging during 60years operation and strain concentration at structural discontinuities. To clarify creep damage by intermediate stress holding, creep-fatigue tests with various kinds of stress holding position were conducted [12]. For considering aging effects, accelerated aging tests which are corresponding to (How reliable is it?)200,000hours and 500,000hours operation were achieved. After that, strength and stress-strain behaviors were measured and were compared with initial data. There were no difference and aging effects in the most of data except fracture toughness[12]. Strain concentration has impact on creep-fatigue strength and their precise evaluation methods are needed. For evaluation of creep-fatigue damages of high temperature components, conventional design rules adopts simplified inelastic analysis methods with a help of conservative strain concentration factors, and their rationalization is required from an economical reason. By utilizing an existence of a unique stress redistribution locus (SRL) , a simplified inelastic analysis method based on SRLs was proposed to evaluate strain concentration[13].

4.2 Validation of strength evaluation methods by reactor vessel models

To validate above strength evaluation method, thermal transient strength tests were conducted on the reactor vessel model (Figure 13)[14]. Electric heater and water cooling system enforced cyclic thermal loads on the cylindrical models made of 316FR without holding tome (fatigue test) and with holding time (creep-fatigue test). After thousands of thermal cycles, cracks were observed on the surfaces as figure 13.

Measured crack initiation cycles and penetration cycles were compared with predictions. In figure 14, circular symbols are fatigue test results. Triangular and diamond symbols are creep fatigue tests. Their failure cycle numbers are measurements. On the other hand, strain ranges are predictions by analysis. Brank symbols mean prediction by elastic analysis. Painted symbols denote predictions by inelastic analysis. The black line is an average fatigue curve from material tests. The red one is a creep fatigue curve. These results showed that inelastic analysis can adequately predict crack initiation cycles for both fatigue and creep fatigue. Furthermore, elastic analysis gave conservative results.

Can you confidently extrapolate from the relatively short-term tests to a design life of 60 yrs?

5. Conclusions

In order to improve total accuracy of design evaluation procedures, a set of new guidelines was proposed with considering characteristics of reactor vessels for thermal load modeling, structural analysis and strength evaluation.

GUIDELINES FOR THERMAL LOAD MODELING

One of main difficulties of thermal load modeling is their inducement mechanism by interaction between thermal hydraulic and structural mechanics. Design evaluation requires envelope load conditions with considering scatter of design parameters. Proposed guidelines enable precise load modeling by grasping sensitivities of thermal stress to design parameters including thermal hydraulic ones.

GUIDELINES FOR INELASTIC DESIGN ANALYSIS

Guidelines are proposed to apply inelastic analysis methods for design of reactor vessels. There are so many influence parameters in inelastic analysis that conservative and unique solutions are hardly found. To overcome such difficulties, mechanism and main parameters of inelastic behaviors of reactor vessels were clarified. Guidelines give conservative results within the same mechanism as expected reactor vessels.

HIGH TEMPERATURE STRENGTH EVALUATION METHOD

Ratcheting deformation and creep fatigue strength evaluation methods were proposed. Accumulated strain is limited within no influence of fatigue and creep-fatigue strength. Taking design conditions of reactor vessels into account, creep fatigue evaluation considers strain concentration and an intermediate stress hold effect on creep-fatigue strength. Influences of thermal aging were also confirmed

ACKNOWLEDGEMENTS

Present study includes the results of “Development of elevated temperature structural design method for fast reactor vessels and failed fuel detection and location system” entrusted to JAEA by the Ministry of Education, Culture, Sports, Science and Technology of Japan (MEXT).

REFERENCES

[1] Sagayama, Y., Okada, K. and Nagata, T., “Progress on Reactor System Technology in the FaCT Project Toward the Commercialization of Fast Reactor Cycle System,” Proceedings of International Conference on Fast Reactors and Related Fuel Cycles (FR2009), IAEA-CN-176-01-02. (2009)

[2] Kawasaki,N., Takakura,K.,Ohtani,T.,Hayashi,M. and Yamada,Y., 1999, Recent Design Improvements of Elevated Temperature Structural Design Guide for DFBR in Japan, SMiRT15, Div.F, F04/4

[3] Naoto KASAHARA, Kenichiro SATO, Kazuyuki TSUKIMORI and Nobuchika KAWASAKI, Development of elevated temperature structural design methods to realize compact reactor vessels, Proceedings of International Conference on Fast Reactors and Related Fuel Cycles (FR2009), IAEA-CN-176/08-03 (2009)

[4] Kasahara.N., Jimbo.M., Hosogai.H., 2003. Mitigation Method of Thermal Transient Stress by Thermal hydraulic-Structure Total Analysis. SMiRT17, F03-1

[5] Yang Xu, Kenichiro Satoh, Yoshio Kamishima and Naoto Kasahara, Proposal of Thermal Transient Load Modeling Method of for Fast Breeder Reactors, SMiRT-21, Div.V, #390,(2011)

[6] Ohno, N. And Wang, J.D., 1993. Kinematic hardening rule with critical state of dynamic recovery, Part I, Int. J. Plasticity. 9. P.375-390

[7] Iwata, K., Tsukimori, K., Kawasaki, N., Yada, H. and Kasahara, N. 2008. Development of constitutive models for fast breeder reactor design – multi-linear kinematic hardening model with stress reversal-on resetting -. Proc. of the 52nd Japan Congress on Material Research. P.65-66.

[8] Corum, J.M. 1981. Future needs for inelastic analysis in design of high-temperature nuclear plant components. Computers & Structures. 13. P.231-240

[9] Iwata, K. 1993. A two-surface cyclic plasticity model consistent with fundamental stress-strain equations of the power-law type. Nuclear Engineering and Design. 139. P.319-326.

[10] Kazuyuki TSUKIMORI,Koji IWATA, Nobuchika KAWASAKI, Naoto KASAHARA, Development of Constitutive Models for Fast Reactor Design, SMiRT-21, Div.I, #82,(2011)

[11] Nobuhiro ISOBE, et al., Design Criteria for Ratcheting Fatigue of 316FR Steel under Fast Reactor Conditions, SMiRT-18,F04-2, F04-2, pp1131/1140(2005)

[12] Nobuchika KAWASAKI, Yuji NAGAE, Shoichi KATO, Naoto KASAHARA, Intermediate dwell creep-fatigue strength：uni-axial and structural strength, SMiRT-20, (2009)

[13] Naoto KASAHARA and Jun MAEDA, Analytical Study on Mechanism of Stress Redistribution Locus in Structures, ICPVT-12, SA3-2(2009)

[14] Daigo Watanabe, Yasuharu Chumann, Masami Otani, Hiroshi Shibamoto,Kazuhiko Inoue, Naoto Kasahara, Constitutive Equations for Inelastic Analysis and their Validation through Structural Model Tests, Nuc. Eng. Des., Volume 238, Issue 2, (2008)

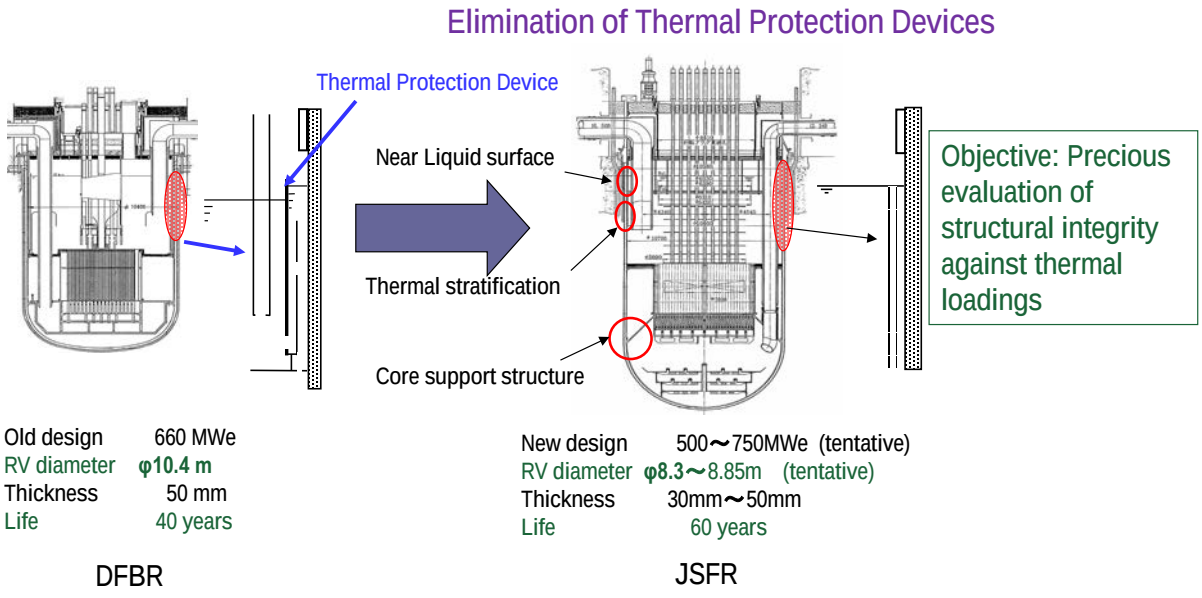

Figure 1 Realization of compact reactor vessel in JSFR by elimination of thermal protection devices

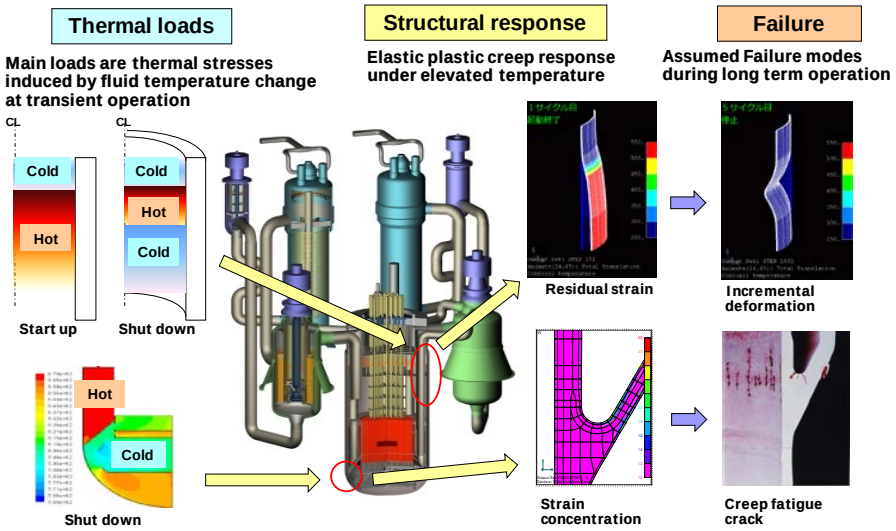

Figure 2 Failure modes and mechanism of reactor vessels in JSFR

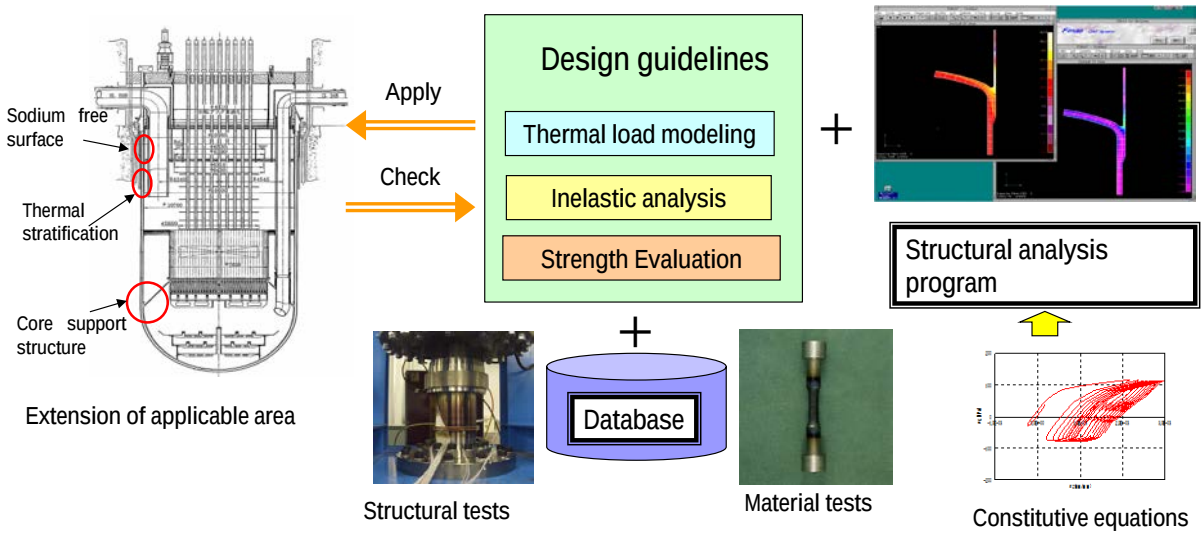

Figure 3 Development of design guidelines for reactor vessels

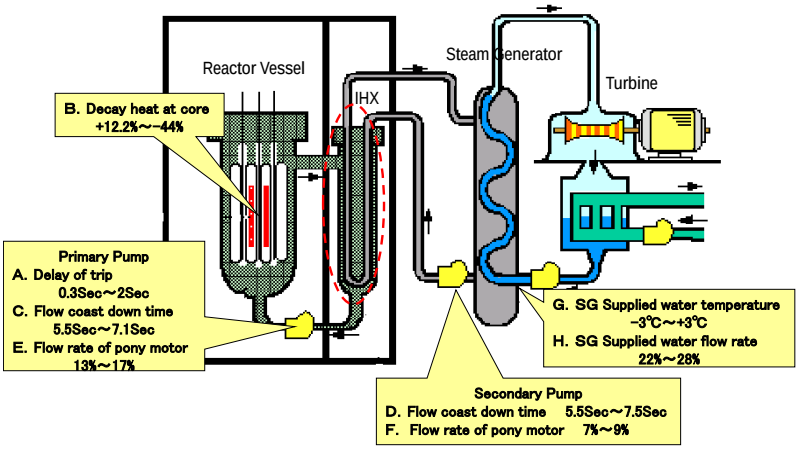

Figure 4 Many influence factors such as system plant parameters for thermal transient loads

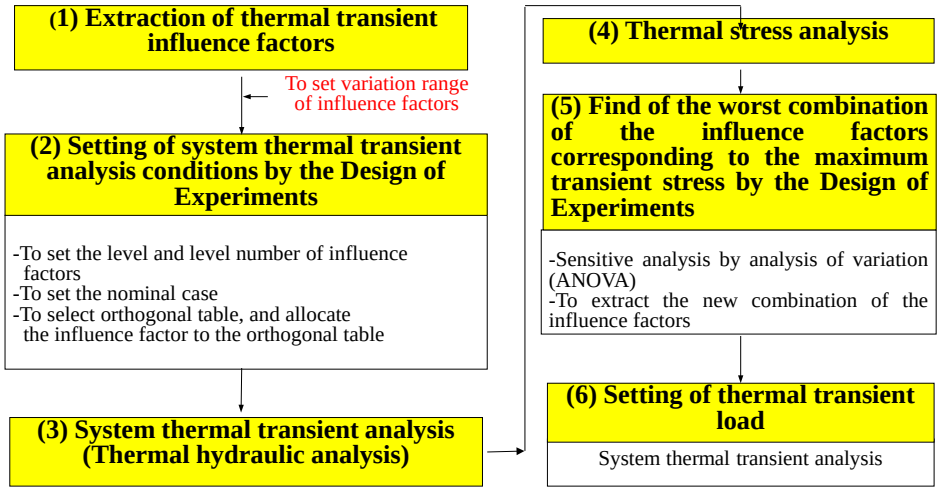

Figure 5 New Proposal of thermal transient modeling method by Design of Experiments

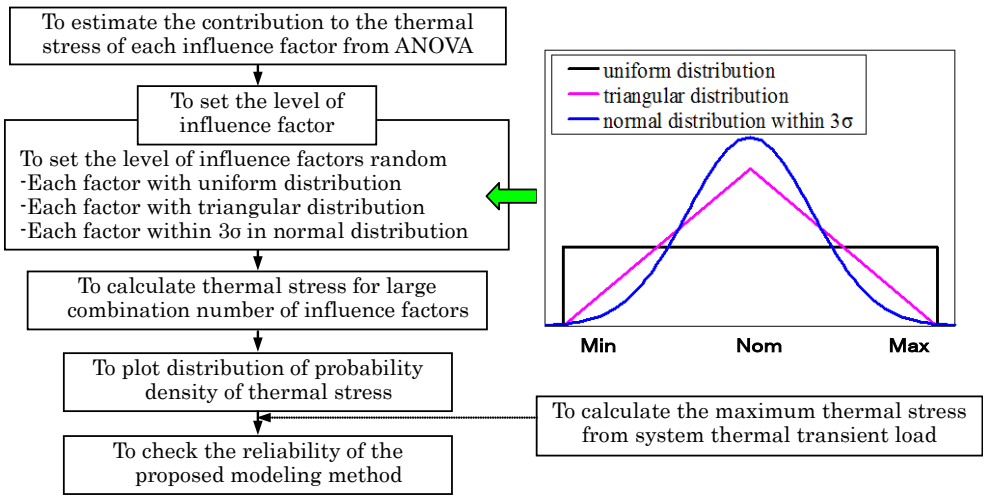

Figure 6 Probabilistic analysis with the Monte Carlo Simulation

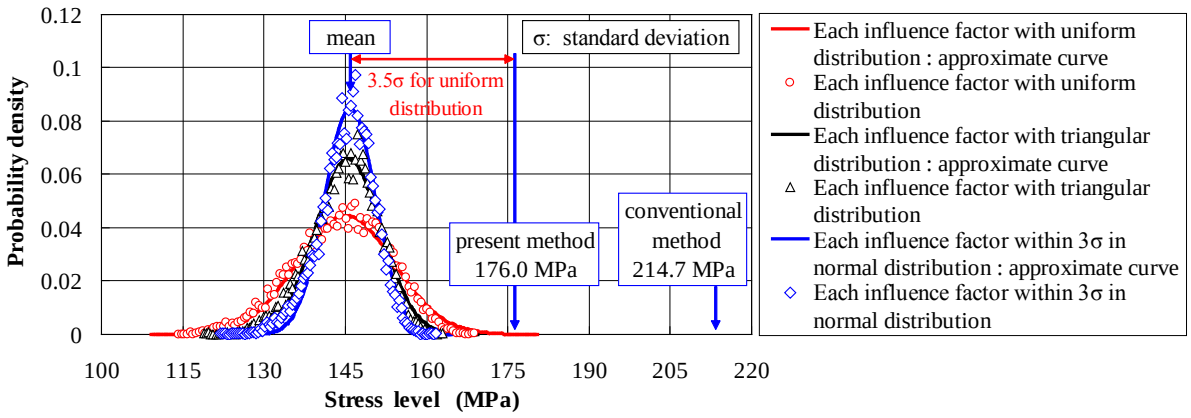

Figure 7 Comparison of modeled thermal loads between Design of Experiments and Monte Carlo Simulation

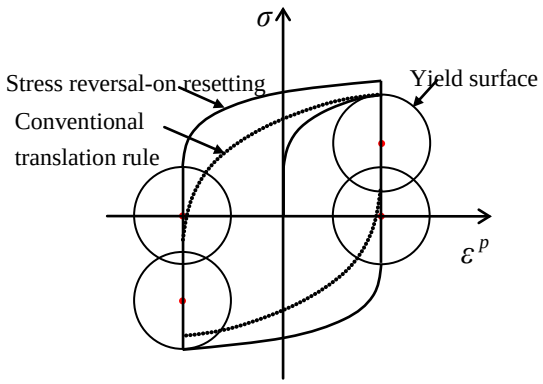

Figure 8 Concept of stress reversal-on resetting

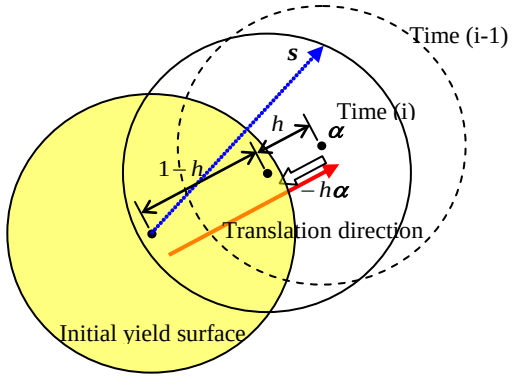

Figure 9 Translation of a yield surface in the stress reversal-on resetting process

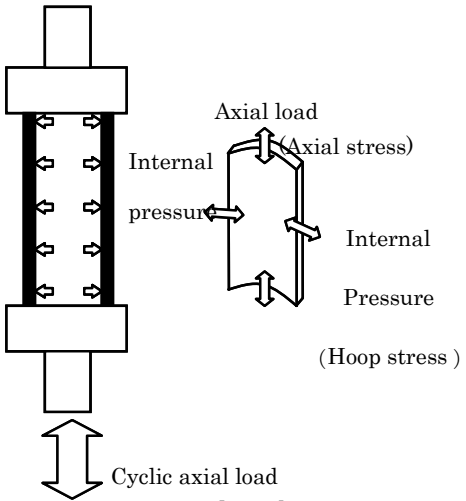

Figure 10. Bi-axial ratcheting test

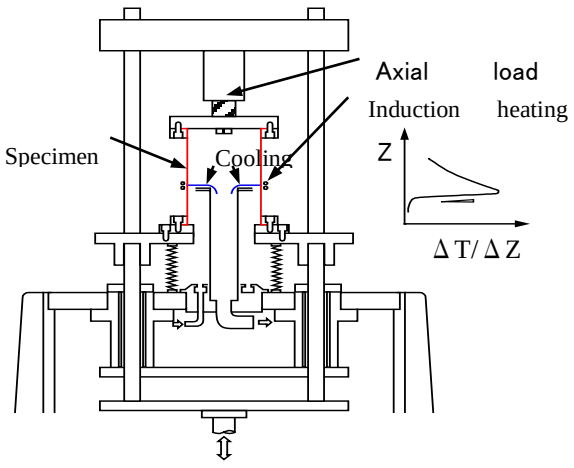

Figure 11. Structure model tests

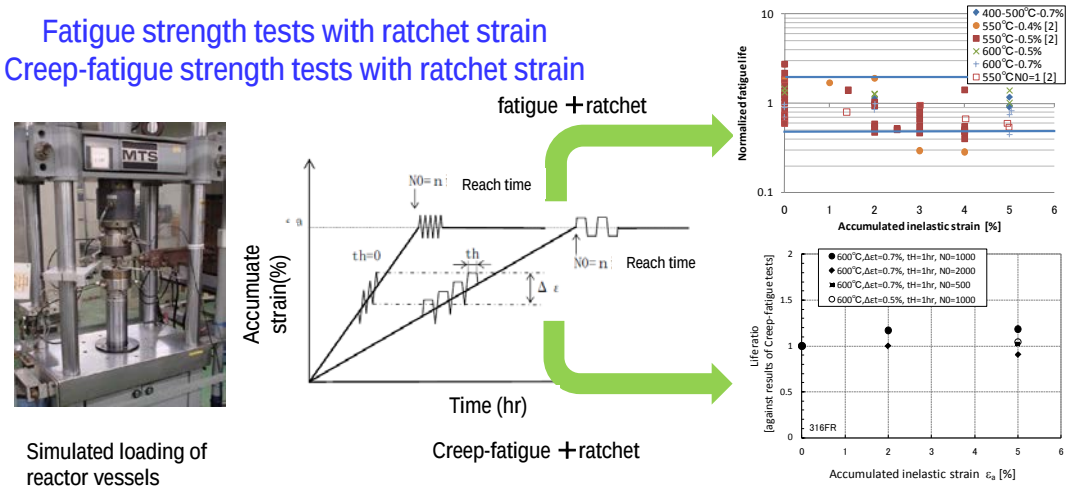

Figure 12 Effects of ratchet strain on fatigue and creep-fatigue strength

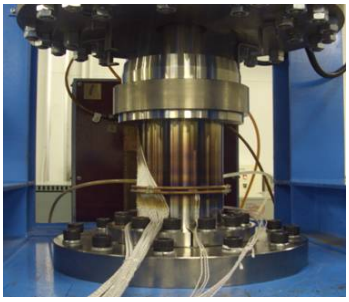

Reactor vessel model

Load conditions

Temperature	600℃		
Thermal stress	1000MPa		
Primary stress	50MPa	30MPa	50MPa
Hold time	0hr	3hr	3hr

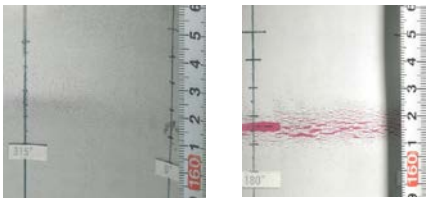

Inner surface Outer surface

Observed cracks after 2000cycles (30MPa, 3hr)

Figure 13 Reactor vessel models for validation of strength evaluation methods

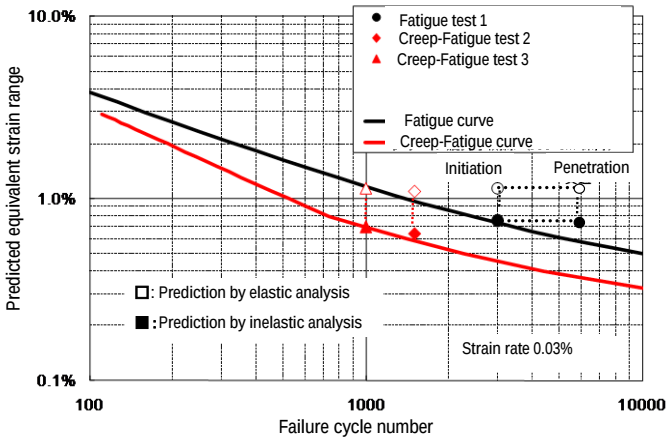

Figure 14 Comparison of creep-fatigue failure cycles between measurements and predictions

Objectives of experimental validation of mechanical equipment for BN-1200 reactor plant

M.A. Lyubimov, A.V. Timofeev

JSC "Afrikantov OKBM", Nizhny Novgorod, Russia

Abstract. As compared with BN-600 and BN-800 reactors, the BN-1200 reactor design incorporates the number of new engineering decisions aimed at improvement of technical-and-economical characteristics. The refuelling system applies the conceptually new mechanical equipment: vertical elevator with varying length of the overhang for FA insertion and overhanging refuelling mechanism. To validate the operability of these components, the equipment mockups and test facilities were developed.

In connection with variation of mass and dimension characteristics of CPS control rods and introduction of some improvements in BN-1200 reactor design, new control rod drive mechanisms are used for each three rod types, which will be tested as per the special program.

The paper presents the information on the design features of the given mechanical equipment, testing equipment characteristics and main parameters of the equipment, which are controlled during tests.

1. Introduction

BN-1200 reactor that is currently under development represents the pilot power unit of a series of large size fast reactors. Its primary objective is to demonstrate feasibility of the installed power cost achievement comparable to that of the PWR reactors. Therefore, much emphasis in reactor development is put on reduction of its overall size, material consumption, optimization of the technical solutions and provision of equipment reliability.

The refueling equipment and CPS CRDMs are referred to the key mechanical equipment of the reactor.

The design of BN-1200 reactor refueling equipment provides an essential unique feature due to application of unique layout decisions aimed at reduction of the reactor's material consumption.

The CPS CRDMs reliability is important both from the viewpoint of reactor economics and safety provision. Therefore, CPS CRDMs design should be proven by the tests as it is stipulated by the regulatory documentation.

2. BN-1200 reactor refueling equipment

Due to application of unique layout decisions, the refueling scheme of BN-1200 reactor design (Fig.1) [1] is essentially different as compared to that of BN-350, BN-600 and BN-800 reactors.

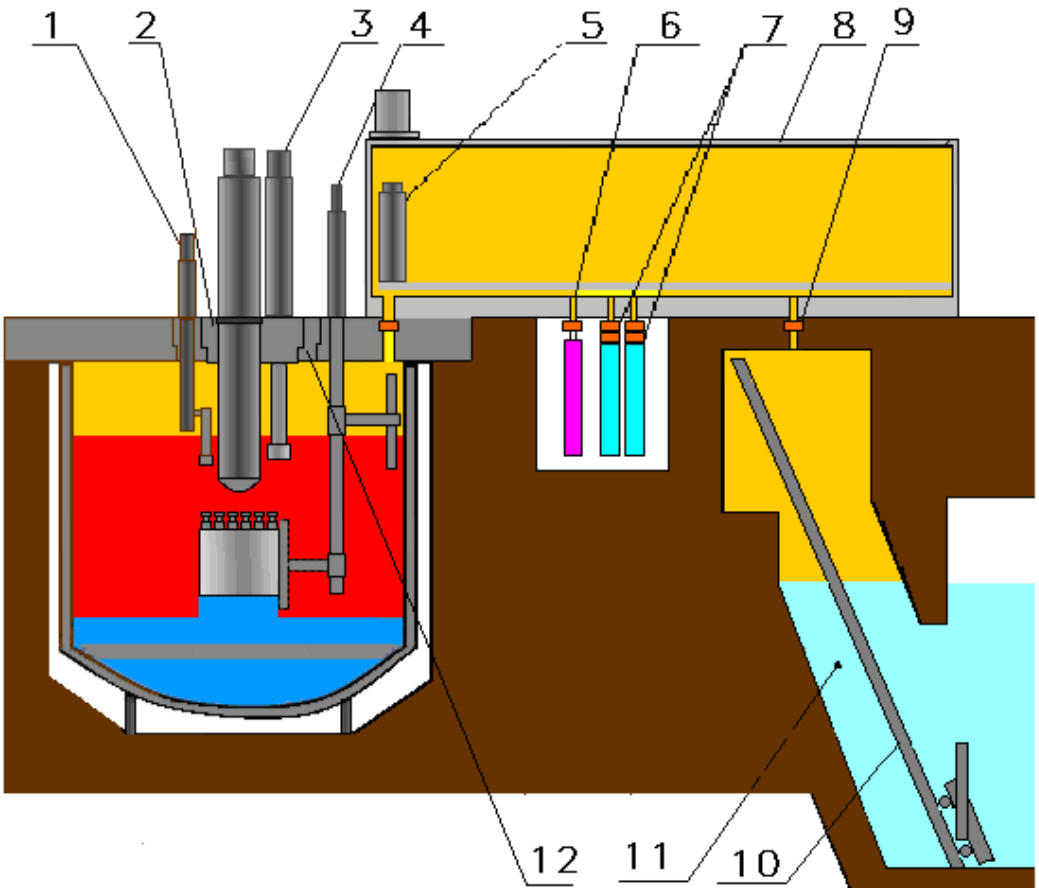

FIG. 1. BN-1200 reactor refueling scheme

1 – cantilever refueling mechanism, 2 – small rotatable plug, 3 – refueling mechanism, 4 – elevator, 5 – refueling machine, 6 – lead washing cell, 7 – steam and water washing cell, 8 – refueling box, 9 – gate valve, 10 – inclined hoist, 11 – water pool, 12 – large rotatable plug.

The elevator and cantilever refueling mechanism of modified design are used in this scheme.

3. BN-1200 RP elevator design and operation

The elevator is a part of the set of in-reactor refueling devices designed to transfer fresh FAs from the refueling machine to the refueling mechanism and spent FAs from the refueling mechanism to the refueling machine. The elevator is required to lift the FA head above the sodium level, which ensures reliable operation of the refueling machine's grapple due to lack of necessity to cross the gas-sodium boundary.

In developing the elevator challenges have been set so as to provide preset movement of the FA along the radius from the service area of the refueling mechanism into the service area of the refueling machine and provide the minimum overall dimensions of the elevator during its withdrawal.

There is one elevator in the reactor plant. The elevator design is illustrated in Fig.2

The elevator is a stationary L-type vertical mechanism arranged inside the assembly plug on the upper fixed shield of the reactor.

Internal cavities of the elevator communicate with the gaseous cavity of the reactor and have leak-tight design in relation to the environment.

The carriage is provided with a sleeve for accommodation of reloaded FAs. At the top of the sleeve there is a bushing with a hexagonal opening, by the aid of which FA's orientation by azimuth is effected. The sleeve is fixed to the carriage by way of pantograph to provide its installation and disassembly. Control over the pantograph is carried out using a special drive installed in the hole of the assembly plug.

There is a rotatable plug in the assembly plug by the aid which the elevator is rotated at a specified angle to align the longitudinal axis of the sleeve with the axis of the reactor refueling channel or channel axis in the core.

In between the refuelings, the elevator is in the parking position with the carriage lifted to the top position.

During refueling the elevator performs the following functions:

- lifting of the carriage from bottom to top position;
- rotation of the carriage until the axis of the sleeve is aligned with that of the reactor refueling channel;
- rotation of the carriage (following withdrawal of a spent FA by the refueling machine or installation of a fresh FA);
- descending the carriage to the bottom position.

The cycle is repeated until refueling of all FAs is completed.

The proven design solutions of BN-600 reactor elevator's major components are adopted in the design of the elevator (i.e. movement of the carriage along the guide rail by the aid of the chain, availability of the plug to arrange the guide rod and tubes, double-reduction wormgear unit and manual drive, limitation of the pulling force by the aid of the overload release clutches, availability of tubes that serve as the channels for the chain and tie rod movement, arrangement and fastening of the drive, identity of materials etc.) that provide its performance within the designed operation life .

The main advantages of the elevator as compared to the inclined elevators used in BN-350, BN-600 and BN-800 RPs are increased convenience of handling and shorter installation and disassembly time.

Changes in the design of the elevator refer to the cantilever arrangement of the sleeve on the carriage and the ability to reduce the length of the cantilever by a special purpose device in regard to the elevator's guide rod during its withdrawal. These design solutions require experimental verification.

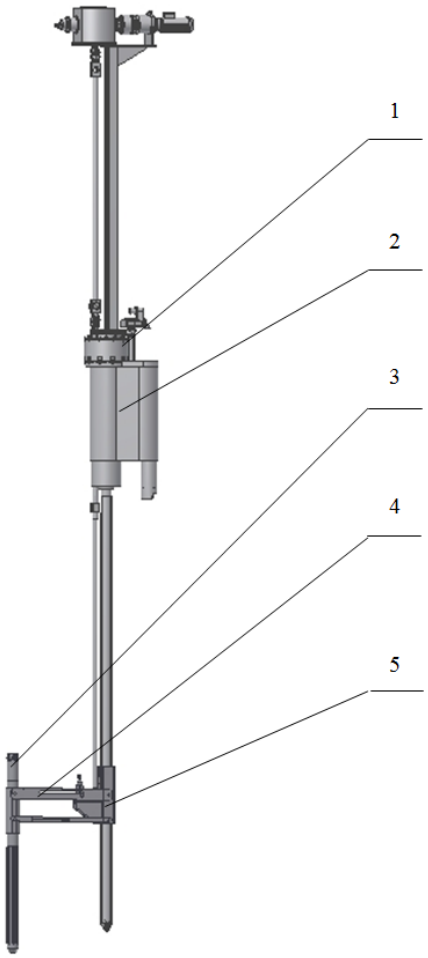

FIG. 2. Elevator

1 – rotatable plug; 2 – assembly plug; 3 – sleeve; 4 – pantograph; 5 – carriage.

4. Experimental validation of the elevator components' operation

Mockups of the carriage with pantograph, guide rod and a special purpose device for remote variation of the cantilever length responsible for the sleeve position in relation to the guide rod have been designed and manufactured in order to test the engineering solutions adopted in the design of the elevator. The fabricated life-size mockups enabled to simulate the elevator operation during the FAs reload and the process of remote variation of the cantilever length providing the sleeve position in relation to the guide rod. During the tests the following is checked:

- carriage movement along the guide rod;
- remote variation of the cantilever length providing position of the sleeve in relation to the guide rod in case of aligned and misaligned position of the special purpose device and the drive's component used to change the cantilever length.

5. Design and operation of BN-1200 RP cantilever refueling mechanism

The cantilever refueling mechanism is designed to perform loading and unloading of the peripheral rows of FAs in the steel and boron shield. It is installed on the large rotatable plug only in case there is a need to reload these FAs. Between the refuelings of the steel and boron shield's FAs, the refueling mechanism is arranged at the test stand in the main reactor hall, and the hole in the large rotatable plug is covered with a special plug.

The cantilever refueling mechanism is used for extraction of FAs from the reactor core, providing orientation of FA hexagonal in case of the FAs removal and installation by turning the large rotatable plug, refueling mechanism's plug and rotation of the refueling mechanism.

The cantilever refueling mechanism's design is illustrated in Fig.3.

While designing the cantilever refueling mechanism the following challenges had to be solved:

- provide required length of the cantilever of the grapple location in regard to the longitudinal axis of the refueling mechanism, enabling to reload infrequently replaceable FAs of the steel and boron shield arranged beyond the boundary of the large rotatable plug diameter.
- provide control over the force applied for extraction of FAs from the core and elevator;
- provide orientation of the hexagonal tube of reloaded FA by the faces during its installation in the core cells and the elevator's sleeve.

Design solutions not yet tested in the existing and currently under development reactors with liquid metal coolant are adopted in the design of the cantilever refueling mechanism i.e. cantilever arrangement of the grappling device with regard to the longitudinal axis of the refueling mechanism and modified sensor unit used to control withdrawal force exerted on the FAs. Therefore, for the development of the entire design and testing designs of the individual units it is necessary to conduct a complex of R&D activities to confirm operation of the refueling mechanism within the designed operation life.

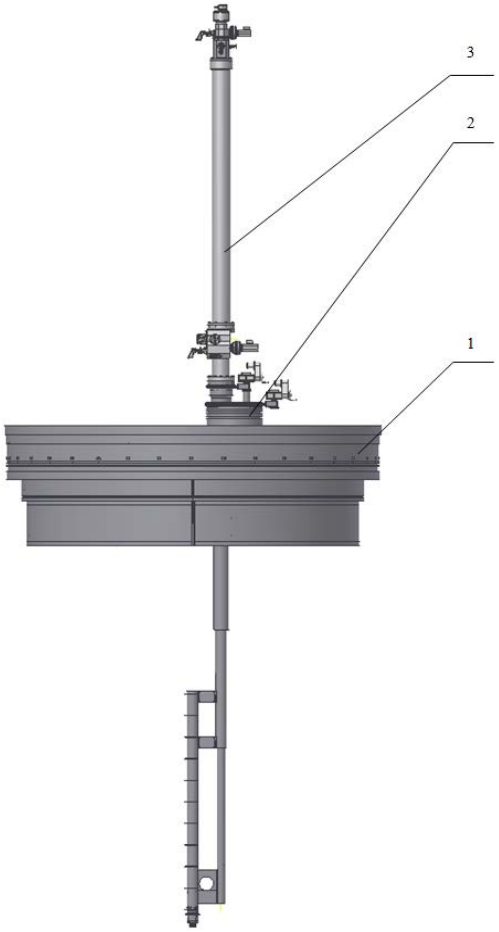

FIG. 3. Cantilever refueling mechanism

1 – large rotatable plug; 2 - plug of the refueling mechanism; 3 - refueling mechanism.

6. Experimental validation of the cantilever refueling mechanism's components performance

A simplified mockup and test stand has been designed and manufactured to check the technical decisions adopted in the design of the cantilever refueling mechanism. During the tests the following is performed:

— testing the operation and modifications of the design and size of the grappling device with the guide tube by conducting operations on withdrawal and installation of the FA simulator:

(1) in case of the aligned and misaligned position of the grappling device and simulator;
(2) in case of mismatch of the hexagon socket angle formed by six simulators and the central simulator's hexagon;
(3) under various deviations of the grappling device and guide tube movement (stroke);

— determination of conditions under which the FA simulator's self-orientation takes place:

(1) determination of the maximum angle of the simulator self-orientation in case of the aligned position of the simulator and socket formed by six simulators;
(2) determination of the maximum angle of the simulator self-orientation in case of the misaligned position of the simulator and socket formed by six simulators;

— determination of the force applied to the guide tube during separation of the heads of imitators forming hexagonal socket;

— testing the operation of the way the sensors are installed to control the force of the simulator withdrawal.

7. Design and operation of CPS CRDMs

CPS CRDMs of BN-1200 likewise those of BN-800 and BN-600 are functionally and structurally divided into compensating rod CRDM, control rod CRDM and emergency protection CRDM. The difference between the compensating rod and control rod CRDM is that the first one has a higher rate of the control member movement and, therefore, more powerful electric motor. To provide quick actuation of the EP CRDM there is an electromagnetic clutch, breaking the kinematic circuit of the control member. The design of emergency protection CRDM, control rod CRDM and compensating rod CRDM is shown in Fig. 4 (a, b, c, respectively).

CPS CRDM operation is to move the control member by a specified value at a preset rate.

The design of BN-800 CPS CRDMs, to a great extent, is based on the decisions adopted in BN-600 reactor and proven by its operation experience. The basis for improving the design of BN-800 CPS CRDM is the use of a step motor that enabled to simplify the kinematic circuit and improve its reliability. The CPS CRDMs of BN-800 and BN-1200 are similar design. The main difference between them is the larger mass of the CPS working members (~15 kg in BN-800 as compared to 50 kg in BN-1200), which entailed the increase of CRDM mass and electric motor drives' power. Similar to the decision adopted in BN-800, some of the CPS control rods with the CR CRDM in BN-1200 are used in the passive emergency protection mode by way of free weighting in the sodium flow, following disengagement of the rods' grapples at the upper position (hydraulically balanced rod) [2].

FIG. 4. CPS CRDMs.

8. Experimental validation of the CPS CRDM performance

The pilot samples of CPS CRDMs have been designed and manufactured to test the technical decisions incorporated in their design. During the test runs checkup of the following key characteristics is being done:

- rate and value of the tie rod movement with the simulator of the CPS control member;
- engagement and disengagement of the tie rod with the simulator of the CPS control member;
- matching of the CPS control member position indicators' readings to its actual position;
- accuracy of the CPS control member stop at the preset position;
- drop time of the EP control member (exceptionally for the EP CRDM).

9. Conclusion

Development of equipment for the BN-1200 RP is based on the available extensive experience of the development and operation of fast sodium cooled reactors in Russia. This serves as the basis of confidence for ensuring reliable operation of the equipment, a high technical and economic performance and safety level of the power unit with BN-1200 RP. Novel engineering decisions adopted in the BN-1200 RP project also have a sufficient degree of validity on the basis of the available experience. However, comprehensive computational and experimental studies should be carried out for their final verification.

REFERENCES

[1] VASILYEV, B.A., TIMOFEEV, A.V., LYUBIMOV, M.A., BUDYLSKY, A.D., Layout and design solutions for the refueling system of the advanced BN reactor. / Atomic Energy, 2010, v.108, No 4, pp. 246-249.

[2] VASILYEV, B.A., KAMANIN, YU.L., GLADKOV, V.V., BARTENEV, V.N., SHEPELEV, S.F., KUZAVKOV, N.G. (JSC "OKBM Afrikantov"), DENISOV, V.V., CARSONOV, V.I. (JSC OKB "Gidropress"), Improvement of the fast reactors' equipment. / Atomic Energy, 2010, v.108, No 4, pp. 241-245.

Development of the LIBS technique for online sodium measurements related to the safety of sodium fast reactors

J.-B. Sirven, C. Maury, E. Vors, J.-L. Courouau, M. Tabarant, T. Vercouter

CEA, DEN, Department of Physical Chemistry, F-91191 Gif sur Yvette, France

Abstract. In previous French sodium fast reactors, the coolant purity was regularly measured to detect potential undesirable phenomena like air ingress, corrosion of structural materials, leakages between cooling circuits, or even fuel clad failures. These events are likely to release chemical elements in the sodium, like oxygen, hydrogen, and corrosion or fission products. Techniques used to monitor their concentration in the coolant were mainly plugging indicators, electrochemical probes, elemental and nuclear analysis of sodium samples taken during a reactor shutdown.

These methods proved efficient, but had several limitations. Plugging indicators are implemented online but only indicate with accuracy a purity level, with no discrimination of the impurity chemical nature. Other measuring techniques can be used to analyze target elements but they are not carried on online. Therefore, the development of new techniques, allowing fast, online, sensitive measurements and enabling to identify the type of impurity, was initiated for future SFRs. Laser-Induced Breakdown Spectroscopy (LIBS) is one of them.

LIBS operates by focusing a laser pulse onto the surface of a sample. The resulting ablation leads to the formation of a plasma, whose optical emission is analyzed by a spectrometer. The sample elemental composition is determined from the atomic lines intensity. The measurement is fast (a few seconds to a few minutes) and can be implemented online.

We will present the development of the LIBS technique for two applications related to the safety of SFRs. The first one is the online monitoring of sodium purity, with a sensitivity in the ppm range for elements soluble in liquid sodium. For this application the challenge is to reach the required detection limits for the events to monitor. The second is the direct real-time detection of sodium aerosols in case of sodium leakage from a pipe. Performances, limitations and challenges of these approaches will be discussed.

1. Introduction

As part of developing Gen-IV reactors , France is currently studying the option of sodium-cooled fast reactors (SFRs). This technology has already been successfully implemented from 70’s to the 90’s, mainly with the Phénix and SuperPhénix reactors. Today, improvements are being considered in all sectors of the reactor conception. In particular, systems ensuring the reactor safety are of special interest to enhance acceptability by the public. In this field, the sodium quality control is a major issue, whether it is related to radiometric, physical or chemical measurements.

The chemical purity of primary liquid sodium can be used to detect different potential incidents that may happen in the reactor. For example, an air ingress can introduce oxygen in the sodium, which may induce a higher corrosion rate of the hot structural materials. Then elements such as iron, chromium or nickel can be released, in different forms, in the coolant, which may lead to reducing the components thickness, hence their lifetime, but also to contamination of the coolant by activated corrosion products. Last but not the least, a fuel clad failure is likely to contaminate the sodium with fission products. Therefore, detecting different impurities allows an operator to identify the related

undesirable situations and helps to simplify the reactor exploitation and to monitor it in a concept of clean primary sodium.

Another issue related to the SFRs safety that must be addressed relates to the quick detection of sodium leaks from pipes in case of breach. Such leaks should be addressed either by countermeasures or by early and accurate detection. Current implemented systems depend on the location where the leak must be detected, and on the pipe geometry. Thus, wire type leak detectors are developed for local measurements, in contact with the pipe [1], whereas global detection is achieved by detectors which sample the ambient air and analyze sodium by flame atomic spectrometry, or by sodium ionization detectors [2]. Several detectors proved efficient for sodium leak detection, but they have a few drawbacks, such as a high false alarm rate, or the introduction of an additional risk in the facility due to the measuring device principle (flame spectrometer).

Optical techniques have powerful advantages for online measurements in nuclear environment [3]. Among them, laser-induced breakdown spectroscopy (LIBS) could be particularly suited for real time elemental analysis, at remote distance and in constrained environment [4]. Therefore it is considered as a possible innovative technique for measurements related to sodium monitoring in SFRs [5]. The principle of LIBS is rather simple: is consists in focusing a laser pulse onto the surface of a sample and in analyzing the resulting plasma emission with a spectrometer. The atomic lines signal enables to retrieve the sample elemental composition.

Due to its unique capability to perform chemically selective measurements, online and in a short time, LIBS has a high potential to provide a significant complementary value to improve detection performances in connection with other systems already used for liquid sodium monitoring, like electrochemical probes [6], plugging indicators [7] or sodium sampling followed by complete dissolution and chemical analysis. For the same reasons, the technique can also be considered as a good alternative for global sodium leak early detection. Therefore, this paper reports on the first application of LIBS for online sodium monitoring, as part of current research on innovative instrumentation dedicated to SFRs safety. Calibrations are obtained for several elements of interest, and detection limits are derived. The potential of the technique is discussed for both applications.

2. Experimental setup

2.1. Liquid sodium analysis

The experimental setup for liquid sodium analysis is presented on Fig. 1. A 266 nm Nd:YAG laser, with a pulse duration of 5 ns (FWHM) and a maximum pulse energy of 15 mJ, is used for ablation at a repetition rate of 20 Hz. It is focused onto the sodium surface by a lens of 1 m focal length. Approximately 300 g of sodium are contained in an oven filled with ultra-pure argon (99.9999% purity) in order to avoid any contamination by oxygen. It is heated by a heating belt up to a temperature of 150°C. As sodium melts at 98°C, it is liquid at this temperature. The heating belt is controlled by a PID controller associated with a temperature probe which measures the liquid sodium temperature inside a thimble. A quartz window placed on the upper part of the oven transmits the laser beam and the light emitted by the plasma. Another window is available for plasma visualization. Both windows are flushed by ultra-pure argon to avoid deposition of ablated matter. Plasma emission is collected in the same direction as that of the laser beam. An achromatic optical system injects it into a 910 µm core, 0.22 numerical aperture optical fiber connected to a Czerny-Turner spectrometer with a 30 cm focal length and a 3600 grooves/mm grating. With a 100 µm entrance slit we get a resolution power $\lambda/\Delta\lambda$ of 2200 at 280 nm. The detector used is an intensified CCD camera (iStar, Andor) with 2048x512 pixels.

The gate delay with respect to the laser pulse and the time integration gate were optimized so that the signal to background noise ratio is maximum for the lines of interest. They are respectively 4 µs and 6

µs. Each spectrum is the result of 4000 accumulated laser shots, i.e. the measurement duration is 3 min 20 s. 10 spectra per concentration are acquired.

For calibration of impurities concentration in liquid sodium, the standard addition method is used. When the sodium cools down and is solid, the oven is flushed with argon so that the overpressure prevents any air ingress. A previously weighed piece of pure metal is then inserted in the oven through the upper window. Lead, indium and thallium were chosen as analytes in this study because they are highly soluble in liquid sodium at 150°C [8]. The maximum concentration obtained at the end of the calibration campaign was between 80 and 130 ppm, depending on the element. Their concentration was confirmed after the last standard addition by an ICP-OES measurement. The analytical lines are at 283.3 nm for lead, 451.1 nm for indium and 276.8 nm for thallium.

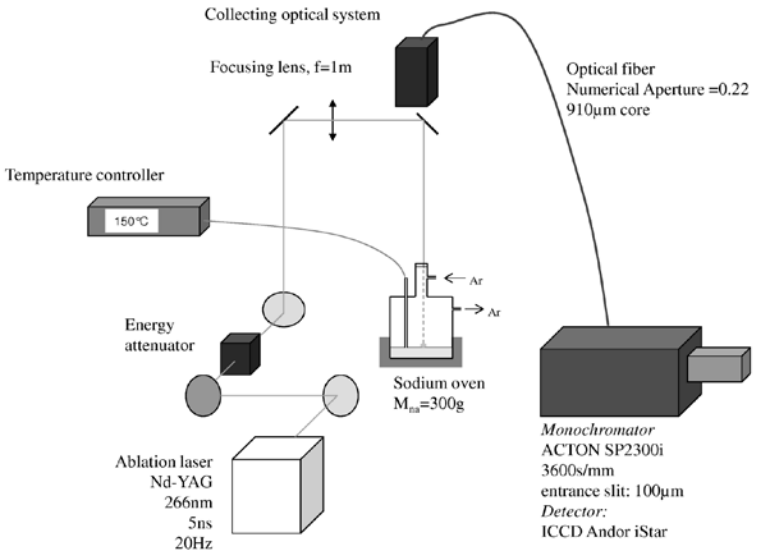

FIG. 1. LIBS setup for liquid sodium analysis.

2.2. Sodium aerosol analysis

For aerosols analysis, the LIBS principle is different than for solids or liquids analysis. It consists in continuously firing the laser. At each laser shot a plasma is formed in the air. When a particle is in the plasma volume, it is vaporized and a specific signal is recorded. For diluted aerosols, most spectra exhibit only the signal of the ambiant gas. Only a few percents of the total number of laser shots, or even fewer, give a particle signal. Those shots are referred to as 'hits'. The aerosol mass concentration is derived from the hits rate and from the average analyte intensity for the hits. Therefore, laser shots are not accumulated in each spectrum, on the contrary, a spectrum is recorded for each shot. The methodology of aerosols measurement by LIBS, known as 'conditional analysis', was detailed by Hahn et al. in ref. [9].

The experimental setup is represented on Fig. 2. An aerosol generator (Sinaptec CH GA80) using an ultrasonic nebulizer is used to produce $NaHCO_3$ micrometric particles from a 5 g/L solution. The theoretical mean particle aerodynamic diameter in this case is about 3 µm, of the order of the particle size expected in case of a sodium leak. The solution flow rate on the nebulizer is of the order of 0.1 mL/min. The aerosol number concentration is varied by changing this flow rate. A flow splitter is placed at the generator output. The aerosol is directed to an electrical low pressure impactor (ELPI, Dekati) for particle size measurement, to a dust-monitoring instrument (DustTrak DRX 8533, TSI) to

measure the aerosol mass concentration in real time, and to a LIBS analysis cell. The flow rate is respectively 10 L/min, 3 L/min and 10 L/min in each sampling line.

For LIBS measurements we use a 1064 nm Nd:YAG laser delivering 415 mJ pulses at 20 Hz with a pulse duration of 5 ns (FWHM). The laser beam is focused inside the cell by a lens of 150 mm focal length. The plasma is formed at the center of the cell and its emission is collected in the same direction as that of the laser beam by a lens of 100 mm focal length. The emitted light is injected into an optical fiber with a 910 µm core diameter and 0.22 numerical aperture. This fiber is connected to a Czerny-Turner spectrometer with a 640 mm focal length and a 1200 grooves/mm grating blazed at 630 nm. The slit width is 50 µm. The spectrometer is equipped with an intensified CCD camera (PI MAX, Princeton Instruments) with 1024x256 pixels. The intensity at 589.0 and 589.6 nm (wavelength of the sodium doublet) is the analytical signal. 10000 laser shots are made for each acquisition, i.e. the measurement duration is 8 min 20 s, and each acquisition is replicated five times at each concentration. The gate delay is 10 µs with respect to the laser shot, and the time integration gate is 20 µs.

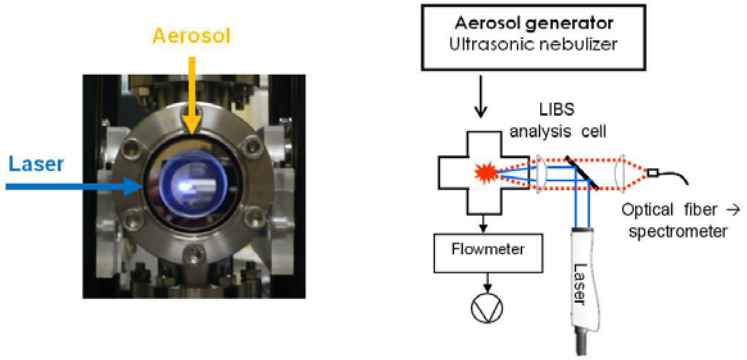

FIG. 2. LIBS setup for sodium aerosols analysis. The photo shows the LIBS analysis cell with the laser-induced plasma formed in the centre.

3. Results and discussion

3.1. Liquid sodium analysis

Typical spectra of the three impurities analyzed in liquid sodium are represented on Fig. 3. We see that the lines lie on an intense background continuum due to the free electrons radiation (Bremsstrahlung). Its intensity is variable with wavelength, higher in the visible than in the UV range. We also observe that the lead line at 283.3 nm is located on the left wing of an intense sodium line at 285.3 nm (not visible on the figure). In spite of that, this line was found to have the highest signal to background noise ratio for this element.

Signal intensity drifts were detected during each acquisition of 10 spectra, which lasted approximately 30 min, but also from one standard addition to the other, i.e. from day to day. These drifts were attributed mainly to uncontrolled variations of the argon pressure inside the oven. The resulting fluctuations were found to be proportional ones, i.e. the lines ratios were unchanged, only the spectra global intensity varied. Consequently, the analytical lines intensity had to be normalized to compensate for these fluctuations. However our setup did not allow to simultaneously measure the intensity of a non self-absorbed sodium line that could have been used for normalization. Then we chose to normalize the lines intensity, previously background corrected, by the continuum intensity measured around 273 nm for lead and thallium, around 453 nm for indium. This approach was found to satisfactorily correct the signal drifts previously mentioned.

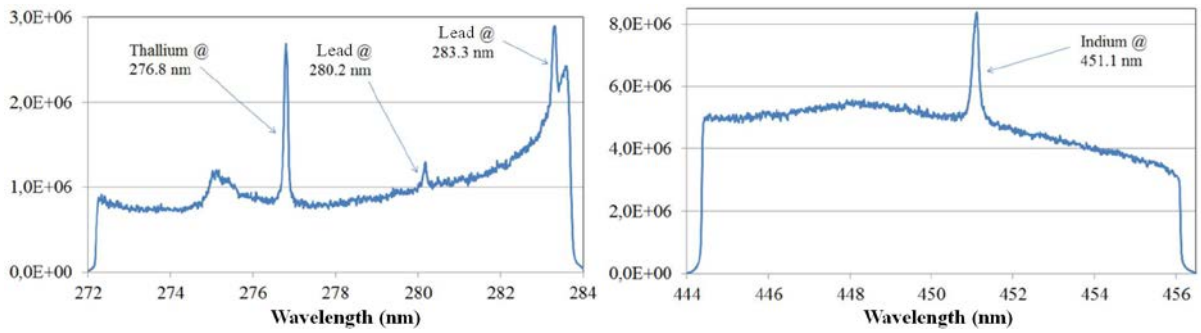

FIG. 3. LIBS spectra of lead (80 ppm), indium (90 ppm) and thallium (126 ppm) in liquid sodium.

Calibration lines obtained with the lines normalized intensity are shown on Fig. 4. Error bars represent one standard deviation calculated from the 10 replicas. Confidence hyperbolas are plotted with a confidence interval of 95%, calculated using the variance-weighted data. The quality of the calibration (linearity, accuracy, repeatability) is very satisfactory for the three elements. The detection limits are 3 ppm for lead and indium, 4 ppm for thallium. They are of the same order of magnitude, or even better than in other studies performed in more standard LIBS configurations and matrices [10], which is very positive in our case given the difficulties of the experiment (unusual matrix, remote analysis, signal drifts to due instrumental constraints…). This performance is close to the requirements of impurities monitoring in liquid sodium in case of corrosion or leakage from one cooling circuit to the other, for which detection is needed at the ~1 ppm level. However they are not sufficient to early detect a fuel clad failure, but this was expected given the extremely low detection limit required in this case, estimated lower than the ppb range.

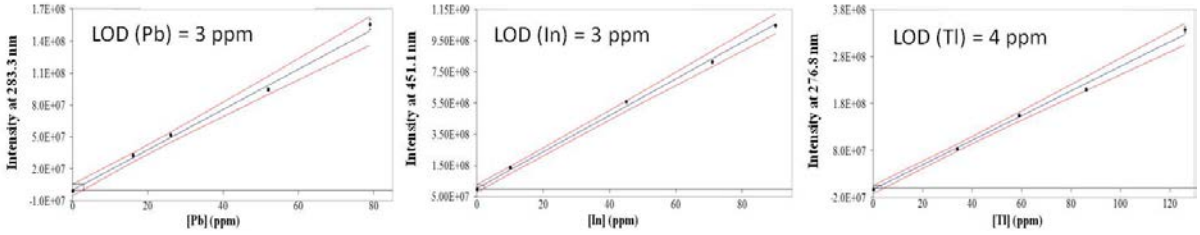

FIG. 4. Calibration by LIBS of lead, indium and thallium concentration in liquid sodium.

This first study was deliberately limited to impurities highly soluble in liquid sodium in order to estimate the sensitivity of the LIBS measurement in such a matrix and at 1 m distance. However, lead, indium and thallium are not really elements of interest for sodium monitoring. Iron, chromium and nickel, for example, are more interesting to detect, but they are much less soluble in sodium, even at the reactor temperature of 550°C. Indeed, their solubility limit, extrapolated from higher temperature data, is respectively 0.5 ppm, 1.45 ppm and 0.03 ppm at this temperature [8]. Note that this restriction does not apply to two other relevant elements to be measured for sodium monitoring, namely hydrogen and oxygen, whose solubility limit in liquid sodium is respectively 620 and 1800 ppm at 550°C [8]. But these elements are more difficult to handmle experimentally than metals. Therefore, two ways of improving this research can be defined. First, we aim at establishing a model to extrapolate the LIBS signal from one element to the other, using the data presented in this paper for three elements to validate the model. The objective is to be able to predict the detection limit of any

other element soluble in sodium. Secondly, the analysis of chemical compounds of interest insoluble in liquid sodium (iron oxides for example, or complexes formed with corrosion products and sodium) must be investigated. These compounds might be present in the form of particles in suspension in liquid sodium, but we lack input data concerning their chemical composition, their speciation, their size, etc. Online LIBS analysis perfomed on dedicated experiments to understand the behavior of these compounds could improve our knowledge of chemistry in liquid sodium. From the LIBS point of view, an approach similar to that implemented for aerosols analysis might be useful.

3.2. Sodium aerosol analysis

Fig. 5 shows two series of 3000 single-shot measurements of the LIBS signal at the 589 nm sodium doublet wavelength, for two mass concentrations of sodium in the aerosol. These series exhibit a background at an intensity of about 100, with hits visible above this level for shots for which a particle is in the plasma volume. The hits intensity is proportional to the particle mass, whereas the number of hits is proportional to the particle number density. For both series the particle size distribution is the same, the difference lies in the particle number density in the aerosol. As a consequence, much fewer hits are observed at 2 µg/m^3 than at 60 µg/m^3, but their intensity is of the same order of magnitude.

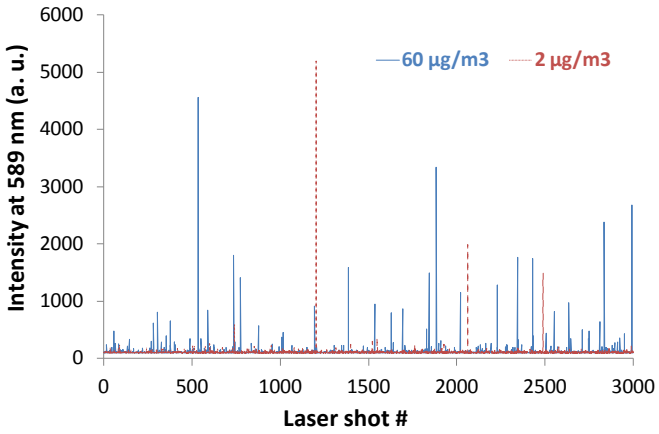

FIG. 5. Single shot measurements of the intensity at 589 nm for two sodium concentrations in the aerosol, 2 and 60 µg/m^3.

From those series, the analytical signal can be calculated using the conditional analysis methodology briefly described in section 2.2. This signal is plotted against the sodium mass concentration in the aerosol on Fig. 6. The confidence hyperbolas with a 95% confidence interval are also shown. They are calculated using the variance-weighted data. The error bars represent one standard deviation calculated from the five replicas at each concentration. We see that the calibration line obtained is very linear, with satisfactory accuracy and repeatability of the measurement. The detection limit of sodium is found to be 4 µg/m^3 in our experimental conditions. This is significantly lower than the detection limit of current Na101 systems used for sodium aerosol détection in the ambient air, which is closer to 100 µg/m^3. Our objective in terms of detection sensitivity was then successfully achieved. The continuation of this work will now focus on the enhancement of the LIBS system robustness, taking into account the constraints of a possible implementation in an SFR (industrial conditions, laser safety…). Indeed, the measurements presented here were obtained using a laboratory system. As the sodium doublet at 589 nm is free from spectral interferences, it is possible to implement a detection system using an interference filter at the sodium wavelength and a photomultiplier instead of the traditional combination of a monochromator and an intensified CCD. This option will be simpler and

more robust, hence more suitable for measurements in industrial conditions inside a nuclear facility. This new detection system will be tested in the near future.

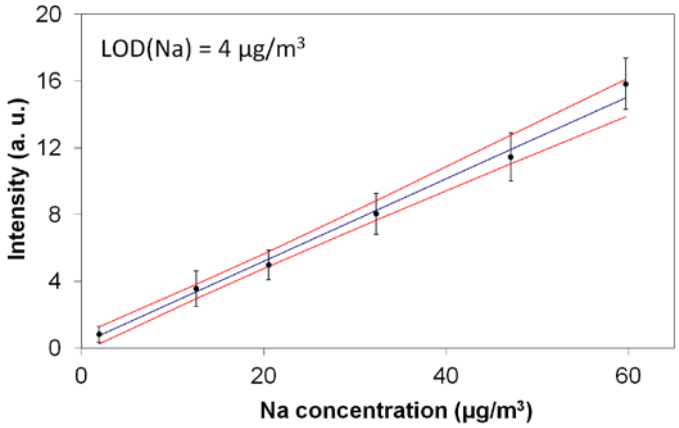

FIG. 6. Calibration by LIBS of sodium concentration in a $NaHCO_3$ aerosol.

4. Conclusion

The laser-induced breakdown spectroscopy (LIBS) technique was investigated as a tool to enhance the safety of sodium-cooled fast nuclear reactors in two ways. First, it was tested to monitor online and in real time the chemical purity of liquid sodium, in order to detect potential undesirable events. The first LIBS measurements on liquid sodium were reported, using a dedicated sodium oven under argon and a LIBS system at 1 m distance. Quantitation of lead, indium and thallium concentration using the standard addition method was performed, with detection limits of 3 ppm for lead and indium, 4 ppm for thallium, for 3 min 20 s measurements in our experimental conditions. However, as this study was focused on the analysis of elements highly soluble in sodium, which is not the case of the elements of interest, the measurement of insoluble compounds will now be investigated, as well as a model aimed at predicting the detection limit of any element in the sodium matrix. Yet accurate knowledge of the chemical behavior of liquid sodium is lacking and might be improved using online LIBS measurements on dedicated experiments. The next challenge would be to distinguish the impurities diluted fraction from particles in suspension.

Secondly, LIBS was implemented for sodium particles monitoring. The objective here was to test a new technique to detect the presence of a sodium aerosol in the ambient air in case of a leakage from a pipe transporting the coolant. Using an aerosol generator and a LIBS laboratory configuration, we found a detection limit for sodium of 4 µg/m^3 for 8 min 20 s measurements. This result shows that the technique is well suited for this type of monitoring. The next step will be to enhance the system robustness using a detection system more suitable for measurements in a nuclear facility.

REFERENCES

[1] VIJAYAKUMAR, G., et al., Performance evaluation of PFBR wire type sodium leak detectors, Nucl. Eng. Design, 241 (2011) 2271-2279.
[2] SYLVIA, J. I., et al., Development of sodium leak detectors for PFBR, , Nucl. Eng. Design, 249 (2012) 419-431.
[3] DOIZI, D. et al., Optical on line techniques for nuclear applications. In Advancements in Nuclear Instrumentation Measurement Methods and their Applications (ANIMMA), 2nd

International Conference (2011), p. 1–6.

[4] MIZIOLEK, A.W. et al., Laser Induced Breakdown Spectroscopy. Cambridge University Press (2008).

[5] MAURY, C., Innovative analytical spectroscopy for improvement of sodium-cooled fast nuclear reactors safety, PhD Thesis, University Pierre and Marie Curie, Paris (2012) (in French).

[6] HAYES, D. J., Instrumentation for liquid sodium in nuclear reactors. Journal of Physics E: Scientific Instruments, 7 (1974) 69–75.

[7] YAMAMOTO, H., et al., Measurement Of Impurity Concentration In Sodium By Automatic Plugging Indicator. Journal of Nuclear Science and Technology, 14 (1977) 452-456.

[8] BORGSTEDT, H. U., MATHEWS, C. K., Applied Chemistry of the Alkali Metals. Plenum Press, New York (1987).

[9] HAHN, D.W. et al., Discrete particle detection and metal emissions monitoring using laser induced breakdown spectroscopy, App. Spectrosc. 51 (1997) 1836-1844.

[10] CREMERS, D. A., et al., Handbook of Laser Induced Breakdown Spectroscopy. John Wiley & Sons LtD, Chichester (2006).

Intermediate Heat Exchanger (IHX) Trade Study in Support of Advanced Fast Reactor-100 Development

M. T. Farmer and C. Grandy

Argonne National Laboratory,
9700 South Cass Avenue
Argonne, IL, 60439 U.S.A.

Presented by M. T. Farmer

Abstract. Reactor fabrication costs are closely linked to the commodities utilized in their construction. One large component of many pool-type sodium fast reactor designs that can significantly impact the overall size of the reactor vessel is the Intermediate Heat Exchanger (IHX). On this basis, a trade study was performed to evaluate four different types of novel IHX designs from the viewpoint of minimizing the impact on the size of the reactor. The four designs that were evaluated as part of this study were: i) conventional shell-with-straight tube design, ii) shell with twisted tube design, iii) Printed Circuit Heat Exchanger (PCHE), and iv) a spiral tube design. The approach was to develop simple thermal-hydraulics models in order to provide a technical basis for assessing the overall size of the units. Simple mechanical stress models were also developed so that component thicknesses could be calculated. This allowed material volumes and commodities for the various designs to be estimated. The results indicate that adopting a twisted vs. straight tube design can reduce commodities by ~ 30 %, and overall height of the units by roughly 30-40%. Aside from the choice of tube design, geometry also plays an important role in reducing commodity and space requirements; i.e., commodities for a kidney-shaped design were found to be ~10% less relative to the circular case, and the reduction is even more (~20%) for an annular design. If a kidney-shaped design is adopted, then the radial thickness of the vessel occluded by the IHXs can be reduced by 20%. Conversely, the reduction for annular designs approaches 75%. Height requirements are also reduced, and this is principally due to the smaller radius of the elliptical heads that are required in the radially thinned designs. Additional costs that may be incurred by fabricating a more complex design have not been factored into these analyses.

Introduction

In terms of fast reactor design development, IHXs for both loop and pool-type plant concepts have received considerable attention since these are large thermo-mechanical devices that occupy a substantial amount of space within the reactor vessel for pool-type plants, and similarly, a substantial amount of floor space on the reactor deck for loop-type plants. Furthermore, they require a large investment in construction materials (e.g., steel) to fabricate. Due to these space and commodity requirements, several different IHX design concepts have been proposed and analysis and testing programs have been carried out to support these concepts. One potential innovation is the use of ferritic steels with increased thermal conductivity that minimizes the heat transfer area required to achieve a specific thermal rating.[1] These materials are also desirable since they have lower thermal expansion coefficients in comparison to the austenitic steels, which translate into reduced design requirements to accommodate thermal stresses.

[1]The thermal conductivity of ferritic steels (e.g. 2-1/4 Cr–1 Mo) is ~ 40 % higher compared to stainless steels at 500 ºC.

A second innovation, proposed for the GE-PRISM concept [1], was the use of kidney-shaped units that fit more compactly within the annular cold-pool region that surrounds the reactor core in most pool-type plant designs. Although this approach has the desired effect of reducing the size of the reactor vessel required to accommodate the IHXs, the unique planar cross section will produce more complex flow behavior in both the inlet and exit plenums on the primary and secondary sides of the unit relative to traditional cylindrical IHX designs. Substantial analysis and testing activities were carried out to develop plenum designs that produced uniform inlet and exit patterns on both the shell and tube sides of conventional (circular) IHXs. Although these designs are reasonably mature, additional work may be required if non-symmetric IHX planar designs such as those proposed in the current study are adopted in the future. In this regard, advanced CFD tools that are able to analyze flow behavior in complex geometries may be useful in supporting the development of plenum designs that produce well-defined flow patterns.

A third issue is longevity. If robust IHX designs that would reliably function over the entire plant life could be developed, then the IHX could be made a permanent part of the reactor vessel internal structure. This would yield a more compact primary plant configuration. A review of the technology indicates that IHXs have performed with a quite high level of reliability in sodium fast reactor plants that have been operated around the world, and thus it seems prudent to capitalize on this success in future fast reactor concepts in terms that minimize the impact of the IHX on the plant configuration.

The remainder of this paper analyzes four potential IHX options for advanced pool-type fast reactor designs. To that end, various IHX design options and tradeoffs are discussed first. Modeling used to analyze the concepts is then summarized, followed by presentation and discussion of the analysis results. The paper concludes with a summary of the findings.

IHX Design Options

The objective of this trade study was to evaluate four IHX design options identified for potential deployment in an advanced sodium fast reactor system with the intent of minimizing the impact on the overall size of the reactor. The study focuses on pool-type plant configurations. Aside from potential size reductions, the designs are also evaluated from the viewpoint of maintaining key IHX functional requirements which include low pressure drop and preservation of natural convection flow paths under shutdown heat removal conditions. As noted above, three ideas have already been identified that reduce the space that IHXs occupy in pool plant configurations: i) high thermal conductance materials, ii) kidney-shaped planar construction, and iii) IHXs that are made as permanent installations. This study builds upon these notions, as well as evaluating other types of novel concepts for potential deployment. Thus, extending the GE approach, one case considers a full annular design that is integrated into the redan[2]. This approach effectively mandates that the units are permanent installations. The units are also assumed to be made from ferritic steel that has a higher thermal conductivity in comparison to austenitic steels. With these innovations as the starting point, the specific IHX designs that are evaluated as part of this study include: i) conventional shell-with-straight tube design, ii) shell with twisted tube® design, iii) Printed Circuit Heat Exchanger (PCHE), and iv) a spiral tube design.

The conventional shell and tube type heat exchanger has been deployed in many fast reactor applications, but not in an annular configuration as investigated as part of this work. This concept consists of a number of round tubes attached to a tubesheet inside a cylindrical vessel, with tube size, tube length, and total number of tubes varying depending on the system requirements. The tube bundle normally contains a number of baffles to accomplish the dual objectives of providing a support structure for the tubes, and to direct the shell-side flow across the tubes rather than along the tubes. The resulting cross-flow on the shell side yields a relatively high pressure drop because energy is used

[2]Redan is a term commonly used to refer to the mechancial structure separating the hot and cold pools in pool-type plants.

to reverse the flow rather than to enhance heat transfer. Finally, fluid flow around the baffles can be non-uniform resulting in areas of low flow and dead spots. In other applications this can cause fouling accumulation, corrosion, and poor heat transfer.

The Twisted Tube® heat exchanger [2] originated in Eastern Europe and became commercially available in Sweden in the mid 1980's. This concept was developed to overcome inherent limitations with conventional shell and tube designs that were noted above. Applications have principally been in areas involving single phase and condensing flows in the pulp and paper industries, as well as chemical process industries. The twisted tube concept consists of a tube bundle assembled from uniquely formed tubes in an arrangement that does not use baffles; see Figure 1. The tubes are formed into an oval cross section with a superimposed helical spiral in the axial direction of the bundle. The tube ends are round to allow conventional tube-to-tubesheet joints. A wide range of tube materials have been used including carbon and stainless steels, Cr-Mo alloys, duplex and super duplex alloys as well as exotic metals such as titanium, zirconium and tantalum. Tube sizes may vary from 1.3 cm to 2.5 cm. The tubes are assembled such that the twists are aligned at every plane along the bundle length, resulting in tubes contacting adjacent tubes at many points. This minimizes flow-induced vibration issues. The shell-side flow path is complex and predominantly axial in nature. The twisted tube design imparts a swirl flow on both the shell and tube sides of the unit that enhances the heat transfer relative to that achieved in traditional parallel flow heat exchanger designs [2,3]. To the best of our knowledge, the twisted tube concept has not been previously employed in fast reactor applications.

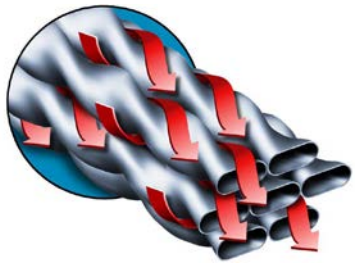

Figure 1 - Illustration of Twisted Tube Bundle Arrangement

Printed Circuit Heat Exchangers (PCHEs) [4] are characterized as high integrity plate type heat exchangers. They are fabricated from flat metal plates (sheets) that have fluid flow channels that are chemically etched using the same process developed for electronic printed circuit board production. The etched plates are stacked and diffusion bonded together to make the core of the heat exchanger. PCHEs can be made of one or several cores welded together to suit the duties required. Headers and nozzles are attached to the core(s) to complete the exchanger. PCHEs are compact and robust, and can achieve high thermal effectiveness of over 98% depending on the process. These units can be four to six times smaller than conventional shell and tube heat exchangers of the equivalent duty cycle, and they have pressure and temperature capabilities in excess of 600 bar and 900°C, respectively. This technology has been deployed in the hydrocarbon processing, oil platform, and oil refining industries. In terms of nuclear applications, the technology has been considered for use as recuperator and cooler modules in advanced CO_2 Brayton cycle power conversion systems, and has recently been evaluated for potential use an IHX for the Lead Fast Reactor (LFR) system [5]. This design can have space and weight advantages, reducing exchanger size together with piping and valve requirements. However, the diffusion bonding method used to manufacture these units leads to size restrictions and, therefore, maximum duty cycle ratings that can limit the range of applicability in large thermal process systems.

The spiral tube heat exchanger concept has also been considered for deployment in the LFR [5]. In industrial applications [6], this design typically features a coil assembly fitted in a compact shell that is intended to optimize heat transfer efficiency and space. The spiral coil assembly is welded to inlet and exit manifolds that in turn are welded to a head and fitted in a compact shell. The gaps between the coils of the spiral bundle become the shell side flow path. As for the twisted tube design, the spiral creates circulating flow patterns that enhance the heat transfer on both the shell and tube sides. The profile of a spiral tube heat exchanger is compact and can generally be accommodated within a smaller footprint relative to a traditional shell and tube design. Since the bundle is coiled, space requirements for bundle removal are reduced. A spiral design also tends to minimize material usage since the

manifolds replace the heads and tube sheets that are used in conventional shell and tube units. The shell side is usually smaller than a comparable shell and tube design and there are no requirements for tube supports or baffle plates.

Summary of Modeling Approach

Heat Transfer and Pressure Drop Analysis

Thermal-hydraulics models for a counter-current flow, shell-and-tube type heat exchanger were developed in order to provide a technical basis for assessing both straight- and twisted-tube IHX designs. For the purposes of this study, the primary sodium flow was assumed to be on the shell side while secondary sodium occupies the tube side. Given the unit thermal power rating as well as the temperature differentials on the primary and secondary sides, the models calculate the required IHX tube length given other input parameters (i.e., number of tubes as well as the tube thermal conductivity, OD, and pitch). The tube wall thickness was evaluated as part of the IHX structural modeling.

The particular form of the heat transfer coefficient depends upon whether the IHX is a straight- or twisted-tube design. For straight tubes, the convective heat transfer coefficients were evaluated using the classic Martinelli correlation that was developed for liquid metal flow in tubes. For spiral tube configurations, the heat transfer correlations on both the shell and tube sides were modified to reflect the increased mixing associated with the swirling flow behavior within the bundle. On the tube interior, the heat transfer correlation recommended by Dzyubenko et al. [3] is of the form:

$$h_i = 0.072\,\mathrm{Re}^{0.76}\,\mathrm{Pr}^{0.4}\,\Omega^{0.16}\,\frac{k}{D_{H,i}} \tag{1}$$

Where *Re* and *Pr* and the fluid Reynolds and Prandtl numbers, respectively, *k* is thermal conductivity, $D_{H,i}$ is the tube interior hydraulic diameter,

$$\Omega = \left[0.5 + \frac{8}{\pi^2}\left(\frac{s}{2D_{H,i}}\right)\right]^{-1}, \tag{2}$$

and *s* is the twist pitch of the tube bundle (the axial distance at which the twisted tube has undergone a 360˚ rotation; see Figure 1). Optimal twist pitch-to-diameter ratios for these types of bundles are reported [3] to be in the range of $P/D_{T,o}$ = 6 – 12 (see Figure 2 for pitch definition and general nomenclature used in the following). There are several different types of tube geometries used in these units; for the purposes of this study, the tubes were taken to be oval. For this geometry, the hydraulic diameter on the interior of the tube can be deduced from the general definition as:

$$D_{H,i} = \frac{\pi D_{T,i}^2 + 4\zeta D_{T,i}}{\pi D_{T,i} + 2\zeta} \tag{3}$$

On the shell side of the twisted bundle, a modified version of the Dittus-Boelter correlation is employed [3]; i.e,

$$h_o = 0.023\omega\,\mathrm{Re}^{0.8}\,\mathrm{Pr}^{0.4}\,\frac{k}{D_{H,o}} \tag{4}$$

where:

$$\omega = 1 + 3.6\left(\frac{s^2}{D_{T,o}D_{H,o}}\right)^{-0.357} \tag{5}$$

For triangular-pitched arrays in which the total width of the oval tubes equals the lateral separation (i.e., W=L in Figure 2), the hydraulic diameter on the shell side is deduced as:

$$D_{H,o} = \frac{4D_{T,o}^2\left(\frac{\sqrt{3}}{2}\beta^2 - \frac{\pi}{4} + 1 - \beta\right)}{D_{T,o}\left[\pi + 2(\beta - 1)\right]} \tag{6}$$

where $\beta = P / D_{T,o}$ is the tube pitch-to-diameter ratio for the bundle.

Aside from the shell and tube side convective heat transfer coefficients, the thermal resistance between the two fluid streams is also a function of tube wall thermal resistance (i.e., k/t_w). As part of this work, the wall thickness was evaluated as part of a simple stress analysis given a peak differential pressure that the secondary side of the unit must tolerate due to a postulated sodium-water reaction (for Rankine steam cycle power conversion system) or CO_2 leak event (for a supercritical CO_2 Brayton cycle power converter).

The particular form of the equations used to evaluate pressure drop across the shell and tube sides is dependent upon whether or not a straight or twisted-tube IHX design is considered. Pressure drop on the tube side was calculated using the standard Bernoulli equation modification to account for frictional drag as well as tube bank entrance and exit form losses.

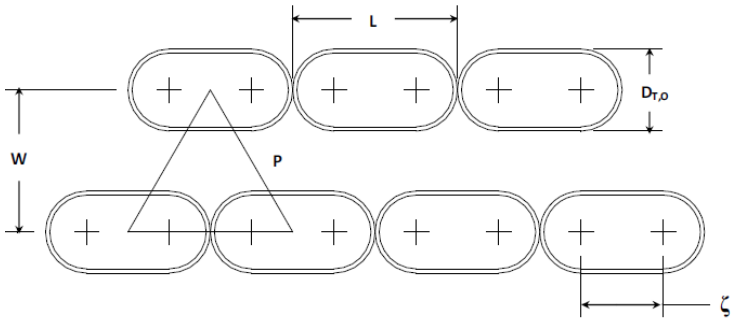

Figure 2 - Nomenclature for Twisted Tube Geometry.

The pressure drop analysis on the shell side is complicated by the fact that an orificed baffle plate design was used for straight tube cases in order to minimize pressure drop while obtaining a fairly uniform flow pattern within the bundle. Orificed baffle plates were also used in the GE-PRISM IHX design [1]. Although well-established correlations have been developed for evaluating pressure drop for the case of impervious plates (e.g., see Kern [7]), suitable correlations for the case of orificed plates could not be identified in the open literature. On this basis, a correlation was developed and validated against the pressure drop data for the kidney-shaped GE-Prism Mod B IHX design which also utilized orificed baffle plates; the agreement was within 8 % of the GE estimate.

For the twisted tube design, pressure losses on both the shell and tube sides are increased relative to straight tube non-baffled case as a result of the additional turbulence imparted to the flow fields. On the tube side, the total pressure drop along the bundle is calculated using the Bernoulli equation, but with the friction factor calculated from the modified expression [3]:

$$f = \frac{0.71}{\mathrm{Re}^{0.2}}\Omega^{0.27} - 0.008\Omega^{0.67} \tag{7}$$

Pressure drop on the shell side is calculated in a similar manner, but with the friction factor evaluated from a modified version of the Blausius correlation [3]:

$$f = \omega\frac{0.3164}{\mathrm{Re}^{0.25}} \tag{8}$$

where ω is given by Eq. 5.

Structural/Commodities Analysis

One of the key objectives of the trade study was to determine the extent that commodities such as steel mass could be reduced or minimized through various design alternatives. Thus, component thicknesses for the IHX were evaluated on the basis of simple stress equations given a design pressure escalation ΔP in the secondary system due to a postulated boundary failure event in the power conversion system. The stress equations for various components were taken from [8]. For example, given the IHX tube OD and pitch specified as part of the problem input, the minimum tube wall thickness was evaluated from:

$$t_w = \frac{\Delta P}{\sigma_{\max}}\left[1+\frac{\Delta P}{\sigma_{\max}}\right]^{-1} R_{T,o} \tag{9}$$

where σ_{max} is the maximum allowable tensile stress in the tubing material. Similar expressions were utilized to calculate material thicknesses for other structural members such as the tube sheets, IHX shell, and the elliptical heads. The downcomer and return line piping wall thicknesses also need to be specified. In liquid metal systems, it is customary to specify a maximum pipe flow velocity[3] below which issues such as erosion and flow-induced vibration are suppressed. This velocity limit, in conjunction with the required mass flow rate of sodium to achieve a given thermal rating, allowed pipe ID's and thereby wall thicknesses to be determined. This result, along with the overall length of the IHX that was principally determined by the tube length, allows the total volume of commodities to be evaluated based upon the particulars of the IHX design. Given the material densities for the various components, the commodity masses could then be calculated.

Results and Discussion

Straight- and Twisted-Tube IHX Designs

The baseline design data assumed in these calculations for both the straight and twisted tube designs are provided in Table 1. All calculations were carried using basic design data (i.e. thermal power level and temperature differentials on the primary and secondary sides) consistent with that used for the Advanced Burner Test Reactor (ABTR) design [9]; see Table 1. This is a 250 MWt (95 MWe) plant in which the IHXs are fabricated from 9Cr-1Mo steel to capitalize on the increased thermal conductivity of this material. In terms of mechanical properties required to estimate commodities, the maximum tensile stress and densities were taken equal to σ_{max} = 110 MPa and ρ = 7900 kg/m^3, respectively. The design pressure loading due to a postulated pressure excursion on the secondary side is assumed to equal ΔP = 6.8 MPa (1000 psig), which is the same as that used in the GE Prism concept [1]. The thickness of the sodium stagnant zone protecting the upper and lower tubesheets from thermal transients is assumed to be 30 cm. The thermophysical properties of sodium assumed in the analysis are also provided in Table 1.

For the straight tube design, tube diameter was selected to 1.59 cm, with the tube pitch-to-diameter set at 1.4. In addition, orificed baffle plates are used with inter-plate spacing, number of holes, and hole diameter kept the same as that used in previous IHX design studies [9].

Given the tube eccentricity for the twisted tube concept, it is not readily clear how to design the bundle so that thermalhydraulic results for the twisted- and straight-tube designs can be directly compared. Thus, the basis chosen here is to approximately preserve the surface flow areas for the two designs, factoring in the eccentricity of the twisted tubes. Under this assumption, the equivalent diameter of the twisted tube is calculated from:

[3]Based on historical experience, a typical peak sodium pipe flow velocity is ~6 m/sec. From a corrosion standpoint, there does not seem to be a velocity dependance above ~4 m/s. To preclude cavitation, the maximum velocity is ~10 m/s.

$$\frac{\pi}{4} D_{straight}^2 = D_{twist}^2 \left(\frac{\sqrt{3}}{2} \beta^2 - \frac{\pi}{4} + 1 - \beta \right)$$

Selecting the tube eccentricity for the twisted case to be $\zeta = D_{T,o}$, then P = $2D_{T,o}$ and so $\beta = P / D_{T,o} = 2$. With these assumptions, the equivalent diameter of the twisted tube is found from the above expression as $D_{twist} = 0.686 \bullet D_{straight} = 1.09\ cm$. With this approach, the unit cell area for a given tube is approximately the same for the twisted and straight designs, and so tube sheet areas are approximately equal for a specified number if IHX tubes.

Table 1 - Baseline Design Data for Straight and Twisted-Tube IHX Designs

Parameter	Value for IHX design:	
	Straight tube	Twisted tube
Tube outer diameter	1.59 cm	1.09 cm
Tube eccentricity, ζ /P	0	1
Tube cross-sectional area	2.0 cm^2	2.0 cm^2
Tube pitch	2.23 cm	2.18 cm
Pitch/diameter ratio, $P/D_{T,o}$	1.4	2.0
Tube twist pitch, s/P	N/A	12
Buffer distance protecting upper and lower tubesheets, L_{dead}	30 cm	30 cm
Shell baffle plates – thickness	6.4 mm	N/A
Shell baffle plate spacing	91 cm	N/A
Baffle plate cut dist. across IHX not occluded by plates)	50 %	N/A
Baffle perforation (open flow area/ total axial flow area)	45%	N/A
Perforation hole diameter	8.12 mm	N/A
Number of perforation holes per IHX tube	2	N/A
Tube material	9Cr-1Mo	9Cr-1Mo
Primary sodium temperature inlet	510 ˚C	510 ˚C
Primary sodium temperature outlet	355 ˚C	355 ˚C
Secondary sodium temperature outlet	333 ˚C	333 ˚C
Secondary sodium temperature inlet	488 ˚C	488 ˚C
Sodium thermal conductivity, *k*	69.4 W/m-K	69.4 W/m-K
Sodium specific heat, *c*	1283 J/kg-K	1283 J/kg-K
Sodium density, ρ	832 kg/m^3	832 kg/m^3
Secondary viscosity, μ	$2.76 \cdot 10^{-4}$ kg/m-s	$2.76 \cdot 10^{-4}$ kg/m-s

The various cases that are considered for the tradeoff study are summarized in Table 2. In terms of geometric assumptions, a traditional straight tube, cylindrical IHX design is considered as the reference Case 1. A twisted tube variation (Case 2) of the cylindrical design is also evaluated. Following the GE approach [1], kidney-shaped straight (Case 3) and twisted tube (Case 4) designs are also considered. For the kidney geometry, the annular thickness of the units must be specified, and in this study that thickness is taken equal to 1.0 m. For these four cases, two discrete IHXs are assumed to be deployed inside the reactor, each of which has a thermal duty rating of 125 MW.

Finally, annular designs are considered for which the IHXs occupy the full 360˚ perimeter of the vessel, and these units are assumed to be constructed as an integral component of the redan. The inner diameter of the IHX is set equal to the assumed redan OD (for this work, taken as 3.9 m), and the outer diameter is then calculated given the tube sheet area. For these cases, the radial thickness of the units is relatively thin, which can constrain the size of a circular downcomer that can be placed in the unit. To minimize the downcomer size, a total of 4 supply/return lines are assumed; each set serves a 90˚ sector of the IHX assembly. Thus, the calculations are carried out for one of these 90˚ sector units, and the other three units are assumed to be identical in design. Cases 5 and 6 for the annular design consider straight and twisted tube variants, respectively.

In terms of the approach for carrying out the parametric calculations, the number of heat exchanger tubes is treated as the independent variable. The required tube length is then calculated as the key model output, and the minimum heat exchanger cross-sectional area is given by tube unit cell cross-sectional area multiplied by the total number of tubes. This approach provides the overall heat exchanger size to be selected on the basis of the available cross sectional area, or the available elevation space, whichever is desired. Component thicknesses and volumes are evaluated along with the sizing calculations so that a cumulative mass estimate can be provided.

Table 2 - Principal Cases and Results of IHX Tradeoff Study

Case No.	Cross-Section	Tube Type	Rating (MW)	No. of Units	Active Tube Length (m)	Overall Unit Height (m)	Radial Depth (m)	Mass per Unit (kg)	% mass of ref.	% heigh t of ref.	% radial depth of ref.
1 (ref)	Circular	straight	125	2	3.61	5.20	1.27	16,420	100	100	100
2	Circular	twist	125	2	1.70	3.26	1.24	11,346	69	63	98
3	Kidney	straight	125	2	3.61	5.01	1.02	14,906	91	96	80
4	Kidney	twist	125	2	1.70	3.09	1.02	10,280	63	47	80
5	Annular	straight	62.5	4	2.07	2.95	0.35	12,920	79	57	28
6	Annular	twist	62.5	4	1.18	2.05	0.34	9,120	56	39	27

Typical results are illustrated in Figure 3 for the Case 1. Results include: i) active and total HX tube length, ii) tube sheet planar area, iii) component thicknesses, iv) ΔP on primary and secondary sides, v) component as well as cumulative unit mass, and finally vi) overall unit dimensions, both in terms of height and radial thickness occupied in the reactor vessel. In terms of making a comparison between the various designs, each unit is assumed to be composed of 2500 tubes. This number is chosen since it is reasonable for fabrication. In addition, for the annular designs, the resultant radial thickness of the tube sheet is large enough to accommodate the 30 cm OD downcomer that is required to maintain sodium flow velocity in the pipe below the 6 m/sec threshold assumed in this analysis.

The calculated overall dimensions and mass of the IHXs for the various cases are shown in Table 2. For comparison, key results (total mass, height, and radial thickness of the units) have been normalized by reference case values to provide a sense of commodity reductions that can be achieved through the various design choices. For each geometry, adopting a twisted vs. straight tube design reduces commodities by roughly 30%, while overall height of the units is reduced by roughly 30-40%. This is due to the fact that the twisted design increases convective heat transfer coefficients on both the shell and tube sides of the unit considerably (see modeling description). The degree of reduction is also a function of tube wall thermal heat transfer resistance, which for these calculations is quite low due to the fact that the tube wall thickness required to tolerate the design pressure transient of 6.8 MPa due to a SWR is thin. If additional thickness is added to accommodate manufacturing tolerances and/or corrosion, then the relative reduction would be reduced for the twisted design option.

Aside from the choice of tube design, geometry also plays an important role in reducing commodity and space requirements for the IHXs. For instance, the amount of steel required for kidney-shaped designs is ~ 10 % less relative to the circular cases, and the reduction is even more (~ 20 %) for the annular design. This is due to the fact that the required tube sheet thicknesses are significantly reduced since the critical width (i.e., annular thickness) that determines plate strength is reduced. If a kidney-shaped design is adopted, then the radial thickness of the vessel occluded by the IHXs can be reduced by 20 %. Conversely, the reduction for annular designs approaches 75 %. The required height is also reduced, and this is principally due to the smaller radius of the elliptical heads on the units that are required in the radially thinned designs. An idea of the degree that commodities can be reduced with this approach is provided in Figure 4, which shows an elevation view on an annular twisted-tube IHX deployed in the AFR-100 [10].

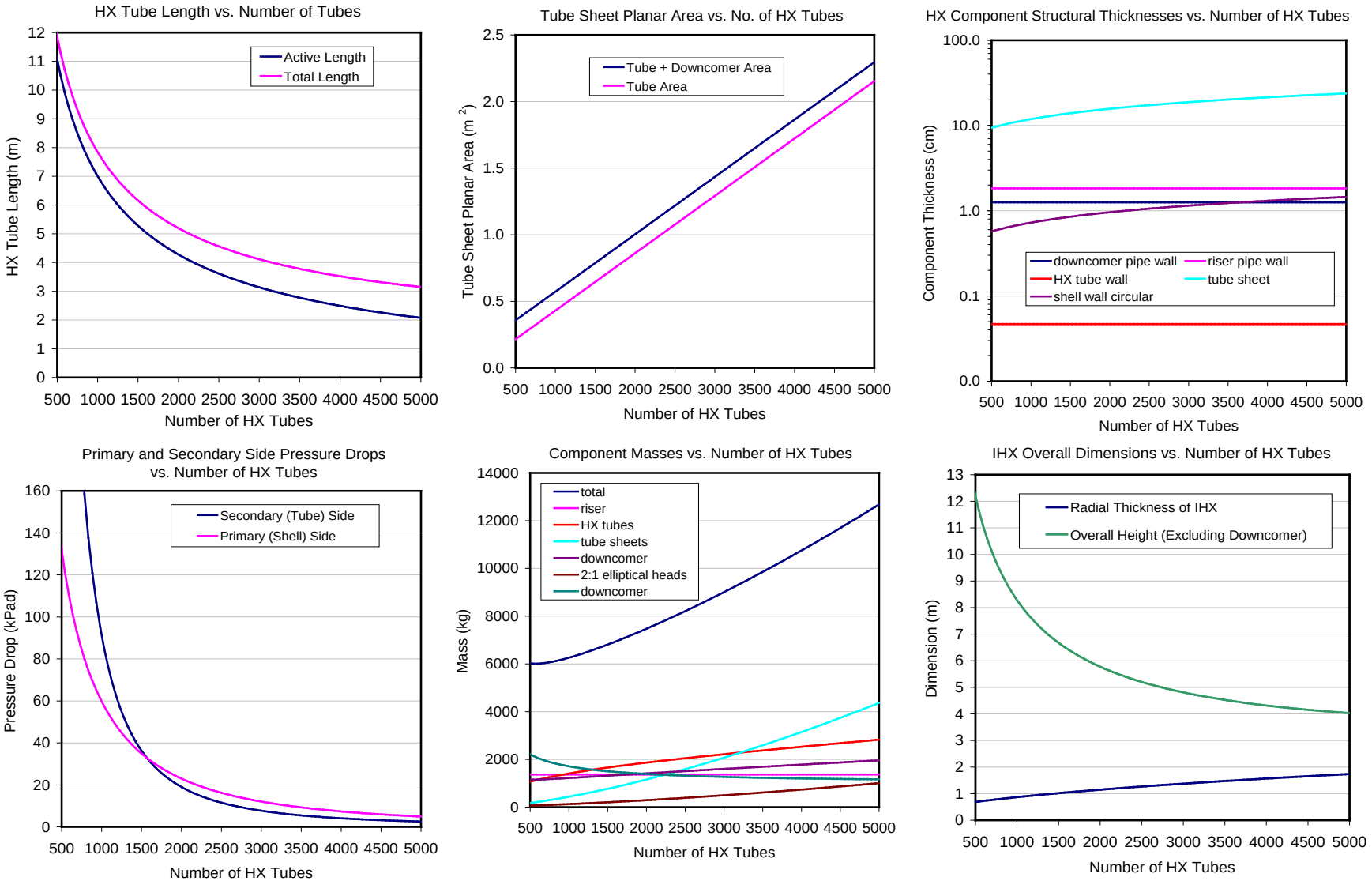

Figure 3 - Principal IHX Design Results for Case 1: Circular Straight Tube Design (data for each of 2 units)

PCHE and Spiral Tube IHX Designs

Two other IHX design options have been identified that may provide promise in future fast reactor designs; i.e. the spiral tube [6] and PCHE [4] options. Although detailed assessments of these options were not completed as part of this study, a qualitative discussion regarding their potential utilization is provided below.

As noted in Section 1, PCHEs [4] are characterized as high integrity plate type heat exchangers that are fabricated from flat metal plates (sheets) that have fluid flow channels that are chemically etched using the same process developed for electronic printed circuit board production. These units can be four to six times smaller than conventional shell and tube heat exchangers of the equivalent duty cycle, and so they may offer an attractive design alternative. However, one potential drawback is that the diffusion bonding manufacturing process for PCHE's limits the maximum thermal capacity for a single unit to the order of tens of MWt. Thus, this option would require a fairly extensive array of headered supply and return piping lines to the PCHEs. This may be practical for loop designs in which the IHXs are not located inside the reactor vessel, but for pool concepts, installation may be problematic. Additional work on how the PCHEs would be configured and piped together inside the vessel for pool plant designs is warranted.

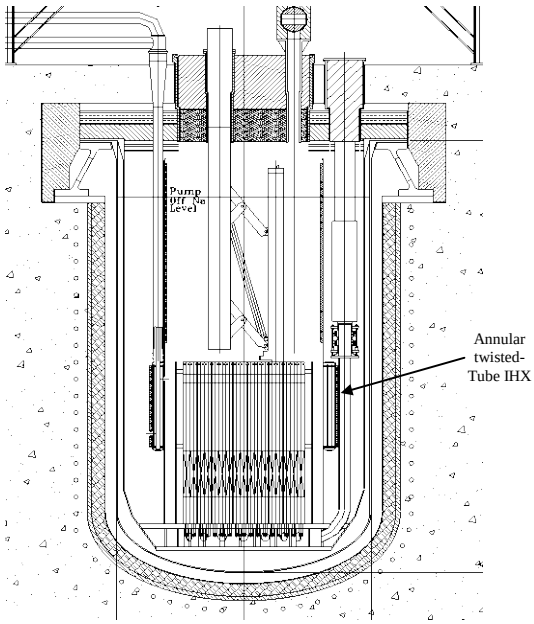

Figure 4 - Illustration of Annular Twisted Tube IHX Deployed in the AFR-100 [10].

The spiral tube heat exchanger concept has been proposed for lead fast reactor systems [5]. In industrial applications [6], this design typically features coiled assemblies that fit in a compact shell that is intended to optimize heat transfer efficiency and space. The coils are welded to inlet and exit manifolds that in turn are welded to a head and fitted in the shell. The spiral design also could limit material usage since the manifolds replace the heads and tubesheets that are used in conventional shell and tube designs. The coils could effectively replace the annular tube configuration considered in the previous section. However, one potential drawback is that the flow across the tube bank would be in cross-flow. This is generally a higher pressure drop option when compared with parallel flow tube designs. Thus, this configuration needs to be analyzed to determine if the bundle size required to remove fission heat under full power operations would inhibit natural convection cooling under shutdown heat removal conditions.

Summary

The objective of this trade study was to evaluate four different types of novel IHX designs for potential deployment in an advanced sodium fast reactor system with the intent of minimizing the impact on the overall size of the reactor. This study focused on pool-type plant configurations. The four designs that were specifically evaluated were: i) conventional shell-with-straight tube design, ii) shell with twisted tube design, iii) Printed Circuit Heat Exchanger (PCHE), and iv) spiral tube design. The approach was to develop simple thermalhydraulics models for a counter-current flow, shell-and-tube type heat exchanger in order to provide a technical basis for assessing both straight- and twisted-tube designs. For a given thermal power rating and temperature differentials on the primary and secondary sides, the model calculates the required IHX tube length, as well as the mechanical design characteristics (i.e., the number of tubes, as well as the tube thermal conductivity, pitch, diameter, and wall thickness). Additional models

were developed for evaluating primary and secondary side pressure drops across the tube bank. Finally, simple mechanical stress models were developed so that component thicknesses could be calculated. This allowed material volumes and thereby commodity requirements for the various designs to be estimated. For the PCHE and spiral tube IHX options, the evaluation was limited to a qualitative discussion regarding the practicality of deploying these types of designs in advanced fast reactor concepts.

The results indicate that adopting a twisted vs. straight tube design can reduce commodities by ~ 30 %, and overall height of the units by roughly 30-40 %. This is due to the fact that the twisted design considerably increases convective heat transfer coefficients on both the shell and tube sides of the unit. Aside from the choice of tube design, geometry also plays an important role in reducing commodity and space requirements. In particular, the amount of steel required for a kidney-shaped designs was found to be ~ 10 % less relative to the circular case, and the reduction is even more (~ 20 %) for the annular design. This is due to the fact that the required tube sheet thicknesses are significantly thinner since the critical width (i.e., annular thickness) that determines plate strength is reduced. If a kidney-shaped design is adopted, then the radial thickness of the vessel occluded by the IHXs can be reduced by 20 %. Conversely, the reduction for annular designs approaches 75 %. The required height is also reduced, and this is principally due to the smaller radius of the elliptical heads on the units that are required in the radially thinned designs.

ACKNOWLEDGEMENTS

This work was performed under the auspices of the U.S. Department of Energy's Advanced Reactor Concepts program. The authors greatfully acknowledge the support provided by DOE especially our sponsors Brian Robinson, Craig Welling, and Thomas O'Connor.

REFERENCES

1. W. Kwant and C.E. Boardman, "PRISM-Liquid Metal Cooled Reactor Plant Design and Performance," Nuclear Engineering and Design, Vol. 136, pp. 111-120 (1992).
2. www.kochheattransfer.com
3. B. V. Dzyubenko, L. –V. Ashmanta, and M. D. Sehgal, Modeling and Design of Twisted Tube Heat Exchangers, Begall House, Inc., New York, NY, 2000.
4. X. Li, R. Le Pierres, and S. J. Dewson, "Heat Exchangers for the Next Generation of Nuclear Reactors," Paper 6105, 2006 International Congress on Advances in Nuclear Power Plants (ICAPP '06), Reno, June 4-8, 2006.
5. L. Cinotti, C. F. Smith, J. J. Sienicki, H. Aït Abderrahim, G. Benamati, G. Locatelli, S. Monti, H. Wider, D. Struwe, A. Orden, and I. S. Hwang, "The Potential of the LFR and the ELSY Project," Paper 7585, 2007 International Congress on Advances in Nuclear Power Plants (ICAPP 2007), Nice, France, May 13-18, 2007.
6. www.sentry-equip.com
7. D. Q. Kern, Process Heat Transfer, McGraw-Hill Book Co., New York, NY, 1950.
8. R. J. Roark and W. C. Young, Formulas for Stress and Strain, 5th Ed., McGraw-Hill Company, New York, NY, 1975.
9. Y. I. Chang et al., "Advanced Burner Test Reactor Preconceptual Design Report," ANL-ABR-1 (ANL-AFCI-173), September 5, 2006.
10. C. Grandy et al., "Advanced Fast Reactor - 100 - Design Overview," International Conference on Fast Reactors and Related Fuel Cycles: Safe Technologies and Sustainable Scenarios, Paris, France, 4-7 March 2013.

Development of a new electromagnetic flow meter for a fast reactor
Feasibility of EMF composed of multi-unit

T. Asada[a], D. Kittaka[a], M. Komai[a], M. Enomoto[a], H. Ota[a], E. Hoashi[b], S. Suzuki[b], H. Horiike[b], M. Hirabayashi[c], M. Otaka[c], K. Ara[c]

[a] Toshiba Corporation Power Systems Company

[b] Osaka University

[c] Japan Atomic Energy Agency

Abstract We have been developing electromagnetic flowmeters (EMFs) for sodium-cooled fast reactors such as 4S (Super-Safe, Small and Simple). The EMF consists of multi-unit that are composed of M- -shaped electromagnets and electrodes anchored on the outside surface of the annular sodium flow path. The EMF enables calibration in one-unit. One-unit calibration can reduce the size of the calibration facility. A calibration factor in one-unit has to agree with a calibration factor in multi-unit. However, the calibration factors has a difference by some factors. In this study, we optimized the magnetic field and induced current profile so that the calibration factor in one-unit agrees with one in multi-unit. To confirm the optimization, two test devices for sodium experiments were also made. The output flow velocity signals of two apparatuses agree within 1% at the flow velocity of 0.8 m/s. The feasibility of calibration in one-unit was confirmed.

1. Introduction

An electromagnetic flowmeter (EMF) is typically used to measure the flow rate in a sodium-cooled Fast Reactor (SFR). The prototype and commercial SFRs will need higher flow rates and flowmeters which can measure high flow rate. As a result, the cost for the calibration of EMF would become high because the sizeable calibration facility would be necessary. We have been developing EMFs for such SFRs like the 4S (Super-Safe, Small and Simple)[(1)] which has a annular flow path to set an Electomagnetic pump. The EMF is composed of M- -shaped electromagnets anchored to the outside surface of the annular sodium flow path. Six EMF units would be evenly spaced around the annular flow path. If the EMF could be calibrated by one-unit, the amount of sodium required in the calibration facility would be also one-sixth and thus this enables to down the size of facility.

A calibration factor measured in one-unit has to agree with one measured in the multi-unit. However, the calibration factor measured in one-unit is different from the calibration factor measured in multi-unit due to the induced current and the magnetic fields which straddle the neighboring EMFs. In this study, we optimized the magnetic field and induced current profile to minimize neighboring EMF interference using a three-dimensional electromagnetic code, FALCON. To confirm the optimization and analyse the error of MHD simulation, two test devices for sodium experiments were also made and tested: one is a 360-degrees full model with six EMF units, and the other is a 60-degrees-cut model with one EMF unit.

2. New EMF Design

2.1. Structure and Theory

Fig.1 shows the configuration of the EMF. It consists of M--shaped magnetic cores and excitation coils for producing a magnetic field perpendicular to the flow path, and a pair of electrodes for measuring an induced voltage. When sodium passes across the magnetic field formed by three electromagnets, induced current flows in sodium and voltage is induced. The induced voltage is

measured with electrodes and converted to flow rate by a calibration factor: (induced voltage)/(average velocity). This calibration factor needs to be determined through experiment.

Fig.2 shows overviews of multi-unit model applied in the actual FR and one-unit model applied in calbration. Six units would be set in multi-unit model and One-unit model has the one-sixth of annular flow path. We called multi-unit and one-unit models as 360-degrees full model and 60-degrees-cut model respectively.

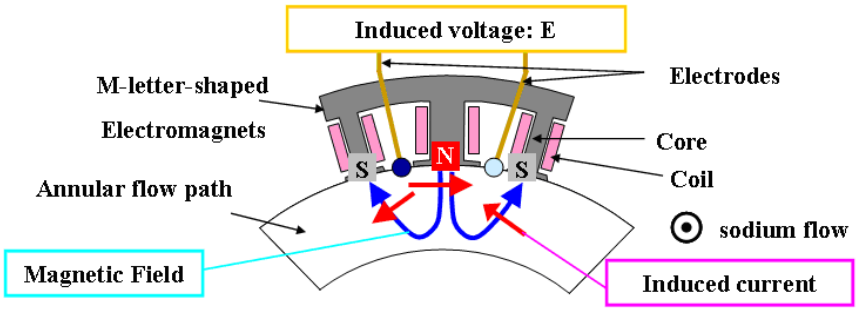

FIG. 1. EMF theory and components

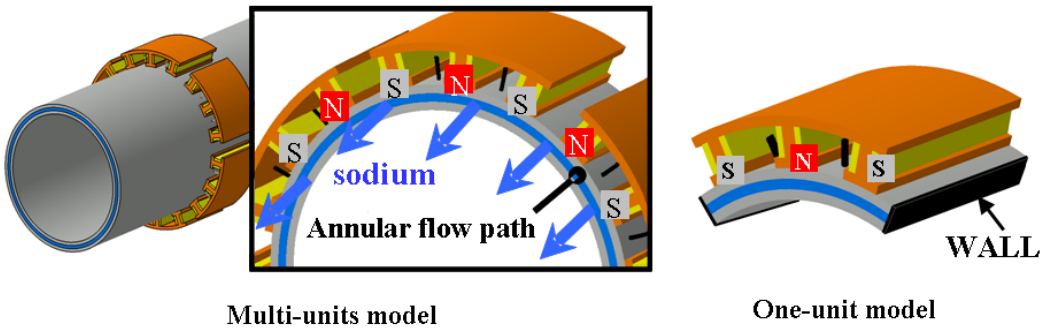

FIG. 2. Two models in measurement and calibration

2.2. Characteristics and Problems

The EMF has two unique characteristics. First, this EMF is applied to measurement of sodium flow rate in annular flow path. Second, calibration of this EMF can be done in one-unit. This EMF is calibrated in one unit to determine a calibration factor and, when this EMF is applied in multiple units to actual flow rate measurement, the same calibration factor can be used.

However, an induced voltage measured by calibration experiments with one-unit is different from one measured in SFRs with multi-unit in conditions of same flow rate. Because there are no neighboring EMFs in 60-degrees-cut model but other EMFs are located next to one EMF in 360-degrees full model. As a result, the magnetic field or induced current profile in 360-degrees full model is different from the profile in 60-degrees-cut model. Therefore we need to reduce the difference of induced voltages between one-unit and multi-unit.

Fig.3 shows two polarity patterns. One is homopolarity which is composed of NSN-NSN polarities. Another is antipolarity which is composed of SNS-NSN polarities. These polarities have different magnetic fields and induced current profile. In case of homopolarity, magnetic field does not straddle both EMFs but induced current straddles to both EMFs. On the other hand, in case of antipolarity, magnetic field straddles to both EMFs but induced current does not straddle to both EMFs. We

calculated two polarity patterns in 360-degrees full model and 60-degrees-cut model and compared their induced voltages and decided better the polarity pattern.

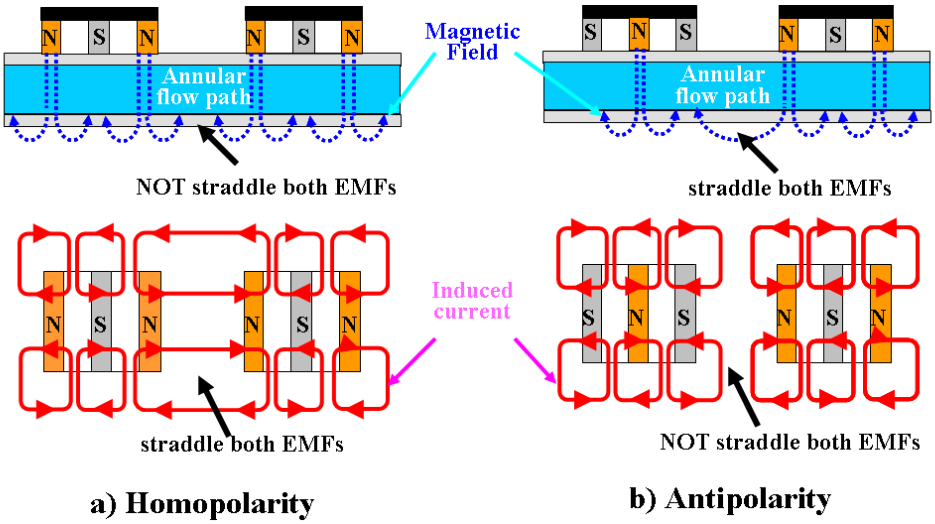

FIG. 3. Overview of homopolarity and antipolarity

3. Simulation method and Experimental apparatus

3.1. MHD simulation method

In 4S, the velocity in annular flow path is from 0.4 to 1.5 m/s. Since the max interaction parameter correnponding to 0.4 m/s is 1.4 and the value is greater than 1.0, the velocity distribution is influenced by electromagnetic forces and the velocity changes. Therefore MHD simulation including an interaction between magnetic field and velocity distribution is necessary to simulate the induced voltage with high accuracy. The interaction parameter N is defined by:

$$N = \frac{2\sigma B^2 SH}{\rho W} \tag{1}$$

where S is the cross section in duct [m^2], H is flow path width [m], W is flow rate [m^3/s] , ρ is density [m^3/kg] , σ is electrical conductivity [1/Ωm] and B is magnetic flux [T].

We had developed a three-dimensional MHD simulation code for EMF [(2)(3)]. The MHD simulation coupled three dimensional finite element code, FALCON with a commercial CFD code, STAR-CD®. Fig. 4 shows weak coupling algorithm of MHD simulation in which the exchanging data between FALCON and STAR-CD is the magnetic force and the sodium velocity. Magnetic force and induced magnetic in annular flow path are solved by FALCON from an external magnetic field and sodium velocity. An external magnetic field formed with electromagnets is solved by a commercial electromagnetic code, Opera-3d®. This external magnetic field is an input condition. A sodium velocity is solved by a STAR-CD.

In the FALCON, induced magnetic field is solved by

$$\nabla \times \left(\frac{1}{\mu_o} \nabla \times \boldsymbol{A} \right) = \sigma \cdot \left[\boldsymbol{u} \times \boldsymbol{B}_{ap} + \boldsymbol{u} \times (\nabla \times \boldsymbol{A}) - \nabla \phi \right] \tag{2}$$

$$\nabla \cdot (\sigma \cdot \nabla \phi) = \nabla \cdot \left[\sigma \cdot \boldsymbol{u} \times \left(\boldsymbol{B}_{ap} + \nabla \times \boldsymbol{A} \right) \right] \tag{3}$$

where A is the vector potential, ϕ is the scalar potential, B_{ap} is the external magnetic flux [T] and μ is magnetic permeability [H/m].
The induced current in annular flow path is computed by:

$$\boldsymbol{J} = \sigma \cdot \left(\boldsymbol{u} \times \boldsymbol{B}_{ap} - \nabla \phi \right) \tag{4}$$

where J is the induced current [A/m^2].
And magnetic force is given by:

$$\boldsymbol{F} = \boldsymbol{J} \times \boldsymbol{B} = \left(J_y B_z - J_z B_y, J_z B_x - J_x B_z, J_x B_y - J_y B_x \right) \tag{5}$$

where F is Lorents force [N/m^3] and B is magnetic flux [T].

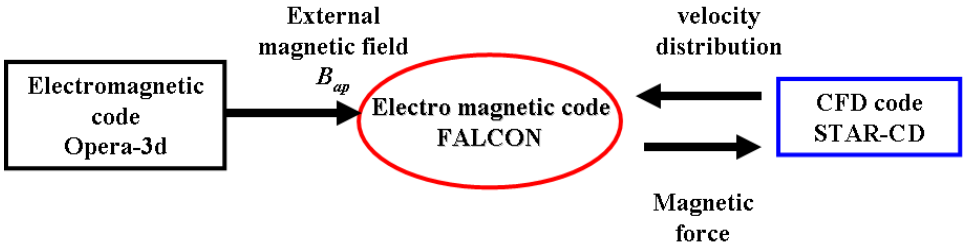

FIG. 4. MHD simulation algorithm

3.2. Simulation models

The simulation model is made from the experimental apparatus referred to section 3.3. We modeled the annular flow path but the length is extended from 1,100mm to 3,000mm to make a fully-developed flow distribution and the Reynolds number is about 30,000. Fig. 5 shows the simulation model. 360-degrees full model uses 120-degrees periodic boundaries.

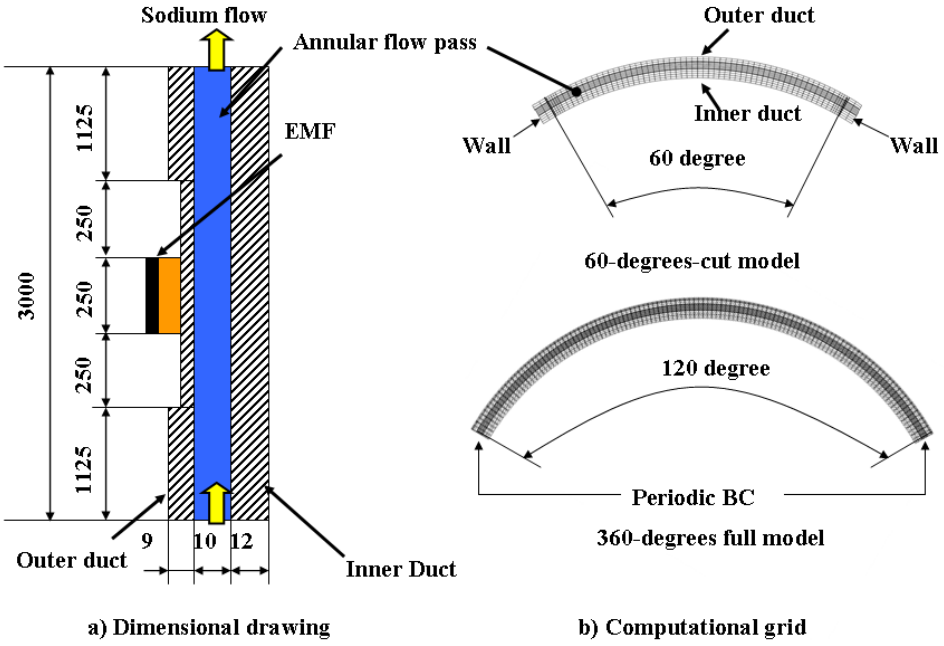

FIG. 5. Simulation model

3.3. Sodium test apparatuses and test loop

Fig.6 shows 360-degrees full model and 60-degrees-cut model. These models are one-third model of EMF for 4S and have inlet buffer, outlet buffer and annular path and are connected to sodium test loop at vertical direction. In 360-degrees full model, six units are anchored on the outside surface of the annular sodium flow path. In 60-degrees-cut model, one unit is anchored on the outside surface of the divided annular sodium flow path. The annular flow path width is 10 mm and the path length is 1100 mm. Fig. 7 shows pictures of 360-degrees full model and 60-degrees-cut model. Fig. 8 shows the layout of sodium loop and picture of the sodium test loop. 360-degrees full model or 60-degrees-cut model is set in the sodium loop.

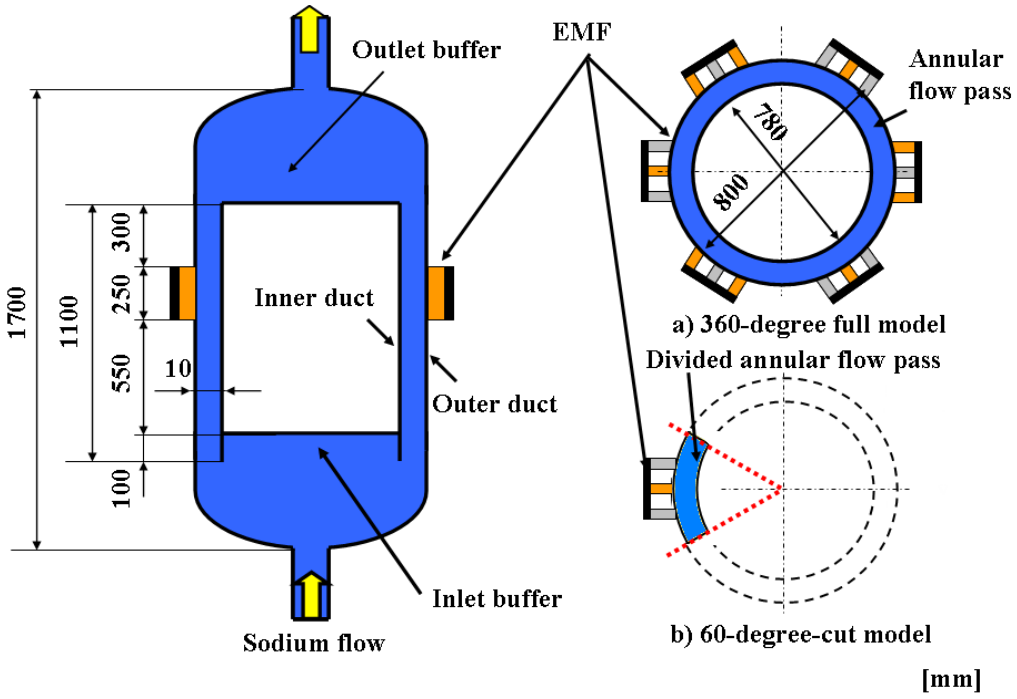

FIG. 6. Overview of 360-degrees full model and 60-degrees-cut model

FIG. 7. Pictures of experiment apparatus

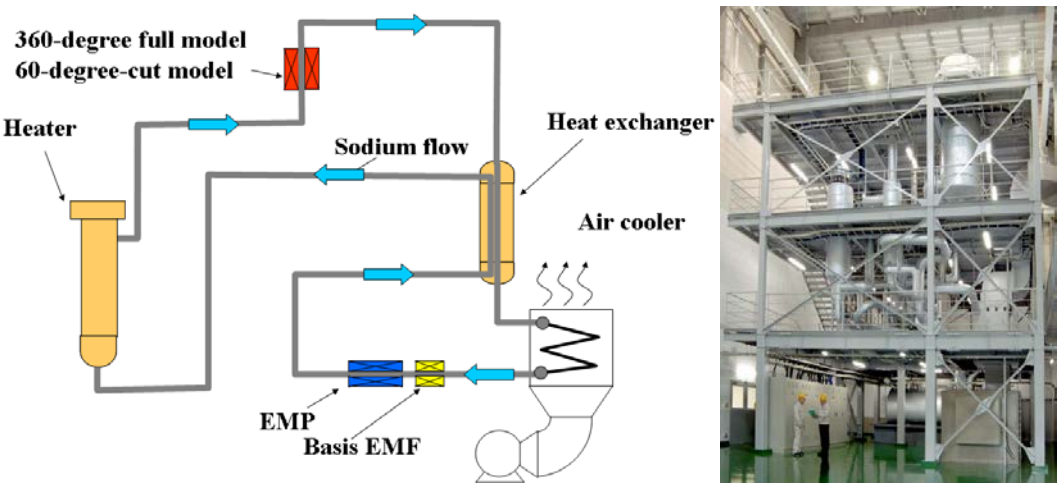

FIG. 8. Sodium test loop

In this experiment, we use ultrasonic flow meters to measure local velocity in sodium to confirm the validity of MHD simulation. Four ultrasonic flow meters are set on the outside surface of the annular flow path in 60-degrees-cut model and their positions are downward from EMF in 195mm. These positions are decided by apparatus structure. Table 1 shows specification of ultrasonic flow meter. Fig. 9 shows pictures of a ultrasonic flow meter and outward attached the flow meters to the test apparatus and Fig.10 shows set position of them. These positions are decided by velocity distribution in upper figure which is changed by magnetic force. As the interaction parameter in upper figure is nearly 1.0, the magnetic force disturbs the sodium flow.

Table 1. Specification of ultrasonic flow meters

Transducer	lithium niobate
Frequency	5 MHz

Transducer Diameter	ϕ 10mm
Max Temp.	400 °C

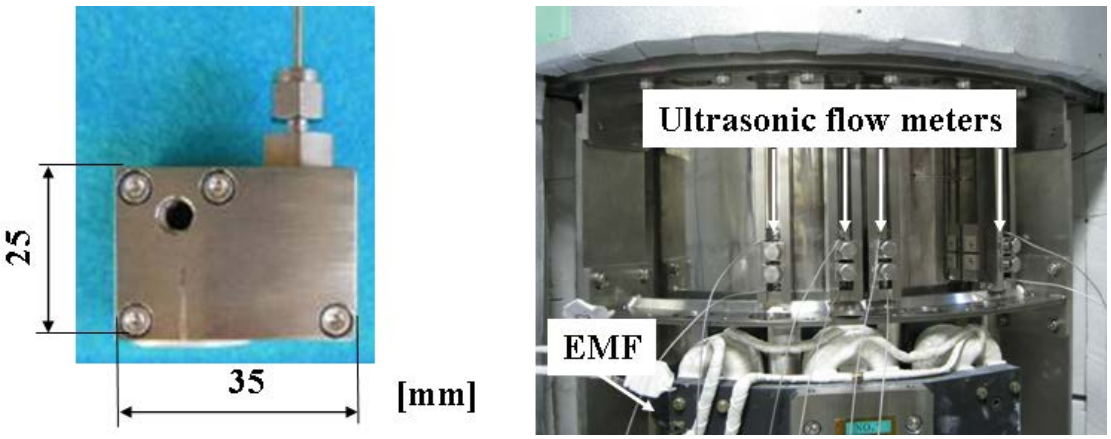

FIG. 9.Pictures of ultrasonic flow meter

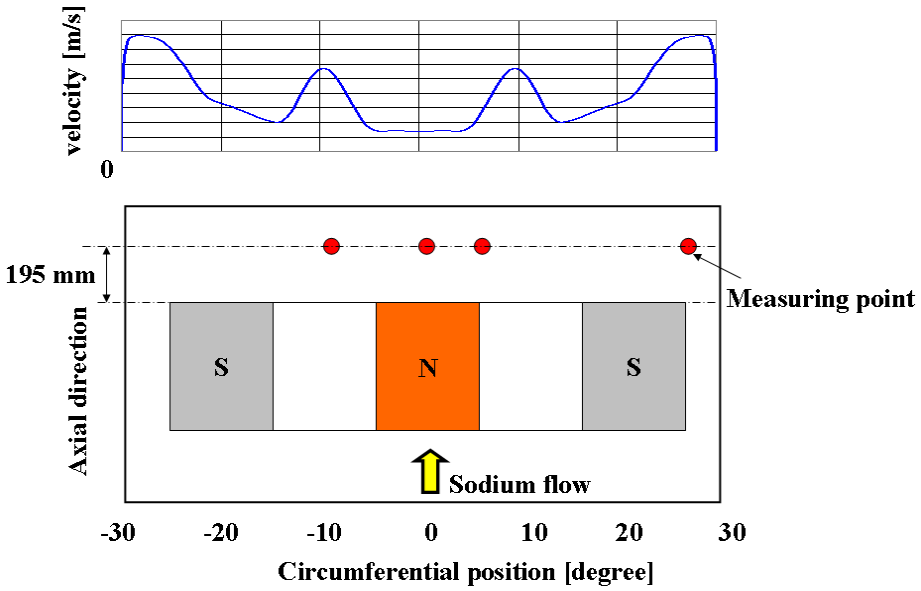

FIG. 10. Positions set on ultrasonic flowmeters in 60-degrees-cut model

4. Predction by simulations

4.1. Simulation conditions

Table 2 shows conditions of simulation. These conditions are same in 360-degrees full model and 60-degrees-cut model.

Table 2. Conditions of simulation

STAR-CD ver.	4.02
Flow	Isothermal, incompressible, steady flow
Turbulence model	Low-Reynolds number k-ε

Boundary conditions	Inlet : fixed velocity
	Outlet : pressure
	Wall: Non-slip
Property	Sodium（temperature 355°C）
	Density : 866.9 [kg/m^3]
	Viscosity coefficient:2.84588×10^{-4} [Pa*s]
	Electrical conductivity: 5.031 [$1/\Omega m$]
	Magnetic permeability: 1.257 [H/m]
Sodium average velocity	0.3, 0.8, 1.0 [m/s]
OPERA-3D ver.	13.0
Coil current	2145 [Amp Turn]

4.2. Simulation results for polarities

Fig. 11 shows a circumferential electric potential distribution in 360-degrees full and 60-degrees-cut model. In the case of antipolarity, the electric potential of 360-degrees full model agrees with the electric potential of 60-degrees-cut model. On the other hand, the electric potential of 360-degrees full model with homopolarity is different from the electric potential of 60-degrees-cut model.

Table 3 shows induced voltage and difference of induced voltage in three cases of sodium average velocity. The difference is calculated by

$$Diff = (\frac{E_{360} - E_{60}}{E_{60}}) \times 100 \quad (6)$$

where E_{360} is induced voltage in 360-degee full model, E_{60} is induced voltage in 60-degrees-cut model. The induced voltage is peak-to-peak of electric potential. The induced voltages of 360-degrees full model with antipolarity and 60-degrees-cut model agree within 1% at an average velocity of 0.3, 0.8 and 1.0 m/s. On the other hand, the induced voltage of 360-degrees full model with homopolity is different from the induced voltage of 60-degrees-cut model and the max difference is 15%. This result indicates that the induced current has more influence to the induced voltage than the magnetic field. Obtained simulation results are as follows:

(1) Antipolarity is better polarity pattern than homopolarity and the induced voltage of 360-degrees full model agrees with one of 60-degrees-cut model.

(2) The induced current that straddles to neighboring EMFs exerts more influence to the induced voltage than the magnetic field that straddles to neighboring EMFs.

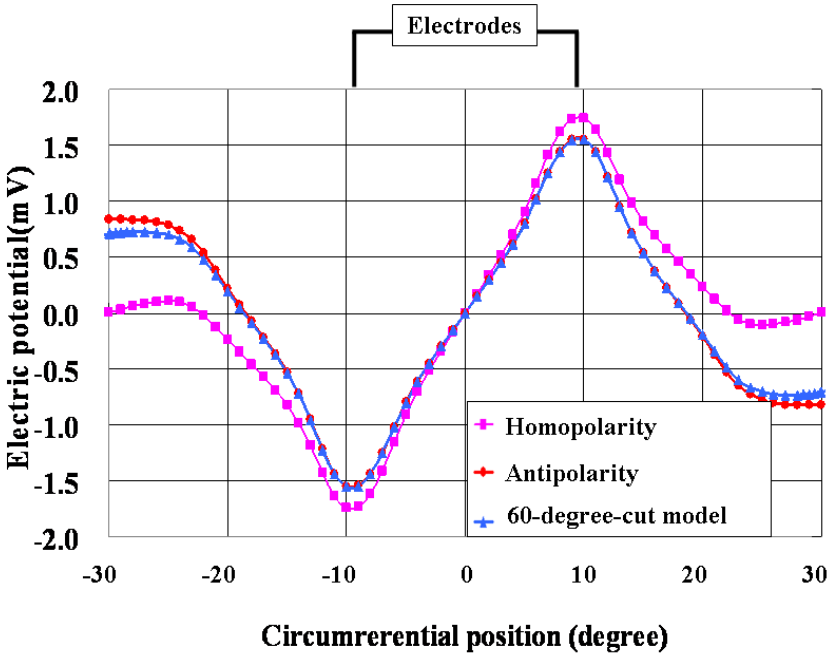

FIG. 11. Electric potential in 360-degrees full model and 60-degrees-cut model

Table 3. Induced voltages in 360-degrees full model and 60-degrees-cut model

Sodium ave. velocity[m/s]	Induced voltage [mV]			Difference [%]	
	Homopolarity	Antipolarity	cut-model	Homopolarity	Antipolarity
0.3	1.179	1.033	1.027	14.8	0.6
0.8	3.468	3.098	3.097	12.0	0.0
1.0	4.444	4.012	4.016	10.7	-0.1

5. Verification with sodium test

5.1. Experimental conditions

Table 4 shows the experimental conditions. We tested 360-degrees full modell in antipolarity and 60-degrees-cut model. The coil currnent and the sodium temperature is fixed at 2145 AT and 300°C and the flow rate is changed. The flow rate is measured by basis EMF in Fig. 8.

Table 4. Experimental conditions

a) 360-degrees full model			b) 60-degrees-cut model		
Flow rate L/min	Ave. velocity m/s	Interaction Parameter	Flow rate L/min	Ave. velocity m/s	Interaction Parameter
1190	0.80	0.35	194	0.78	0.35
1001	0.67	0.41	160	0.64	0.43
801	0.54	0.51	125	0.50	0.55
603	0.41	0.68	107	0.43	0.64
402	0.27	1.02	70	0.28	0.98
197	0.13	2.09			

5.2. Sodium test results and evaluation

Fig. 12(a) shows induced voltages as a function of average velocity in the annular flow path. In the 60-degrees-cut model and the 360-degrees full model, the induced voltage increases with increasing of average velocity. The induced voltage in 60-degrees-cut model agrees with the one in 360-degrees model with antipolarity. The calibration factor of the 360-degrees full model and 60-degrees-cut model agreed within 1%. This calibration factor's error is the same value predicted by MHD simulation.

Fig. 12(b) shows that the simulated induced voltage agrees with the experimental one. These induced voltages is simulated in condition that the inlet velocity is same as experiments. The analysis error is within 4%. The analysis error is calculated by

$$Err = \left(\frac{E_S - E_E}{E_E}\right) \times 100 \qquad (7)$$

where E_S is induced voltage calculated by MHD simulation, E_E is induced voltage measured by experiment in 60-degrees-cut model. MHD simulation can predict MHD phenomenon on condition that the velocity is distorted by magnetic force.

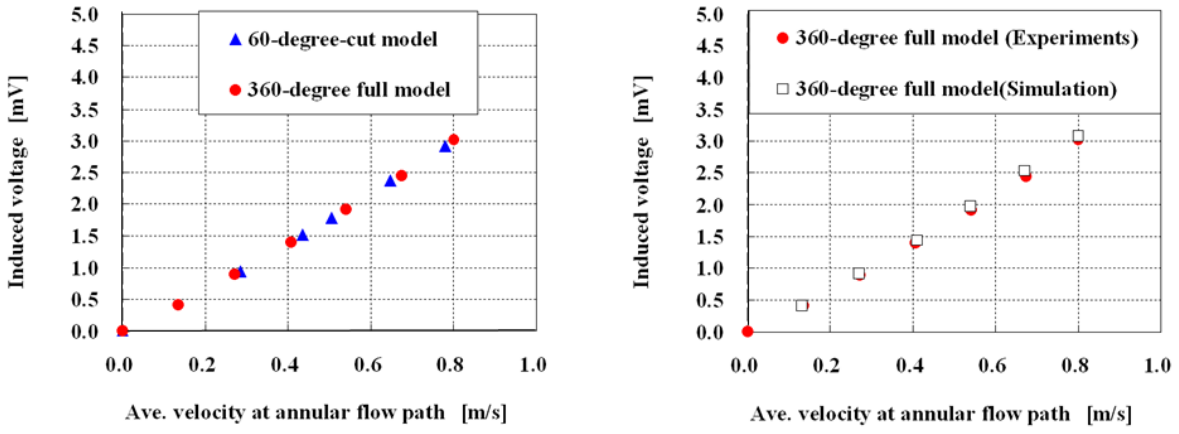

a) Comparison between experiments

b) Comparison of experiments with simulations

FIG. 12. Experiment results

Fig. 13 shows local velocity measured with ultrasonic flowmeters and simulated velocity distribution in 60-cut-model. The test condition is below: Sodium temperature is 200°C. Ave. velocity at annular flow path is 0.4 m/s. The interaction parameter is 0.98. The measured velocity distribution agrees with simulated one. The MHD simulation can predict flow distribution distorted by magnetic force.

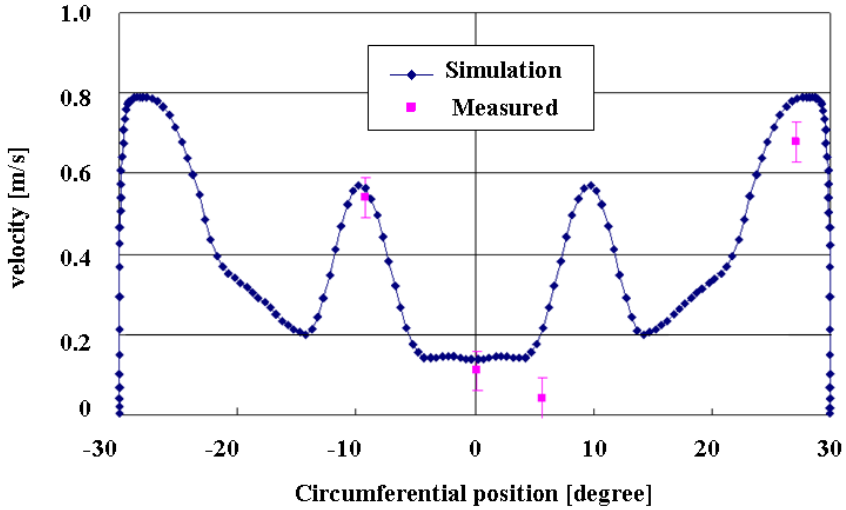

FIG. 13. Local velocity measured with ultrasonic meters

6. Conclusions

We have confirmed the feasibility of the EMF for calibration by simulation and Sodium test.
Obtained results are as follows:

(1) The induced voltage in 360-degrees full model with antipolarity (NSN-SNS) agrees with the induced voltage in 60-degrees-cut model. The calibration factors of the 360-degrees full model (6 units) and 60-degrees-cut model (1 unit) agreed within 1%.

(2) The induced current that straddles to neighboring EMFs exerts more influence to the induced voltage than the magnetic field that straddles to neighboring EMFs.

(3) MHD simulation that is coupled STAR-CD and FALCON solved the induced voltage within error 4% on conditions that the velocity distorted by magnetic force.

ACKNOWLEDGEMENTS

This study is the result of "Development of a new EMF in Sodium-cooled Fast Reactor" entrusted to "Toshiba" by the Ministry of Education, Culture, Sport, Science, and Technology (MEXT) of Japan.

REFERENCES

[1] M. Komai et, al., Development of a new electromagnetic flow meter in Sodium-cooled Fast Reactor, International Conference on Fast Reactors and Related Fuel Cycles –Challenges and Opportunities-(FR09)

[2] T. Shimizu et, al., A Numerical Study on Faraday-Type Electromagnetic Flow—meter simulation in Liquid Metal System, (I) A Numerical Method Based on Magnetic Field and Electric Potential Field: FALCON code, Journal of Nuclear Science and Technology, Vol.37, No.12, pp1038-1048(2000)

[3] T. Shimizu et, al., A Numerical Study on Faraday-Type Electromagnetic Flow-meter simulation in Liquid Metal System, (II) Analysis of End effect due to Saddle-Shaped Small-Sized Magnets with FALCON code, Journal of Nuclear Science and Technology, Vol.38, No.1, pp19-29

The Viscous and End Effects on an Electromagnetic Pumps for Sodium Circulation

Hee Reyoung Kim

Ulsan National Institute of Science and Technology, Ulsan, Rep. of Korea

Abstract. Analyses of the viscous and end effects on an electromagnetic (EM) pump for the sodium coolant circulation in Fast Reactors was carried out based on the MHD laminar flow analysis and the electromagnetic field theory. A one-dimensional MHD analysis for the liquid metal flowing through an annular channel has been performed on the basis of a simplified model of equivalent current sheets instead of three-phase currents in the discrete primary windings. The calculations show that the developed pressure difference resulted from electromagnetic and viscous forces in the liquid metal is expressed in terms of the slip, and that the viscous loss effects are negligible compared with electromagnetic driving forces except in the low-slip region where the pumps operate with very high flow velocities comparable with the synchronous velocity of the electromagnetic fields, which is not applicable to the practical EM pumps. A two-dimensional electromagnetic field analysis based on an equivalent current sheet model has found the vector potentials in closed form by means of the Fourier transform method. The resultant magnetic fields and driving forces exerted on the liquid metal reveal that the end effects due to finiteness of the pump length are formidable. Calculations of each magnetic force contribution indicate that the end effects are originated from the magnetic force caused by the induced current generated by the liquid metal movement across the magnetic field rather than the one produced by externally applied magnetic fields by three-phase winding currents. It is concluded that since the influences of the end effects in addition to viscous losses are extensive particularly in high-velocity operations of the EM pumps, it is necessary to find ways to suppress them, such as proper selection of the pump parameters and compensation of the end effects.

1. Introduction

A great interest in the linear induction EM pumps has been given as an elemental device for circulating the sodium coolant in Liquid-Metal Fast Breeder Reactors. The EM pumps have the advantage over the mechanical pumps due to the fact that they have no rotating parts, which results in simplicity and convenience of maintenance and repair. The basic operational experiments on pilot linear induction EM pumps with various geometrical shapes have been carried out, and the practical applications have been made for the other areas of research like liquid metal chemistry. The linear induction EM pump gets the driving power from Lorentz's forces generated by the time-varying magnetic fields and the current induced in the electrically conductive liquid metal. Mathematical solutions for the driving forces are obtained by solving MHD equations of incompressible viscous flow coupled with Maxwell's equations under appropriate assumptions. It is found that the mechanical pressure gradients developed in the pump duct are given as a function of the slip including other pump variables. Since the pumping pressures are developed by Lorentz's forces experiencing viscous drag forces, viscous loss effects on the electromagnetically-developed liquid metal flow need to be investigated. Generally, the Hartmann number given by the system scale length and magnetic field with viscosity and electrical conductivity is used as a measurement of viscous effect [1]. In the present work, direct comparison of the electromaqgnetic force with viscous force is carried out by analytical solutions obtained from related equations. The calculated results show, at the nominal conditions, that the pump performance can be analyzed by electromagnetic treatment due to negligible viscous effects. In addition to viscous loss effects, there are end effects at inlet and outlet of the EM pump due to finite pump length. It is known that braking forces by these end effects result in a reduction in the driving force of the EM pump. Solving Maxwell's equations analytically, radial and axial magnetic fields are

found along the pump axial direction in the cases with and without end effects. respectively. Force density distributions obtained by calculations indicate that end effects are mainly due to the electromagnetic force caused by the induced current generated by the liquid metal movement across the magnetic field rather than the one produced by externally applied magnetic fields by three-phase winding currents. In this paper, MHD flow and electromagnetic analyses on the annular linear induction EM pumps with flowrates of 60 L/min are carried out by solving MHD and Maxwell's equations.

2. Analysis of Viscous Losses by MHD Laminar Flow Analysis

The driving power of the annular linear induction EM pump is generated from Lorentz's force given by products of magnetic field (**B**) and induced current (**J**) perpendicular to it. Electrically conductive liquid fluid also experiences viscous forces while being developed by Lorentz's force. Therefore, a real hydrodynamical pressure difference at both the ends of pump appears to be reduced by viscous forces. In this respect, an attempt has been made to obtain the expression for the pressure gradient mathematically by analyzing MHD equations coupled with Maxwell's field equation. As shown in Fig.1, a typical annular linear induction EM pump has sloted external cores in which exciting coils are inserted to generate $\boldsymbol{J} \times \boldsymbol{B}$ force in the liquid metal flowing in the annular duct [2].

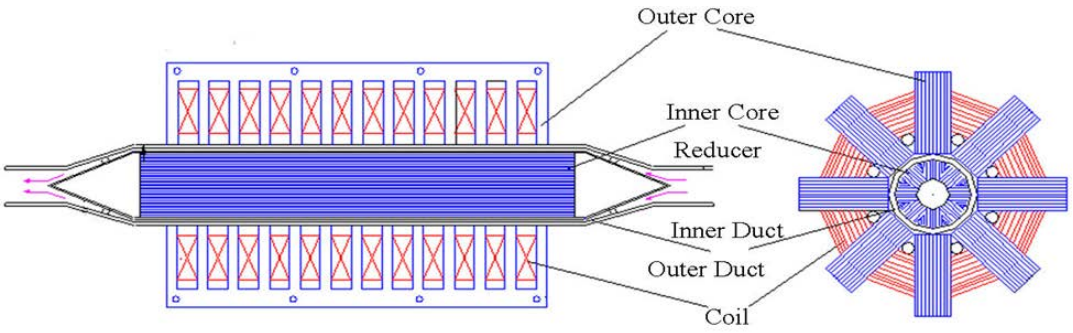

FIG. 1. Cross-sectional view of annular linear induction EM pump

But, to simplify the problem, the real pump core shape of is turned into a smooth core face replacing exciting coils by an equivalent current sheet to real coil arrangement as depicted in Fig.2 [5].

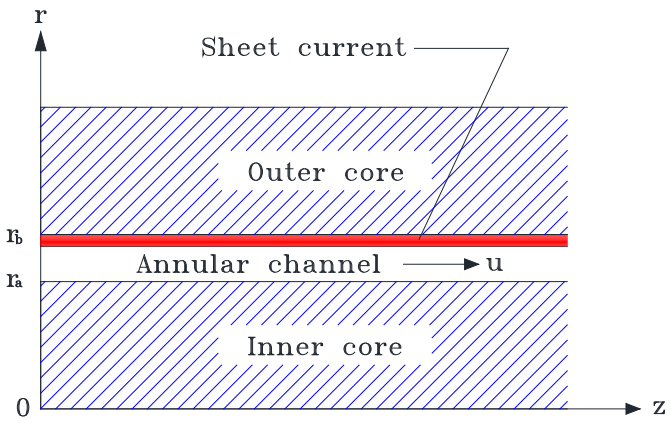

FIG. 2. Simplified laminar model with equivalent current sheet

A few more assumptions are introduced as follows [5].

(1) The pump has an infinitely-long annular channel with an equivalent current sheet replaced by discrete primary windings slotted in the outer core.

(2) All fields in the pump are axisymmetric ($\frac{\partial}{\partial\theta}=0$) in view of cylindrical arrangement of the pump system.
(3) The equivalent current sheet representing the three-phase currents (I) of continuous primary windings of N turns having pole pairs of p and pole pitch of τ is given by $\boldsymbol{J}_a(r_2,z,t)=J_m e^{i(\omega t-kz)}\hat{\boldsymbol{\theta}}$ where $J_m=3\sqrt{2}k_w NI/p\tau$.
(4) The sheet current produces traveling sinusoidal fields in the same form of $\boldsymbol{J}_a$ with angular frequency of ω and wave number of k for ***B, E*** and ***J***.
(5) Radial magnetic field (B_r) is uniform due to negligible skin effect in a narrow liquid metal gap.
(6) The liquid metal flow is incompressible.

To analyze the system, first of all, MHD equations are needed for expressing conservations of fluid and momentum. The pressure gradient (∇P) arouses from the combined action of electromagnetic driving and hydrodynamic drag forces in the conducting fluid of density ρ, viscosity η, and fluid velocity $\boldsymbol{u}$. Electromagnetic term by Lorentz's force is related with Maxwell's equations. Besides, induced current density ($\boldsymbol{J}$) in the Lorentz's force is represented from Ohm's law given by electrical conductivity (σ) and fields ($\boldsymbol{E}+\boldsymbol{u}\times\boldsymbol{B}$) induced both by traveling sinusoidal magnetic fields and conductive flow movement across them. Then governing equations are given as :

- MHD equations

$$\nabla\cdot\boldsymbol{u}=0$$

$$\rho\left\{\frac{\partial u}{\partial t}+(\boldsymbol{u}\cdot\nabla)\boldsymbol{u}\right\}=-\nabla P+\eta\nabla^2\boldsymbol{u}+\boldsymbol{J}\times\boldsymbol{B}$$

- Maxwell's equations

$$\nabla\times\boldsymbol{B}=\mu_0\boldsymbol{J}$$
$$\nabla\times\boldsymbol{E}=-\frac{\partial\boldsymbol{B}}{\partial t}$$
$$\boldsymbol{B}=\nabla\times\boldsymbol{A}$$
$$\boldsymbol{E}=-\frac{\partial\boldsymbol{A}}{\partial t}$$
$$\boldsymbol{J}=\sigma(\boldsymbol{E}+\boldsymbol{u}\times\mathrm{B})$$

In the MHD equations, we are interested in the time-averaged value of velocity. In practical sense, when velocity and flowrate are indicated, they generally mean the averaged values over time. Therefore, we will try to analyze the system in the time-averaged point of view. The time-averaged MHD equations are resulted in two reduced equations for flow velocity and magnetic field.

$$\frac{d^2\bar{u}}{dr^2}+\frac{1}{r}\frac{d\bar{u}}{dr}-\alpha^2\bar{u}=\frac{1}{\eta}\frac{dP}{dz}-\alpha^2U_s$$

$$\frac{dB_z}{dr}=\{\mu_0\sigma(-U_s+u)+j\}B_r$$

where

$$\alpha^2=\frac{\sigma B_r^2}{2\eta},\ U_s=\frac{\omega}{k}\ \text{(synchronous speed)}$$

B_r can be treated as a constant since radial magnetic field does rarely change at a narrow inter-core gap in induction machines having negligible skin effects. In general, magnetic core materials have very large permeabilities compared with those of liquid metals, and the differences of tangential magnetic fields between core ($\boldsymbol{H_1}$) and liquid metal ($\boldsymbol{H_2}$) regions are given by sheet current density ($\boldsymbol{K}$) as

$$\boldsymbol{n}\times(\boldsymbol{H_1}-\boldsymbol{H_2})=\boldsymbol{K}$$

Thus for the present pump model, we get

$B_z(r_2)=\mu_0 J_m\,,\quad B_z(r_1)=0$

Applying no-slip boundary conditions for velocity ($\bar{u}$) at the cylindrical walls (r_1, r_2), i.e., $\bar{u}(r_1)=\bar{u}(r_2)=0$, we have solutions for the time-averaged velocity expressed in terms of the modified Bessel functions, I_0 and K_0, of zeroth order as

$$u(r)=\{AI_0(\alpha r)+BK_0(\alpha r)-1\}\left\{\frac{1}{\alpha^2\eta}\frac{d\bar{P}}{dz}-U_s\right\}$$

where

$$A=\frac{K_0(\alpha a)-K_0(\alpha b)}{K_0(\alpha a)I_0(\alpha b)-K_0(\alpha b)I_0(\alpha a)}$$

$$B=\frac{I_0(\alpha b)-KI_0(\alpha a)}{K_0(\alpha a)I_0(\alpha b)-K_0(\alpha b)I_0(\alpha a)}$$

If an average slip (s) over the channel gap is defined by

$$s=\frac{1}{r_2-r_1}\int_{r_1}^{r_2}(1-\frac{\bar{u}}{U_s})dr$$

The radial magnetic field (B_r) and axial pressure gradient ($\frac{d\bar{P}}{dz}$) are obtained as function of s together with other pump parameters.

$$B_r=\frac{\mu_0 J_m}{(-\mu_0\sigma s U_s+jk)(r_2-r_1)}$$

$$\frac{d\bar{P}}{dz}=\frac{1}{2}\sigma U_s B_r^2\left\{s+(1-s)\left(1+\frac{1}{\frac{1}{r_2-r_1}\int_{r_1}^{r_2}(AI_0(\alpha r)+BK_0(\alpha r)-1)\,dr}\right)\right\}$$

The axial pressure gradient has been developed by two components, Lorentz's force and viscous term. The first term of right-hand side, $\frac{1}{2}\sigma U_s B_r^2$ is originated from the electromagnetic force density which is simply obtained by direct calculation of $\boldsymbol{J}\times\boldsymbol{B}$. The other terms of right-hand side correspond to viscous force density. To compare the viscous force density with electromagnetic force density, as a example, numerical values of pressure differences versus slip (or flowrate) are represented graphically in Fig.3 for a pump system with flowrate of 40,000 L/min under a pressure difference of 15 atm. Fig.3 indicates that viscous force density is negligible compared with electromagnetic force density through all flowrate values except for near synchronous speed (s = 0). Practically induction pumps are not operated at near the synchronous speed with very low slip. Due to real hydraulic load like valve or piping system, such low slip value needs to be avoided so that the system can generate quite realistic developing force. Since EM pumps are generally operated at sufficiently high slip region to generate a considerable developing force overcoming heavy hydraulic pressure load (more than a few atms), the pump system analyses can be treated by electromagnetic analysis alone

neglecting viscous effects. After all, it is thought that mechanical pressure gradient in the system can be replaced by electromagnetic force density ($\boldsymbol{J} \times \boldsymbol{B}$) alone.

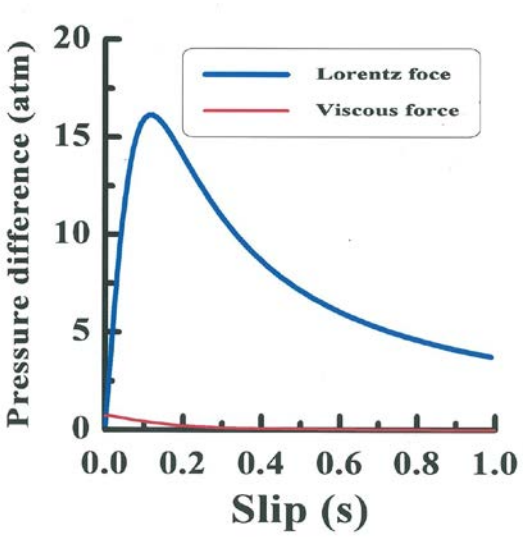

FIG. 3. Comparison of viscous force effects with Lorentz's ones on producing the pressure difference between the inlet and the outlet of a 40,000 L/min pump

3. Analyses of End Effects by Electromagnetic Theory

In the previous section, it is shown that EM pumps at nominal conditions can be analyzed by electromagnetic treatment. In this section, end effects caused by finite pump length are investigated from the results of calculated magnetic field and force density distributions. Applying linear induction motor theory with constant flow velocity, Maxwell's equations are to be solved analytically [5]. To solve Maxwell's equations analytically, an equivalent current sheet model with a finite axial length as in the Fig.2 is used. Then, assumptions are the same in the MHD flow analyses of previous section except an infinite axial extension. Maxwell's equation represented by magnetic vector potential ($\boldsymbol{A}$) yields

$$\nabla^2 \boldsymbol{A} = \mu\sigma\left\{\frac{\partial \boldsymbol{A}}{\partial t} - \boldsymbol{u} \times (\nabla \times \boldsymbol{A})\right\}$$

where

$$\boldsymbol{A} = \boldsymbol{A}(r,z)e^{i\omega t}\hat{\boldsymbol{\theta}} = \boldsymbol{R}(r)\boldsymbol{Z}(z)e^{i\omega t}\,\hat{\boldsymbol{\theta}}$$

Taking the Fourier transforms with respect to z, we have

$$A(r,z) = \frac{1}{2\pi}\int_{-\infty}^{\infty} \tilde{A}(r,\zeta)e^{ikz}d\xi$$

$$\tilde{A}(r,z) = R(r)\int_{-\infty}^{\infty} Z(z)e^{-i\xi z}dz$$

$$J(\xi) = \int_0^L Je^{-ikz}e^{-i\xi z}dz = \frac{iJ}{\xi + k}\left[e^{-i(\xi+k)L} - 1\right]$$

Then, a reduced field equation is resulted as

$$\frac{d^2R}{dr^2}+\frac{1}{r}\frac{dR}{dr}-\left(\frac{1}{r^2}+\alpha^2\right)R=0$$

where

$$\alpha^2=\xi^2+i\mu\sigma(u\xi+\omega)$$

From the reduced equation, magnetic vector potential is obtained in terms of first (I_0, I_1) and second (K_0, K_1) kinds of modified Bessel functions of zeroth and first orders.

$$A(r,z)=\frac{i\mu J}{2\pi}\int_{-\infty}^{\infty}\frac{e^{-i(\xi+k)L}-1}{\xi+k}\frac{G(r,\xi)}{\alpha H(\xi)}e^{ikz}d\xi$$

where

$$G(r,\xi)=K_0(\alpha r_1)I_1(\alpha r)+I_0(\alpha r_1)K_1(\alpha r)$$

$$H(\xi)=K_0(\alpha r_1)I_0(\alpha r_2)-I_0(\alpha r_1)K_0(\alpha r_2)$$

Applying the residue theorem and the asymptotic expression of Bessel functions,

$$A(r,z)=\mu JA_{1,0}+\mu J\sum_{n=1}^{\infty}A_{1,n} \qquad (z<0)$$

$$A(r,z)=\mu J\frac{\mathrm{G(r,-k)}}{\alpha(-\mathrm{k})\mathrm{H}(-\mathrm{k})}e^{-ikz}+\mu JA_{2,0}+\mu J\sum_{n=1}^{\infty}A_{2^-,n}+\mu J\sum_{n=1}^{\infty}A_{2^+,n} \qquad (0<z<L)$$

$$A(r,z)=\mu JA_{3,0}+\mu J\sum_{n=1}^{\infty}A_{3,n} \qquad (z>L)$$

where terms from residues at ξ_0^+ are given by

$$A_{1,0}=\frac{\mu J}{r\ln(\frac{r_2}{r_1})}\frac{e^{-i(\xi_0^-+k)L}-1}{\xi_0^-+k}\frac{e^{-i\xi_0^-z}}{\xi_0^--\xi_0^+}$$

$$A_{2,0}=\frac{\mu J}{r\ln(\frac{r_2}{r_1})}\left\{\frac{e^{-i(\xi_0^-+k)L}}{\xi_0^-+k}\frac{e^{-i\xi_0^-z}}{\xi_0^--\xi_0^+}+\frac{1}{\xi_0^++k}\frac{e^{i\xi_0^+z}}{\xi_0^+-\xi_0^-}\right\}$$

$$A_{3,0}=\frac{\mu J}{r\ln(\frac{r_2}{r_1})}\frac{1-e^{-i(\xi_0^++k)L}}{\xi_0^++k}\frac{e^{i\xi_0^+z}}{\xi_0^+-\xi_0^-}$$

and terms from residues at ξ_n^+ (n>0) are obtained as

$$A_{1,n}=\frac{G(r,\xi_n^-)}{\alpha(\xi_n^-)H'(\xi_n^-)}\left\{\frac{e^{-i(\xi_n^-+k)L}-1}{\xi_n^-+k}\right\}e^{i\xi_n^-z}$$

$$\mathrm{A}_{2,\mathrm{n}}^-=\frac{G(r,\xi_n^-)}{\alpha(\xi_n^-)H'(\xi_n^-)}\left\{\frac{e^{-i(\xi_n^-+k)L}}{\xi_n^-+k}\right\}e^{i\xi_n^-z}$$

$$\mathrm{A}_{2,\mathrm{n}}^+=\frac{G(r,\xi_n^+)}{\alpha(\xi_n^+)H'(\xi_n^+)}\left\{\frac{1}{\xi_n^++k}\right\}e^{i\xi_n^+z}$$

$$A_{3,n}=\frac{G(r,\xi_n^+)}{\alpha(\xi_n^+)H'(\xi_n^+)}\left\{\frac{1-e^{-i(\xi_n^++k)L}}{\xi_n^++k}\right\}e^{i\xi_n^+z}$$

Using $I_0' = I_1$ and $K_0' = -K_1$,

$$H'(\xi) = \alpha'(\zeta)\{-r_1[K_1(\alpha r_1)I_0(\alpha r_2) + I_1(\alpha r_1)K_0(\alpha r_2)] + -r_2[K_0(\alpha r_1)I_1(\alpha r_2) + I_0(\alpha r_1)K_1(\alpha r_2)]\}$$

The vector potential *A*(*r*, *z*) consists of three kinds of travelling waves along *z* characterized by three poles *-k*, ξ_0^- and ξ_0^+. Noting that *k*>0, Re$|\xi_0^+|$<0 and Im$|\xi_0^+|$>0, and Re$|\xi_0^-|$>0 and Im$|\xi_0^-|$<0, $e^{i(\omega t - kz)}$ term represents a normal wave moving to +z, $e^{i(\omega t + \xi_0^+ z)}$ term is an inlet-end-effect wave damping along +z and $e^{i(\omega t + \xi_0^- z)}$ term is an outlet-end-effect wave damping along *-z*, respectively. Taking curl of magnetic vector potential ($\boldsymbol{B} = \nabla \times \boldsymbol{A}$) yields radial and axial magnetic fields as shown in Fig. 4 and Fig. 5.

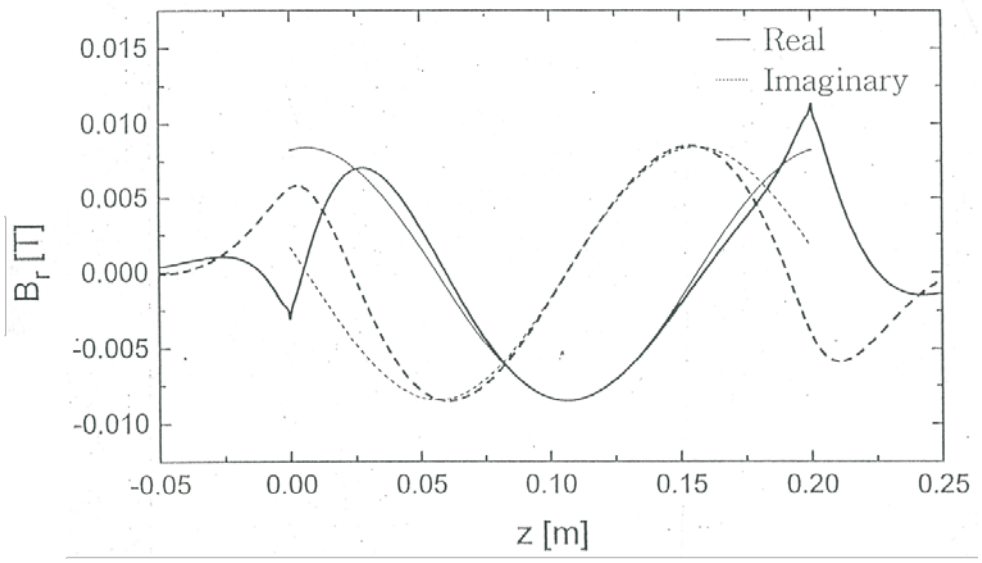

FIG. 4. Radial magnetic field distributions with (heavy curves) and without (light curves) end effects along pump axial direction

The magnetic fields are seen to be distorted at both ends of the pump due to end effects. The time-averaged driving force density is given by

$$\boldsymbol{F} = |\overline{\boldsymbol{J} \times \boldsymbol{B}}| = \frac{1}{2}\{\sigma(-i\omega \boldsymbol{A} + u B_r)B_r^*\}$$

from which Fig.6 presents the calculated force density distributions in an EM pump of 60 L/min. It appears in the figure that, at both entry and exit ends, the force densities are dropped rapidly in their values due to end effects. Especially, at the inlet region locally the force has opposite direction to the normal motion of liquid metal, and it is thought that such phenomena cause a reduction of a pump efficiency or thrust.

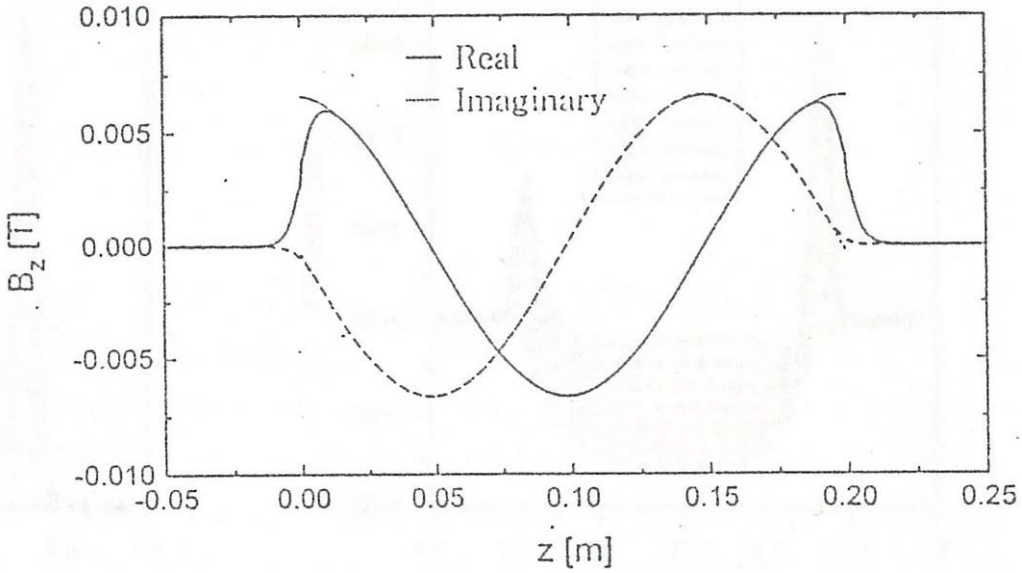

FIG. 5. Axial magnetic field distributions with (heavy curves) and without (light curves) end effects along pump axial direction

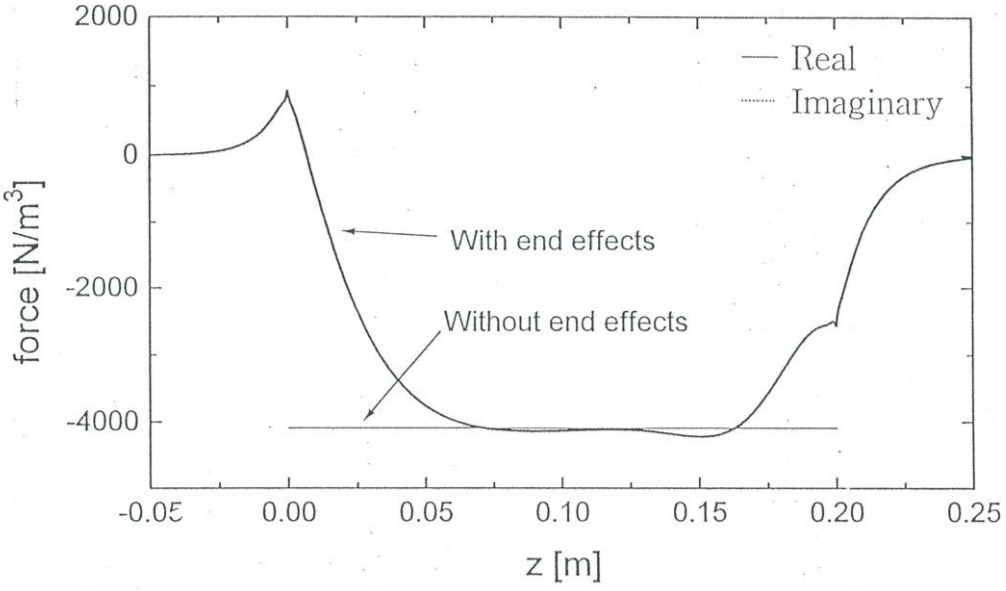

FIG. 6. *Developing force with (heavy curves) and without (light curves) end effects along pump axial direction*

4. Conclusion

Calculated results of the MHD flow analysis shows that the viscous loss effects on producing pressure differences are negligible compared with electromagnetic driving forces except in the low slip region where the pumps operate with very high flow velocities comparable with the field synchronous speed. The closed-form solutions obtained from the Fourier transform method for the current sheet model reveal that the end effects due to finiteness of the pump length, which are originated from the magnetic force caused by $(\boldsymbol{u}\times \boldsymbol{B})\times \boldsymbol{B}$ rather than $\boldsymbol{E}\times \boldsymbol{B}$, are formidable. Since the influence of the end effects in addition to viscous losses are extensive particularly in high-velocity operations of the EM pumps, it is

necessary to find ways to suppress them, such as proper selection of the pump parameters and compensation of the end effects.

REFERENCES

[1] H. Branover, Magnetohydrodynamic flow in ducts, A John Wiley & Sons, New York, 1978.
[2] S. A. Nasar, Linear motion electromagnetic systems, A John Wiley & Sons, New York, 1985.
[3] S. A. Nasar, Linear motion electric machines, A John Wiley & Sons, New York, 1976.
[4] Hee Reyoung Kim and Yong Bum Lee, Design and Characteristic Experiment of the Small Annular Linear Induction Electromagnetic Pump, Annals of Nuclear Energy,38, 1046-1052, 2011.
[5] Lawson. P. Harris, Hydromagnetic channel flows, A John Wiley & Sons, New York, 1960.

EXPERIMENTAL INVESTIGATION OF GAS-LIFT USE IN NUCLEAR REACTORS

Jiri Polansky

Pavel Zitek

Vaclav Valenta

University of West Bohemia in Pilsen

ABSTRACT.

This work briefly describes the selection of type of a two-phase flow [1], suitable for intensifying of a natural flow of nuclear reactors [4] with liquid fuel – cooling mixture molten salts and the description of a „Two-phase flow demonstrator“ (TFD) [6] used for experimental study of the „gas-lift“ system [2], [3] and its influence on the support of natural convection. The experimental device works with water and the air is used as a gas. The used perspex limits the temperature to 60°C. There are stated relations for the description of a natural flow in model device and relations for determination of suitable liquid/gas ratio of the gas-lift in the study [5].

There is described the measuring device and the application of the TFD sensor. The flow rate of water is measured by the induction flow meter that gives a voltage signal, which is brought into a computer for processing. Measuring of the velocity distribution and the size of the bubbles is performed by using the PIV method (Particle Image Velocimetry) [7], [8].

There was created a model of dispersive bubble flow for application in nuclear reactors. The basic calculation is performed by using the homogeneous flow, where is considered, that the velocity of the fluid and the gas is equal and there is measured the relative share of the gas in homogeneous mixture with the fluid for this case. There are considered the temperature, pressure and flow rate velocity changes of the fluid and gas in the gas-lift cylinder and their influence on the size and velocity of the bubbles for the heat and mass transport of this mixture by the gas-lift cylinder.

INTRODUCTION

There is possible to use a very well known gas-lift for the intensification of natural flow in nuclear reactors. Gas-lift is replaced classic pumps with which they are currently problems in the case of high-temperature reactors. With the intensification of the natural flow are able to pay 1/2 to 4/5 the paid thermal performance when using forced air, depending on the total pressure loss of the primary circuit.

It is only possible to use the continual gas delivery method in nuclear reactors. It is possible to use He as a gas. In MSR the gas-lift is suitable for cleaning the fuel-cooling mixture of fluoride salts from gaseous fission products and therefore removing the problems with „Xenon Fission product poisoning“ of classic reactors. There is applicable the bubble mode and the disperse bubble mode that allows larger flow intensification - from the types of the two-phase flow. The other modes like slug mode, churn mode and annular mode are unsuitable for non-homogeneous distribution of the phases.

Jiri Polansky
Pavel Zitek
Vaclav Valenta

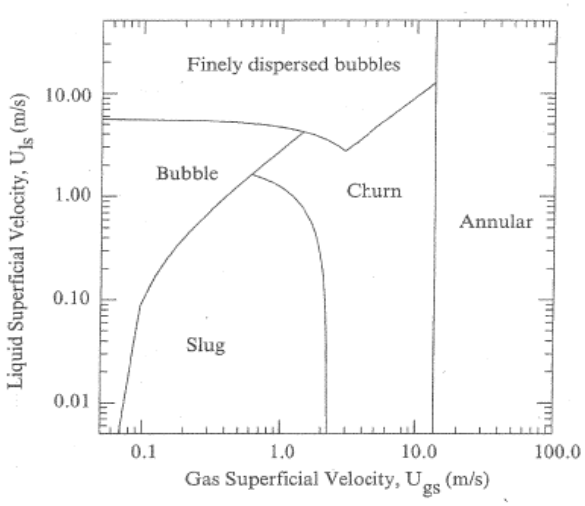

FIG. 1. Map of distribution of the types of a two-phase flow (Taitel) [1]

There is a problem in determination of weight flow rates of the fluid and gas [kg/s] W_∞ a W_g to get to the sphere of the disperse bubble flow. It means for the fluid, that its superficial velocity (the fluid is alone in the cross sectional area) of flow is $v_{sl} \geq 6\ m/s$ and at the same time the superficial gas velocity is $v_{sg} \leq 8\ m/s$. (according to the picture from Taitel)

There applies:

$W_l = \rho_l(T_{max}).A_k.v_{sl}$ a $W_g = \rho_g\ (T_g\ ).\ A_k.v_{sg.}$ where the cross-sectional area of the tractive "chimney" is $A_k = \pi.D^2/4$, ρ is density, index l is the fluid,g is the gas, m [kg/s] is the weight flow rate.

We obtain this relation for natural heat flowing in the primary circuit - on condition that the temperature changes only in the active zone and the heat exchanger - from the solution of the continuity equation and the Bernoulli's equation:

$$\tilde{\chi}_{pr} = \frac{\chi_{pr}}{\overline{\overline{A}}^2} \tag{1}$$

χ_{pr} Are total hydraulic losses in the primary circuit, $\bar{A}$ is the medium flow cross-section of the circuit, $\overline{\rho}$ is the medium density of the coolant in the circuit.

It applies:

$$\frac{1}{\overline{\overline{A}}} = \frac{}{L}\int_{x_0}^{x_L} \frac{dx}{\rho(x).A(x)} \tag{2}$$

$$\overline{\rho} = \frac{1}{V}\int_{x_0}^{x_L} \rho(x).A(x).\,dx \tag{3}$$

$$W_\infty = \left[\frac{2\cdot\overline{\rho}^2\cdot g\cdot\beta\cdot P}{\tilde{\chi}_{pr}\cdot c_p}\cdot\left(z_v - z_c\right)\right]^{\frac{1}{3}} \tag{4}$$

P [W] is the total heat output of the zone.

$$W_{\infty}^{gas-lift} = \left(W_{l\infty} + W_g\right)\left[\frac{\text{kg}}{\text{s}}\right] \tag{5}$$

Using $W_{\infty}^{gas-lift}$ it is necessary to use in general c_p a ρ for a two-phase mixture and simultaneously determine the new losses, because $W_{\infty}^{gas-lift}$ increases the flow velocity in the whole primary circuit.

The amount of the gas supplied by the m vents into the tractive cylinder of the gas-lift W_g [kg/s] is determined by the following relation from [3]

$$W_g = C_d \cdot \frac{\pi}{4} \cdot d^2 \cdot m \cdot p_1 \cdot \sqrt{\frac{1}{r \cdot T_g} - \left(\frac{2 \cdot \kappa}{\kappa - 1}\right)} \cdot \sqrt{\left(\frac{p_2}{p_1}\right)^{\frac{2}{\kappa}} - \left(\frac{p_2}{p_1}\right)^{\frac{\kappa-1}{\kappa}}} \tag{6}$$

Changes and flow properties at various temperatures and pressures of the gas and the liquid in tension and chimney losses in two-phase flow in the entire circuit are described in [5].

DEMONSTRATOR OF THE TWO-PHASE FLOW

The experimental device that is in this work signed as the Two-phase flow demonstrator (TFD) is a model device that is used for experimental studies of the gas-lift system and its influence on the natural convection support. There was provided space in the lab L136 at the Department of Power System Engineering, Faculty of Mechanical Engineering, University of West Bohemia in Pilsen. for this purpose.

The device represents a very simplified model of the primary circuit of the reactor with fuel in liquid salts. In the TFD unlike the MSR there is normal water flowing and the supplied gas is air. The measurings in water and air provide series of interesting results and points out the problems that can occur during the construction of the device with flowing liquid salts.

The experimental device consists of the series of construction parts that have been named after the parts of the primary circuit, that they represent. The model of the whole device including the description of its main parts is shown in the figure 3.

There were used two types of the construction material – metal from the carbonaceous steel and perspex. The most parts are welded from the 2mm thick metal plates. The remaining parts, that have to be transparent in order to perform the PIV measurements are made from the 5mm or 10mm thick perspex depending on the strain of the part. The maximum dimensions of the device are 2160 x 1100 x 360 mm (height x length x width).

The active zone (AZ) is represented here by the cylindrical metal container of 360 mm diameter and height of 300 mm. There is a conic crossing in its upper part and the are of air intake for the gas-lift follows. The heat source in the model AZ secures a 2000 W heating unit that is bolted and correctly sealed to the wall of the container in its bottom part in order not to obstruct the flowing water and therefore not to increase the pressure losses. The bottom of AZ, that has to be removable in order of assembling and potential exchange of the heating unit, is connected with the cylindrical part of AZ using the flange and twelve screws. There is bolted a ball valve for filling and drainage in the bottommost part of the AZ.

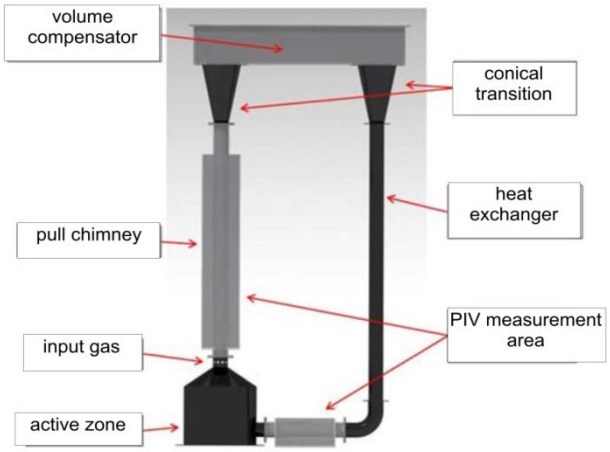

FIG. 2. The model of the two-phase flow demonstrator

There is welded a short tube of a 70 mm diameter with ten vents for the air intake above the conic crossing. In the wall of the tube there are drilled ten vents and then welded the M12 nuts for these purposes. There is one pressure pipe welded via inserted reduction to every nut, that transfers the compressed air from the compressor to the area of the tractive cylinder intake. One point of the measurements is to determine the influence of the size of supplied air on the water flow rate TFD water loop. Therefore it is essential to change the diameter of individual vents for air intake easily in order to control the size of the created bubbles in the tractive cylinder. There are used changeable brass insets that are situated in the reduction in between the pressure pipe and the tractive cylinder entry for these purposes. The reduction - that is actually a drilled-through screw with one inside and one outside threading – and the changeable brass inset determining the size of the air intake vent are shown in the figure 4. There is a number of the changeable insets with vent diameters of 0,5 mm, 1 mm and 2 mm available. In case we don't use the inset in the reduction, the diameter of the entry vent is 7 mm, therefore we have four options of the air intake vent size.

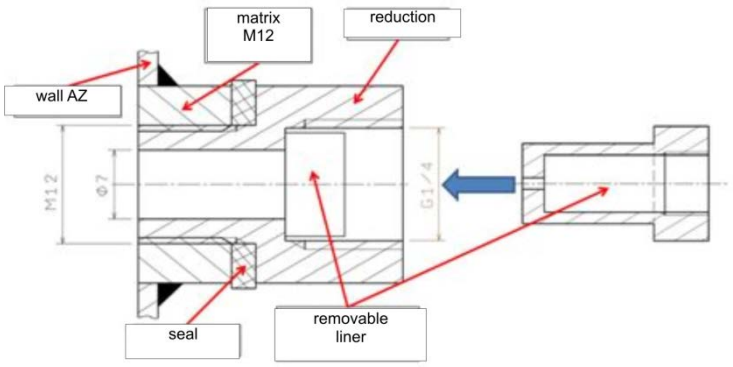

FIG. 3. The reduction with changeable inster

Tractive cylinder is made of the perspex pipe of a circular cross-section with inside diameter of 70 mm and the wall thickness of 5 mm. Its height is 1200 mm. It is connected (using the flange) to a metal pipe with previously mentioned ten vents that are used for the air intake.

The temperature of water is measured by using the thermocouple in three different spots. The air pressure is measured by the classic analogue pressure gauge and its capacity flow rate is measured by 3 flow-meter that can be switched over.

Alongside the height of the tractive chemney is situated a pool of a square cross-section made of perspex with the wall thickness of 5 mm that is necessary for possibility of measuring of the flow using PIV. The pool is during the measurements filled with water and therefore eliminates the influence of different light refraction index in water and on air. The light spreads faster in the air than in the water, while in the water and perspex is the light velocity very similar. It is necessary to create a plane that is perpendicular to the axis of the camera in the crossing between the air and water, if the picture recorded by the camera should correspond with reality. This is secured when the pool is full.

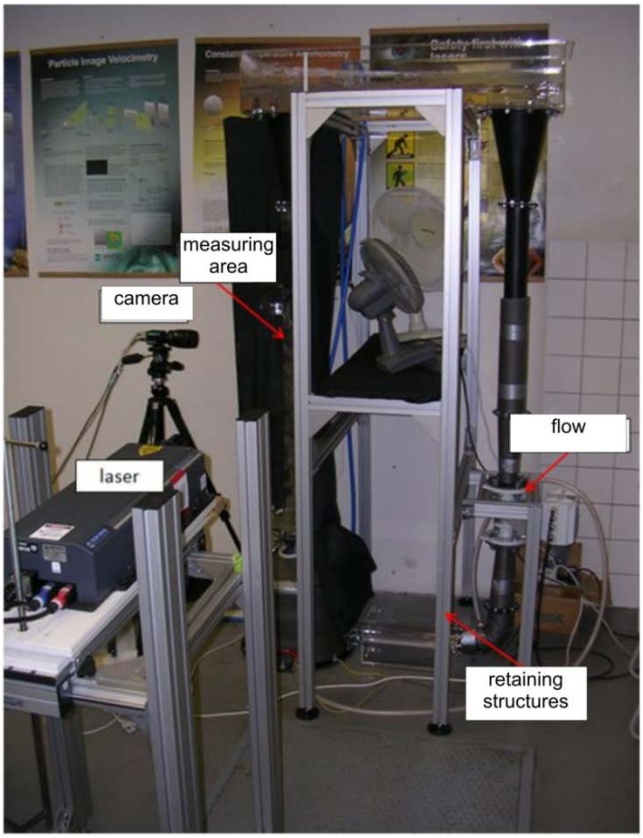

FIG. 4. Two-phase flow demonstrator

MEASURING DEVICES AND SENSORS ON THE TFD

It is necessary to install some measuring devices and sensors on the TFD to enable studying of the gas-lift and natural flow due to the water heating in the AZ. The water flow rate is measured by the induction flow meter from the lab equipment, that is attached by flanges to a vertical metal pipe under the area of the heat exchanger. The request of the minimum calming length ahead and behind the flow meter given by the manufacturer has been taken into consider during the flow meter assembly. The output of the flow meter is a voltage signal of 0 to 10V, which is transferred to the computer using the A/D converter by National Instruments (NI) and the LabView software.

At the beginning of 2012 there were supplied 3 rotameters of different extents for the air volume flow rate measuring. They were situated next to each other on a simple panel, where it is possible to switch the air flow between the individual devices using the valves. This way we can measure the air flow rate in the extent of 0,1 to 60 1/min. The air flow rate is displayed on the scale and the manufacturer claims ± 5% accuracy, when reading directly. The rotameter is the most suitable option regarding the request of measuring of a small air flow rate and simultaneously significantly large flow rate extents.

The air pressure is measured behind the pressure container outlet of the compressor by a classic analogue pressure gauge with range of 0 to 10 bar, which is a part of the compressor. The measurings have been performed for three different air pressures – 1,5; 3 and 5 bar.

The water temperature is measured using the thermocouple in three different spots for the purposes of natural convection studies. It is at the outlet of the AZ (maximum temperature in the circuit), above the tractive cylinder and behind the heat exchanger (minimum temperature in the circuit). The cold end of the thermocouple is compensated electronically in the convertor for thermocouple from NI. The advantage of the thermocouple is their low price if we don't take into consider the price of the NI hardware and software, which is available at the Department of Power System Engineering. Next advantages of the thermocouple are quick reactions to the temperature changes, easy use, wide extent and a rather good accuracy.

The last and most extensive measuring device is the PIV apparatus, that has been described in a separate chapter. We can watch in detail the flowing in the tractive cylinder using the PIV. The advantage of this method is an exact description of the velocity field in a specific spot and the possibility of an extensive numerical analysis of the results.

THE PRINCIPLE OF THE PIV METHOD

Particle Image Velocimetry (PIV) is a whole-flow-field technique providing instantaneous velocity vector measurements in a cross-section of a flow. Two velocity components are measured, but use of a stereoscopic approach permits all three velocity components to be recorded, resulting in instantaneous 3D velocity vectors for the whole area. The use of modern digital cameras and dedicated computing hardware, results in real-time velocity maps.

THE MEASURING APPARATUS

The cross-section of the fluid, in which there are evaluated the instantaneous velocities, is realised using the laser. The laser beam is shaped to a light sheet using the special optical system. The display of reference particles is recorded by a camera, of which axis is placed perpendicularly to the cross-section level.

The recorded images are divided into smaller square fields that are called „Interrogation Area". In order to measure the flowing velocity, it is necessary to have two images of the interrogated area with exactly defined time interval. The gained images are processed by the software, that uses the mathematical apparatus of a quick Fourier transform and mutual correlation for investigation of an average move of the particles in every interrogated area. The results of the measuring can be very illustratively visualised using the vector field.

There are used the CCD cameras for image recording. The main parameters determining the quality of the camera are speed, sensitivity and resolution. There are used pulse lasers that are able to issue a sufficiently strong radiation, which enables to reach a very short exposition and therefore to capture the most exact images. The essential part of the apparatus is the synchronizer that provides the time synchronization of the camera shutter and the laser pulse. The synchronizer is also able to exactly determine the time interval between the two pulses, which is one of the essential conditions for correct flow velocity determination.

Jiri Polansky
Pavel Zitek
Vaclav Valenta

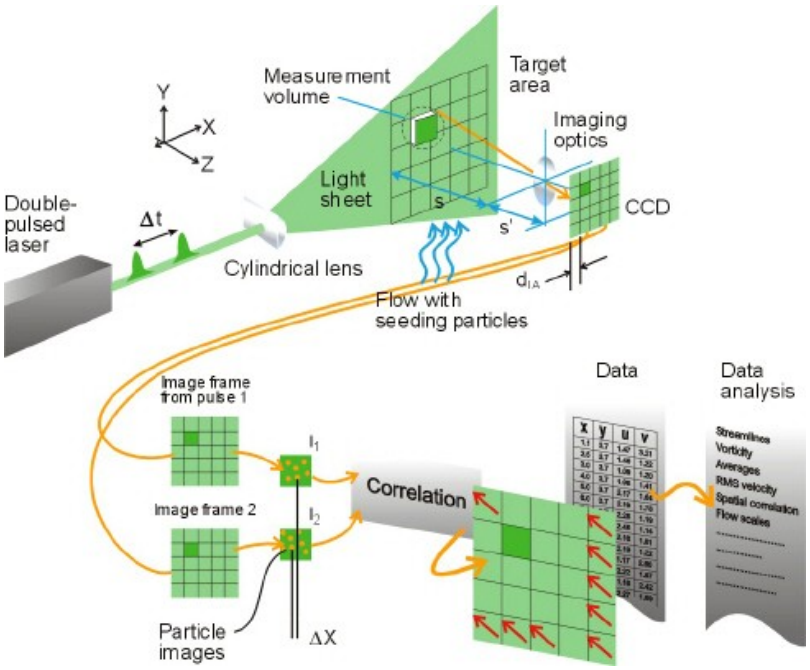

FIG. 5. The scheme of the PIV measuring layout [9]

RESULT

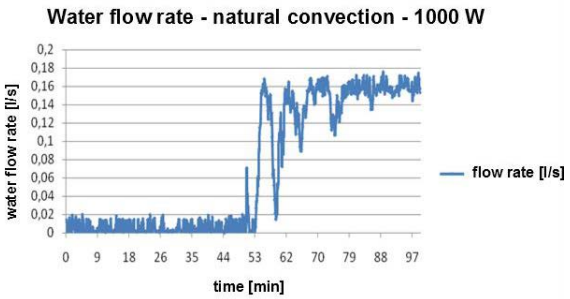

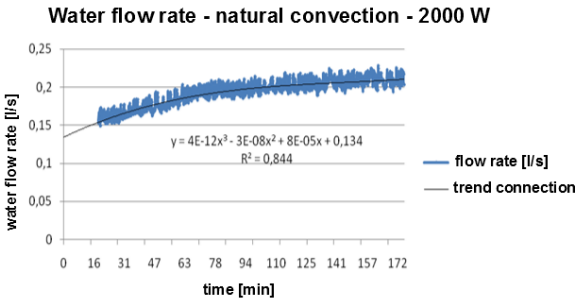

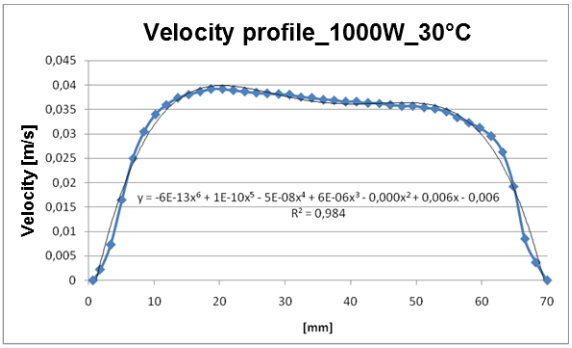

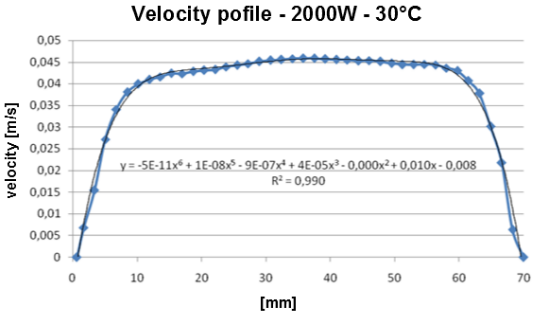

Jiri Polansky
Pavel Zitek
Vaclav Valenta

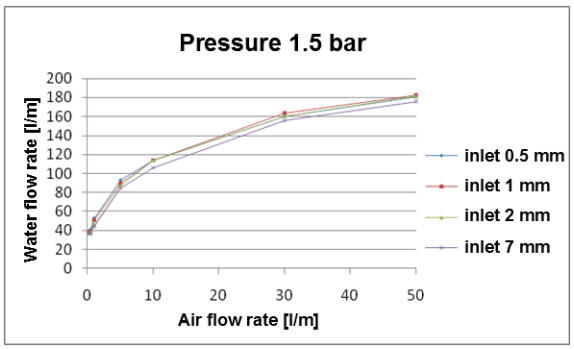

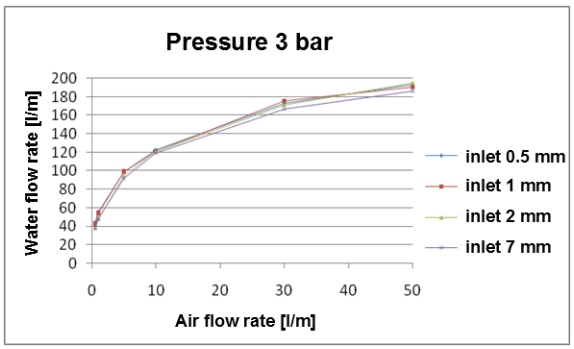

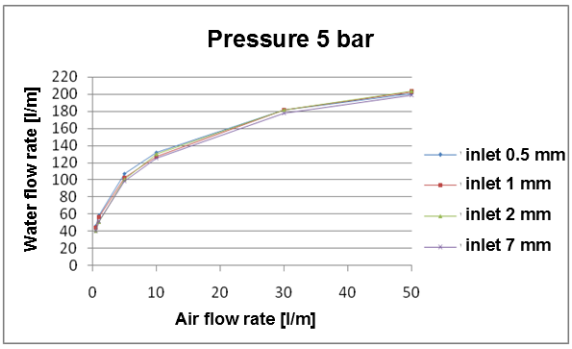

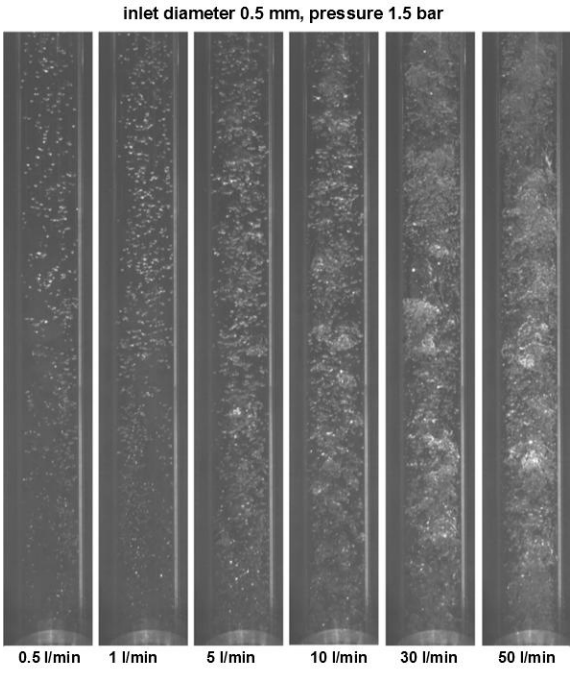

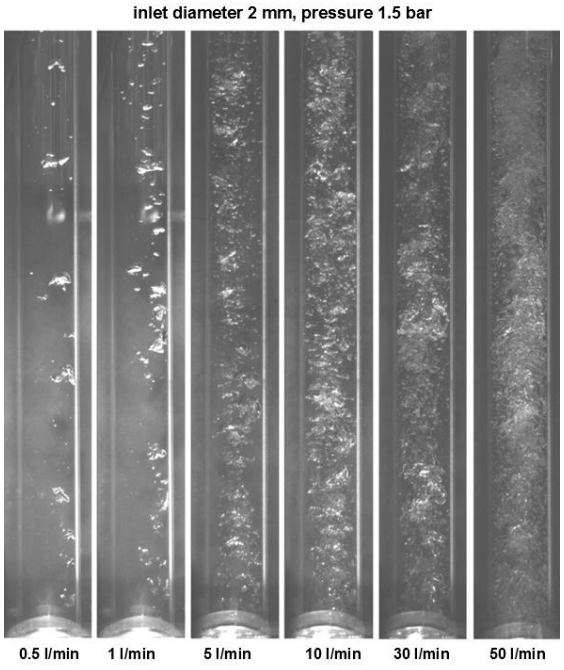

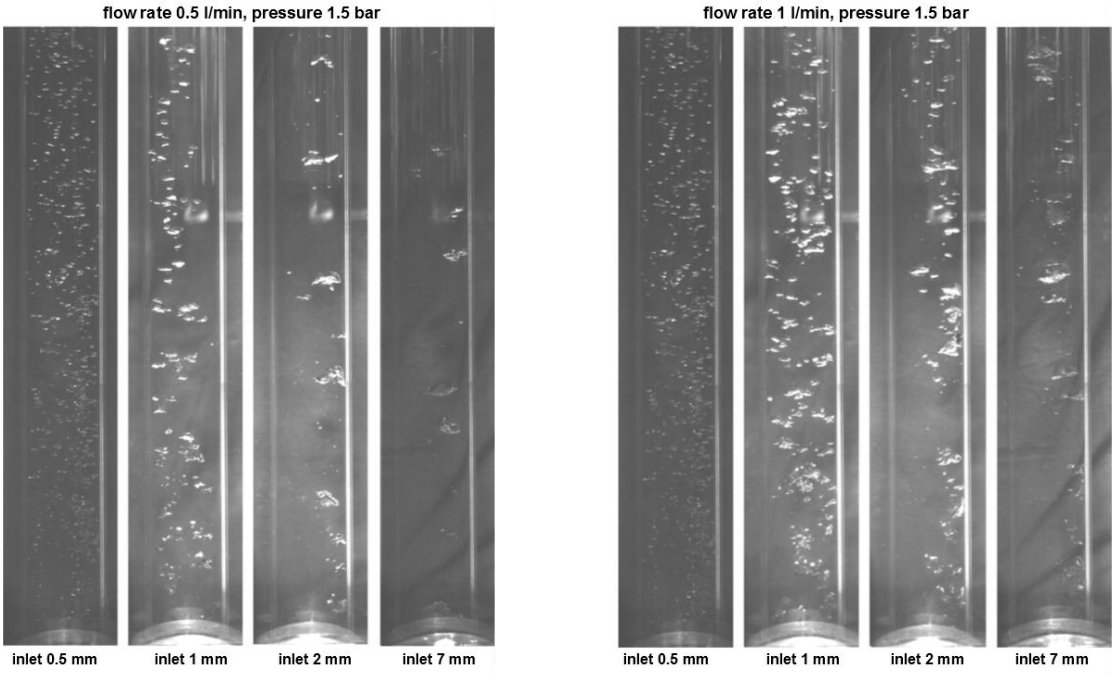

CONCLUSION

Flow fields on simplified model of MSR using Gas lift was measured by PIV and also predicted by two-phase flow theory. Methodology of measurement and calculation was estaliched.

Particle image velocimetry device and two-phase flow demonstrator (TFD) was used for experimental investigation.

Presently two-phase flow demonstrator is on the reconstruction. Measuring and controlling of heat exchanger and gas input device will be more accurate for future.

Other scheduled updates:

- Measuring and data evaluation improving.
- Inductive flow meter coupled with PIV device.
- Velocity and size of bubbles as a gas-lift parameters function.
- Size of bubbles as a distance from gas input function.
- Different spectrums of bubbles measuring. Measuring the spectra of bubbles will be used in the design of the separator gas cleaning compounds from gaseous fission products.
- From the measurements in our experimental facility is due to the release of most of the gas in the pressurized located above the tensile chimney. In the entrance of liquids before heating were measured during operation no bubbles, which confirms leak bubbles in the compensator. For use molten salt reactors will need to be supplemented by further separation of gas equipment. By application of this device, we have already started to look at our work [10].
- For future work needs to be thoroughly developed similarity theory.

Jiri Polansky
Pavel Zitek
Vaclav Valenta

ACKNOWLEDGEMENTS

Research works were supported by Ministry of Education of Czech Republic – ESF grant No. CZ.1.07/2.3.00/20.0139 and in specific research.

REFERENCES

[1] Salomon Levy: Two-Phase Flow in Complex Systems. John Wiley & Sons, INC., New York, 1999, (ISBN 0-471-32967-3)
[2] Takacz G.: Gas-lift Manual, Penn Well, 2003
[3] Vaclav Valenta: Introduction to Gas-lift, research report, University of West Bohemia, 2009
[4] Vaclav Valenta, Pavel Zitek: Two-phase flow in Nuclear Reactor, research report, UWB, 2012
[5] Vaclav Valenta, Pavel Zitek: Gas-lift Calculation technique, research report, UWB, 2012
[6] Jan Culik: Design of Primary Heat Exchanger and Two-Phase Flow Demonstrator for the Development of MSR, theses , University of West Bohemia, 2012
[7] Jiri Polansky: PIV and UVP using in energetics, habilitation lecture, UWB, 2007
[8] Markus Raffel: Particle Image Velocimetry A Practical Guide, Springer, ISBN 978-3-540-72307-3, 2007
[9] DANTEC DINAMICS: Measurement Principles of PIV, http://www.dantecdynamics.com
[10] Ivo Zlabek: The design of components for cleaning fluorides MSR from gaseous fission products, bachelor thesis , University of West Bohemia, 2011